AD-A078 683 NIELSEN ENGINEERING AND RESEARCH INC MOUNTAIN VIEW CALIF F/G 20/4
THE DEVELOPMENT OF RAPID PREDICTIVE METHODS FOR THREE-DIMENSION--ETC(U)
JUL 79 A J CRISALLI , S S STAHARA F44620-75-C-0047
UNCLASSIFIED NEAR-TR-198 AFOSR-TR-79-1281 NL

1 OF 4
AD-
A078683

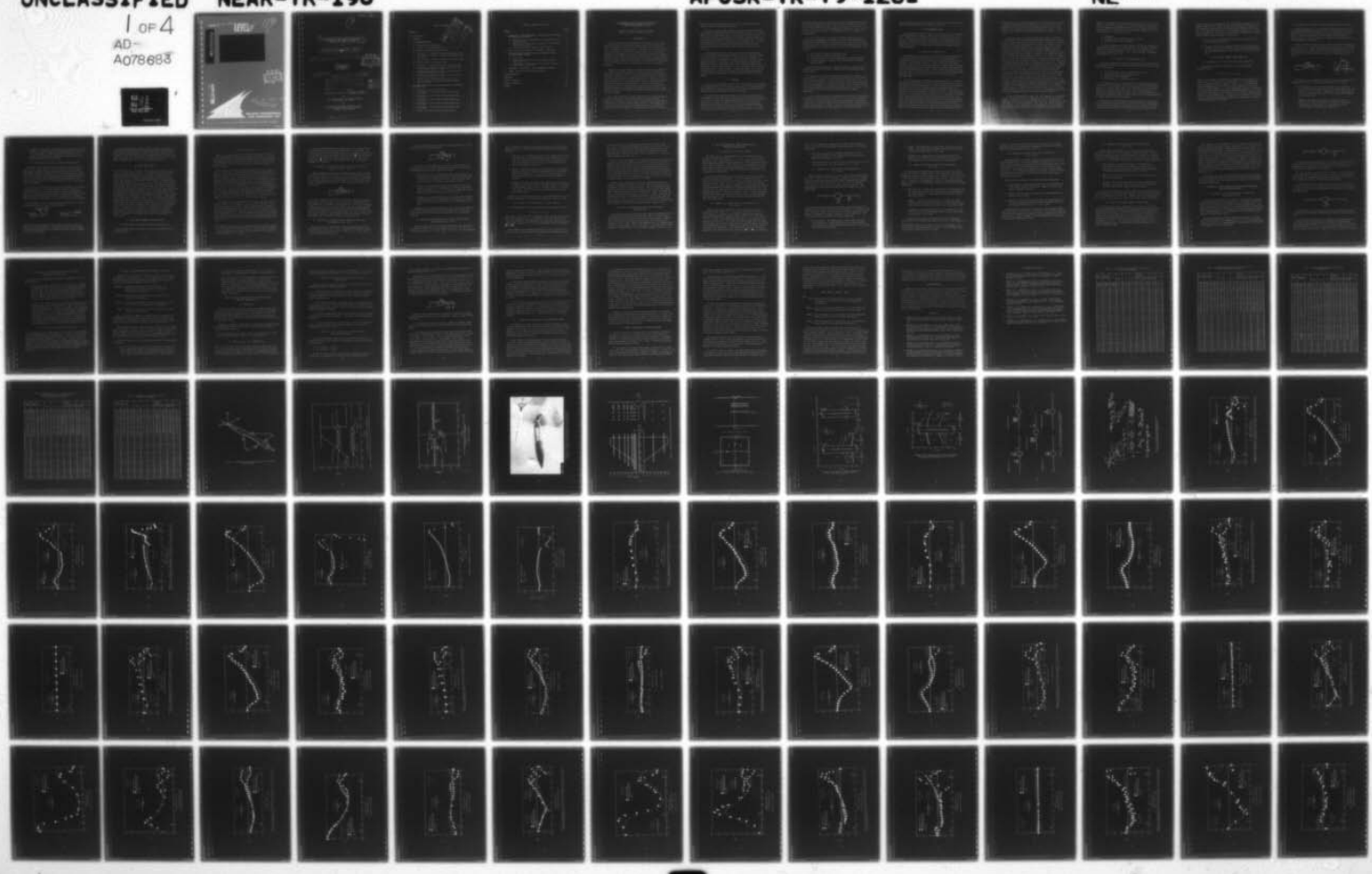

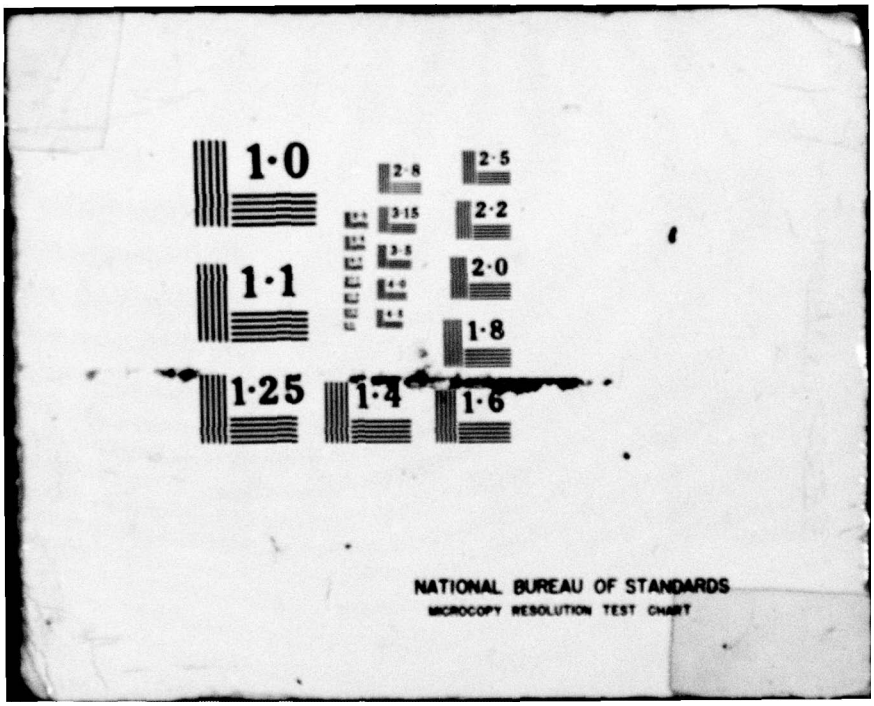
1·0
1·1
1·25
1·4
1·6
2·8
3·15
2·5
2·2
2·0
1·8
NATIONAL BUREAU OF STANDARDS
MICROCOPY RESOLUTION TEST CHART

AFOSR-TR- 79-1281

LEVEL II

(17)

SC

ADA078683

DDC
RECEIVED
DEC 18 1979
E

DDC FILE COPY

79 12 18 2

Approved for public release;
distribution unlimited.

NIELSEN ENGINEERING
AND RESEARCH, INC.

OFFICES: 510 CLYDE AVENUE / MOUNTAIN VIEW, CALIFORNIA 94043 / TELEPHONE (415) 968-9457

COPY NO. 10

(1)

(6) THE DEVELOPMENT OF RAPID PREDICTIVE METHODS FOR THREE-DIMENSIONAL TRANSONIC FLOW FIELDS ABOUT FIGHTER BOMBER AIRCRAFT. Part I.

by

(10) Anthony J. Crisalli, Stephen S. Stahara, Jack N. Nielsen, John R. Spreiter

(9) Final rept. 1 Jan 75 - 30 Sep 79,

(14) NEAR-TR-198
(11) July 1979

(18) AFOSR (19) TR-79-1281 (12) 305

(16) 2307
(17) A1

(15) Prepared under Contract No. F44620-75-C-0047

for

AIR FORCE OFFICE OF SCIENTIFIC RESEARCH
Washington, D.C. 20332

by

NIELSEN ENGINEERING & RESEARCH, INC.
510 Clyde Avenue, Mountain View, CA 94043
Telephone (415) 968-9457

389 783

JOB

TABLE OF CONTENTS

TABLE OF CONTENTS (Concluded)

THE DEVELOPMENT OF RAPID PREDICTIVE METHODS FOR THREE-DIMENSIONAL TRANSONIC FLOW FIELDS ABOUT FIGHTER BOMBER AIRCRAFT

by

Anthony J. Crisalli, Stephen S. Stahara,
Jack N. Nielsen, and John R. Spreiter

1. INTRODUCTION

The safe and controllable separation of external stores, either powered or unpowered, from modern fighter-bomber aircraft remains a current problem of significant military importance for the U.S. Air Force. Operational limitations due to dangerous store release characteristics can reduce aircraft mission effectiveness and survivability. Consequently, development of accurate engineering predictive methods for describing store trajectories fills a critical dual role. Use of such methods not only enhances the performance and safety of weapon delivery, but also provides a means for reducing the time required for both wind-tunnel and full-scale flight tests relating to store certification programs.

Recognition of this need has lead Nielsen Engineering & Research, Inc. (NEAR) through AFFDL support to develop the most comprehensive engineering predictive method currently available for determining store separation characteristics at subcritical subsonic speeds. A similar program for developing the analogous capability at supersonic speeds is currently underway. At transonic speeds, however, the problem becomes significantly more complicated because of the essential nonlinear character of the flow. Nevertheless, the need for an accurate store trajectory predictive technique at transonic speeds is even more compelling as unusual store separation phenomena are more likely to occur in this speed regime.

This report presents an overall account of the progress made on an essential component of the transonic store trajectory problem: the prediction of transonic flow fields about wing-body/pylon combinations representative of modern fighter-bomber aircraft. The emphasis here is on the development of predictive techniques which are sufficiently economical from the standpoint of computer cost to enable an aircraft

designer to employ the techniques over a wide range of Mach number, angle of attack, and geometric parameters.

The report presents several candidate transonic predictive methods and evaluates them by comparing their predictions of various flow field quantities with experimental data. The experimental data are taken from a parallel wind-tunnel test phase of the project, designed specifically for evaluating the predictive methods. The experimental data have been documented and archived in several test reports (refs. 1-4). The extensive comparisons of the theoretical predictions from the various predictive methods with the data comprise the major portion of this report.

In the following sections, work on the transonic flow field prediction problem as performed under AFOSR Contract No. F44620-75-C-0047 will be reviewed in its entirety, in such a way as to highlight the evolution of the various predictive methods from the initiation of the research project to the present. Both experimental and theoretical phases are covered. Many comparisons of the predictive methods with experimental data are shown and used to draw conclusions about the relative merits of the various methods. A subsequent report will deal with the application of the flow field predictive techniques discussed in this report to the computation of external store loadings at transonic speeds.

2. OVERVIEW

In this section we present an overview of the theoretical and experimental phases of the project insofar as they relate to the computation of three-dimensional transonic flow fields about transonic wing-body configurations with pylons under the wing or fuselage.

The goal of the theoretical phase is to develop a transonic flow field predictive technique which is sufficiently economical and accurate to be used as a basis for computing store loadings and trajectories. In particular, the force and moment distributions on a store which is separated from the parent aircraft (i.e. the wing-body/pylon combination) can be found by first calculating the flow field in the vicinity of the parent aircraft without the store in the flow field. The force

and moment distribution on the store can then be determined by inputing the velocity components at the position the store occupies in the flow into a store loading calculation. Thus, the ability to predict the flow field in the vicinity of the wing-body/pylon combination, without store, is the essential first step in the computation of store loadings and trajectories.

In view of the above, the theoretical phase of the project has focused on the development and testing of several flow-field predictive methods about wing-body/pylon configurations and, more basically, wing-body configurations. These flow-field predictive methods are now listed chronologically in the order in which they have been investigated in the project:

1. The classical transonic equivalence rule
2. An extended transonic equivalence rule
3. Three-dimensional linear solutions based on paneling methods
4. A three-dimensional transonic small-disturbance finite-difference method

In this report application of the above methods to the flow-field predictive problem are described, compared against experimental data, and evaluated.

The purpose of the parallel experimental phase of the project is to provide data for critically analyzing and evaluating the various flow-field predictive methods. In two 4T wind-tunnel experiments (ref. 1 and refs. 2-4), an idealized F-16 model was tested over a range of angles of attack at Mach numbers in the transonic regime. Flow-field data as well as surface pressure and force/moment distributions were obtained. This report deals exclusively with the flow-field data from these experiments.

In the following section the experimental and theoretical phases of the project will be presented in detail. In the next section, section 3, a description of the wind-tunnel tests and data obtained is presented. In sections 4 through 9, analyses and evaluations of the predictive techniques discussed above are given. Section 10 contains an analysis of the effects of wind-tunnel wall interference on the experimental data.

Finally, section 11 presents the overall conclusions and possible future directions suggested by the investigation thus far.

3. THE EXPERIMENTAL DATA

The experimental data to be used in the evaluation of the transonic flow-field predictive methods is taken from two AEDC 4T wind tunnel tests. These tests are described in detail in the data reports (refs. 1 and 2-4). Here we give a brief description of the experiments with emphasis on the flow-field data. The question of the validity of the experimental data for the evaluation of theoretical methods is also briefly discussed.

3.1 Description of Experiments

Both experiments utilized the same idealized F-16 wing-body model in configurations with and without pylons. (Some configurations contained stores, but that data, which involves store loadings, will be utilized in the subsequent report.) Figure 1 shows the body-fixed coordinate system which is used throughout this report. Figure 2 shows planform and cross-sectional views, including key geometrical locations of the wing-body/pylon/store model. Figure 3 shows a photograph of the wing-body model in the 4T tunnel and the conical flow-field survey probe which was used to obtain flow-field data in the vicinity of the wing-body model.

In the first transonic wind-tunnel experiment (ref. 1), the wing-body model was employed in the AEDC 4T tunnel without pylons. The primary purpose of this experiment was to obtain transonic flow-field data, including axial velocity, upwash velocity, and sidewash velocity, throughout the region surrounding the wing-body model. The data were obtained at very closely-spaced intervals in order to capture the steep variations in flow-field quantities which occur in the vicinity of shock waves. Both inner and outer flow-field surveys were obtained. The inner flow-field data were obtained to evaluate the various theoretical predictive methods discussed in this report. The outer flow-field data, taken on a cylindrical surface as far from the model centerline as possible, were obtained to provide measured outer boundary conditions as input to the theoretical model in order to evaluate wind-tunnel inter-

ference effects. The locations of the inner and outer flow-field grids are shown in figures 4 and 5, respectively. In this report, a representative subset of the flow-field surveys from the first test are employed. The selected data involves two angles of attack, $\alpha = 0^{\circ}, 5^{\circ}$, and the three transonic free-stream Mach numbers, $M_{\infty} = 0.925, 0.975, 1.025$.

A thorough survey of these 4T experimental results of reference 1 has verified that the test parameters were exceptionally well selected in view of providing as wide a range of transonic phenomena as possible. The data display flow conditions from subcritical to slightly supercritical, to strongly supercritical, to mildly supersonic, as were desired. For the two subsonic free-stream Mach numbers, figure 6 illustrates this fact and displays the growth of the supersonic pockets on the pressure and suction sides of the wing. The results are for an (x,z) plane located at the spanwise location y = 2 inches (25% semispan) and are for the wing-body model having a thickness-only wing profile based on the actual thickness distribution of the F-16 wing. The figure on the top indicates the extent of the supersonic zone at $M_{\infty} = 0.925$ for the three angles of attack, while corresponding results for $M_{\infty} = 0.975$ are shown in the bottom plot. The symbol M_L denotes the local Mach number. Since the vertical limits of the inner flow surveys was $1 \leq |z| \leq 5$ inches, the maximum lateral locations of the larger supersonic pockets on the suction side were beyond the last inner survey location at z = 5 inches. However, only for the $M_{\infty} = 0.975$, $\alpha = 5^{\circ}$ case did the pocket extend out to the outer flow survey location at z = 14 inches. These results indicate the extreme sensitivity of the flow at supercritical conditions. Analogous results for $M_{\infty} = 1.025$ are shown in figure 7 which displays the variation and growth of the embedded subsonic pocket. Of particular note in both figures 6 and 7 is that, at modest angles of attack, flow conditions on the pressure side of the wing remain primarily subsonic for a wide range of conditions.

In the second experiment (refs. 2-4), the wing-body in combination with various pylon and store arrangements was tested at several Mach numbers and angles of attack in the AEDC 4T tunnel. The purpose of this experiment was to obtain systematic inner and outer flow-field data as well as store surface pressures, forces and moments. The wing-body/pylon/store configurations used in the flow-field testing are shown in

figure 8. The symbol x in figure 8 denotes the position in the cross plane of the flow-field survey. The flow-field data includes axial velocity, upwash, and sidewash velocities. This report utilizes only flow-field data in the vicinity of the following configurations (configurations 21, 22, and 26 in fig. 8):

1. Wing-body
2. Wing-body with a single pylon on each wing
3. Wing-body with pylon on fuselage

This report presents, for the purpose of theoretical evaluation, a representative subset of the flow-field data for the above configurations from the second experiment (refs. 2-4). The selected data includes two angles of attack, $\alpha = 0^{\circ}, 5^{\circ}$, and transonic free-stream Mach numbers, $M_{\infty} = 0.95, 1.05$.

3.2 Validity of the Experimental Data

The use of experimental data to evaluate predictive theories must be qualified by several considerations pertaining to the quality of the data. These are:

1. Data uncertainties due to instrumentation errors
2. Tunnel flow-field quality imperfections
3. Flow-field lateral asymmetry
4. Wind-tunnel wall interference effects

In references 1 and 2, it was seen that the probable maximum uncertainties due to the combined effect of the first three considerations above are $\pm$ .015 for axial velocity as normalized by the free-stream velocity, $\pm .40^{\circ}$ for upwash angle, and $\pm .40^{\circ}$ for sidewash angle. Therefore, the maximum precision that one can reasonably demand from a theoretical prediction method is that it agree with the experimental data to within these uncertainty tolerances.

The importance of assessing the fourth consideration, wind-tunnel wall interference effects, stems from the fact that wall interference effects have been assumed to be negligible in the theoretical predictions whereas for some of the data, particularly that taken at Mach

numbers close to one, they may not be. The detailed discussion of interference effects, which relates to some of the computational results of the following sections as well as the data from a companion wind-tunnel test in the AEDC 16T tunnel (ref. 1) is deferred to section 10. At this point we simply limit ourselves to the conclusions regarding wall interference effects which are drawn in section 10:

1. For $M_\infty \leq 0.975$, the experimental data are relatively free of wall interference effects.

2. For $M_\infty \geq 1.025$, wall interference effects are not significant over most of the wing. However, they may be significant before the wing leading edge and in the vicinity of the wing trailing edge.

4. THE CLASSICAL TRANSONIC EQUIVALENCE RULE

4.1 Description of Classical Transonic Equivalence Rule

The classical transonic equivalence rule can be expressed mathematically as

$$\phi = \phi_{2,\alpha} + \phi_{2,t} + \phi_B - \phi_{2,B}$$

where ϕ is the composite perturbation potential for the transonic flow field, and $\phi_{2,\alpha}$, $\phi_{2,t}$, and $\phi_{2,B}$ are solutions of the two-dimensional Laplace equation as shown in figure 9. Here, $\phi_{2,\alpha}$ is the two-dimensional incompressible flow solution for the translation of the cross section (lifting problem), $\phi_{2,t}$ the corresponding solution for expansion (or contraction) of the cross section (thickness problem), and $\phi_{2,B}$ the solution for the expansion (or contraction) of a circular cylinder having identical cross-sectional area. Finally, ϕ_B is the solution to the nonlinear transonic small-disturbance equation for axisymmetric flow past the equivalent body of revolution.

4.2 Comparisons of Classical Transonic Equivalence Rule with Data

Extensive comparisons of the classical transonic equivalence rule with the experimental data obtained in the initial 4T test (ref. 1) have been made. Only a sample of those results will be presented in this report. Representative examples of these comparisons are shown in figures 10 and 11. Table 1 contains an index of these comparisons and the corresponding page numbers.

Figure 10 shows the axial velocity, upwash and sidewash comparisons at $M_\infty = 0.925$, $\alpha = 0^o$ at the longitudinal survey whose (y,z) coordinates are (y,z) = (2,-1). Figure 11 shows the same comparisons for $M_\infty = 0.975$. Cross-sectional planform sketches of the wing-body showing the approximate position of this survey are shown below (all dimensions are in inches):

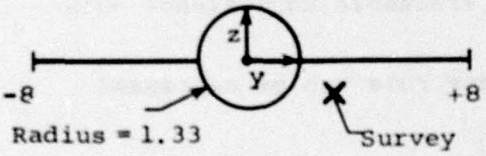

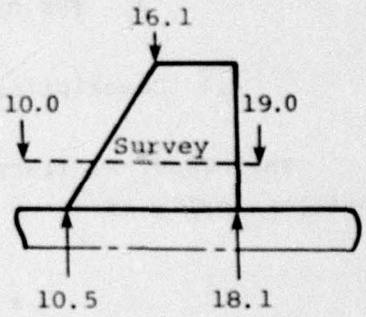

On the basis of the comparisons indicated, as well as numerous other comparisons not shown, the following observations can be drawn:

1. Axial velocity: The classical equivalence rule prediction is satisfactory for points ahead of the leading edge of the wing tip, i.e., x = 16.1 inches. Downstream of the leading edge of the wing tip the predicted axial velocity shows large disagreement with the data.

2. Upwash: The classical equivalence rule predictions are generally satisfactory except for a tendency in some cases to overpredict the experimental data just before the wing trailing edge, as illustrated in figure 11(b).

3. Sidewash: The classical equivalence rule predictions are satisfactory at locations ahead of the leading edge of the wing tip (x = 16.1 inches). Beyond this point, the prediction is generally unsatisfactory, exhibiting a severe overprediction and/or underprediction of the data.

4.3 Shortcomings of Classical Transonic Equivalence Rule

The overall conclusions that can be drawn from the above comparisons, as well as many others (not shown) made over a broad range of Mach numbers, angles of attack, and survey locations is that for the configuration geometry considered, the classical transonic equivalence rule is reliable at locations upstream of the leading edge of the wing tip (x = 16.1 inches), but generally unreliable downstream of the leading edge of the wing tip in its predictions of axial velocity, upwash, and sidewash.

Initially, it was believed that the poor performance of the equivalence rule beyond x = 16.1 inches could be ascribed to numerical problems caused by: (1) the sharp break in the wing planform at the wing tip, (2) trailing-edge singularities caused by inaccuracies in the wing profile second derivatives, and (3) the presence of a boundary layer of signficant thickness in the vicinity of the wing trailing edge.

In an attempt to correct these problems, the geometry of the wing was smoothed as shown in the illustration below,

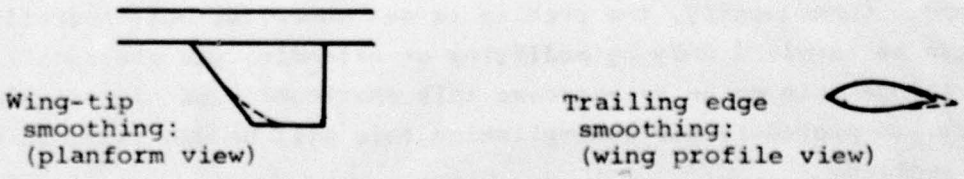

where the solid line represents the actual wing and the dotted line indicates the smoothing used. Additionally, the wing profile second derivatives were smoothed using a least-squares cubic spline representation of the wing profile.

The above modifications ameliorated the problem only slightly. Further analysis indicated that the disagreement between theory and data resulted from a more fundamental cause. Consider the unsatisfactory agreement of the axial velocity u/V_∞ as predicted by the original transonic equivalence rule with data for a nonlifting flow at $M_\infty = 0.975$ as shown in figure 10(a). For $\alpha = 0$, u/V_∞ can be written as

$$\frac{u}{V_\infty} = \frac{u_B}{V_\infty} + \frac{u_{2,t}}{V_\infty} - \frac{u_{2,B}}{V_\infty}$$

The variation of u_B/V_∞ is shown in figure 12(a) while that for $u_{2,t}/V_\infty - u_{2,B}/V_\infty$ is shown in figure 12(b). It is apparent that u_B/V_∞ is quite smooth and behaves qualitatively like the data. However, $u_{2,t}/V_\infty - u_{2,B}/V_\infty$ does not and exhibits a discontinuous derivative at $x = 16.1$ inches (the location of the wing-tip leading edge). An examination of the analytic expression for $u_{2,t}/V_\infty - u_{2,B}/V_\infty$ shows that this is caused by discontinuities in the wing planform (i.e., at the wing tip and the trailing edge) which induce true three-dimensional effects--the prediction of which are beyond the capability of slender-body theory which forms the basis of the classical equivalence rule. The reason behind this breakdown is that slender-body theory performs satisfactorily as long as the wing-span is increasing and the planform is slender. These restrictions become even more important when $\alpha \neq 0$, since slender-body theory predicts that beyond the point of maximum span, a trailing vortex sheet emanates from the wing and extends downstream parallel to the flow direction. Beyond that point of maximum span, the axial lift distribution is zero. Consequently, the problem is not numerical but theoretical, and can be resolved only by modifying or extending the classical equivalence rule so as to overcome this shortcoming of slender-body theory. A procedure for accomplishing this will be discussed in the next section.

5. THE EXTENDED TRANSONIC EQUIVALENCE RULE

5.1 Description of Extended Transonic Equivalence Rule

The extended transonic equivalence rule can be represented by the following formula:

$$\phi = \phi_{3,t+\alpha} + \phi_B - \phi_{3,B}$$

Here $\phi_{3,t+\alpha}$ is the solution to the three-dimensional linear flow around the configuration at an arbitrary angle of attack α, ϕ_B is the usual solution to the axisymmetric nonlinear transonic equation around the equivalent body, at zero angle of attack, and $\phi_{3,B}$ is the axisymmetric linear solution to the flow around the equivalent body at zero angle of attack.

The rationale behind the extended equivalence rule will now be discussed. In section 4, it was seen that the classical equivalence rule does not properly account for planform discontinuities at the wing tip and trailing edge. This is due to the fact that the components $\phi_{2,t}$ and $\phi_{2,B}$ of the classical equivalence rule are two-dimensional solutions computed in crossflow planes perpendicular to the longitudinal axis of the aircraft. In order to represent the proper three-dimensional behavior of the solution in these regions, it therefore seems appropriate to replace $\phi_{2,t}$, $\phi_{2,\alpha}$, and $\phi_{2,B}$ by their three-dimensional counterparts $\phi_{3,t+\alpha}$ and $\phi_{3,B}$, respectively. This yields the extended equivalence rule. It should be noted that the composite velocity potential ϕ in the above equation is asymptotically equivalent to ϕ_B at infinity and asymptotically equivalent to $\phi_{3,t+\alpha}$ on the aircraft surface.

An advantage of the extended equivalence rule is the fact that the solution method for the component $\phi_{3,t+\alpha}$ is already available in the form of operational codes (refs. 5 and 6) based on panel methods.* A conceivable disadvantage of the extended equivalence rule is the fact that the linear-theory solution, $\phi_{3,t+\alpha}$, may not be calculable at free-stream Mach numbers near 1. Extensive calculations which are discussed below, however, have shown that the linear theory paneling methods can be used to provide useful results even at free-stream Mach numbers quite close to 1.

---

* The supersonic paneling code of reference 6 has been modified slightly for this report. The code of reference 6 includes special treatment of nonlinearities due to shocks. That treatment has been removed for the work presented in this report.

In the following subsections the comparisons of the extended transonic equivalence rule with data from reference 1 are presented. The notation used is that the extended transonic equivalence rule predictions are represented by the solid symbol with tick mark, ●, the experimental data by the open symbol ⊙, and the linear-theory predictions by the solid symbol ●. The linear-theory predictions will be discussed separately in section 6.

5.2 Comparison of Extended Transonic Equivalence Rule with Wing-Body Data, $M_\infty = 0.925$

Typical comparisons between the extended equivalence rule and the wing-body alone data at $M_\infty = 0.925$, $\alpha = 0^\circ$ are shown in figures 13 and 14. In these figures the predicted axial velocity upwash, and sidewash are compared with data at surveys located at (y,z) = (2,-1) and (y,z) = (4,-1). The approximate positions of these surveys are shown in the sketch below.

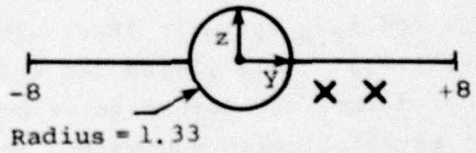

It is seen in figures 13 and 14 that the agreement between the extended equivalence rule and the data is almost exact for these cases. Many other comparisons (not shown in this report) at $\alpha = 0^\circ$ and $= 5^\circ$ and over a range of various survey locations confirm that the agreement between the extended equivalence rule flow-field predictions and experimental data for this configuration is generally very good at $M_\infty = 0.925$. Thus, at this Mach number, the extended equivalence rule provides a distinct improvement over the classical transonic equivalence rule.

5.3 Comparison of Extended Transonic Equivalence Rule with Wing-Body Data, $M_\infty = 0.975$

We now consider the comparisons of the extended equivalence rule with experimental data at $M_\infty = 0.975$. Comparisons for angles of attack $\alpha = 0^\circ$, 5° at survey locations (y,z) = (0,-2), (2,-1), (2,-3), (4,-1) are provided in figures 15 to 22.

A sketch of the wing-body illustrating the approximate (y,z) locations noted above is provided below.

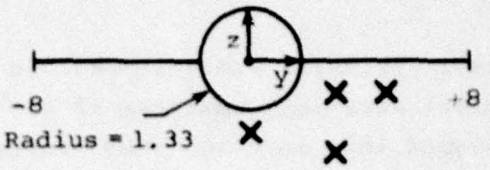

On the basis of the comparisons indicated in these figures, the following general conclusions regarding the extended equivalence rule flow-field predictions at $M_\infty = 0.975$ can be made.

1. Axial velocity: The extended equivalence rule predictions are satisfactory at axial locations up to roughly the leading edge of the wing tip. Beyond this location predictions are qualitatively correct but generally overpredict the data.

2. Upwash: The extended equivalence rule predictions are satisfactory upstream of the trailing edge of the wing except just under the fuselage (y,z) = (0,-2) where the comparison is poor downstream of the leading edge of the wing tip.

3. Sidewash: The extended equivalence rule predictions are satisfactory upstream of the leading edge of the wing tip. Beyond this point the theory overpredicts and then underpredicts the data.

Comparison of the extended equivalence flow field predictions with the classical equivalence rule flow-field predictions for the cases shown provides the conclusion that the extended rule is definitely superior.

5.4 Comparison of Extended Transonic Equivalence Rule with Wing-Body Data, $M_\infty = 1.025$

Analogous comparisons of the extended equivalence rule and data are presented in figures 23 to 30 for angles of attack $\alpha = 0^\circ, 5^\circ$ at the surface locations (y,z) = (0,-2), (2,-1), (2,-3), (4,-1). The following

general conclusions regarding the extended equivalence rule flow-field predictions at $M_\infty = 1.025$ can be drawn on the basis of the above comparisons:

1. Axial velocity: Extended equivalence rule predictions are satisfactory at axial locations upstream of the leading edge of the wing tip. Beyond this location they greatly overpredict the data. This however, may be due to wall interference effects which are discussed in section 10.

2. Upwash: Extended equivalence rule predictions are satisfactory upstream of the wing trailing edge except for the survey just under the fuselage $(y,z) = (0,-2)$ where beyond the wing tip leading edge the theory underpredicts and then overpredicts the data.

3. Sidewash: Extended equivalence rule predictions are generally satisfactory up to the wing trailing edge except for the survey at about midspan $(y,z) = (4,-1)$. For this case at $\alpha = 5^\circ$ [see fig. 30(c)], the theory greatly overpredicts the data at the wing leading edge.

Overall, the extended equivalence rule is generally superior to the classical equivalence rule for the mildly supersonic case $M_\infty = 1.025$.

5.5 Analysis of Extended Equivalence Rule Behavior

As stated previously, the extended transonic equivalence rule is

$$\phi = \phi_{3,t+\alpha} + \phi_B - \phi_{3,B}$$

Since $\phi_{3,t+\alpha}$ is the full three-dimensional linear solution for the wing-body, it follows that $\phi_B - \phi_{3,B}$ represents a nonlinear correction to that linear solution. The magnitude of the nonlinear correction term is represented in figures 13 to 30 by the differences between the symbols ◐ and ●.

With regard to the extended equivalence rule axial velocity predictions at $M_\infty = 0.975$ we observe that between the leading edge of the

wing tip and the wing trailing edge the nonlinear correction term $\phi_B - \phi_{3,B}$ is too large near the body [see figs. 15(a), 16(a), 19(a),20(a), and 21(a)]. It should be noted that the cross-sectional area of the equivalent body changes 40% in this region. It appears that such a sudden change in area is too much for the equivalence rule to handle at subsonic speeds so close to $M_\infty = 1$.

At $M_\infty = 1.025$, the tendency of the extended equivalence rule to overpredict the data with regard to axial velocity is due to an entirely different cause. From figure 23 to 30, we note that the nonlinear correction term is fairly small so that the disagreement with the data is primarily due to the linear component rather than the nonlinear correction. The problem with the linear theory which occurs at low supersonic free-stream Mach numbers is related to multiple reflections and oscillations occuring in the panel method (refs. 5 and 6) and can be corrected by modifications of the existing panel technique.

Regarding the extended equivalence rule upwash predictions at subsonic or supersonic speeds, we note that the predictions are quite reasonable for most of the surveys shown. Under the fuselage the comparison between theory and data for upwash is poor between the leading edge of the wing tip and the wing trailing edge. Again, the reason for this is that the nonlinear correction term is too large. Regarding the extended equivalence rule sidewash predictions, we note that under the wing (e.g., at $(y,z) = (2,-1)$ and $(4,-1)$ the sidewash predictions are poor between the leading edge of the wing tip and the wing trailing edge, again because of overcorrection by the nonlinear transonic term.

5.6 Overall Conclusions Regarding Extended Transonic Equivalence Rule

The overall conclusions drawn from these numerous comparisons is that the extended equivalence rule is generally superior to the classical equivalence rule for the prediction of flow-field quantities. Comparisons of the theoretical predictions with data exhibit almost exact agreement at $M_\infty = 0.925$. However, discrepancies with the extended equivalence rule theory exist at $M_\infty = 0.975$ and $M_\infty = 1.025$ and seem to be due primarily to overcorrection by the nonlinear transonic term $\phi_B - \phi_{3,B}$.

6. THE THREE-DIMENSIONAL LINEAR METHOD APPLIED TO WING-BODY CONFIGURATIONS

6.1 Description of the Linear Theory

The linear theory is represented by the first component of the extended transonic equivalence rule $\phi = \phi_{3,t+\alpha} + \phi_B - \phi_{3,B}$ described in section 5.1. The linear potential, $\phi_{3,t+\alpha}$ is a solution of the linear three-dimensional Prandtl-Glauert equation for a wing-body/pylon combination at angle of attack α, obtained by using a panel method. The panel method used at subsonic free-stream Mach numbers is described in reference 5 while the panel method used for the supersonic free-stream case is described in reference 6.

In the following subsections the comparisons of the linear theory with wing-body data are presented. All of the comparisons of the extended equivalence rule and data which were presented in section 5 also contain the linear theory. Thus, it is possible to evaluate both the performance of the linear theory as compared to experimental data and its relative performance as compared to the extended equivalence rule. The complete index of comparisons of the linear theory with data and corresponding page numbers is contained in Tables 2 and 3. We note that Table 2 refers only to wing-body data while Table 3 refers to both wing-body and wing-body/pylon data. This section deals only with the wing-body data from these tables.

6.2 Comparison of Linear Theory with Wing-Body Data, $M_\infty = 0.925$

Typical comparisons between the linear theory and the experimental data at $M_\infty = 0.925$, $\alpha = 0^\circ$ are shown in figures 13 and 14. In these figures the predicted axial velocity, upwash and sidewash are compared with data at the surveys located at $(y,z) = (2,-1)$ and $(y,z) = (4,-1)$. A sketch of the approximate locations of these positions was provided in section 5.2. It is seen from these figures that the linear theory agrees very well with data except for some discrepancy at the wing trailing edge and, in fact, is essentially identical with the extended equivalence rule prediction. This implies that nonlinear effects, as measured by the difference between the symbols ◐ and ●, are negligible

at $M_\infty = 0.925$. Additional comparisons (not shown in this report) at $\alpha = 0^o$, 5^o and over a range of survey locations confirm the following conclusions:

1. The linear theory and the extended equivalence rule are virtually identical in their predictions of axial velocity, upwash and sidewash at $M_\infty = 0.925$.

2. The comparisons of the linear-theory flow-field quantities with experimental data show good agreement at $M_\infty = 0.925$.

6.3 Comparison of Linear Theory with Wing-Body Data, $M_\infty = 0.950$

Typical comparisons between the linear theory and the experimental data at $M_\infty = 0.95$, $\alpha = 0^o$, 5^o are shown in figures 31 to 39. In these figures the predicted axial velocity, upwash and sidewash are compared with data at the survey locations (y,z) = (0,-2.208), (0,-2.958), (.750,-2.208), (3.5,-1.230), (3.5,-1.980), and (4.25,-1.230). The approximate (y,z) positions are designated by the symbol "x" in the sketch below.

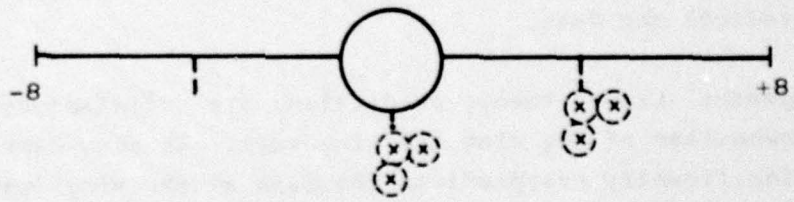

In the above sketch the dotted lines indicate the positions which the pylons and stores would occupy if they were present. (In section 7, the data with pylons present will be given, and then the above data will be useful in assessing the effect of the pylon on the flow field). The following conclusions are drawn from these comparisons:

1. Axial velocity: The comparisons of linear theory with data are satisfactory. Some discrepancies can be seen for most cases between the leading edge of the wing tip (x = 16.1 inches) and the wing trailing edge.

2. Upwash: The comparisons of linear theory with data are satisfactory. The theory does overpredict the data near the wing leading and trailing edges in some cases.

3. Sidewash: The comparisons of linear theory with data are satisfactory. The theory does overpredict the data near the wing leading edge and the leading edge of the wing tip.

6.4 Comparison of Linear Theory with Wing-Body Data, $M_\infty = 0.975$

We now discuss the comparisons of the linear theory with experimental data for the wing-body at $M_\infty = 0.975$. Figures 15 to 22 show comparisons of axial velocity, upwash and sidewash for angles of attack $\alpha = 0^\circ$ and 5° at the survey locations $(y,z) = (0,-2)$, $(2,-1)$, $(2,-3)$, $(4,-1)$. A sketch of the approximate location of these positions was shown in section 5.3. The following conclusions can be drawn from these comparisons:

1. Axial velocity: *Linear theory predictions are satisfactory* up to roughly the leading edge of the wing tip. Beyond this point the linear prediction is unsatisfactory and generally underpredicts the data.

2. Upwash: Linear theory predictions are satisfactory except downstream of the wing trailing edge. In some cases the theory significantly overpredicts the data at the wing leading edge.*

3. Sidewash: Lineary theory predictions are satisfactory in all cases except for some disagreement near the wing leading edge for the $(y,z) = (4,-1)$ case.

A comparison of the above conclusions with the corresponding conclusions for the extended equivalence rule for $M_\infty = 0.975$ presented in

*The discrepancy between the theory and data for the upwash at the leading edge of the wing appears to be due to an insufficient number of chordwise lifting panels on the wing.

section 5.3 shows that the linear theory is superior to the extended equivalence rule in the prediction of upwash and sidewash and somewhat inferior in the prediction of axial velocity.

6.5 Comparison of Linear Theory with Wing-Body Data, $M_\infty = 1.025$

The comparisons of the linear theory with experimental data for the wing-body alone at $M_\infty = 1.025$ are included in figures 23 to 30. It is seen in these figures that the predictions sometimes display small oscillatory behavior at axial locations ahead of the leading edge of the wing tip ($x = 16.1$ inches) and large oscillations at locations beyond that point. It is believed this behavior is caused, in part, by multiple wave reflections occurring in the supersonic paneling method used in reference 6 for M_∞ near 1.

The following conclusions can be drawn from these comparisons:

1. Axial velocity: Linear-theory predictions are satisfactory up to the leading edge of the wing tip. Beyond this point they greatly overpredict the data.

2. Upwash: The linear-theory predictions are satisfactory up to the wing trailing edge.

3. Sidewash: The linear-theory predictions are satisfactory up to the wing trailing edge except for some disagreement near the wing leading edge for the $(y,z) = (4,-1)$ case.

Comparing these conclusions with those for the extended transonic equivalence rule in section 5.4, it is seen that under the wing there is little difference between the upwash and sidewash predictions of the two theories at $M_\infty = 1.025$. However, under the fuselage the linear theory yields superior upwash predictions.

6.6 Comparison of Linear Theory with Wing-Body Data, $M_\infty = 1.050$

Typical comparisons between linear theory and the experimental data at $M_\infty = 1.05$, $\alpha = 0^\circ$, 5° are shown in figures 40 to 48. In these figures the predicted axial velocity, upwash, and sidewash are compared with data at the same survey locations as in section 6.3 (see sketch in section 6.3). The following conclusions are drawn from these comparisons:

1. Axial velocity: Linear-theory tends to overpredict the deceleration of the flow under the model. The predictions also tend to give a much stronger compression wave downstream of the wing trailing edge than is seen in the data.

2. Upwash: The linear-theory predictions are satisfactory up to the wing trailing edge.

3. Sidewash: The linear-theory predictions are satisfactory up to the wing trailing edge. The theory does tend to overpredict the data near the wing leading and trailing edges.

It is seen from figures 40 to 48 that some minor oscillatory behavior is still present in the predictions although it is less than for the case $M_\infty = 1.025$ discussed in section 6.5. However, some of the oscillations are not small [see figs. 41(a), 42(b), 43(c), 44(c), 45(c), and 48(c)].

6.7 Overall Conclusions Regarding Linear Theory

On the basis of the above comparisons it is seen that the linear theory yields satisfactory upwash and sidewash predictions over a range of survey positions under the fuselage and wing at free-stream Mach numbers relatively close to one. The axial velocity as predicted by the linear theory is reasonably good at $M_\infty = 0.925$ and $M_\infty = 1.05$, but increasingly deteriorates beyond the wing tip leading edge as $M_\infty \to 1$. Furthermore, for $M_\infty \geq 1$, the linear theory predictions of all three velocity components show an increasingly oscillatory behavior as $M_\infty \to 1$ from the supersonic side.

When compared with the performance of the classical transonic equivalence rule and the extended transonic equivalence rule, it is seen that the linear theory yields more reliable predictions of both upwash and sidewash over a broad range of conditions for $0^{\circ} \leq \alpha \leq 5^{\circ}$ and $M_{\infty} \leq 0.975$, $M_{\infty} \geq 1.025$. It is also seen that the axial velocity predictions of the linear theory are better than those of the classical equivalence rule but not so good as those of the extended rule. However, it appears that axial velocities may have only a second-order effect on the normal and sidewash forces and the pitching and yawing moments of a separated store. Thus, on balance, the linear theory is considered the best of the flowfield predictive methods in the low angle of attack range, $M_{\infty} \leq 0.975$ or $M_{\infty} \geq 1.025$, for the wing-body configuration considered for angles of attack up to 5°.

It should be noted that the above conclusions are based on comparisons with experimental data for wing-body configurations without pylons. In the next section the linear theory will be compared with wing-body/pylon experimental data.

7. COMPARISON OF THREE-DIMENSIONAL LINEAR THEORY PREDICTIONS *WITH WING-BODY/PYLON DATA*

7.1 Description of the Wing-Body/Pylon Configuration and Survey Locations

In this section we examine the effects on the flow field of adding wing and fuselage pylons to the wing-body. As discussed in section 3, the second 4T experiment involved the following configurations: wing-body, wing-body with two wing pylons, and wing-body with fuselage pylon. The survey (y,z) positions associated with the wing-body/pylon configurations are described below. The comparisons, with corresponding page numbers, are contained in Table 3.

For the wing-body with two wing pylons configuration, the survey (y,z) positions used in the comparisons are (y,z) = (3.5,-1.230), (3.5, -1.980), (4.250,-1.230). The approximate (y,z) positions are designated by the symbol "X" in the sketch below.

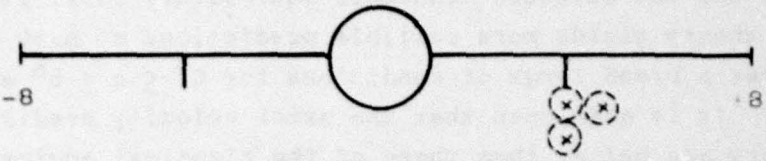

In the above and following sketch, the dotted lines represent the positions which the stores would occupy if they were present. Note that the surveys are located along the centerlines of stores for which loading data were obtained in the experiment.

Note that the above survey positions are among the survey positions for wing-body data discussed in sections 6.3 and 6.6. These wing-body data together with wing-body/pylon data allow the effect on the flow field of adding the pylon to be assessed experimentally.

For the wing-body with fuselage pylon configuration, the survey (y,z) positions used in the graphical comparisons are (y,z) = (0-2.208), (0.-2.958), (.750,-2.208). The approximate (y,z) positions are shown in the sketch below.

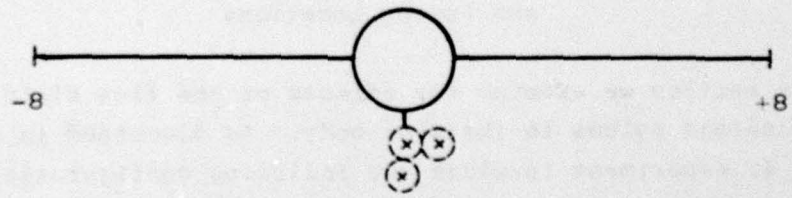

Note again that these survey positions are also among the survey positions for the wing-body configurations discussed in sections 6.3 and 6.6.

The linear-theory predictions are compared with experimental data involving the above wing-body/pylon configurations and designated survey locations in figures 49 to 63, as indexed in Table 3. Two free-stream Mach numbers, M_∞ = 0.95, 1.05, and two angles of attack, $\alpha = 0^o$, 5^o, are treated. The effect of adding the pylon is treated in section 8.

7.2 Discussion of Linear-Theory Predictions for Wing-Body/Pylon Configurations

A scan of all the comparisons discussed above supports the following conclusions:

1. At $M_\infty = 0.950$ (figs. 49-54 and 61-63), the upwash and sidewash, as computed by the linear theory, are in satisfactory agreement with the data. The axial velocity shows good agreement with the data upstream of the wing tip-wing pylon trailing edge region. However, the linear theory does not model correctly the flow expansion and contraction in this region due to the presence of an embedded pocket of supersonic flow.

2. For $M_\infty = 1.050$ (figs. 55-60), the linear-theory predictions show varying degrees of oscillatory behavior in axial velocity, upwash, and sidewash when the pylons are present. The oscillations generally span the data. The oscillating behavior is expecially pronounced beyond $x \approx 16.5$ inches. Comparing these wing-body/pylon predictions with the corresponding predictions for the wing-body at the same Mach number as discussed in section 6.6, it is seen that the presence of the pylon has intensified the oscillatory behavior. As mentioned before, these oscillations are associated with the use of panel methods near $M_\infty = 1$.

7.3 Overall Conclusions Regarding Linear Theory

On the basis of the results shown in this section, it is concluded that for wing-body/pylon configurations at $M_\infty = 0.95$, the linear theory predicts upwash and sidewash reasonably well. Axial velocity is not satisfactorily predicted beyond $x = 16.5$ inches. At $M_\infty = 1.050$ the linear-theory predictions are generally unsatisfactory because of oscillations in the axial velocity, upwash, and sidewash predictions. Without the pylons present, the oscillations are much milder. Possible improvements to the linear theory in this respect will be discussed in section 11.

8. EFFECT OF PYLON ADDITION ON THE TRANSONIC FLOW FIELD

Figures 64 to 78, as indexed in Table 4, show the direct effect of pylon addition to the flow field. In each of these figures, the symbol ⊙ represents the differences [WBP(EXP) - WB(EXP)] and the symbol X represents the difference [WBP(LT) - WB(LT)], where

WBP(EXP) = experimentally measured flow-field quantity (as specified on the y-axis) in the vicinity of the wing-body/pylon combination.

WB(EXP) = experimentally measured flow-field quantity in the vicinity of the wing-body.

WBP(LT) = linear theory prediction of flow field quantity in the the vicinity of the wing-body/pylon combination.

WB(LT) = linear theory prediction of flow field quantity in the vicinity of the wing-body.

Thus, the difference [WBP(EXP) - WB(EXP)] directly represents the experimentally-measured effect of pylon addition on a particular flow field quantity. The difference [WBP(LT) - WB(LT)] similarly represents the effect of pylon addition as predicted by 3-D linear theory.

These comparisons provide numerous physical insights into the effect of pylon addition on the flow field. For example, examining figure 64(b) which illustrates the effect of pylon addition on upwash, we observe that the leading edge of the pylon turns the flow sharply downward while the trailing edge of the pylon turns the flow sharply upward.

A thorough examination of these graphs provides the following general conclusions:

1. At M = 0.950 (figs. 64-69 and 76-78), the effect of pylon addition on upwash and sidewash is satisfactorily predicted by 3-D linear theory. The effect of pylon addition on axial velocity is not always satisfactorily predicted by the linear theory in

the vicinity of the pylon trailing edge, x = 16.8 inches for wing pylons. For body pylons, the results are satisfactory.

2. At M = 1.050 (figs. 70-75), the effect of pylon addition on upwash and sidewash is not well predicted. As before, the predicted effect shows strong oscillatory behavior which is not present in the test data. The oscillatory behavior is associated with use of panel methods at supersonic speeds near $M_\infty = 1$, and is intensified by the presence of the pylon. The linear theory must therefore be improved in this case. This will be discussed further in section 11.

9. THREE-DIMENSIONAL TRANSONIC SMALL-DISTURBANCE FINITE-DIFFERENCE THEORY RESULTS

9.1 Description

In order to provide a bench mark predictive capability with which to assess the various rapid predictive methods discussed in this report and for other reasons discussed below, it was decided to utilize the Bailey-Ballhaus three-dimensional transonic small-disturbance code. The code was modified somewhat to provide the flow-field output required for the present study.

NEAR, Inc. gratefully acknowledges the cooperation and support given by the NASA/Ames Research Center both in providing the code and the required computational time.

The Bailey-Ballhaus code (refs. 7 and 8) was employed to solve the transonic small-disturbance equation in the following form

$$(1 - M_\infty^2)\,\phi_{xx} + \phi_{yy} + \phi_{zz} = M_\infty^2\left(\frac{\gamma+1}{V_\infty}\right)\phi_x\phi_{xx}$$

where V_∞ and M_∞ refer to the free-stream velocity and Mach number, and $\gamma = 1.4$. This form is directly compatible with the classical transonic equivalence rule. The computer run time for a reasonable engineering grid is approximately 20 minutes on the CDC 7600. The present version of

the code is limited to subsonic free-stream Mach numbers. It can treat only clean wing-body configurations, i.e., without pylons or stores.

9.2 Utility of Three-Dimensional Nonlinear Transonic Theory Results

There are several reasons for comparing the prediction of the three-dimensional transonic code with experiment.

1. The predictions are interesting in their own right. The comparisons to be discussed below are probably the first extensive comparisons of three-dimensional transonic small-disturbance results with experimental flow-field data.

2. Since the three-dimensional transonic code can be expected to be more accurate than all the rapid predictive methods, its prediction when compared with data fixes an error bracket which rapid predictive methods cannot be expected to surpass.

3. The three-dimensional transonic code provides a tool to analyze wind-tunnel wall interference effects. This aspect will be discussed in section 10.

4. The three-dimensional transonic code can serve as a basis upon which to develop improved rapid predictive methods. This will be discussed more fully in section 11.

9.3 Comparison of Three-Dimensional Nonlinear Transonic Theory Result with Data

The three-dimensional transonic code was utilized to obtain flow field predictions in the vicinity of the wing-body configuration for the following cases:

1. $M_\infty = 0.950$, $\alpha = 0^\circ, 5^\circ$
2. $M_\infty = 0.975$, $\alpha = 0^\circ, 5^\circ$

In each of the above cases, axial velocity, upwash, and sidewash predictions were obtained at a variety of survey locations in the

vicinity of the wing-body, including all survey locations contained in the data reports (refs. 1-4).

In this report, the three-dimensional transonic code predictions will be compared with experimental data only for the cases $M_\infty = 0.975$, $\alpha = 0^\circ$, 5°. Although predictions at many survey locations were obtained, only the representative surveys (y,z) = (0,-2), (2,-1), (2,-3), (4,-1), (4,-3), (7,-1), and (7,-3) will be used for the axial velocity, upwash and sidewash comparisons. These comparisons are shown in figures 79 to 92. A detailed listing of the comparisons shown in this report with corresponding page numbers is contained in Table 5. The approximate location of these surveys is shown in the sketch below.

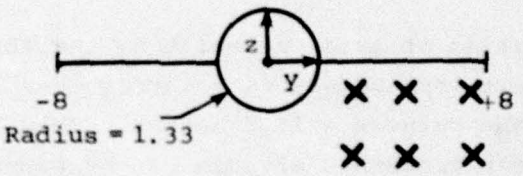

Based on these comparisons the following conclusions can be drawn regarding capabilities of the three-dimensional transonic small-distribution result:

1. The predictions of axial velocity, upwash and sidewash compare satisfactorily in most cases with the data except at the wing trailing edge.

2. The only predictions which are quantitatively only fair (but, nevertheless, qualitatively correct) are the upwash prediction at (y,z) = (0,-2) and $\alpha = 5^\circ$ [fig. 86(b)] and the sidewash prediction at (y,z) = (2,-1) [figs. 80(c) and 87(c)]. The probable cause of these discrepancies is that these surveys, which are located close to the fuselage, are more strongly affected by the approximation used in the present version of the code to treat the fuselage boundary conditions, i.e, that of transferring the boundary conditions from the actual circular fuselage to a square box fuselage. In fact, linear theory is somewhat better than transonic theory at these points as can be seen by

comparing figures 16(c) and 80(c), 19(b) and 86(b), and 20(c) and 87(c). Comparisons (not shown) of the 3-D transonic theory with data for surveys farther away from the fuselage, (y,z) = (0,-3), (0,-4), (0,-5), show excellent agreement.

3. The predictions of upwash and sidewash by the three-dimensional transonic code are comparable in accuracy to the predictions of upwash and sidewash by the linear theory. This supports the belief that for the angle of attack and wing-body geometry considered here, nonlinear transonic effects are small insofar as upwash and sidewash are concerned. Therefore, it is appropriate to use a (rapid) linear theory procedure to predict these quantities at low angles of attack up to $M_\infty = 0.975$.

4. The prediction of axial velocity by the three-dimensional transonic code is a great improvement in accuracy over the linear theory prediction beyond the point x = 16.5 inches. This is the region of the shock where nonlinear transonic effects can be expected to be strongest. It appears inappropriate to use a linear-theory code to predict axial velocity in the shock region of a transonic flow field, as would be expected.

10. ASSESSMENT OF WIND-TUNNEL, WALL-INTERFERENCE EFFECTS

The assessment of wind-tunnel, wall-interference effects in the transonic experimental data is important because all predictive methods discussed in this report use a free-air outer boundary condition. Consequently, if the effect of the wind tunnel walls on the data is not negligible, there could be a signficant discrepancy between the theoretical predictions and the data.

The fact that the three-dimensional nonlinear transonic results (which use a free-air boundary condition) was observed in section 9 to agree well with the experimental data, supports the conclusion that the experimental data at $M_\infty \leq 0.975$ are relatively free of wall interference effects. What differences do exist between theory and experiment may be due to minor wall-interference effects, wind-tunnel flow irregularities, measurement inaccuracies, model fabrication, viscous effects, or approximations in the theory.

The assessment of wall-interference effects at $M_\infty = 1.025$ must proceed differently than for $M_\infty = 0.975$ because the current version of the Bailey-Ballhaus code cannot handle supersonic free-stream Mach numbers. Instead the method developed under this contract and reported in reference 9 is used. This method employs measured outer boundary conditions, as obtained in the wind-tunnel tests of references 1-4, as the outer boundary condition for the transonic axisymmetric equivalent-body calculation. The measured outer boundary condition results for the equivalent body are then compared with corresponding results using a free-air outer boundary condition. This comparison is shown for equivalent body surface pressure in figure 93 for $M_\infty = 1.025$. It is seen in figure 93 that the only regions of disagreement are in the vicinities of $x = 11.0$ inches (i.e., before the wing leading edge over most of the span) and $x = 17.0$ inches. Therefore this lends support to the conclusion that wall interference effects in the case $M_\infty = 1.025$ are not significant over the bulk of the wing but may be significant only in front of the wing leading edge and behind $x = 17.0$ inches. This result may apply more to u/V_∞ than to downwash and sidewash angles.

Finally, we note that above conclusions regarding the relatively minor influence of wind-tunnel wall interference at $M_\infty = 0.975$ and 1.025 are consistent with the conclusions drawn in reference 10. There, the conclusion that wall-interference effects had only a minor influence on the flow field was drawn on the basis of a comparison between 4T experimental data and 16T experimental data.

11. OVERALL CONCLUSIONS AND FUTURE DIRECTIONS

The main conclusion to emerge from the investigation described in this report is that the three-dimensional linear theory predictive technique yields generally satisfactory rapid predictions of upwash and sidewash in a transonic flow field around the wing-body or wing-body/pylon configurations considered, over a range of transonic free-stream Mach numbers and angles of attack.

For the subsonic free-stream Mach numbers considered ($M_\infty = 0.925$, 0.950, and 0.975) and the angles of attack considered ($\alpha = 0^\circ$ and 5°), the linear theory yielded satisfactory agreement in upwash and sidewash upstream of the wing trailing edge for both the wing-body and wing-body/

pylon configurations. Axial velocity was satisfactorily predicted at $M_\infty = 0.925$, but deteriorated as $M_\infty \to 1$.

For the supersonic free-stream Mach numbers considered ($M_\infty = 1.050$ and 1.025) and angles of attack considered ($\alpha = 0^o$ and 5^o), the linear theory yielded satisfactory agreement in upwash and sidewash for the wing-body configuration. Axial velocity was satisfactorily predicted at $M_\infty = 1.050$ but deteriorated as $M_\infty \to 1$, i.e., $M_\infty = 1.025$. For the wing-body/pylon configurations at supersonic free-stream Mach numbers, all flow-field predictions were generally unsatisfactory due to an oscillatory behavior of the linear-theory predictions which is intensified by the presence of pylons. This oscillatory behavior is due to difficulties with multiple reflections and resonance phenomena in the current panel method.

The above conclusions are supported by the extensive comparisons between the linear theory and experimental data which were presented in this report. Additionally, the agreement between the linear theory predictions of upwash and sidewash and the three-dimensional nonlinear transonic finite-difference predictions of the same quantities gives support to the claim that upwash and sidewash are only weakly influenced by nonlinear transonic effects. The effectiveness of the linear theory in predicting upwash and sidewash over a wide range of transonic free-stream Mach numbers, angles of attack, and wing-body/pylon combinations implies that the linear theory may serve as a basis of a rapid economical method for the prediction of store loadings (normal force and side-force distributions and coefficients). However additional effort will be required to avoid oscillatory behavior associated with adding the pylons for very low supersonic Mach numbers.

Any attempt to improve the linear-theory flow field predictive capability should first focus on the problem of oscillatory behavior of the solutions at supersonic free-stream Mach numbers near $M_\infty = 1$. The current panel method used in the linear theory technique should be modified to alleviate these difficulties.

Any further attempt to improve the linear-theory flow field predictive capability in the vicinity of wing-body/pylon combinations should incorporate nonlinear effects which are intrinsic to transonic flow

fields. The three-dimensional transonic code, which does incorporate nonlinear effects, was seen to yield good agreement with data in the vicinity of the wing-body alone combination at $M_\infty = 0.975$, $\alpha = 0^\circ, 5^\circ$. As presently constituted, it cannot handle configurations involving pylons. Additionally, it is not computationally economical and is presently limited to subsonic free-stream Mach numbers. Nevertheless, the possibility exits that the three-dimensional transonic code could be incorporated on a limited basis as part of a larger scheme for the computation of transonic flow fields. Such a scheme can be formulated as follows:

$$WBP = (WBP)_{LT} + (WB)_{NL} - (WB)_{LT}$$

Here

WBP = predicted flow field quantity (axial velocity, upwash, or sidewash) in the vicinity of the wing-body/pylon configuration.

$(WBP)_{LT}$ = flow field quantity as predicted by the three-dimensional linear theory for the wing-body/pylon configuration

$(WB)_{NL}$ = flow field quantity as predicted by the three-dimensional transonic theory for the wing-body configuration

$(WB)_{LT}$ = flow field quantity as predicted by the three-dimensional linear theory for the wing-body configuration.

The above scheme handles wing-body/pylon combinations and it utilizes the three-dimensional transonic code (no pylons) to produce nonlinear transonic effects. Thus the extension of the 3-D transonic method to handle pylons would be circumvented by this device. The problem of economy in the above formulation can be solved by utilizing perturbation techniques (refs. 11-12) which enable one to approximate an entire range of 3-D transonic predictions from just two or three 3-D transonic predictions. For example, the 3-D transonic code could be used to predict the flow field for the cases $\alpha = 0^\circ, 5^\circ$ and then, from these two cases, an entire range of nonlinear predictions could be obtained via a highly economical and accurate perturbation technique. The accuracy of this procedure could be checked by comparing the procedure's flow field pre-

dictions at $\alpha = 10^{\circ}$ or 15°, or by obtaining wind-tunnel test data at $\alpha = 10^{\circ}$ and 15° and using the data as a check. Finally, the extension of the existing 3-D transonic code to supersonic free-stream Mach numbers requires both the implementation of a supersonic free-air outer boundary conditions as well as some grid modifications and should be carried out.

ACKNOWLEDGEMENTS

Support for the research reported in this investigation was provided by the Air Force Office of Scientific Research under Contract No. F44620-75-C-0047 with Lt. Col. Robert C. Smith and Dr. James D. Wilson as Technical Monitor. Support for the wind-tunnel test program was provided by the Air Force Flight Dynamic Laboratory with Mr. Calvin L. Dyer as Technical Monitor. Special thanks are given to Janice Walters for extensive programming support, to Dr. Michael J. Hemsch for careful review of the final manuscript, and to Ames Research Center for providing the code and the computational time needed to determine the 3-D nonlinear transonic results reported herein.

REFERENCES

1. Perkins, S. C., Jr., Stahara, S. S., and Hemsch, M. J.: Data Report for a Test Program to Study Transonic Flow Fields About Aircraft with Application to External Stores. NEAR TR 138, July 1977.

2. Stahara, S. S. and Crisalli, A. J.: Data Report for a Test Program to Study Transonic Flow Fields About Wing-Body Pylon/Store Combinations, Volume I. - Summary Report, Tunnel Empty Flow Survey Data, Wing-Body Force/Moment/Surface Pressure Data, and Pressure Store/Force/Moment/Surface Pressure Data. NEAR TR 163, May 1978.

3. Stahara, S. S. and Crisalli, A. J.: Data Report for a Test Program to Study Transonic Flow Fields About Wing-Body/Pylon/Store Combinations, Volume II. - Flow Field Survey Data for Configurations 21 and 22. NEAR TR 163, May 1978.

4. Stahara, S. S. and Crisalli, A. J.: Data Report for a Test Program to Study Transonic Flow Fields About Wing-Body/Pylon/Store Combinations, Volume III. - Flow Field Survey Data for Configurations 24, 25 and 26. NEAR TR 163, May 1978.

5. Goodwin, F. K. and Dillenius, M. F. E.: Extension of the Method for Predicting Six-Degree-of-Freedom Store Separation Trajectories at Speeds up to the Critical Speed to Include a Fuselage with Noncircular Cross Section, Volume I. - Theoretical Methods and Comparisons with Experiment. AFFDL-TR-74-130, Nov. 1974.

REFERENCES (Concluded)

6. Dillenius, M. F. E., Goodwin, F. K., and Nielsen, J. N.: Prediction of Supersonic Store Separation Characteristics, Volume I - Theoretical Methods and Comparisons with Experiment. AFFDL-TR-76-41, May 1976.

7. Mason, W. H., Mackenzie, D., Stern, M., Ballhaus, W. F., and Frick, J.: An Automated Procedure for Computing the Three-Dimensional Transonic Flow Over Wing-Body Combinations, Including Viscous Effects; Volume I - Description of Analysis Methods and Applications. AFFDL-TR-77-122, Oct. 1977.

8. Mason, W. H., MacKenzie, D., Stern, M., Ballhaus, W. F., and Frick, J.: An Automated Procedure for Computing the Three-Dimensional Transonic Flow Over Wing-Body Combinations, Including Viscous Effects; Volume II Program User's Manual and Code Description. AFFDL-TR-77-122, Oct. 1977.

9. Stahara, S. S. and Spreiter, J. R.: A Transonic Wind Tunnel Interference Assessment - Axisymmetric Flows. 17th Aerospace Sciences Meeting, New Orleans, Louisiana, Jan. 15-17, 1979, AIAA Paper No. 79-0203.

10. Stahara, S. S., Hemsch, M. J., Perkins, S. C., Jr., and Spreiter, J. R.: A Rapid Predictive Method for Three-Dimensional Transonic Flow Fields About Parent Aircraft with Application to External Stores. Paper presented at Fourth JTCG Aircraft/Stores Compatibility Symposium, Eglin Air Force Base, FL, Oct. 1977.

11. Nixon, D.: Perturbation of a Discontinuous Transonic Flow. AIAA Journal, Vol. 10, No. 1, Jan. 1978.

12. Stahara, S. S., Chaussee, D. S., and Spreiter, J. H.: Perturbation Solutions for Transonic Flow on the Blade-to-Blade Surface of Compressor Blade Rows. NASA CR-2941, Jan. 1978.

TABLE 1.- COMPARISONS OF CLASSICAL TRANSONIC EQUIVALENCE RULE WITH DATA OF REFERENCE 1

Experiment	Configuration	M_∞	α (deg)	y (in.)	z (in.)	Axial Velocity Ratio (Page no.)	Upwash (Page no.)	Sidewash (Page no.)	Figure
Ref. 1	WB	.925	0	2.0	-1.0	51	52	53	10
Ref. 1	WB	.975	0	2.0	-1.0	54	55	56	11

TABLE 2.- COMPARISONS OF EXTENDED TRANSONIC EQUIVALENCE RULE, LINEAR THEORY AND DATA OF REFERENCE 1

Experiment	Configuration	M_∞	α (deg)	y (in.)	z (in.)	Axial Velocity Ratio (Page no)	Upwash (Page no)	Sidewash (Page no)	Figure
Ref. 1	WB	.925	0	2	-1	59	60	61	13
				4	-1	62	63	64	14
		.975	0	0	-2	65	66	67	15
				2	-1	68	69	70	16
				2	-3	71	72	73	17
				4	-1	74	75	76	18
			5	0	-2	77	78	79	19
				2	-1	80	81	82	20
				2	-3	83	84	85	21
				4	-1	86	87	88	22
		1.025	0	0	-2	89	90	91	23
				2	-1	92	93	94	24
				2	-3	95	96	97	25
				4	-1	98	99	100	26
			5	0	-2	101	102	103	27
				2	-1	104	105	106	28
				2	-3	107	108	109	29
				4	-1	110	111	112	30

TABLE 3.- COMPARISONS OF LINEAR THEORY WITH DATA FOR REFERENCES 2-4

Experiment	Configuration	M_∞	α (deg)	y (in.)	z (in.)	Axial Velocity Ratio (Page no)	Upwash (Page no)	Sidewash (Page no)	Figure
Refs. 2-4	WB	.95	0	0	-2.208	113	114	115	31
				0	-2.958	116	117	118	32
				.75	-2.208	119	120	121	33
				3.5	-1.230	122	123	124	34
				3.5	-1.980	125	126	127	35
				4.25	-1.230	128	129	130	36
			5	3.5	-1.230	131	132	133	37
				3.5	-1.980	134	135	136	38
				4.25	-1.230	137	138	139	39
		1.05	0	0	-2.208	140	141	142	40
				0	-2.958	143	144	145	41
				.75	-2.208	146	147	148	42
				3.5	-1.230	149	150	151	43
				3.5	-1.980	152	153	154	44
				4.25	-1.230	155	156	157	45
			5	3.5	-1.230	158	159	160	46
				3.5	-1.980	161	162	163	47
				4.25	-1.230	164	165	166	48
	WB/WP	.95	0	3.5	-1.230	167	168	169	49
				3.5	-1.980	170	171	172	50
				4.25	-1.230	173	174	175	51
			5	3.5	-1.230	176	177	178	52
				3.5	-1.980	179	180	181	53
				4.25	-1.230	182	183	184	54
		1.05	0	3.5	-1.230	185	186	187	55
				3.5	-1.980	188	189	190	56
				4.25	-1.230	191	192	193	57
			5	3.5	-1.230	194	195	196	58
				3.5	-1.980	197	198	199	59
				4.25	-1.230	200	201	202	60
	WB/FP	.95	0	0	-2.208	203	204	205	61
				0	-2.958	206	207	208	62
				.75	-2.208	209	210	211	63

TABLE 4.- COMPARISONS OF EFFECT OF PYLON ADDITON AS GIVEN BY LINEAR THEORY WITH EFFECT OF PYLON ADDITION AS GIVEN BY DATA OF REFERENCES 2-4

Experiment	Configuration	M_∞	α (deg)	y (in.)	z (in.)	Axial Velocity Ratio (Page no)	Upwash (Page no)	Sidewash (Page no)	Figure
Refs. 2-4	WP	.95	0	3.5	-1.230	212	213	214	64
↓	↓	↓	↓	3.5	-1.980	215	216	217	65
↓	↓	↓	↓	4.25	-1.230	218	219	220	66
↓	↓	↓	5	3.5	-1.230	221	222	223	67
↓	↓	↓	↓	3.5	-1.980	224	225	226	68
↓	↓	↓	↓	4.25	-1.230	227	228	229	69
↓	↓	1.05	0	3.5	-1.230	230	231	232	70
↓	↓	↓	↓	3.5	-1.980	233	234	235	71
↓	↓	↓	↓	4.25	-1.230	236	237	238	72
↓	↓	↓	5	3.5	-1.230	239	240	241	73
↓	↓	↓	↓	3.5	-1.980	242	243	244	74
↓	↓	↓	↓	4.25	-1.230	245	246	247	75
↓	FP	.95	0	0	-2.208	248	249	250	76
↓	↓	↓	↓	0	-2.958	251	252	253	77
↓	↓	↓	↓	.75	-2.208	254	255	256	78

TABLE 5.- COMPARISONS OF 3-D TRANSONIC PREDICTIONS WITH DATA OF REFERENCE 1

Experiment	Configuration	M_∞	α (deg)	y (in.)	z (in.)	Axial Velocity Ratio (Page no)	Upwash (Page no)	Sidewash (Page no)	Figure
Ref. 1	WB	.975	0	0	-2	257	258	259	79
↓	↓	↓	↓	2	-1	260	261	262	80
↓	↓	↓	↓	2	-3	263	264	265	81
↓	↓	↓	↓	4	-1	266	267	268	82
↓	↓	↓	↓	4	-3	269	270	271	83
↓	↓	↓	↓	7	-1	272	273	274	84
↓	↓	↓	↓	7	-3	275	276	277	85
↓	↓	↓	5	0	-2	278	279	280	86
↓	↓	↓	↓	2	-1	281	282	283	87
↓	↓	↓	↓	2	-3	284	285	286	88
↓	↓	↓	↓	4	-1	287	288	289	89
↓	↓	↓	↓	4	-3	290	291	292	90
↓	↓	↓	↓	7	-1	293	294	295	91
↓	↓	↓	↓	7	-3	296	297	298	92

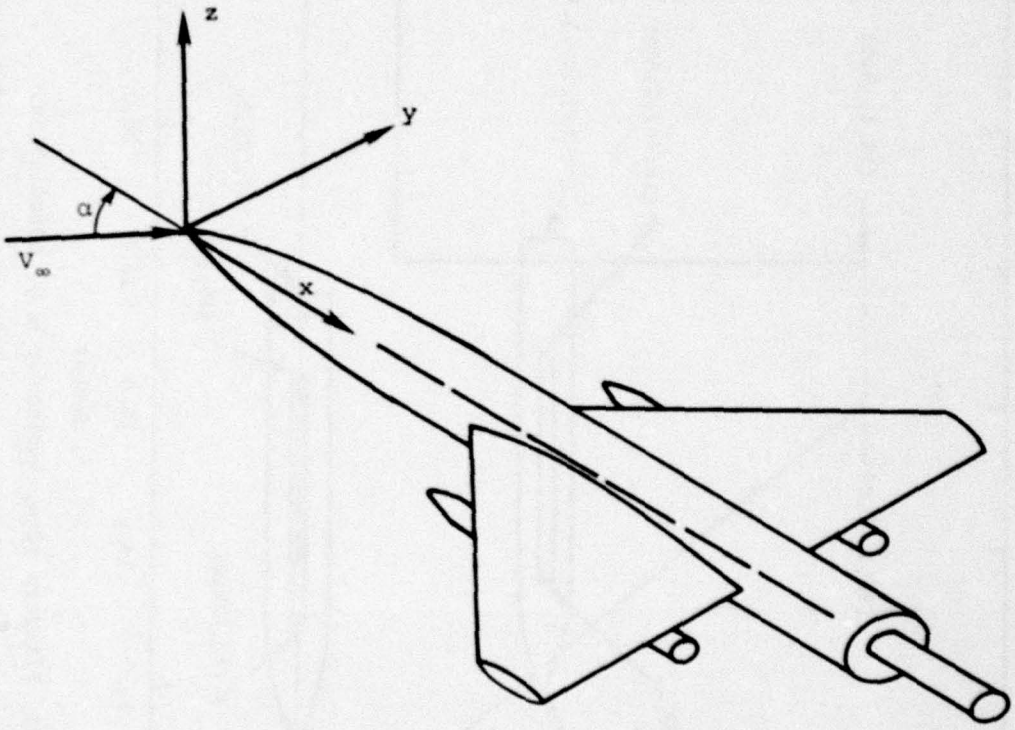

Figure 1.- Body-fixed coordinate system for inner flow field surveys.

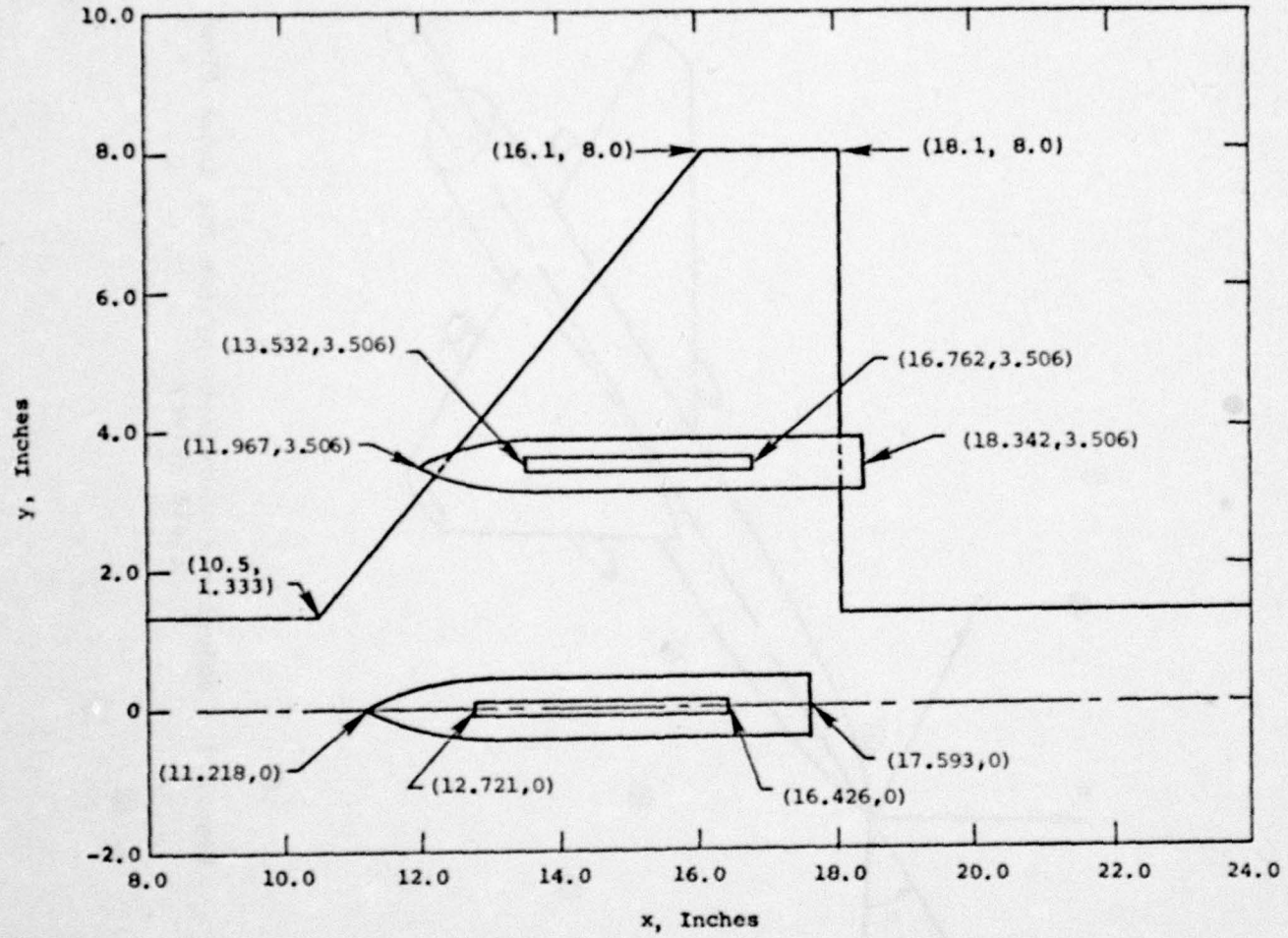

(a) Planform view, including (x,y) coordinates.

Figure 2.- Wing-body with pylons and stores, including measured body-fixed coordinates.

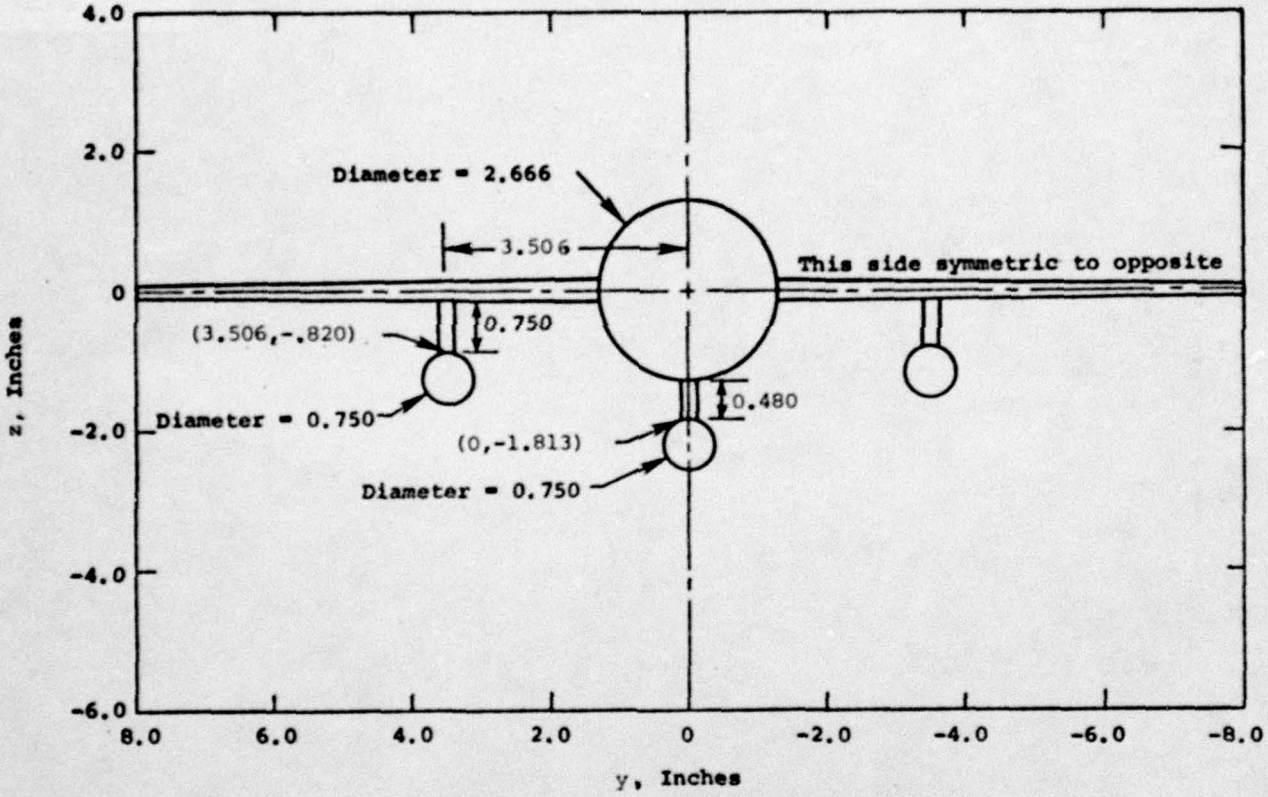

(b) Cross-sectional view (viewed from front of model), including (y,z) coordinates.

Figure 2.- Concluded.

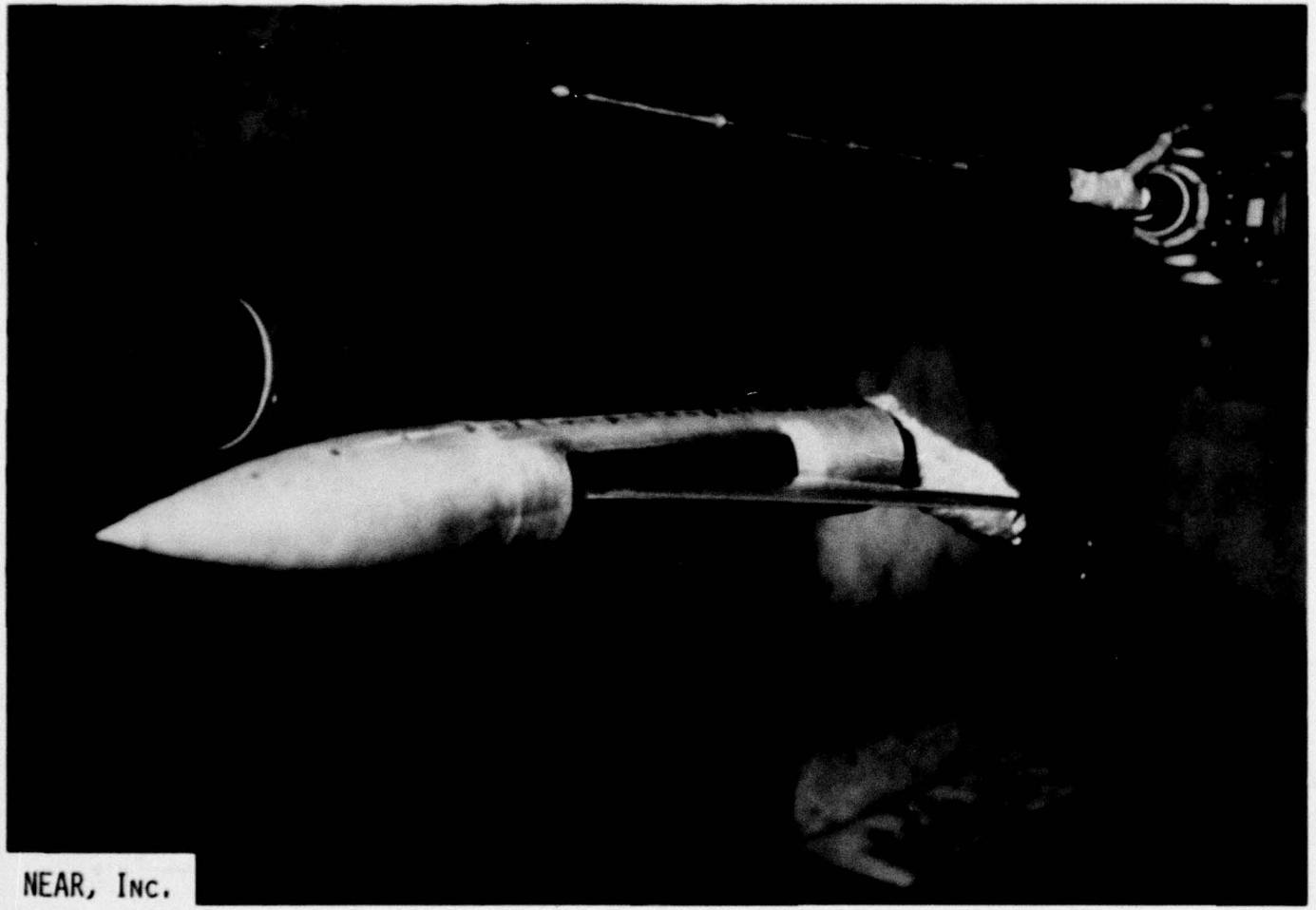

Figure 3. - Conical flow-field survey probe on CTS and wing-body combination with 4-percent thick airfoil.

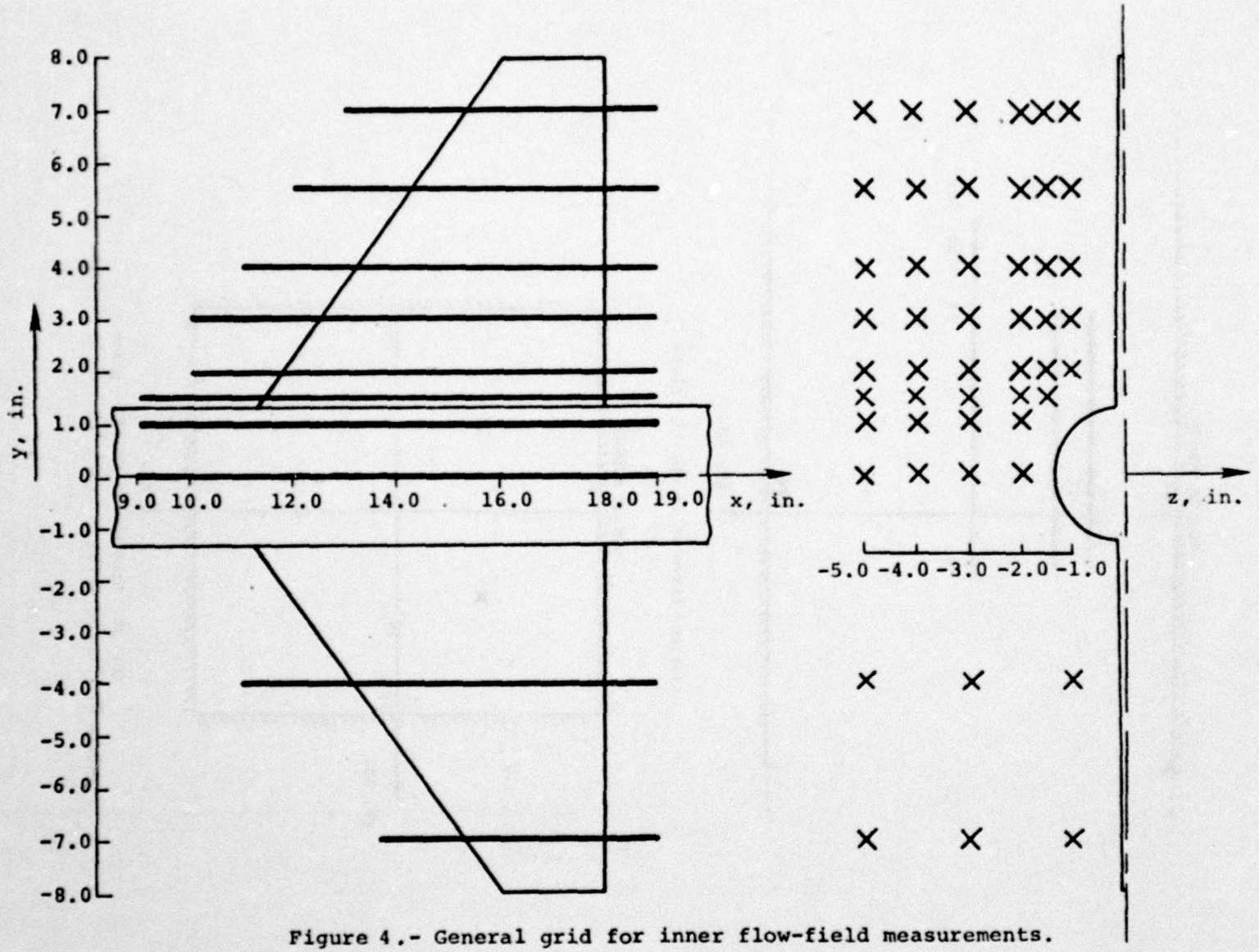

Figure 4.- General grid for inner flow-field measurements.

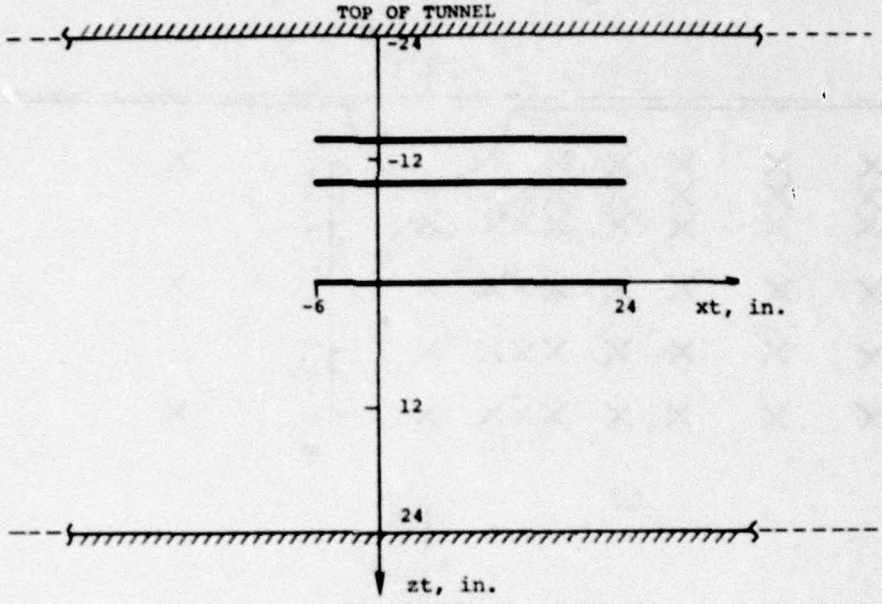

(a) xt traverse in xt, zt plane.

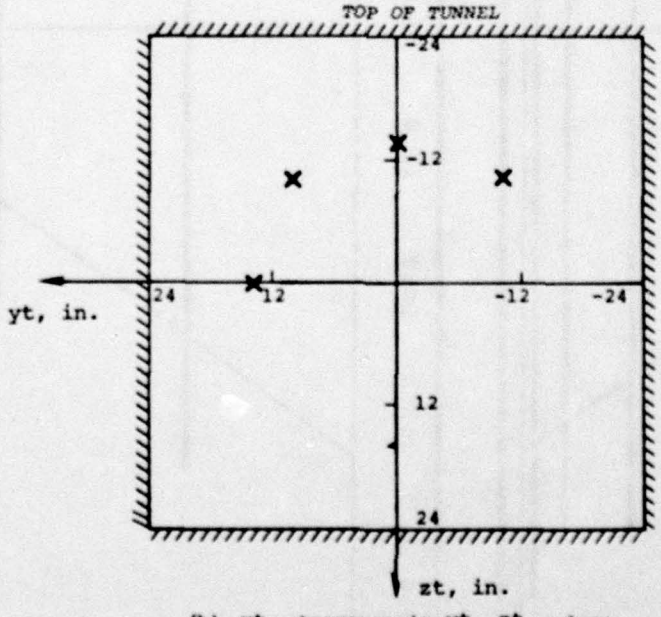

(b) xt traverse in yt, zt plane.

Figure 5.- General grids for outer flow-field surveys.

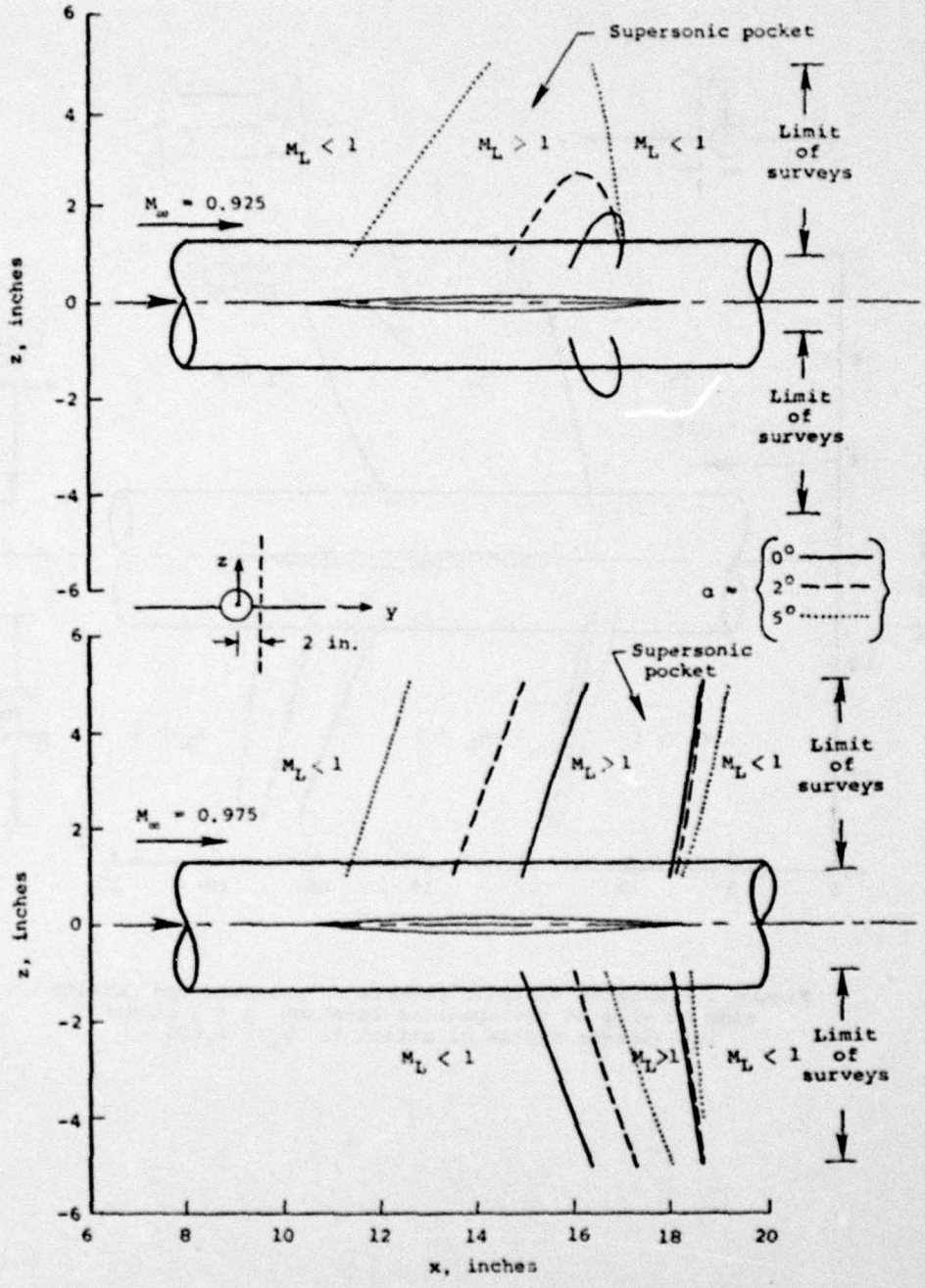

Figure 6.- Size of supersonic pockets on pressure and suction side of wing at the spanwise location y = 2 inches.

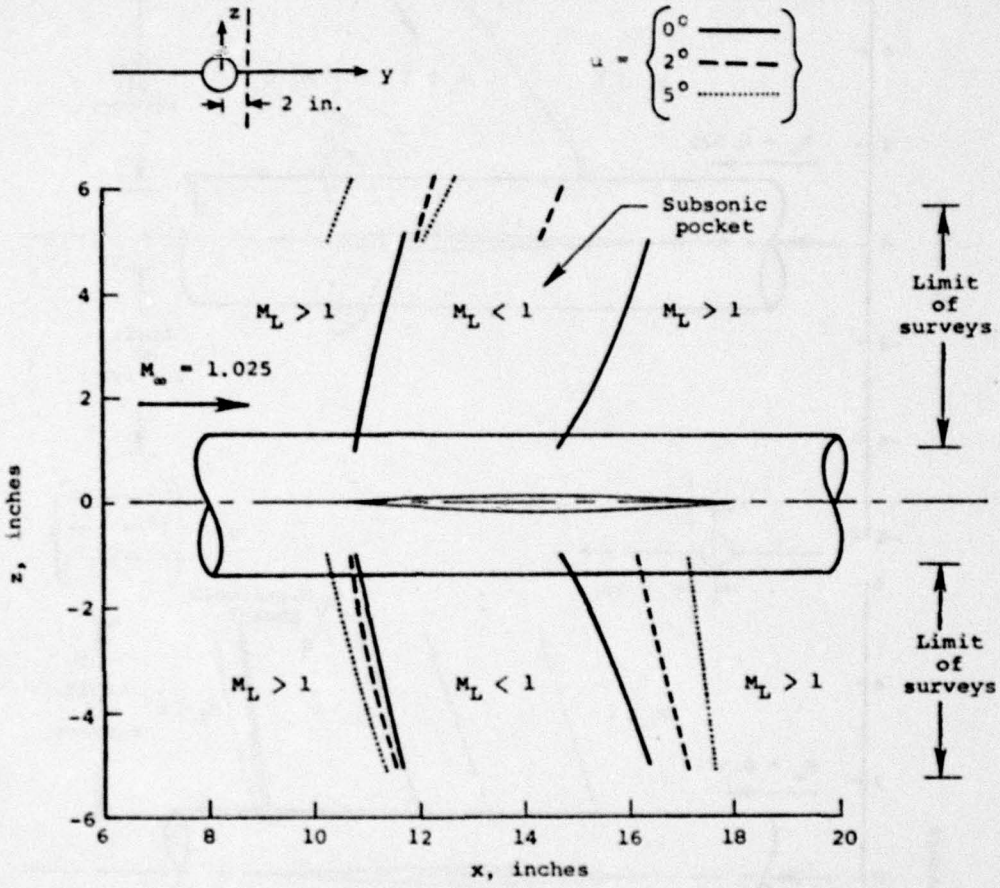

Figure 7.- Size of subsonic pockets on pressure and suction side of wing at the spanwise location y = 2 inches for various angles of attack at $M_\infty = 1.025$.

Configuration 21

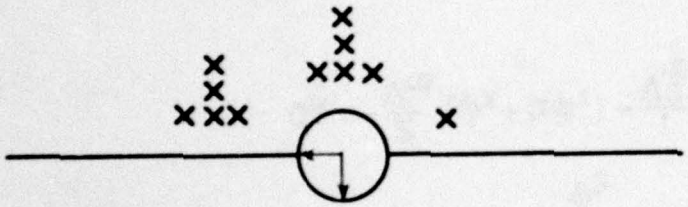

Configuration 22

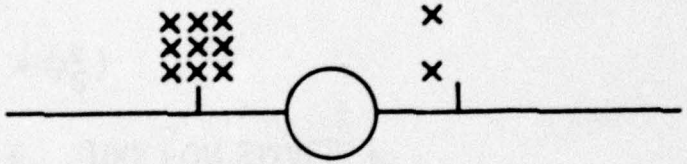

Configuration 24

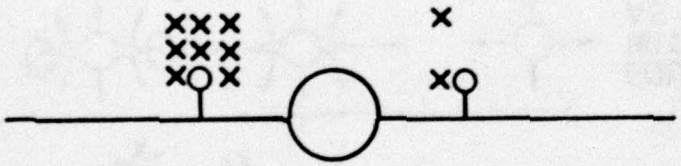

Configuration 25

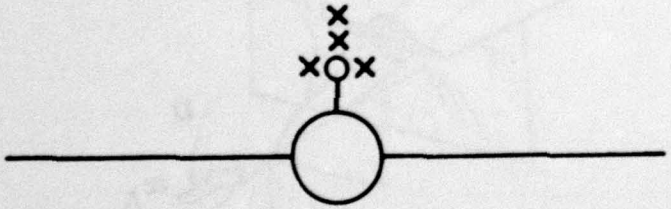

Configuration 26

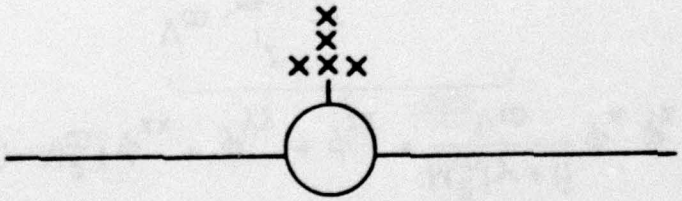

Figure 8.- Cross-sectional illustration of configurations 21, 22, 24, 25 and 26 viewed from rear of model.

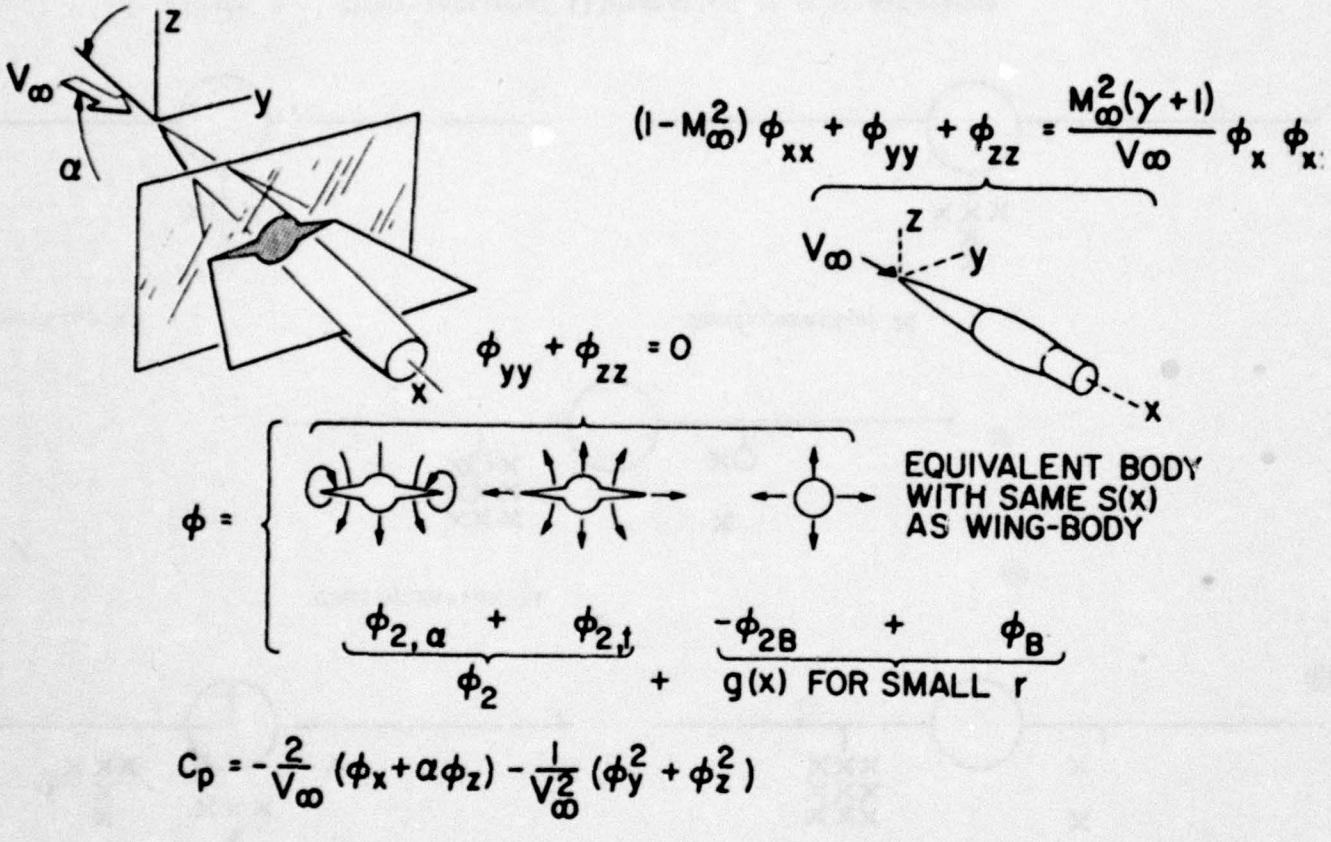

Figure 9.- Transonic equivalence rule for slender wing-body combinations.

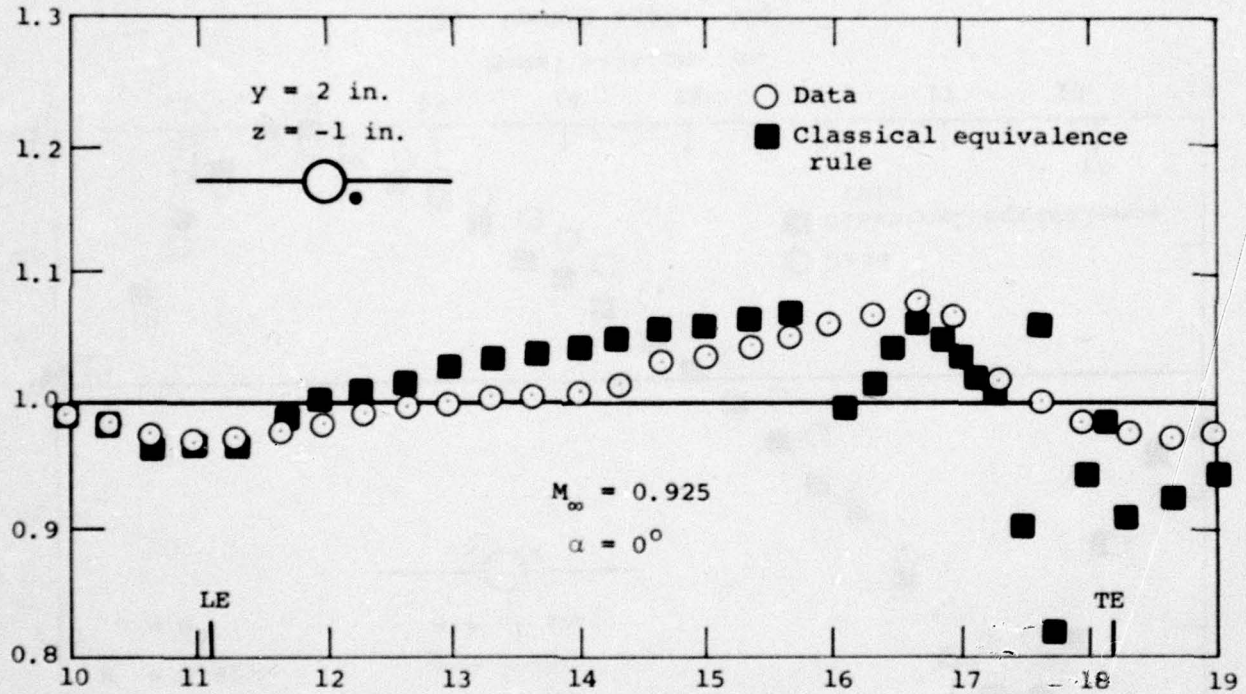

(a) Axial velocity ratio.

Figure 10.- Comparison of measured and theoretical flow field quantities under wing of wing-body combination at $M_\infty = 0.925$, $\alpha = 0^\circ$, y = 2 in., z = -1 in.

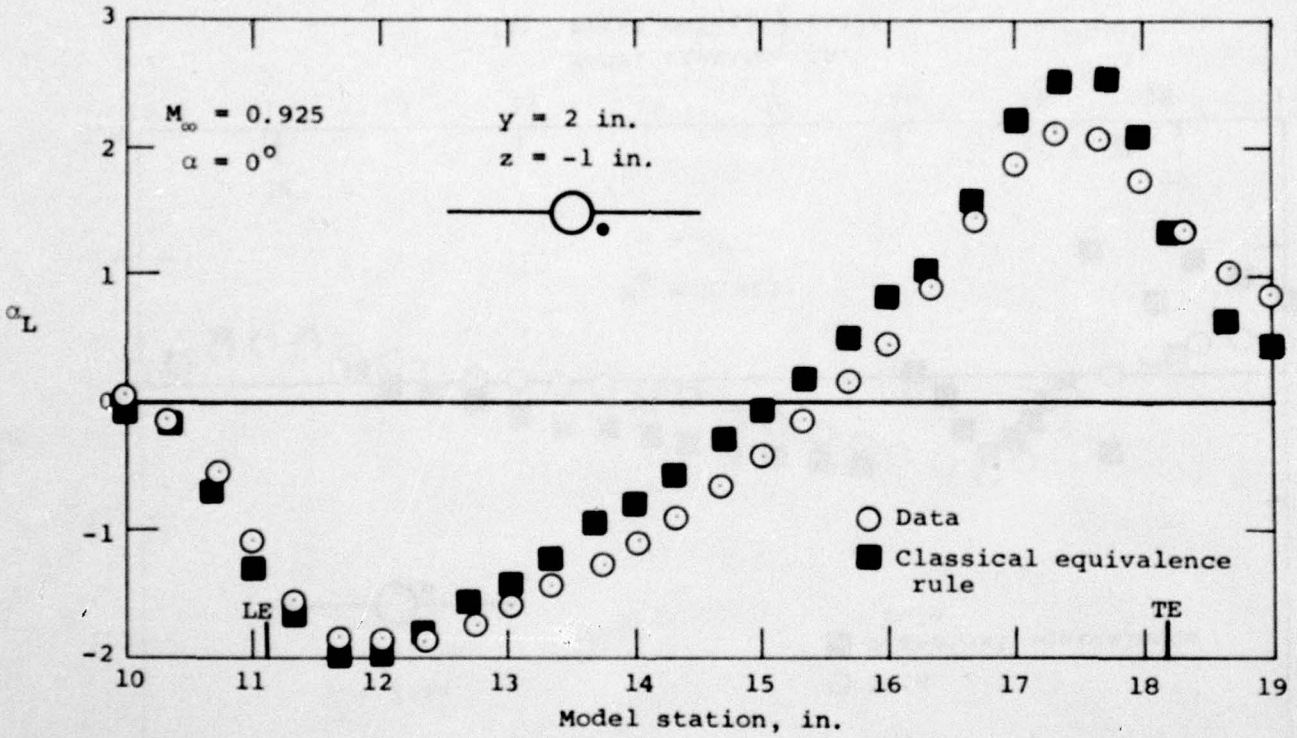

(b) Upwash angle, deg.

Figure 10.- Continued.

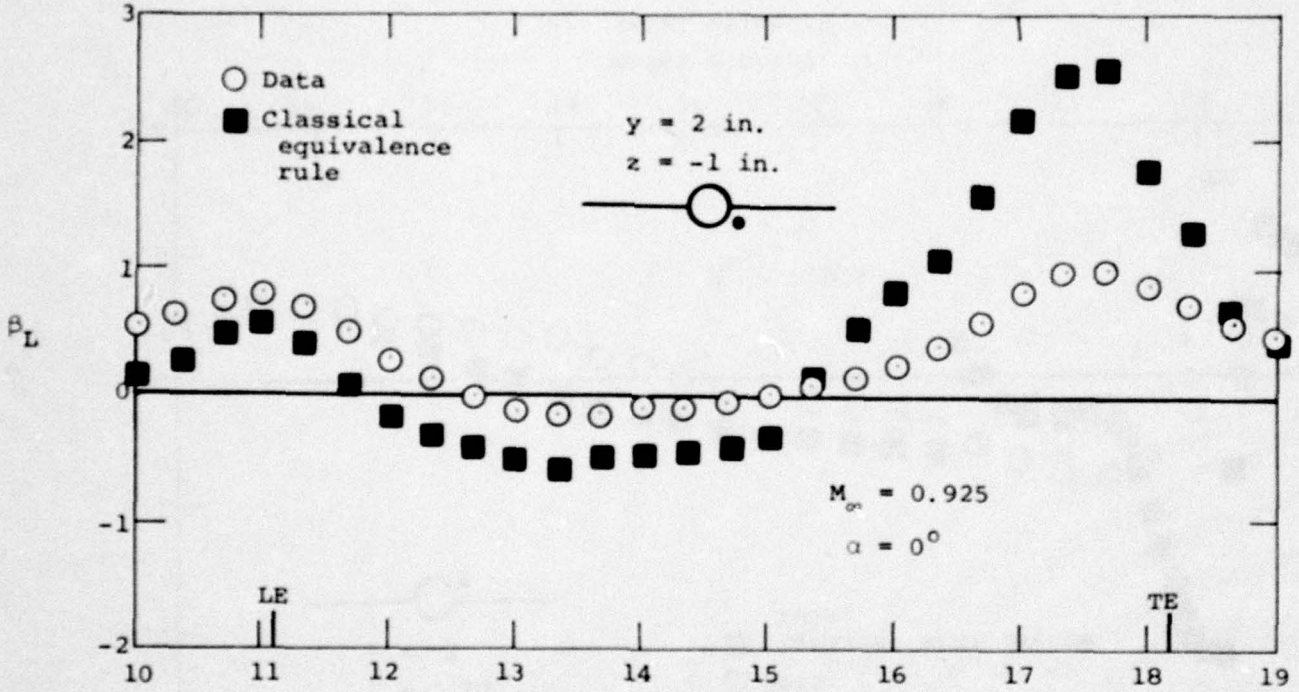

(c) Sidewash angle, deg.

Figure 10.- Concluded.

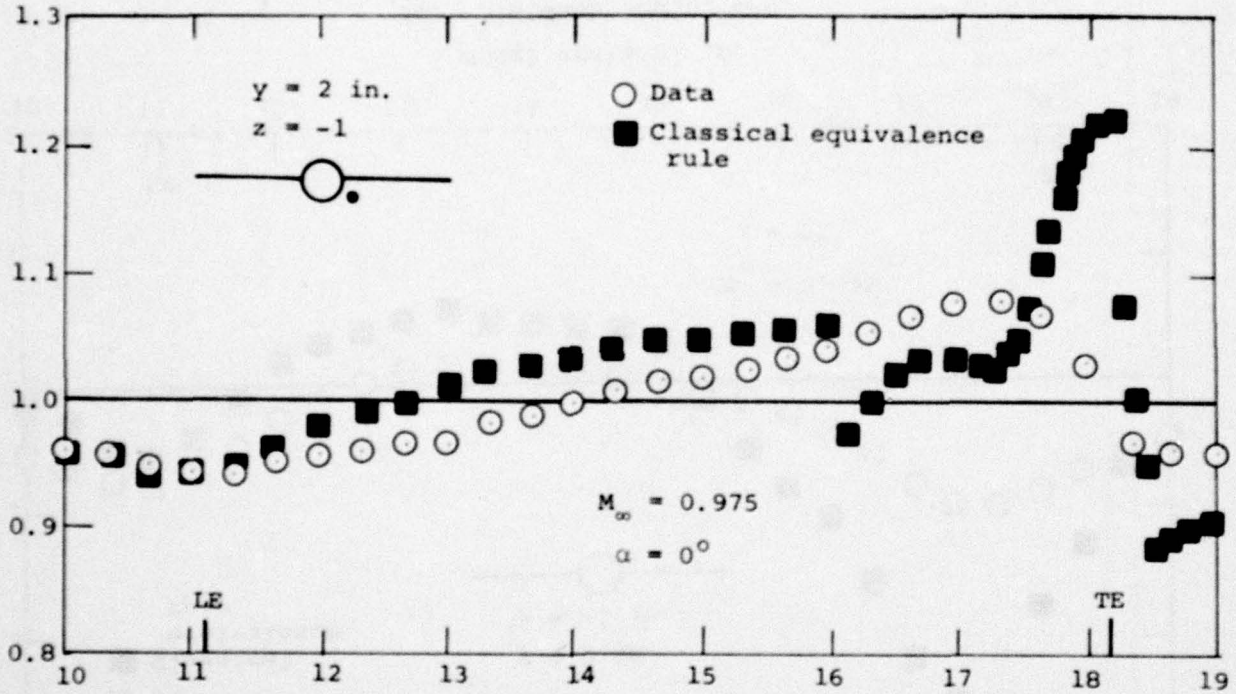

(a) Axial velocity ratio.

Figure 11.- Comparison of measured and theoretical flow field quantities under wing of wing-body combination at $M_\infty = 0.975$, $\alpha = 0^\circ$, y = 2 in., z = -1 in.

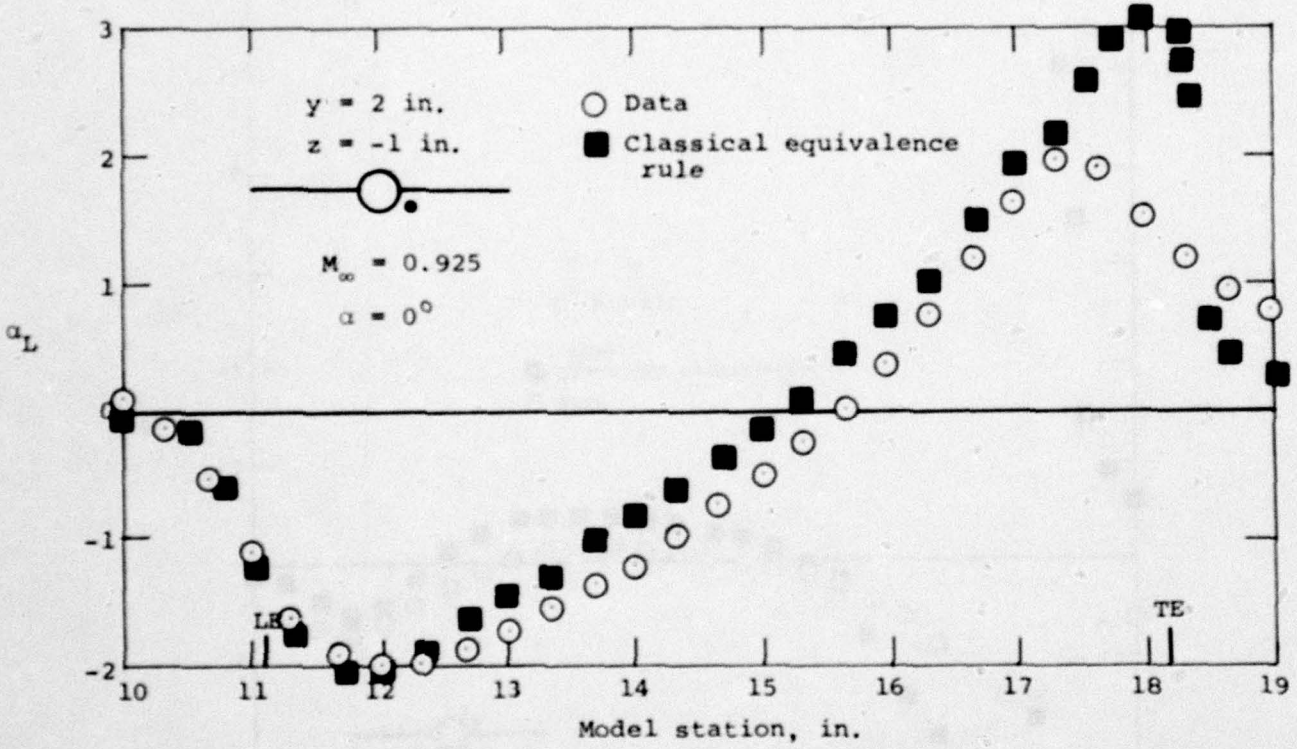

(b) Upwash angle, deg.

Figure 11.- Continued.

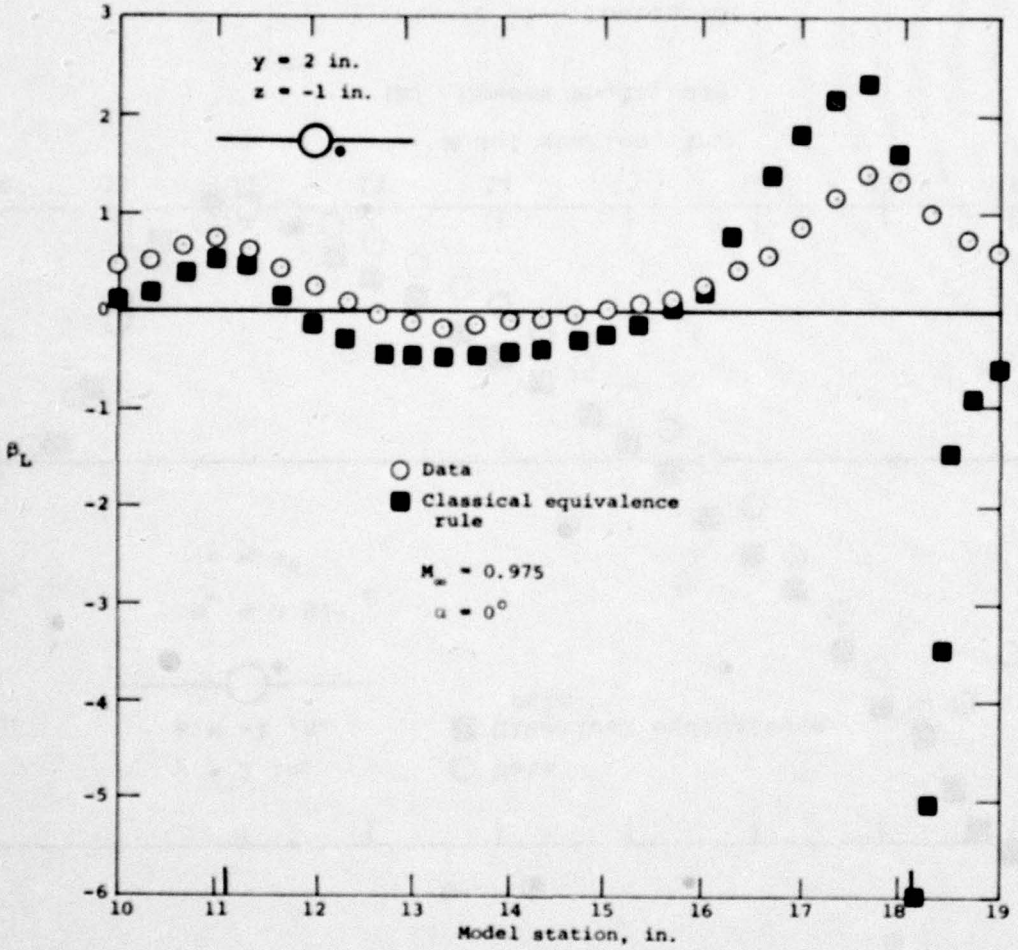

(c) Sidewash angle, deg.

Figure 11.- Concluded.

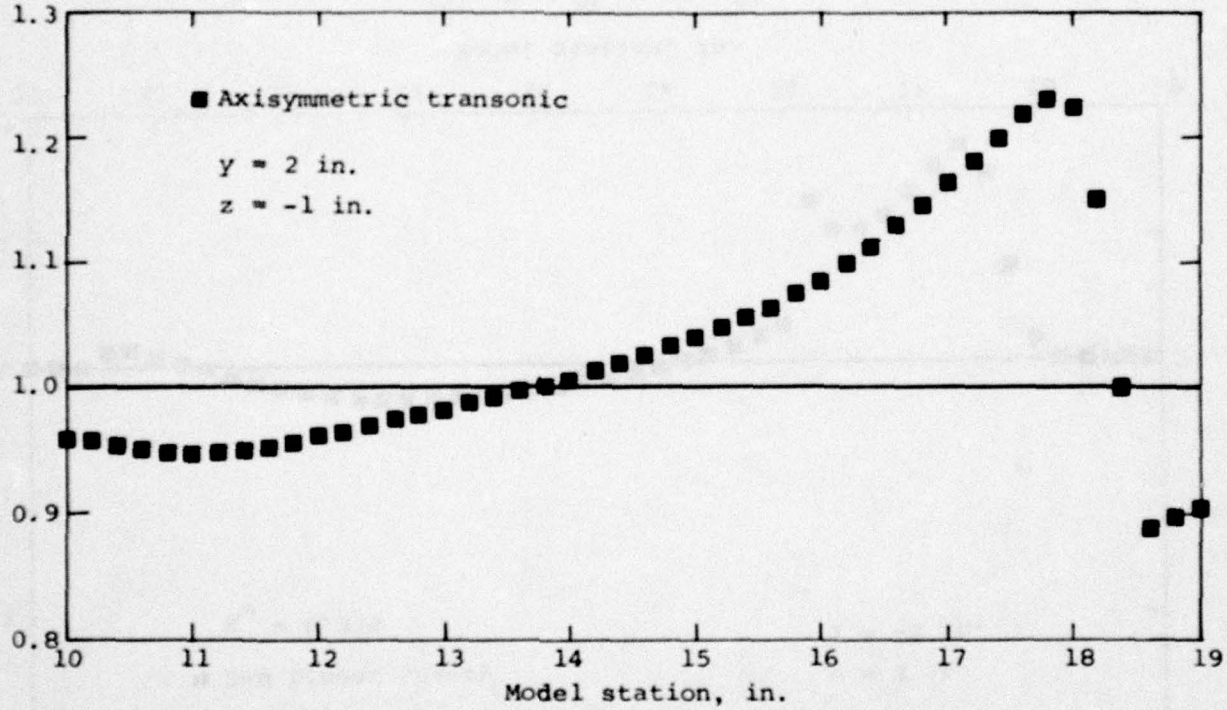

(a) u_B/V_∞.

Figure 12.- Components of axial velocity ratio.

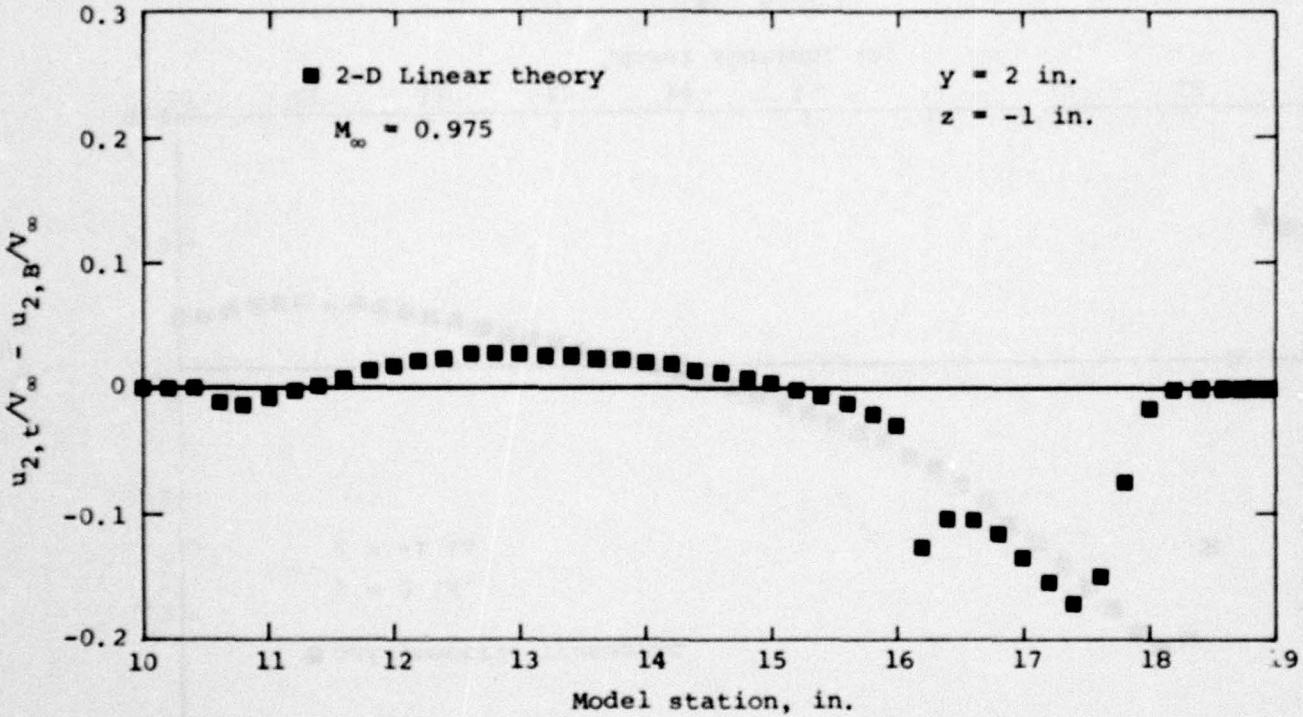

(b) $u_{2,t}/V_\infty - u_{2,B}/V_\infty$.

Figure 12.- Concluded.

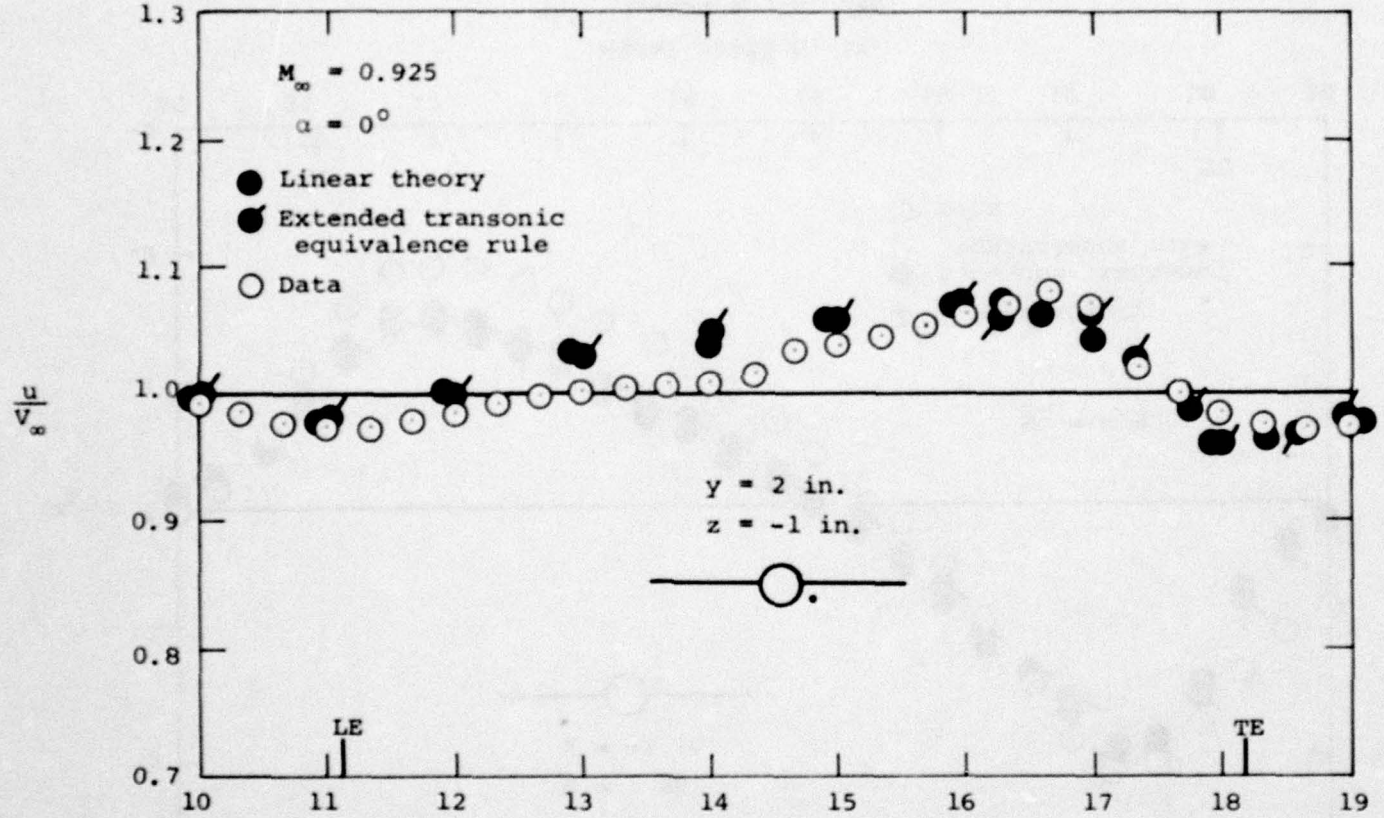

(a) Axial velocity ratio.

Figure 13.- Comparison of measured and theoretical flow field quantities for wing-body combination: $\alpha = 0°$, $M_\infty = 0.925$, y = 2 in., z = -1 in.

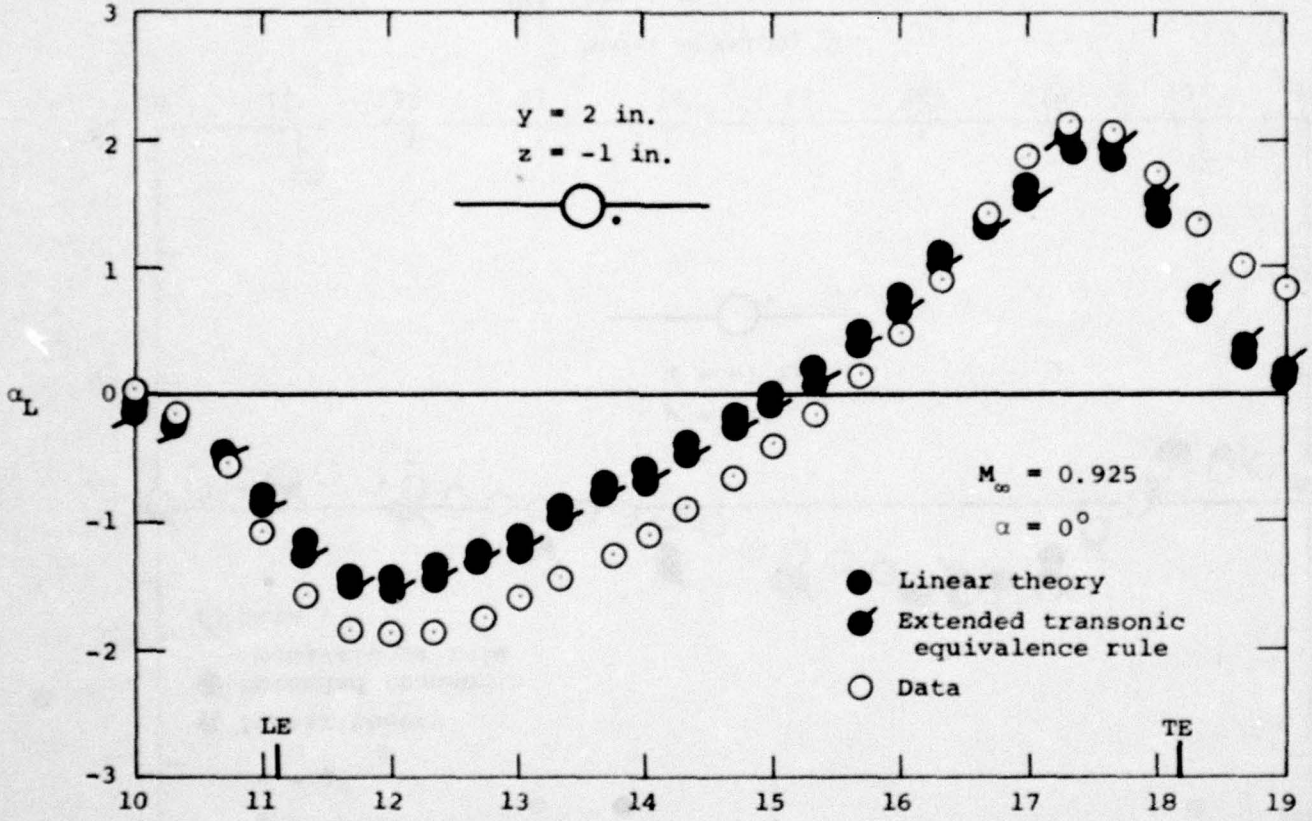

(b) Upwash angle, deg.

Figure 13.- Continued.

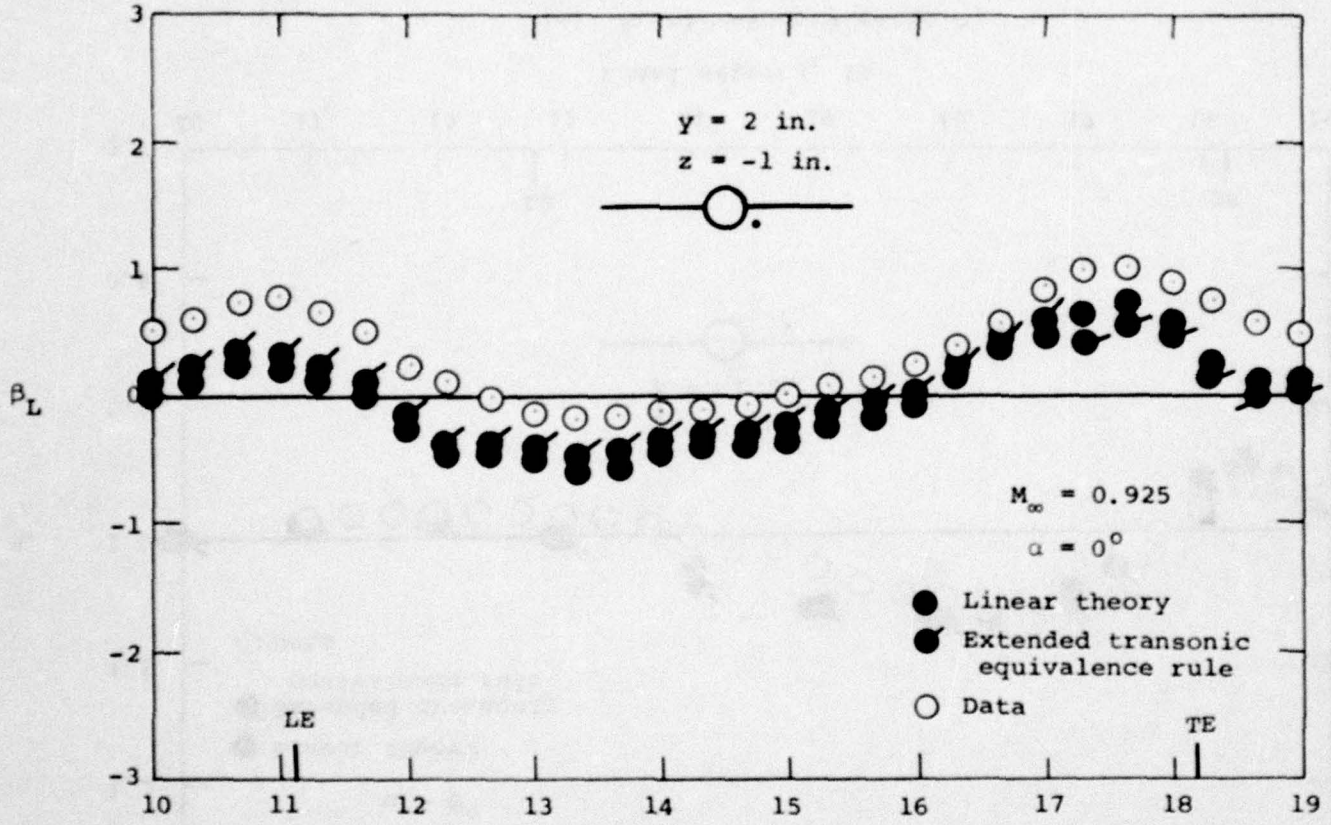

(c) Sidewash angle, deg.

Figure 13.- Concluded.

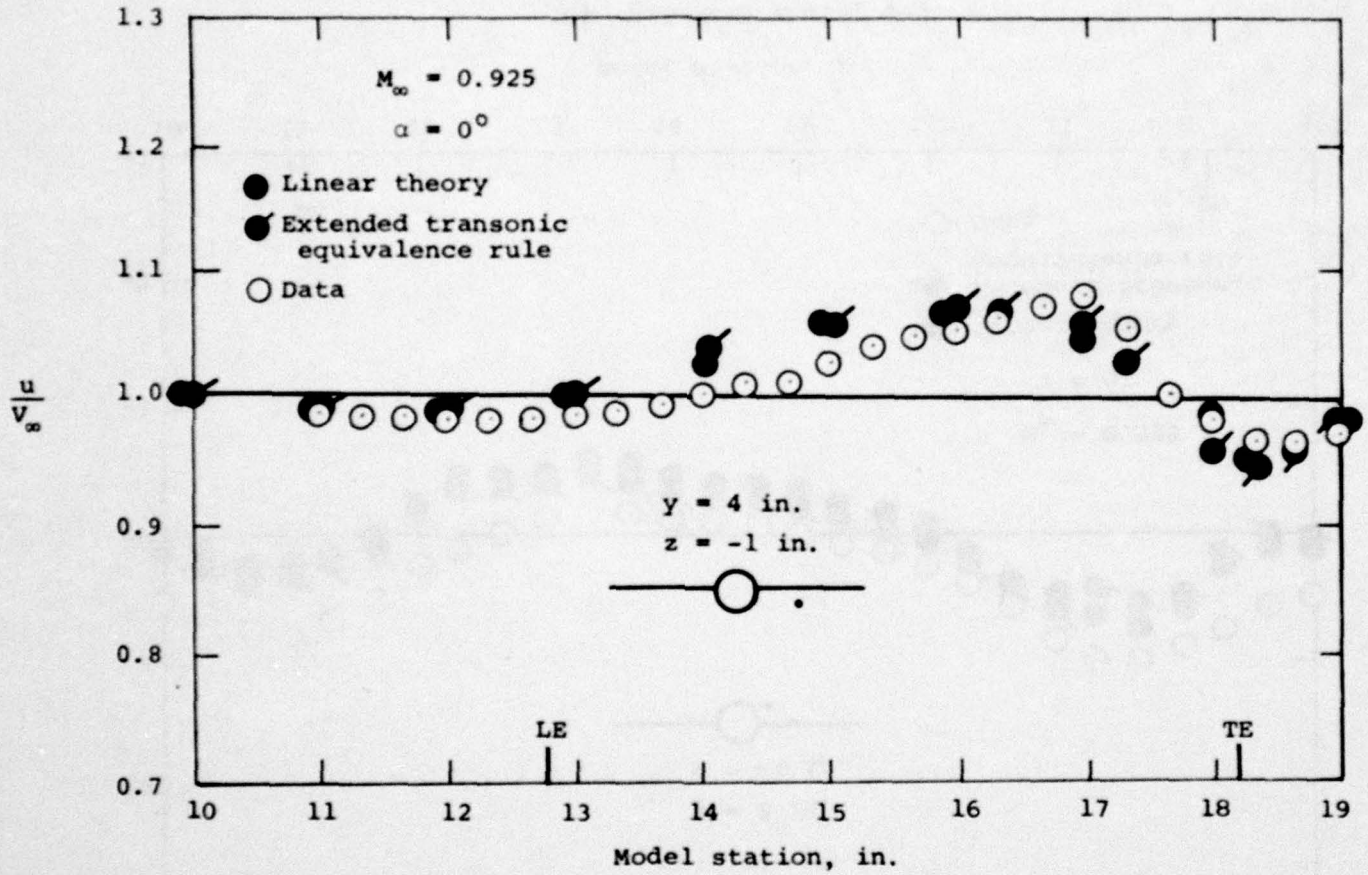

(a) Axial velocity ratio.

Figure 14.- Comparison of measured and theoretical flow field quantities for wing-body combination: $\alpha = 0^\circ$, $M_\infty = 0.925$, y = 4 in., z = -1 in.

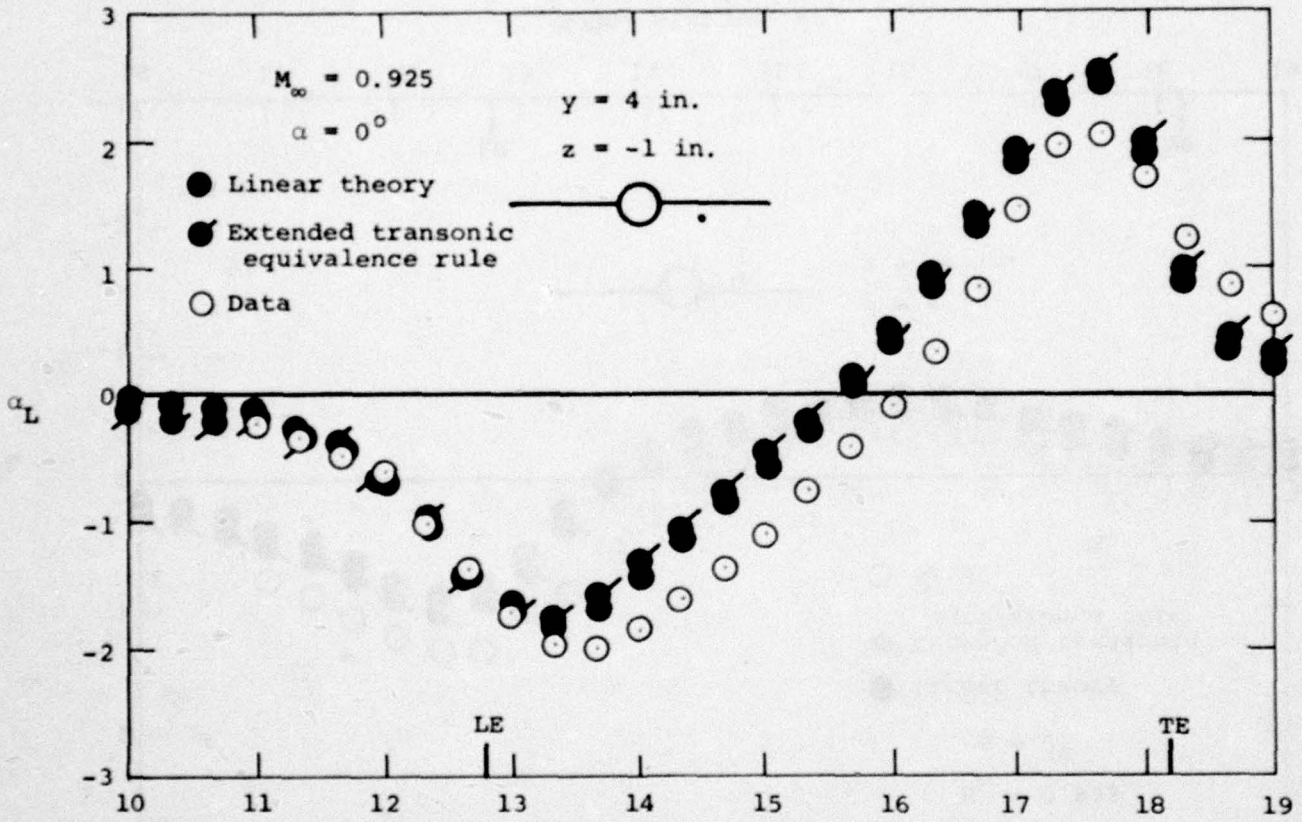

(b) Upwash angle, deg.

Figure 14.- Continued.

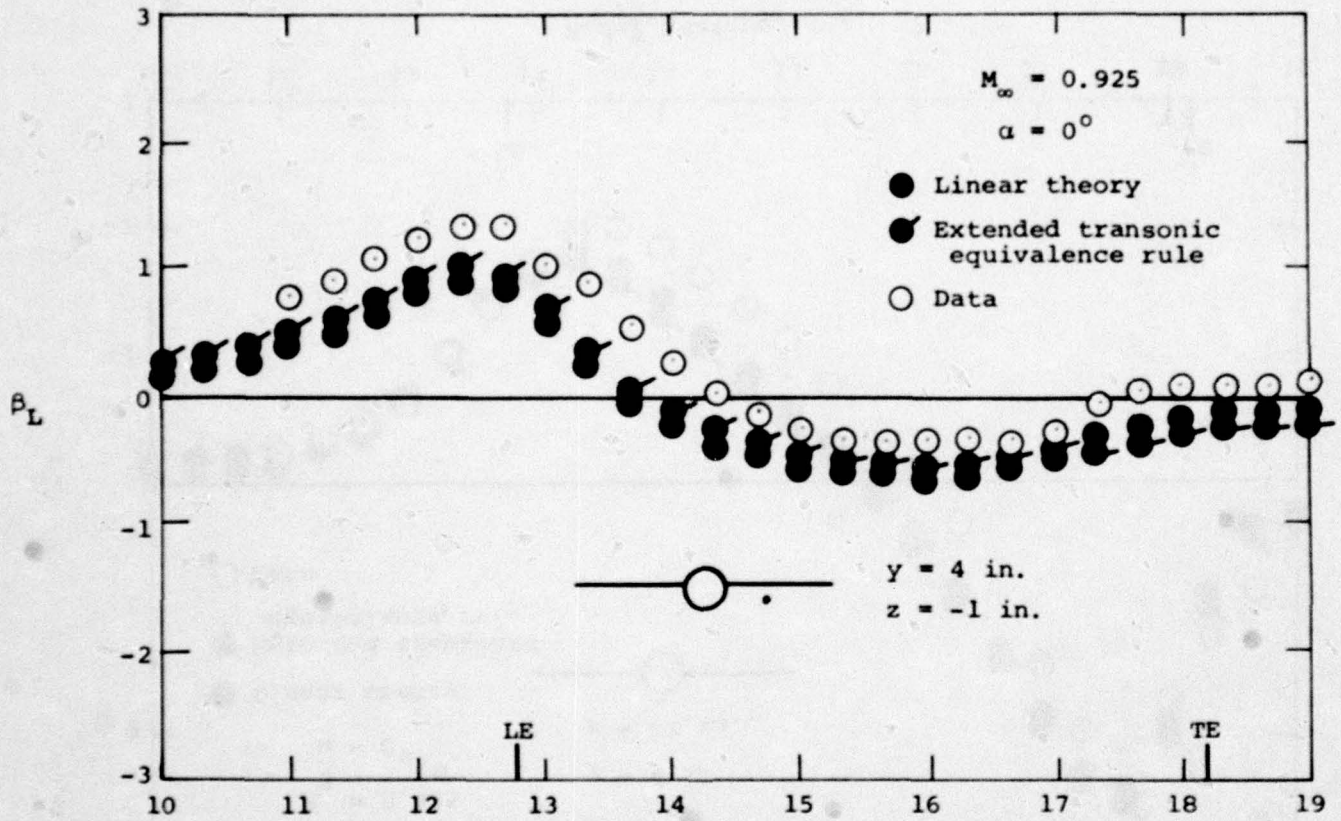

(c) Sidewash angle, deg.

Figure 14.- Concluded.

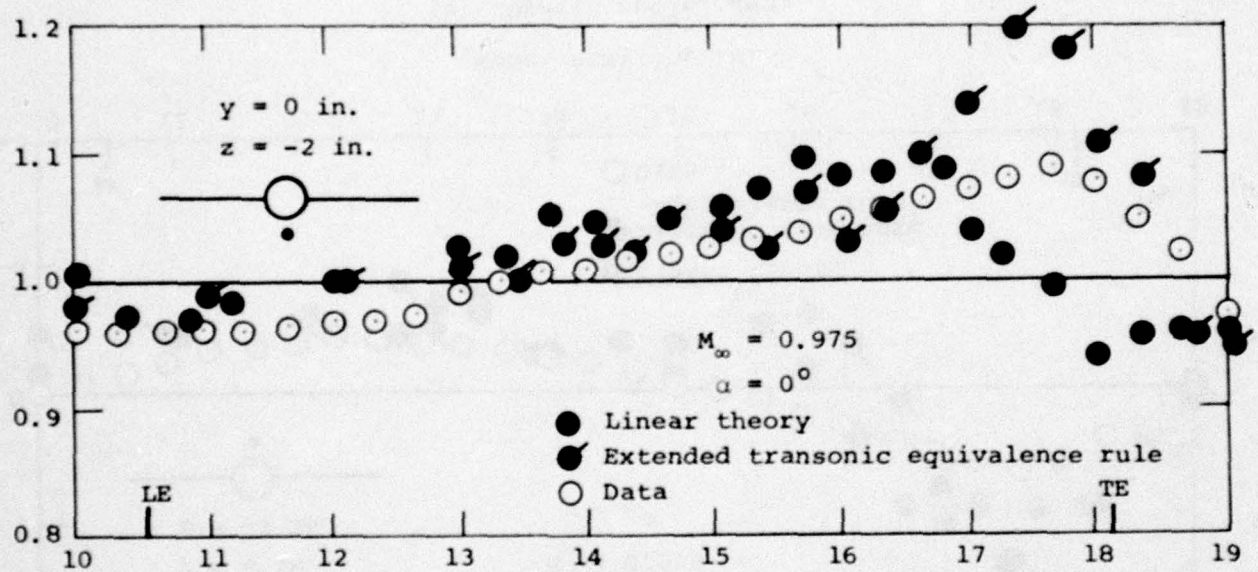

(a) Axial velocity ratio.

Figure 15.- Comparison of measured and theoretical flow field quantities for wing-body combination; $\alpha = 0^\circ$, $M_\infty = 0.975$, y = 0 in., z = -2 in.

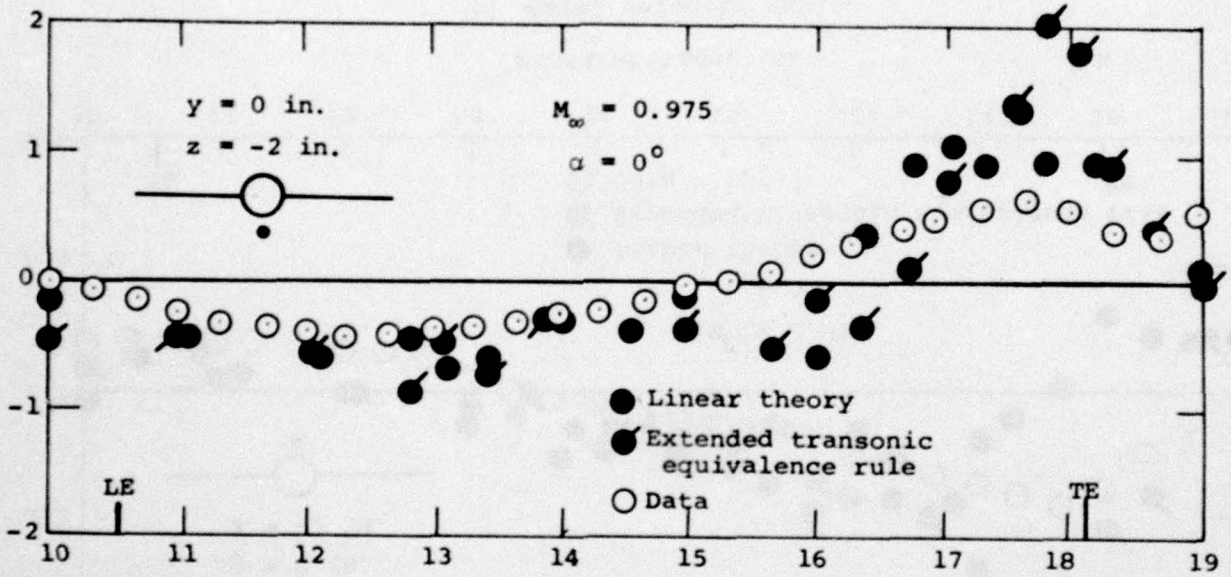

(b) Upwash angle, deg.

Figure 15.- Continued.

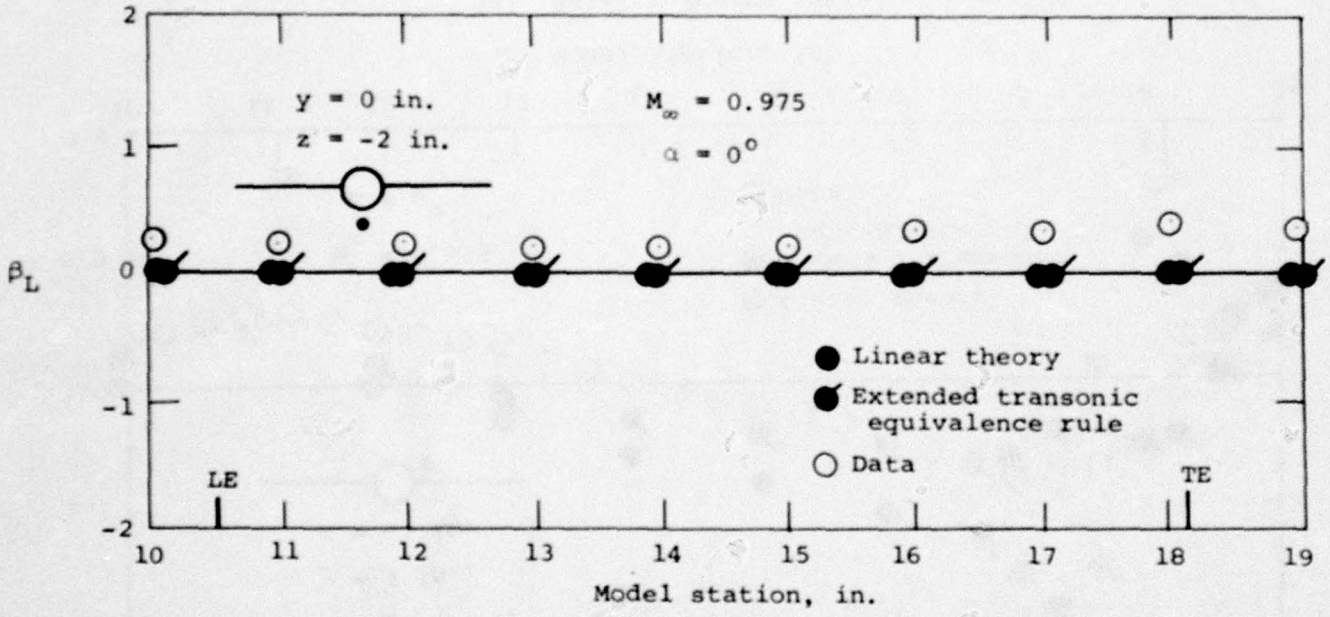

(c) Sidewash angle, deg.

Figure 15.- Concluded.

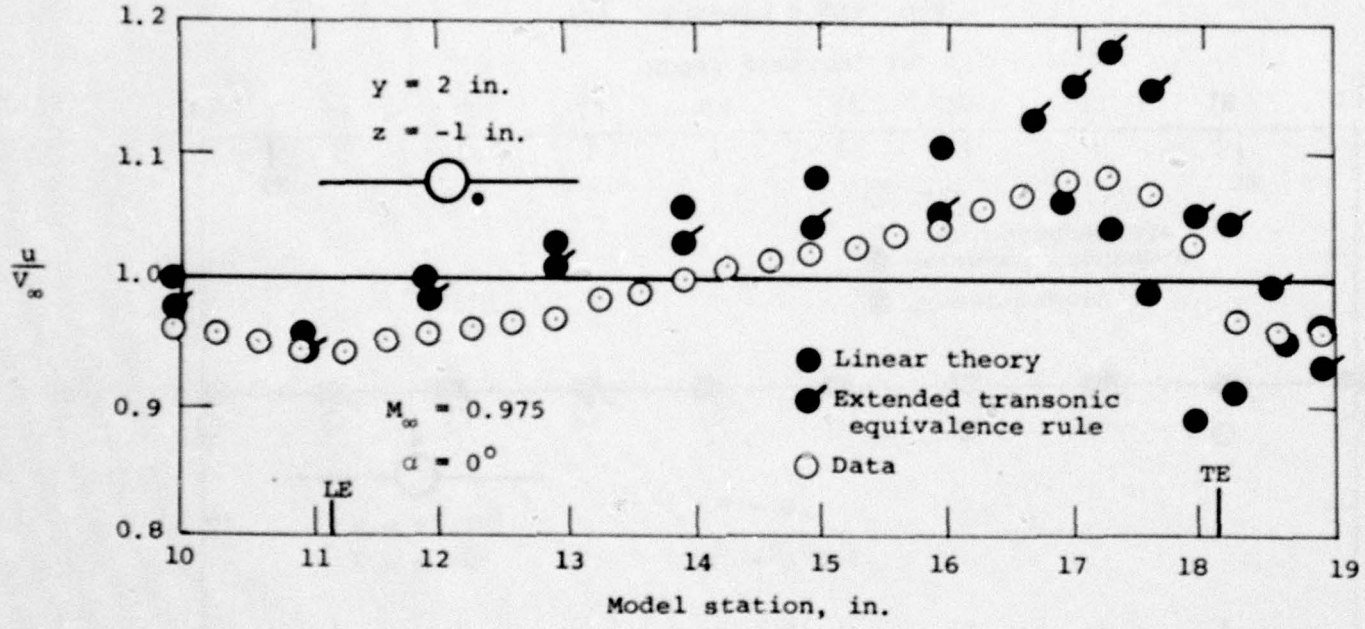

(a) Axial velocity ratio.

Figure 16.- Comparison of measured and theoretical flow field quantities for wing-body combination; $\alpha = 0^\circ$, $M_\infty = 0.975$, y = 2 in., z = -1 in.

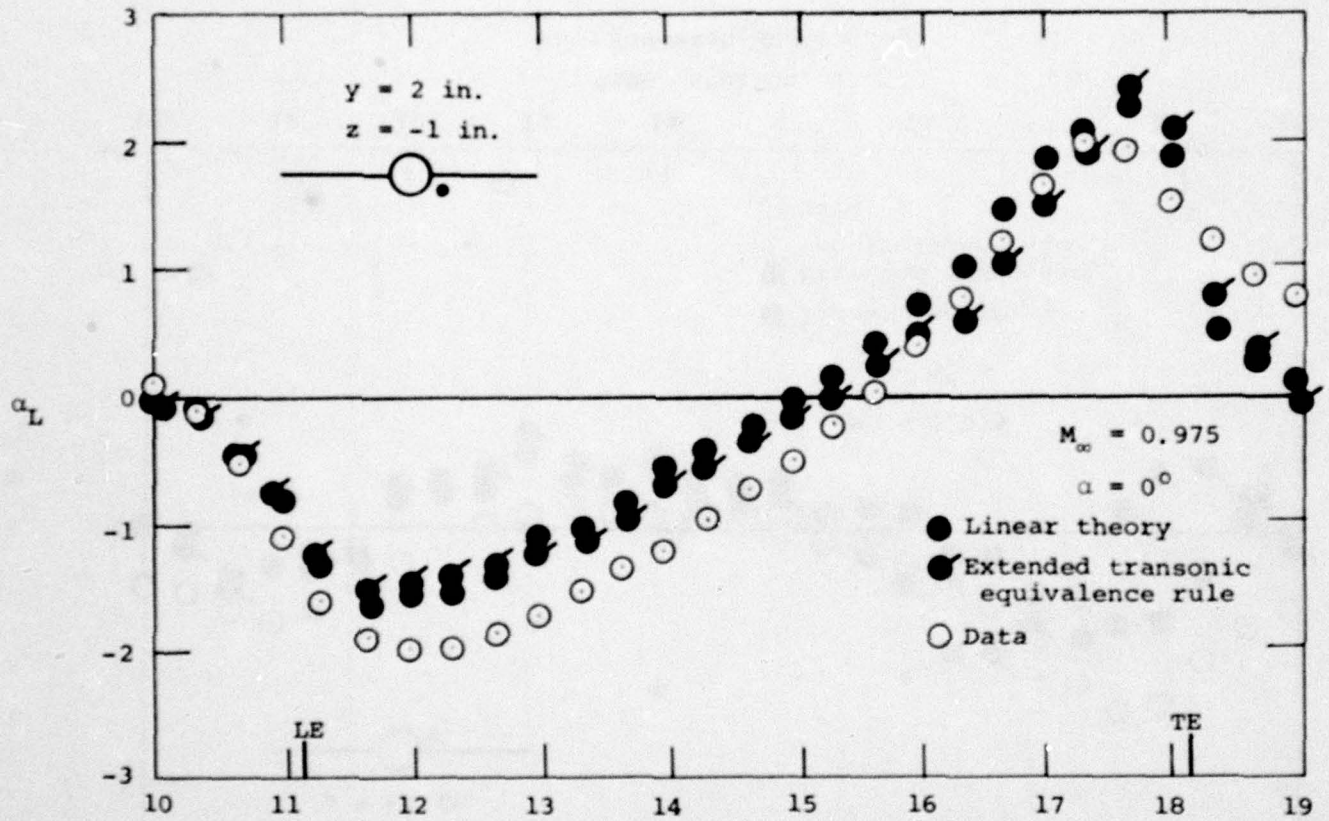

(b) Upwash angle, deg.

Figure 16.- Continued.

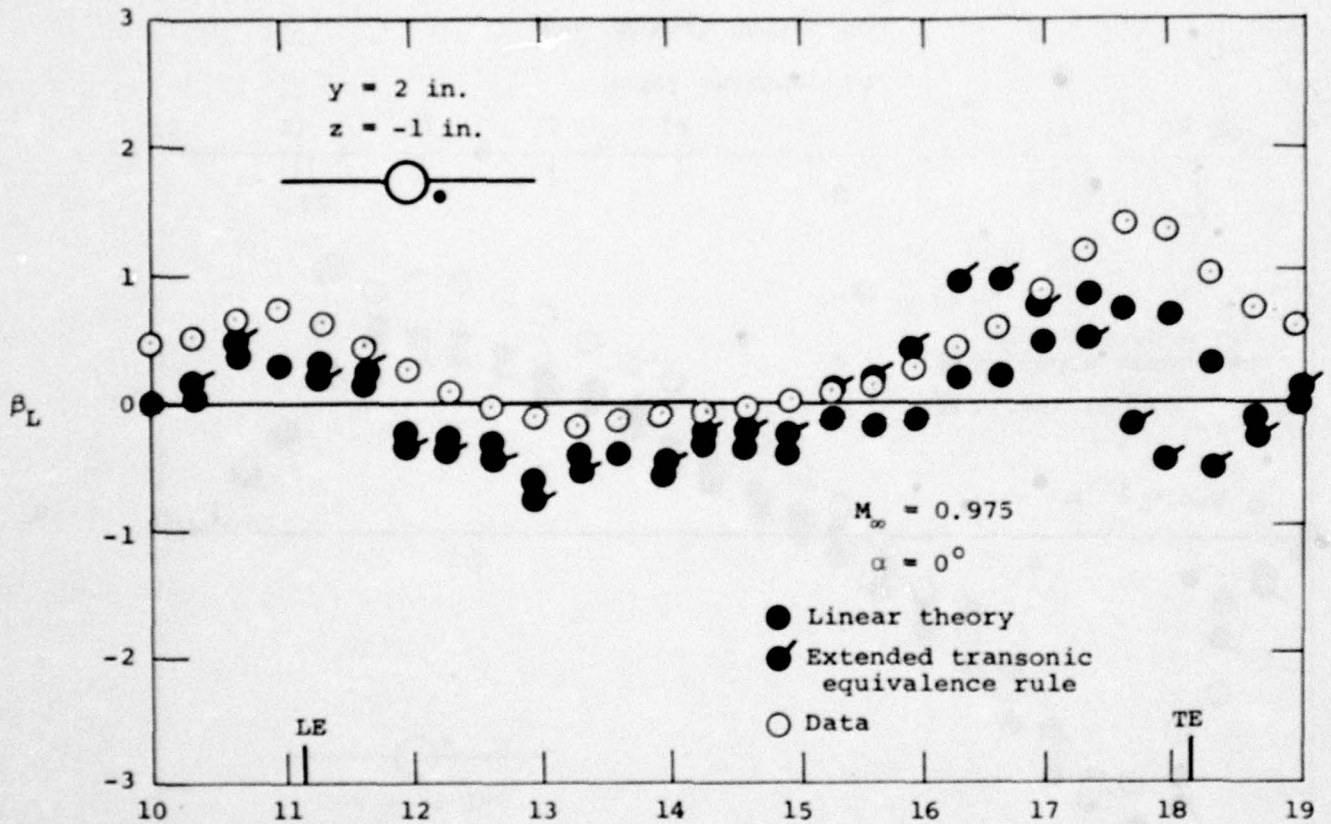

(c) Sidewash angle, deg.

Figure 16.- Concluded.

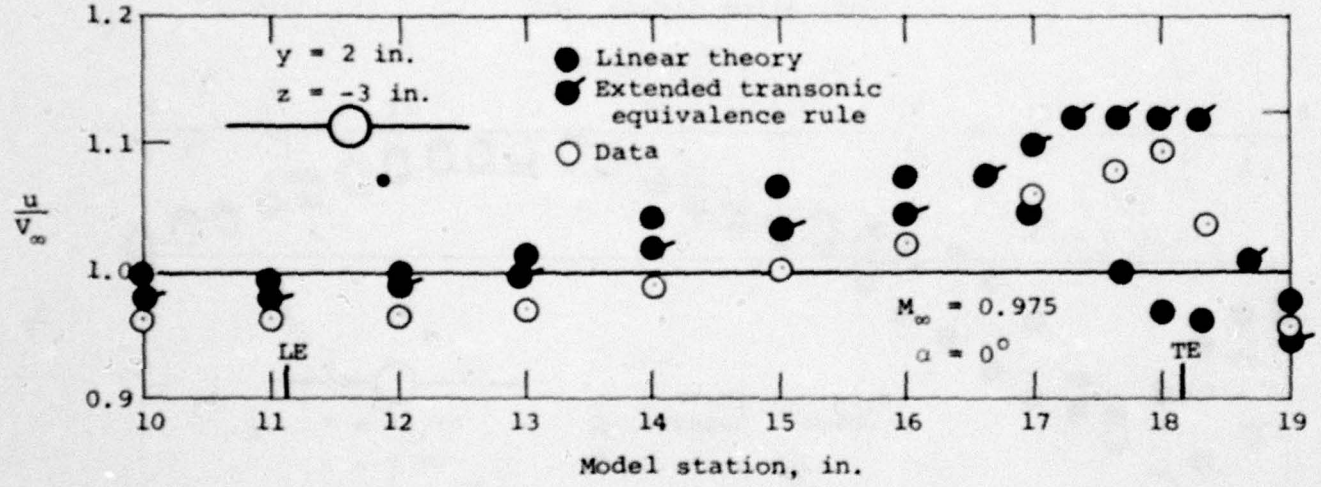

(a) Axial velocity ratio.

Figure 17.- Comparison of measured and theoretical flow field quantities for wing-body combination; $\alpha = 0^\circ$, $M_\infty = 0.975$, y = 2 in., z = -3 in.

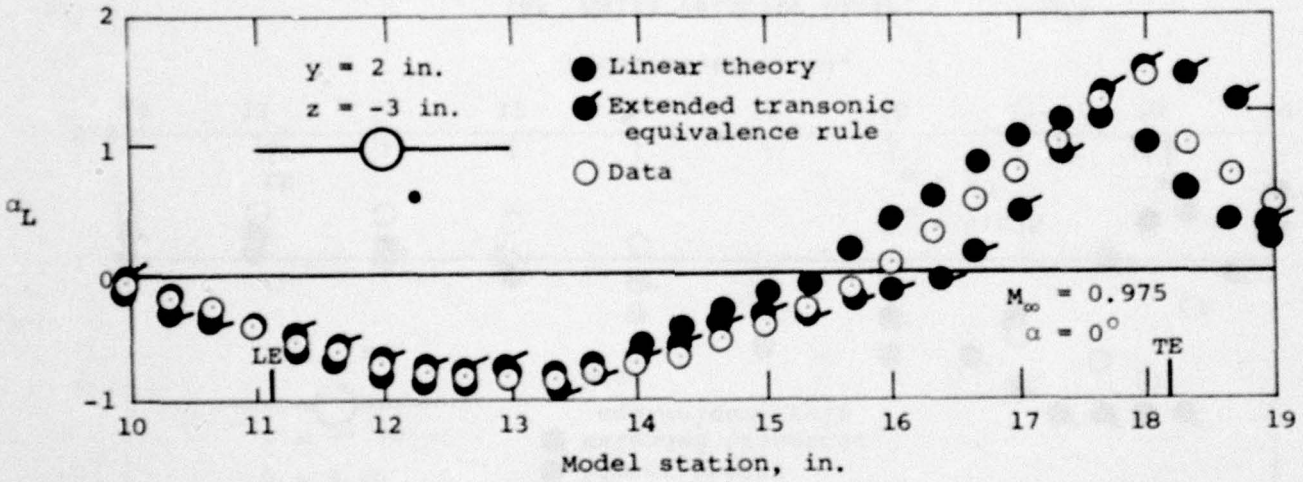

(b) Upwash angle, deg.

Figure 17.- Continued.

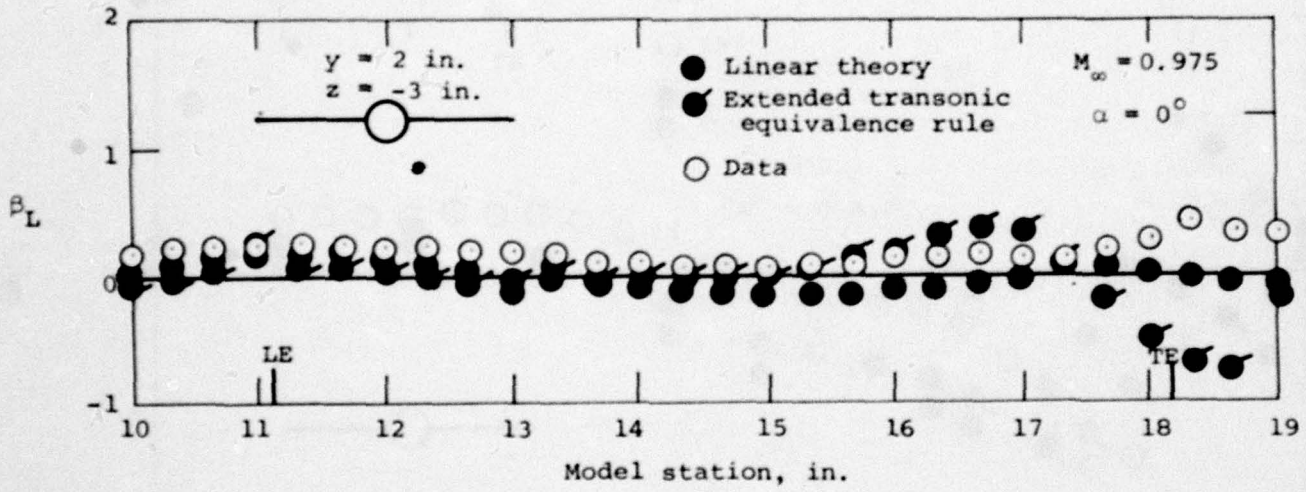

(c) Sidewash angle, deg.

Figure 17.- Concluded.

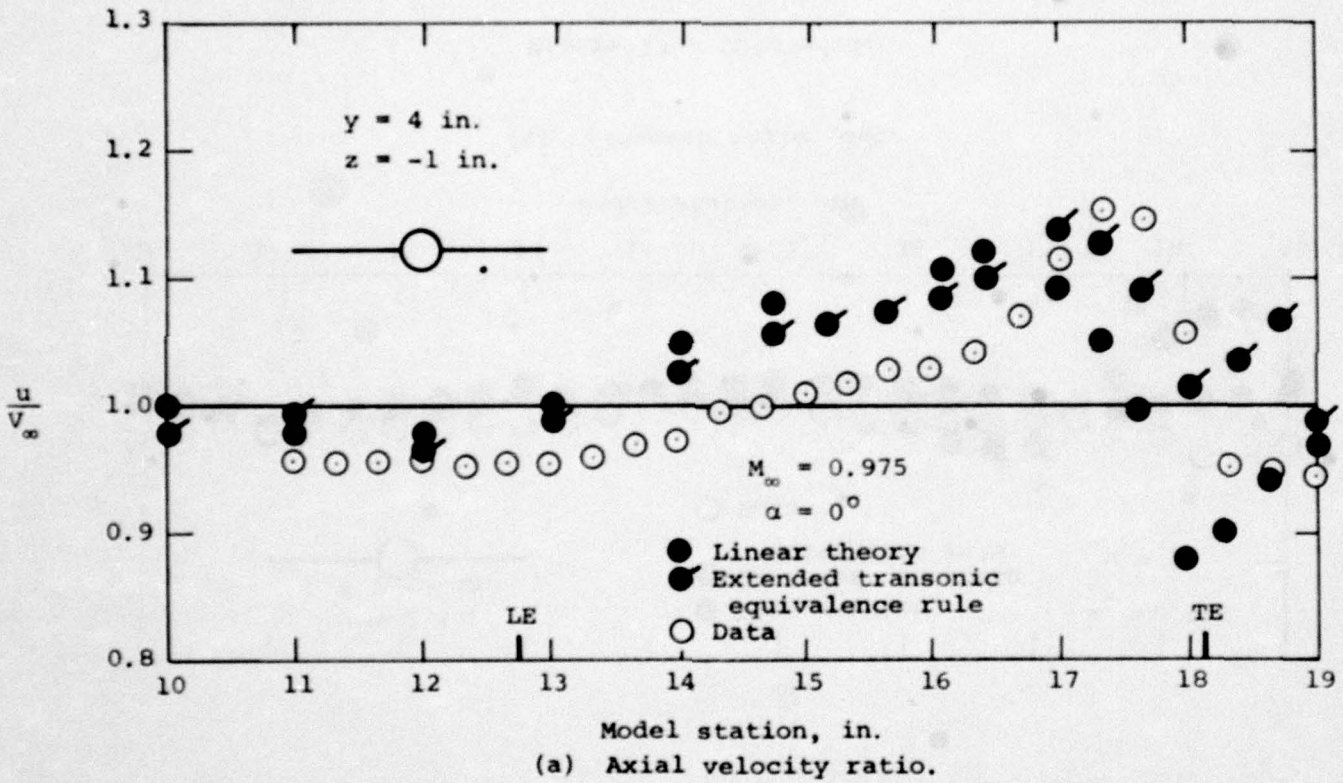

(a) Axial velocity ratio.

Figure 18.- Comparison of measured and theoretical flow field quantities for wing-body combination; $\alpha = 0^\circ$, $M_\infty = 0.975$, y = 4 in., z = -1 in.

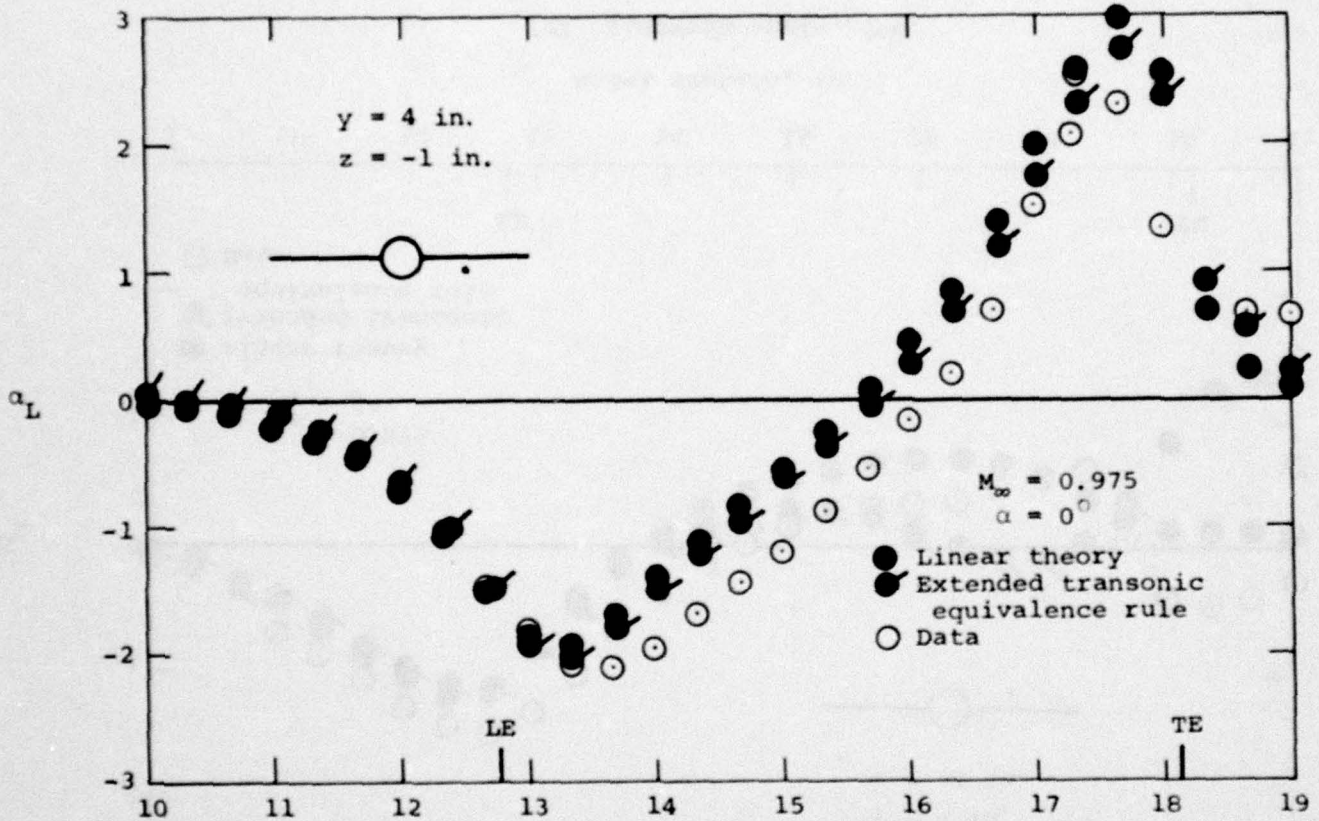

(b) Upwash angle, deg

Figure 18. - Continued.

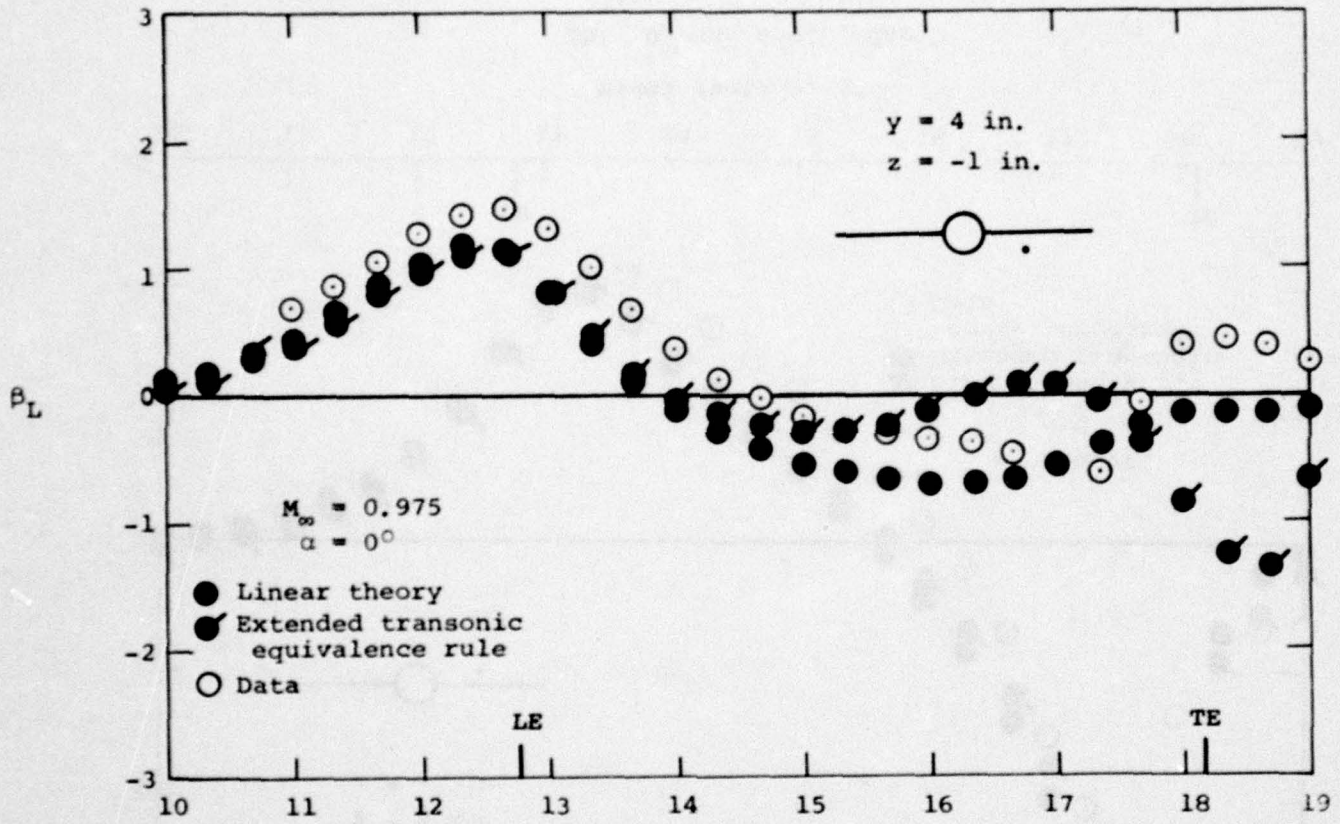

(c) Sidewash angle, deg.

Figure 18.- Concluded.

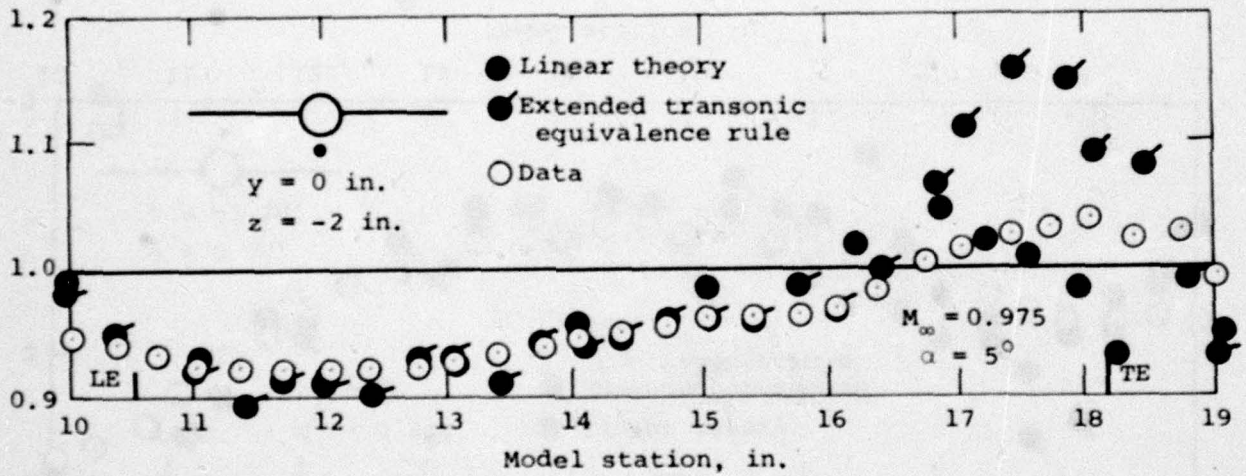

(a) Axial velocity ratio.

Figure 19.- Comparison of measured and theoretical flow field quantities for wing-body combination; $\alpha = 5^\circ$, $M_\infty = 0.975$, y = 0 in., z = -2 in.

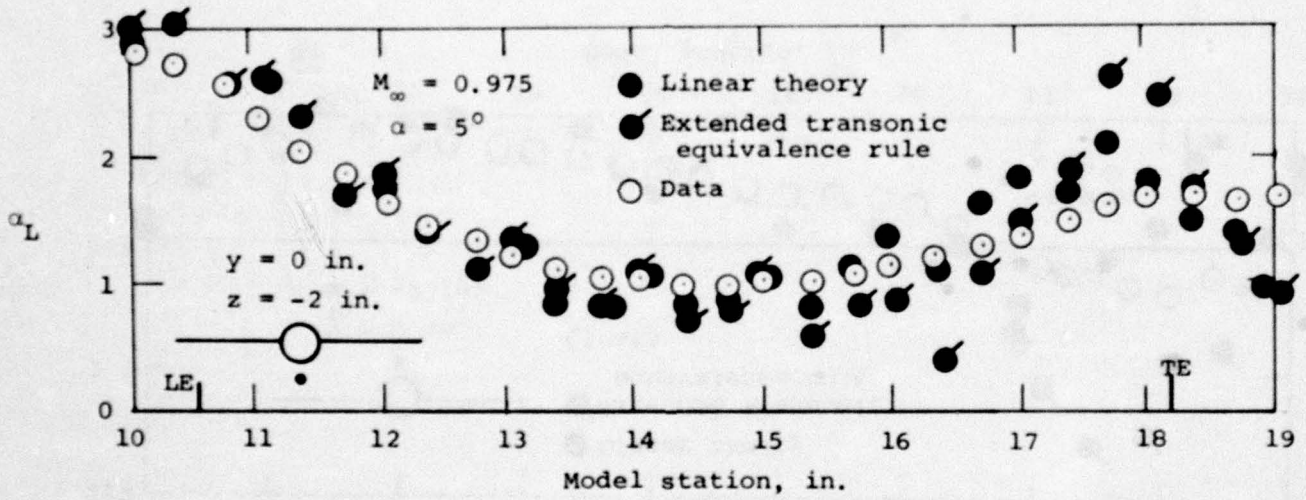

(b) Upwash angle, deg.

Figure 19.- Continued.

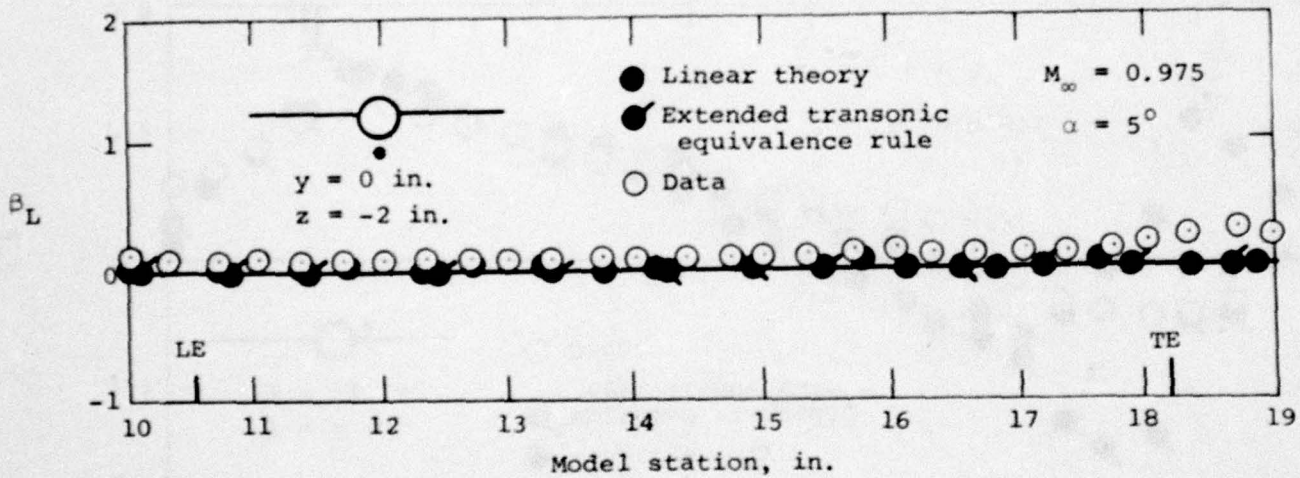

(c) Sidewash angle, deg.

Figure 19.- Concluded.

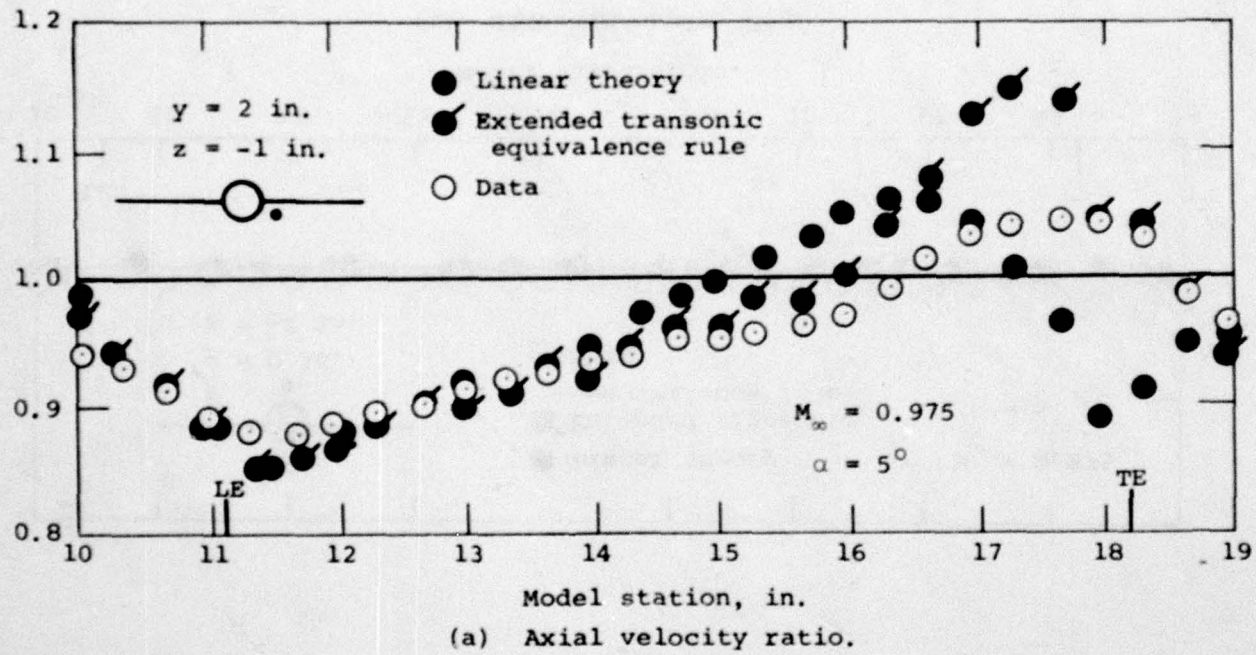

(a) Axial velocity ratio.

Figure 20.- Comparison of measured and theoretical flow field quantities for wing-body combination: $\alpha = 5^\circ$, $M_\infty = 0.975$, y = 2 in., z = -1 in.

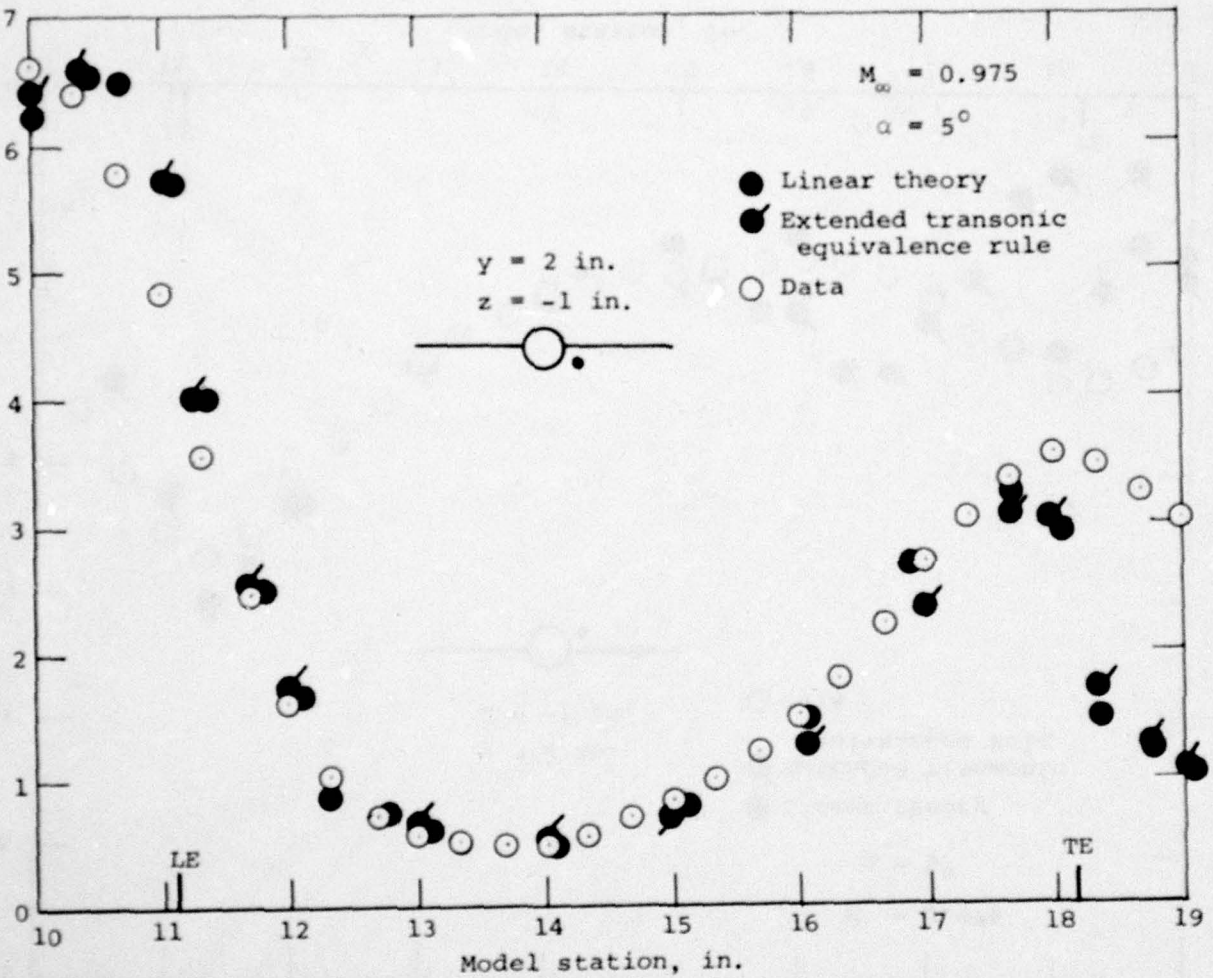

(b) Upwash angle, deg.

Figure 20.- Continued.

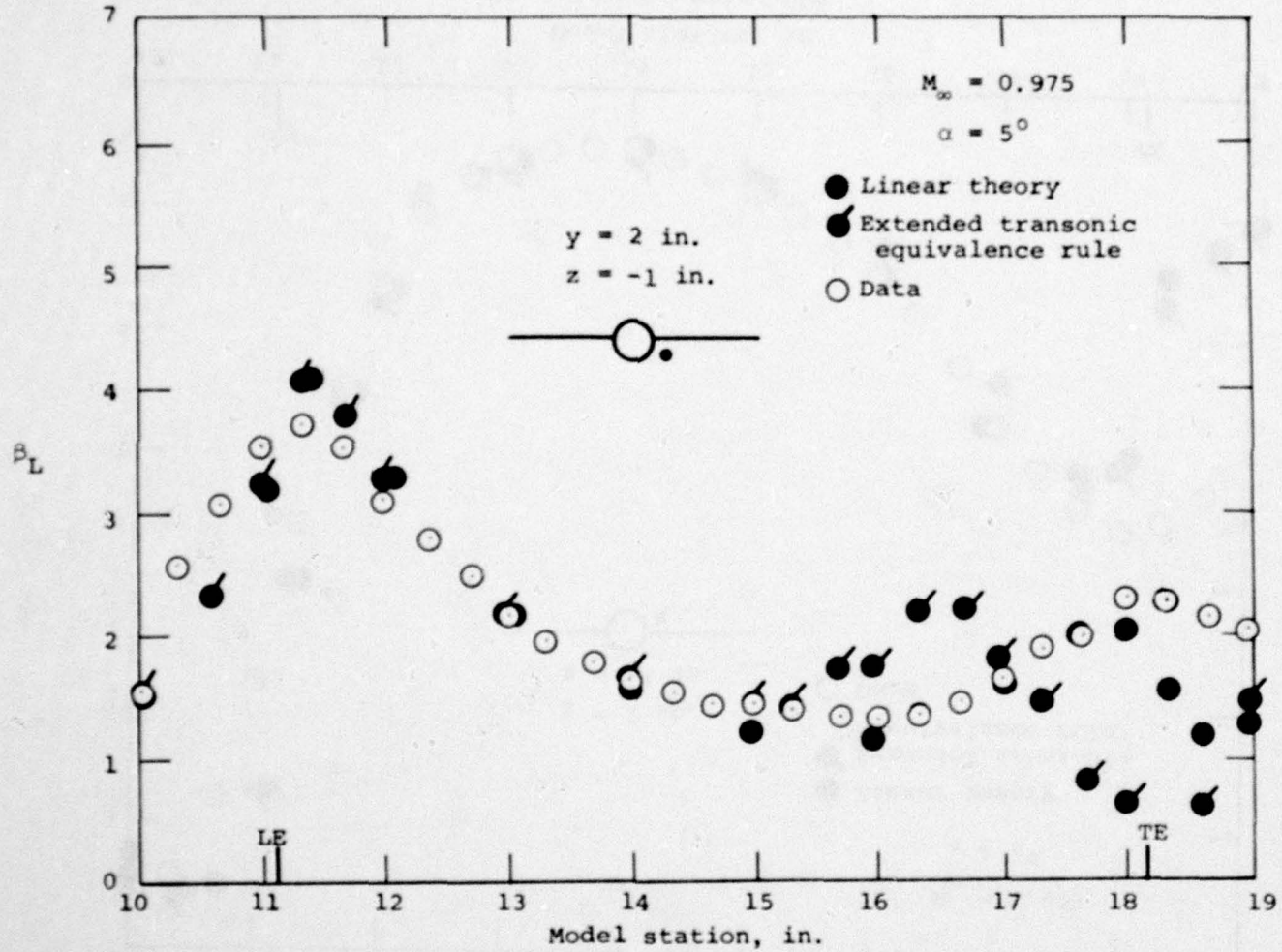

(c) Sidewash angle, deg.

Figure 20.- Concluded.

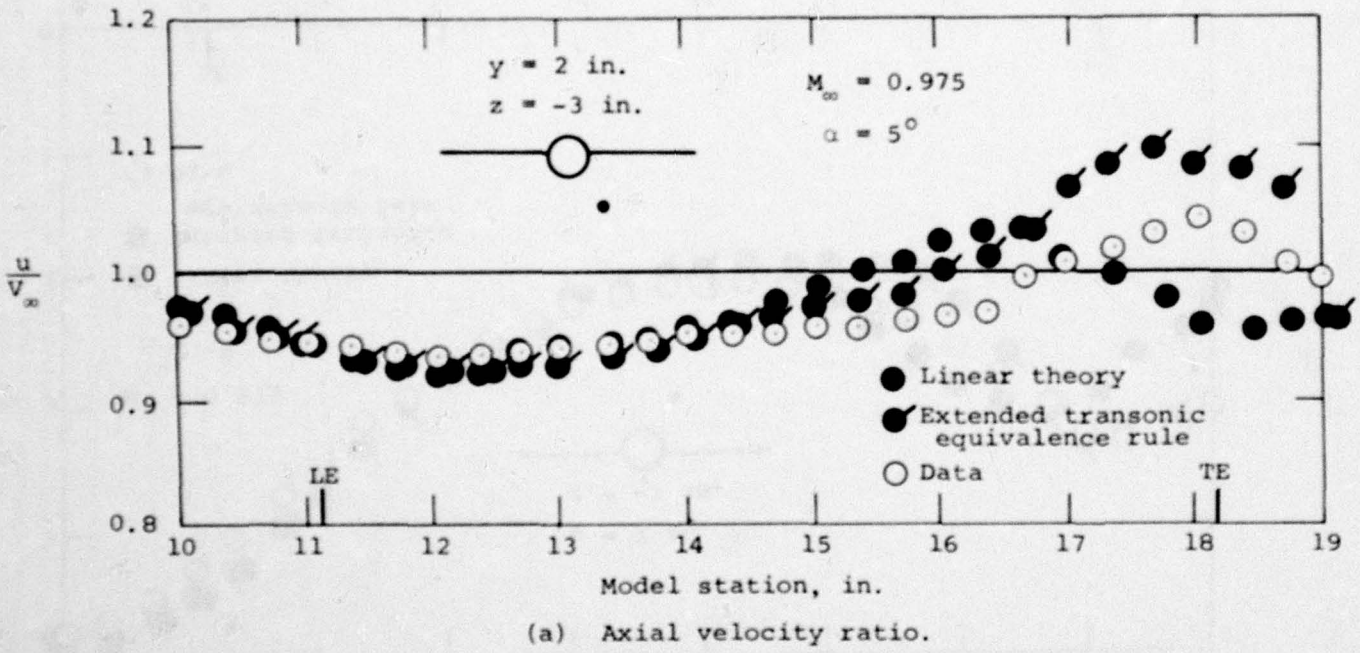

(a) Axial velocity ratio.

Figure 21.- Comparison of measured and theoretical flow field quantities for wing-body combination: $\alpha = 5^\circ$, $M_\infty = 0.975$, y = 2 in., z = -3 in.

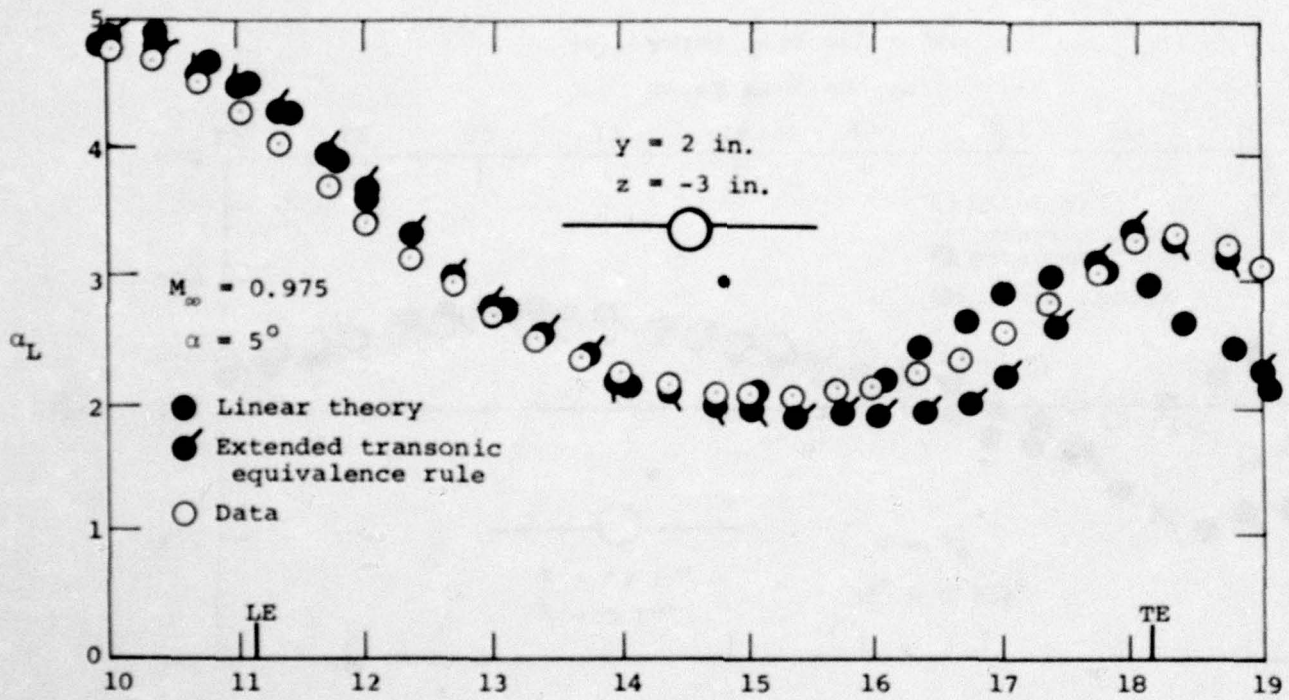

(b) Upwash angle, deg.

Figure 21.- Continued.

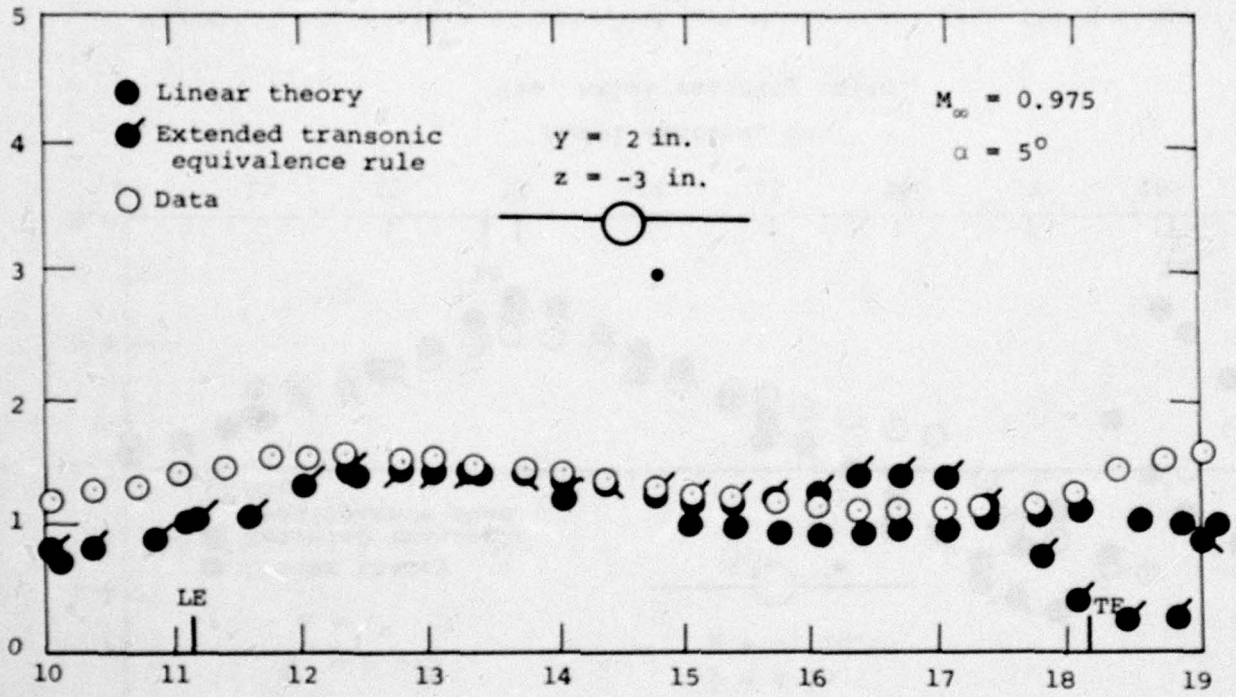

(c) Sidewash angle, deg.

Figure 21.- Concluded.

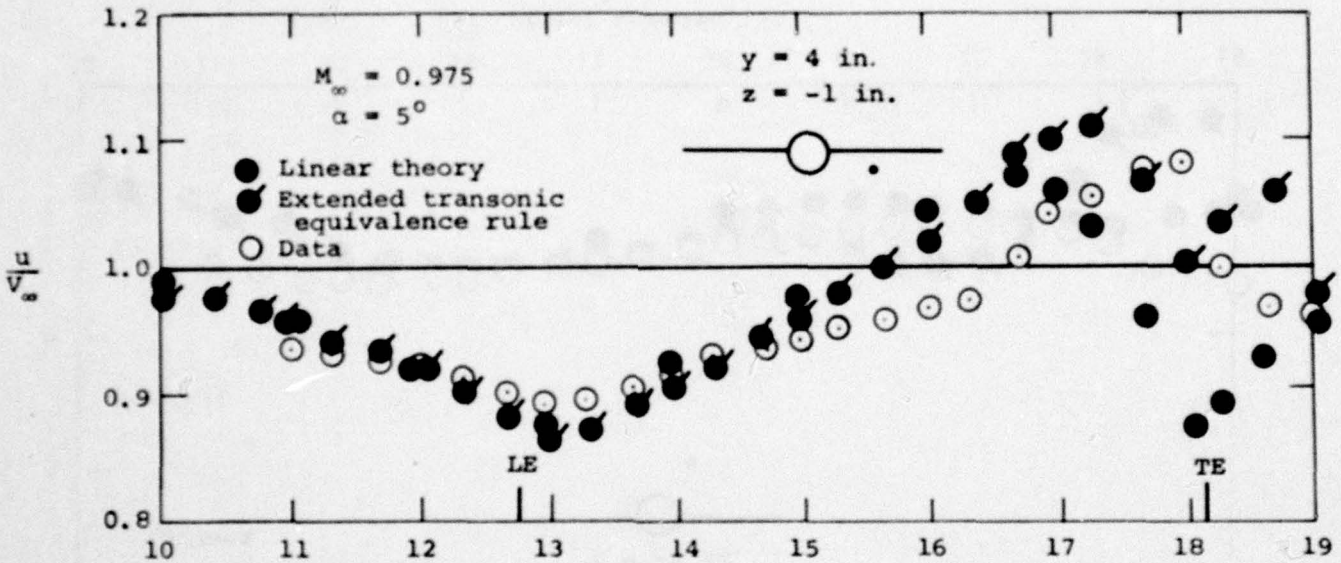

(a) Axial velocity ratio.

Figure 22.- Comparison of measured and theoretical flow field quantities for wing-body combination; $\alpha = 5^\circ$, $M_\infty = 0.975$, y = 4 in., z = -1 in.

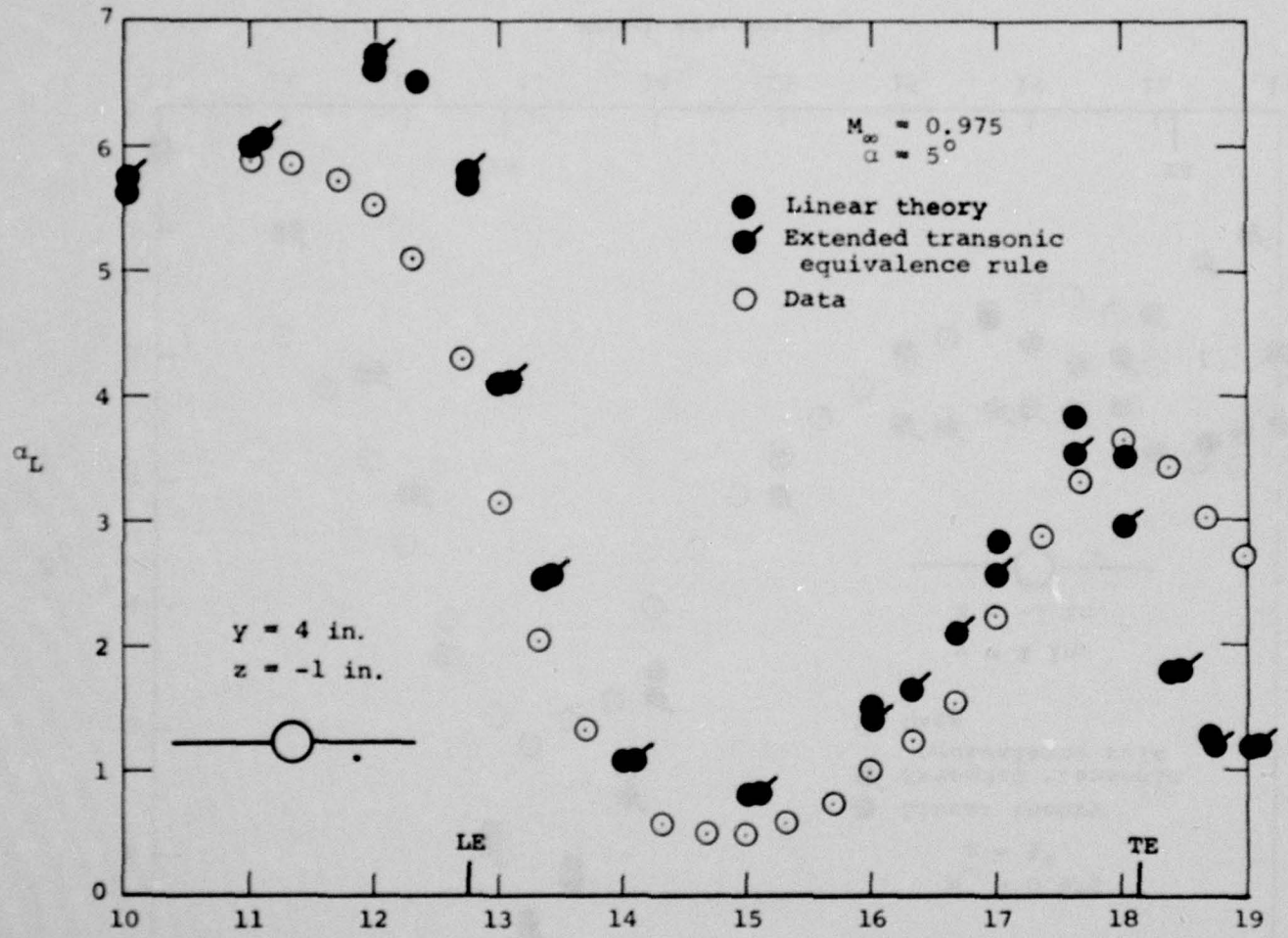

(b) Upwash angle, deg.

Figure 22.- Continued.

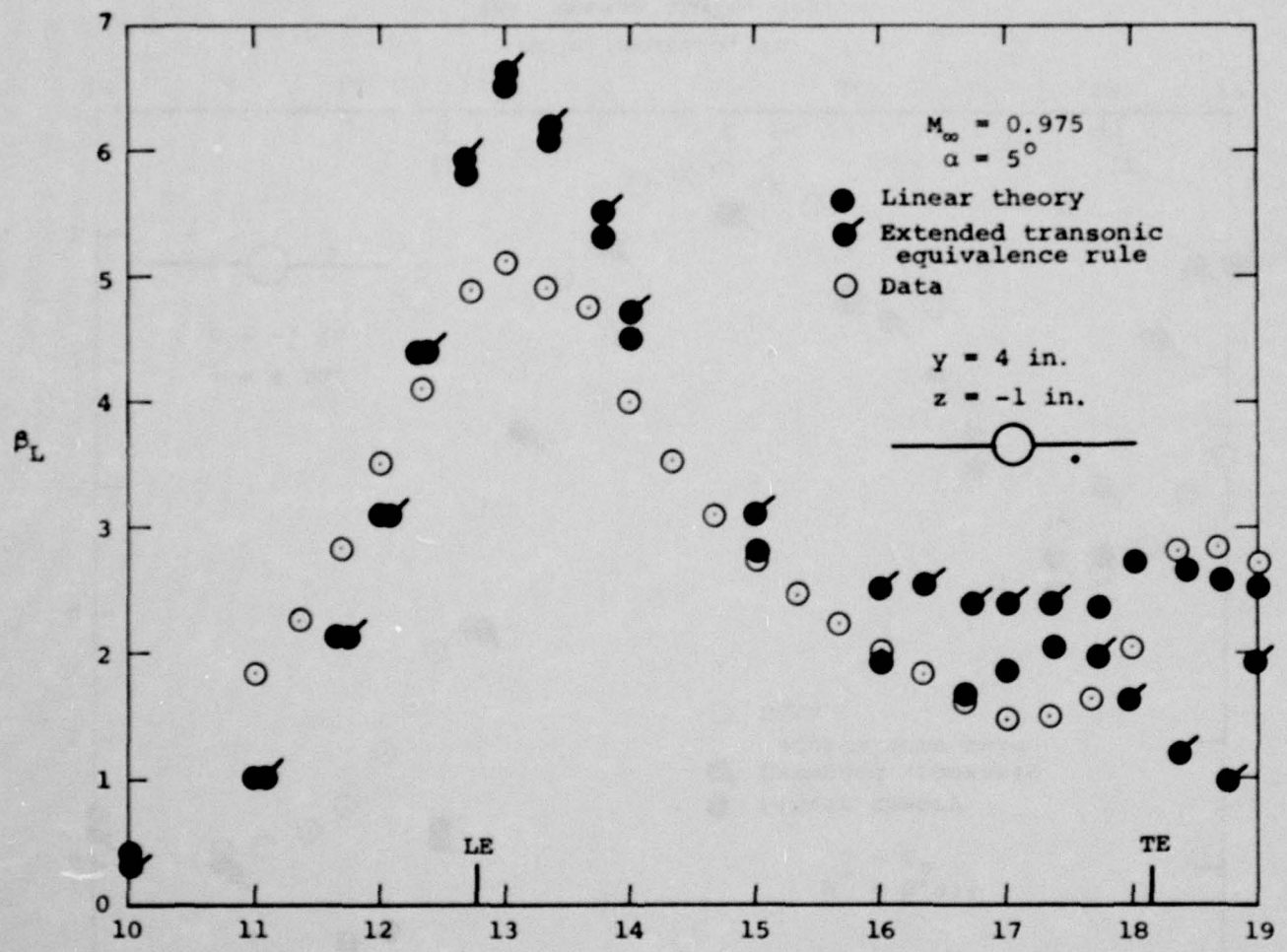

(c) Sidewash angle, deg.

Figure 22.- Concluded.

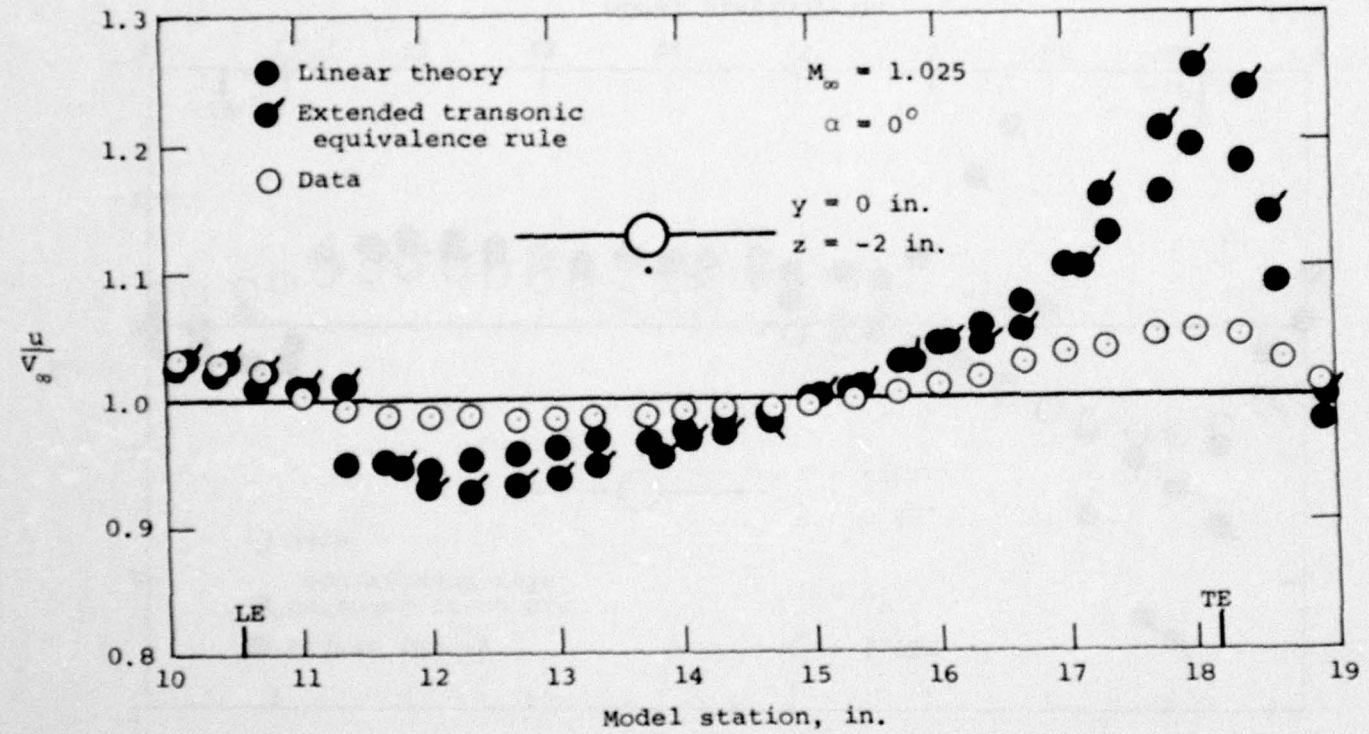

(a) Axial velocity ratio.

Figure 23.- Comparison of measured and theoretical flow field quantities for wing-body combination; α = 0°, M_∞ = 1.025, y = 0 in., z = -2 in.

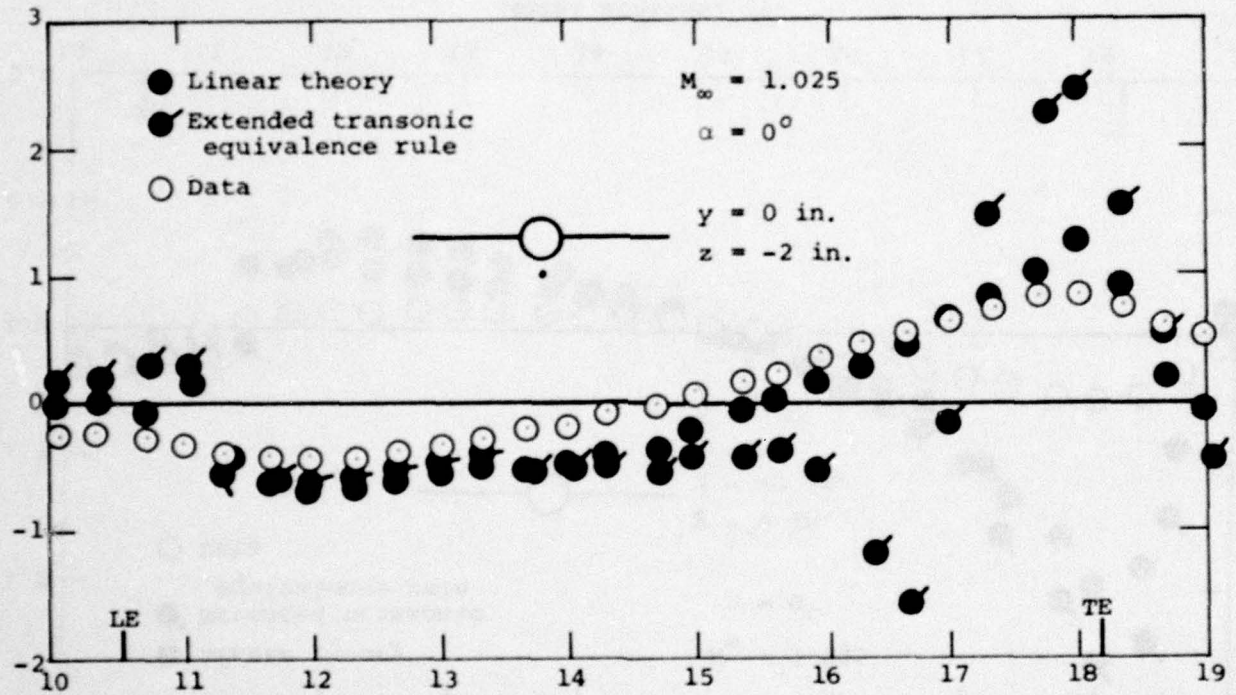

(b) Upwash angle, deg.

Figure 23.- Continued.

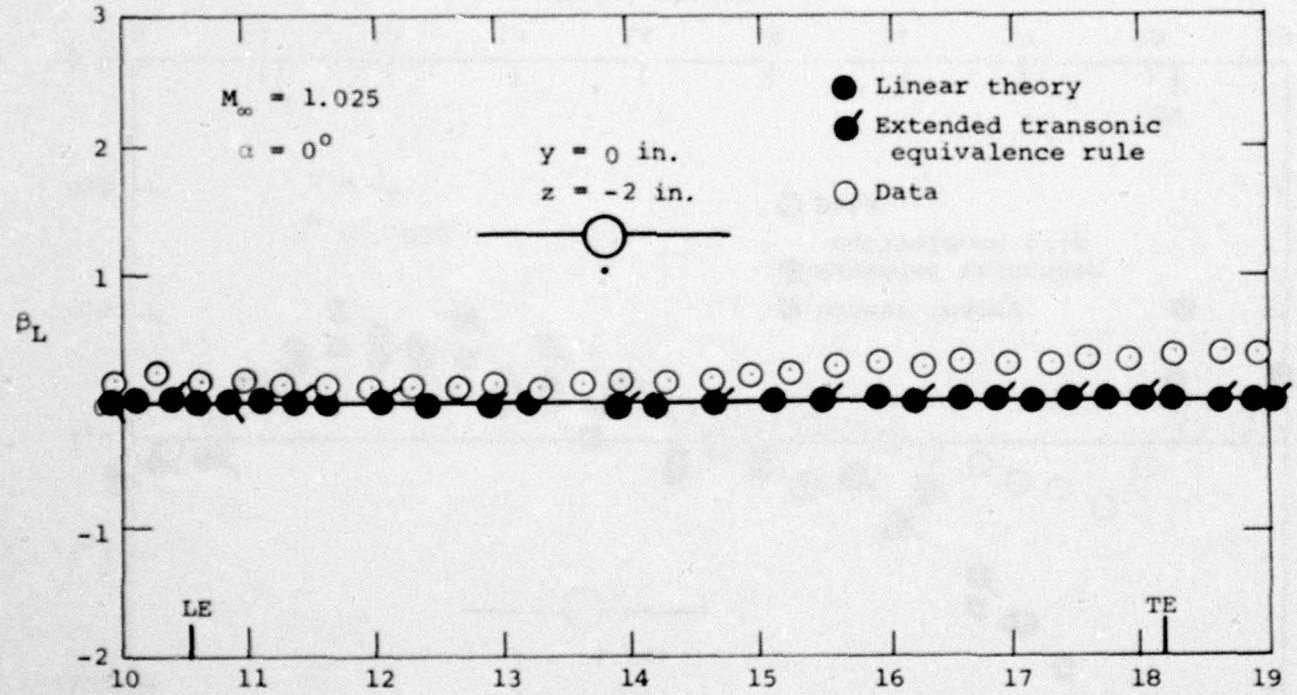

(c) Sidewash angle, deg.

Figure 23.- Concluded.

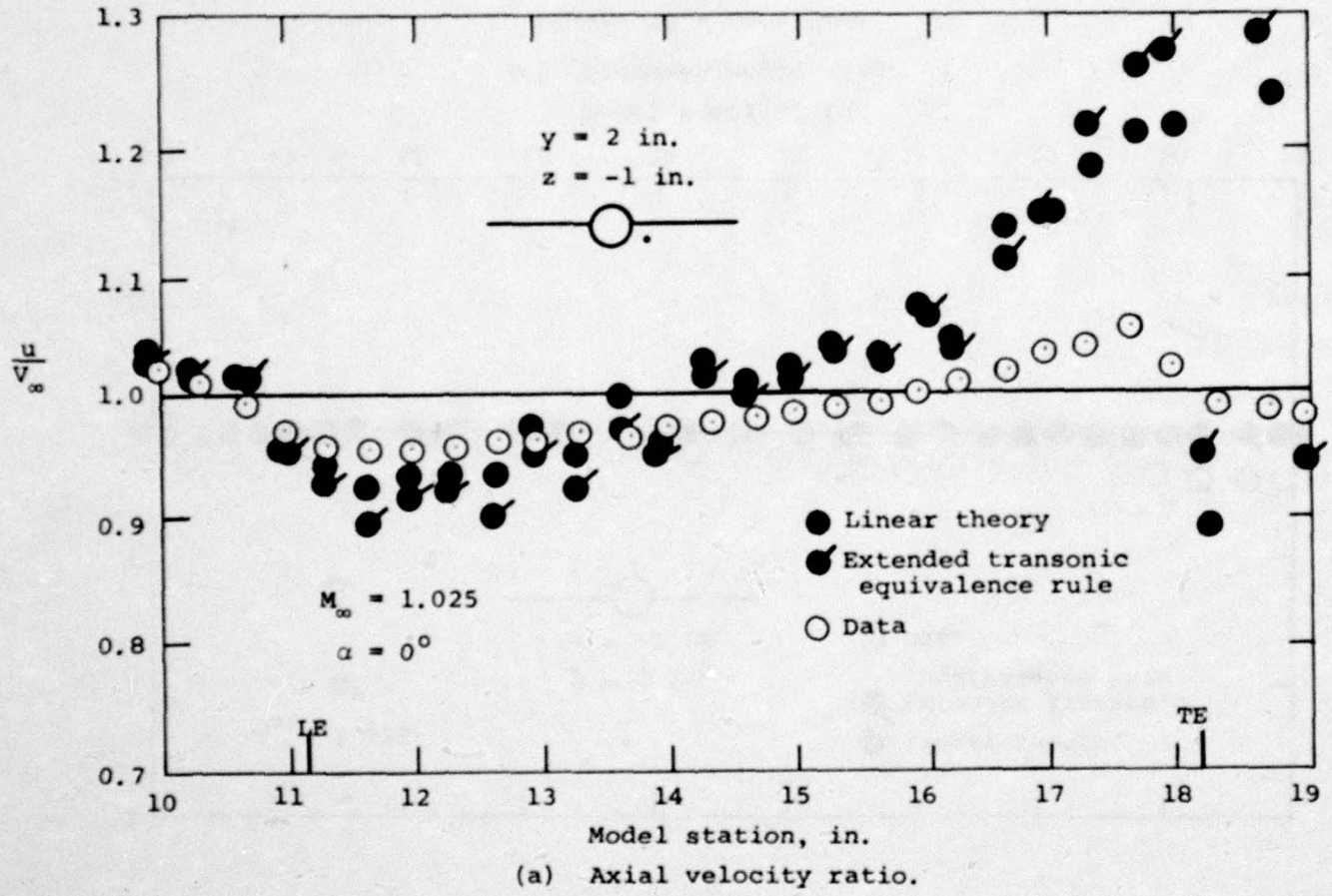

(a) Axial velocity ratio.

Figure 24.- Comparison of measured and theoretical flow field quantities for wing-body combination; $\alpha = 0^\circ$, $M_\infty = 1.025$, y = 2 in., z = -1 in.

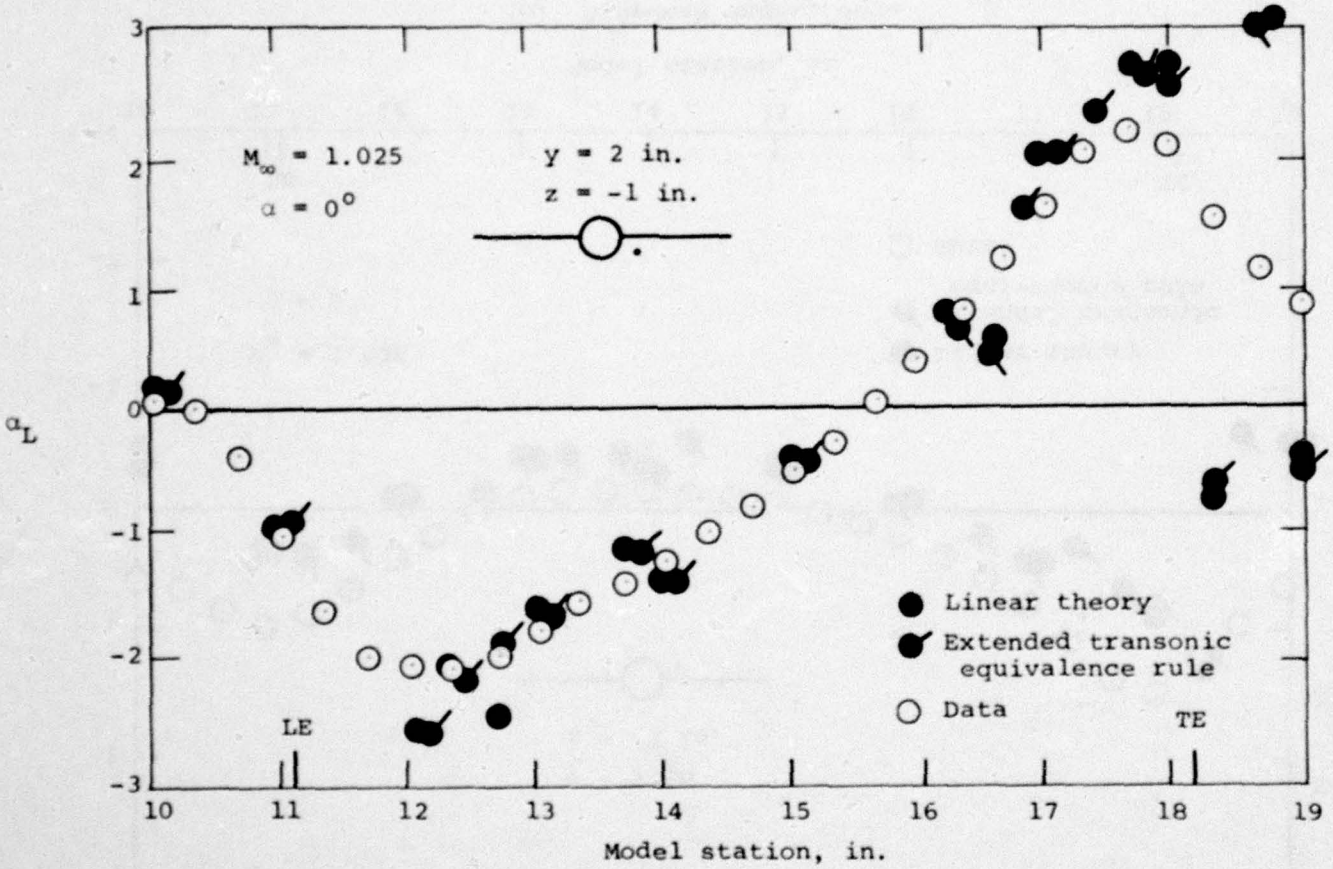

(b) Upwash angle, deg.

Figure 24.- Continued.

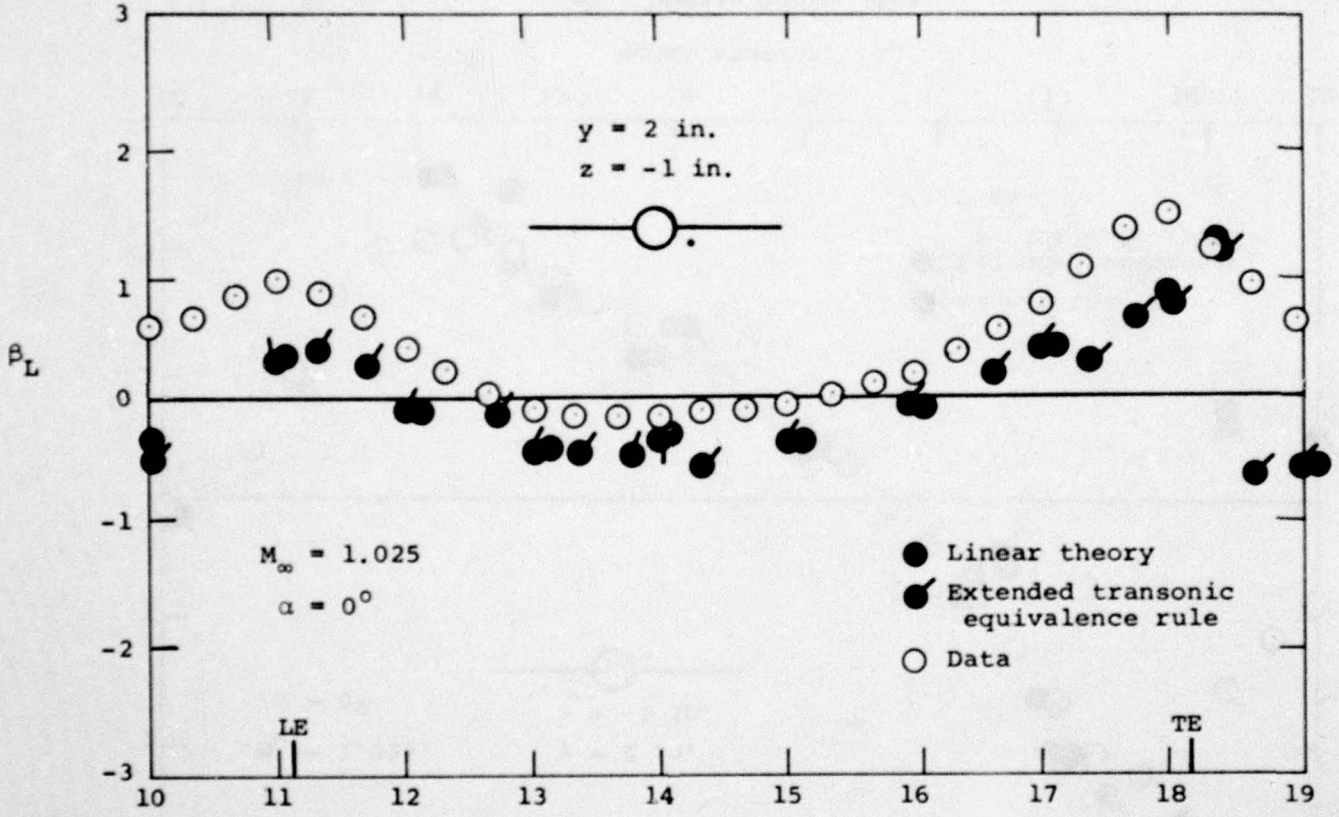

(c) Sidewash angle, deg.

Figure 24.- Concluded.

AD-A078 683 NIELSEN ENGINEERING AND RESEARCH INC MOUNTAIN VIEW CALIF F/G 20/4
THE DEVELOPMENT OF RAPID PREDICTIVE METHODS FOR THREE-DIMENSION--ETC(U)
JUL 79 A J CRISALLI , S S STAHARA F44620-75-C-0047
UNCLASSIFIED NEAR-TR-198 AFOSR-TR-79-1281 NL

2 OF 4
AD-
A078683

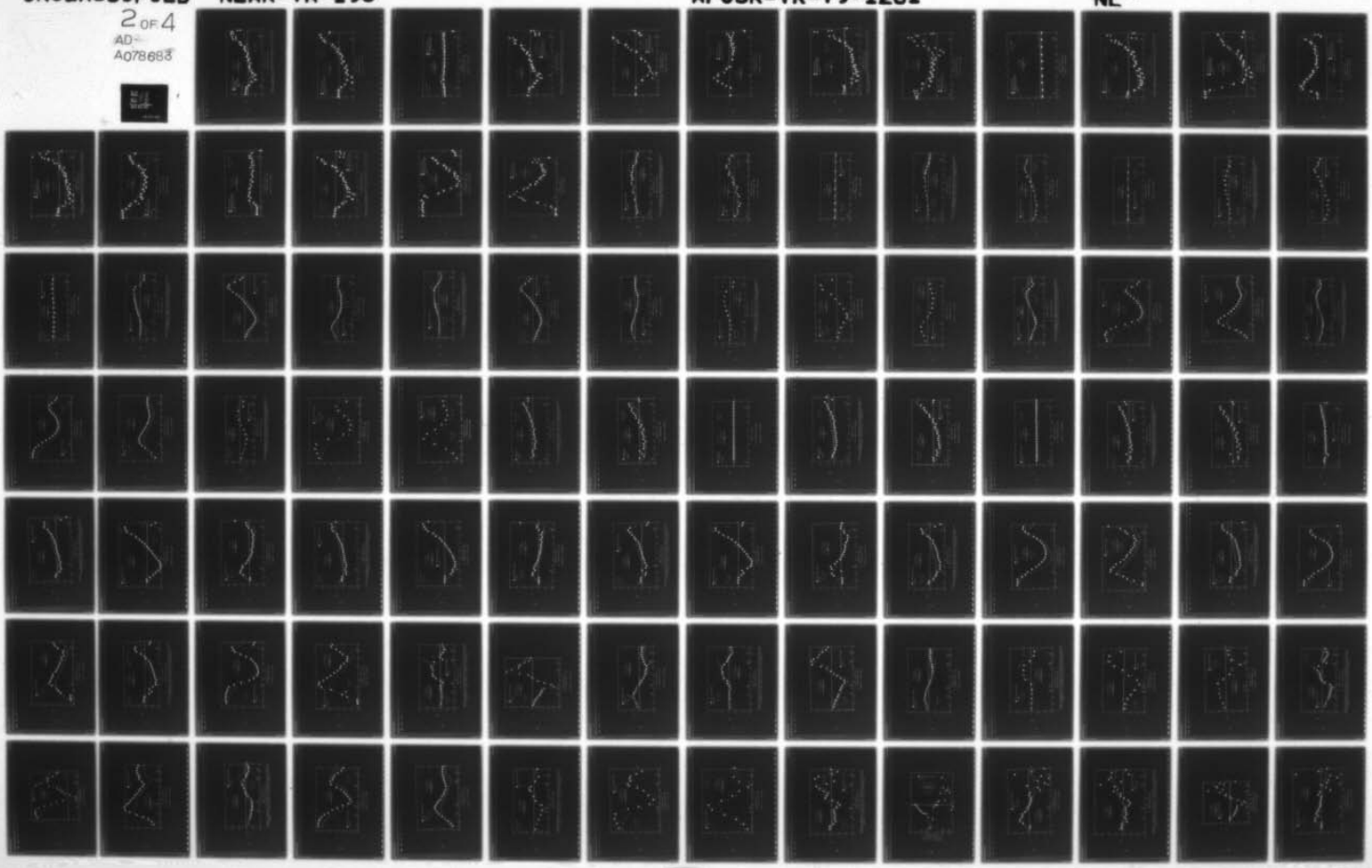

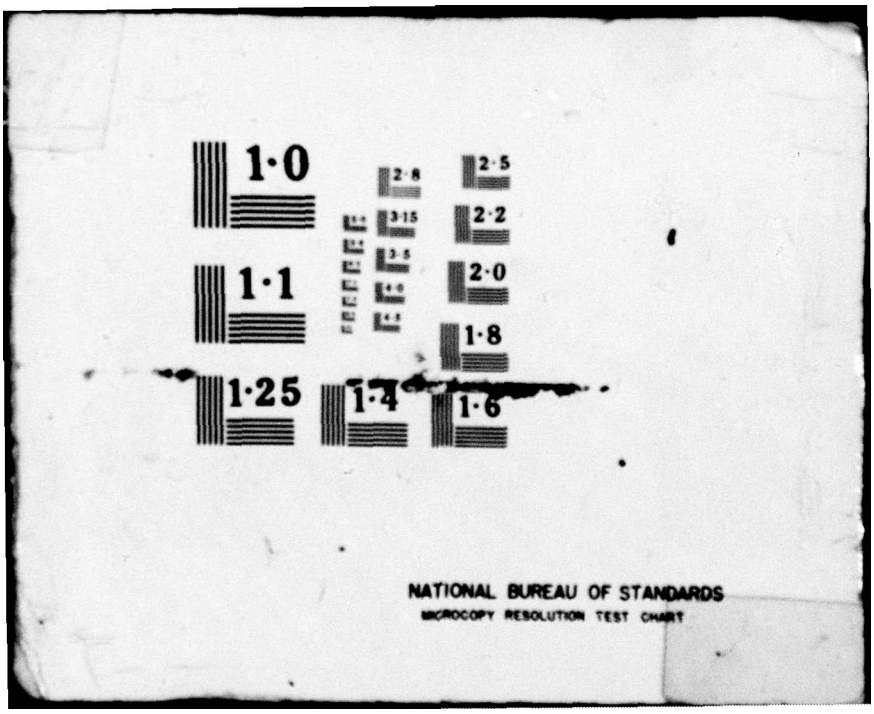
1·0
1·1
1·25
1·4
1·6
1·8
2·0
2·2
2·5
NATIONAL BUREAU OF STANDARDS
MICROCOPY RESOLUTION TEST CHART

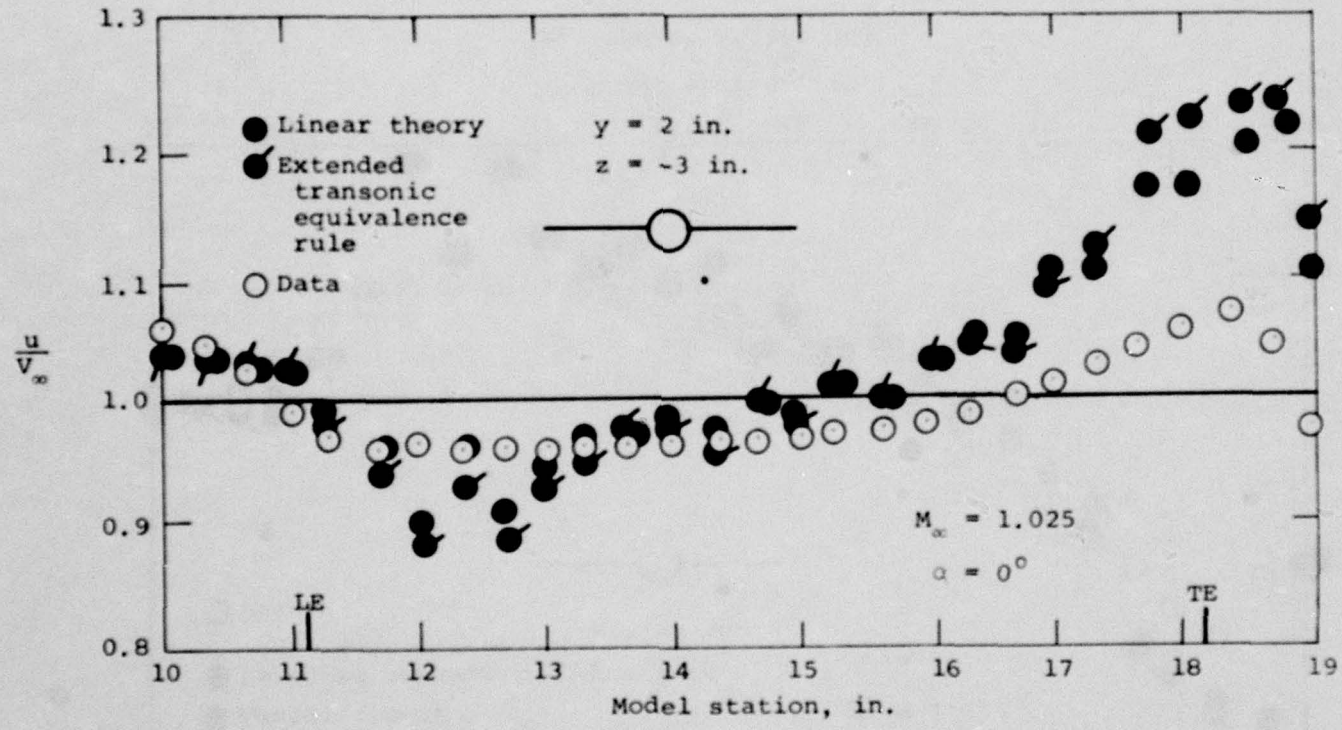

(a) Axial velocity ratio.

Figure 25.- Comparison of measured and theoretical flow field quantities for wing-body combination; $\alpha = 0^\circ$, $M_\infty = 1.025$, y = 2 in., z = -3 in.

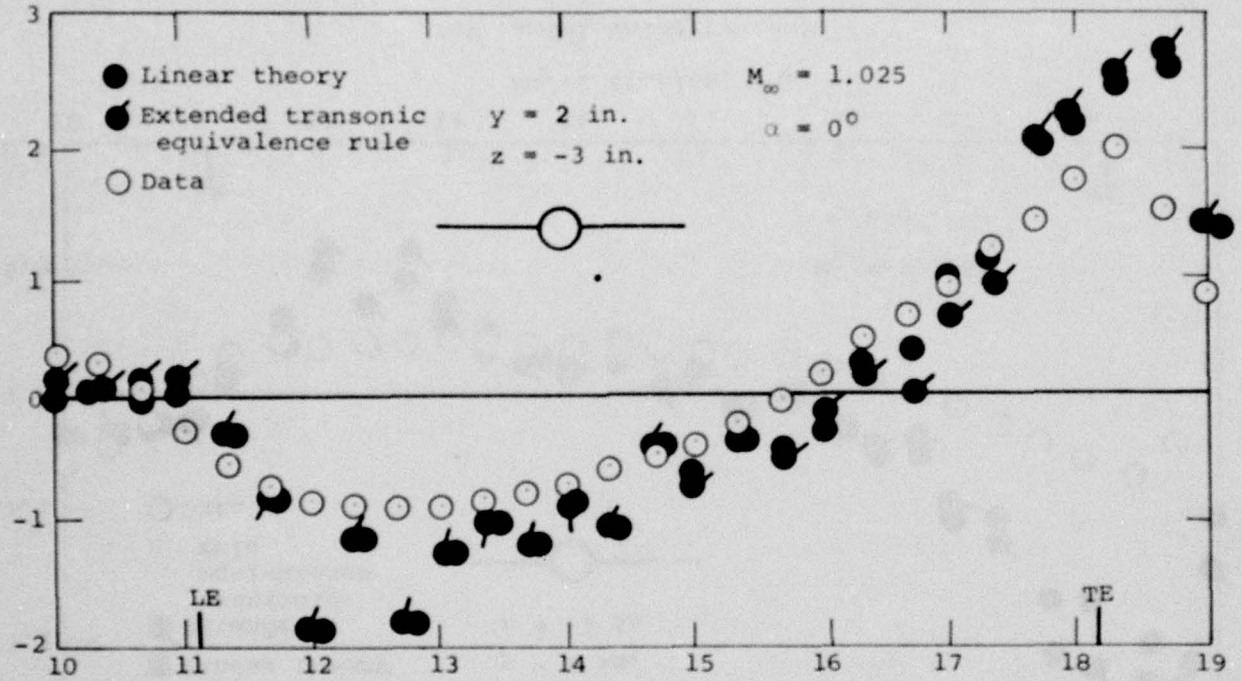

(b) Upwash angle, deg.

Figure 25.- Continued.

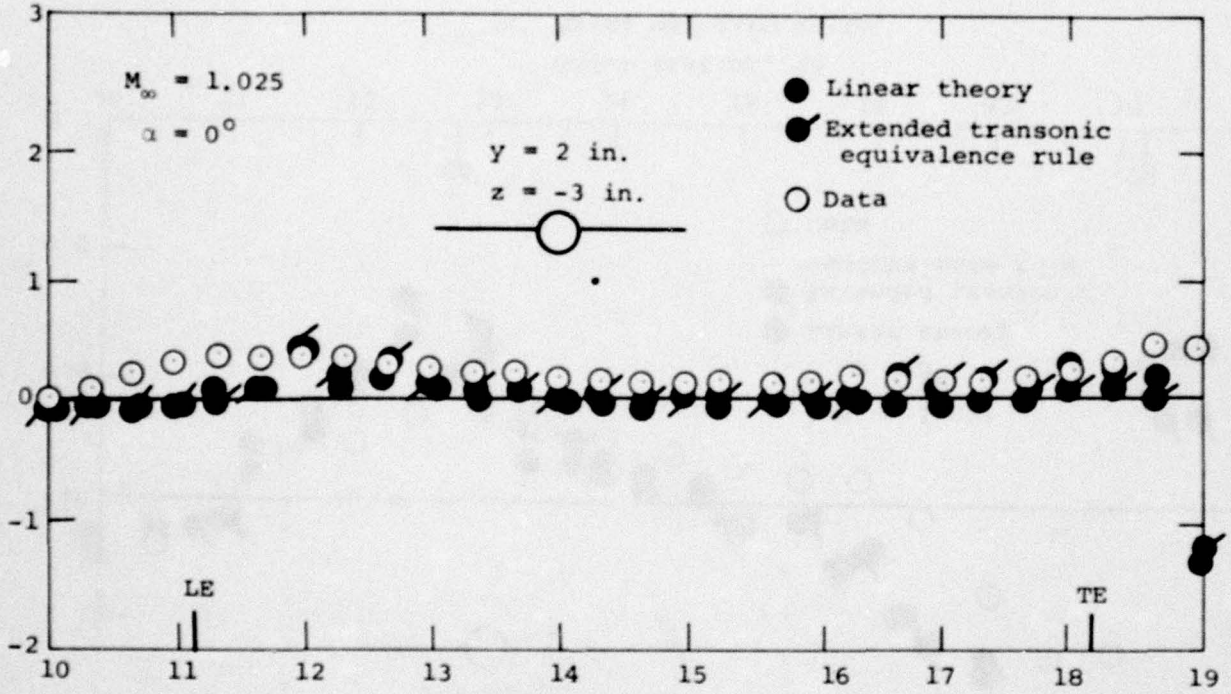

(c) Sidewash angle, deg.

Figure 25.- Concluded.

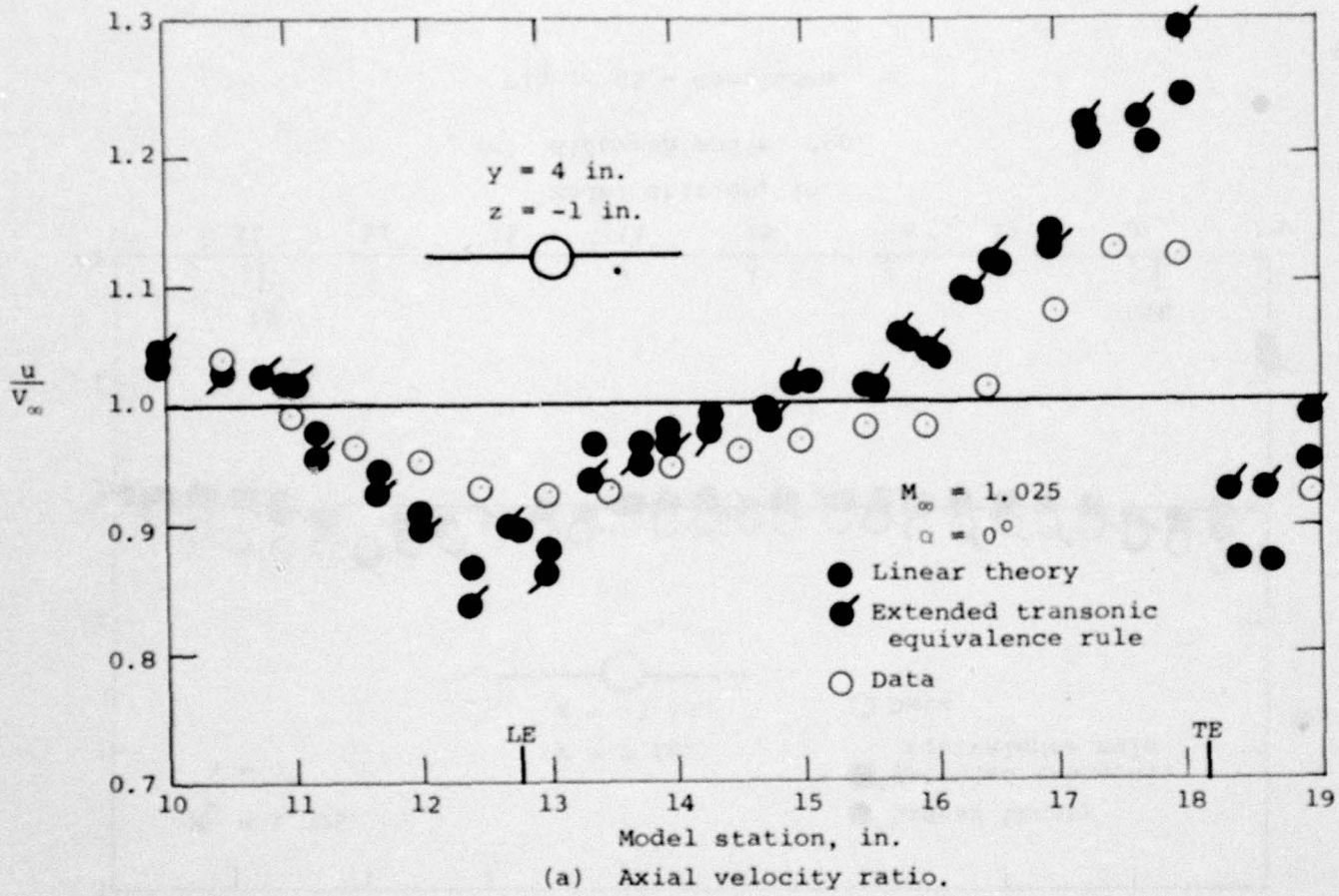

(a) Axial velocity ratio.

Figure 26.- Comparison of measured and theoretical flow field quantities for wing-body combination; $\alpha = 0°$, $M_\infty = 1.025$, y = 4 in., z = -1 in.

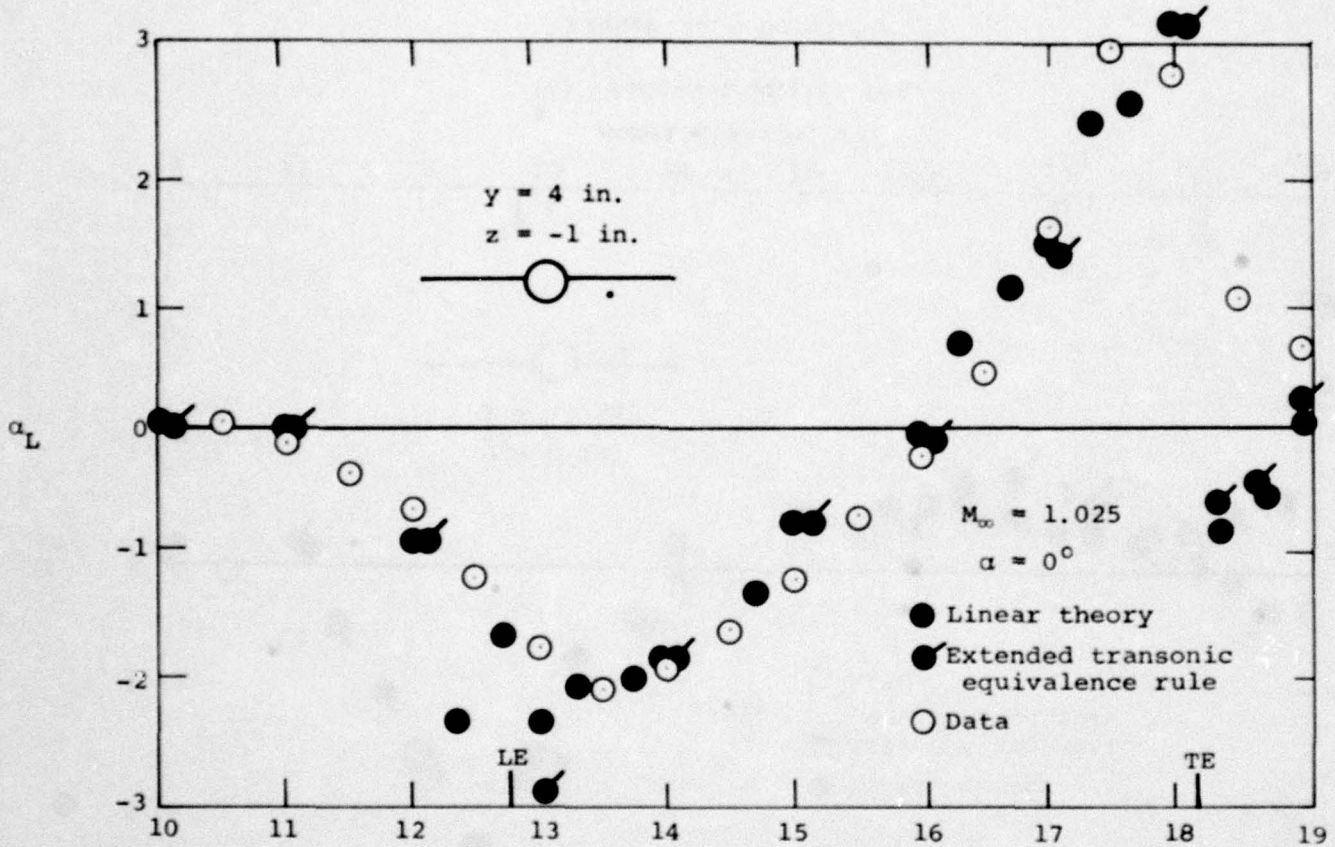

(b) Upwash angle, deg.

Figure 26.- Continued.

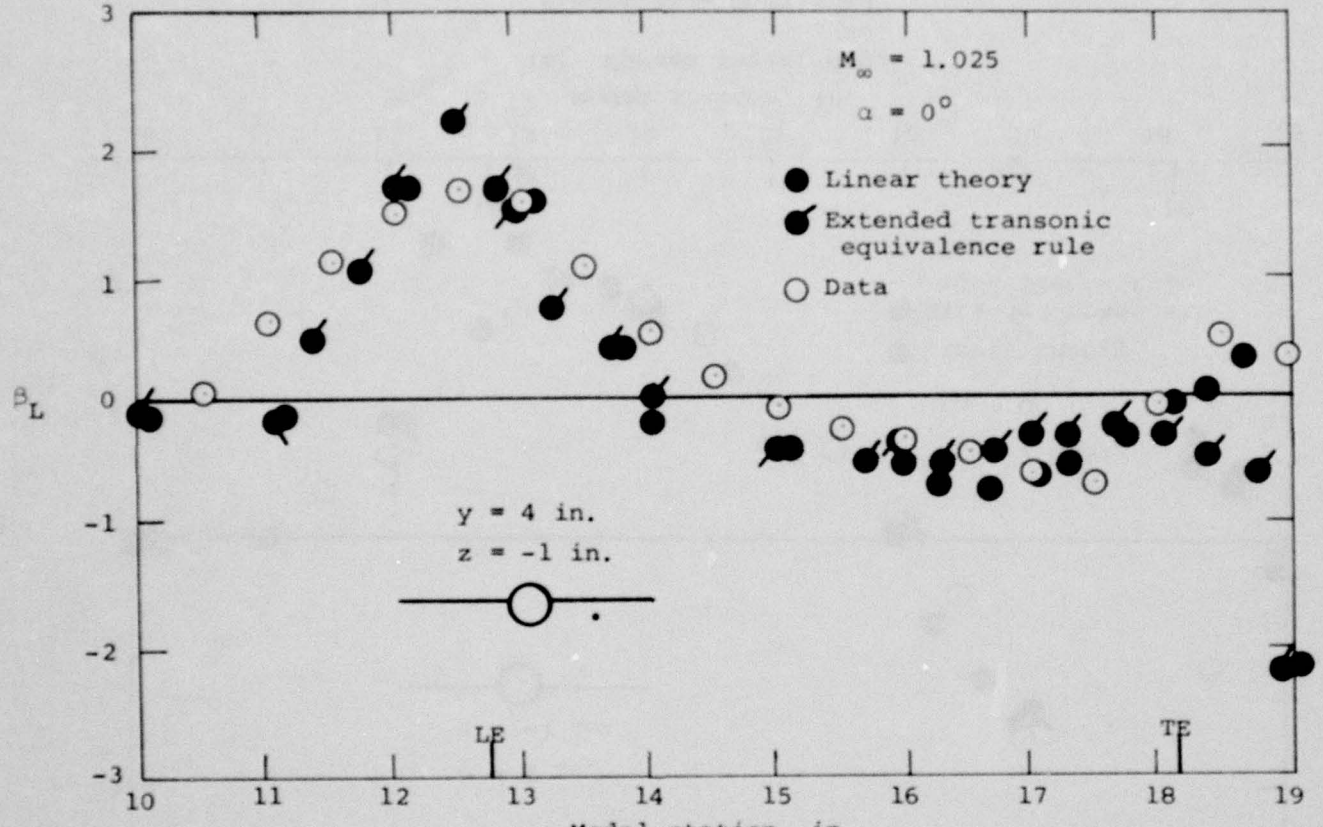

(c) Sidewash angle, deg.

Figure 26.- Concluded.

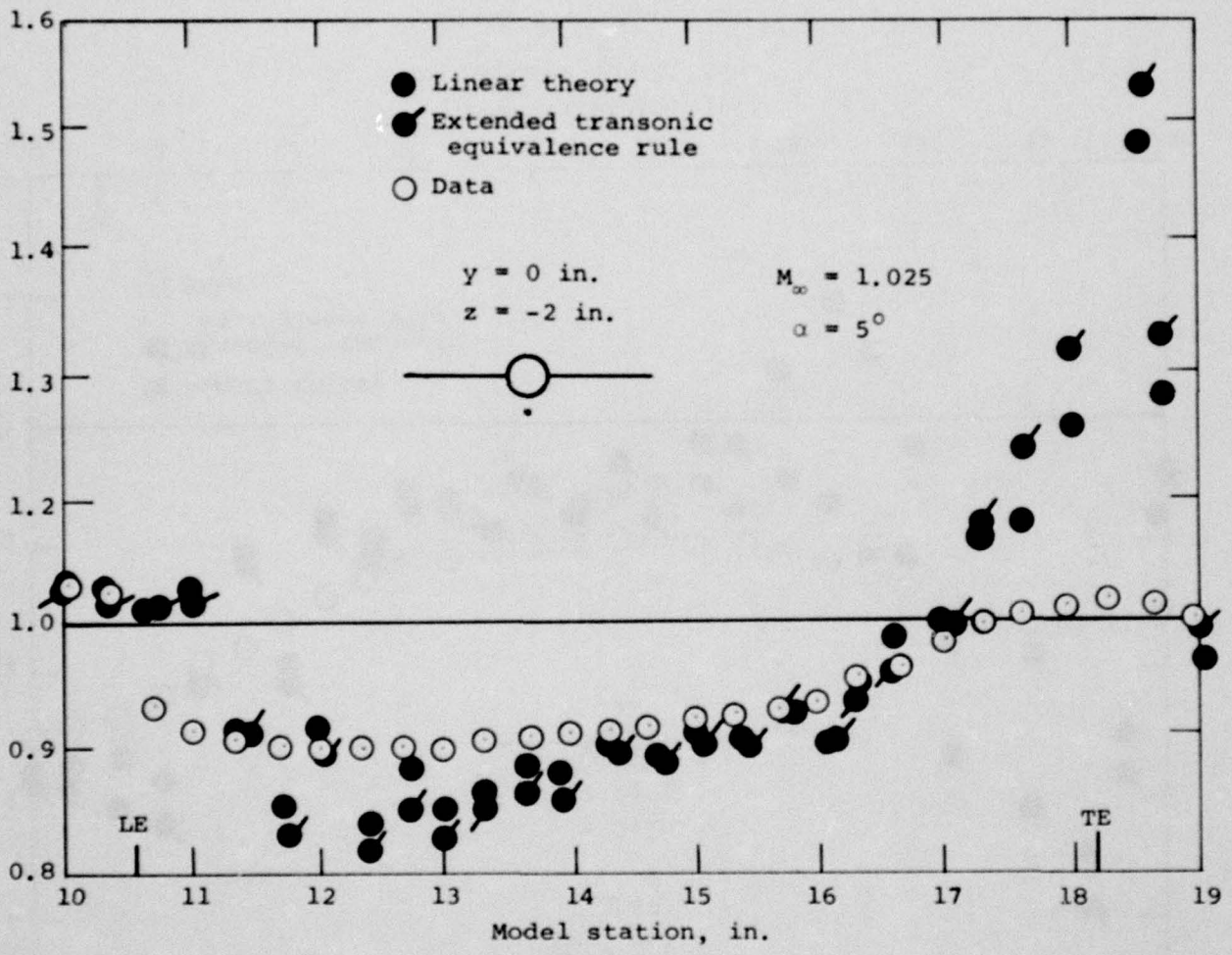

(a) Axial velocity ratio.

Figure 27.- Comparison of measured and theoretical flow field quantities for wing-body combination; α = 5°, M_∞ = 1.025, y = 0 in., z = -2 in.

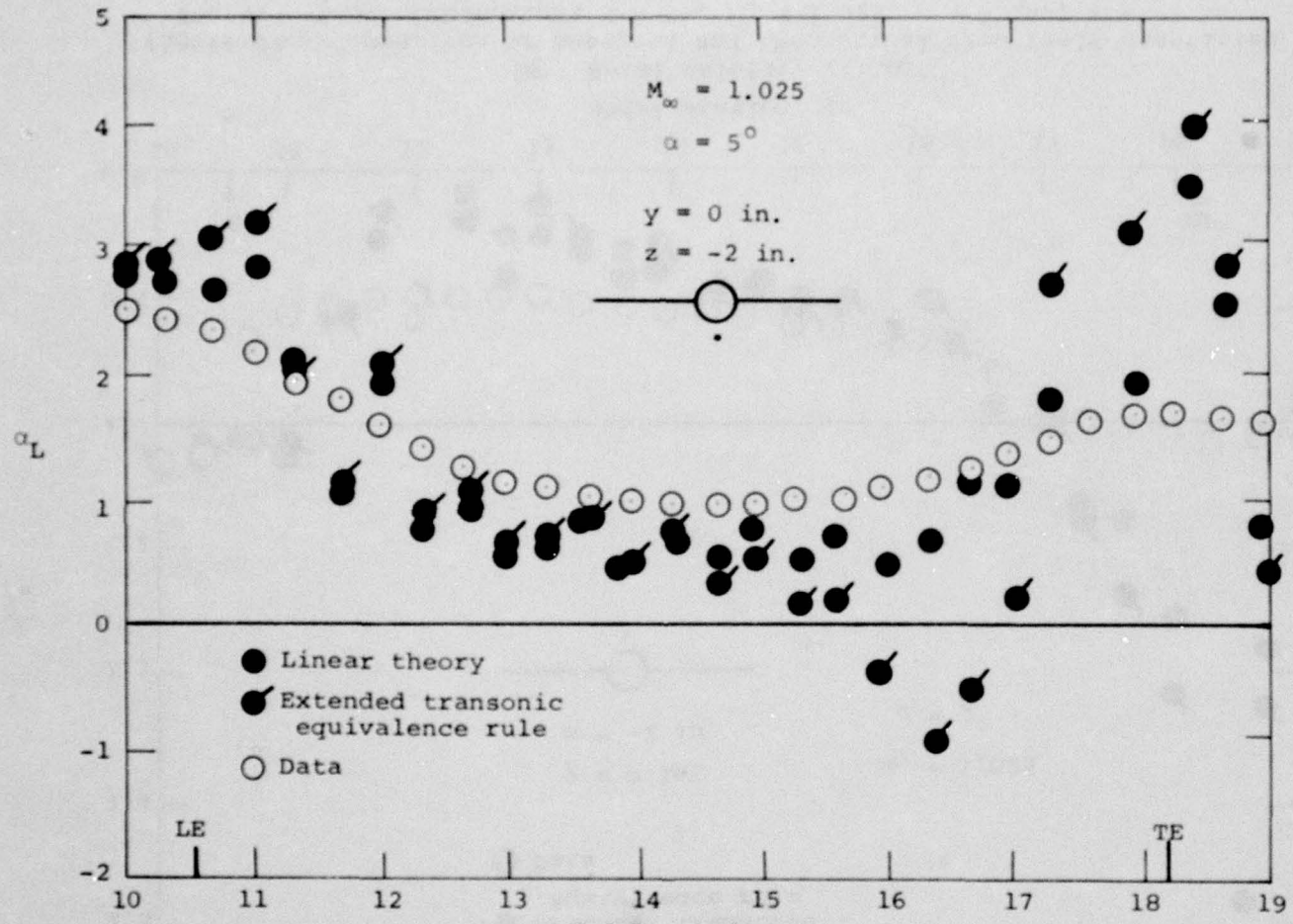

(b) Upwash angle, deg.

Figure 27.- Continued.

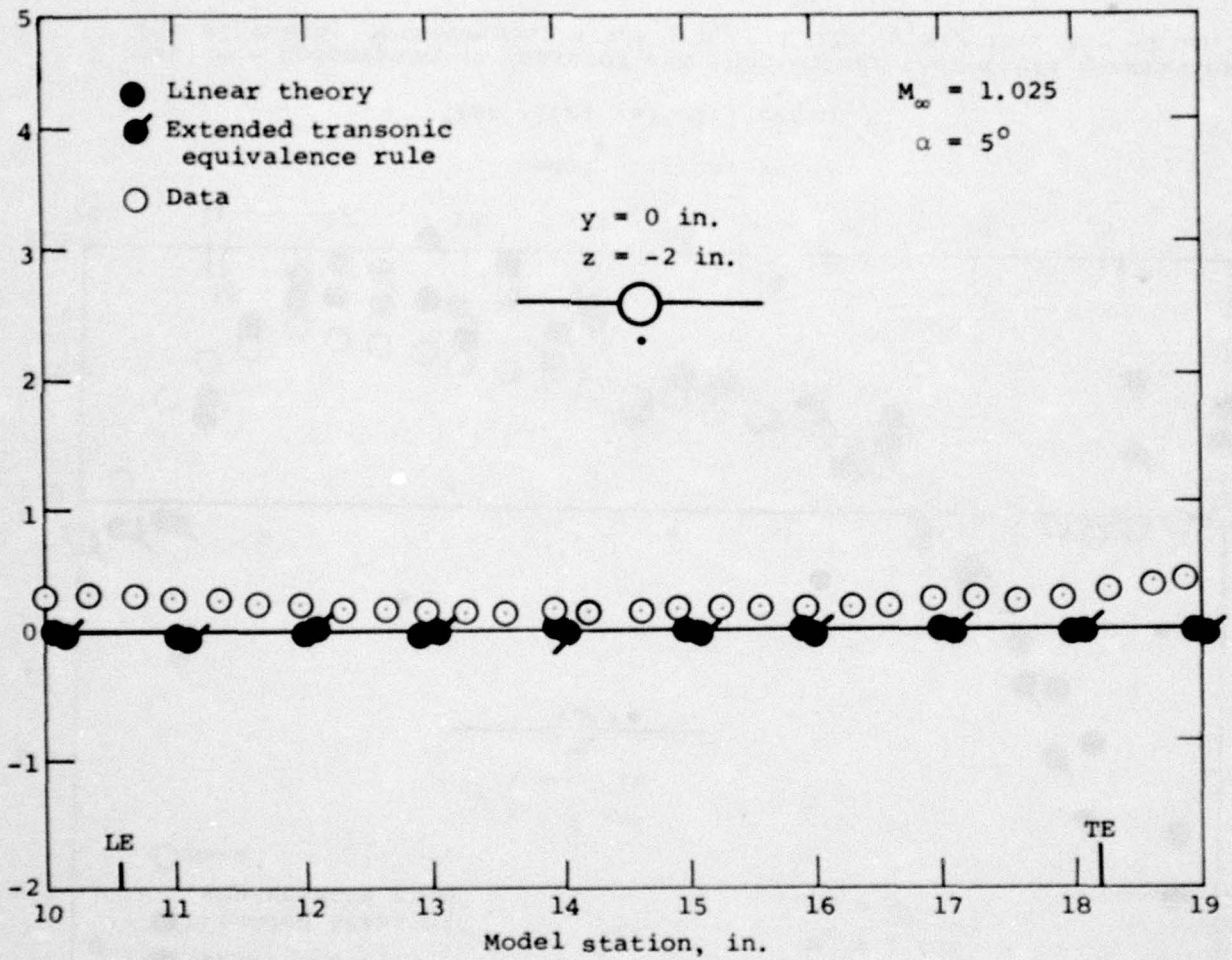

(c) Sidewash angle, deg.

Figure 27.- Concluded.

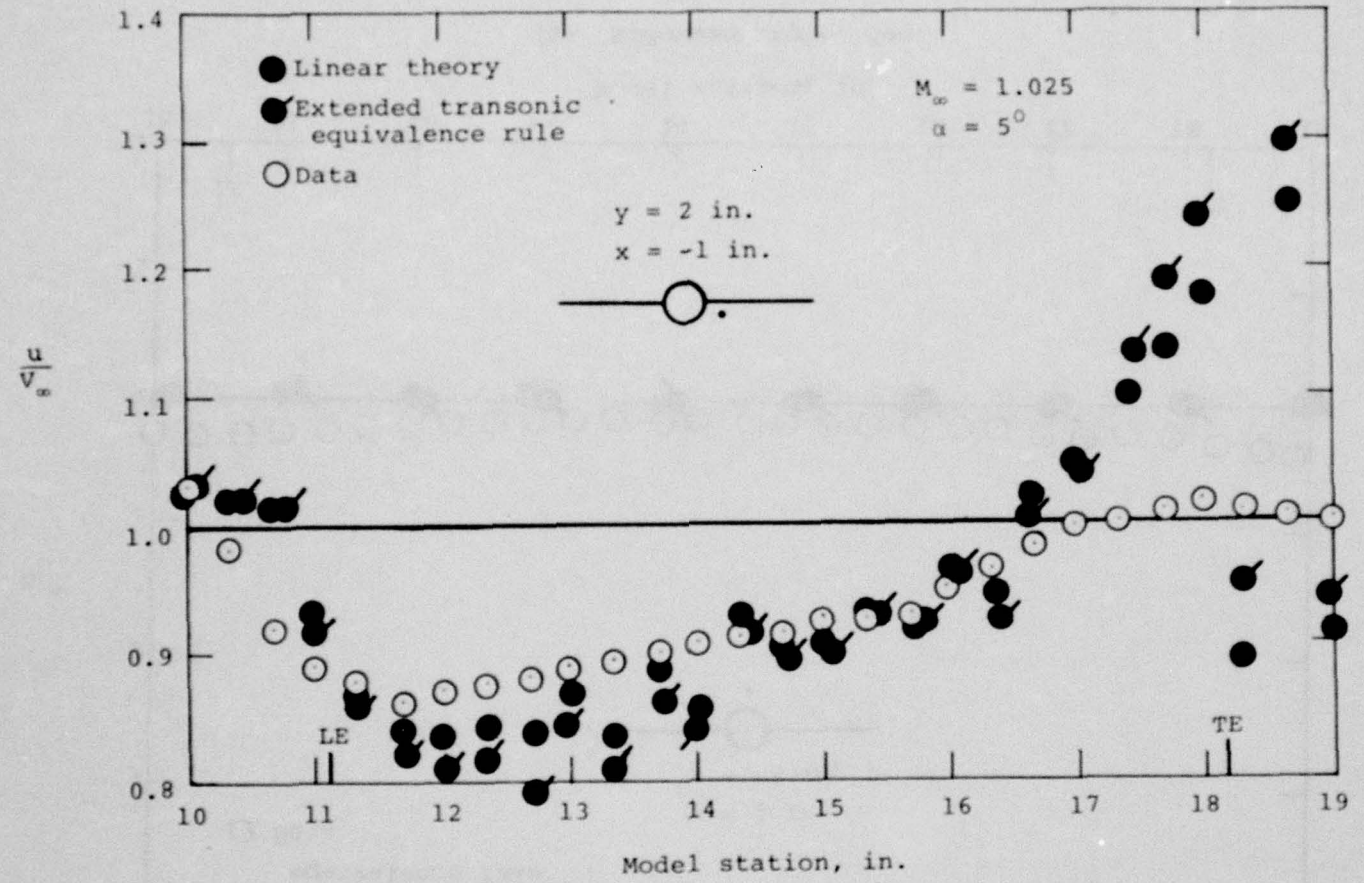

(a) Axial velocity ratio.

Figure 28.- Comparison of measured and theoretical flow field quantities for wing-body combination; $\alpha = 5^\circ$, $M_\infty = 1.025$, y = 2 in., z = -1 in.

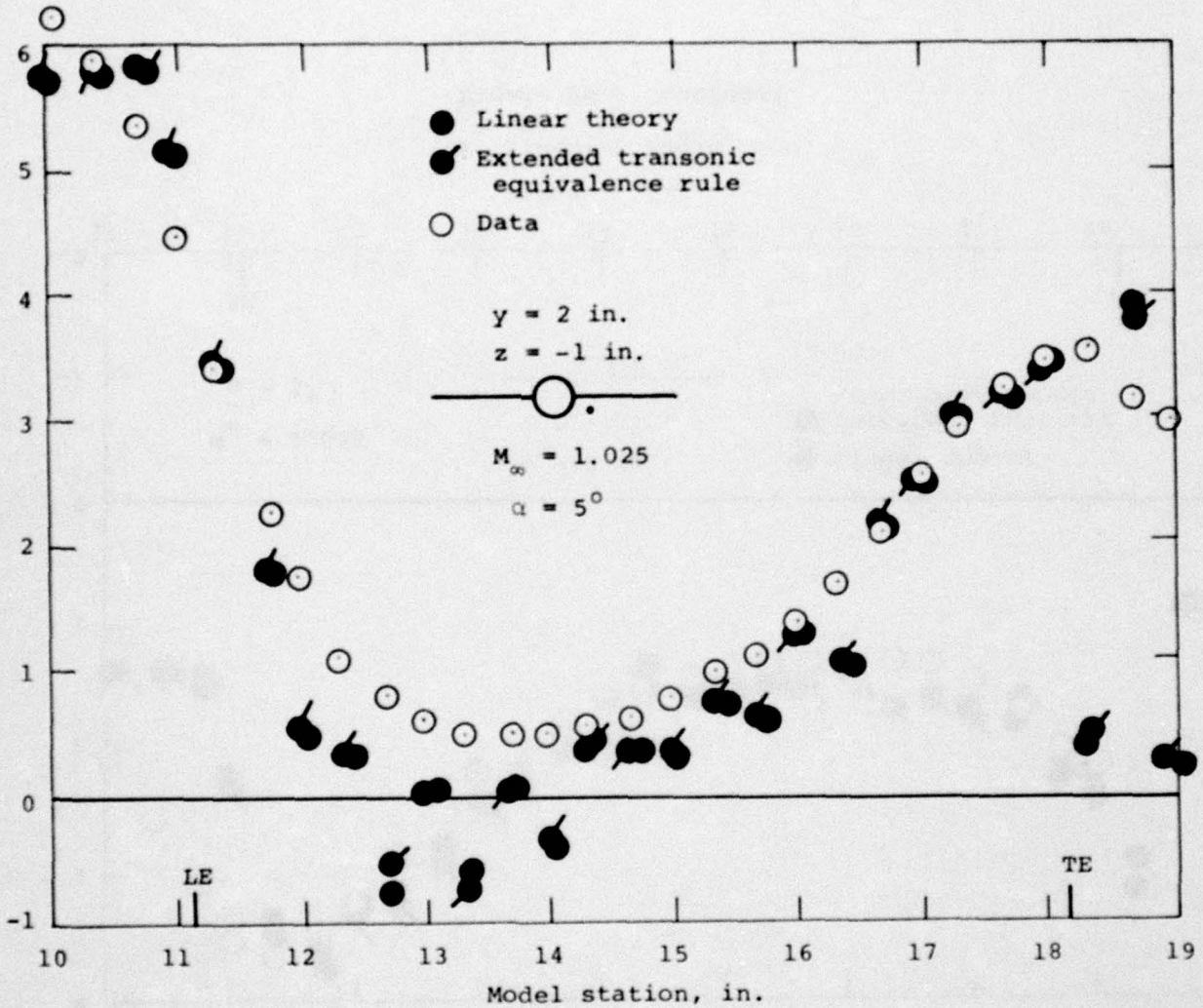

(b) Upwash angle, deg.

Figure 28.- Continued.

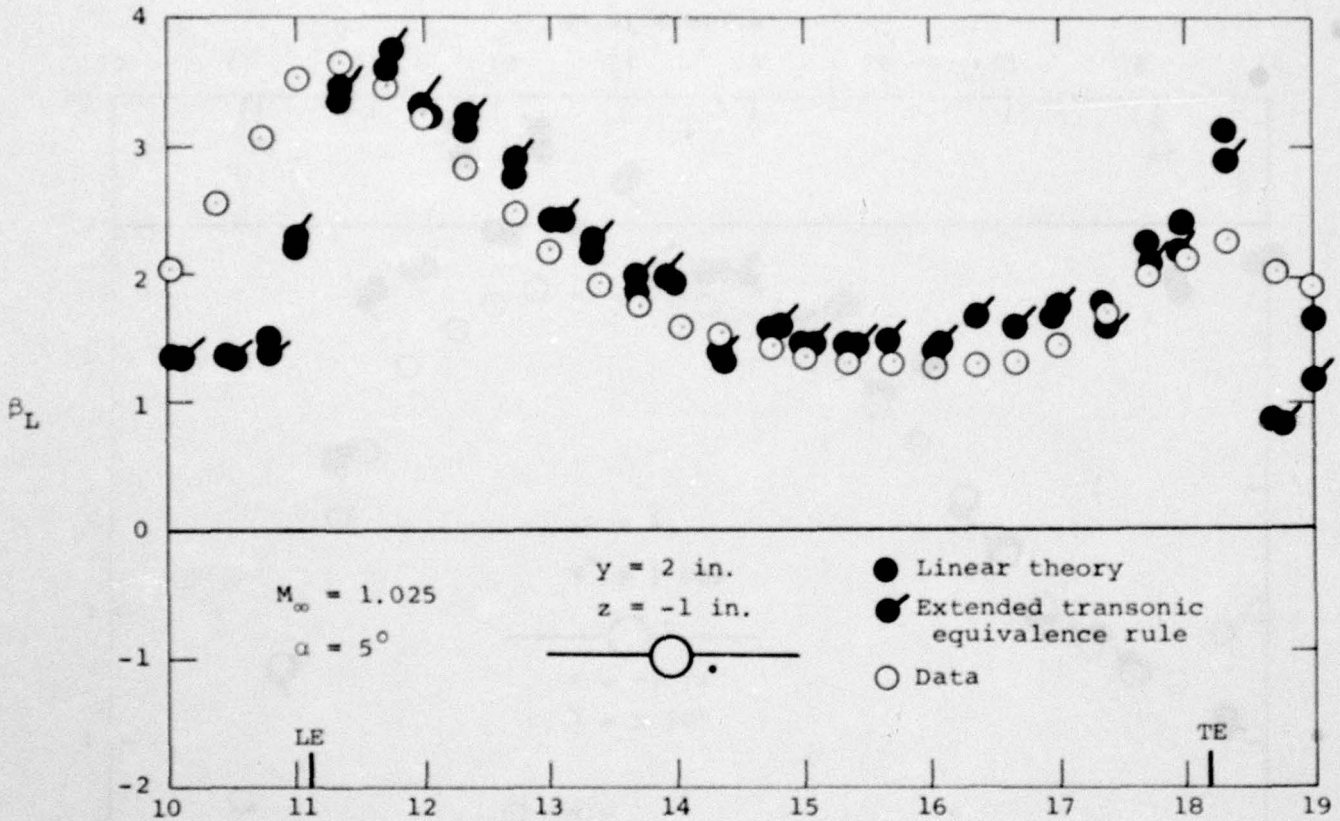

(c) Sidewash angle, deg.

Figure 28.- Concluded.

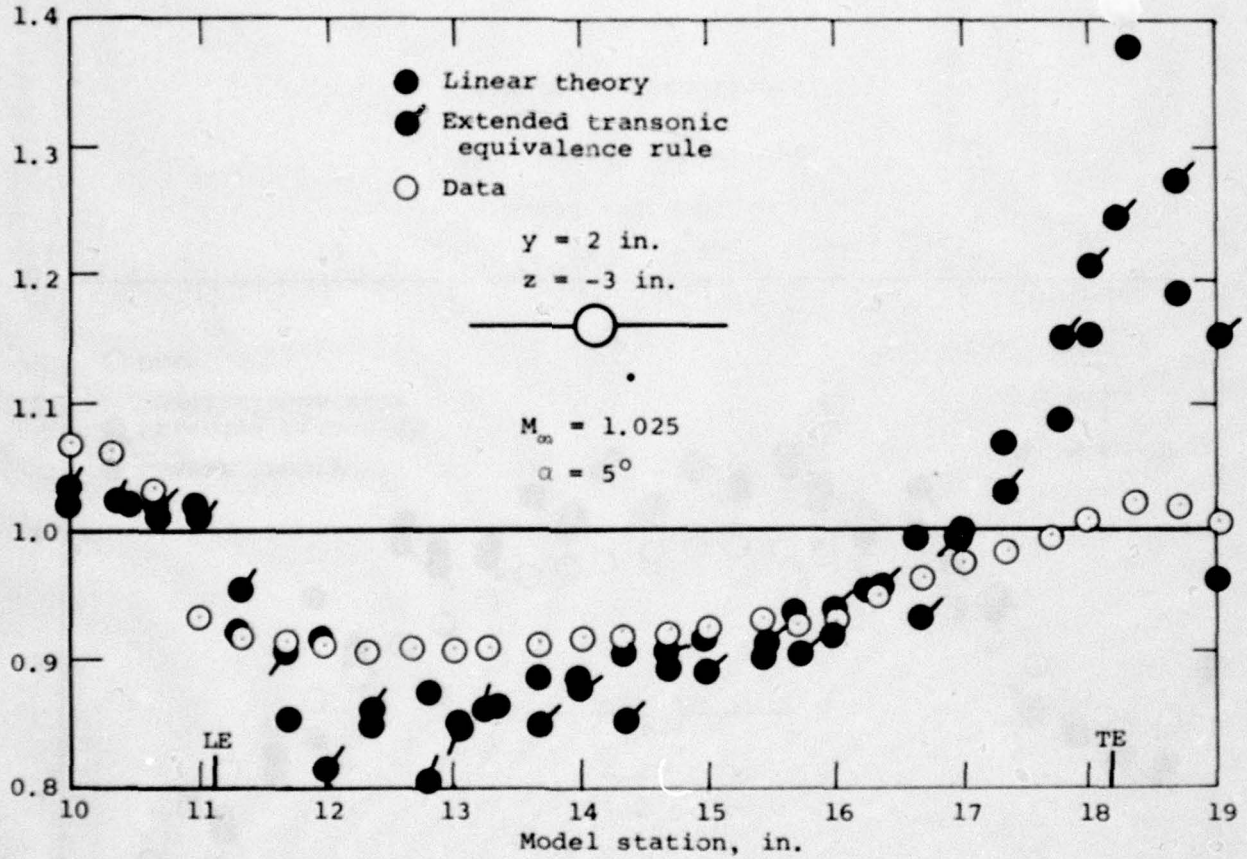

(a) Axial velocity ratio.

Figure 29.- Comparison of measured and theoretical flow field quantities for wing-body combination; $\alpha = 5^\circ$, $M_\infty = 1.025$, y = 2 in., z = -3 in.

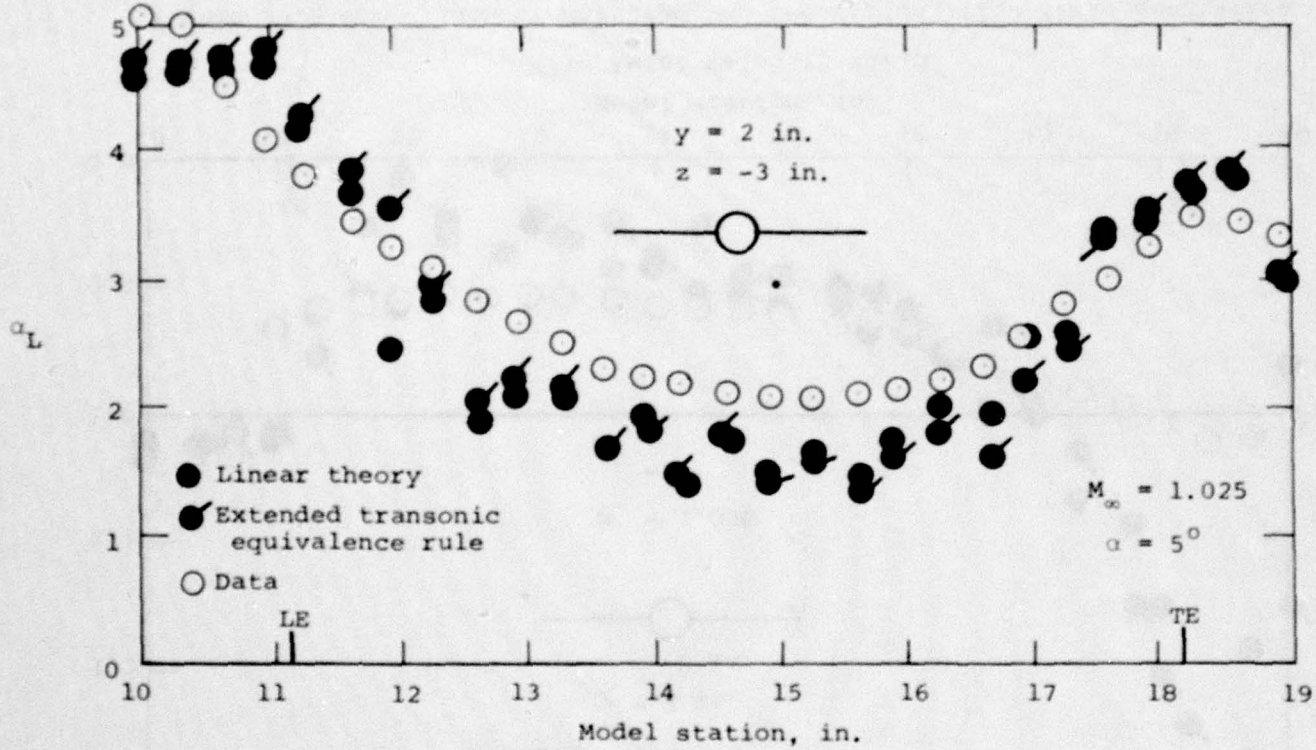

(b) Upwash angle, deg.

Figure 29.- Continued.

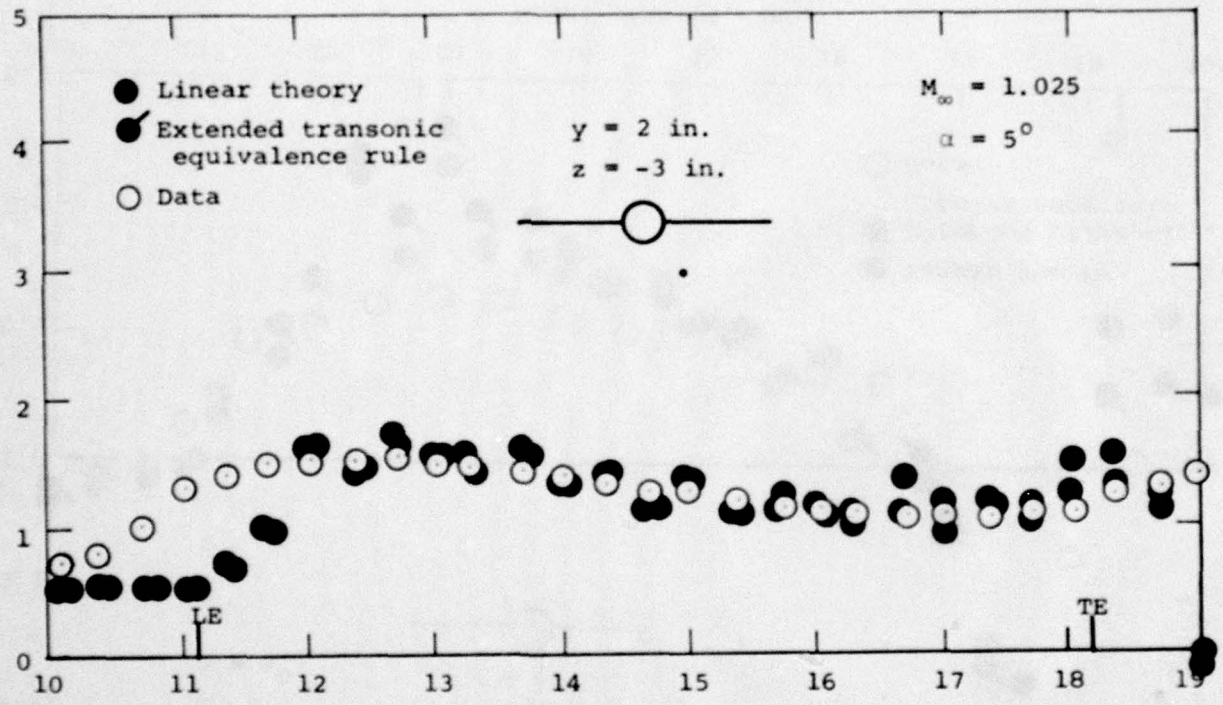

(c) Sidewash angle, deg.

Figure 29.- Concluded.

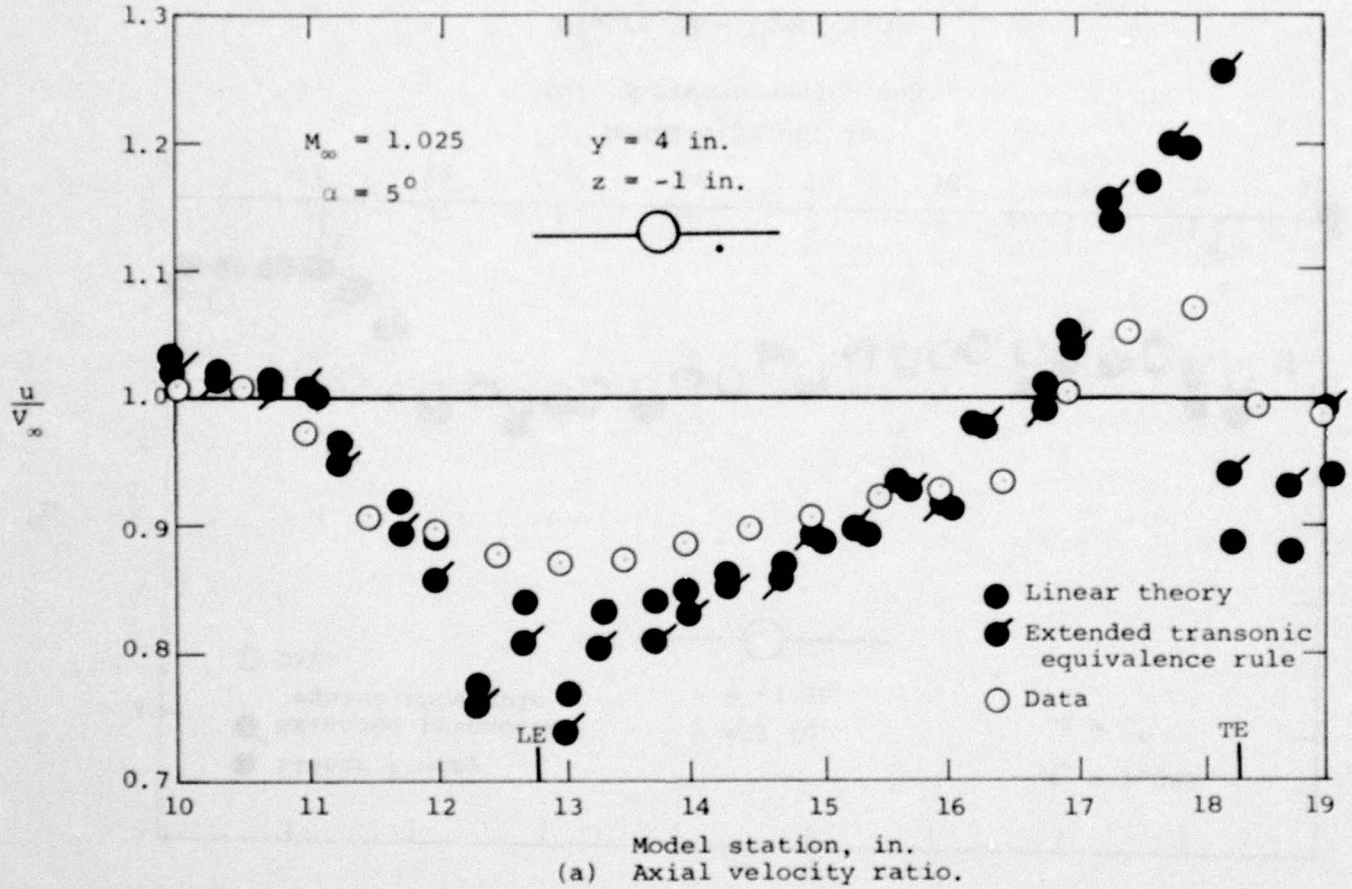

(a) Axial velocity ratio.

Figure 30.- Comparison of measured and theoretical flow field quantities for wing-body combination; $\alpha = 5^\circ$, $M_\infty = 1.025$, y = 4 in., z = -1 in.

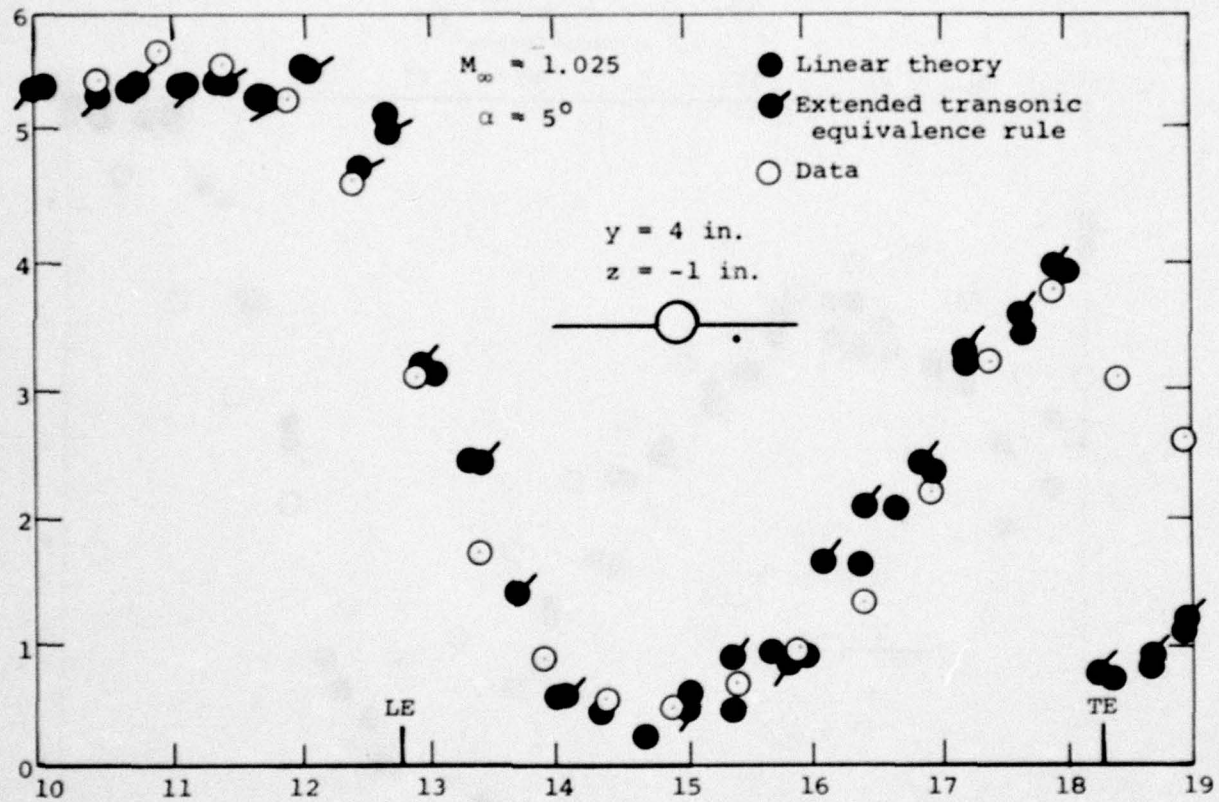

(b) Upwash angle, deg.

Figure 30.- Continued.

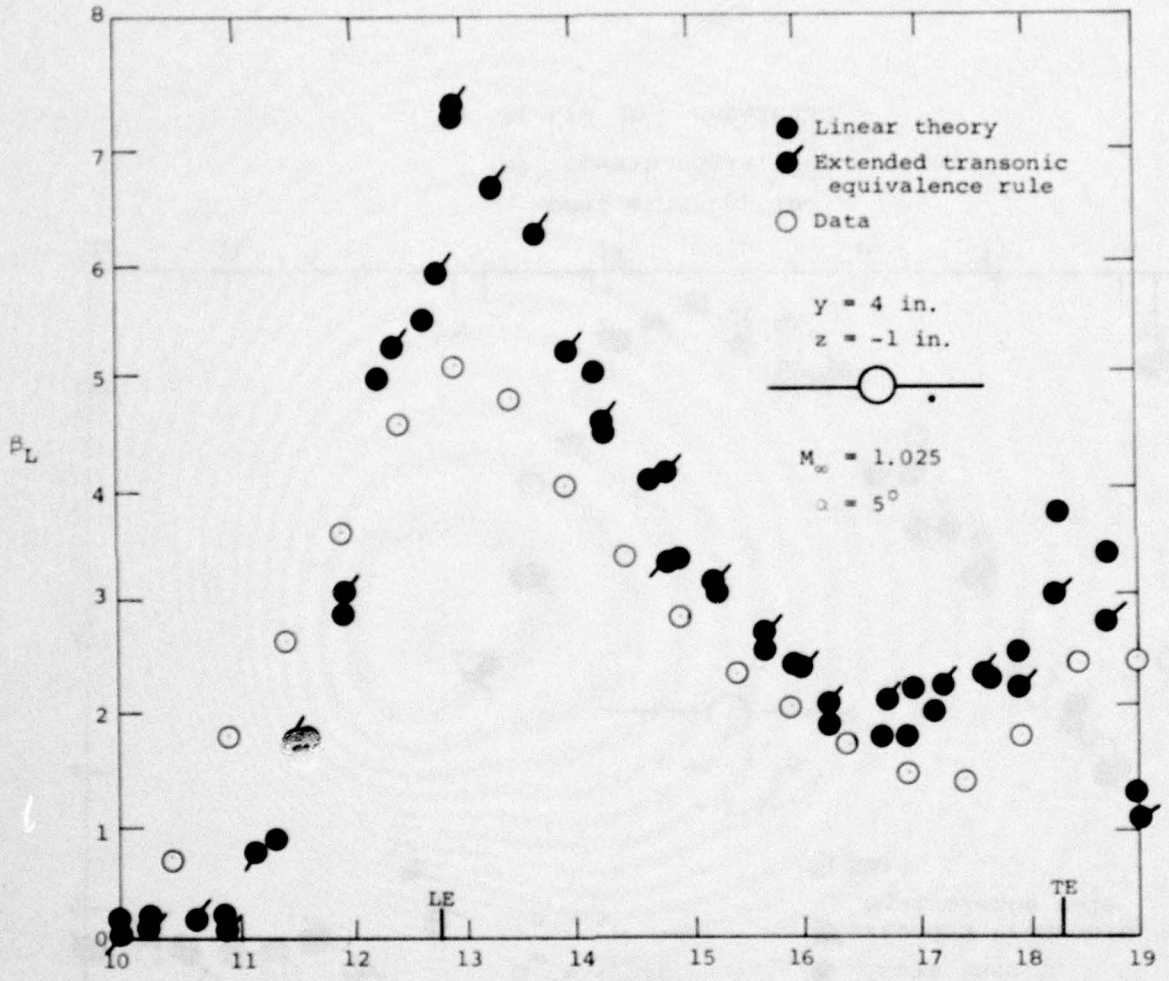

(c) Sidewash angle, deg.

Figure 30.- Concluded.

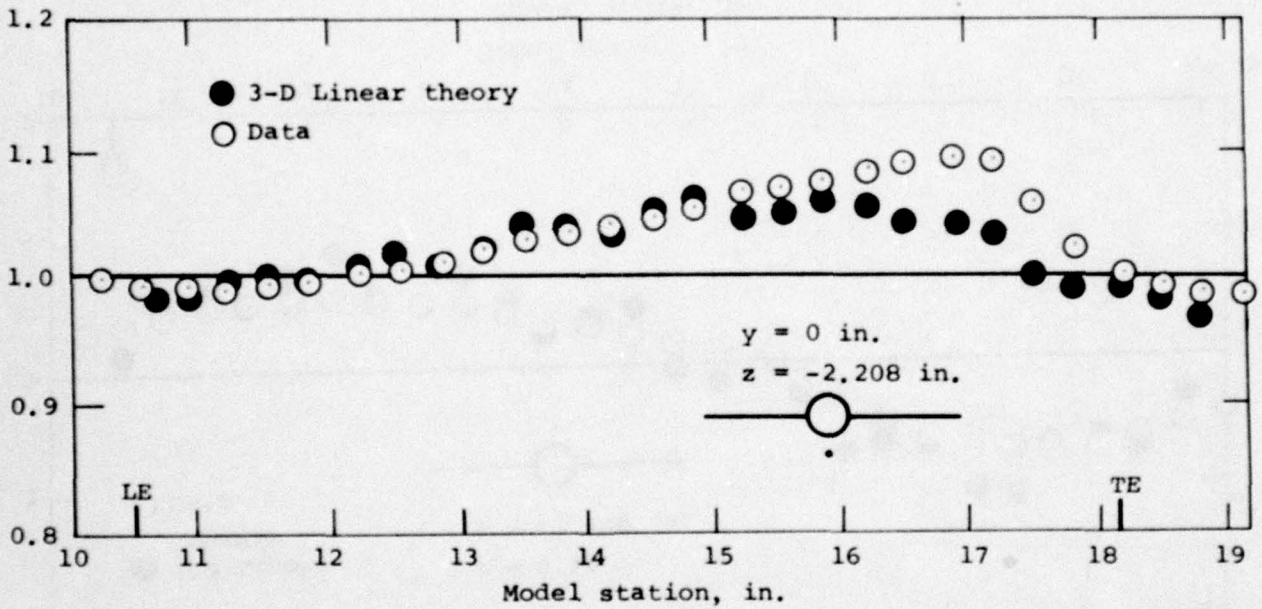

(a) Axial velocity ratio.

Figure 31.- Comparison of measured flow field quantities with prediction of three-dimensional linear theory for wing-body combination, $\alpha = 0^\circ$, $M_\infty = 0.95$, y = 0 in., z = -2.208 in.

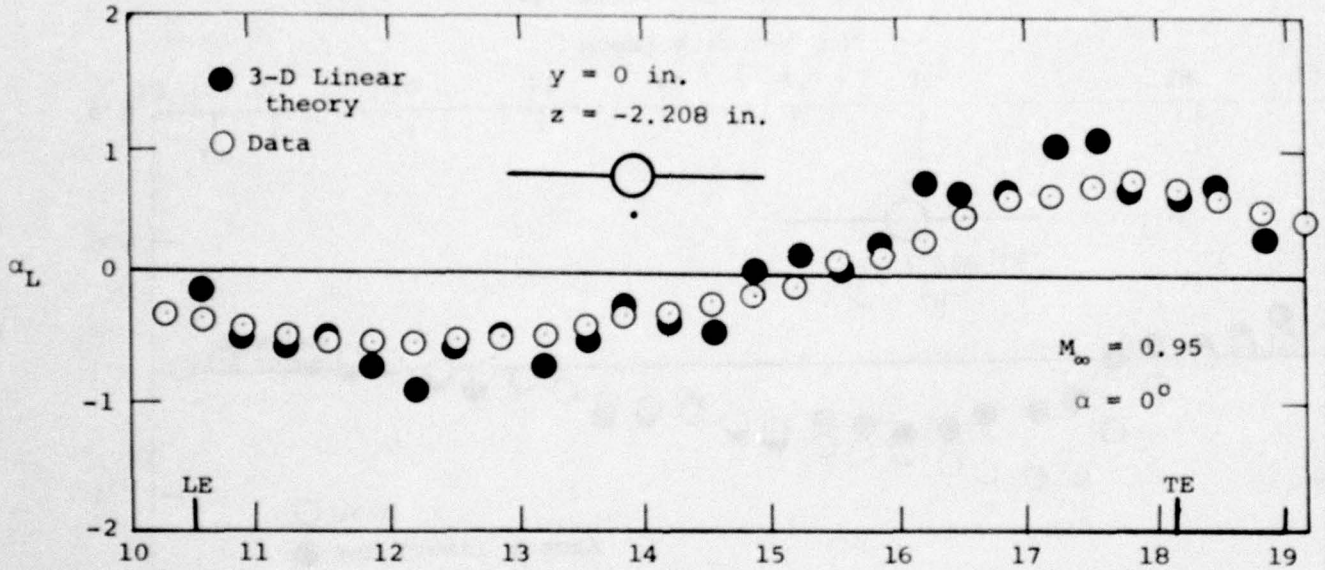

(b) Upwash angle, deg.

Figure 31.- Continued.

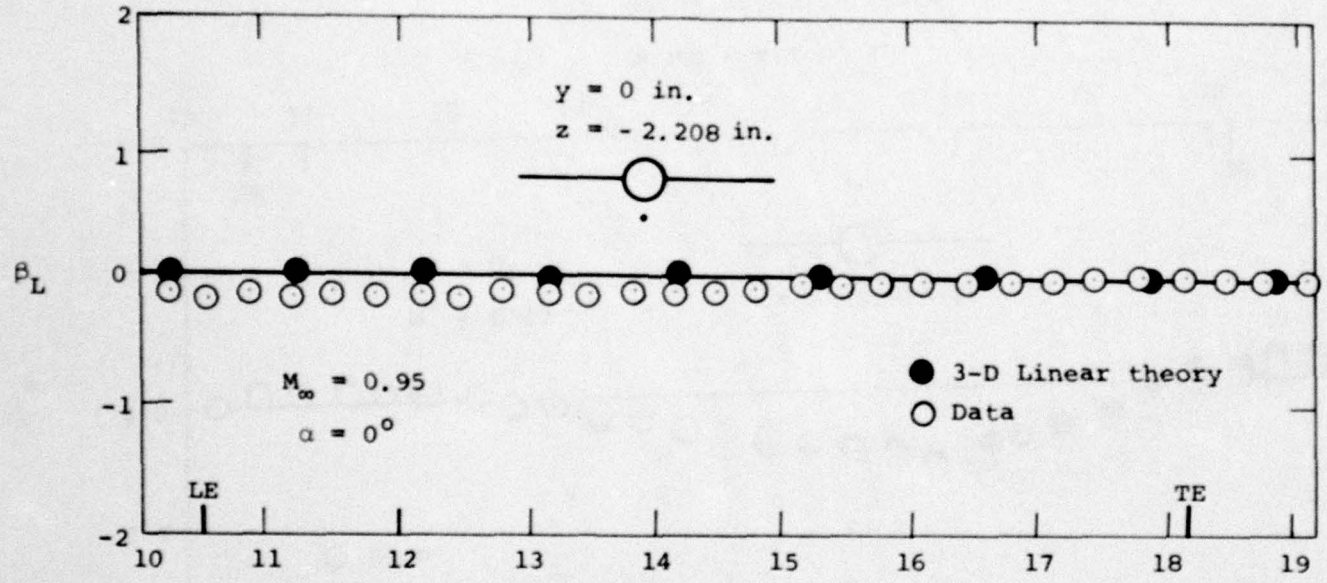

(c) Sidewash angle, deg.

Figure 31.- Concluded.

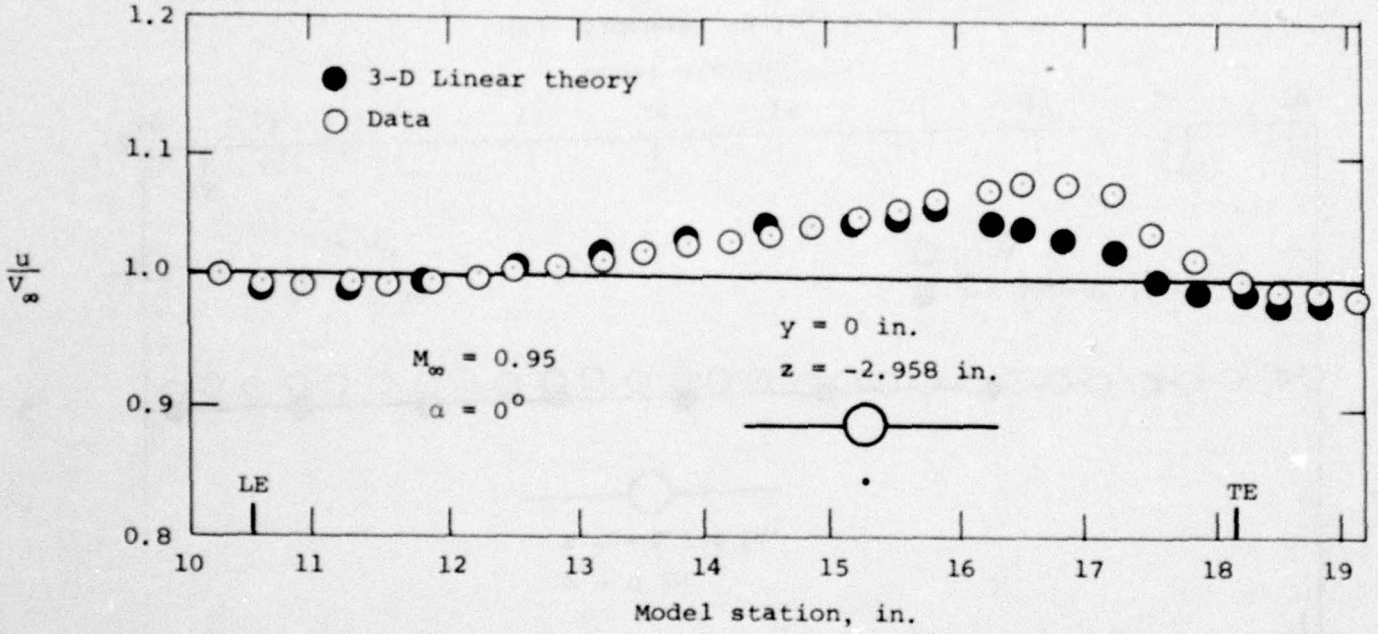

(a) Axial velocity ratio.

Figure 32.- Comparison of measured flow field quantities with prediction of three-dimensional linear theory for wing-body combination, $\alpha = 0^\circ$, $M_\infty = 0.95$, y = 0 in., z = -2.958 in.

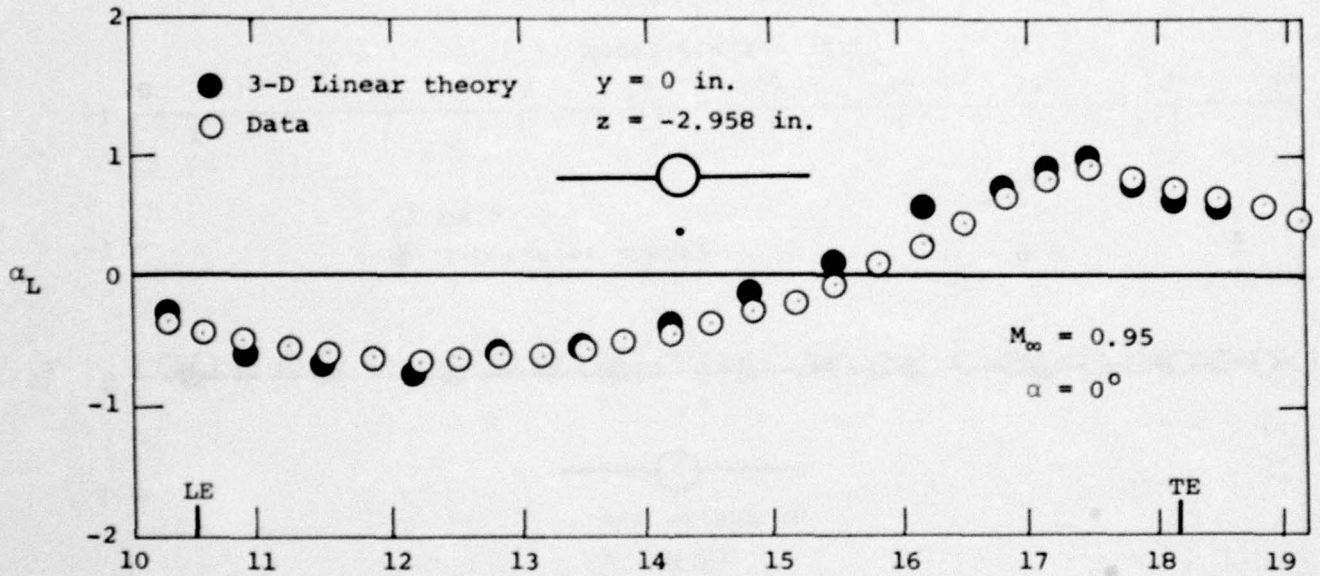

(b) Upwash angle, deg.

Figure 32.- Continued.

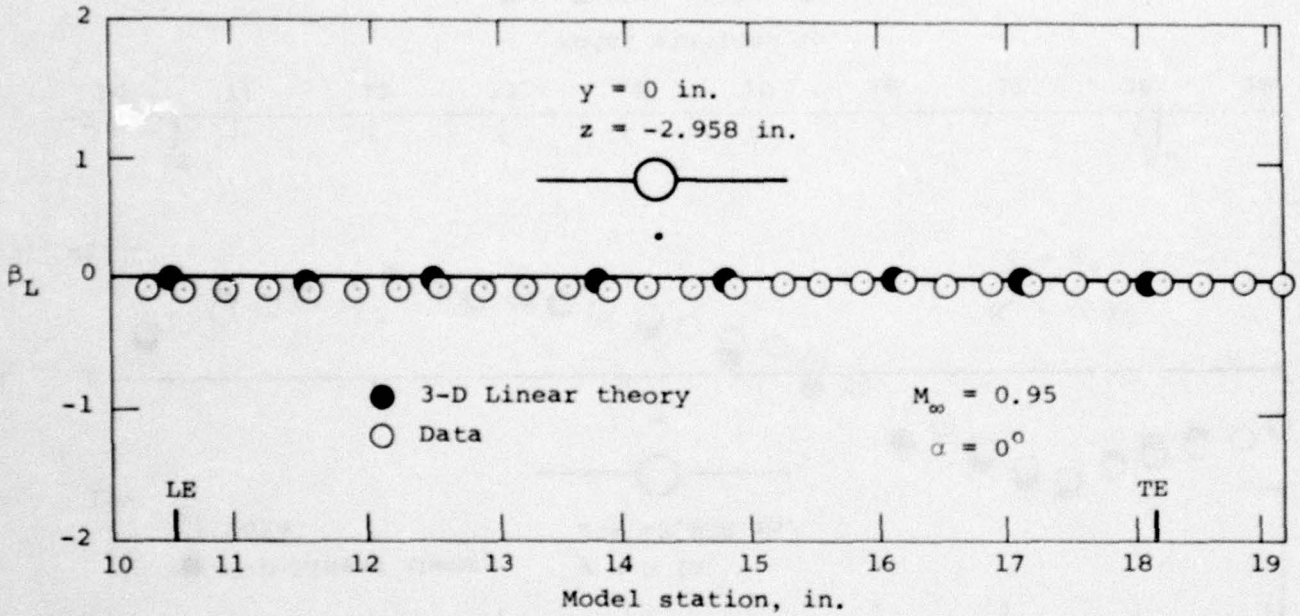

(c) Sidewash angle, deg.

Figure 32.- Concluded.

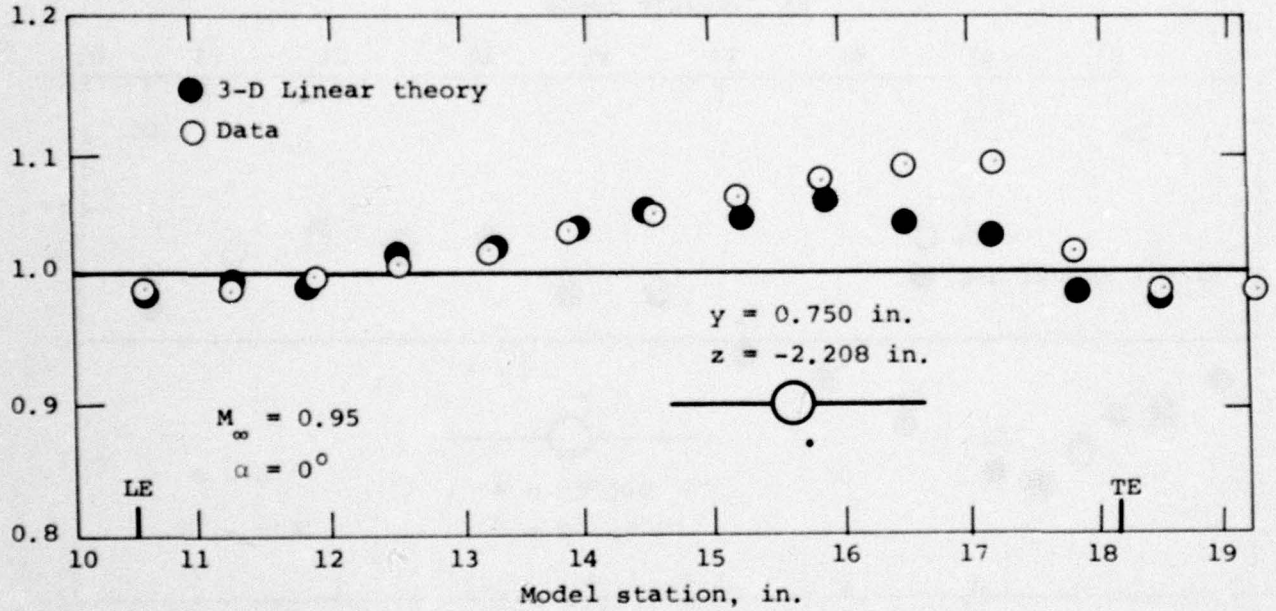

(a) Axial velocity ratio.

Figure 33.- Comparison of measured flow field quantities with prediction of three-dimensional linear theory for wing-body combination, $\alpha = 0^{\circ}$, $M_{\infty} = 0.95$, y = 0.750 in., z = -2.208 in.

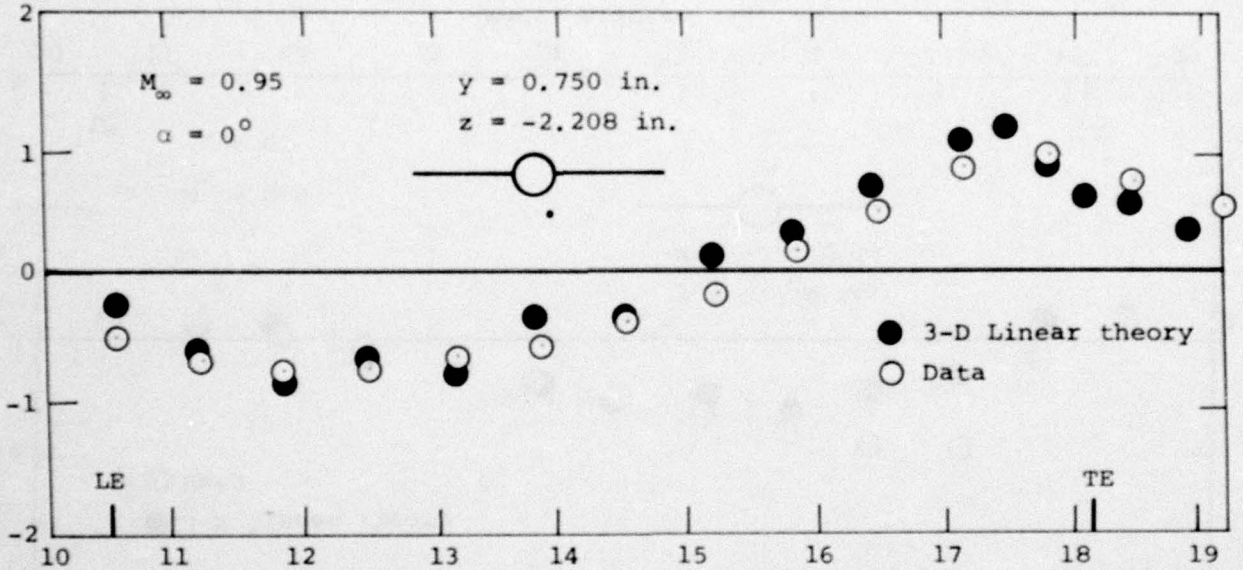

(b) Upwash angle, deg.

Figure 33.- Continued.

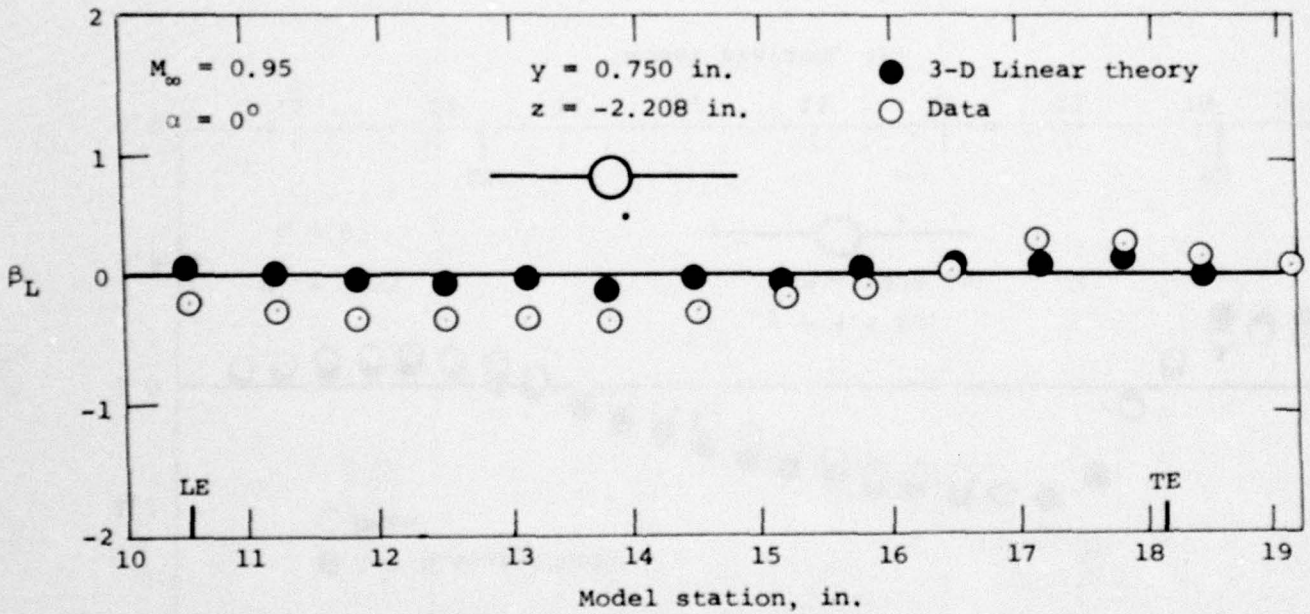

(c) Sidewash angle, deg.

Figure 33.- Concluded.

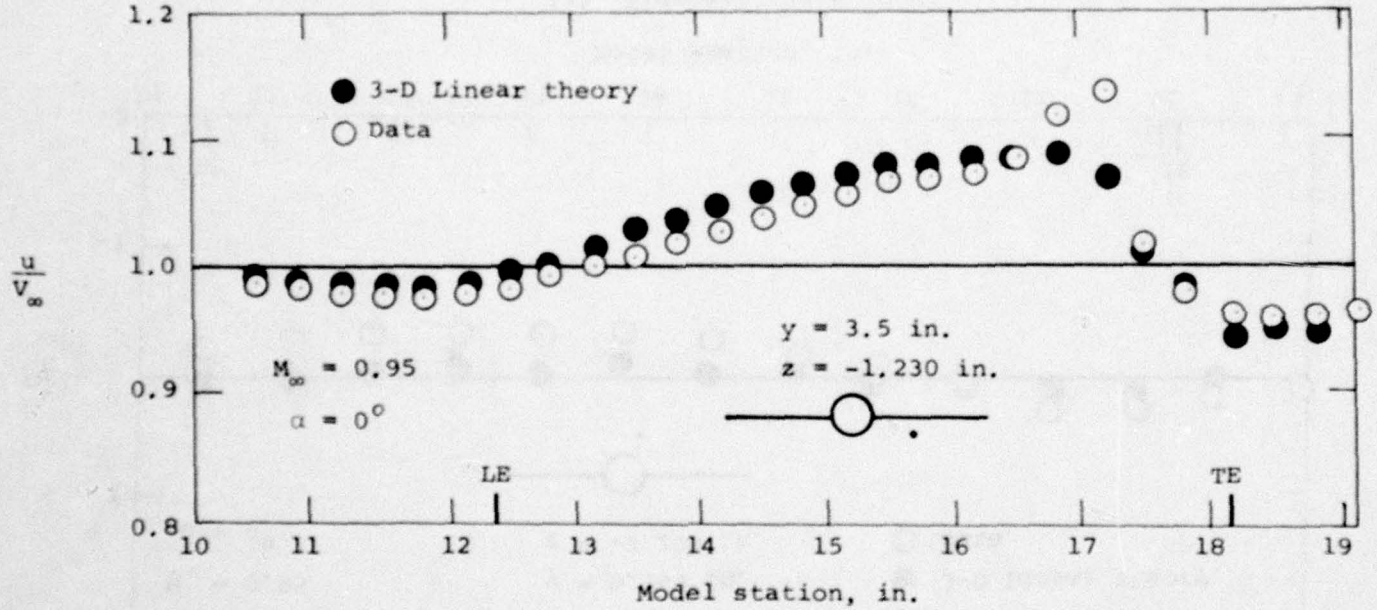

(a) Axial velocity ratio.

Figure 34.- Comparison of measured flow field quantities with prediction of three-dimensional linear theory for wing-body combination, $\alpha = 0°$, $M_\infty = 0.95$, y = 3.5 in., z = -1.230 in.

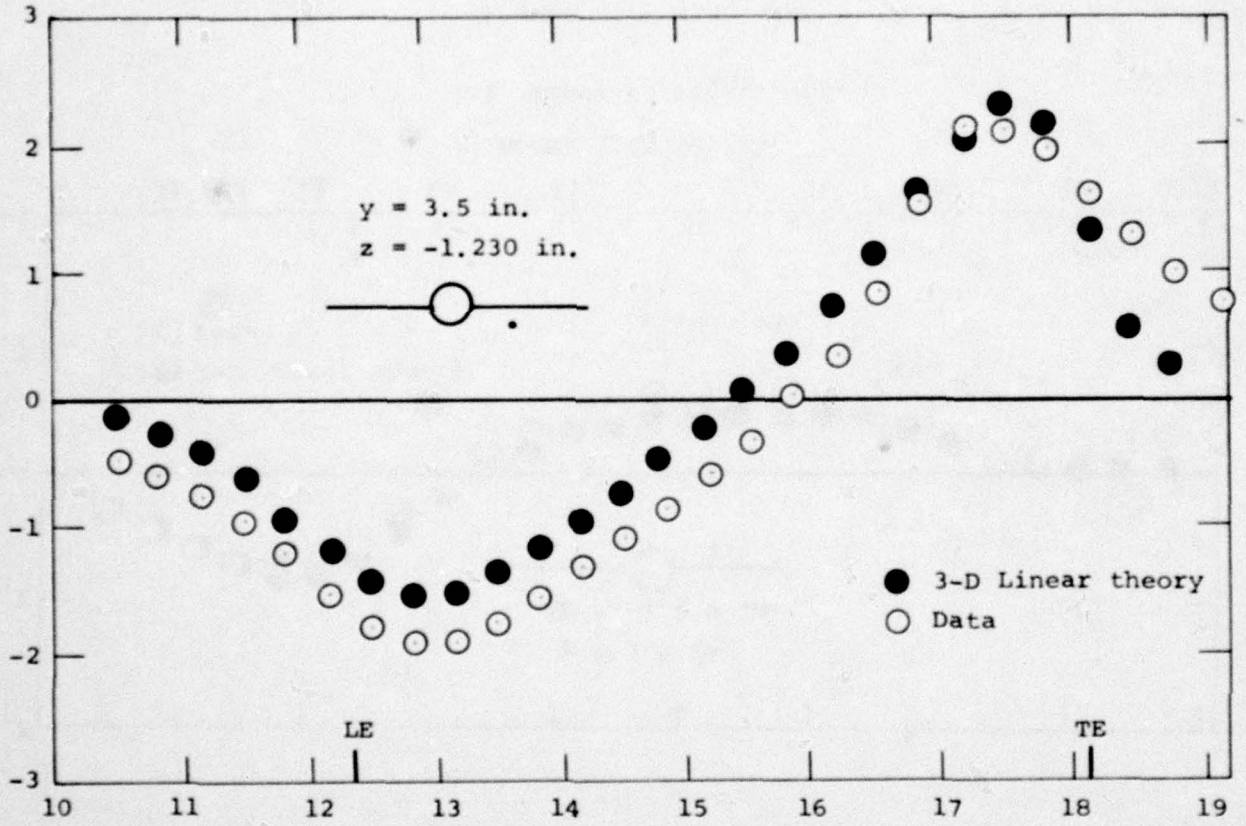

Model station, in.

(b) Upwash angle, deg.

Figure 34.- Continued.

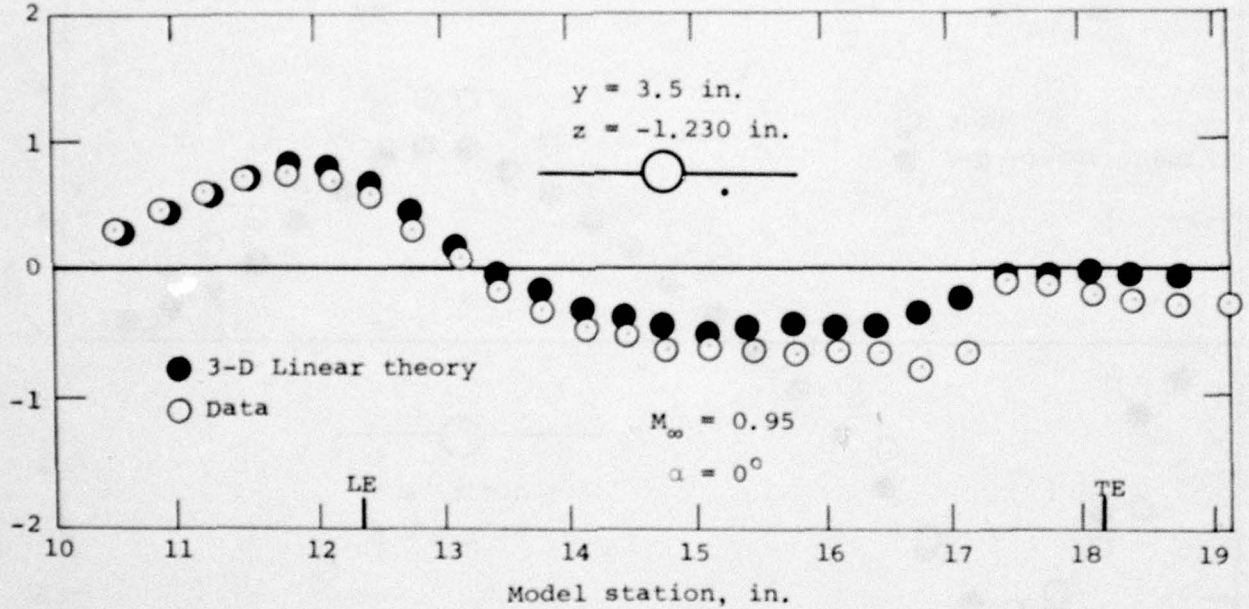

(c) Sidewash angle, deg.

Figure 34.- Concluded.

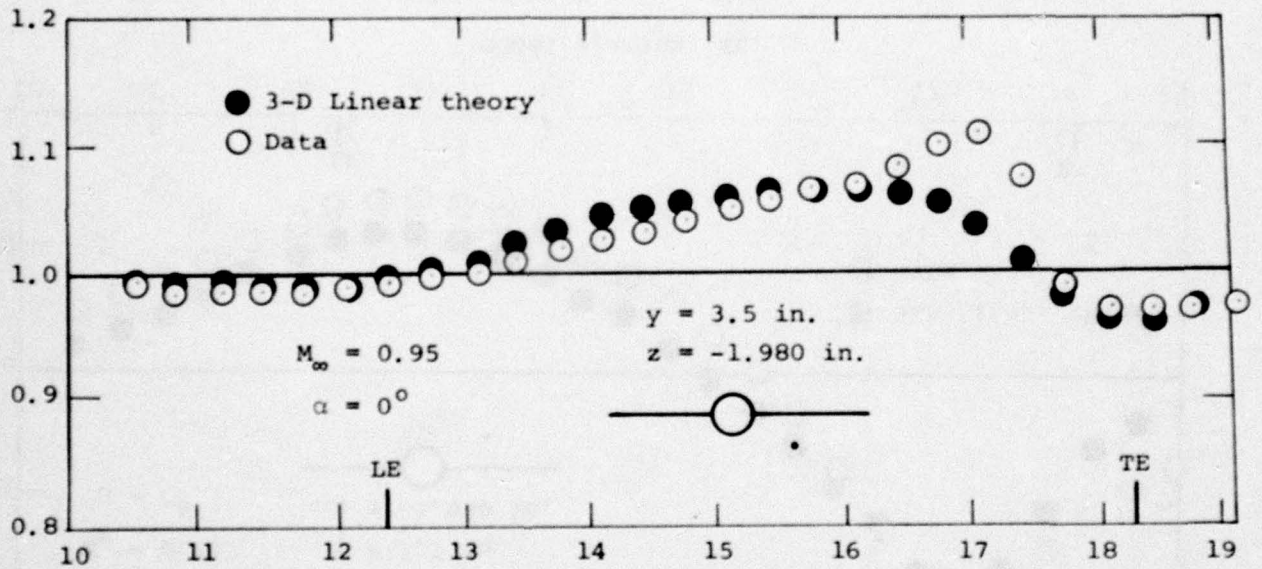

(a) Axial velocity ratio.

Figure 35.- Comparison of measured flow field quantities with prediction of three-dimensional linear theory for wing-body combination, $\alpha = 0^\circ$, $M_\infty = 0.95$, y = 3.5 in., z = -1.980 in.

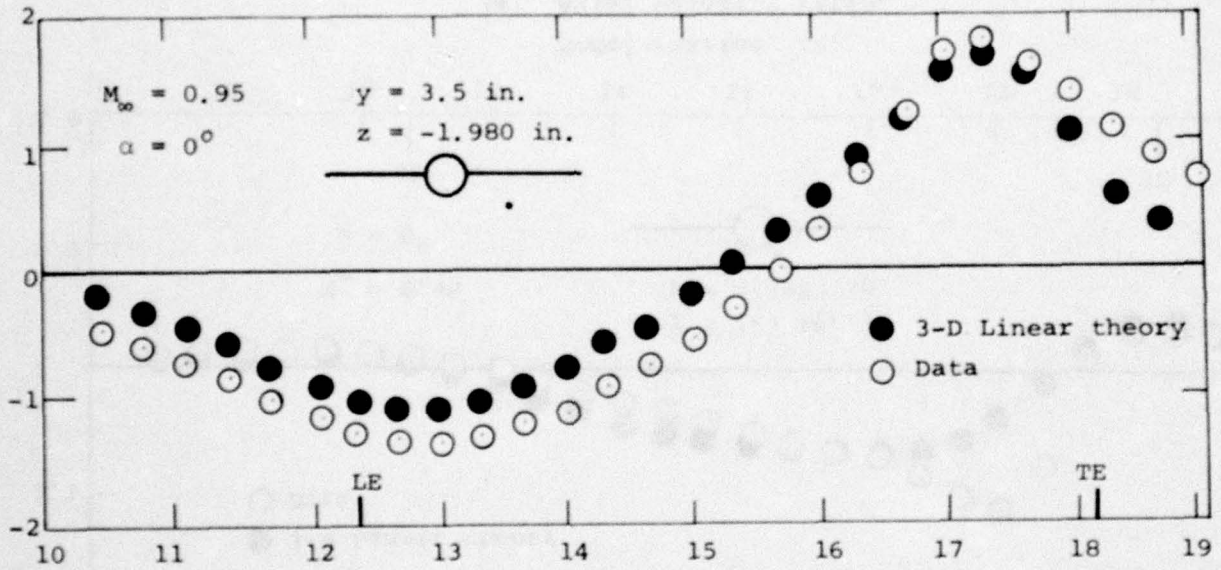

(b) Upwash angle, deg.

Figure 35.- Continued.

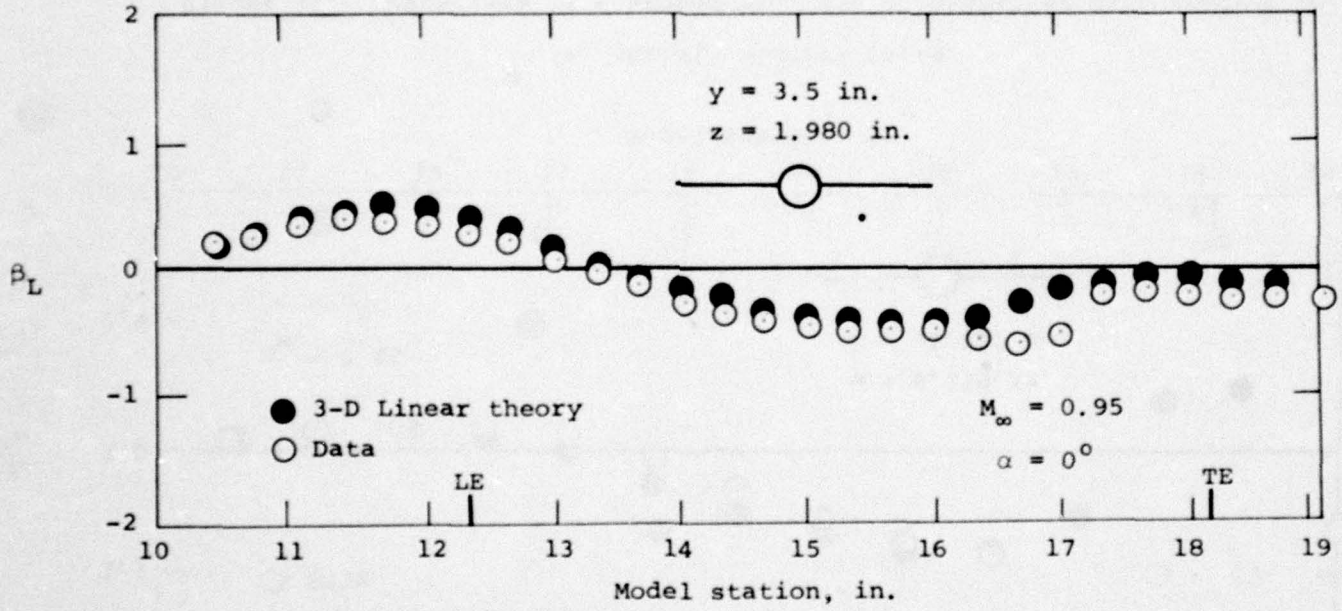

(c) Sidewash angle, deg.

Figure 35.- Concluded.

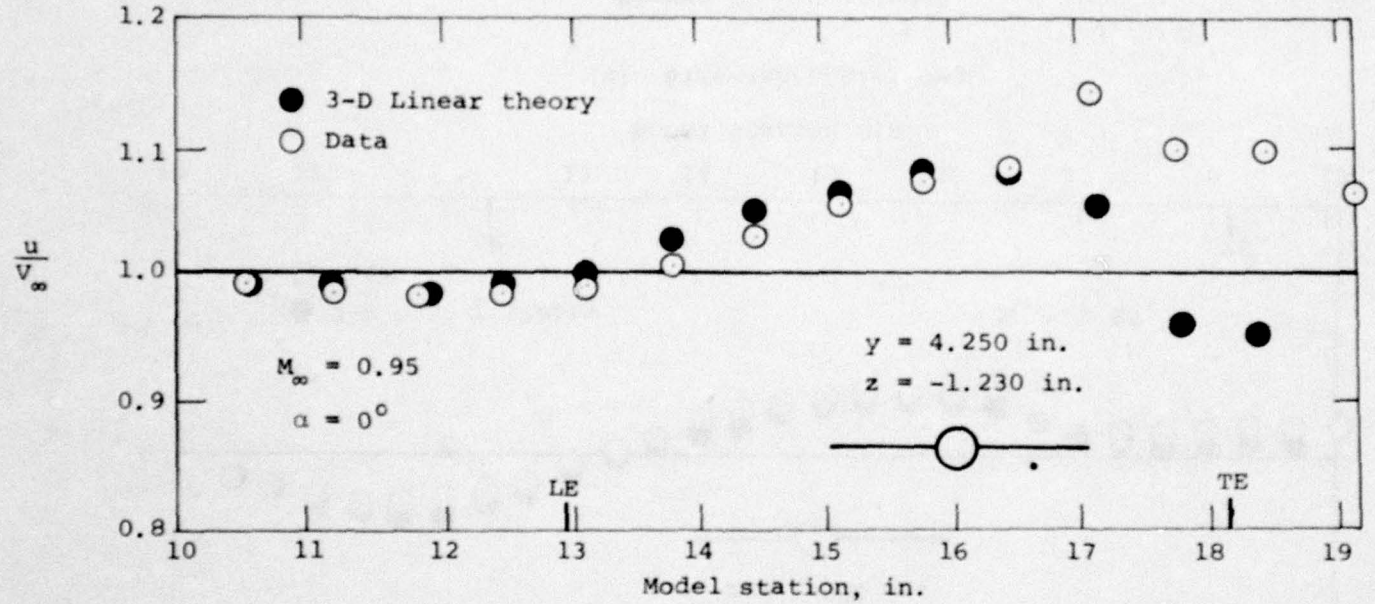

(a) Axial velocity ratio.

Figure 36.- Comparison of measured flow field quantities with prediction of three-dimensional linear theory for wing-body combination, $\alpha = 0^\circ$, $M_\infty = 0.95$, y = 4.250 in., z = -1.230 in.

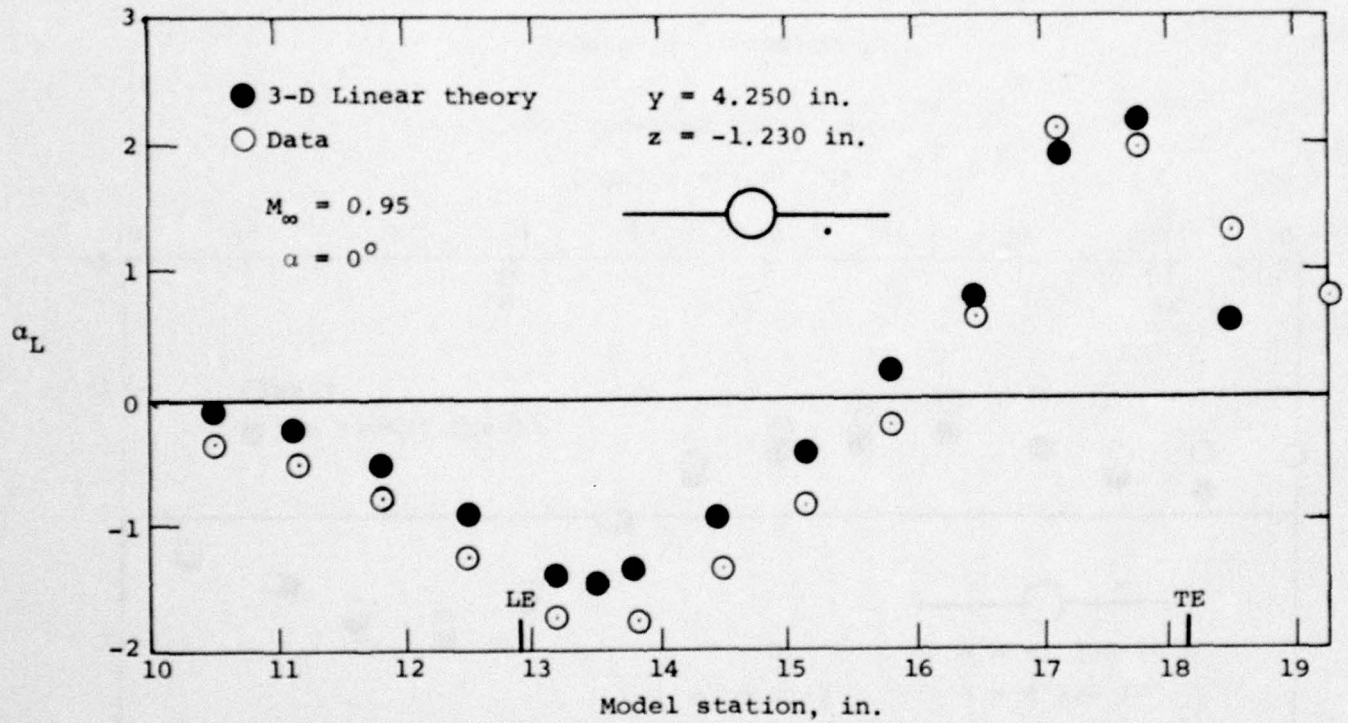

(b) Upwash angle, deg.

Figure 36.- Continued.

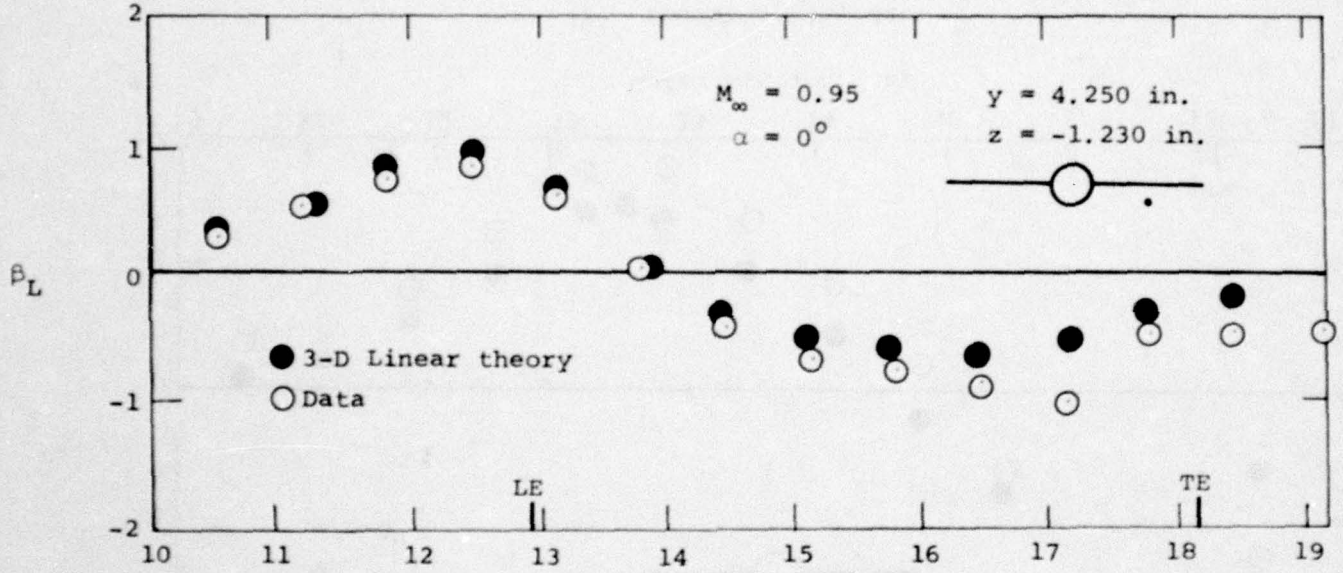

(c) Sidewash angle, deg.

Figure 36.- Concluded.

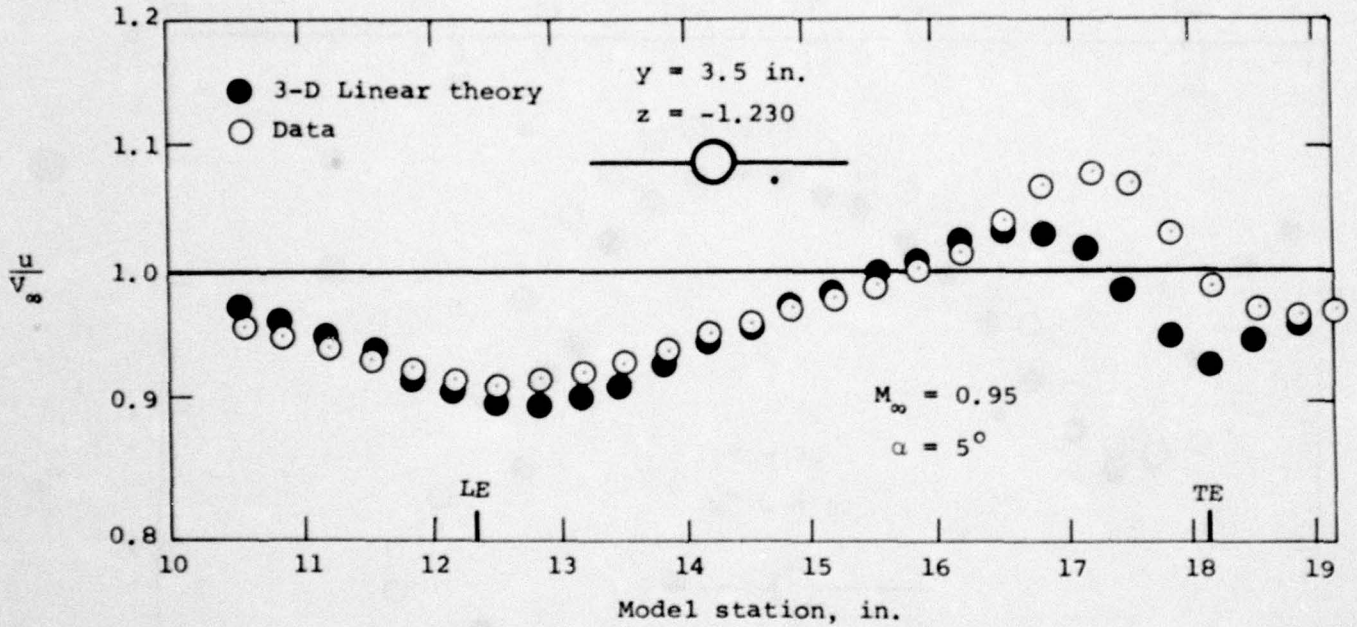

(a) Axial velocity ratio.

Figure 37.- Comparison of measured flow field quantities with prediction of three-dimensional linear theory for wing-body combination, $\alpha = 5^\circ$, $M_\infty = 0.95$, y = 3.5 in., z = -1.230 in.

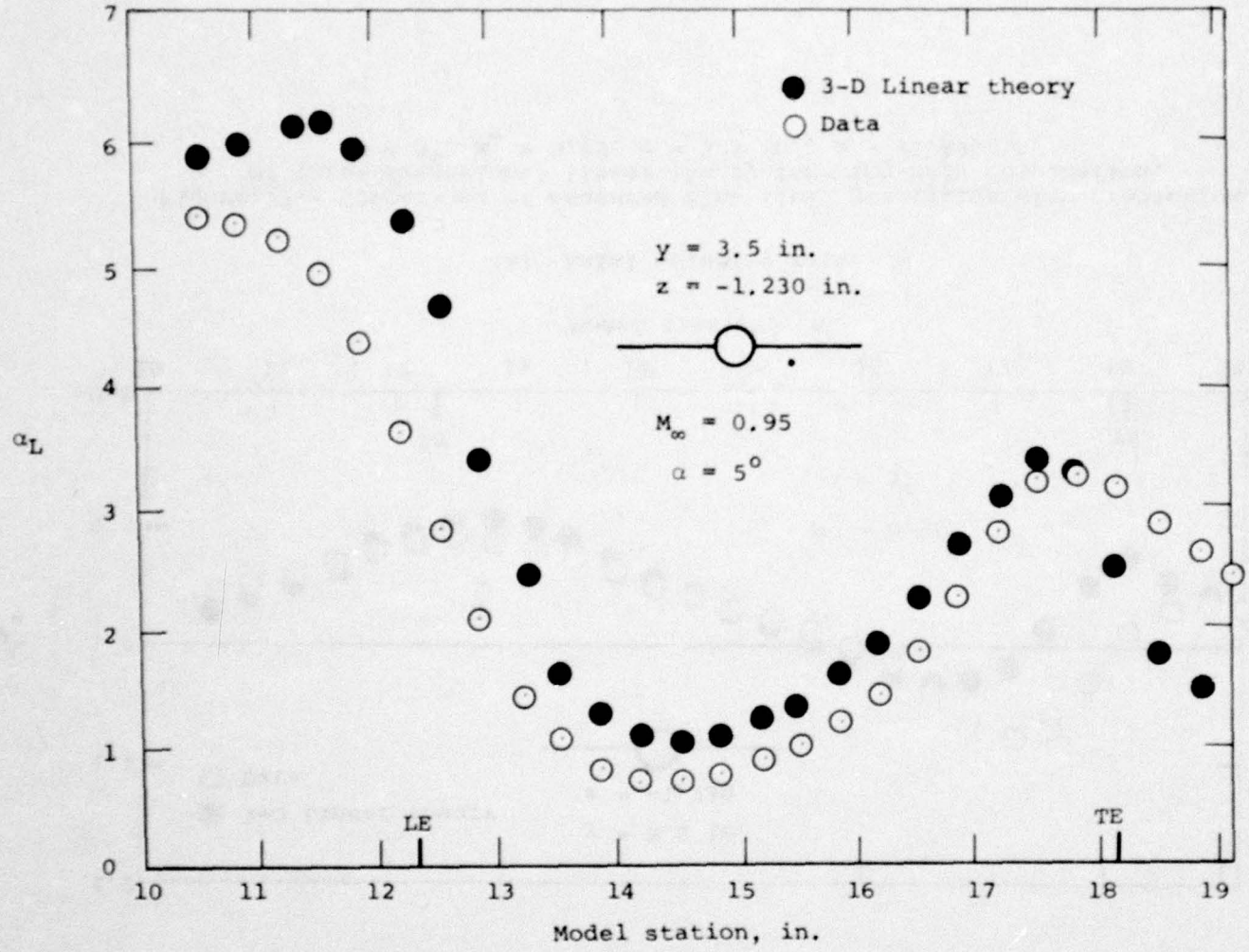

(b) Upwash angle, deg.

Figure 37.- Continued.

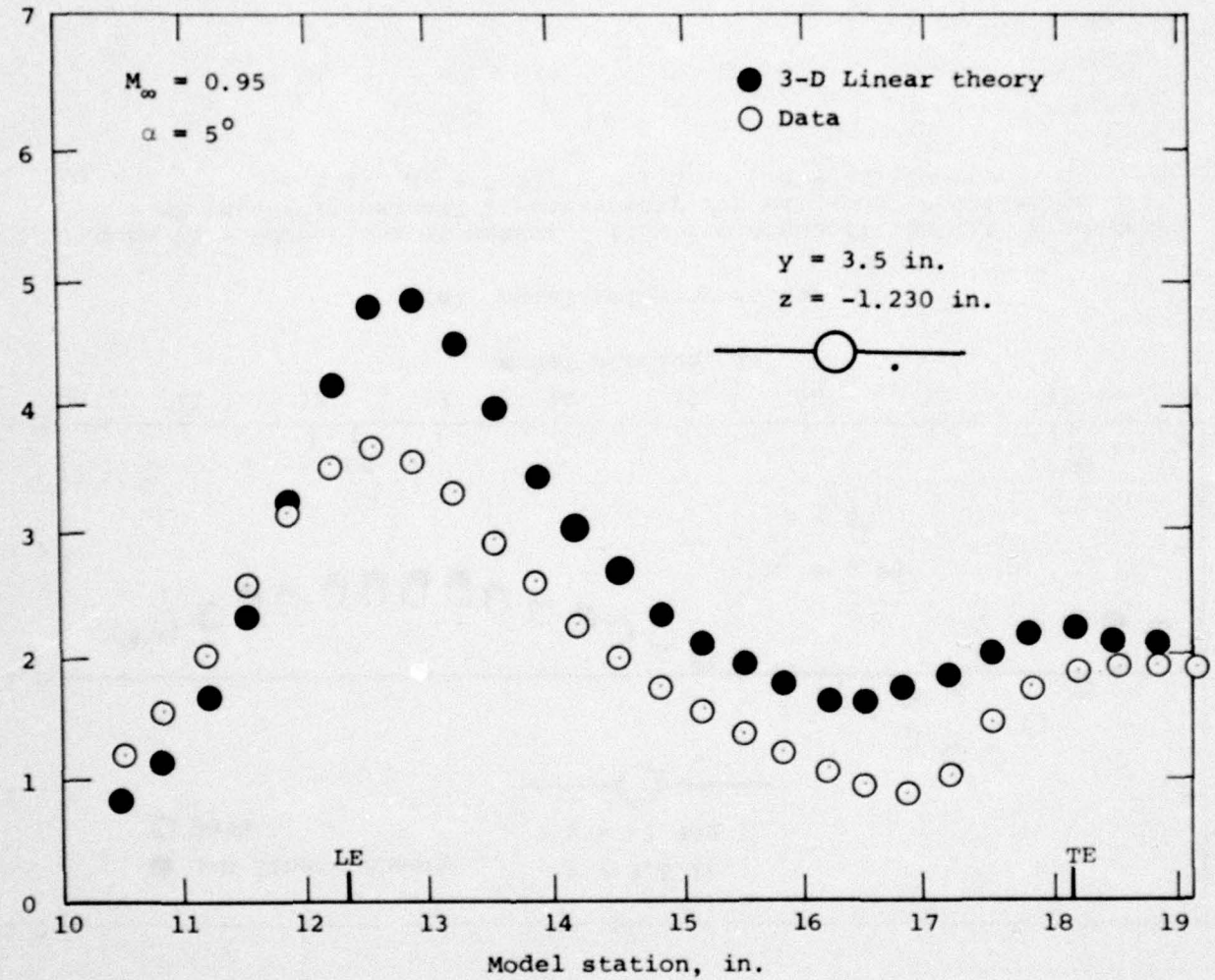

(c) Sidewash angle, deg.

Figure 37.- Concluded.

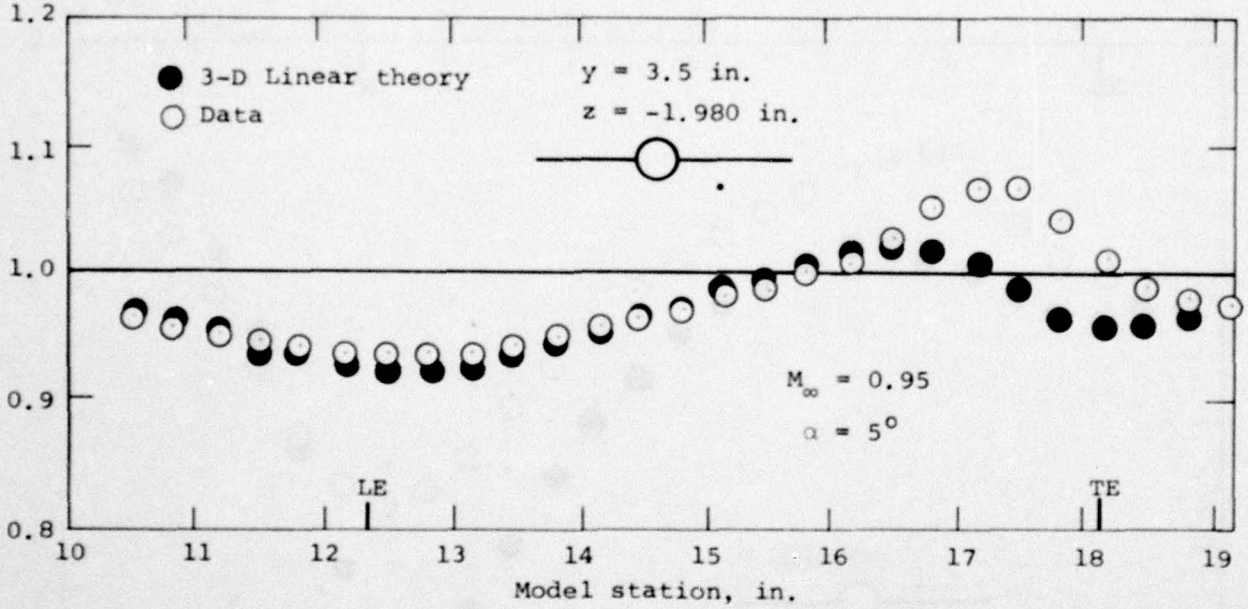

(a) Axial velocity ratio.

Figure 38.- Comparison of measured flow field quantities with prediction of three-dimensional linear theory for wing-body combination, $\alpha = 5^\circ$, $M_\infty = 0.95$, y = 3.5 in., z = -1.980 in.

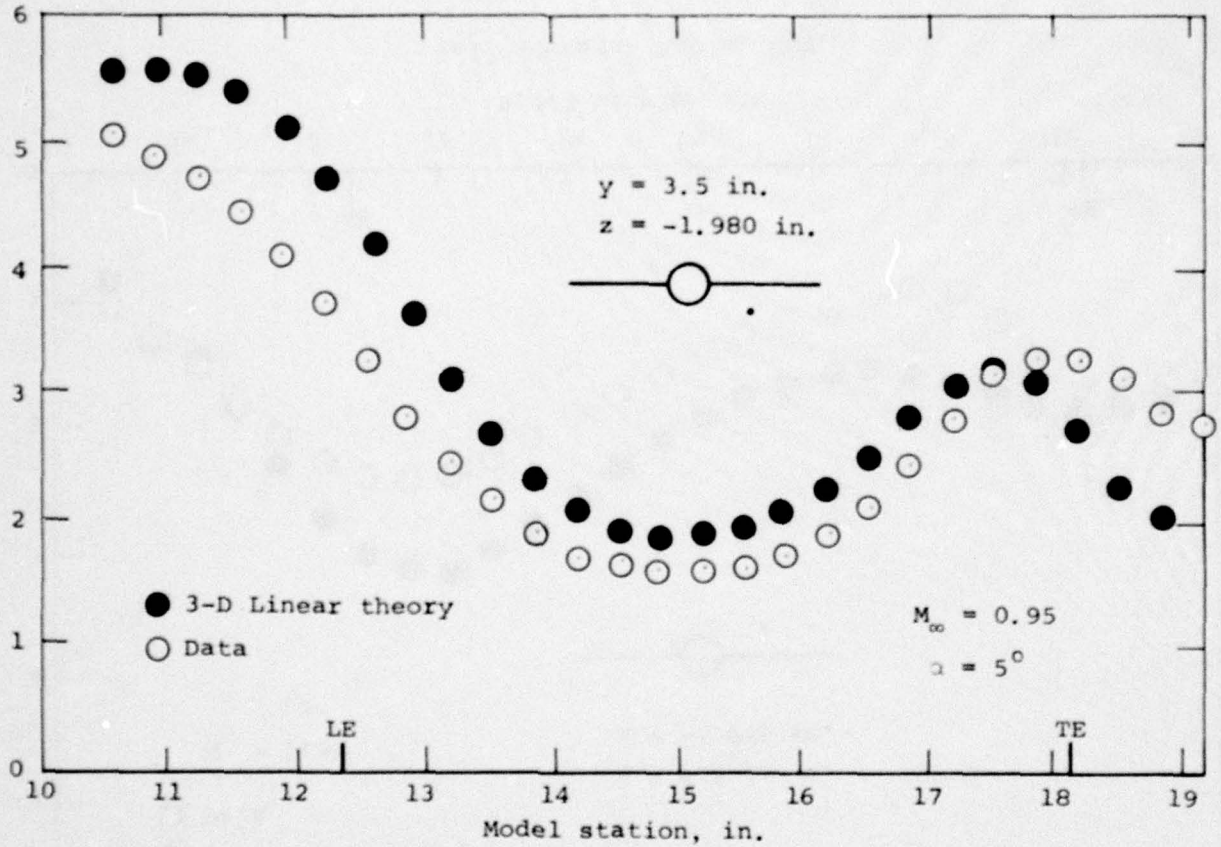

(b) Upwash angle, deg.

Figure 38.- Continued.

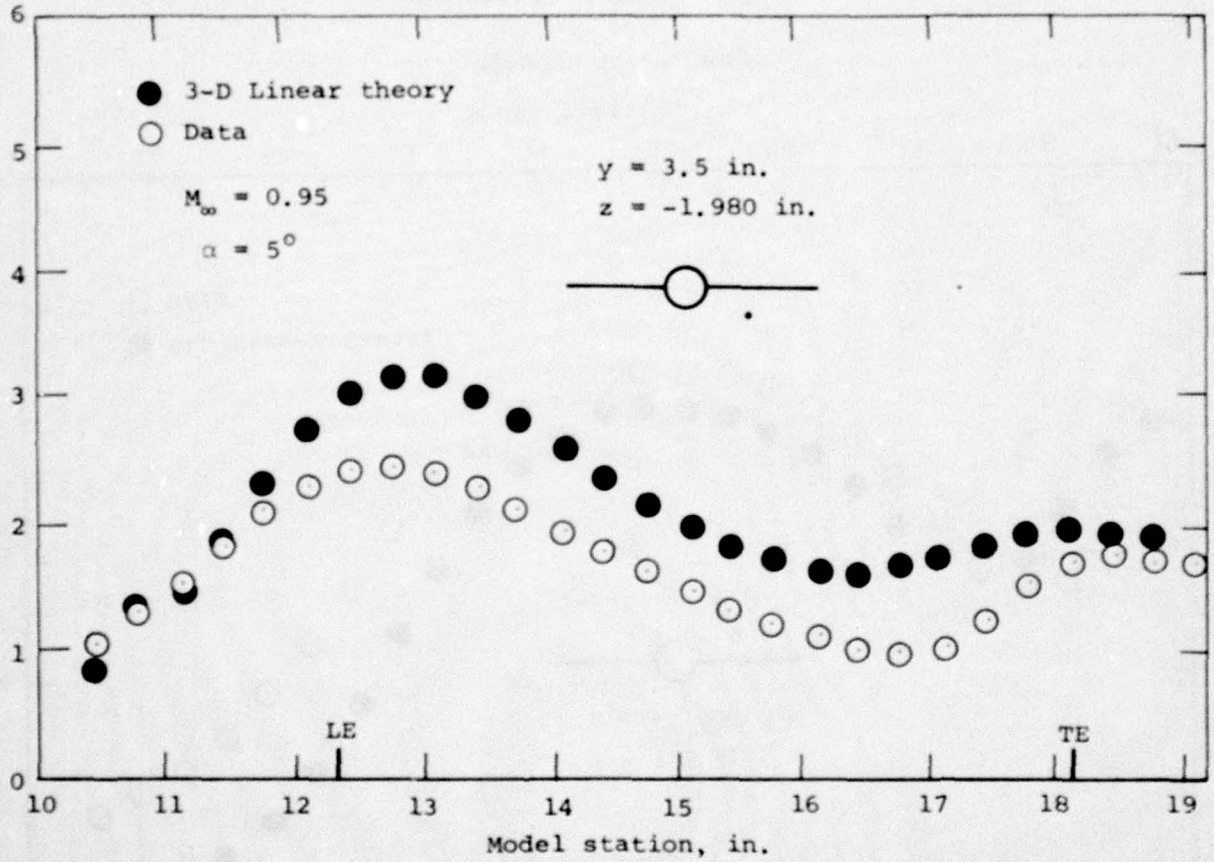

(c) Sidewash angle, deg.

Figure 38.- Concluded.

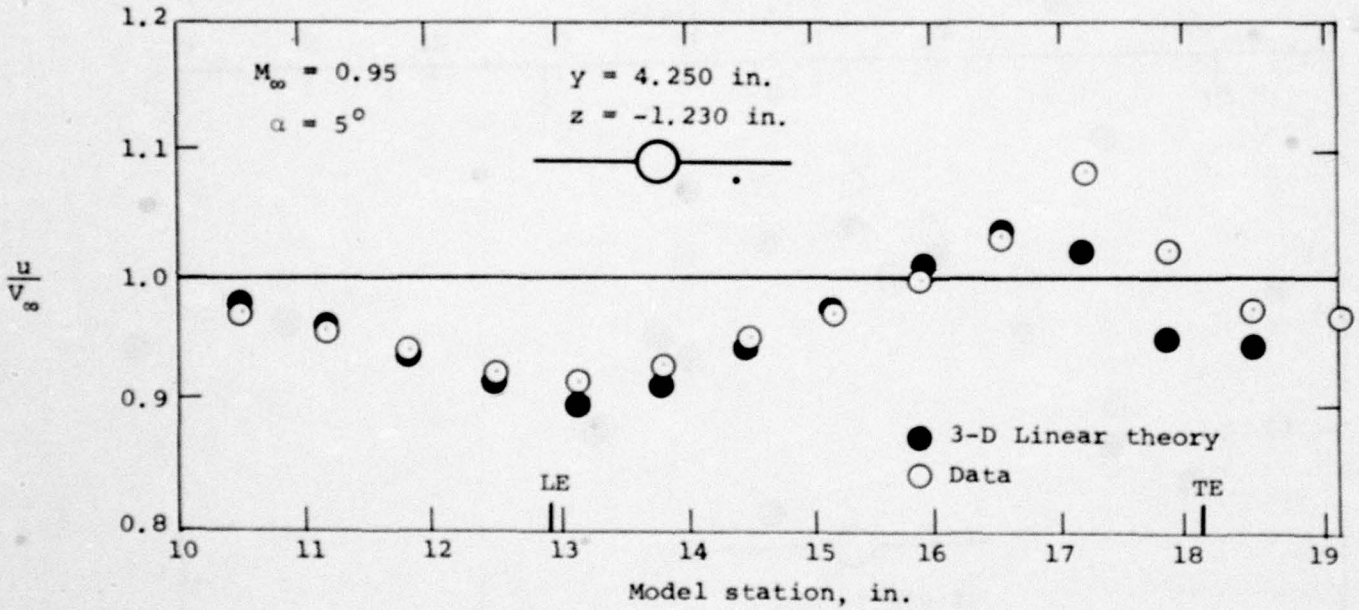

(a) Axial velocity ratio.

Figure 39.- Comparison of measured flow field quantities with prediction of three-dimensional linear theory for wing-body combination, $\alpha = 5^\circ$, $M_\infty = 0.95$, y = 4.250 in., z = -1.230 in.

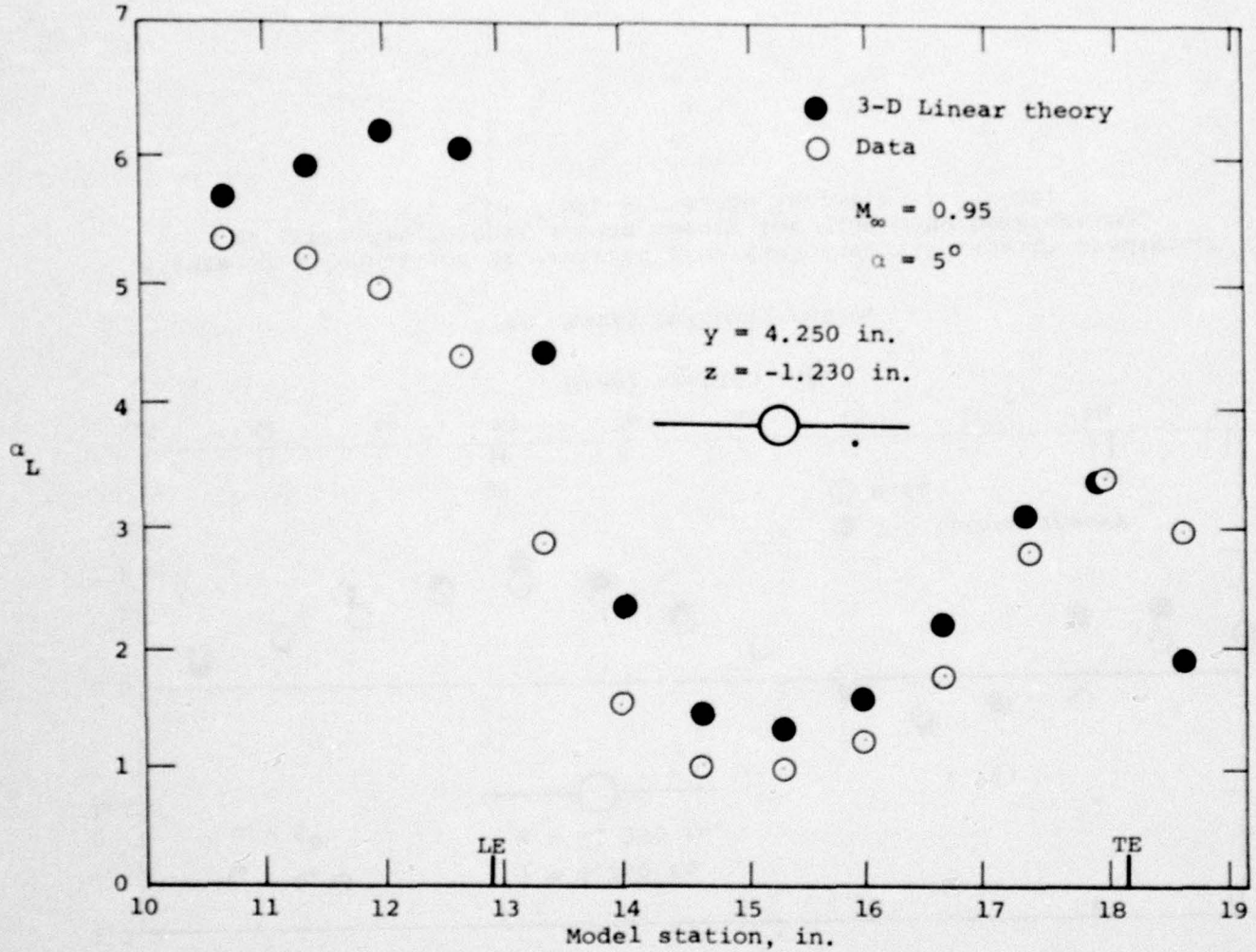

(b) Upwash angle, deg.

Figure 39.- Continued.

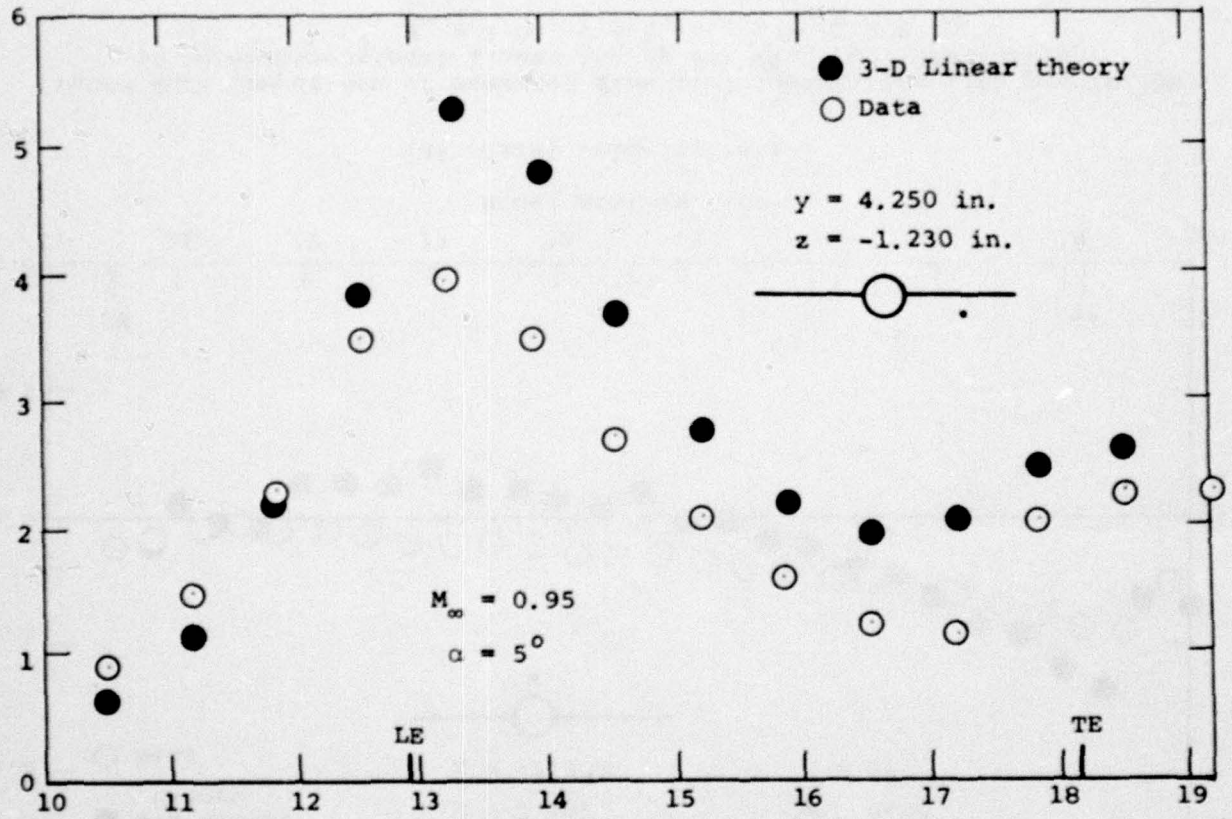

(c) Sidewash angle, deg.

Figure 39.- Concluded.

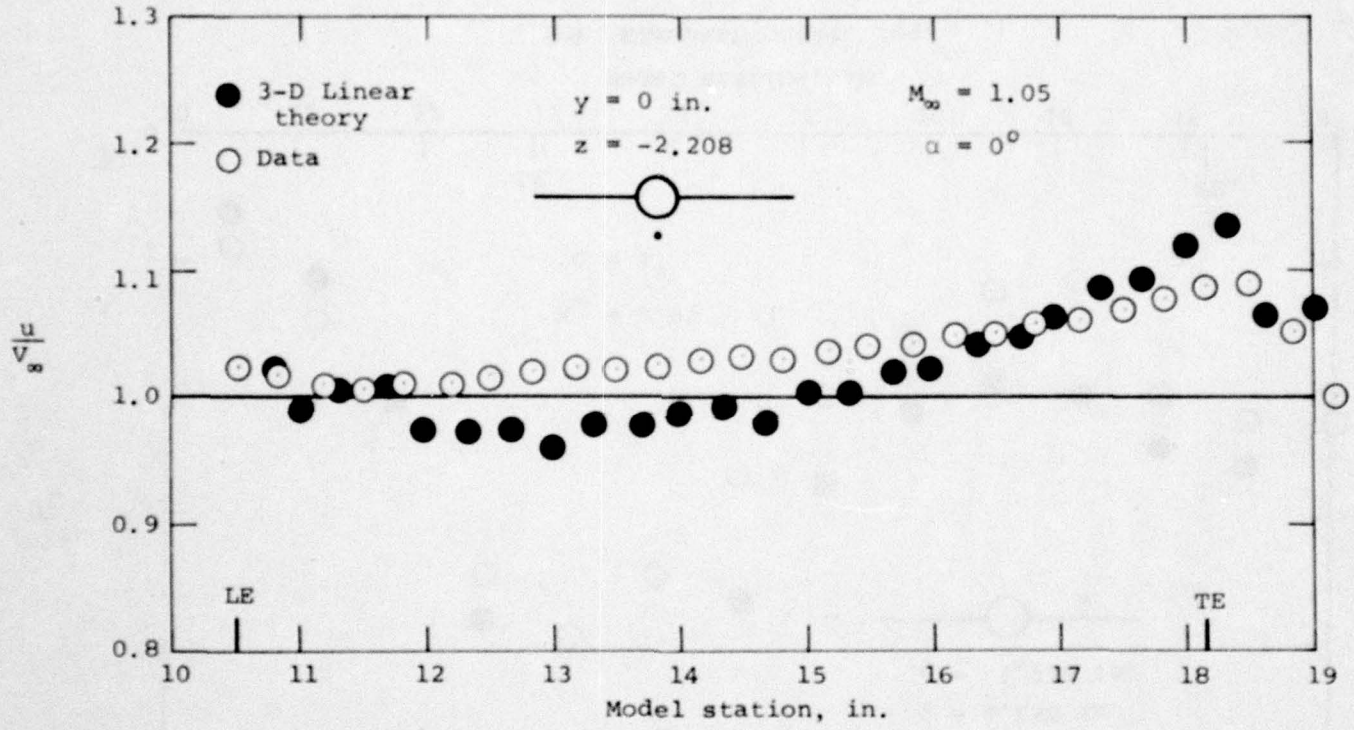

(a) Axial velocity ratio.

Figure 40.- Comparison of measured flow field quantities with prediction of three-dimensional linear theory for wing-body combination, $\alpha = 0^\circ$, $M_\infty = 1.05$, y = 0 in., z = -2.208 in.

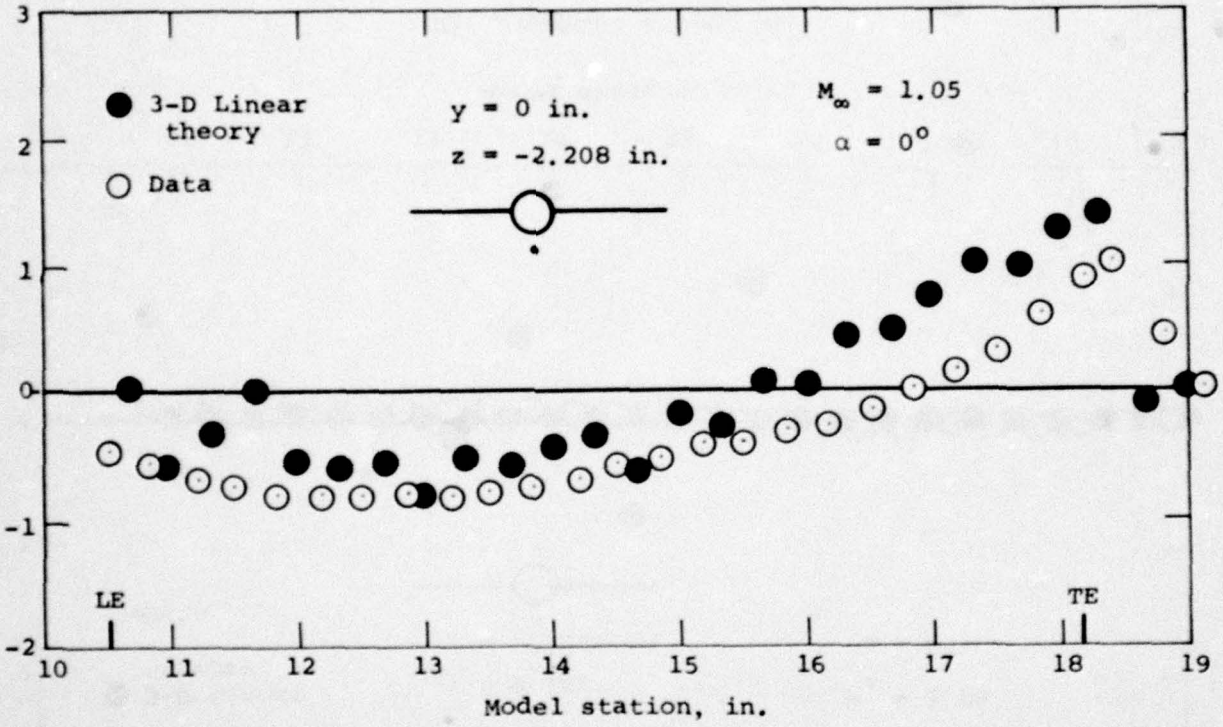

(b) Upwash angle, deg.

Figure 40.- Continued.

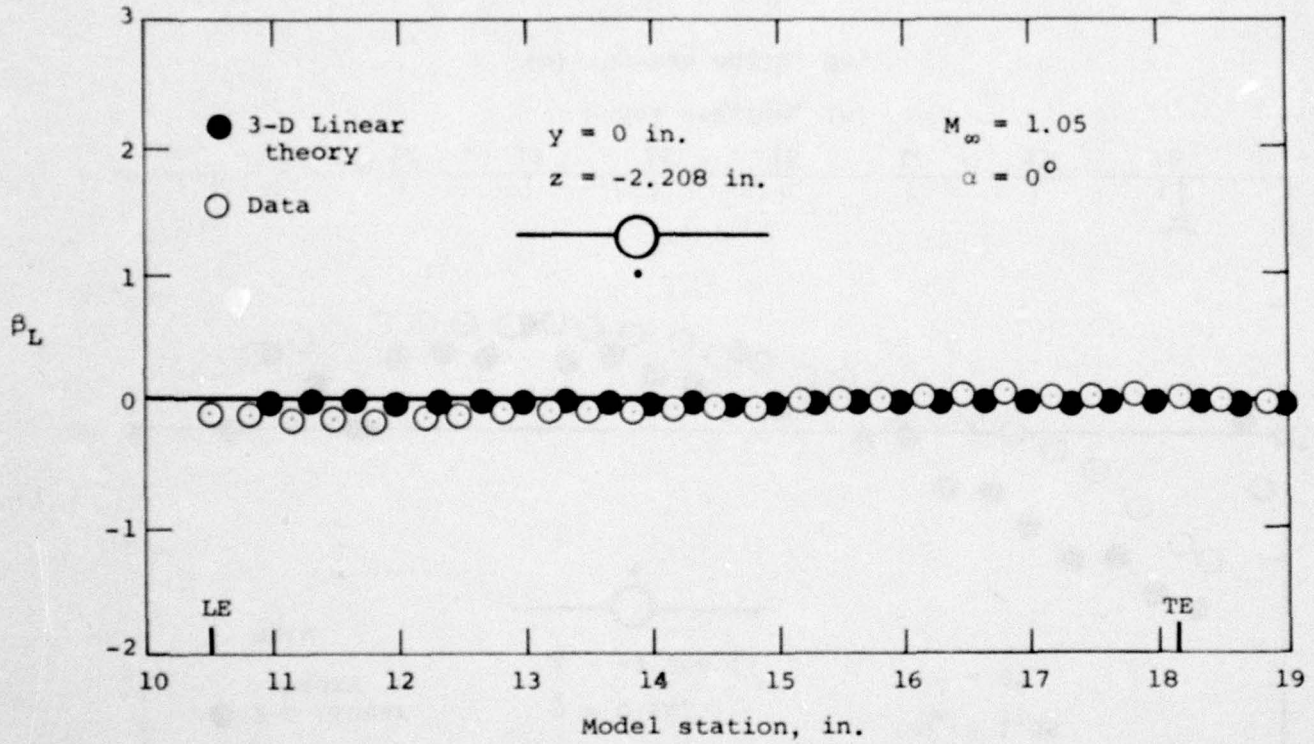

(c) Sidewash angle, deg.

Figure 40.- Concluded.

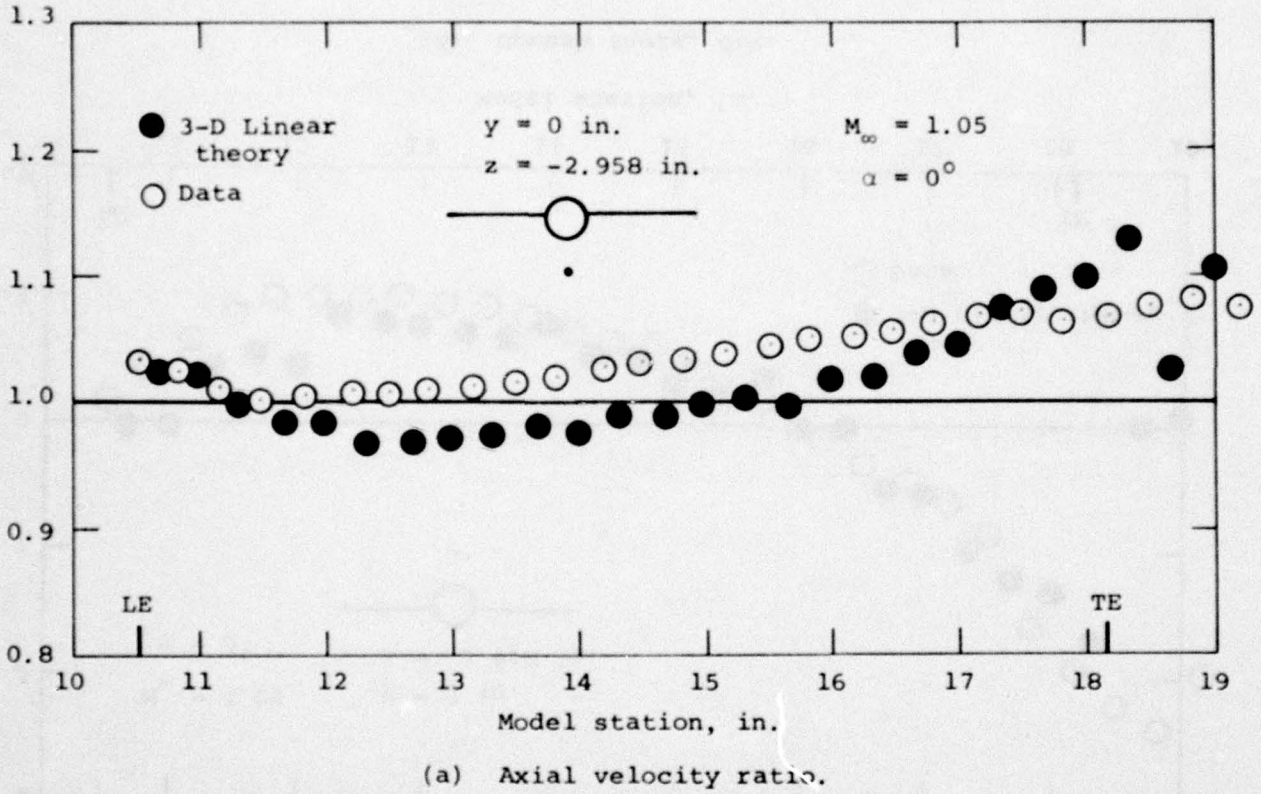

$\frac{u}{V_\infty}$

(a) Axial velocity ratio.

Figure 41.- Comparison of measured flow field quantities with prediction of three-dimensional linear theory for wing-body combination, $\alpha = 0^\circ$, $M_\infty = 1.05$. y = 0 in., z = -2.958 in.

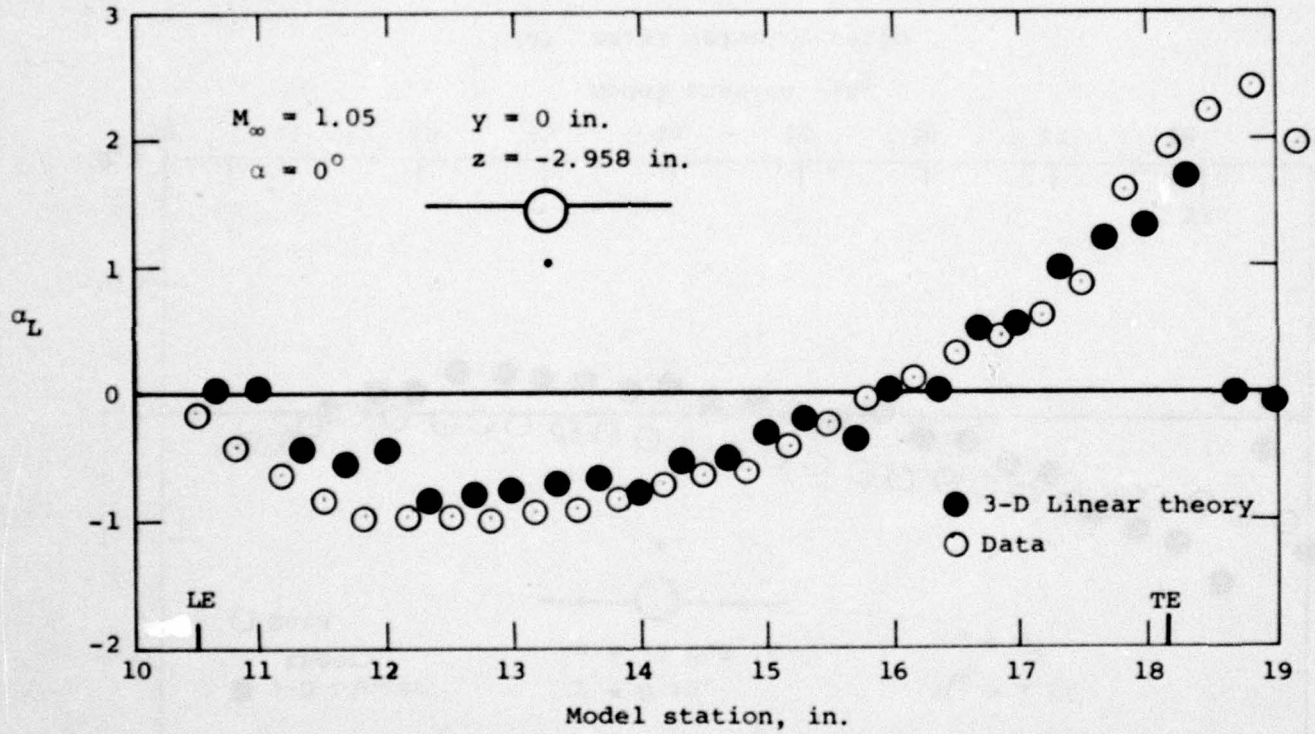

(b) Upwash angle, deg.

Figure 41.- Continued.

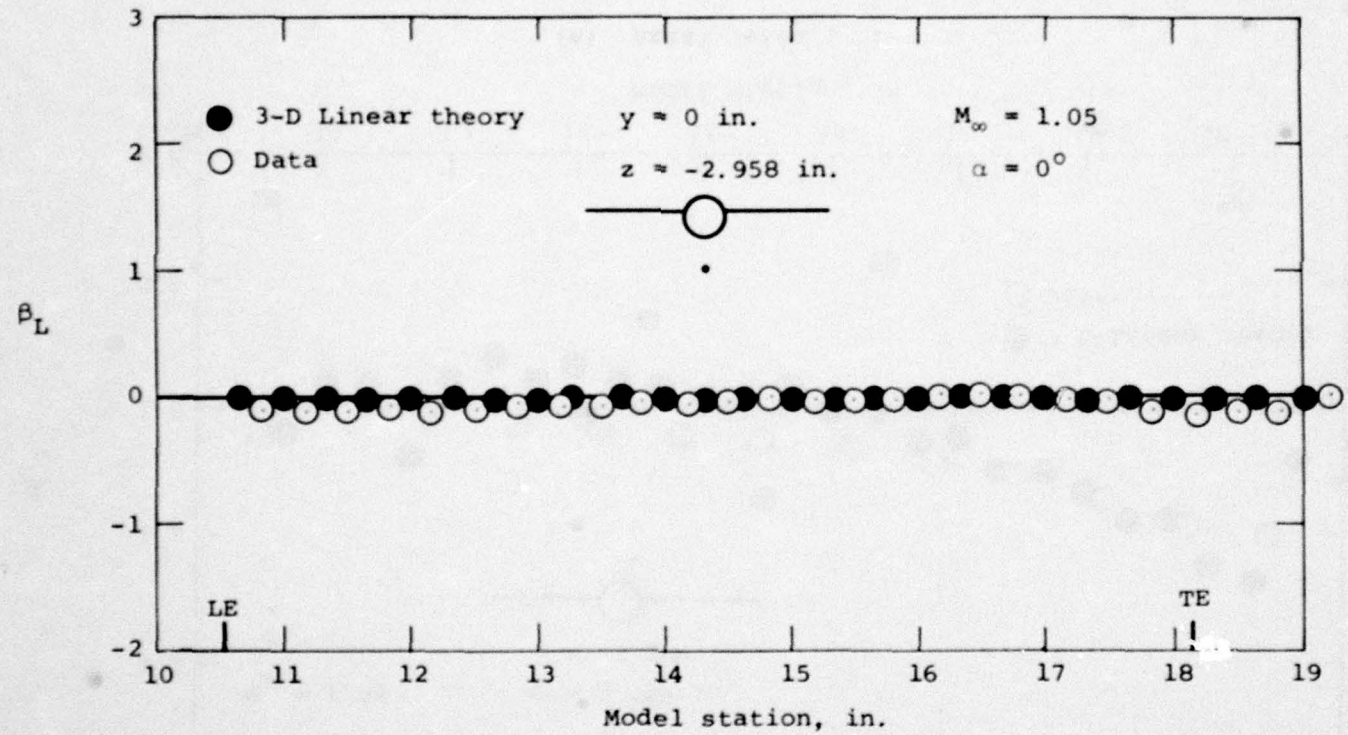

(c) Sidewash angle, deg.

Figure 41.- Concluded.

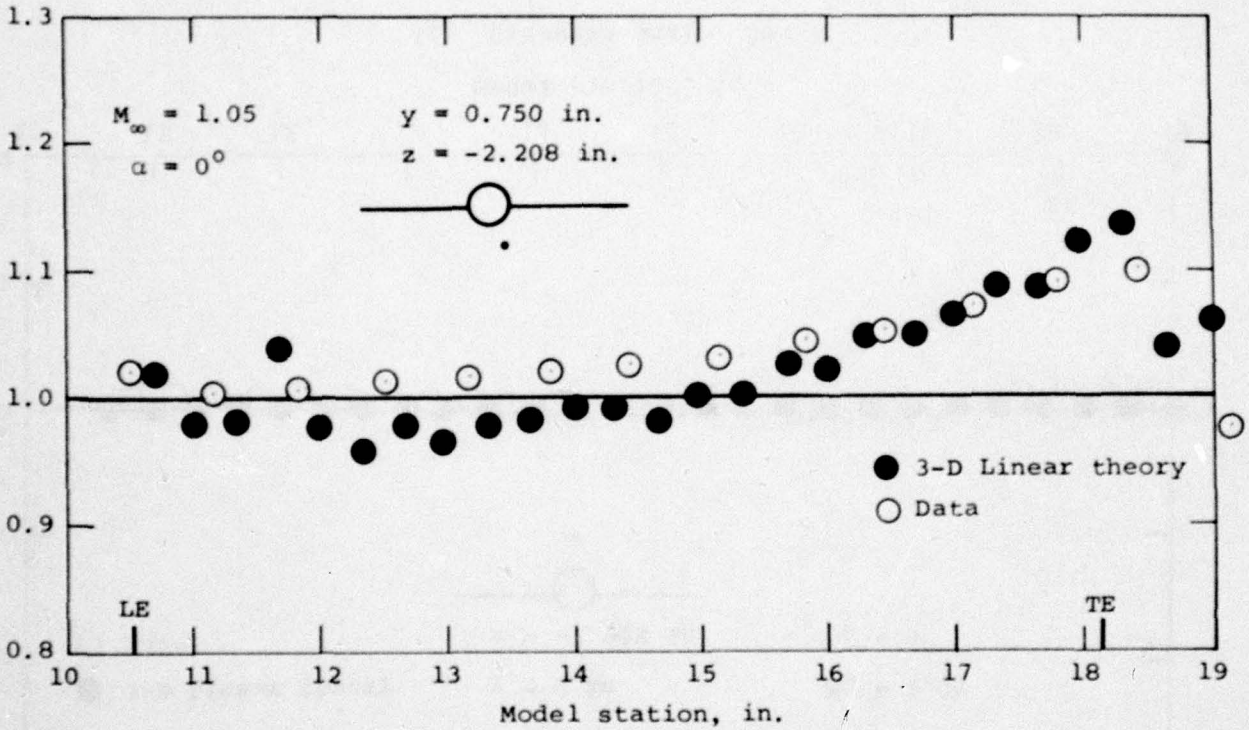

(a) Axial velocity ratio.

Figure 42.- Comparison of measured flow field quantities with prediction of three-dimensional linear theory for wing-body combination, $\alpha = 0^\circ$, $M_\infty = 1.05$, y = 0.750 in., z = -2.208 in.

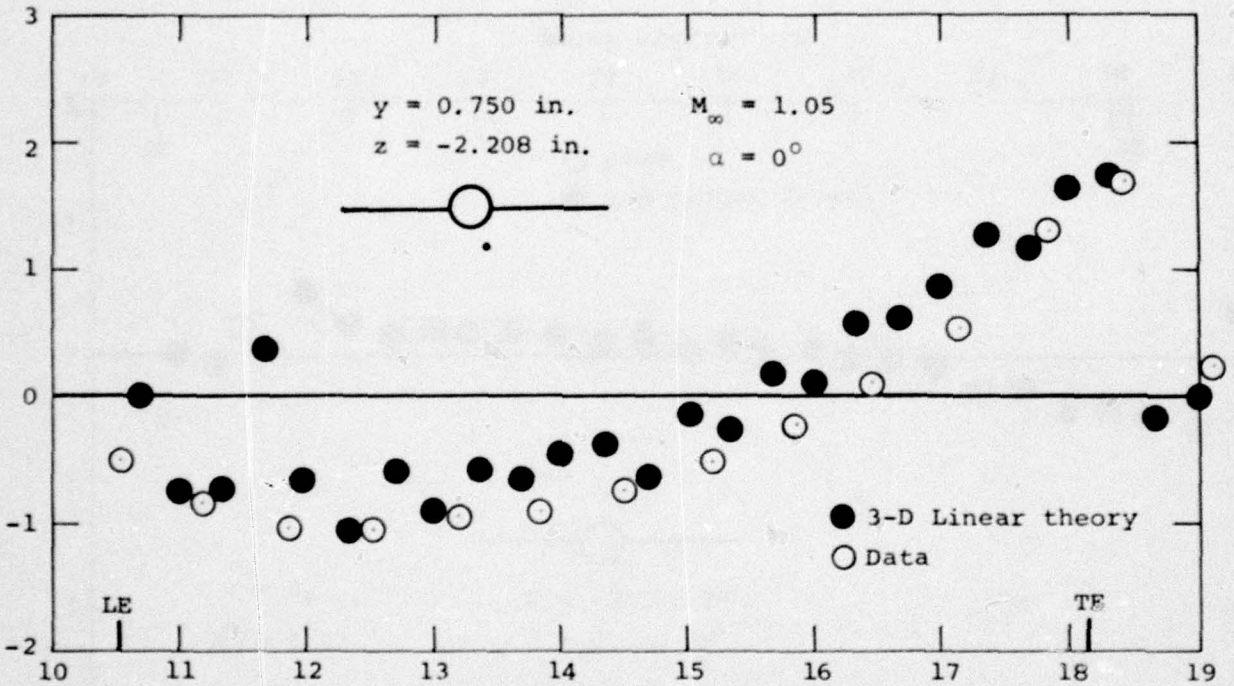

(b) Upwash angle, deg.

Figure 42.- Continued.

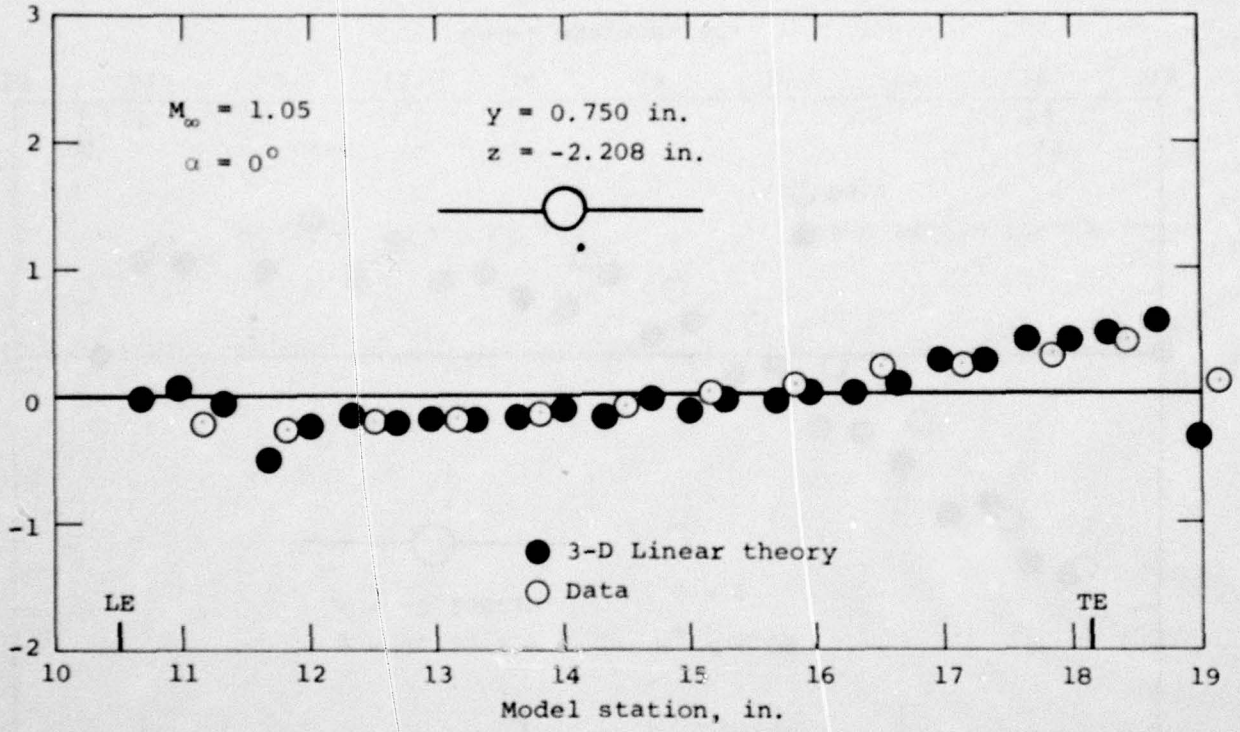

(c) Sidewash angle, deg.

Figure 42.- Concluded.

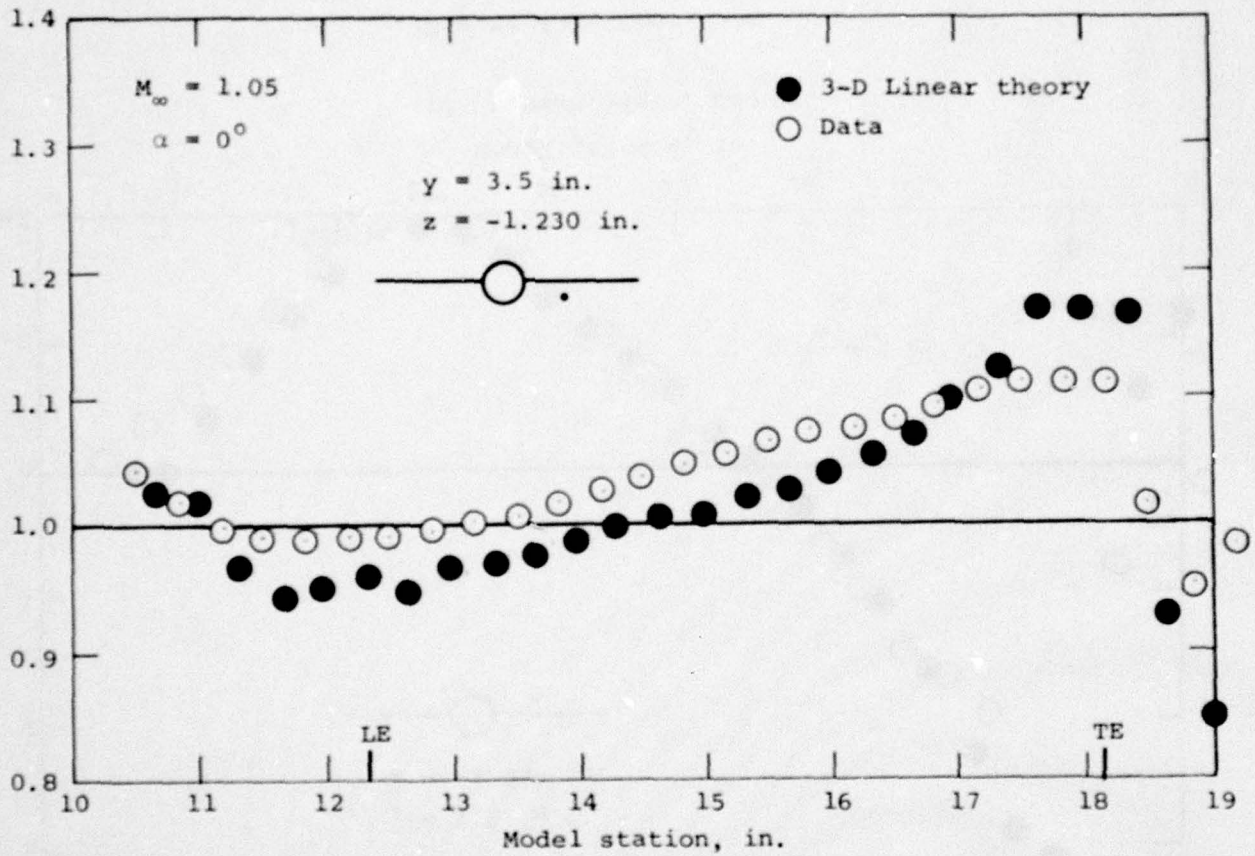

(a) Axial velocity ratio.

Figure 43.- Comparison of measured flow field quantities with prediction of three-dimensional linear theory for wing-body combination, $\alpha = 0°$, $M_\infty = 1.05$, y = 3.5 in., z = -1.230 in.

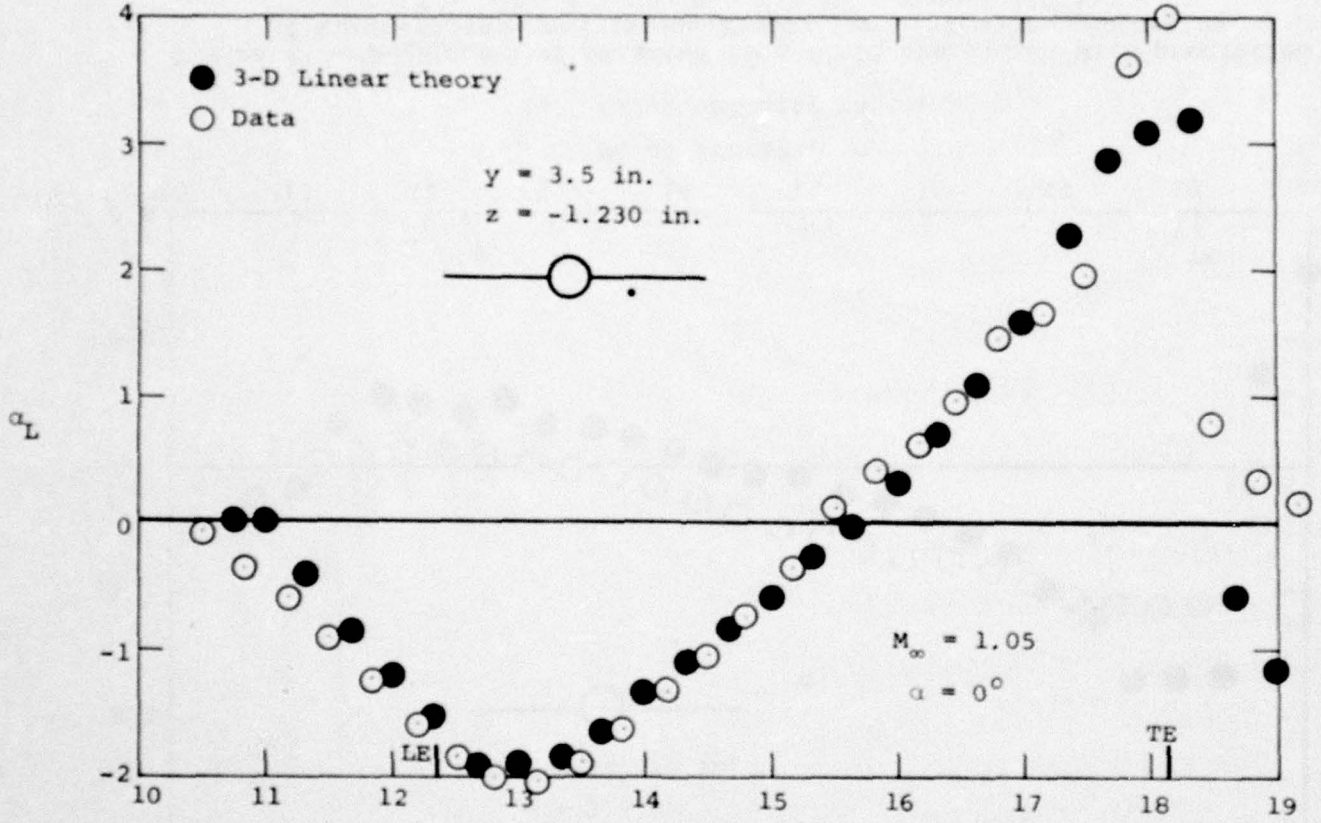

(b) Upwash angle, deg.

Figure 43.- Continued.

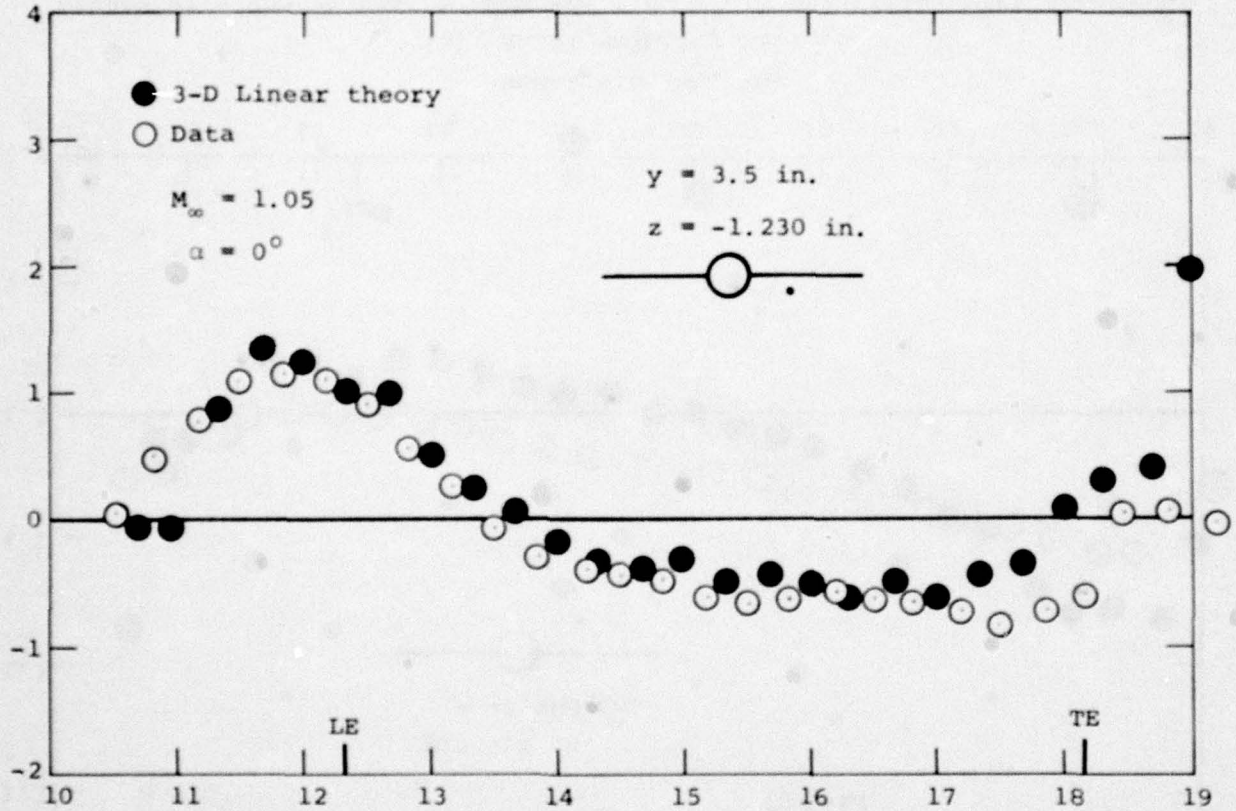

(c) Sidewash angle, deg.

Figure 43.- Concluded.

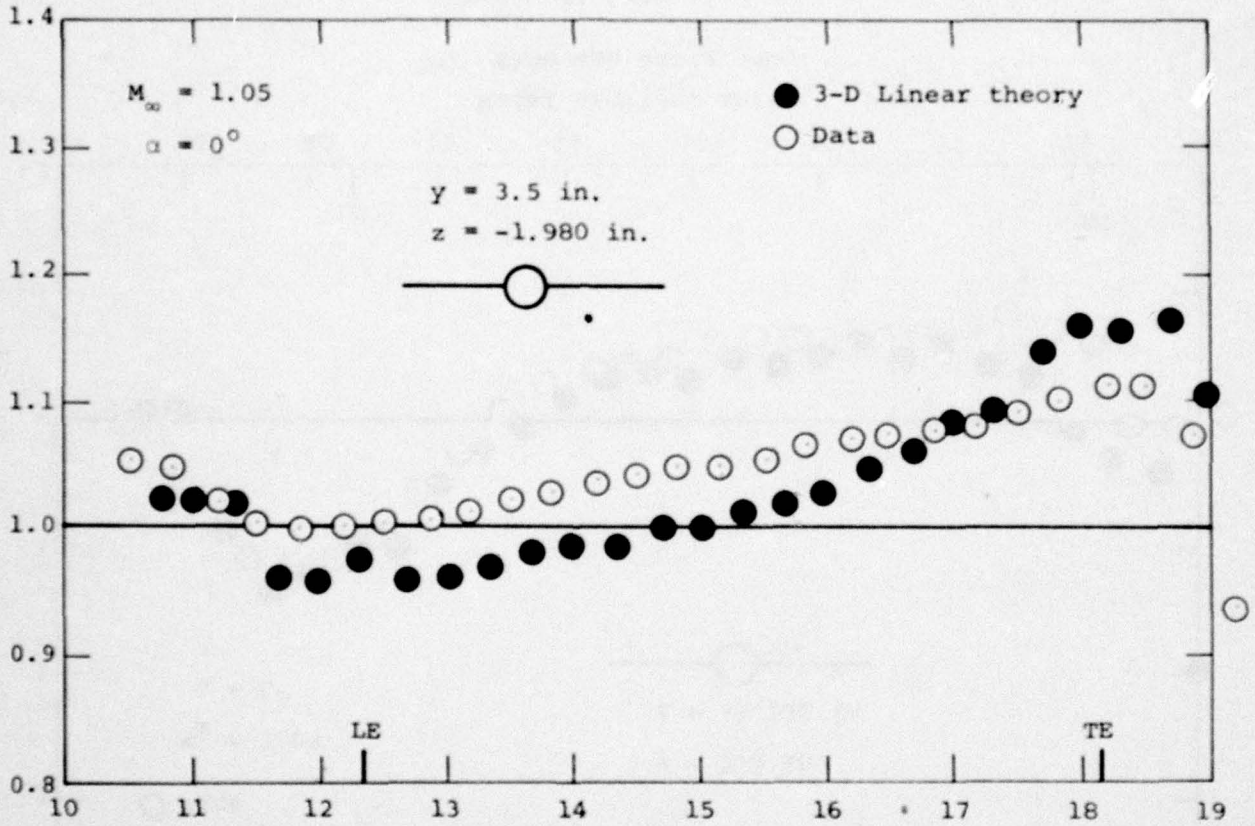

(a) Axial velocity ratio.

Figure 44.- Comparison of measured flow field quantities with prediction of three-dimensional linear theory for wing-body combination, $\alpha = 0^\circ$, $M_\infty = 1.05$, y = 3.5 in., z = -1.980 in.

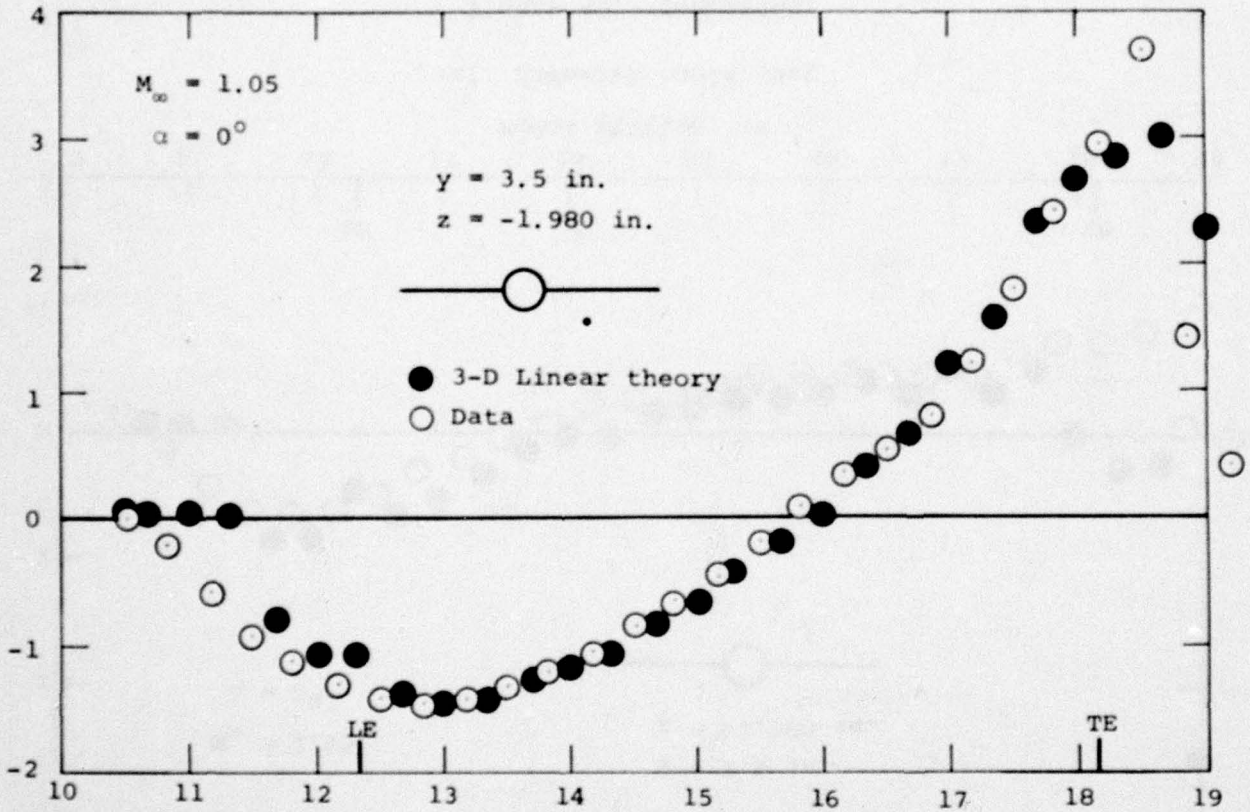

(b) Upwash angle, deg.

Figure 44.- Continued.

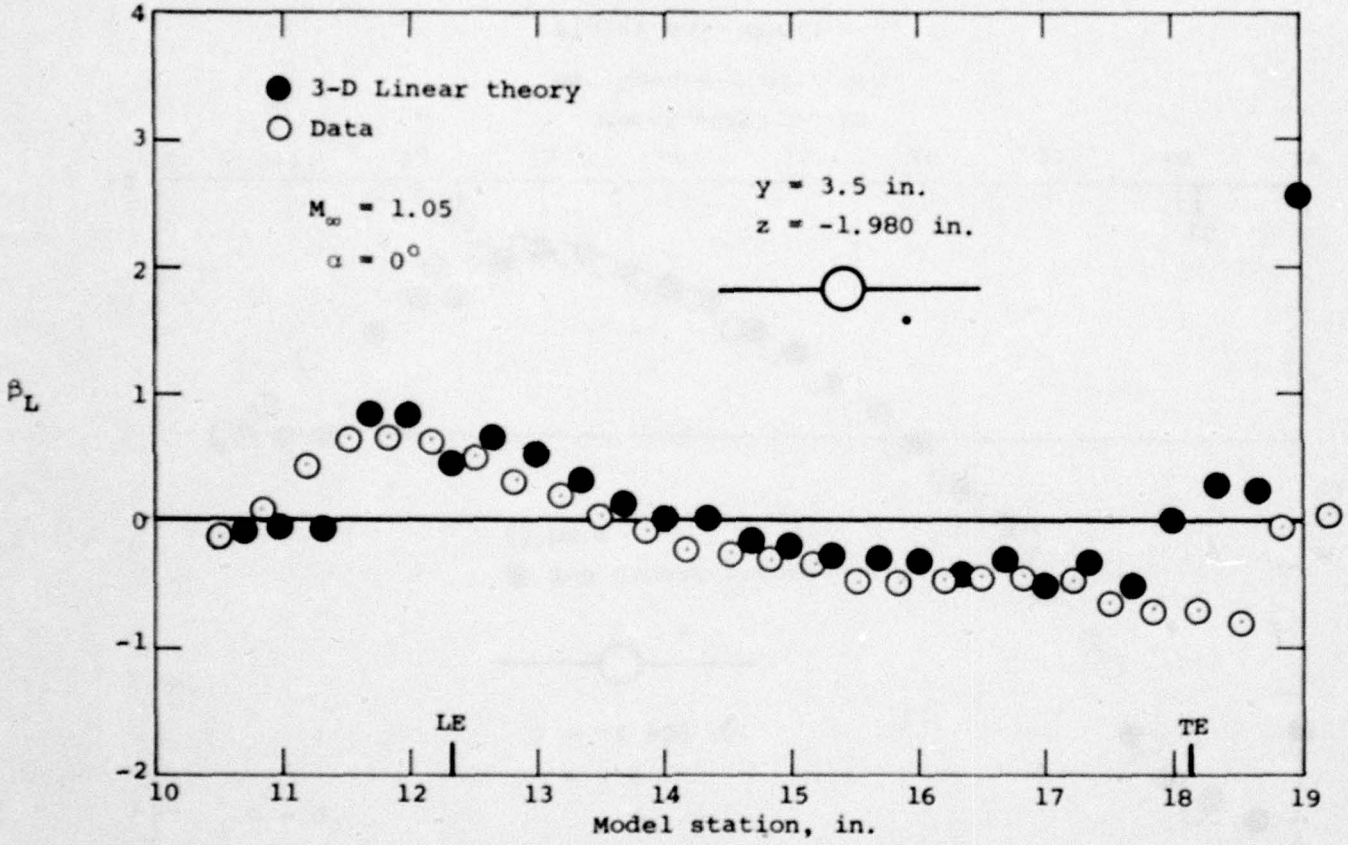

(c) Sidewash angle, deg.

Figure 44.- Concluded.

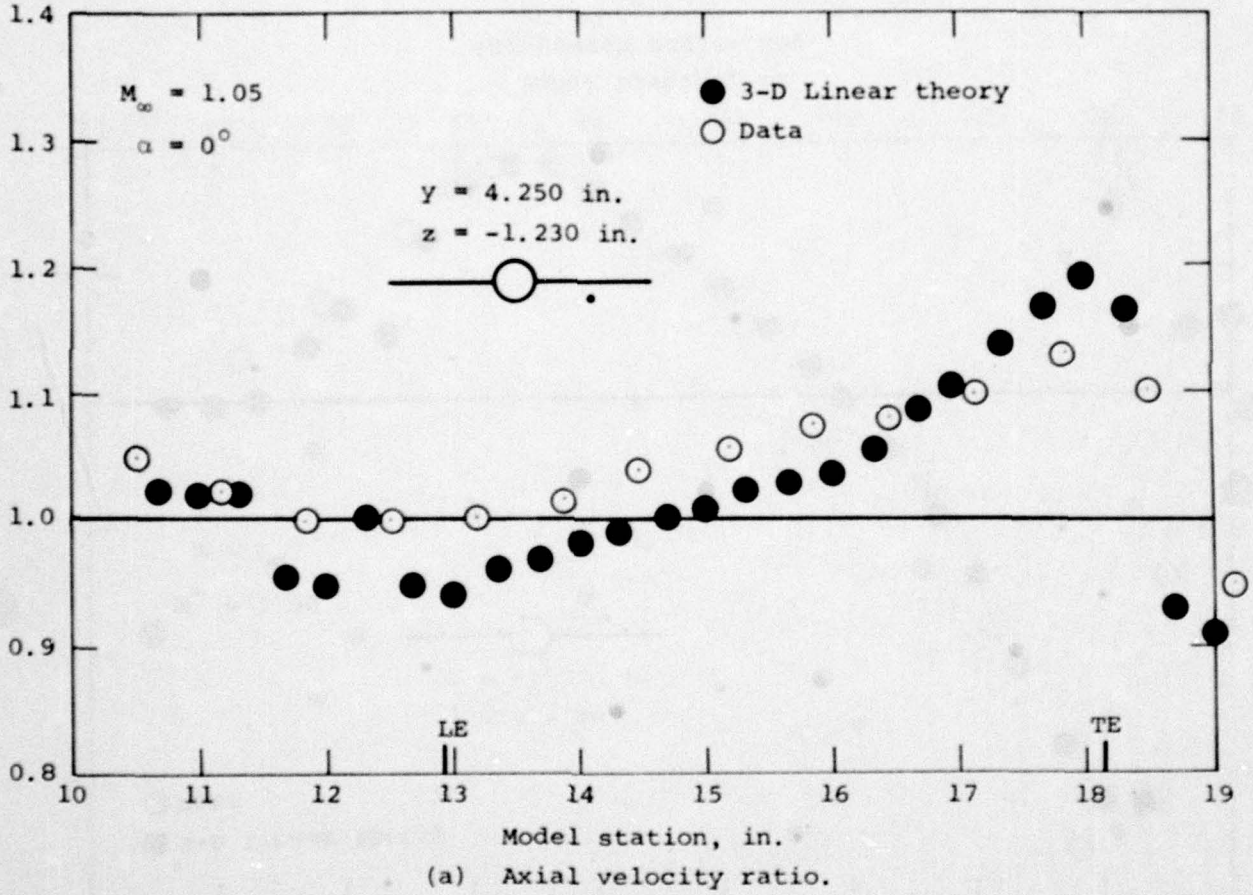

(a) Axial velocity ratio.

Figure 45.- Comparison of measured flow field quantities with prediction of three-dimensional linear theory for wing-body combination, $\alpha = 0°$, $M_\infty = 1.05$, y = 4.250 in., z = -1.230 in.

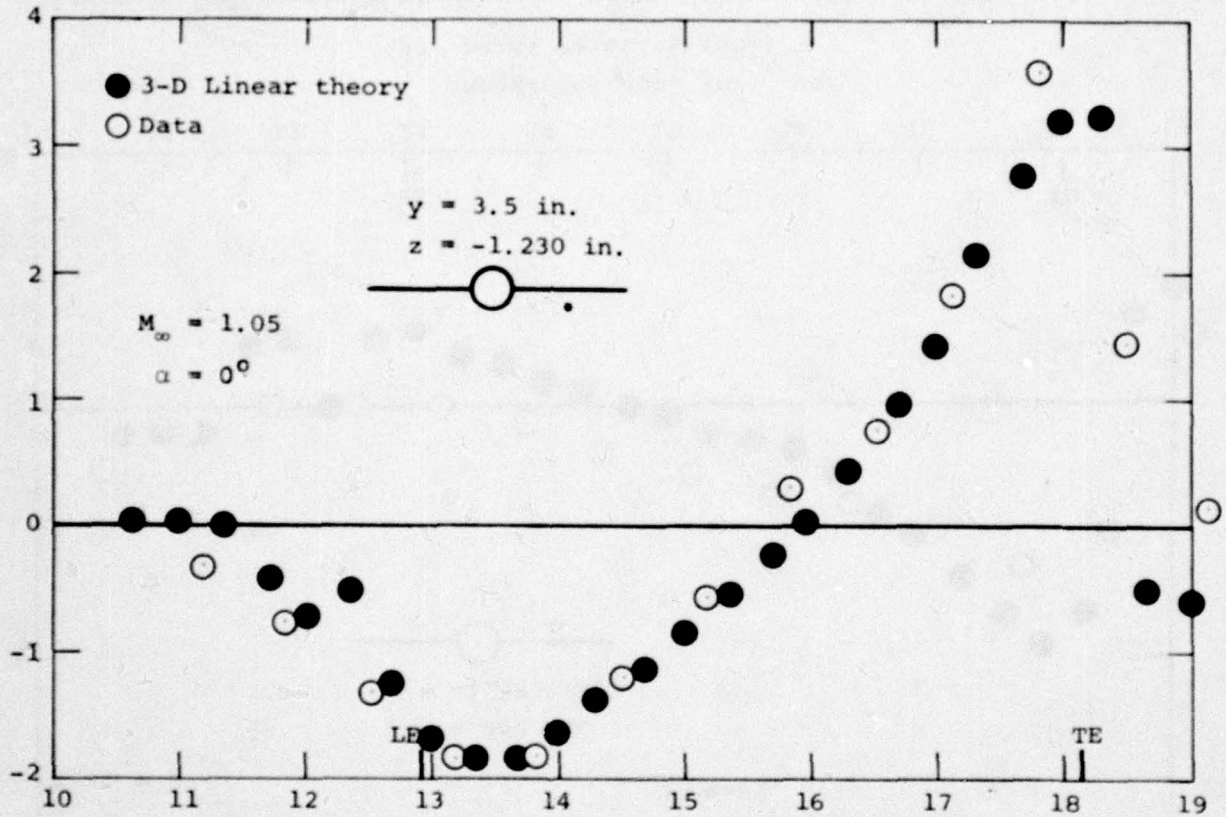

(b) Upwash angle, deg.

Figure 45.- Continued.

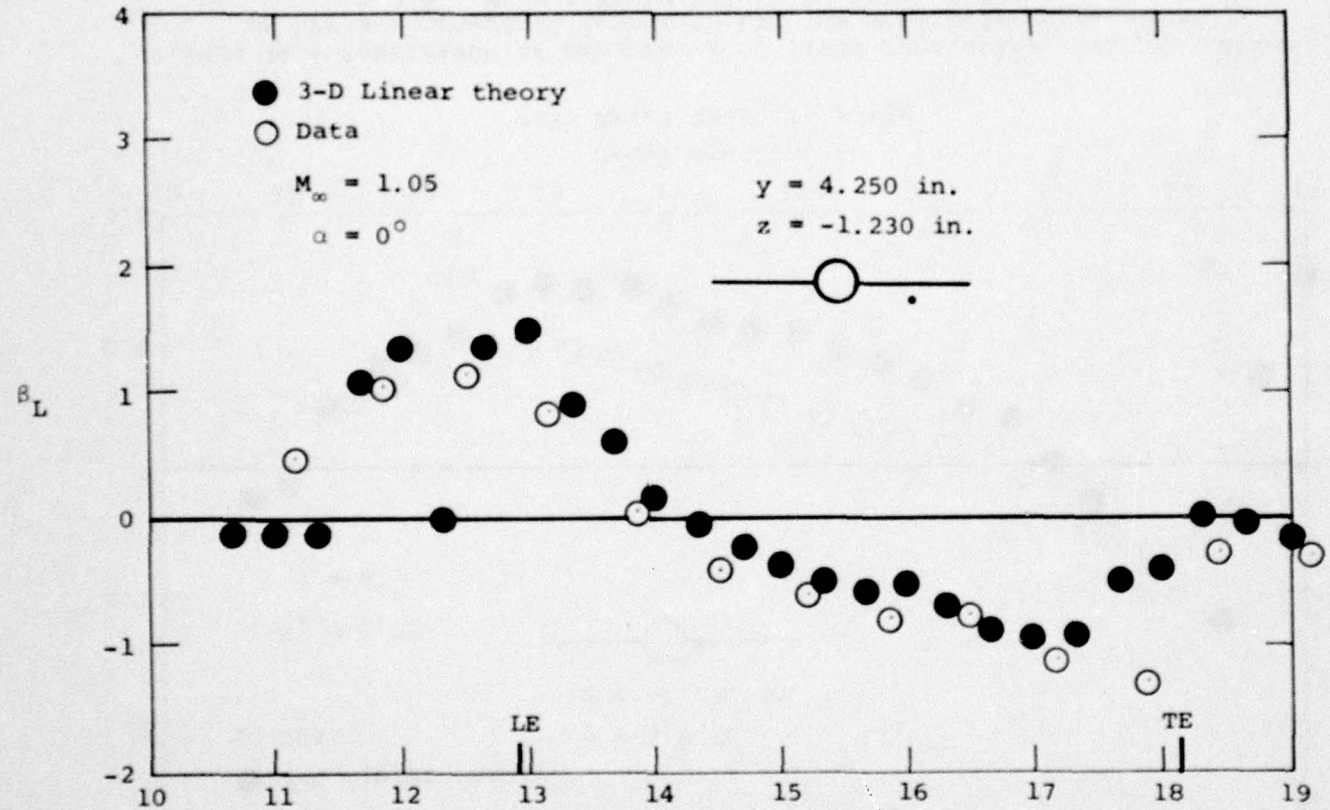

(c) Sidewash angle, deg.

Figure 45.- Concluded.

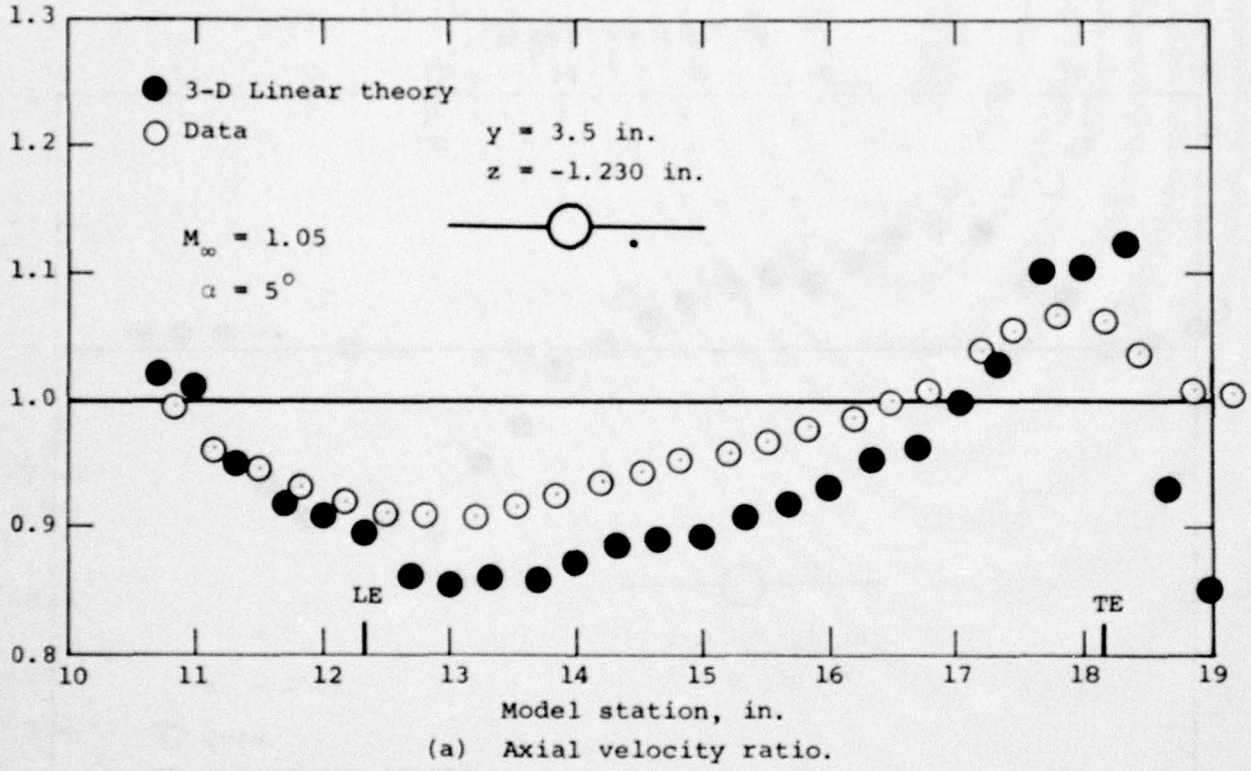

(a) Axial velocity ratio.

Figure 46.- Comparison of measured flow field quantities with prediction of three-dimensional linear theory for wing-body combination, $\alpha = 5^\circ$, $M_\infty = 1.05$, y = 3.5 in., z = -1.230 in.

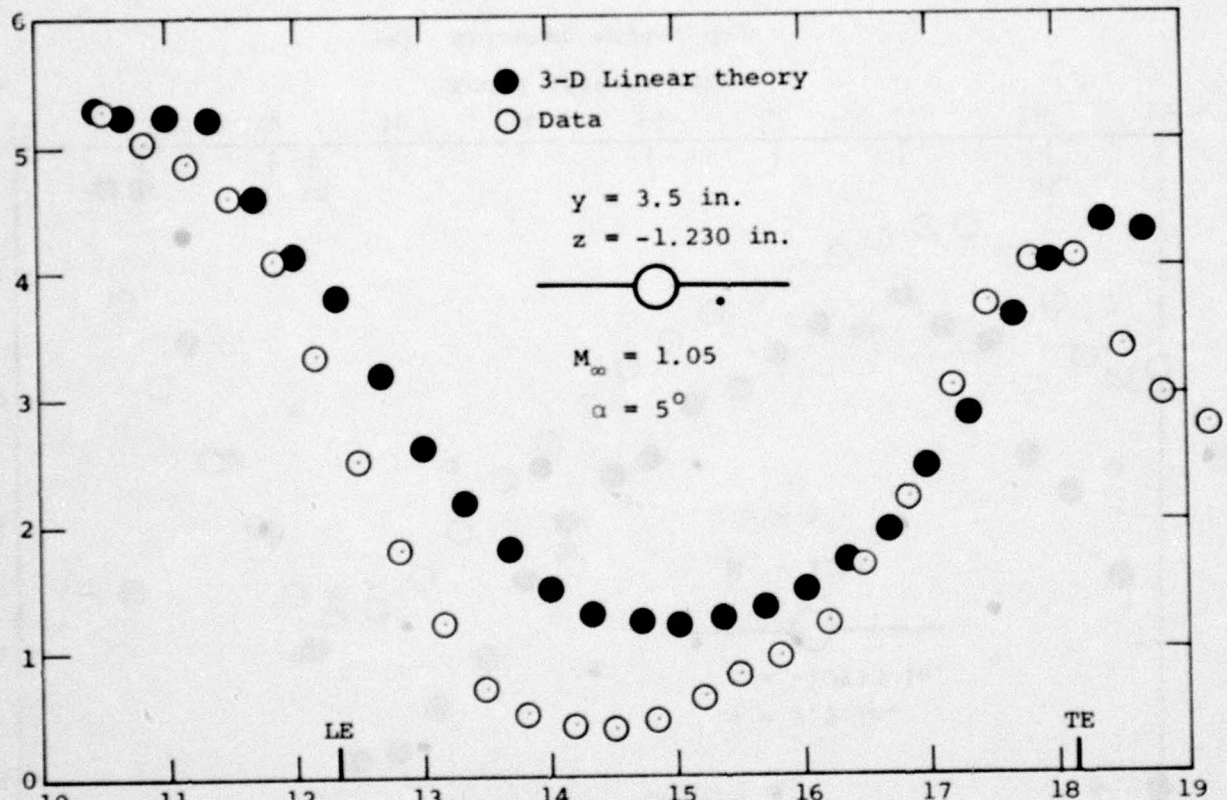

(b) Upwash angle, deg.

Figure 46.- Continued.

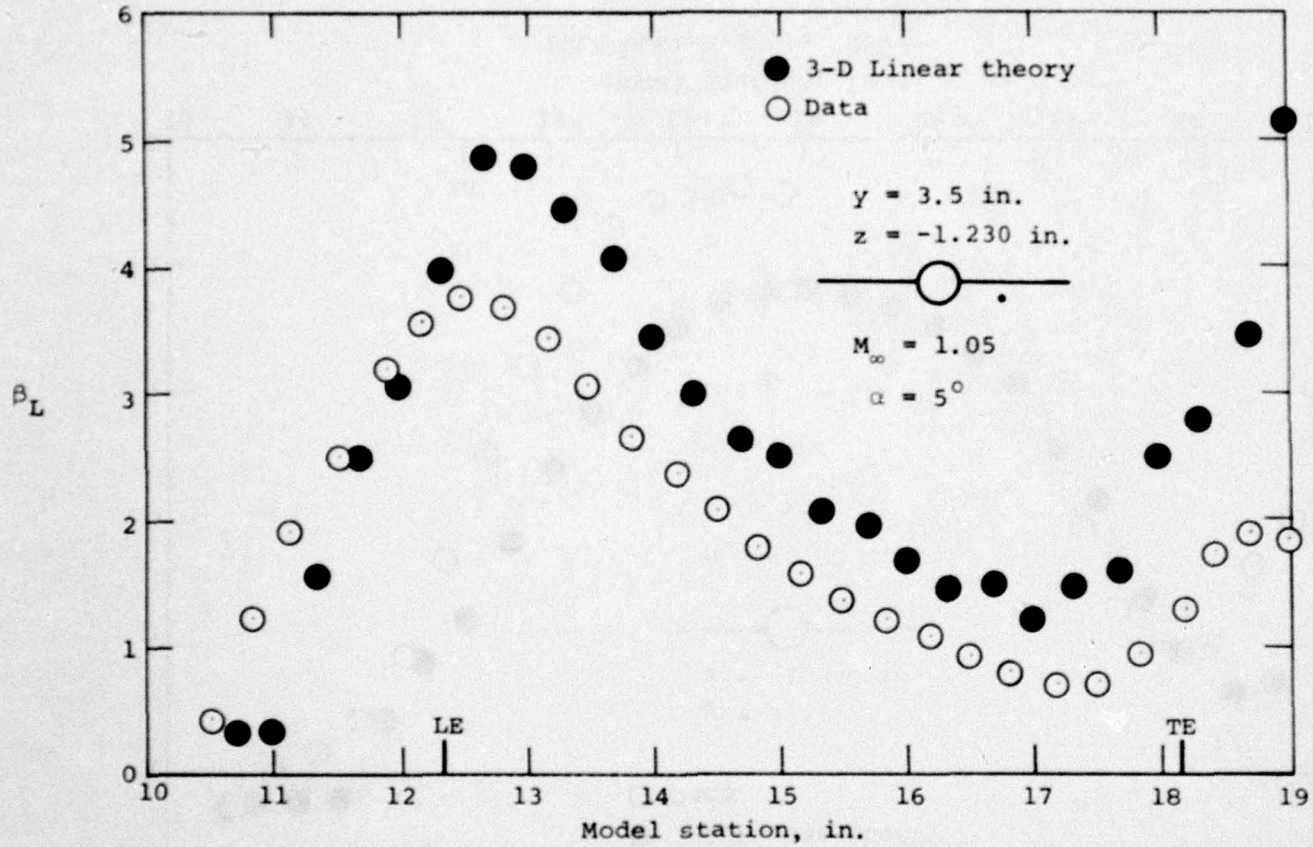

(c) Sidewash angle, deg.

Figure 46.- Concluded.

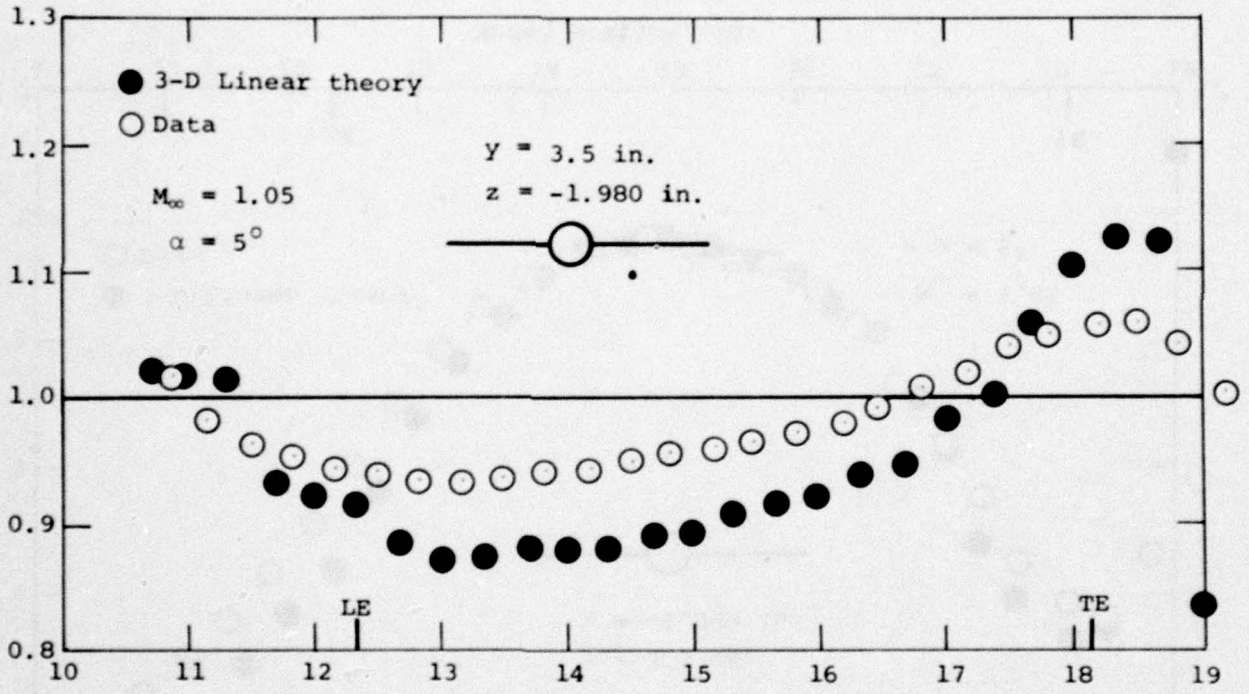

(a) Axial velocity ratio.

Figure 47.- Comparison of measured flow field quantities with prediction of three-dimensional linear theory for wing-body combination, $\alpha = 5^\circ$, $M_\infty = 1.05$, y = 3.5 in., z = -1.980 in.

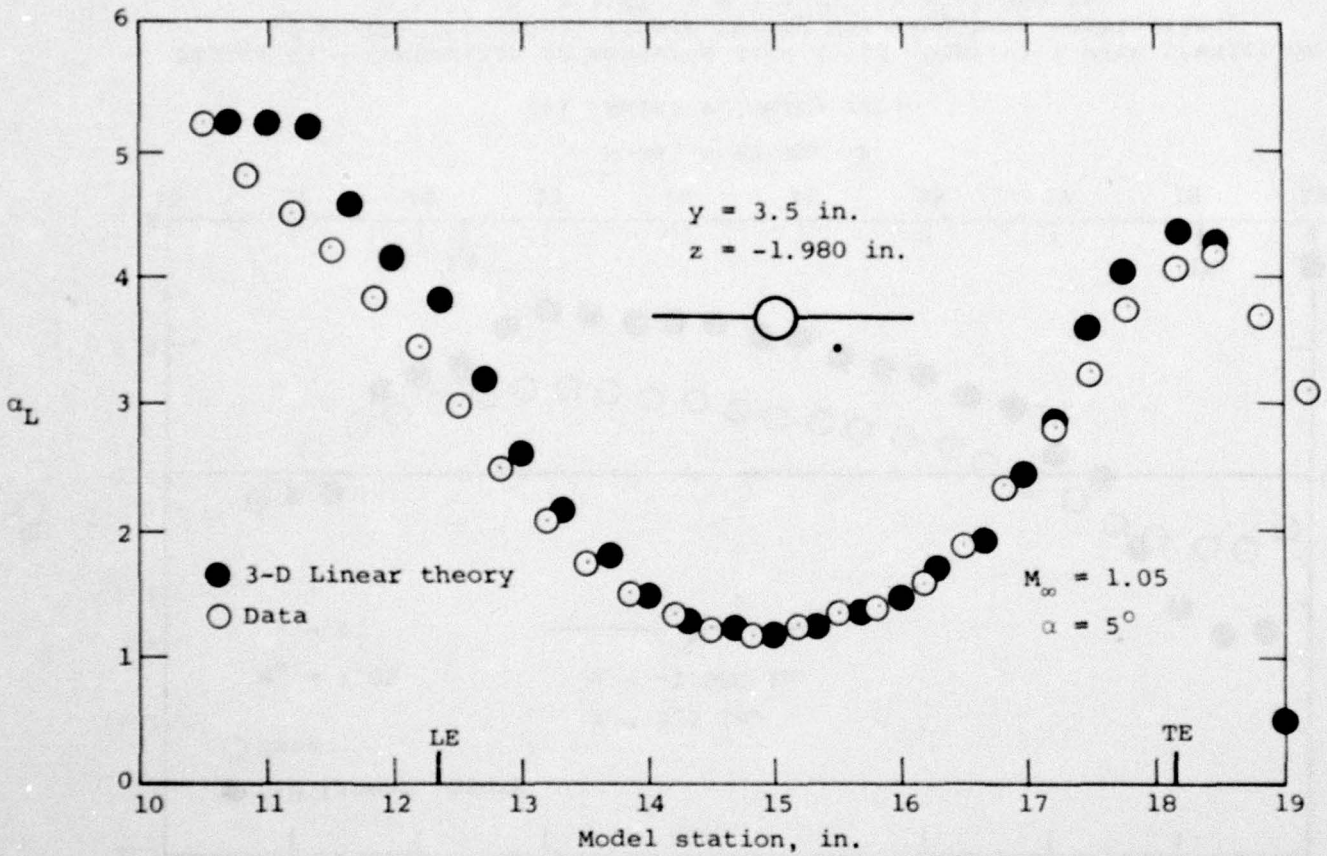

(b) Upwash angle, deg.

Figure 47.- Continued.

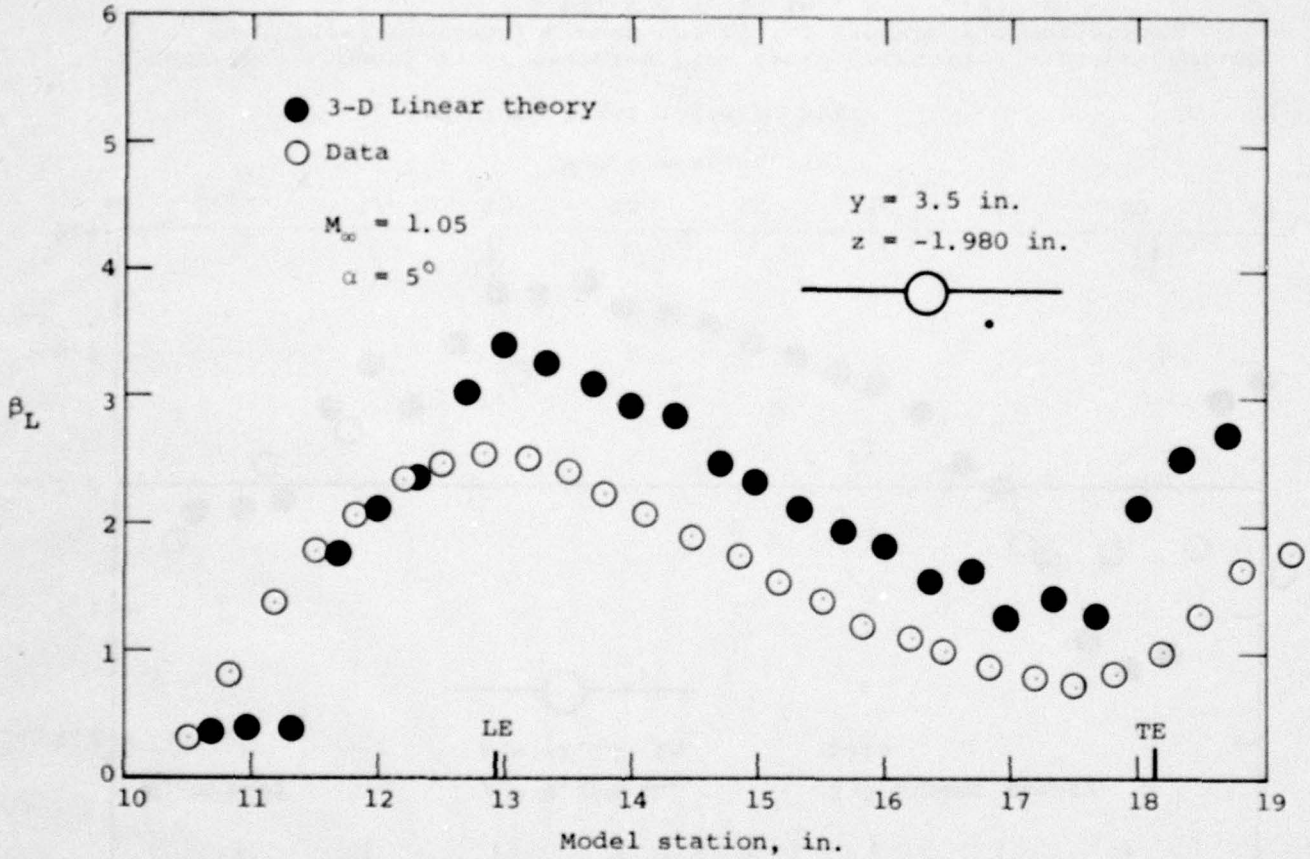

(c) Sidewash angle, deg.

Figure 47.- Concluded.

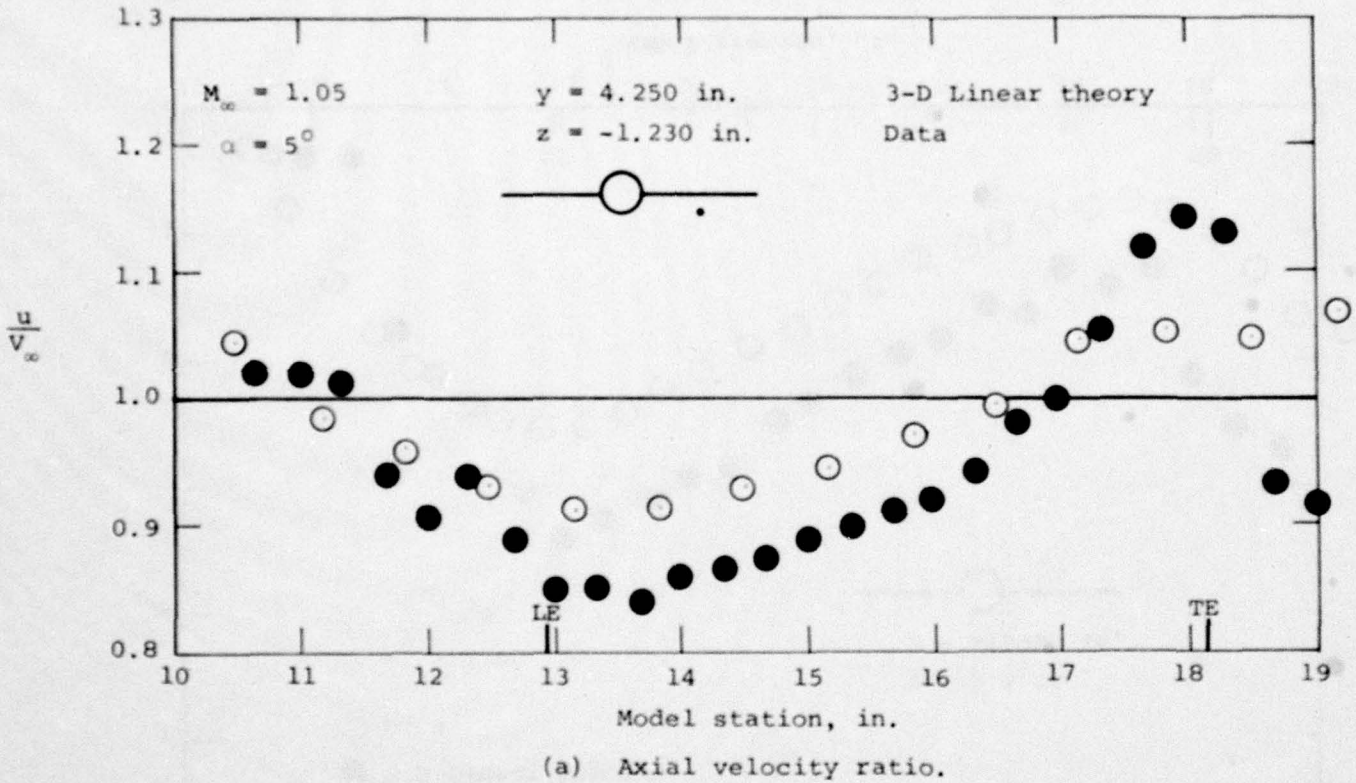

(a) Axial velocity ratio.

Figure 48.- Comparison of measured flow field quantities with prediction of three-dimensional linear theory for wing-body combination, $\alpha = 5^\circ$, $M_\infty = 1.05$, $y = 4.250$ in., $z = -1.230$ in.

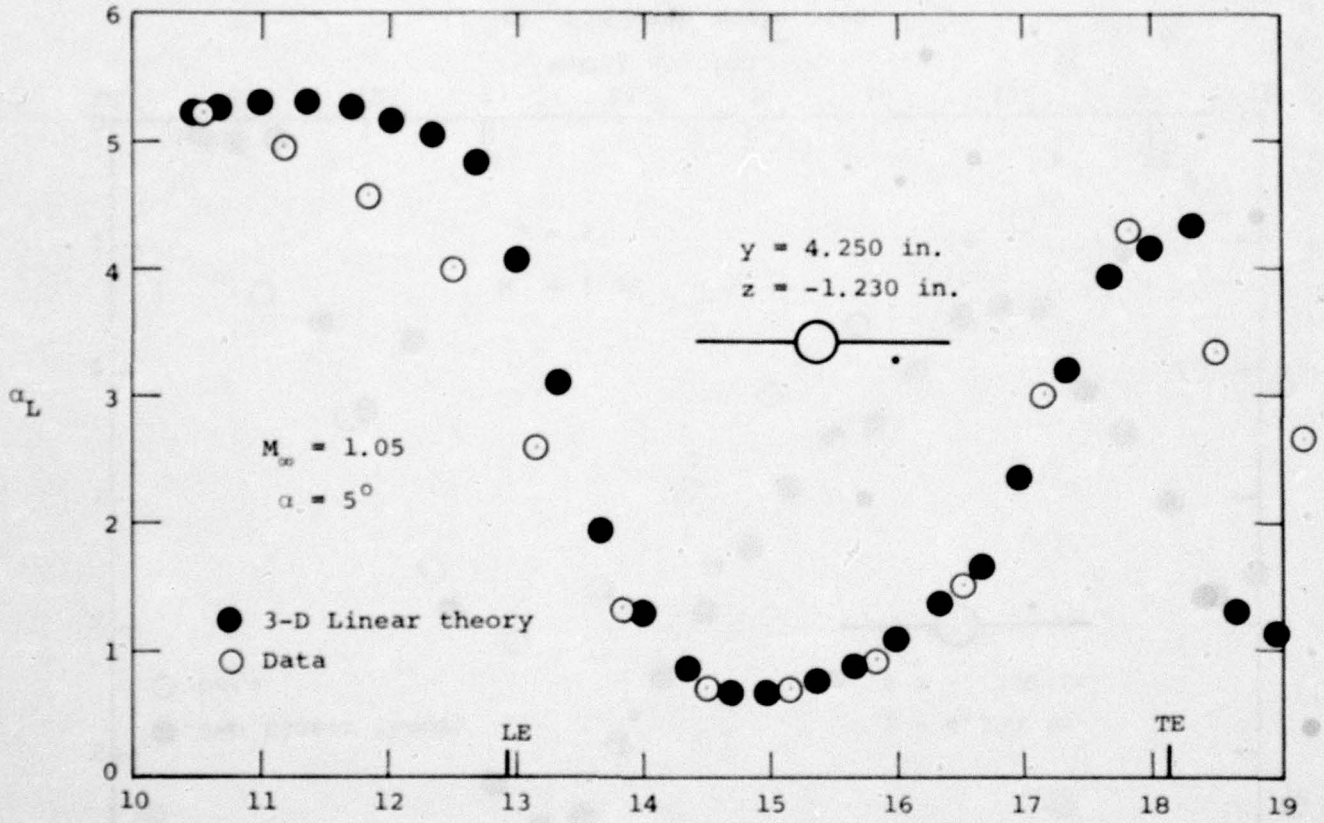

(b) Upwash angle, deg.

Figure 48.- Continued.

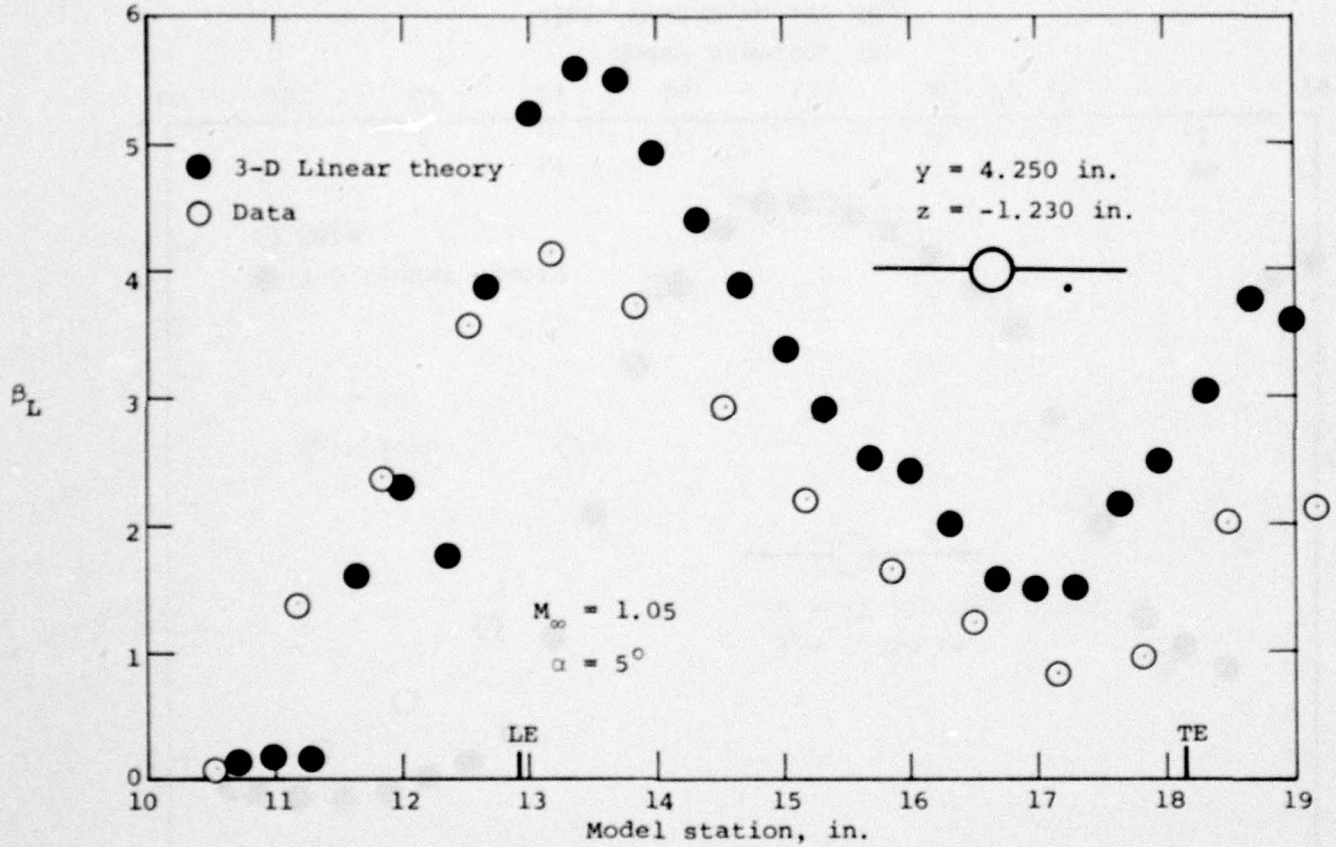

(c) Sidewash angle, deg.

Figure 48.- Concluded.

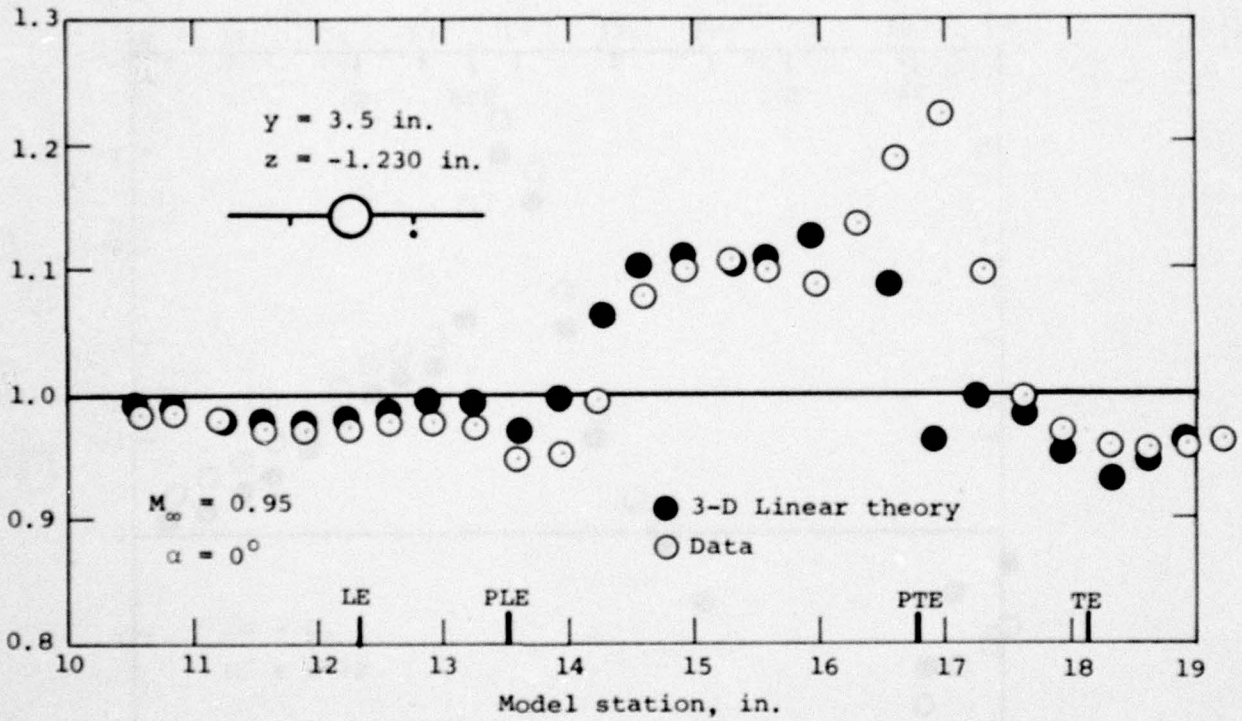

(a) Axial velocity ratio.

Figure 49.- Comparison of measured flow field quantities with prediction of three-dimensional linear theory for wing-body combination with wing pylons, $\alpha = 0^\circ$, $M_\infty = 0.95$, y = 3.5 in., z = -1.230 in.

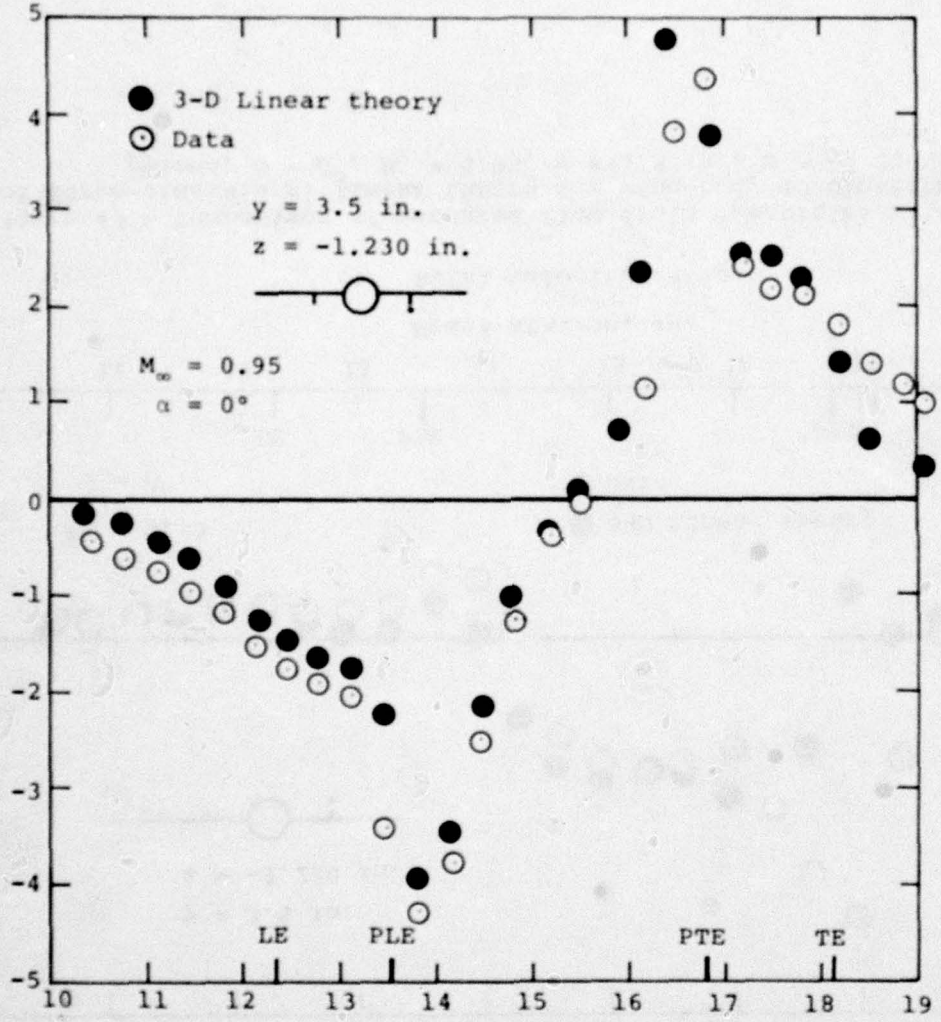

(b) Upwash angle, deg.

Figure 49.- Continued.

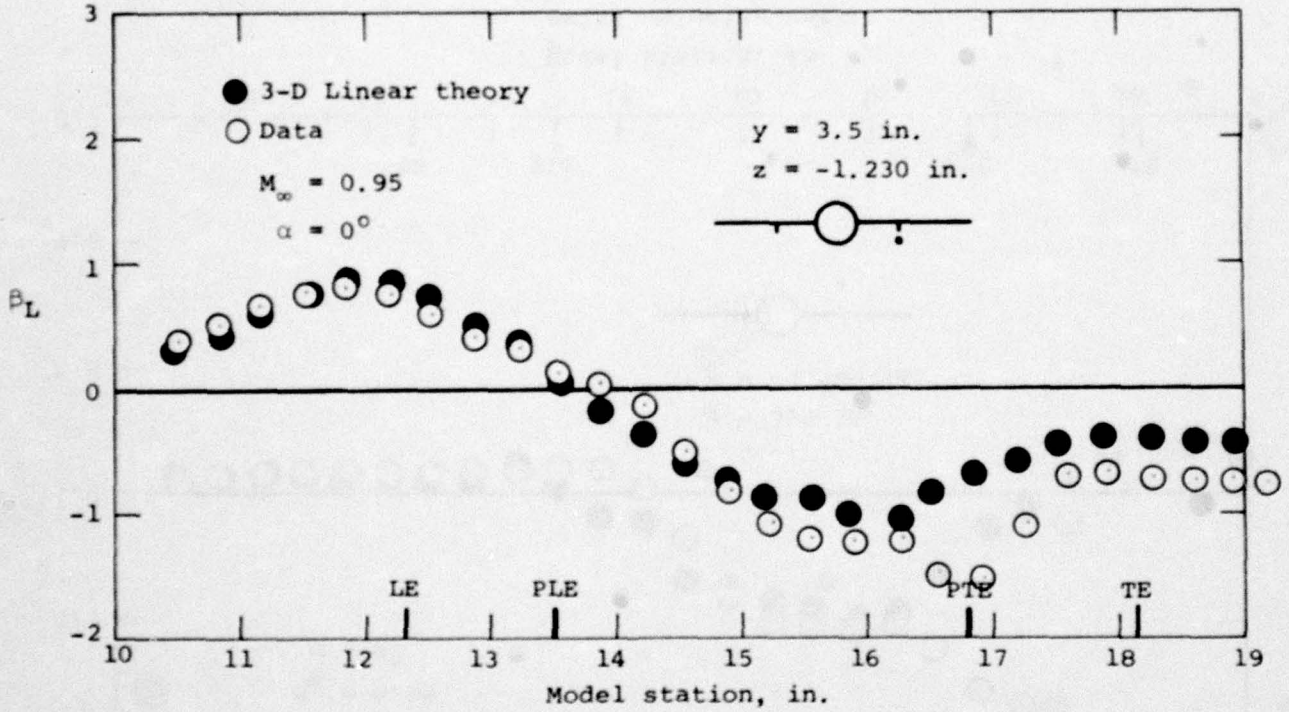

(c) Sidewash angle, deg.

Figure 49.- Concluded.

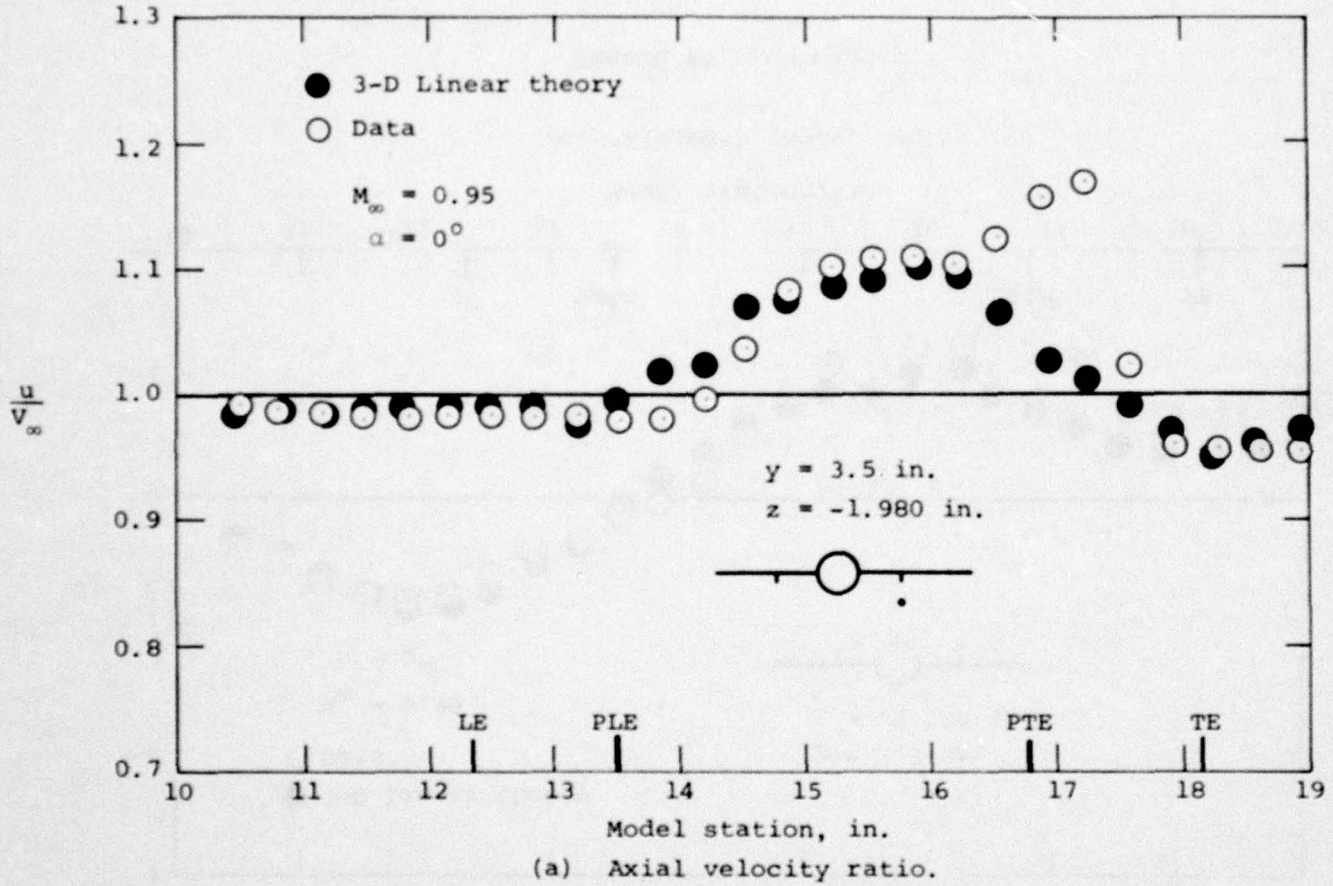

(a) Axial velocity ratio.

Figure 50.- Comparison of measured flow field quantities with prediction of three-dimensional linear theory for wing-body combination with wing pylons, $\alpha = 0°$, $M_\infty = 0.95$, y = 3.5 in., z = -1.980 in.

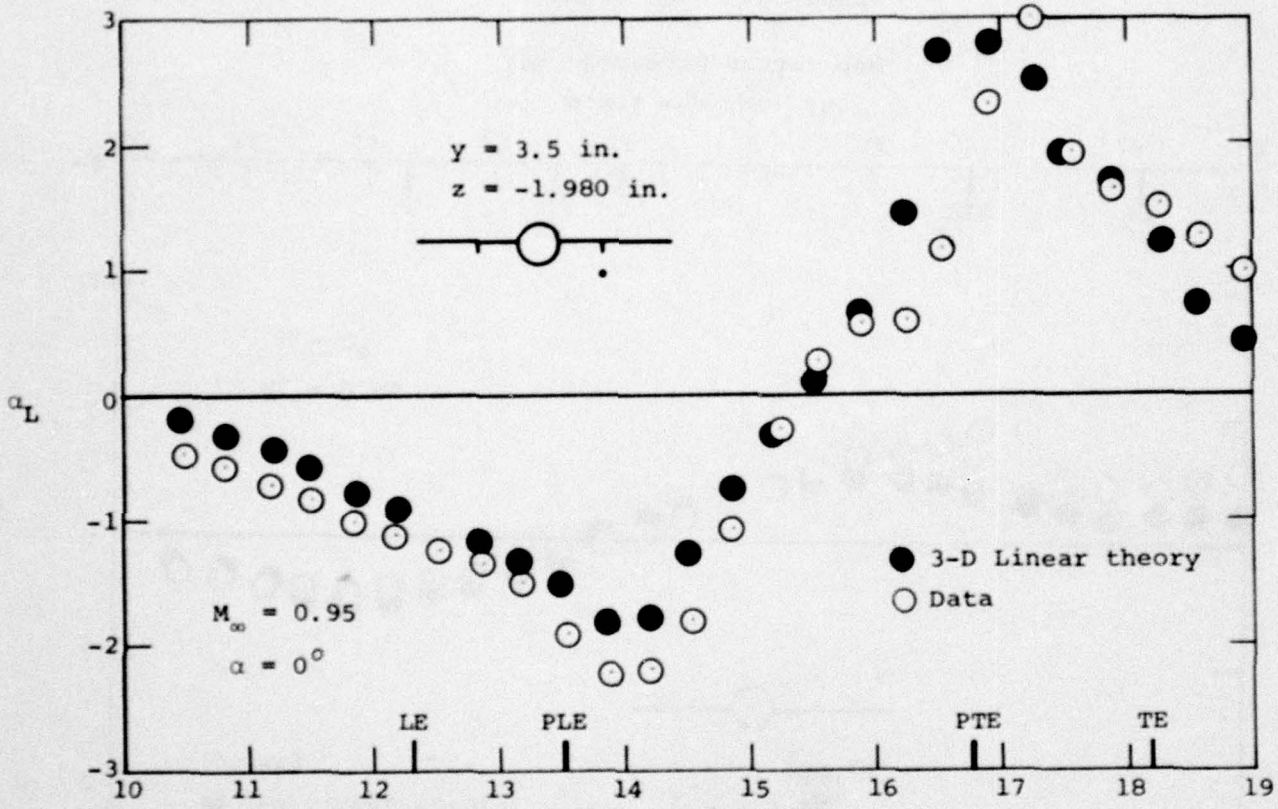

(b) Upwash angle, deg.

Figure 50.- Continued.

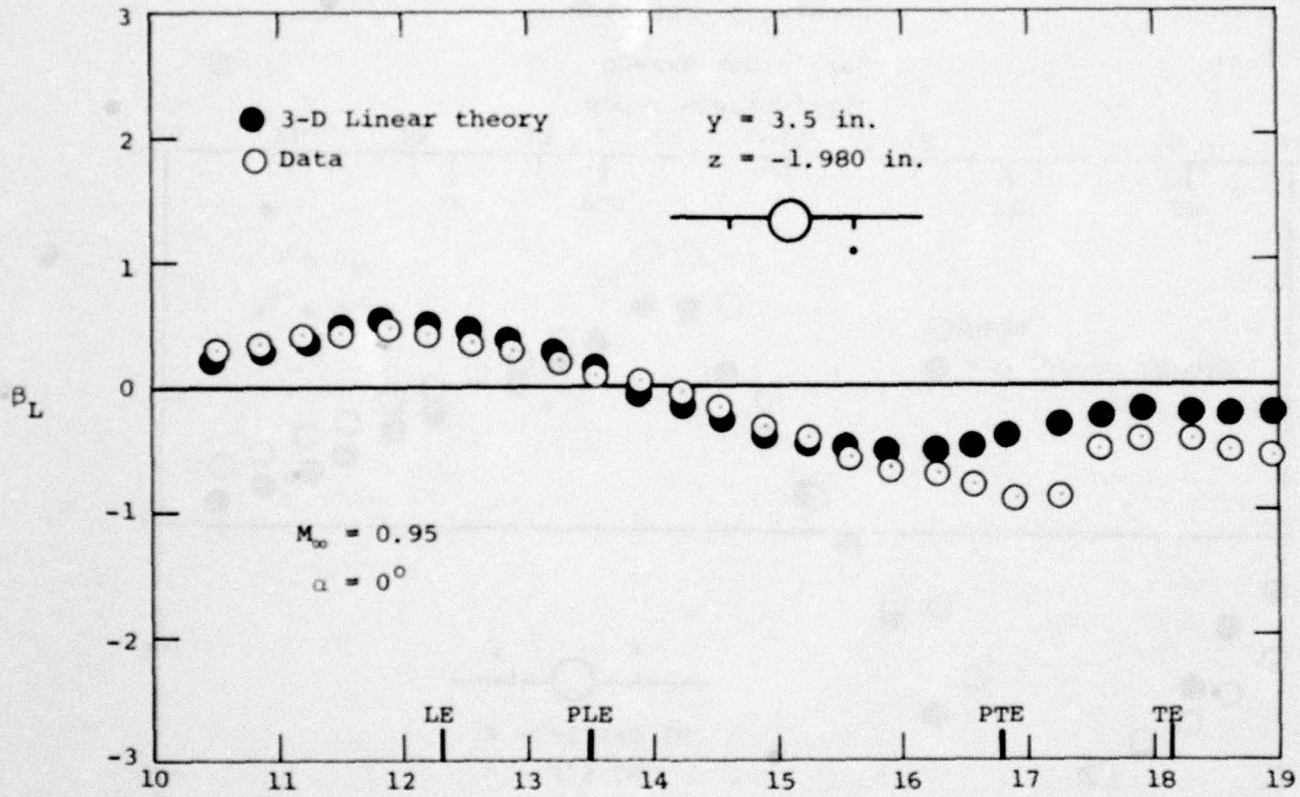

(c) Sidewash angle, deg.

Figure 50.- Concluded.

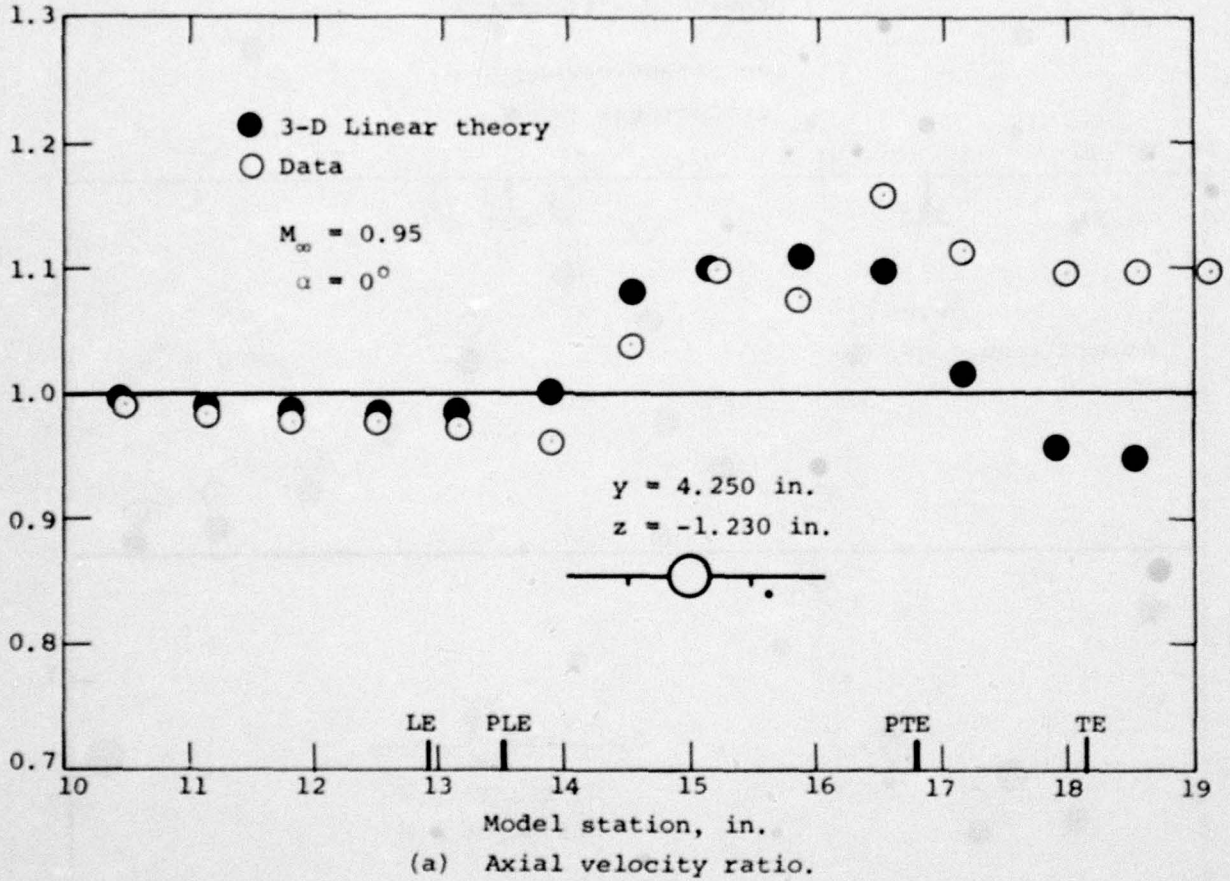

(a) Axial velocity ratio.

Figure 51.- Comparison of measured flow field quantities with prediction of three-dimensional linear theory for wing-body combination with wing pylons, $\alpha = 0°$, $M_\infty = 0.95$, y = 4.250 in., z = -1.230 in.

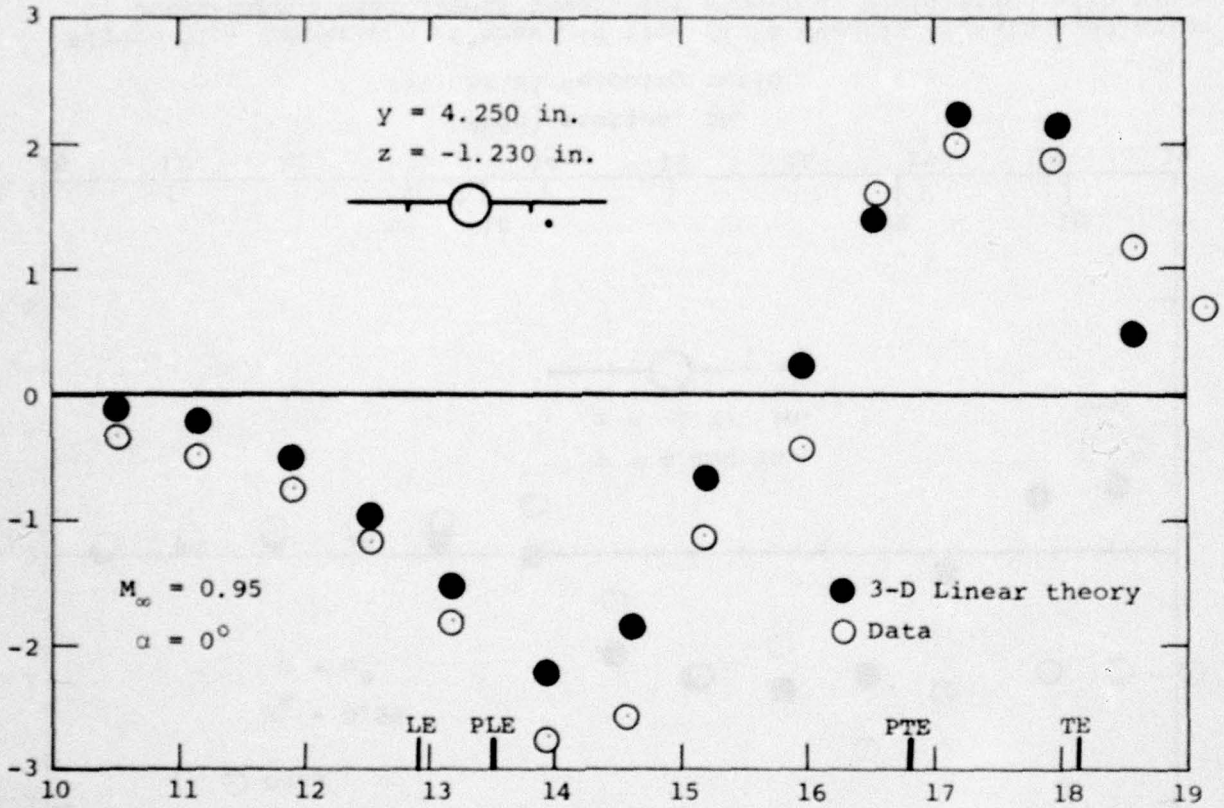

(b) Upwash angle, deg.

Figure 51.- Continued.

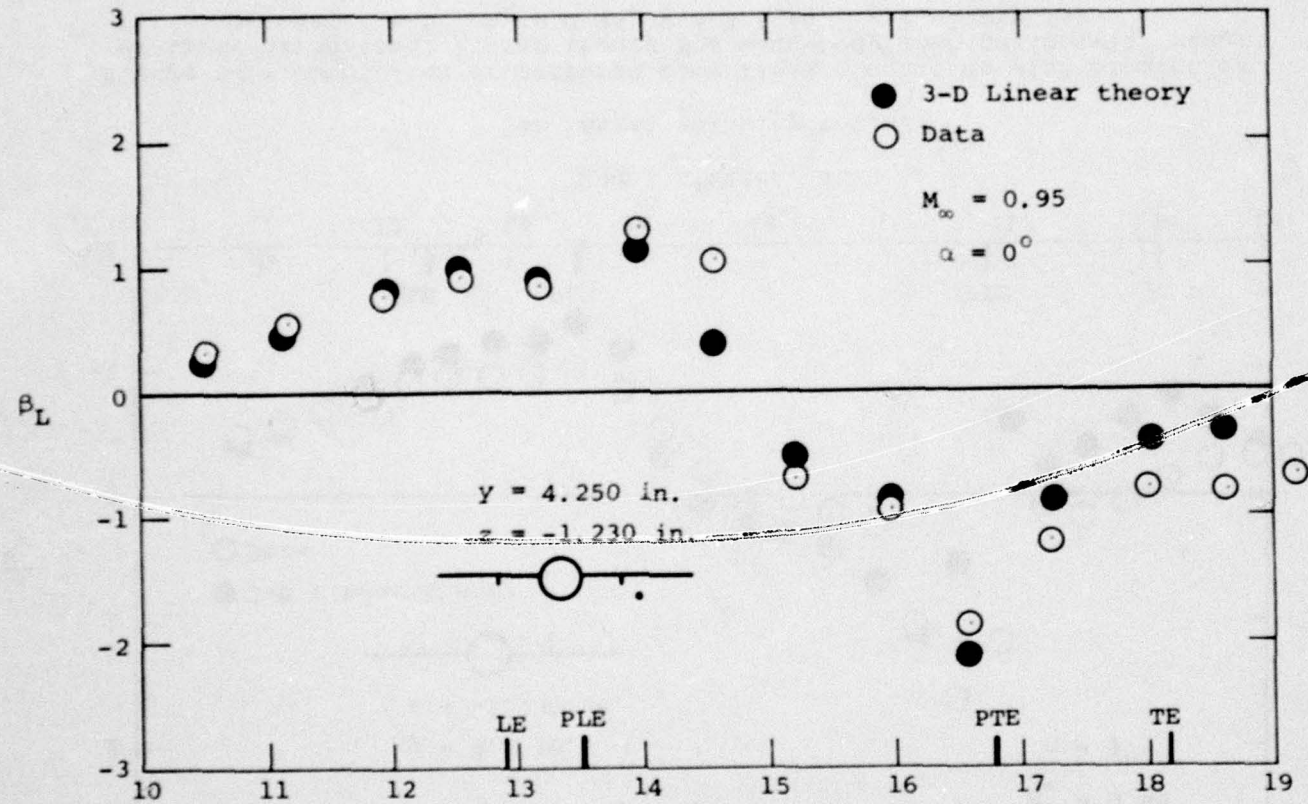

(c) Sidewash angle, deg.

Figure 51.- Concluded.

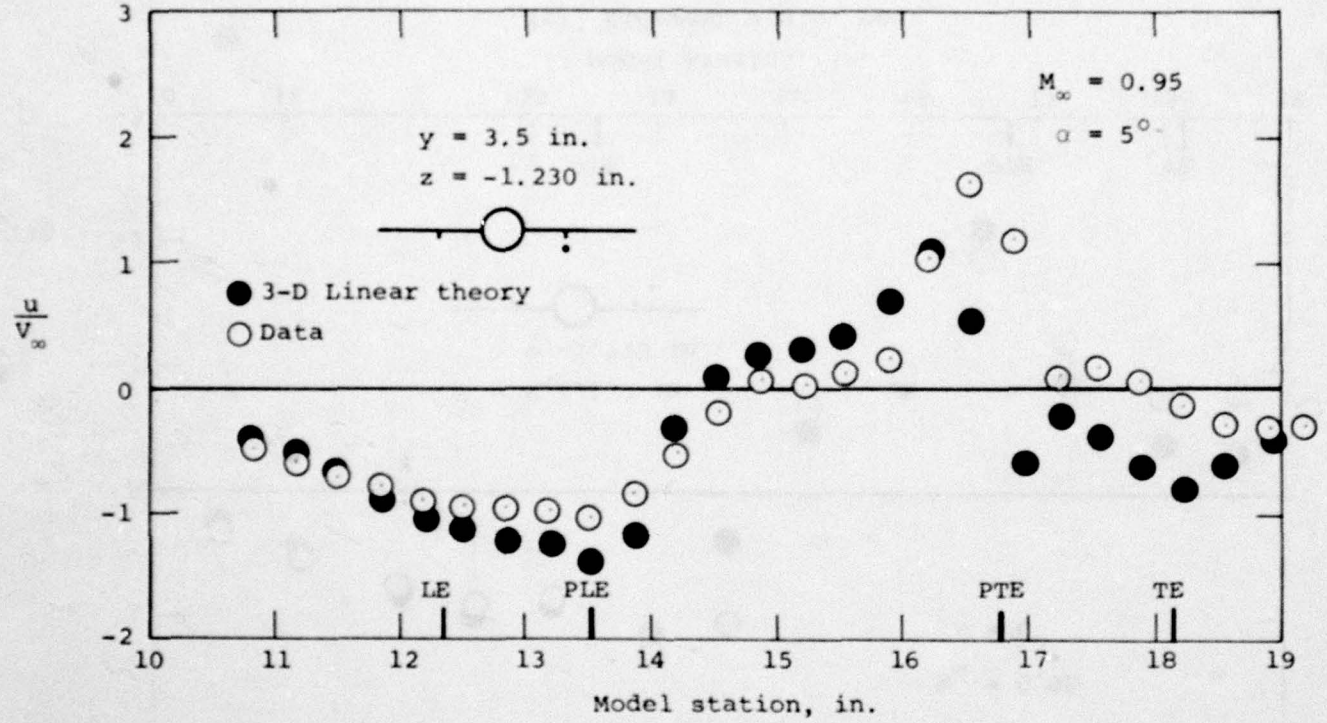

(a) Axial velocity ratio.

Figure 52.- Comparison of measured flow field quantities with prediction of three-dimensional linear theory for wing-body combination with wing pylons, $\alpha = 5°$, $M_\infty = 0.95$, y = 3.5 in., z = -1.230 in.

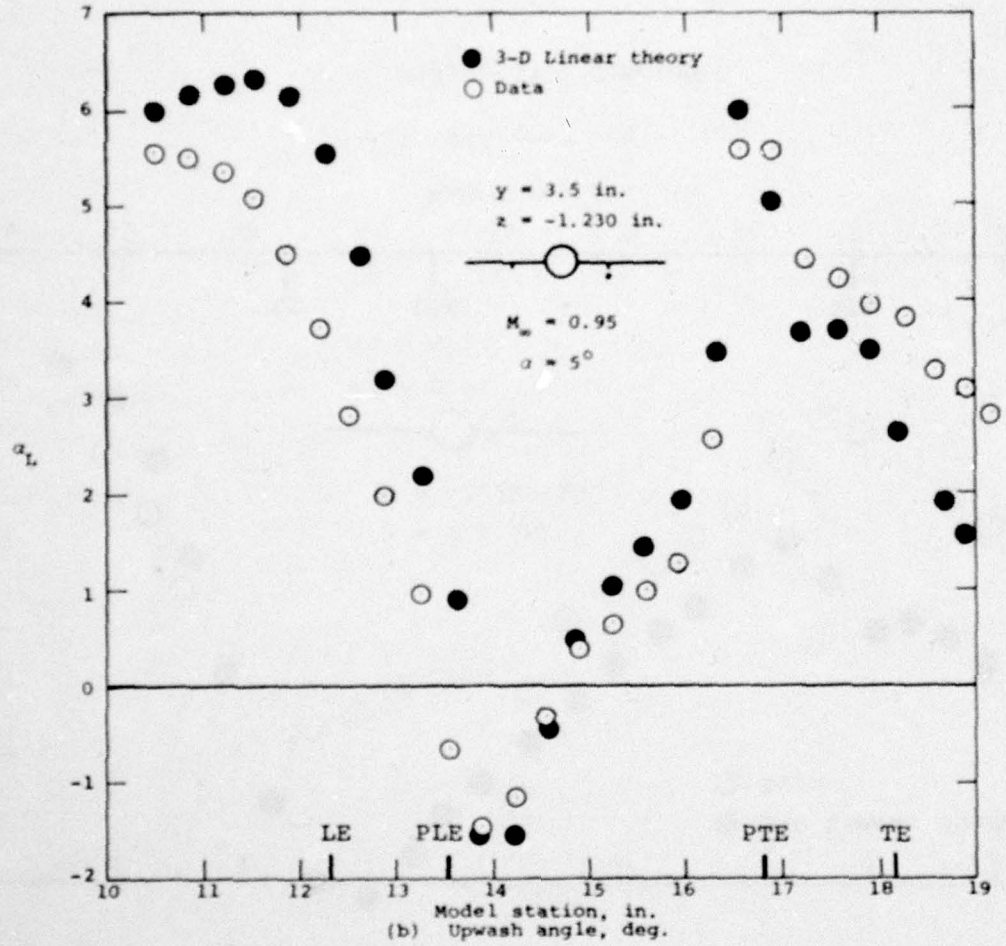

(b) Upwash angle, deg.

Figure 52.- Continued.

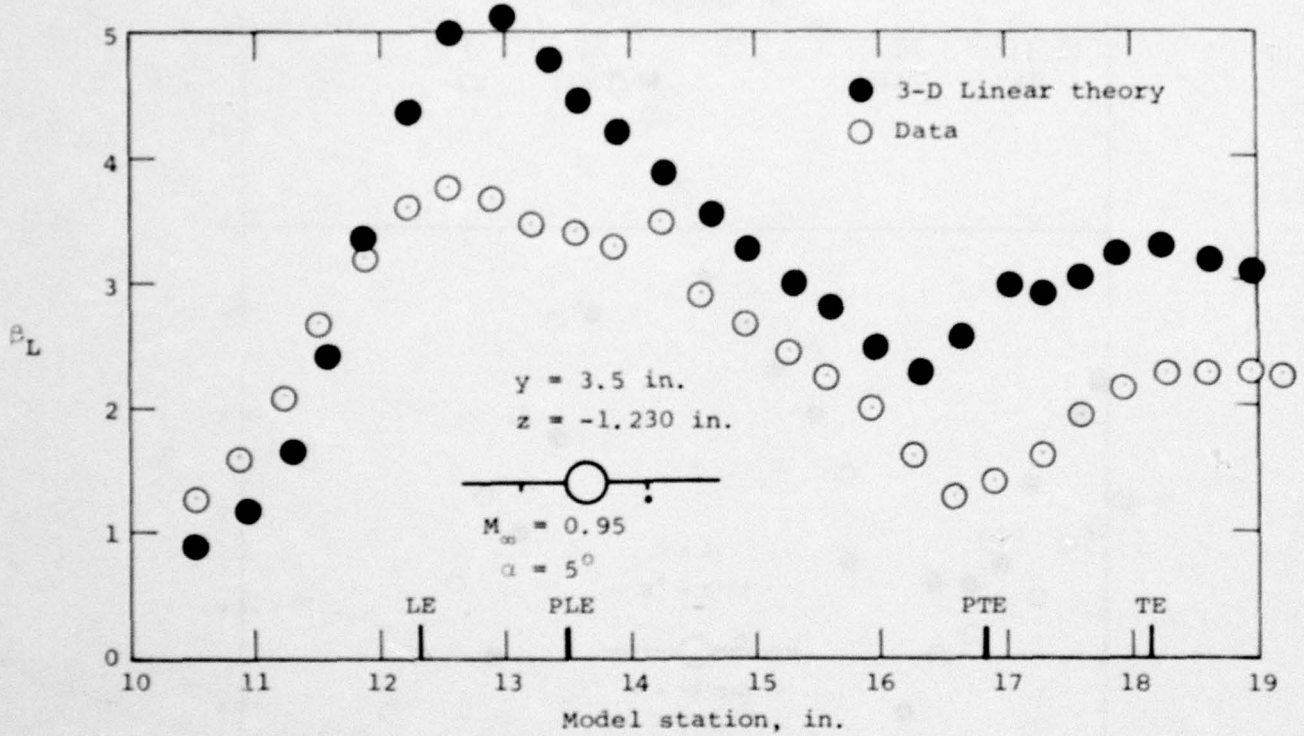

(c) Sidewash angle, deg.

Figure 52.- Concluded.

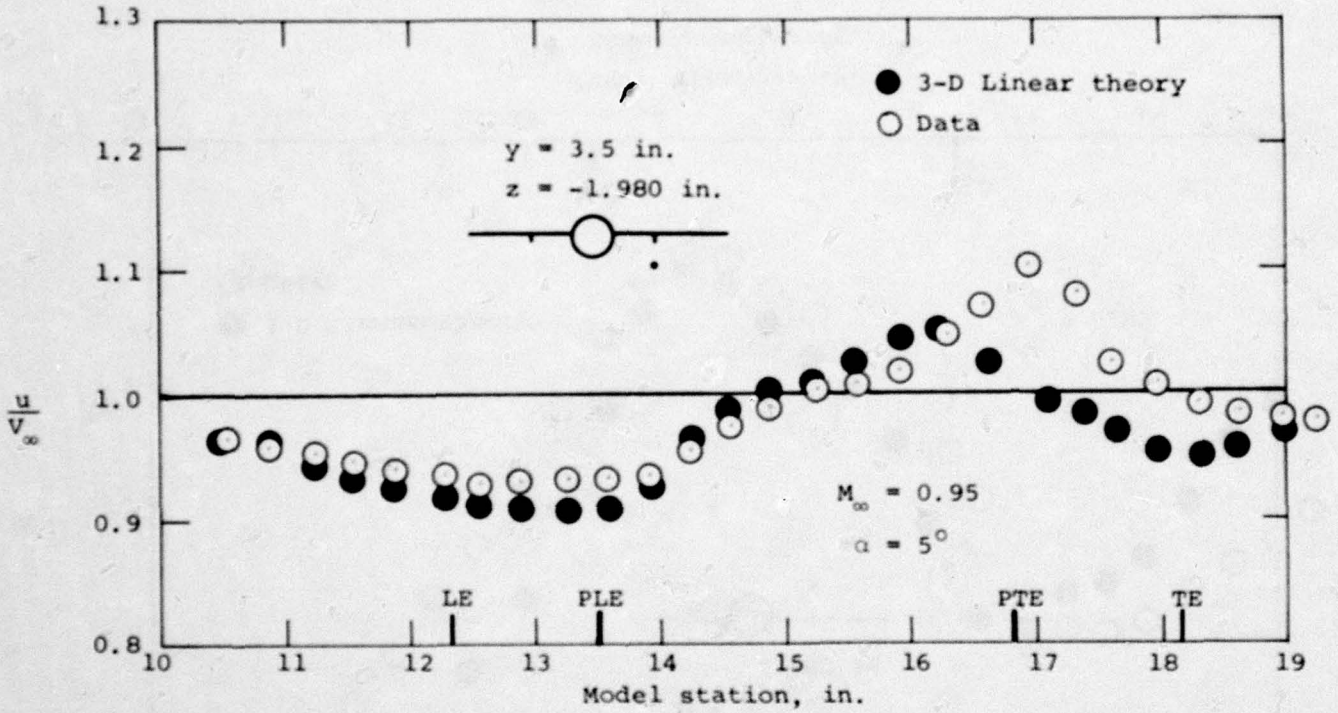

(a) Axial velocity ratio.

Figure 53.- Comparison of measured flow field quantities with prediction of three-dimensional linear theory for wing-body combination with wing pylons, $\alpha = 5^\circ$, $M_\infty = 0.95$, y = 3.5 in., z = -1.980 in.

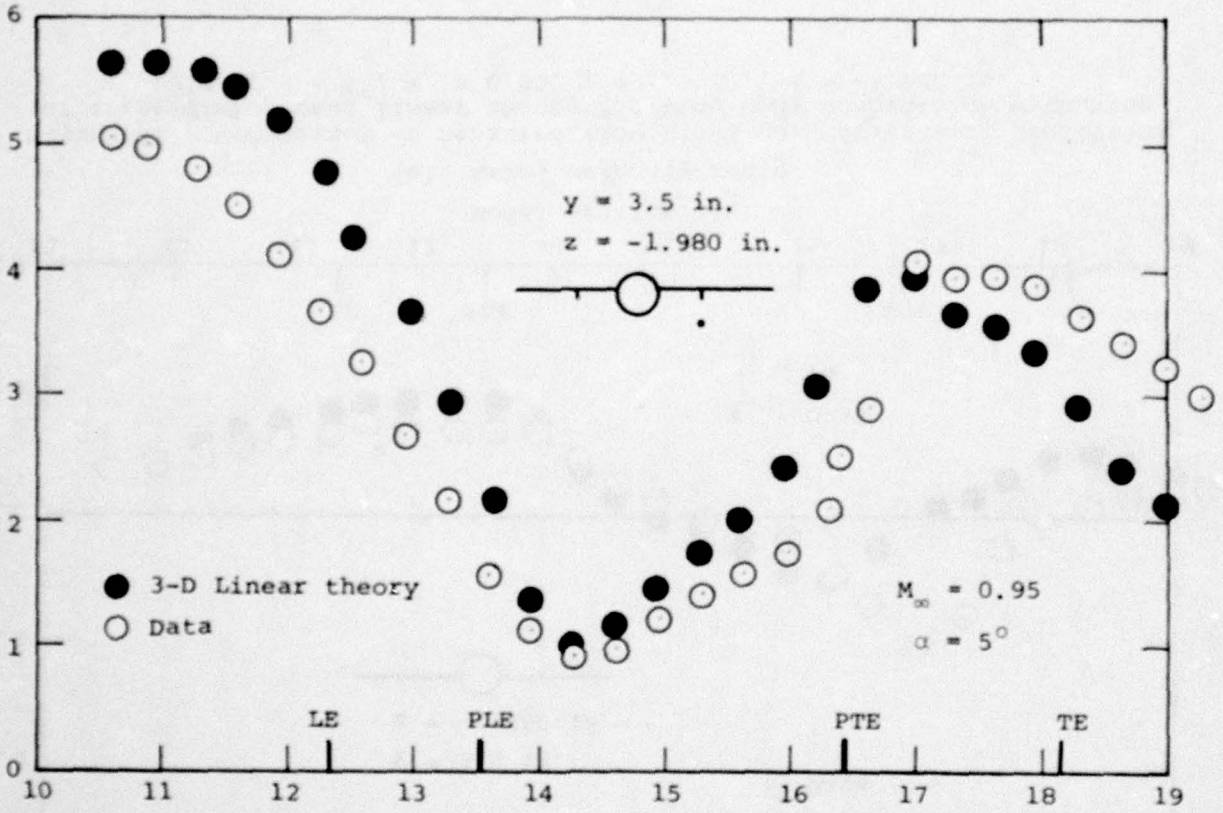

(b) Upwash angle, deg.

Figure 53.- Continued.

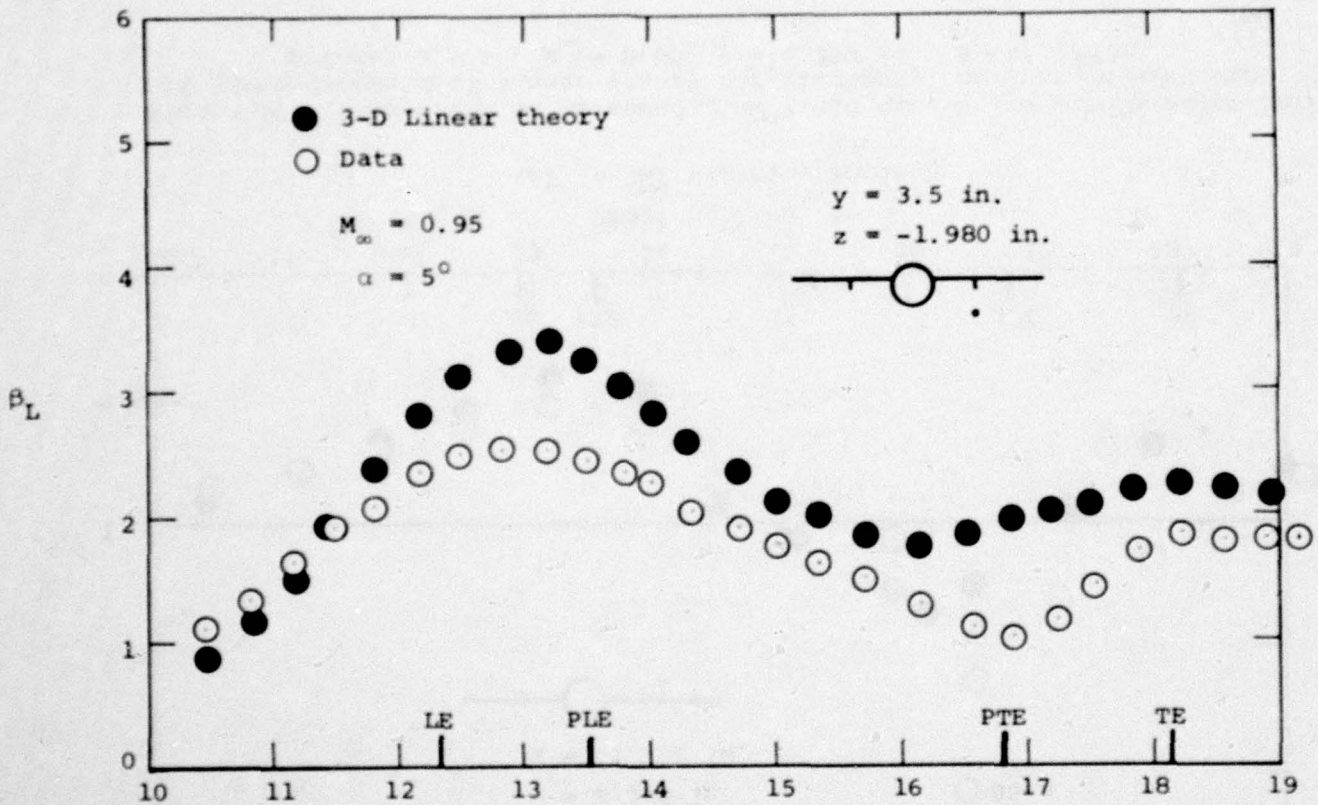

(c) Sidewash angle, deg.

Figure 53.- Concluded.

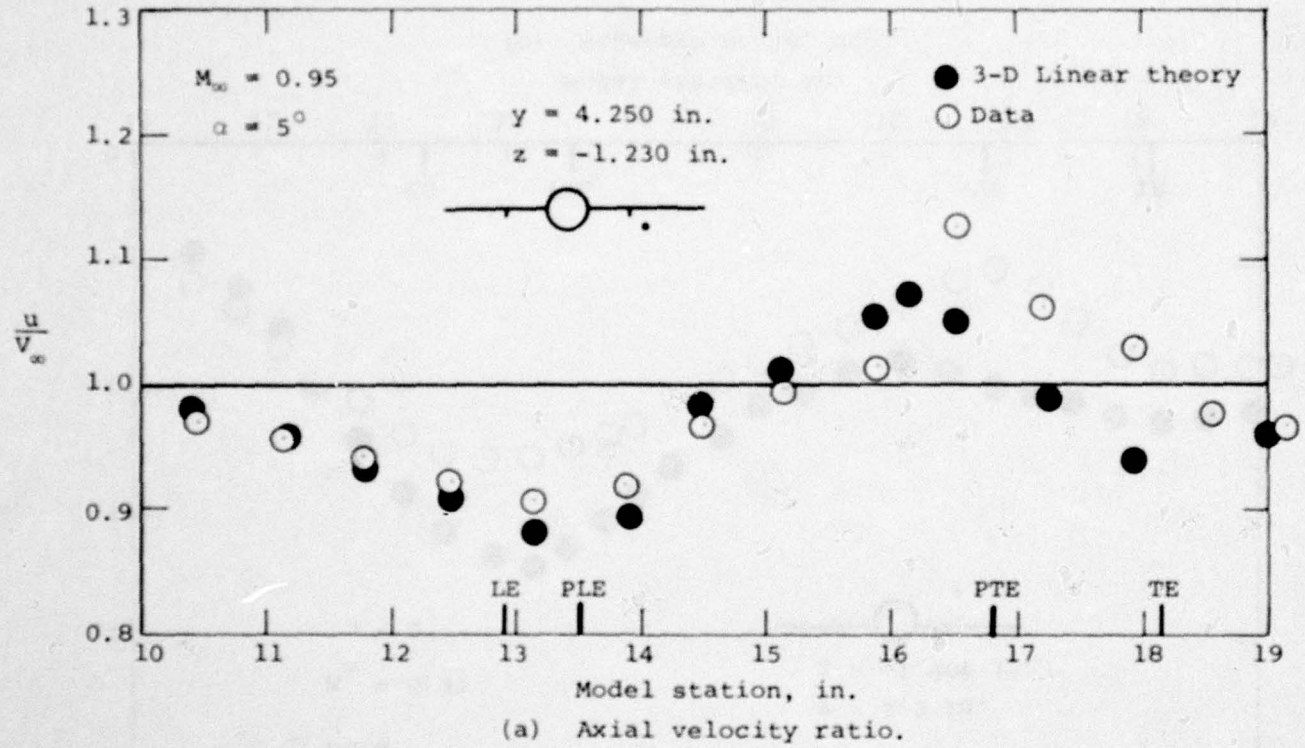

(a) Axial velocity ratio.

Figure 54.- Comparison of measured flow field quantities with prediction of three-dimensional linear theory for wing-body combination with wing pylons, $\alpha = 5^\circ$, $M_\infty = 0.95$, y = 4.250 in., z = -1.230 in.

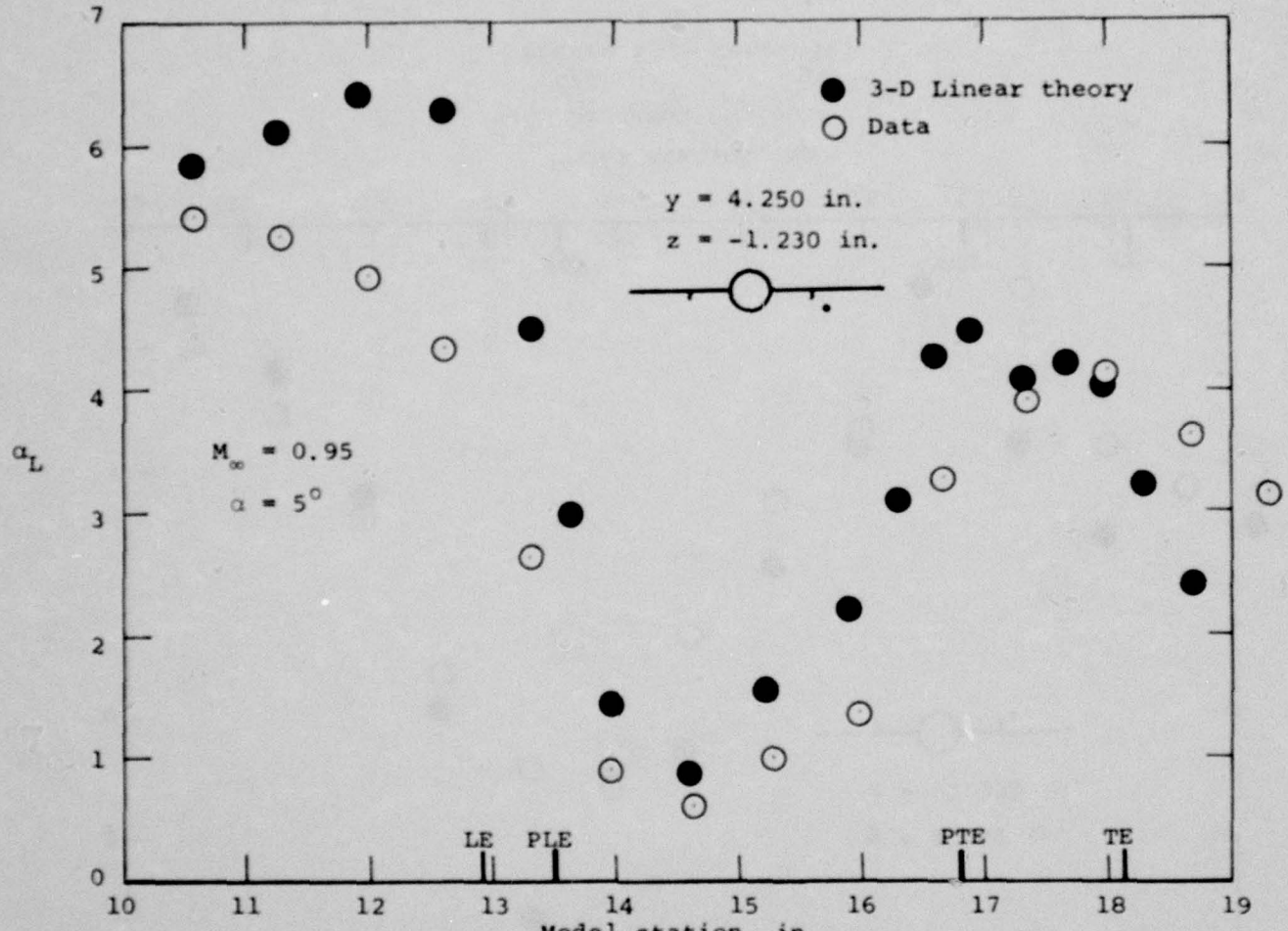

(b) Upwash angle, deg.

Figure 54.- Continued.

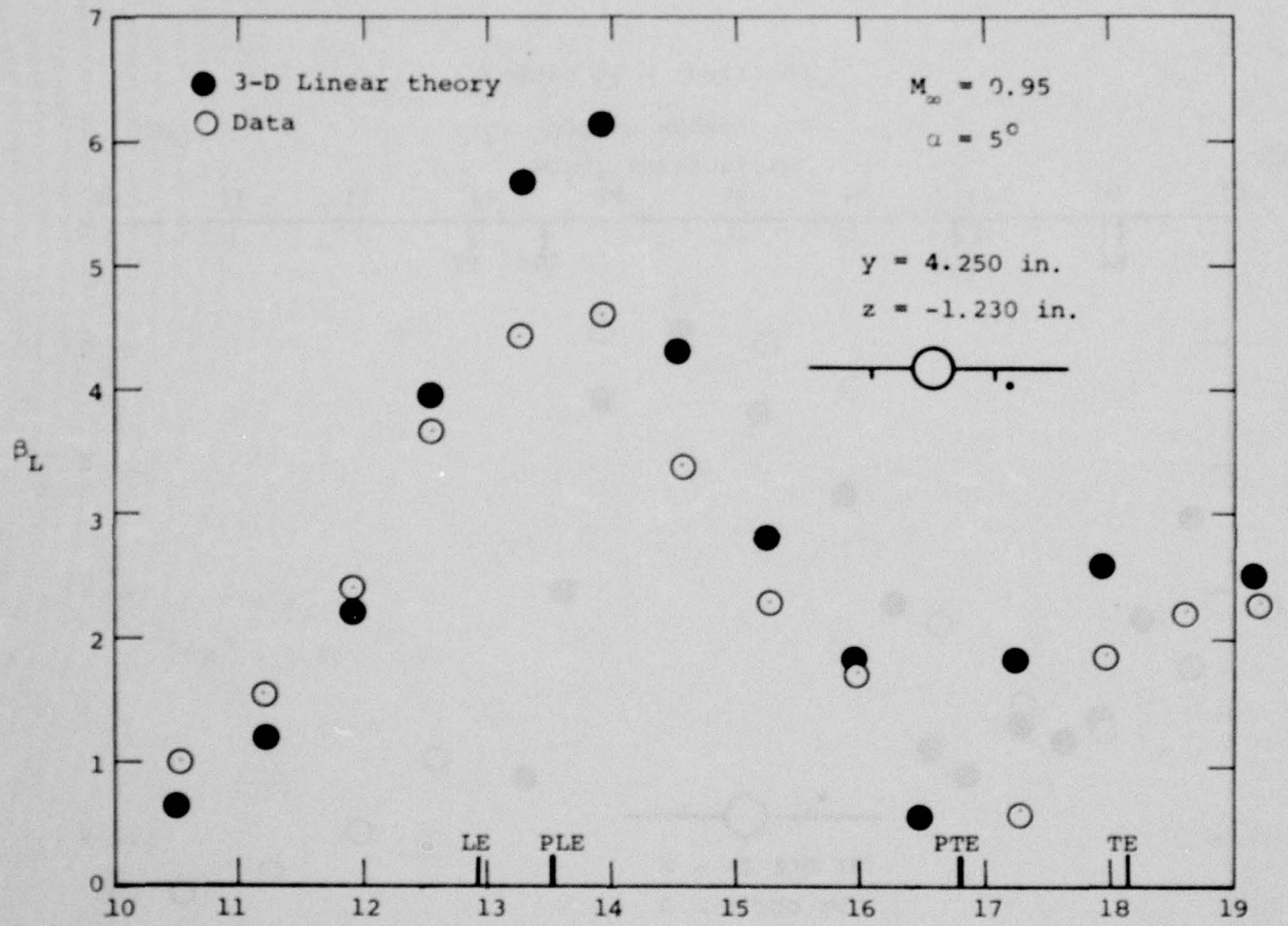

(c) Sidewash angle, deg.

Figure 54.- Concluded.

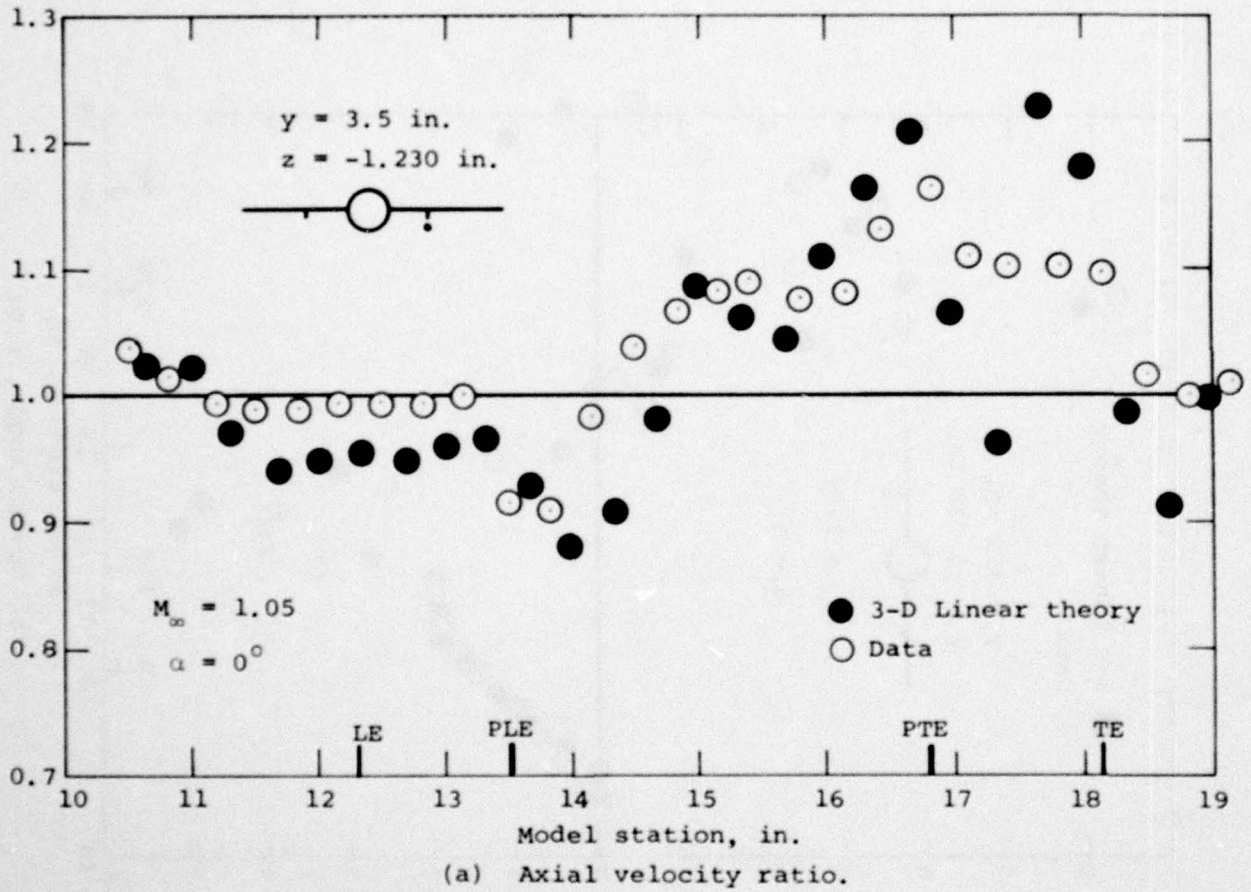

(a) Axial velocity ratio.

Figure 55.- Comparison of measured flow field quantities with prediction of three-dimensional linear theory for wing-body combination with wing pylons, $\alpha = 0^\circ$, $M_\infty = 1.05$, y = 3.5 in., z = -1.230 in.

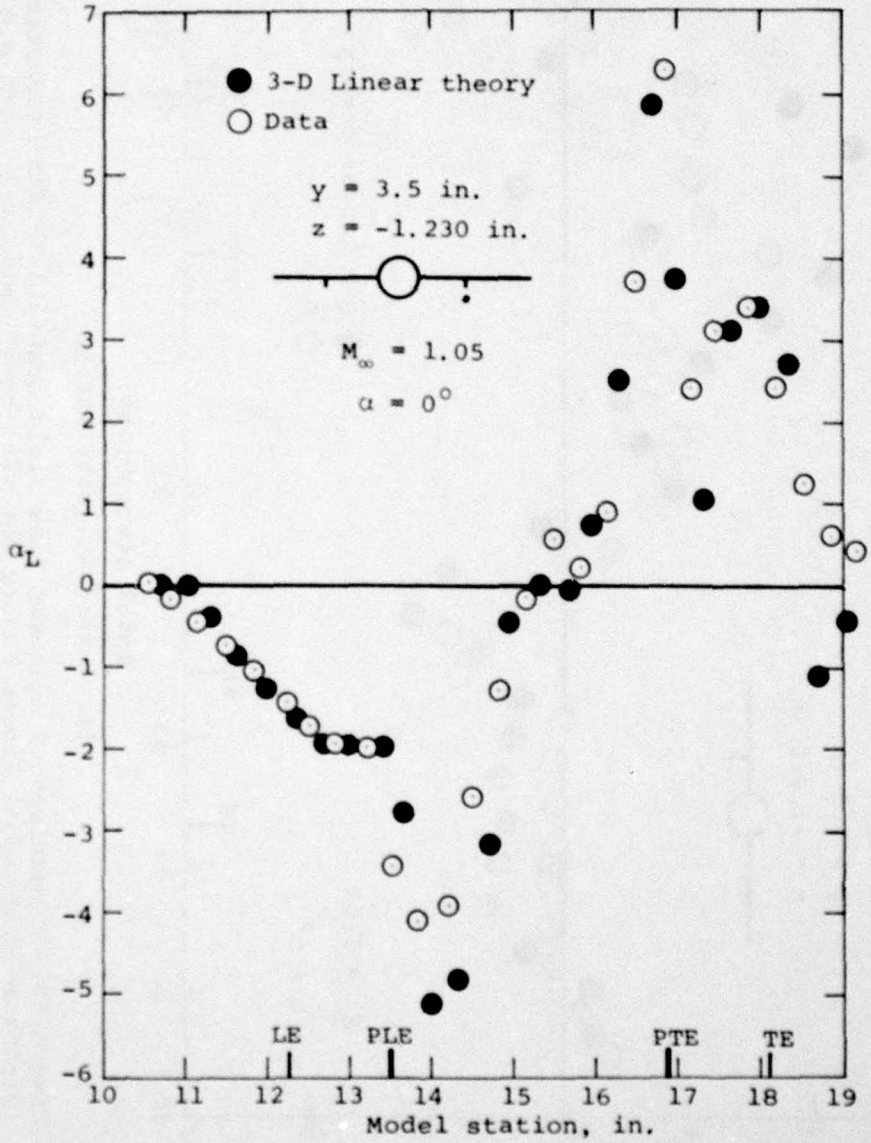

(b) Upwash angle, deg.

Figure 55.- Concluded.

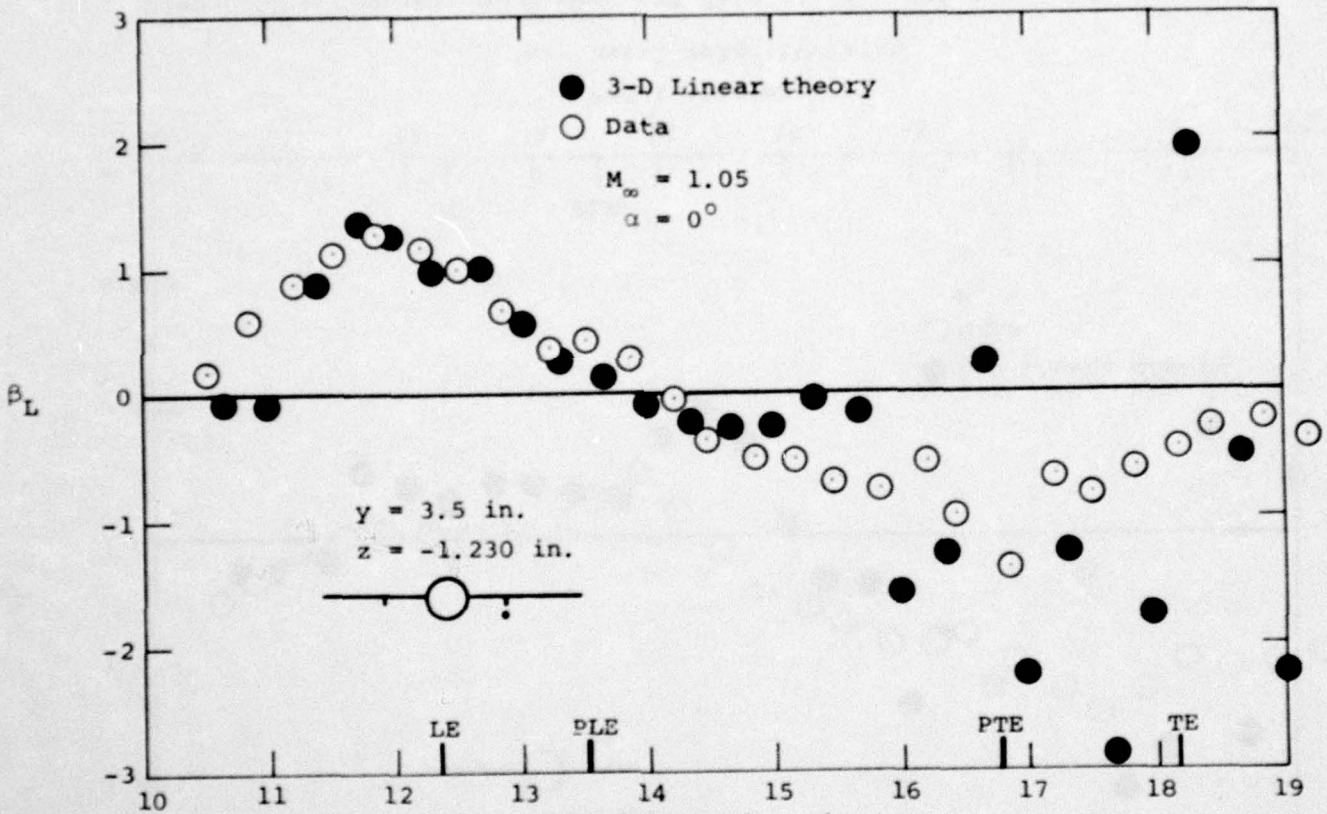

(c) Sidewash angle, deg.

Figure 55.- Concluded.

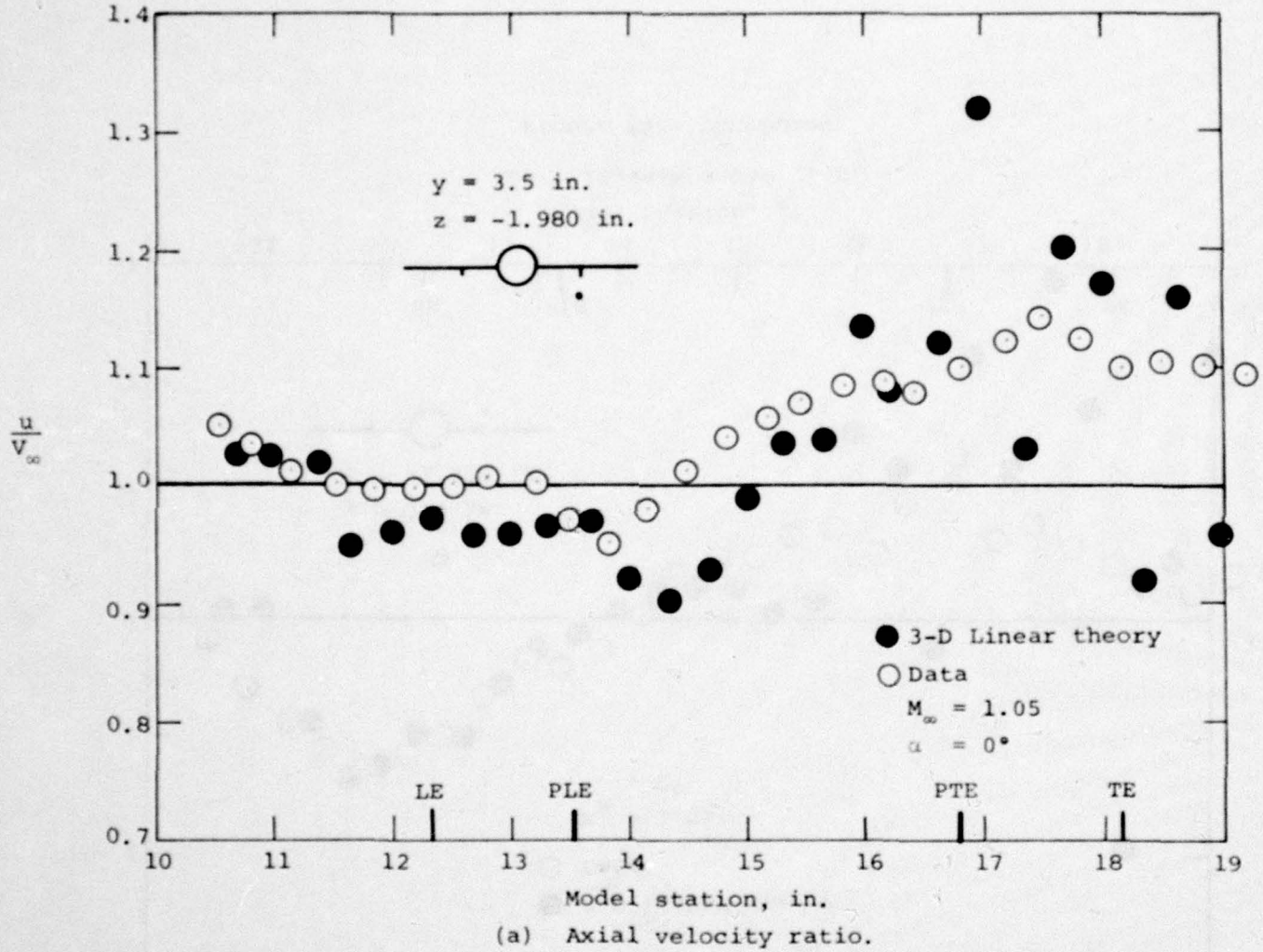

(a) Axial velocity ratio.

Figure 56.- Comparison of measured flow field quantities with prediction of three-dimensional linear theory for wing-body combination with wing pylons, $\alpha = 0^\circ$, $M_\infty = 1.05$, y = 3.5 in., z = -1.980 in.

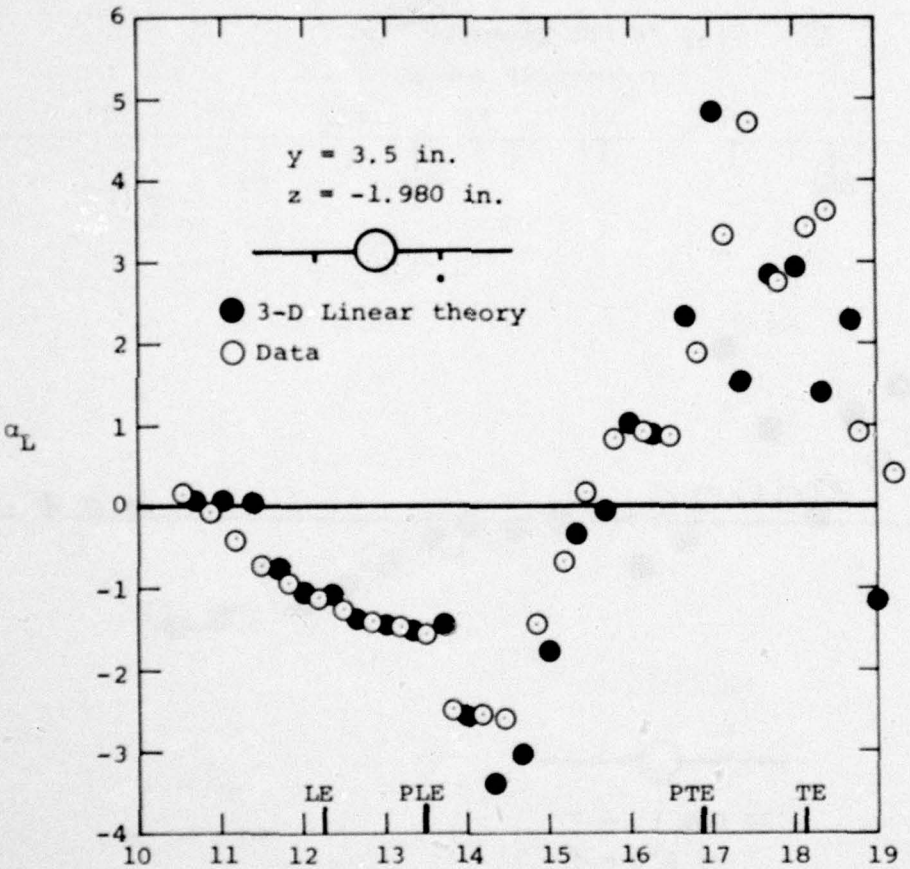

(b) Upwash station, deg.

Figure 56.- Concluded.

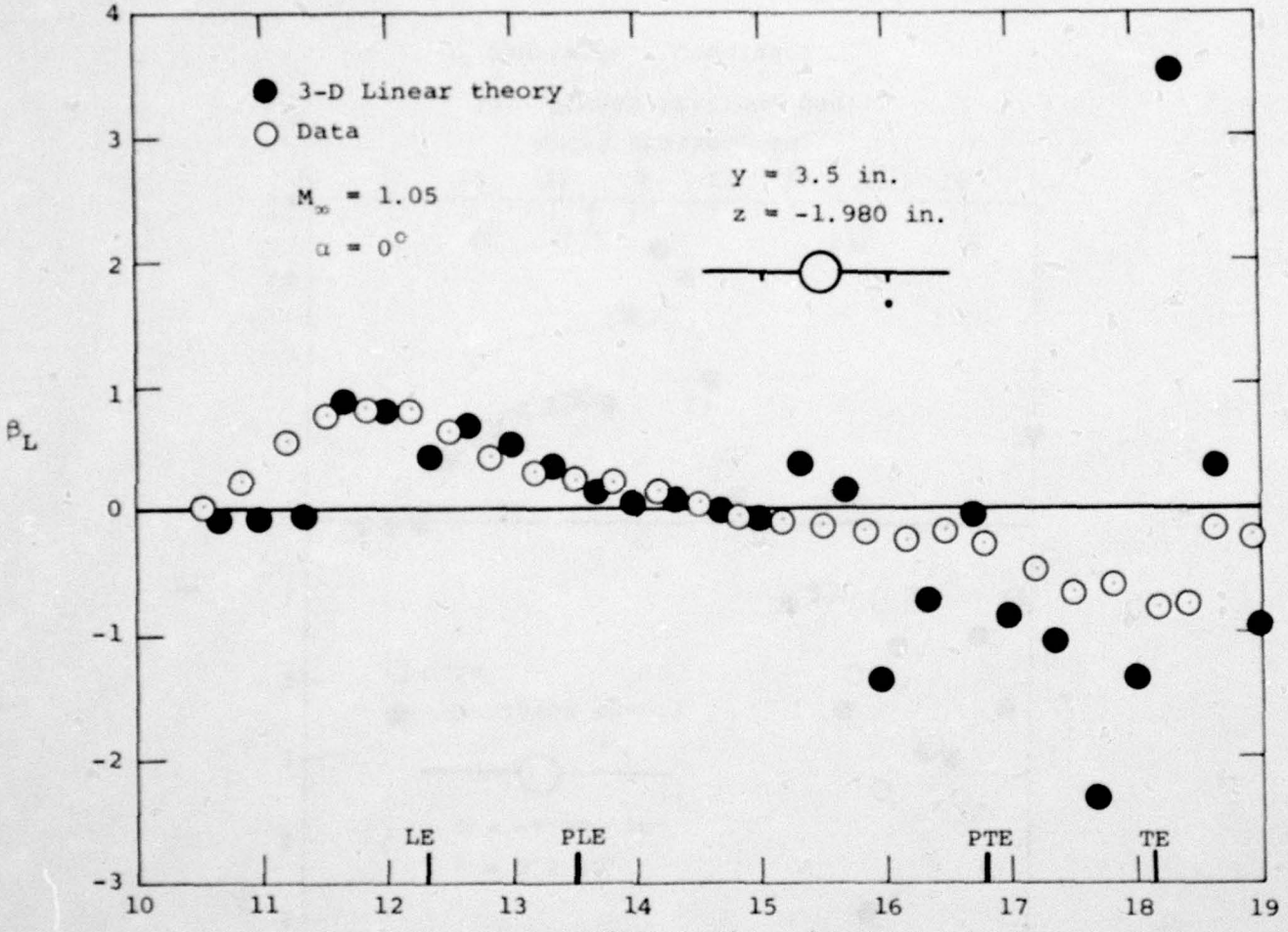

(c) Sidewash angle, deg.

Figure 56.- Concluded.

AD-A078 683 NIELSEN ENGINEERING AND RESEARCH INC MOUNTAIN VIEW CALIF F/G 20/4
THE DEVELOPMENT OF RAPID PREDICTIVE METHODS FOR THREE-DIMENSION--ETC(U)
JUL 79 A J CRISALLI , S S STAHARA F44620-75-C-0047
UNCLASSIFIED NEAR-TR-198 AFOSR-TR-79-1281 NL

3 OF 4
AD-
A078683

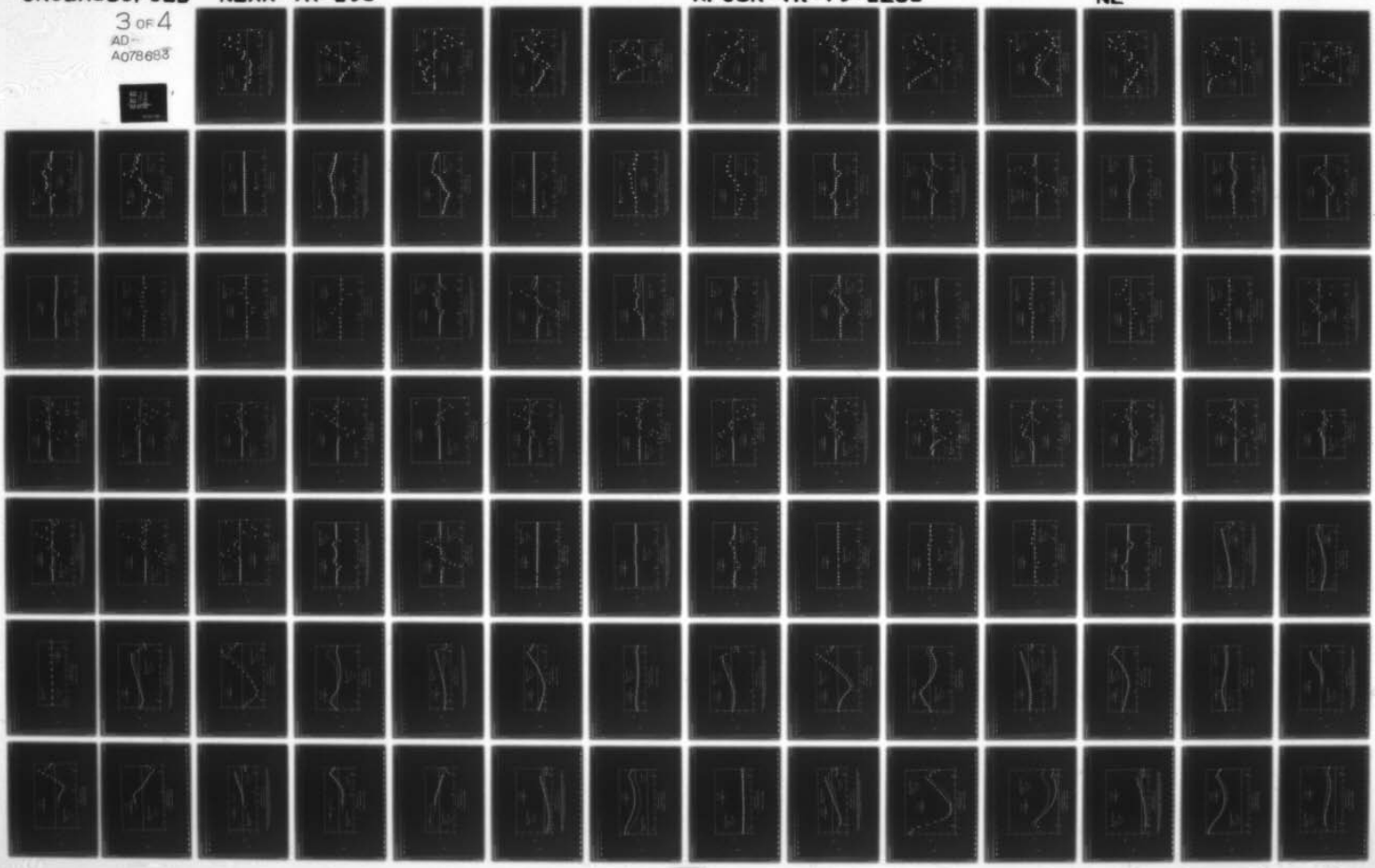

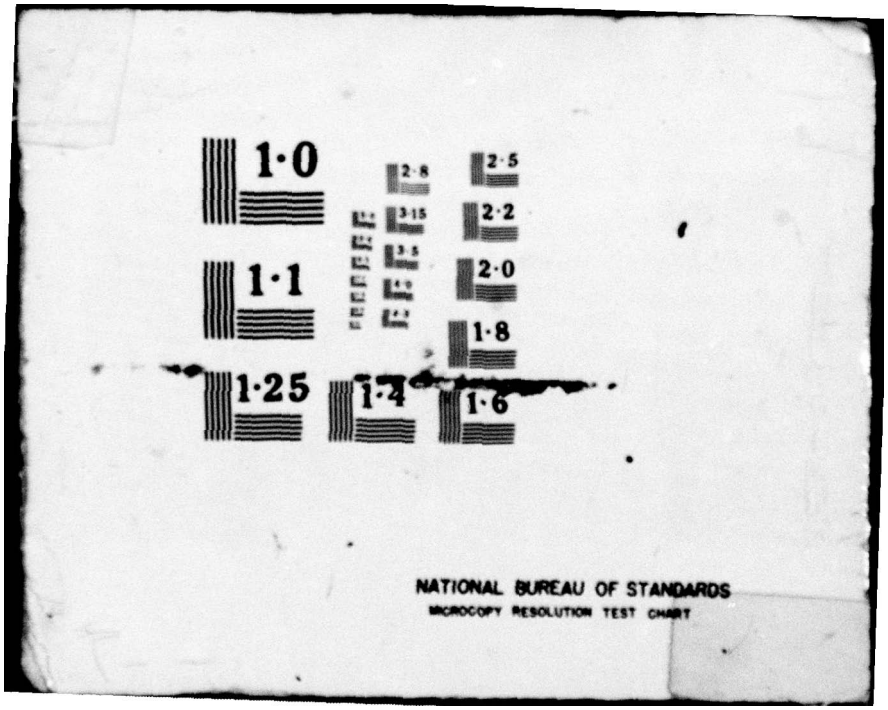
1·0
1·1
1·25
1·4
1·6
1·8
2·0
2·2
2·5
2·8
3·15
3·5
NATIONAL BUREAU OF STANDARDS
MICROCOPY RESOLUTION TEST CHART

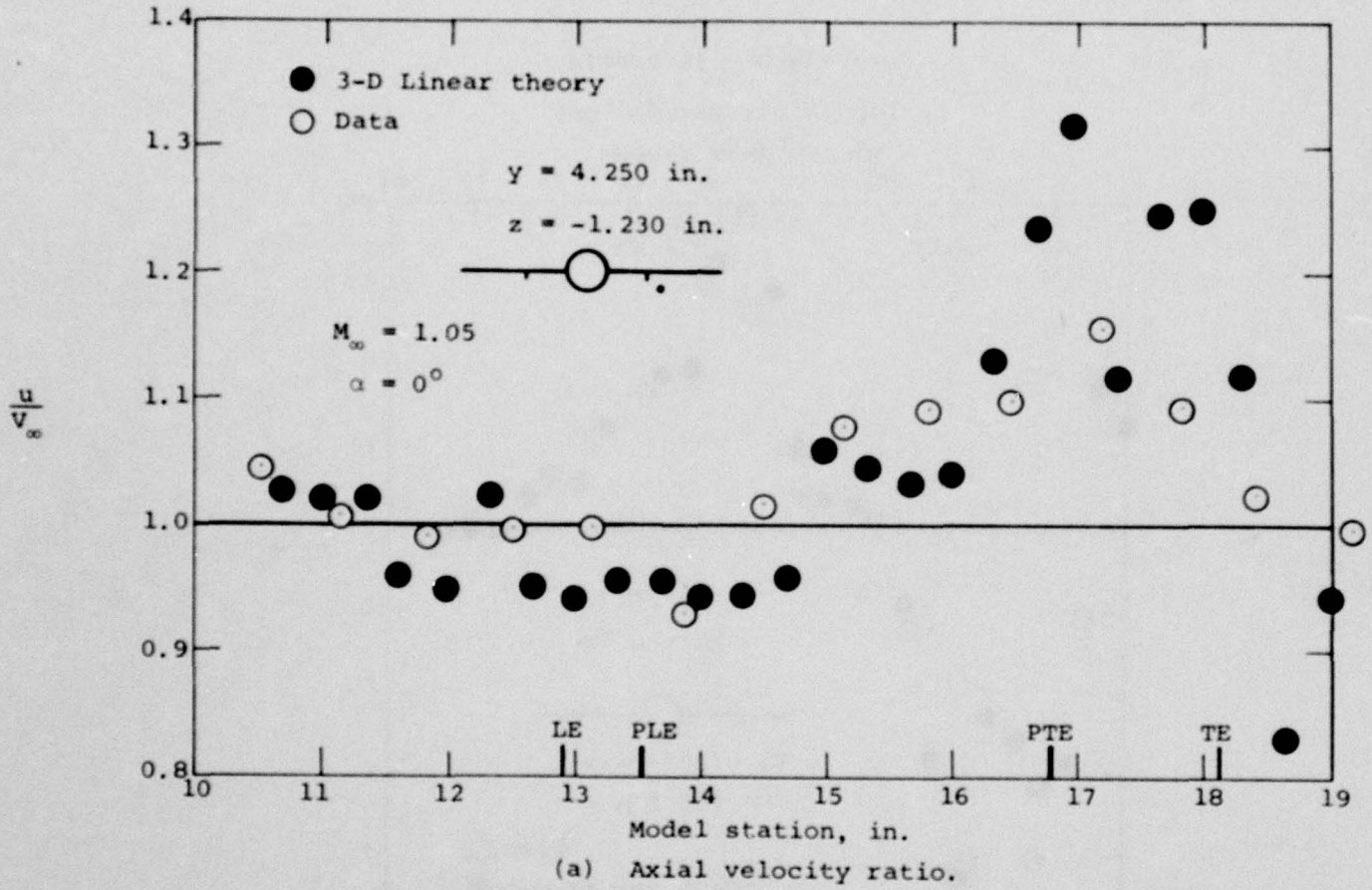

(a) Axial velocity ratio.

Figure 57.- Comparison of measured flow field quantities with prediction of three-dimensional linear theory for wing-body combination with wing pylons, $\alpha = 0°$, $M_\infty = 1.05$, y = 4.250 in., z = -1.230 in.

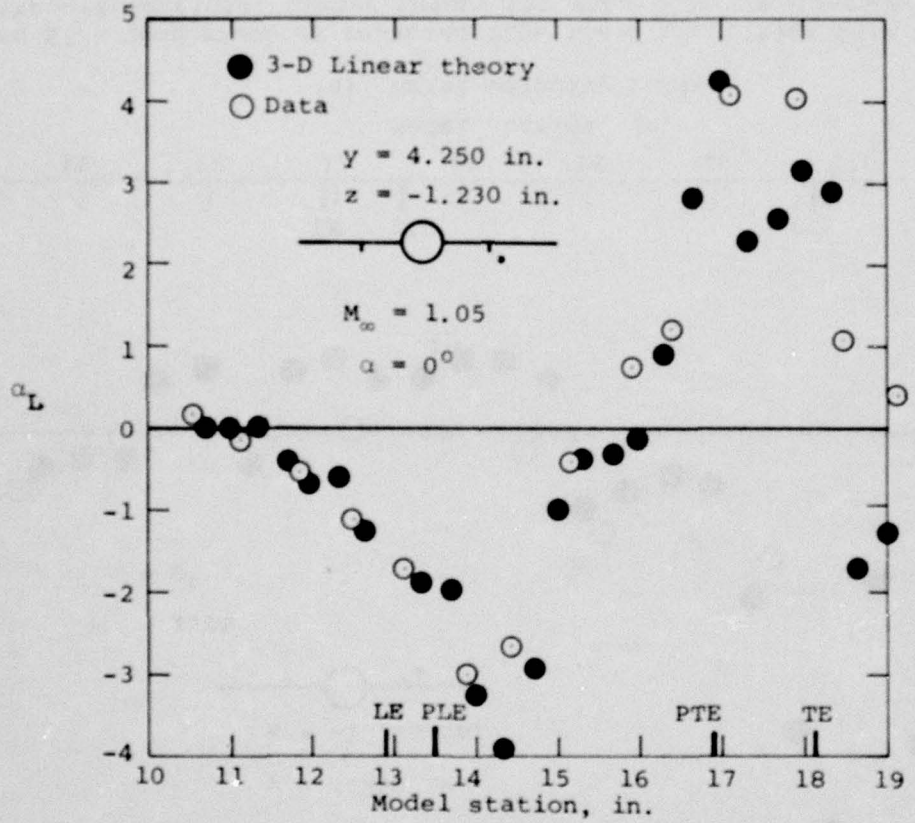

(b) Upwash angle, deg.

Figure 57.- Continued.

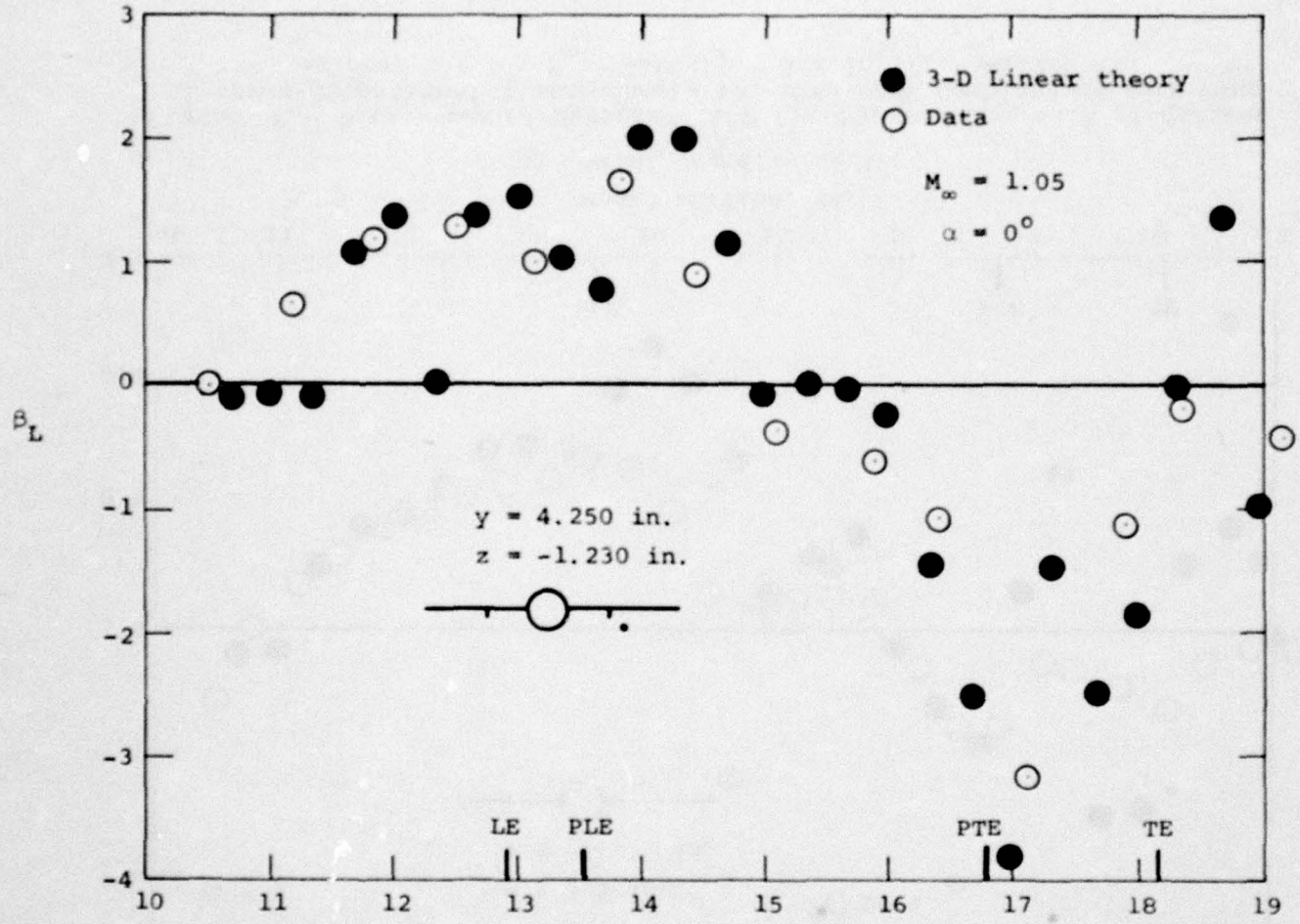

(c) Sidewash angle, deg.

Figure 57.- Concluded.

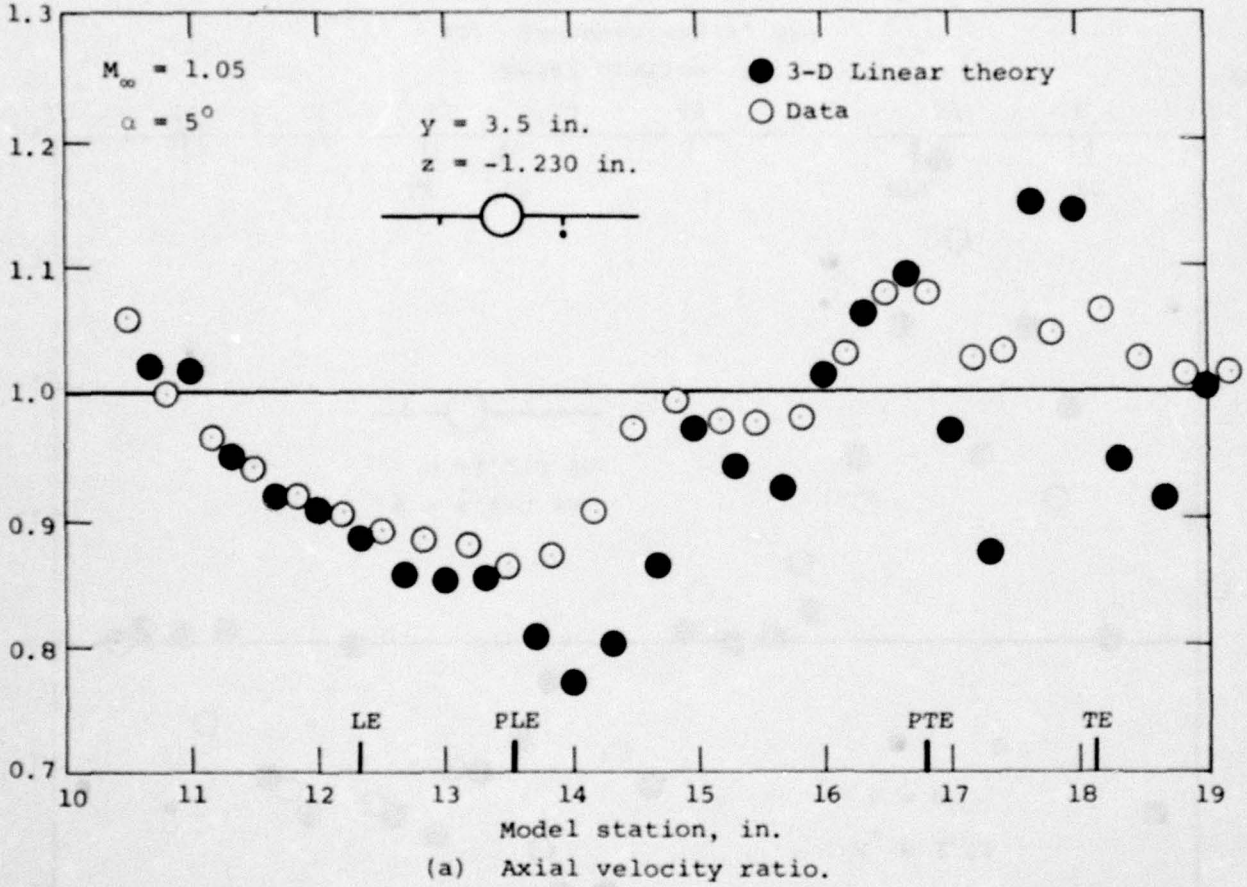

(a) Axial velocity ratio.

Figure 58.- Comparison of measured flow field quantities with prediction of three-dimensional linear theory for wing-body combination with wing pylons, $\alpha = 5^\circ$, $M_\infty = 1.05$, y = 3.5 in., z = -1.230 in.

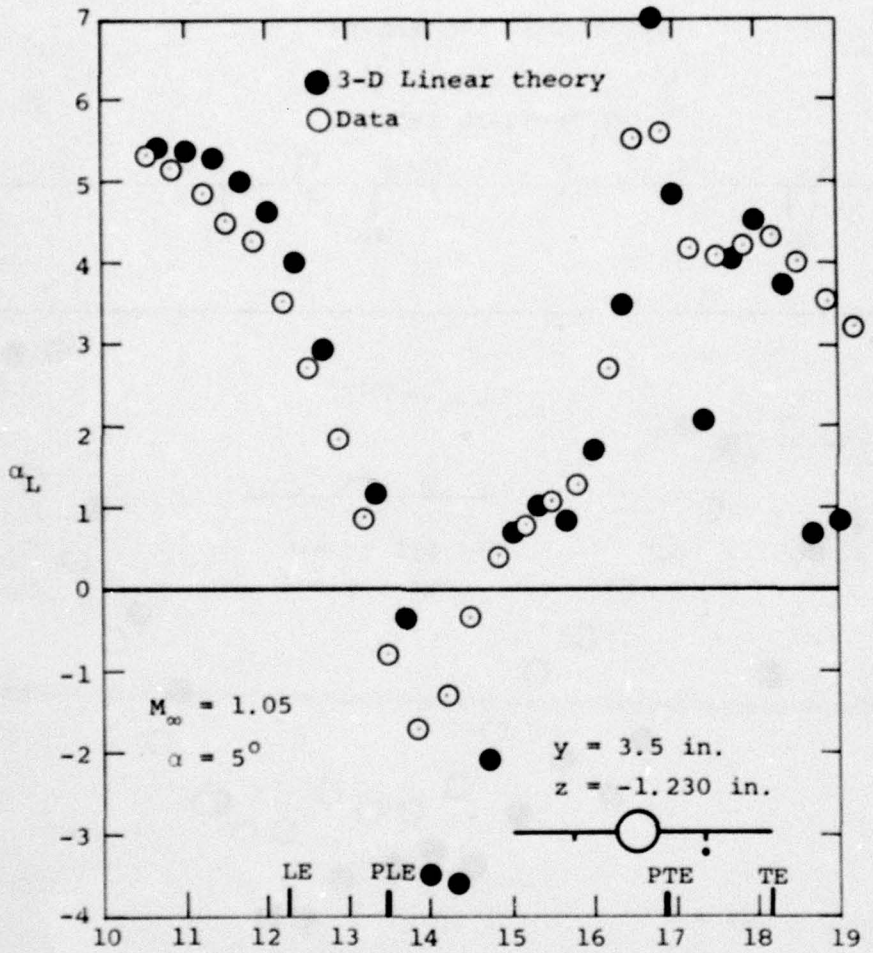

(b) Upwash angle, deg.

Figure 58.- Continued.

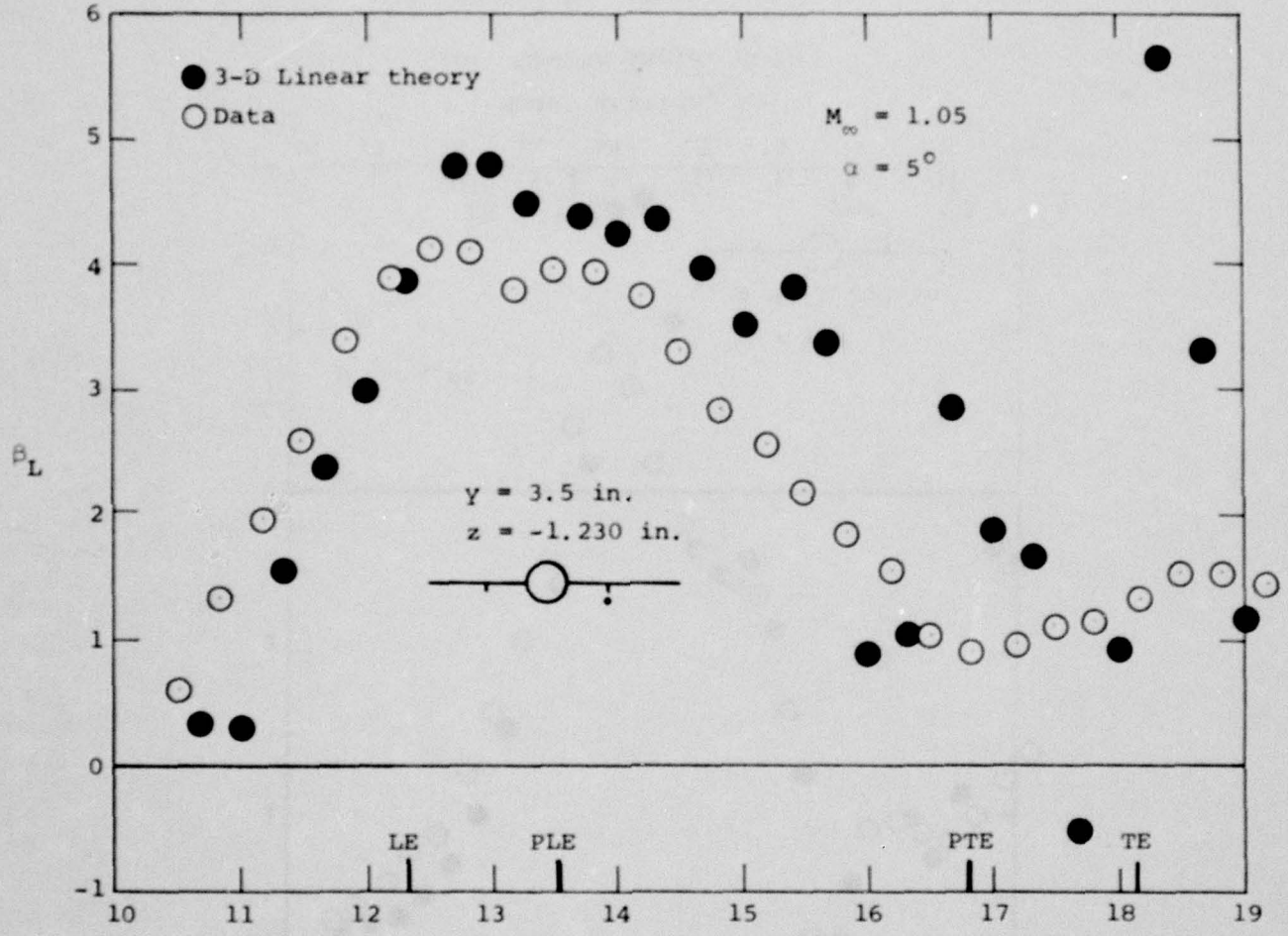

(c) Sidewash angle, deg.

Figure 58.- Concluded.

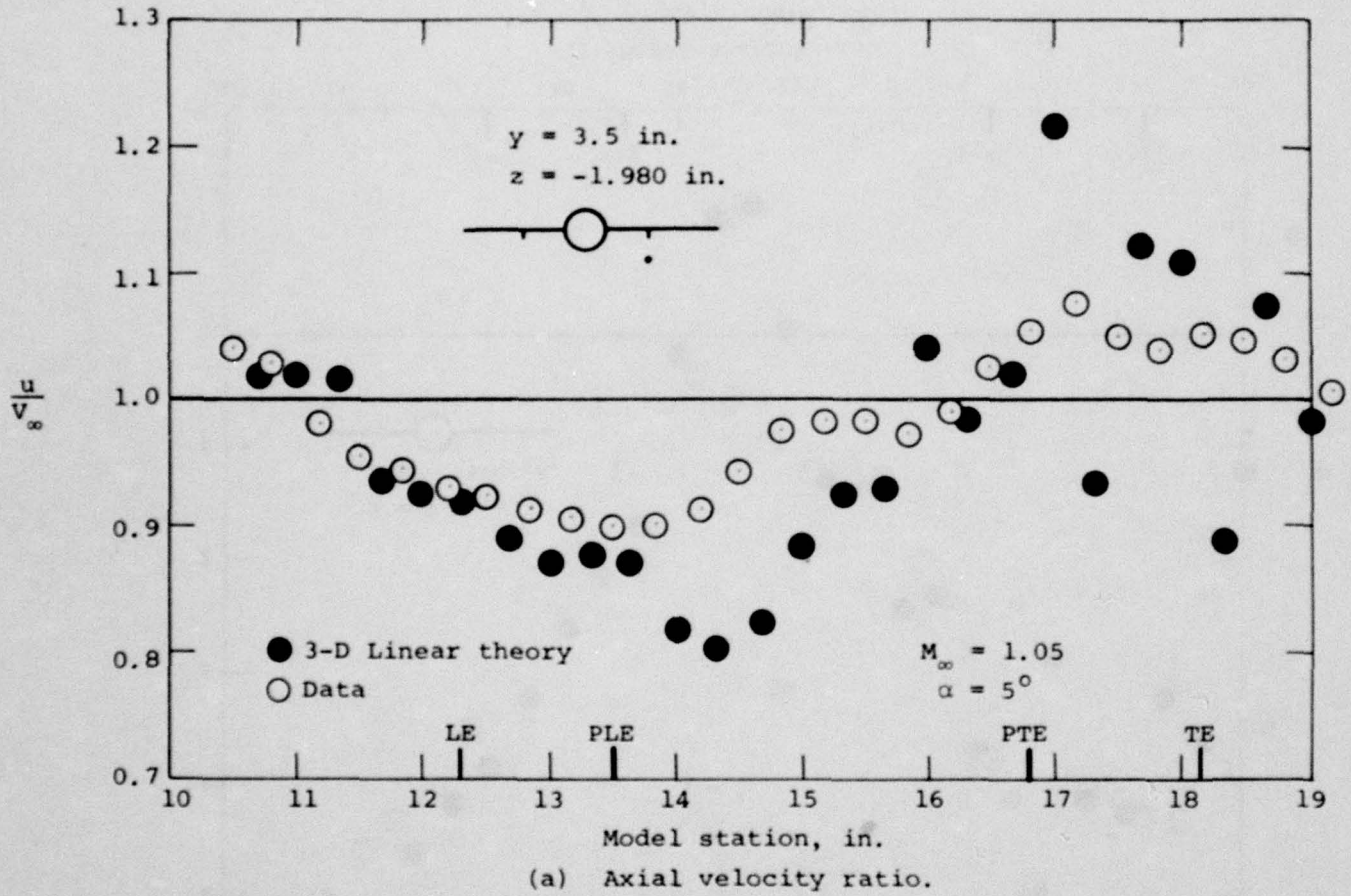

(a) Axial velocity ratio.

Figure 59.- Comparison of measured flow field quantities with prediction of three-dimensional linear theory for wing-body combination with wing pylons, $\alpha = 5^\circ$, $M_\infty = 1.05$, y = 3.5 in., z = -1.980 in.

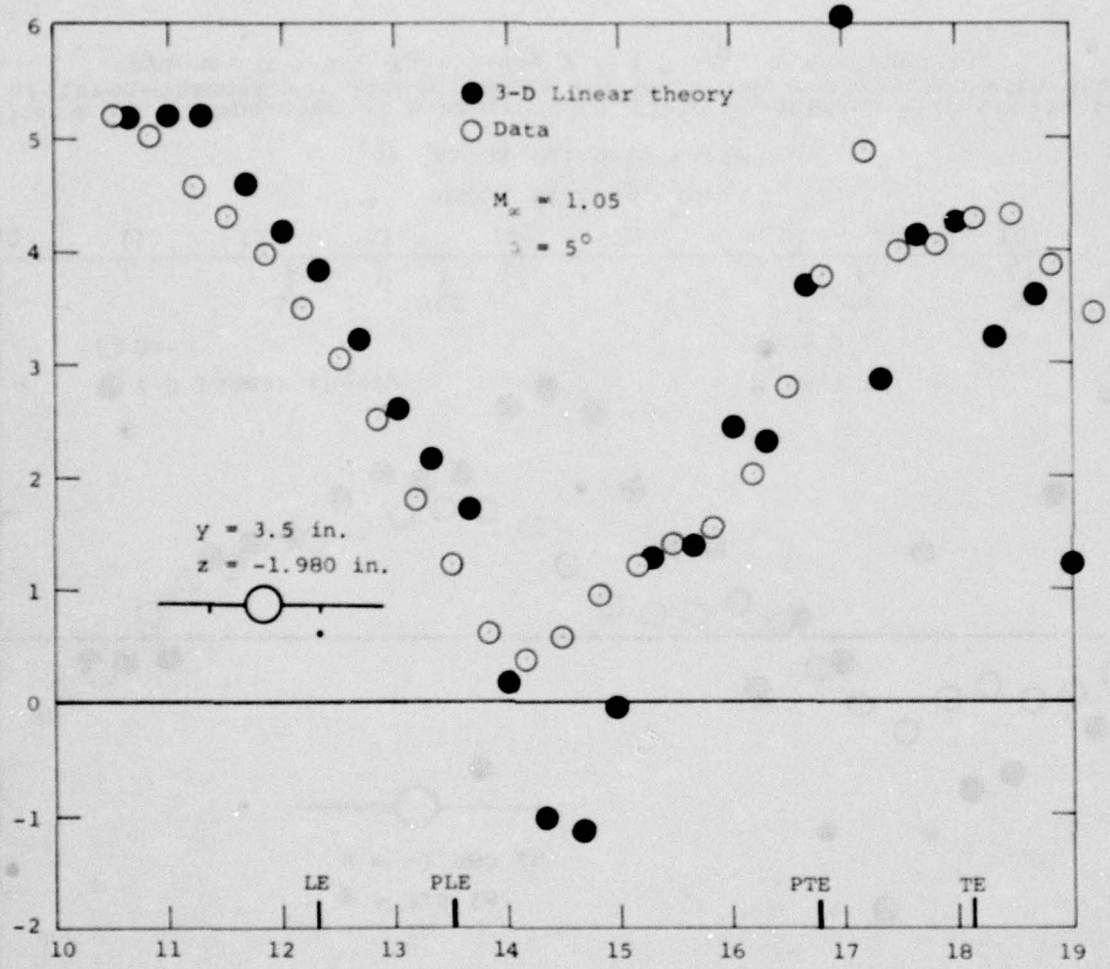

(b) Upwash angle, deg.

Figure 59.- Continued.

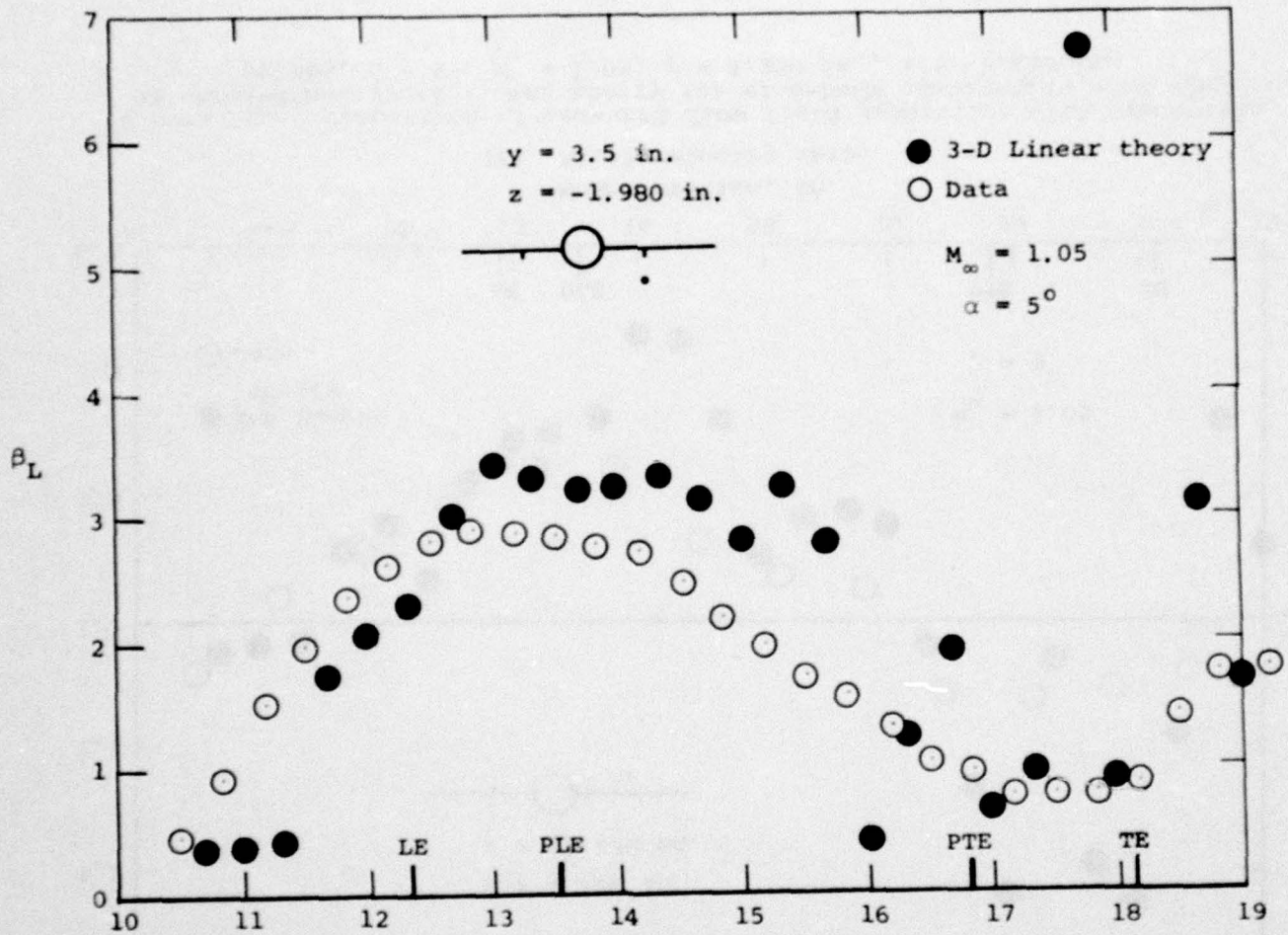

(c) Sidewash angle, deg.

Figure 59.- Concluded.

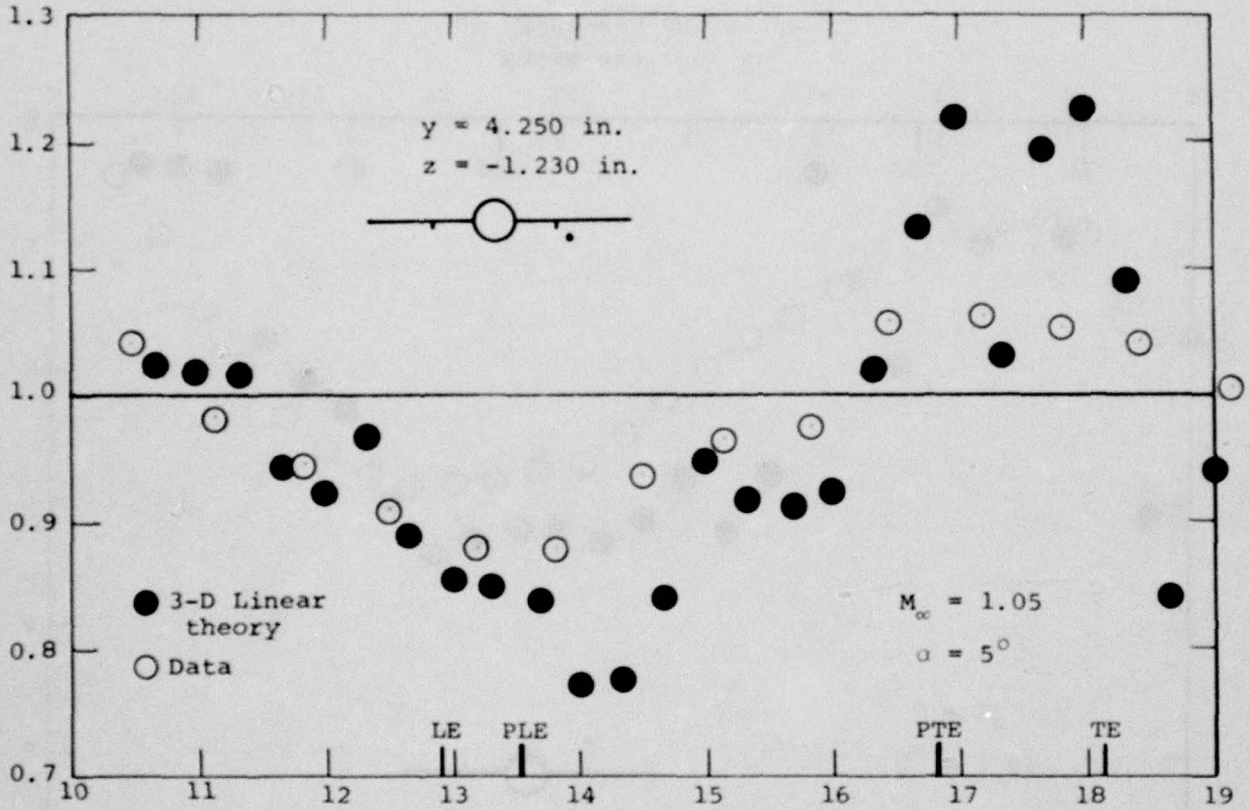

(a) Axial velocity ratio.

Figure 60.- Comparison of measured flow field quantities with prediction of three-dimensional linear theory for wing-body combination with wing pylons, $\alpha = 5°$, $M_\infty = 1.05$, y = 4.250 in., z = -1.230 in.

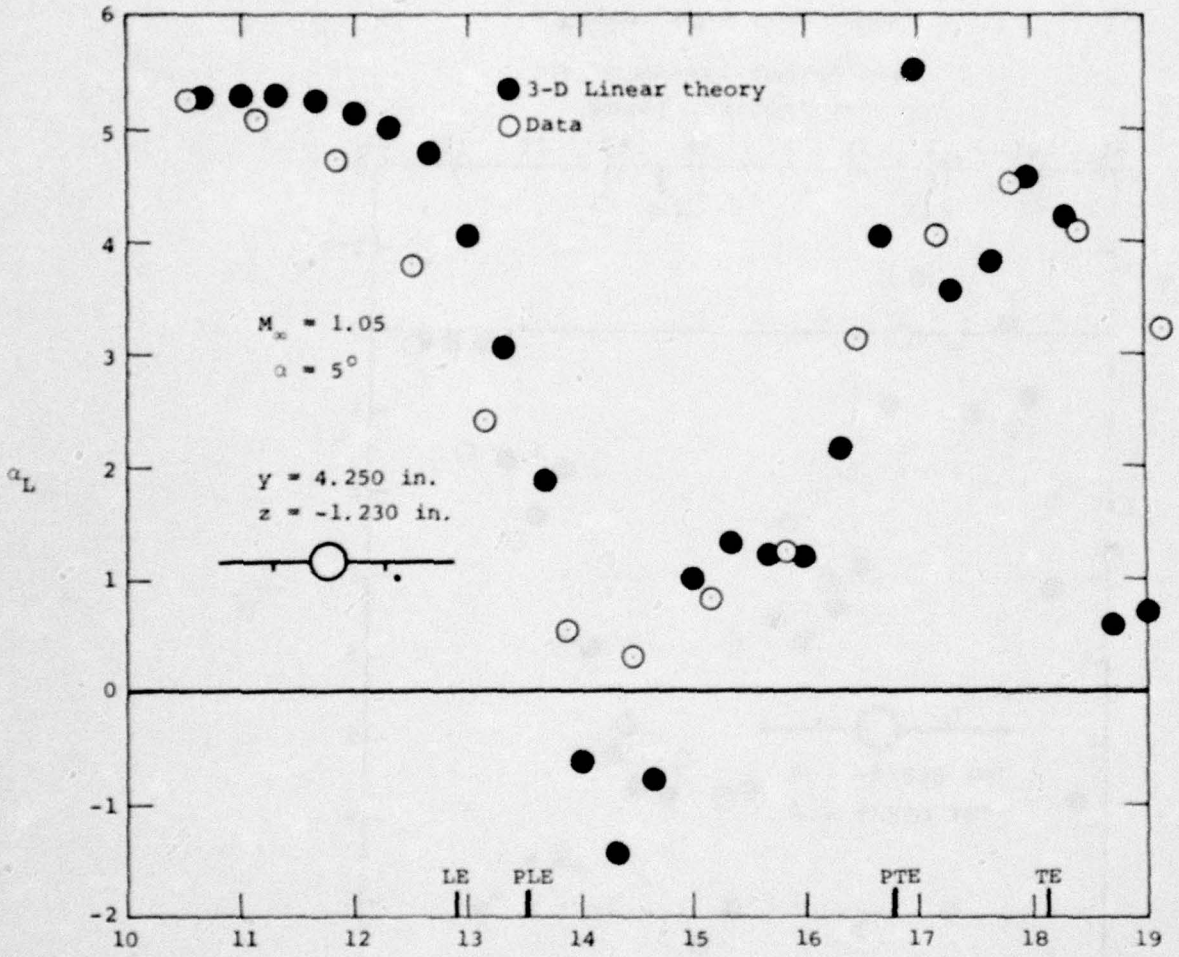

(b) Upwash angle, deg.

Figure 60.- Continued.

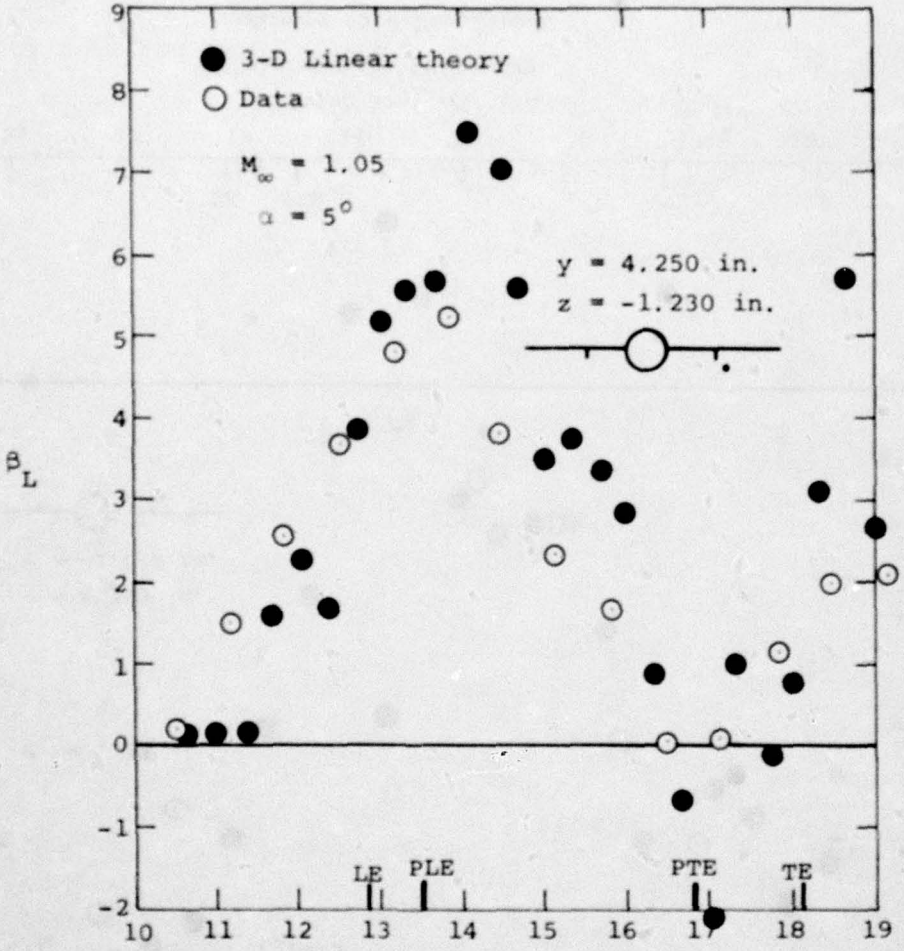

(c) Sidewash angle, deg.

Figure 60.- Concluded.

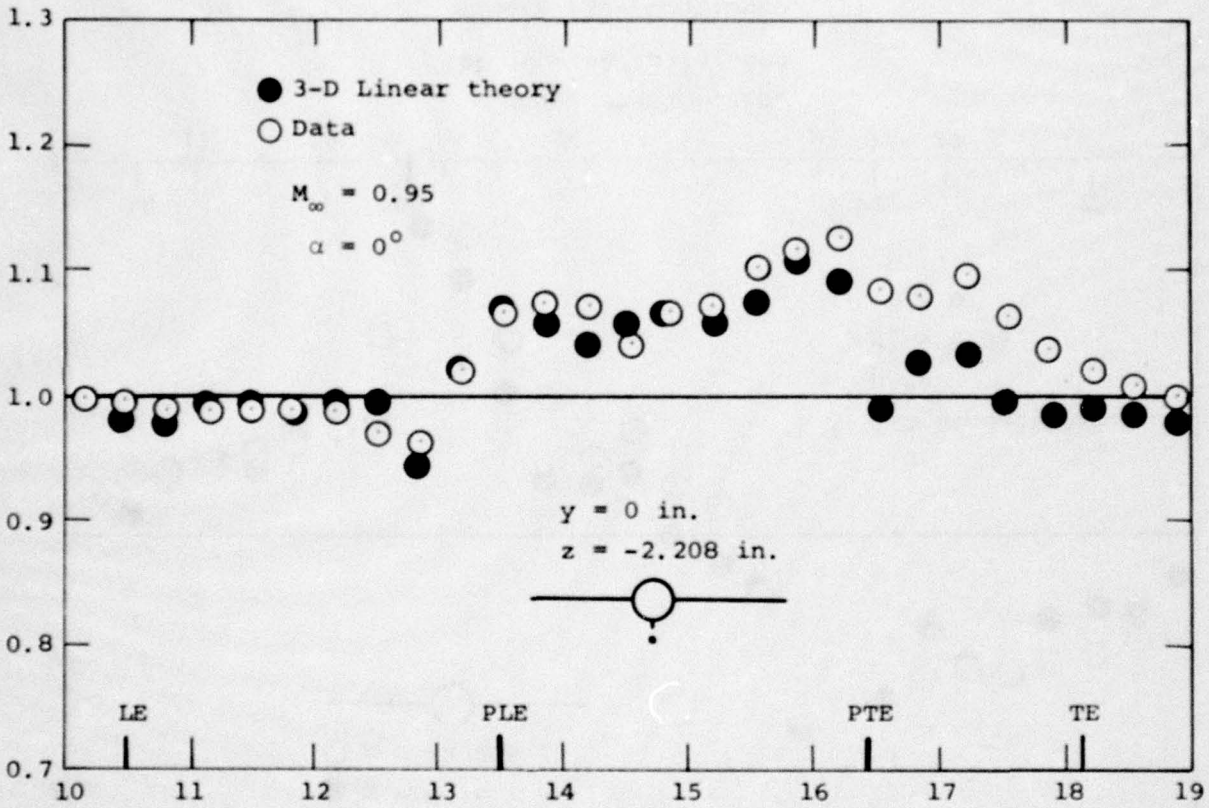

(a) Axial velocity ratio.

Figure 61.- Comparison of measured flow field quantities with predictions of three-dimensional linear theory for wing-body combination with fuselage pylon, $\alpha = 0^{\circ}$, $M_{\infty} = 0.95$, y = 0 in., z = -2.208 in.

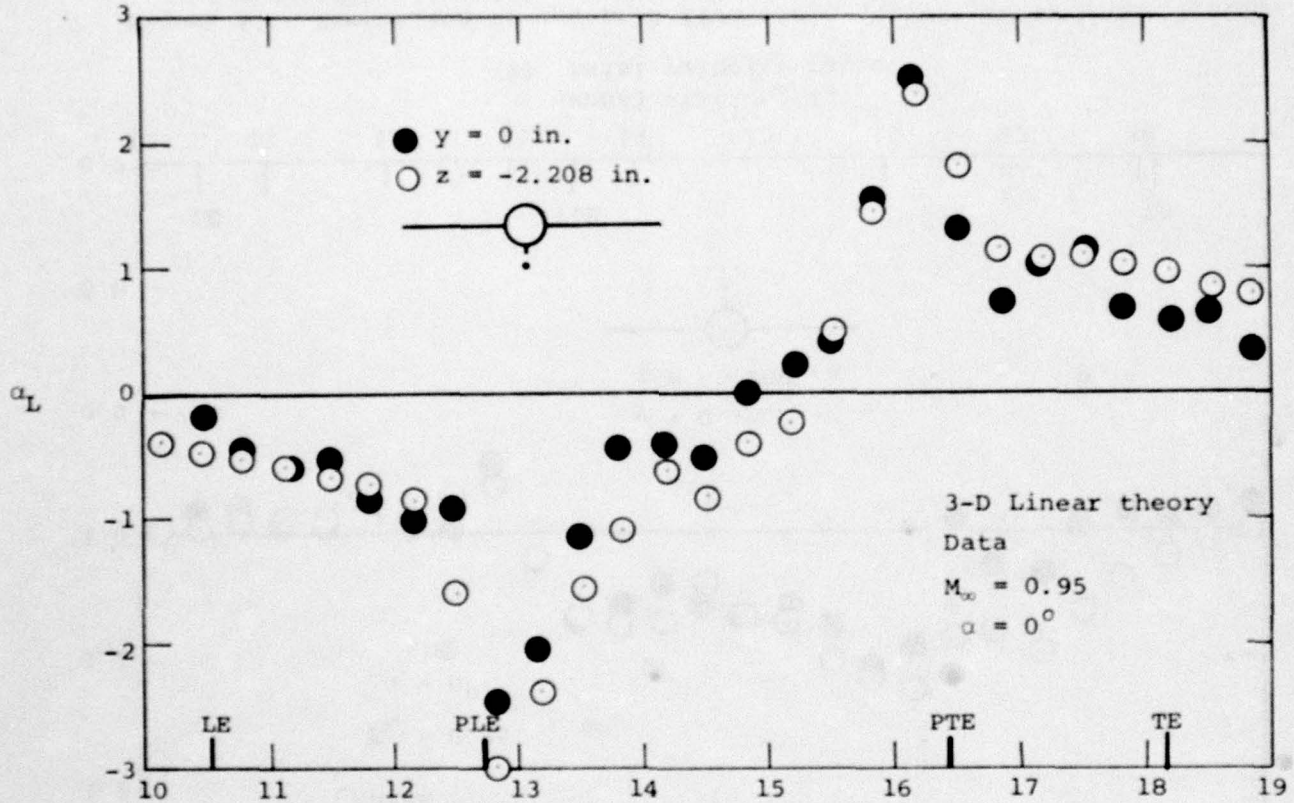

(b) Upwash angle, deg.

Figure 61.- Continued.

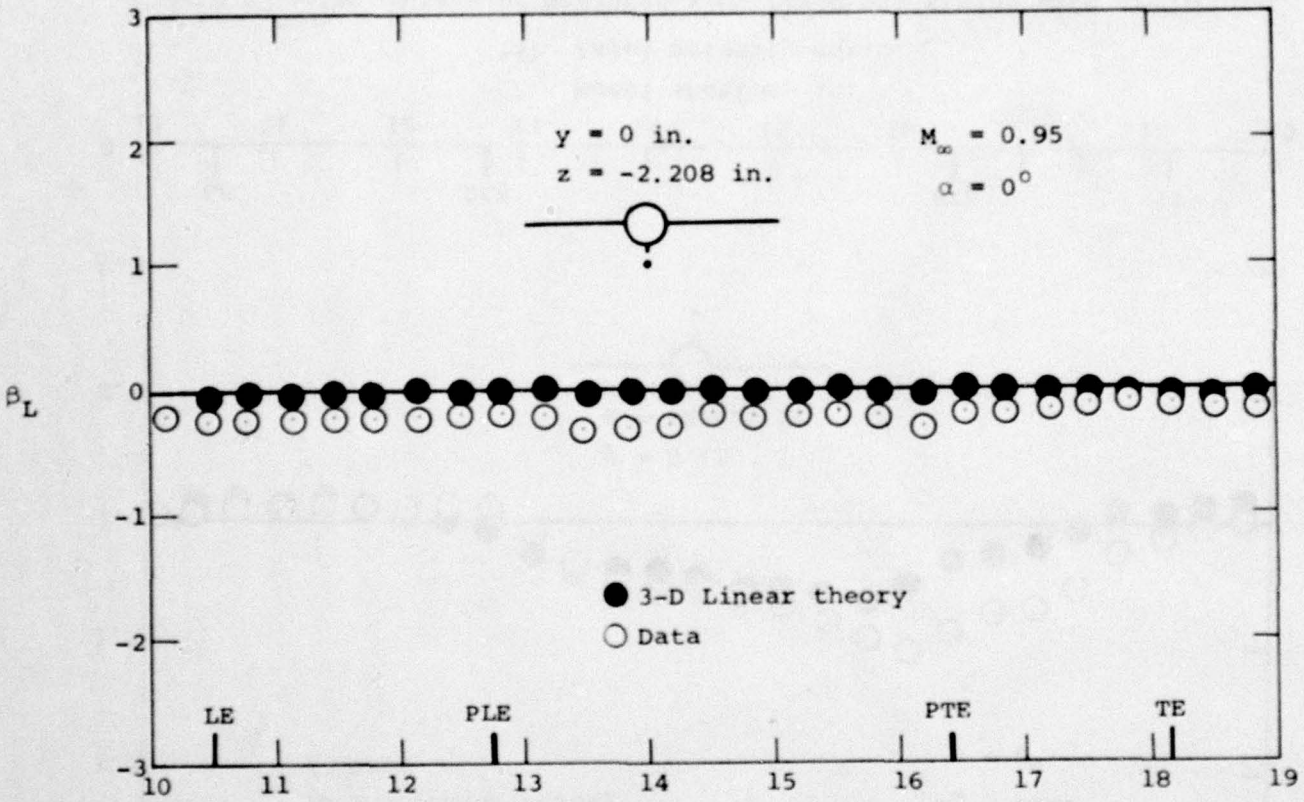

(c) Sidewash angle, deg.

Figure 61.- Concluded.

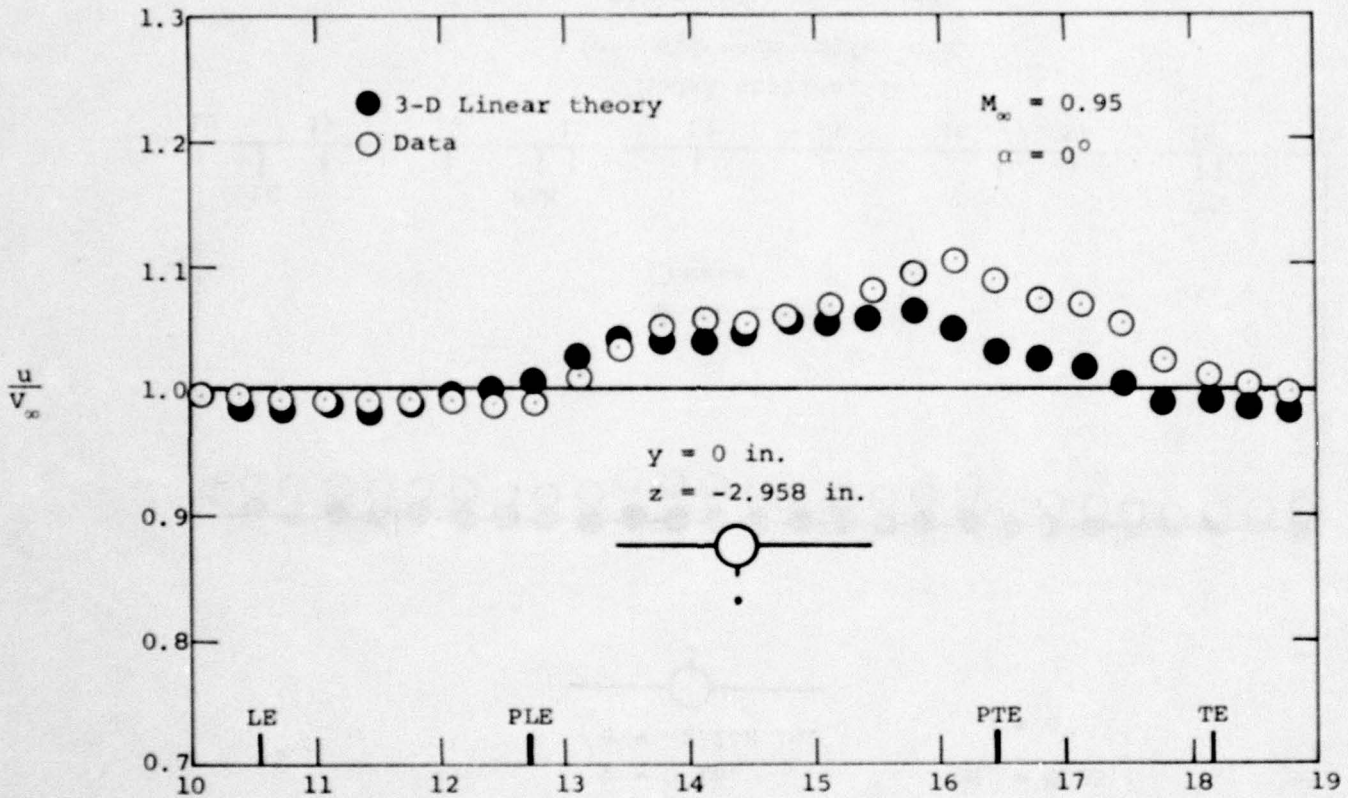

(a) Axial velocity ratio.

Figure 62.- Comparison of measured flow field quantities with prediction of three-dimensional linear theory for wing-body combination with fuselage pylon, α = 0°, M_∞ = 0.95, y = 0 in., z = -2.958 in.

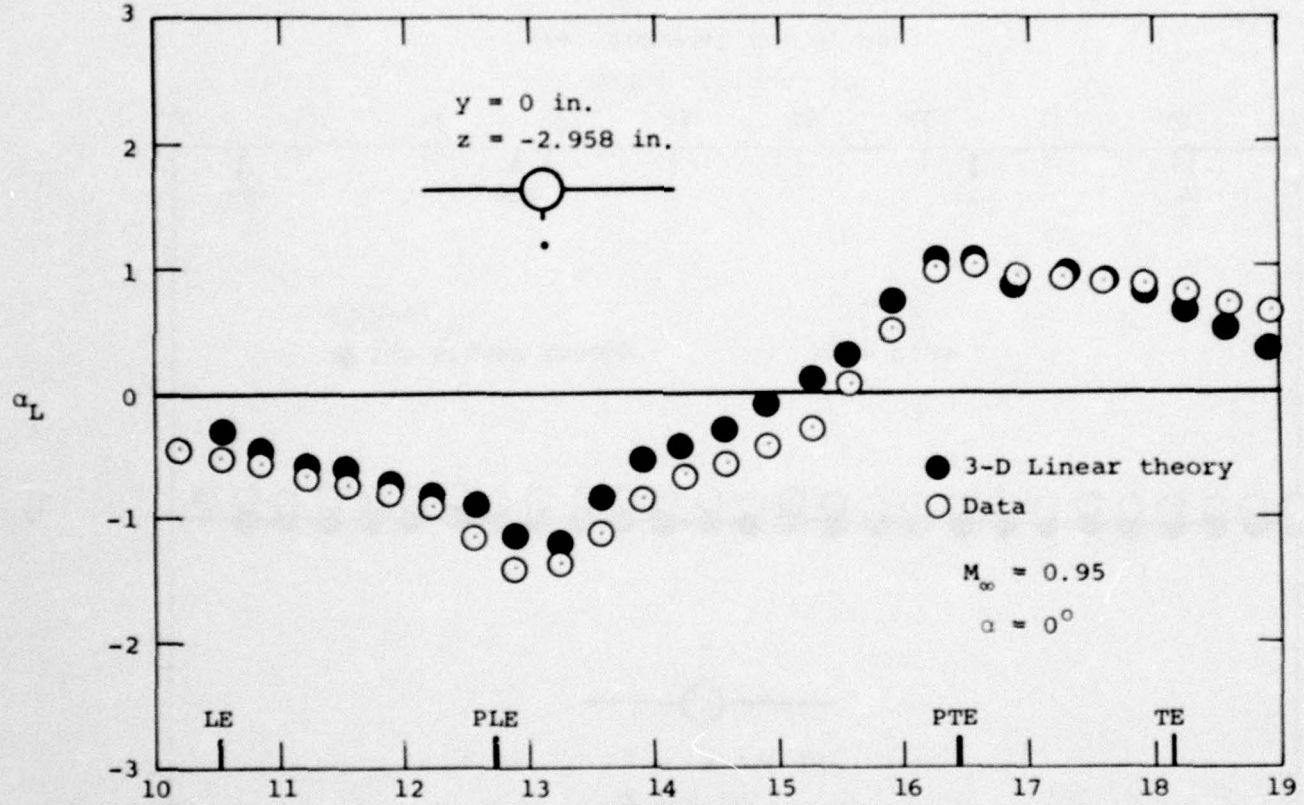

(b) Upwash angle, deg.

Figure 62.- Continued.

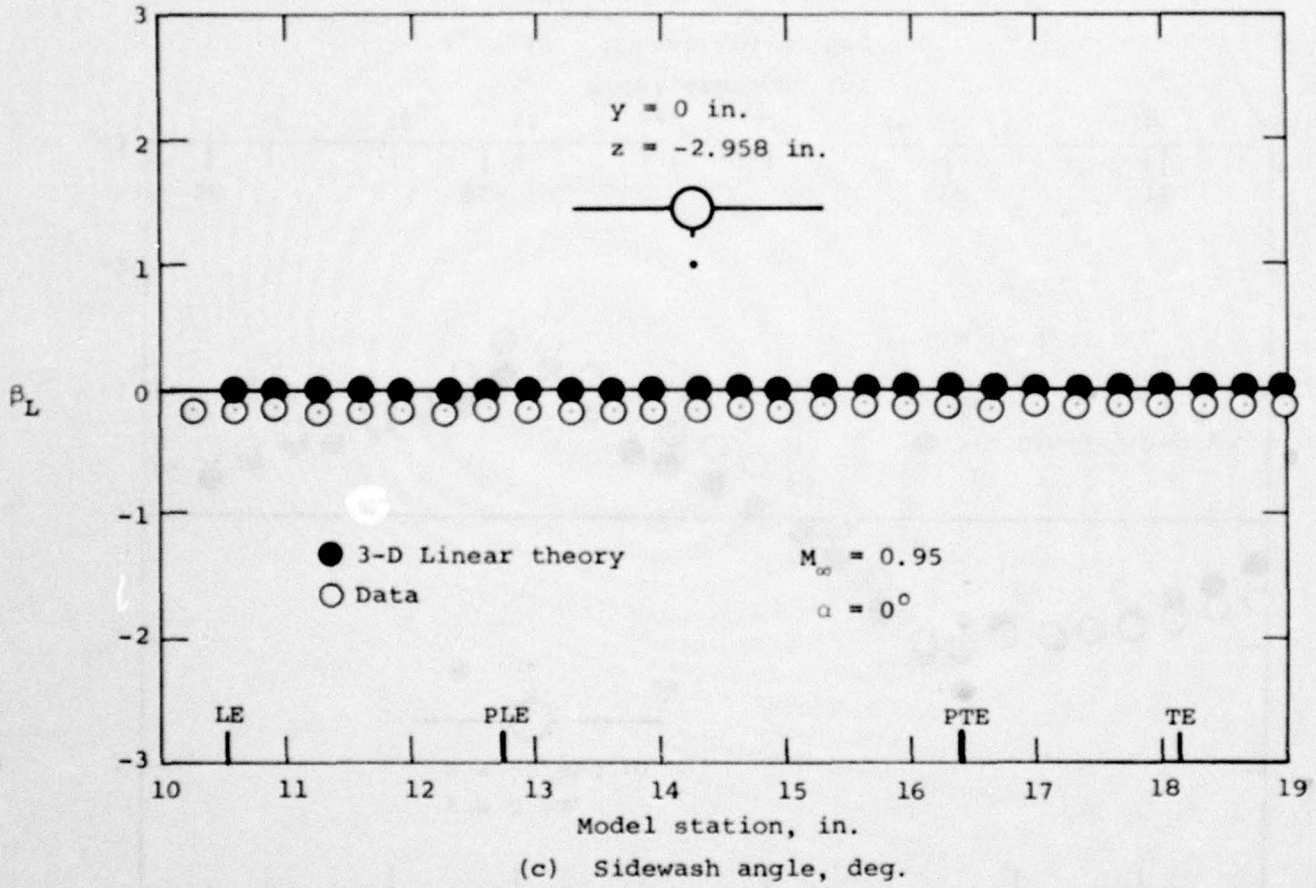

(c) Sidewash angle, deg.

Figure 62.- Concluded.

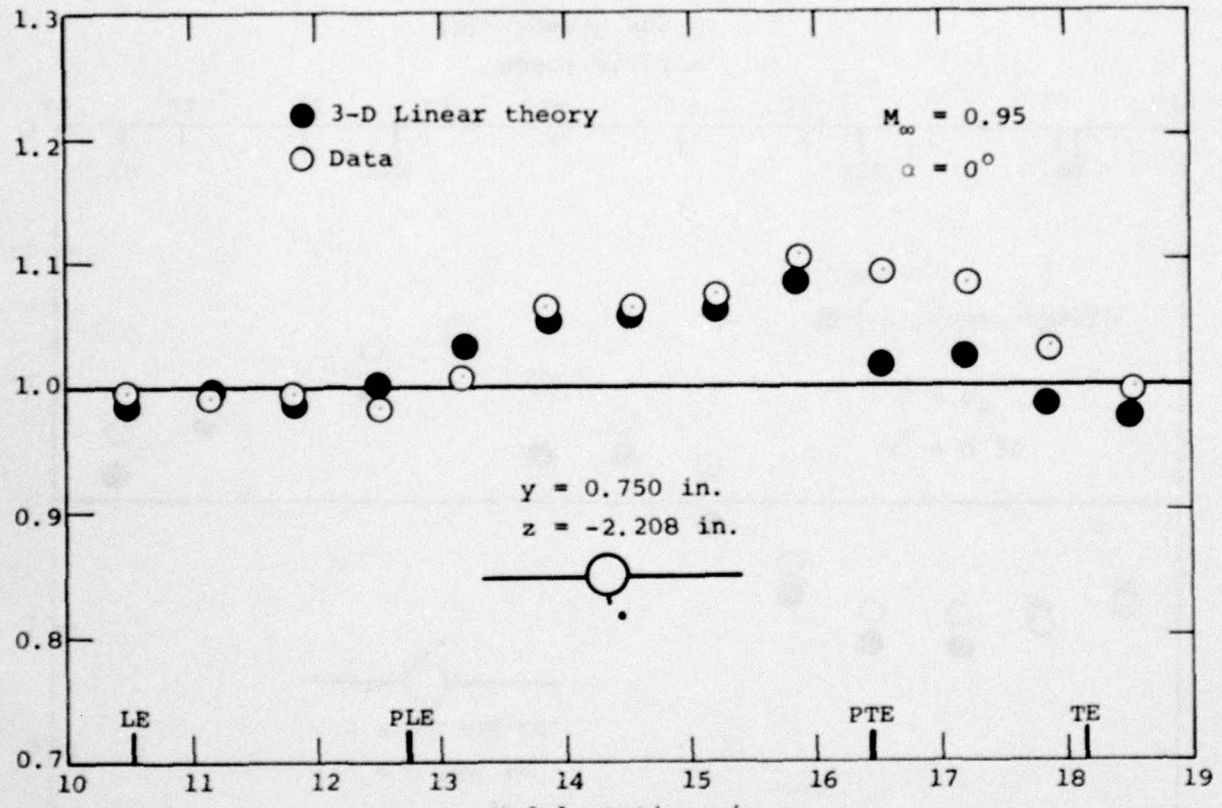

(a) Axial velocity ratio.

Figure 63.- Comparison of measured flow field quantities with predictions of three-dimensional linear theory for wing-body combination with fuselage pylon, $\alpha = 0^\circ$, $M_\infty = 0.95$, y = 0.750 in., z = -2.208 in.

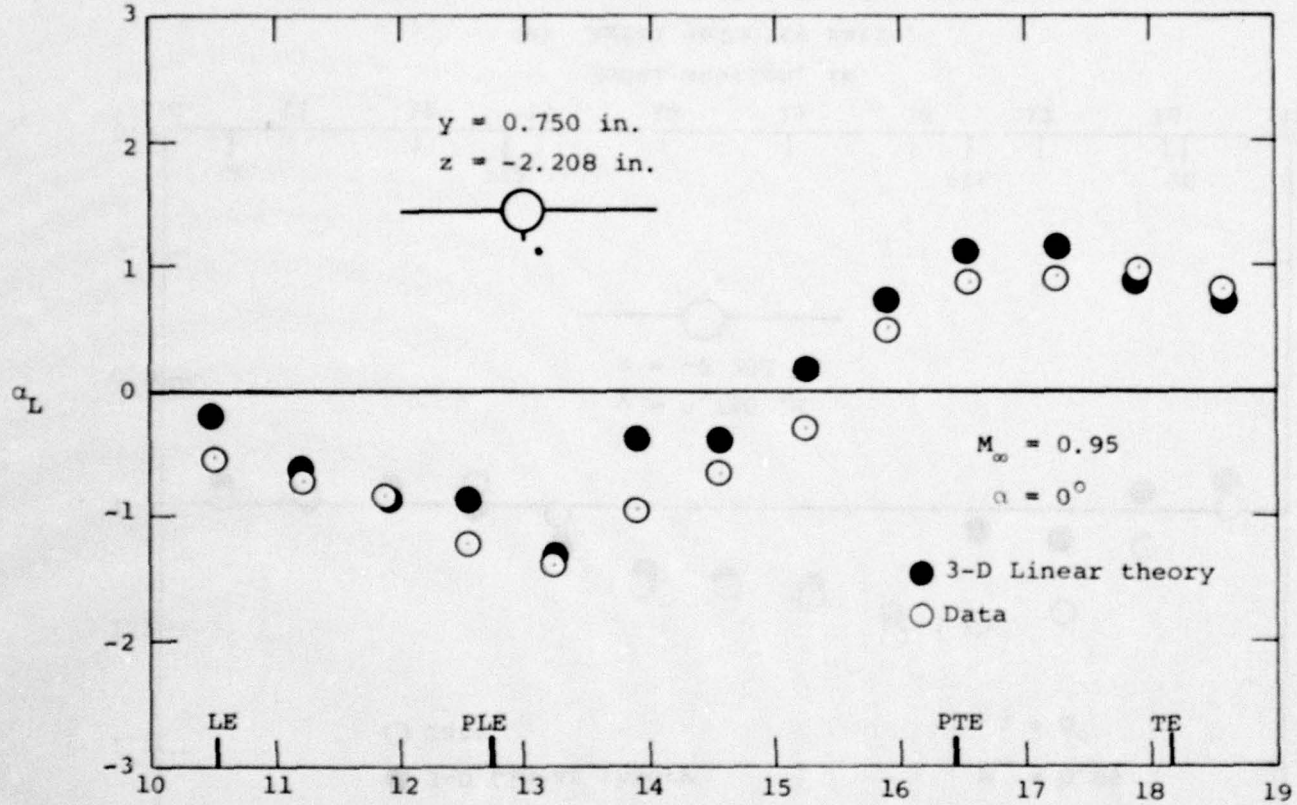

(b) Upwash angle, deg.

Figure 63.- Continued.

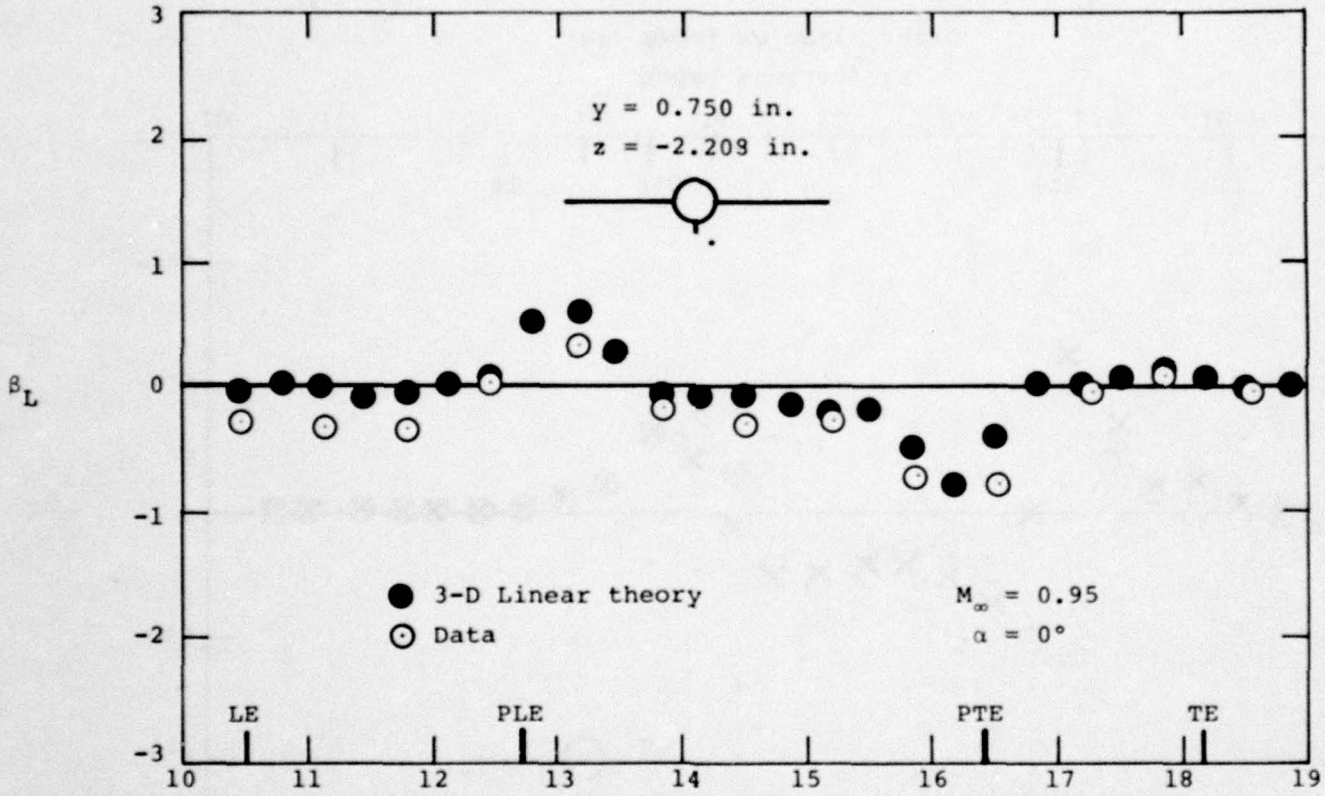

(c) Sidewash angle, deg.

Figure 63.- Concluded.

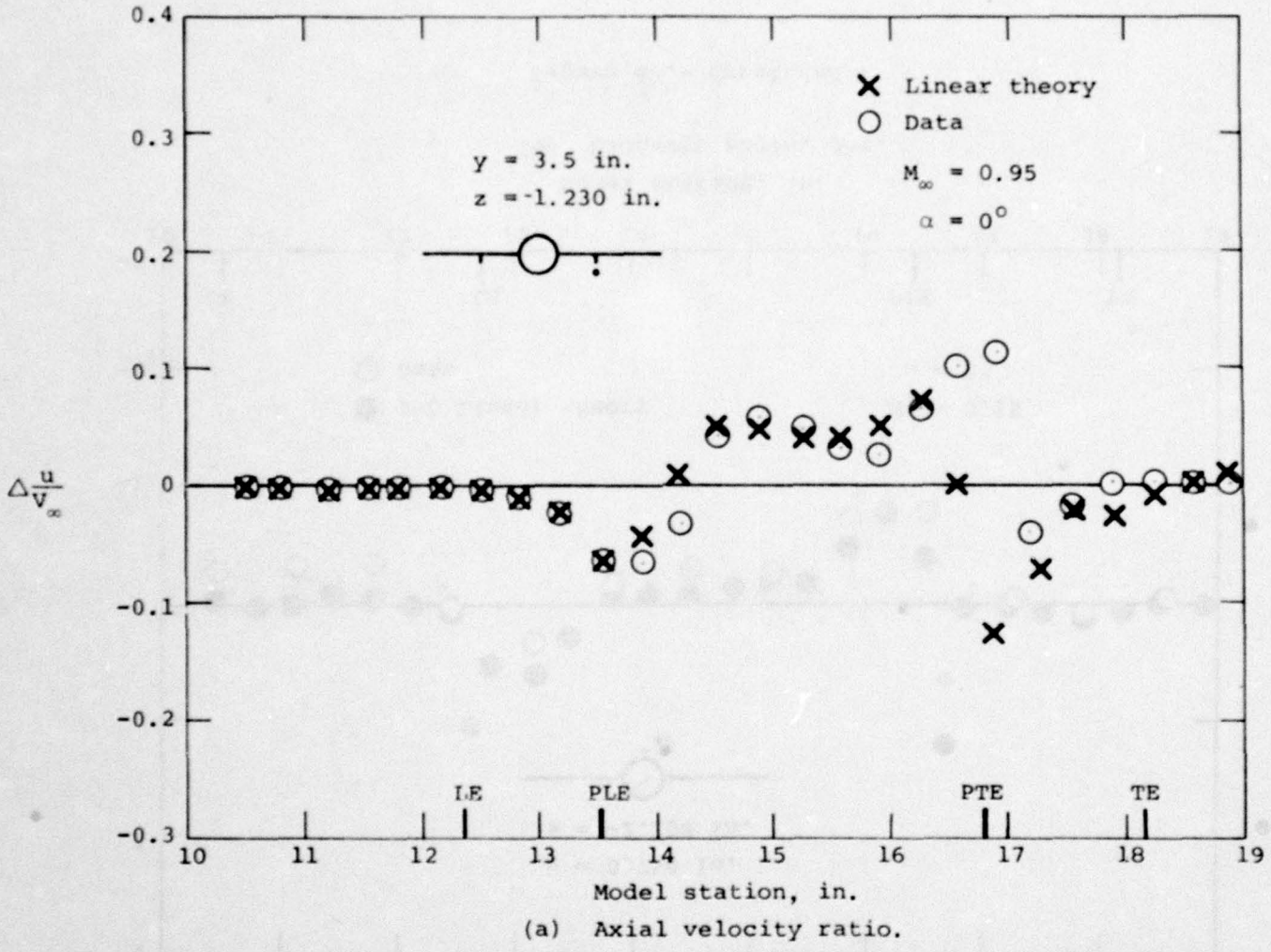

(a) Axial velocity ratio.

Figure 64.- Comparison of measured and theoretical differences between wing-body-pylon and wing-body flow field quantities, α = 0°, M_∞ = 0.95, y = 3.5 in., z = -1.230 in.

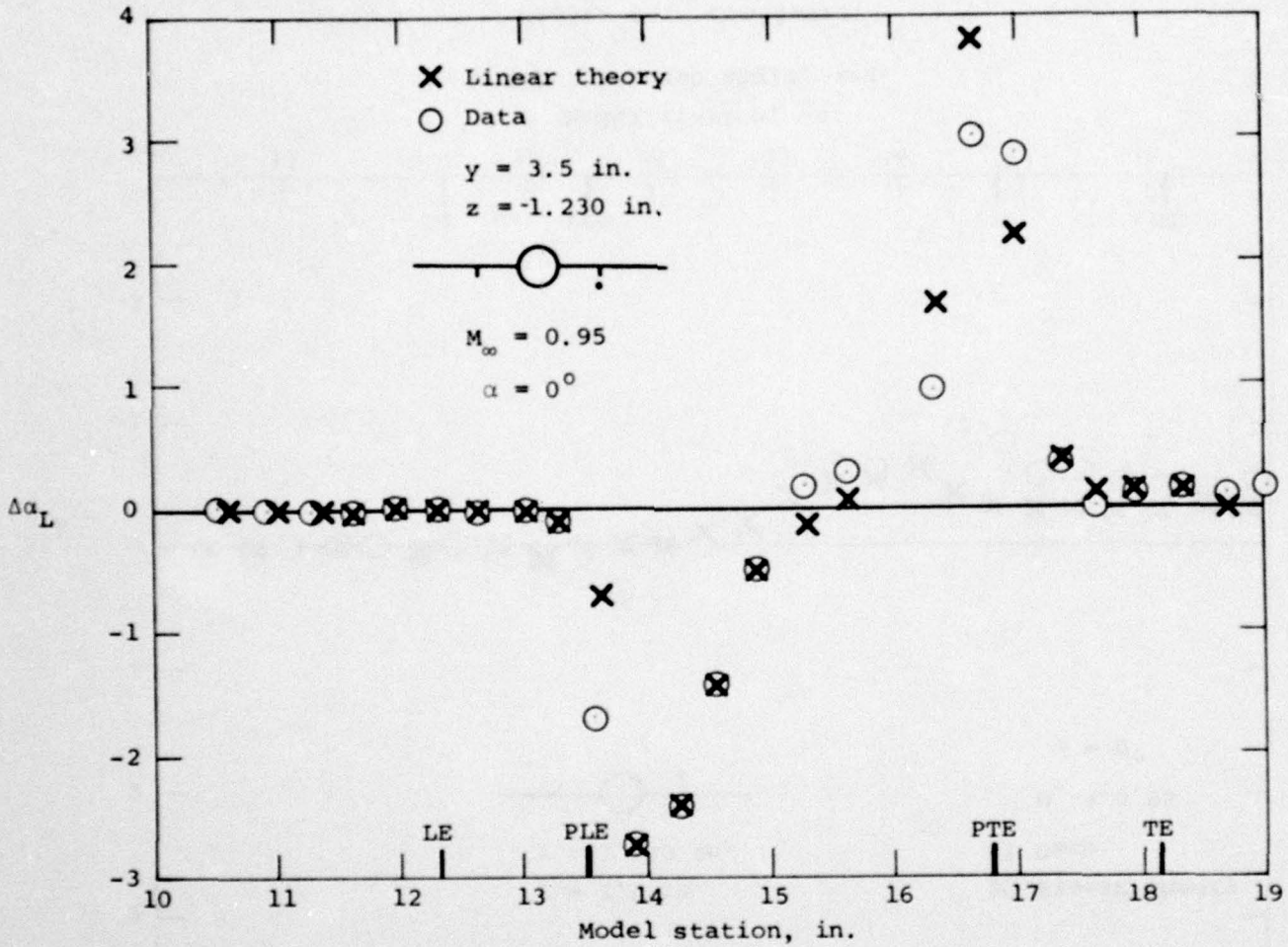

(b) Upwash angle, deg.

Figure 64.- Continued.

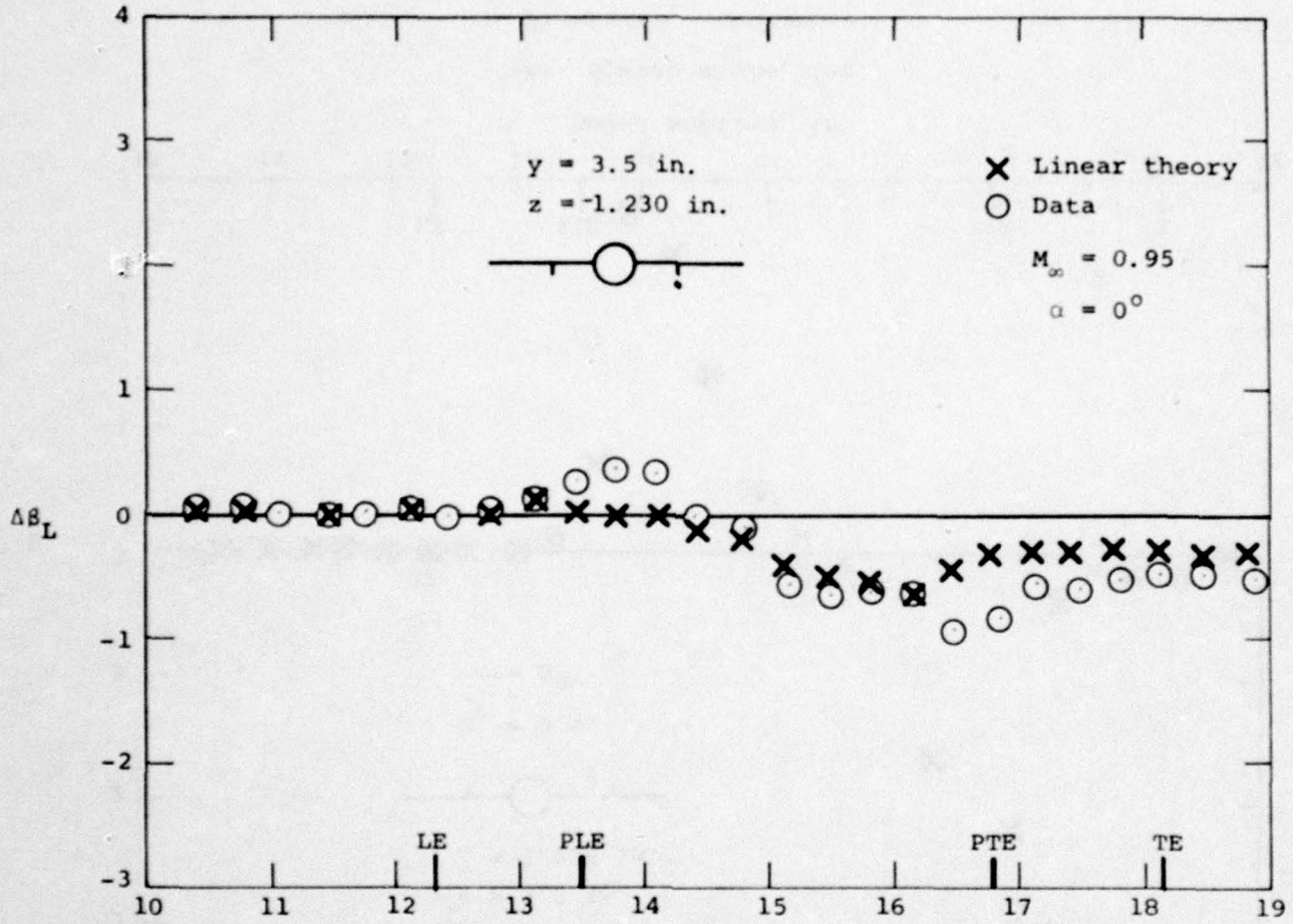

(c) Sidewash angle, deg.

Figure 64.- Concluded.

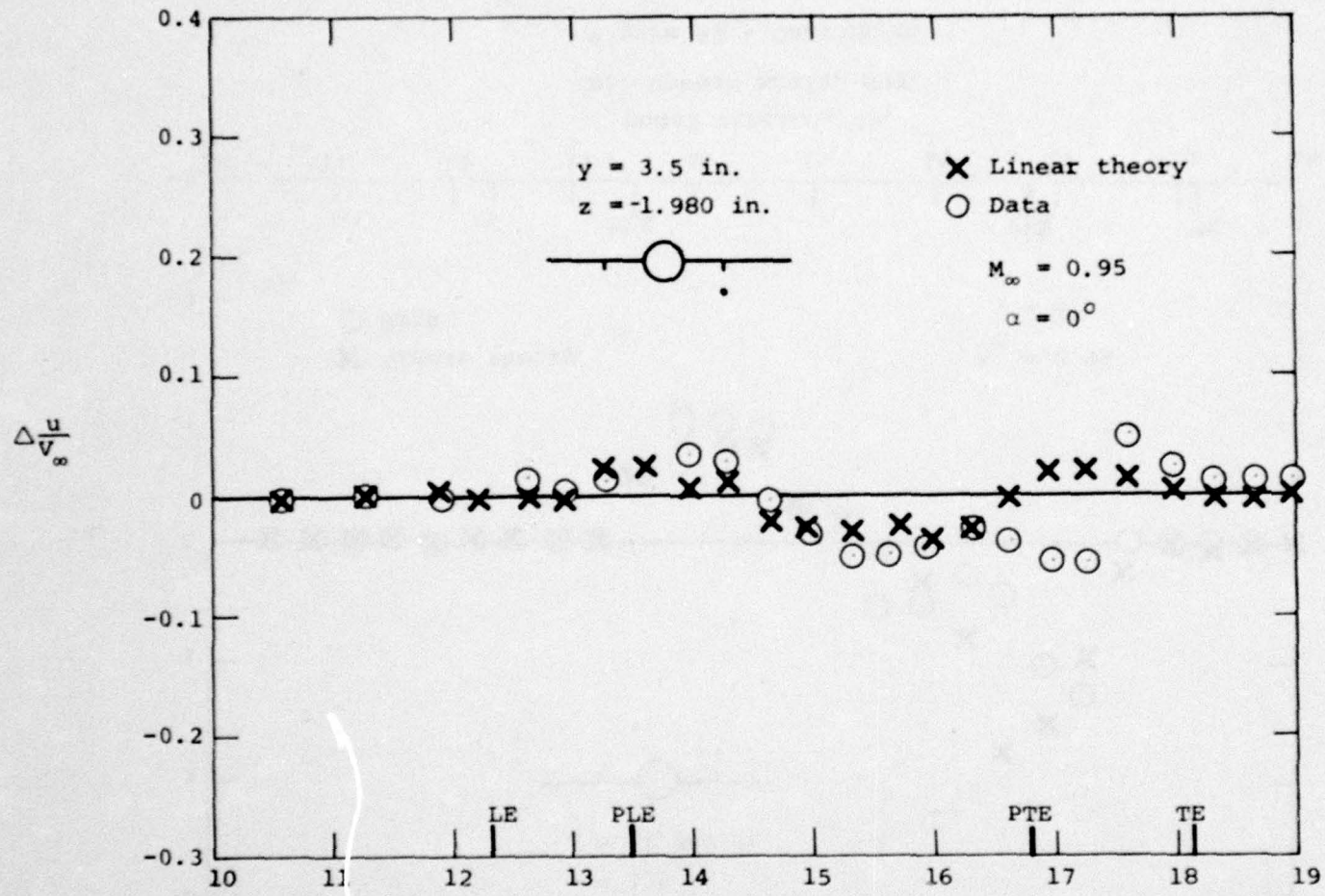

(a) Axial velocity ratio.

Figure 65.- Comparison of measured and theoretical differences between wing-body-pylon and wing-body flow field quantities, $\alpha = 0^\circ$, $M_\infty = 0.95$, y = 3.5 in., z = -1.980 in.

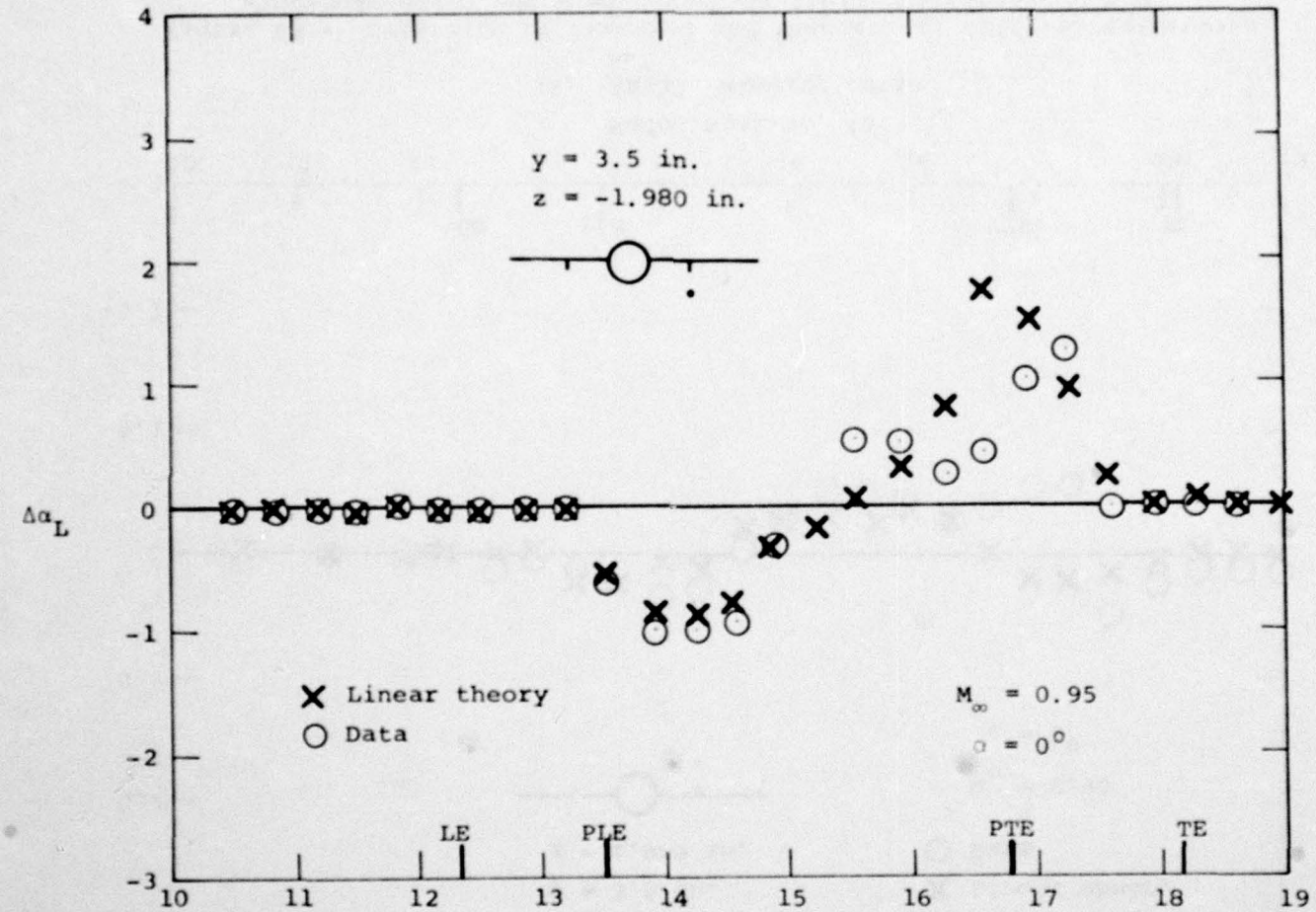

(b) Upwash angle, deg.

Figure 65.- Continued.

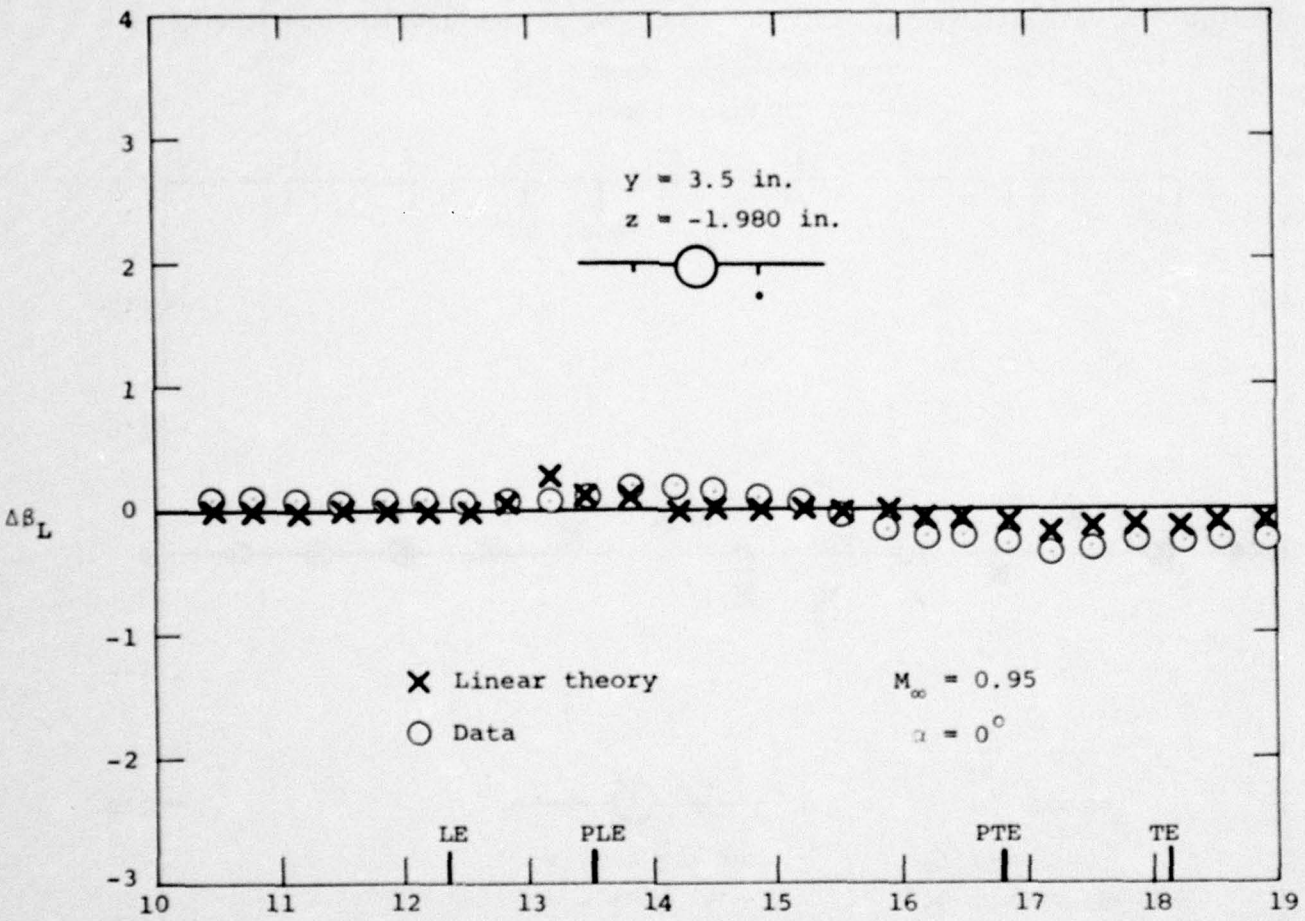

(c) Sidewash angle, deg.

Figure 65.- Concluded.

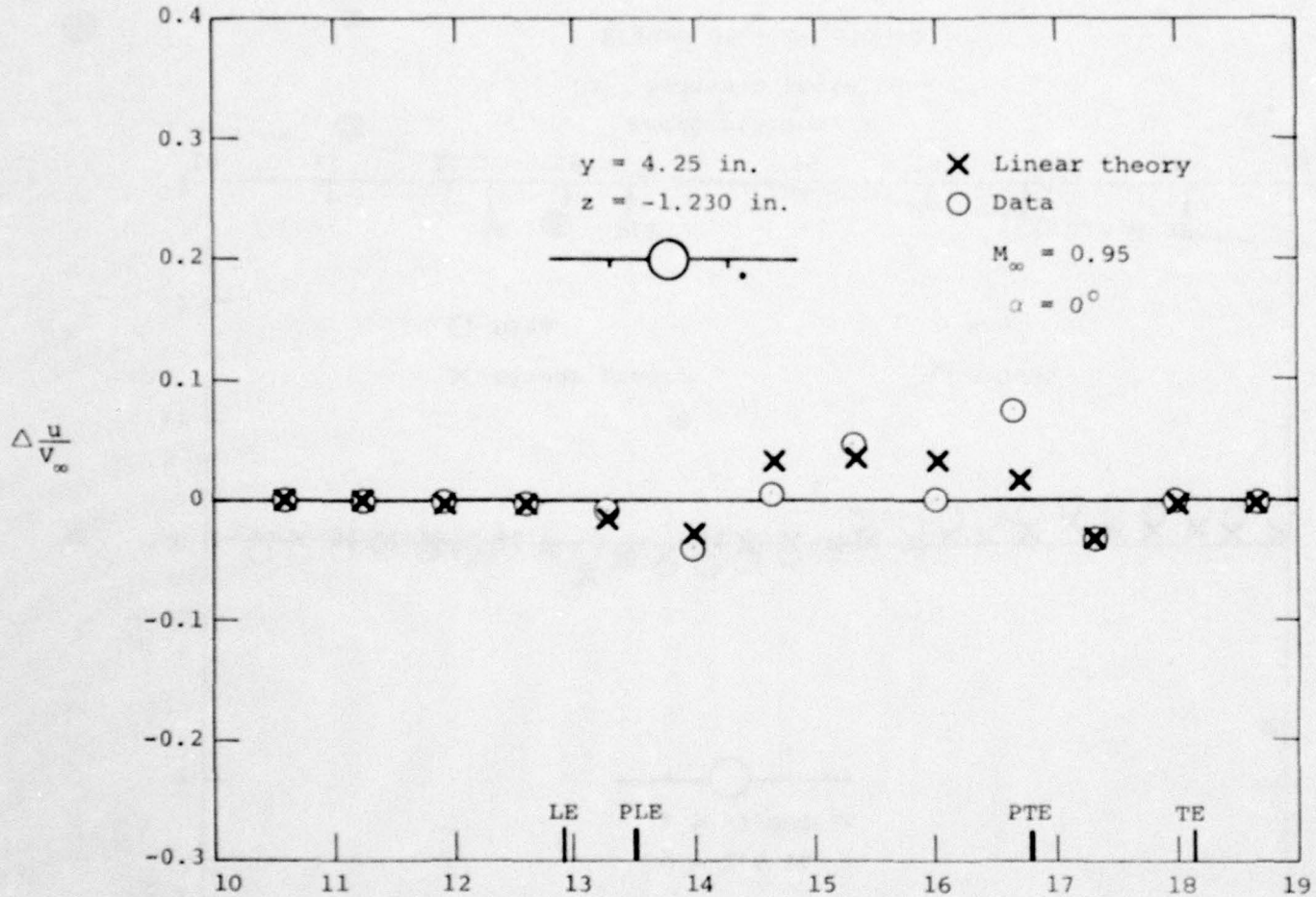

(a) Axial velocity ratio.

Figure 66.- Comparison of measured and theoretical differences between wing-body-pylon and wing-body flow field quantities, α = 0°, M_∞ = 0.95, y = 4.25 in., z = -1.230 in.

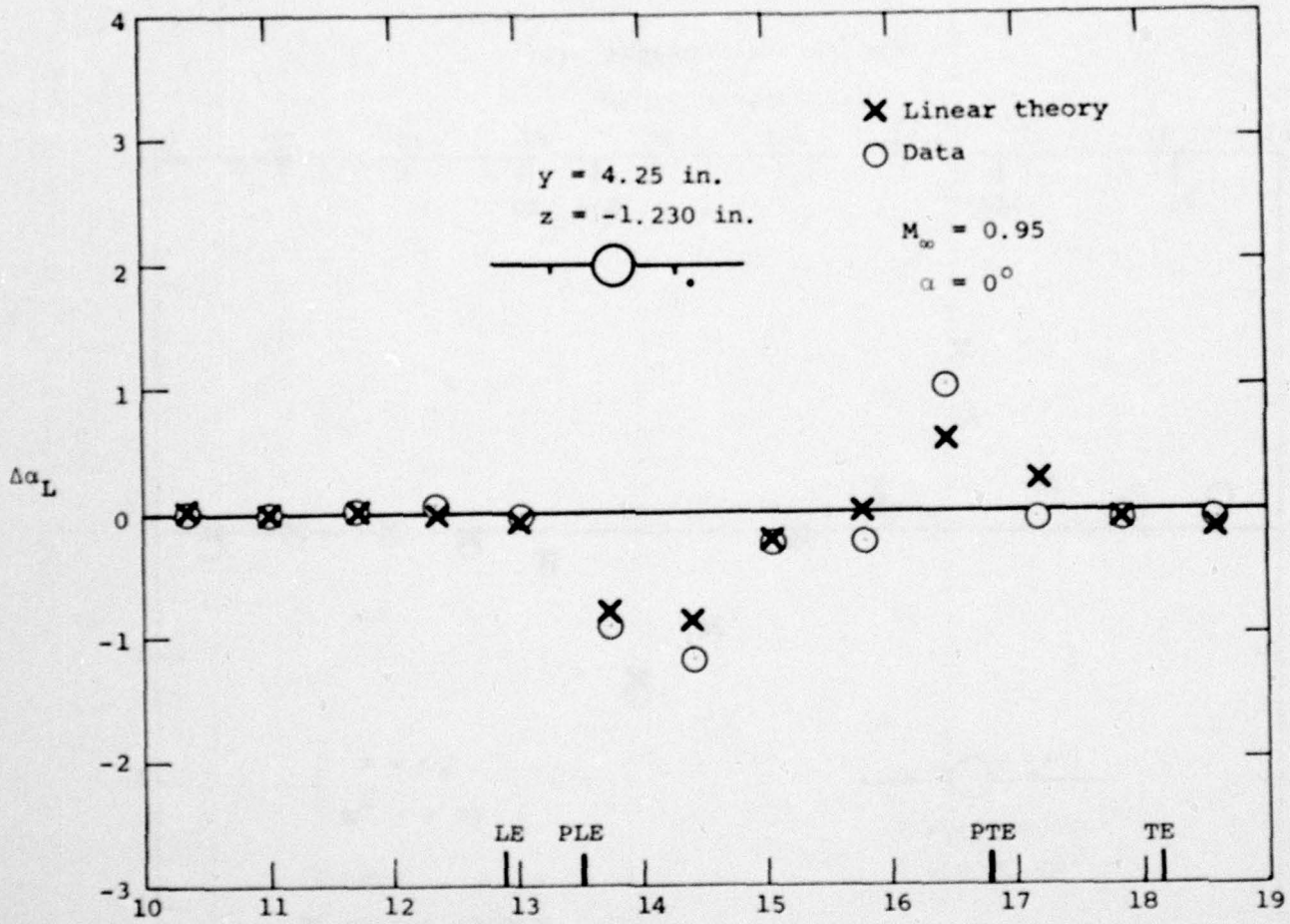

(b) Upwash angle, deg.

Figure 66.- Continued.

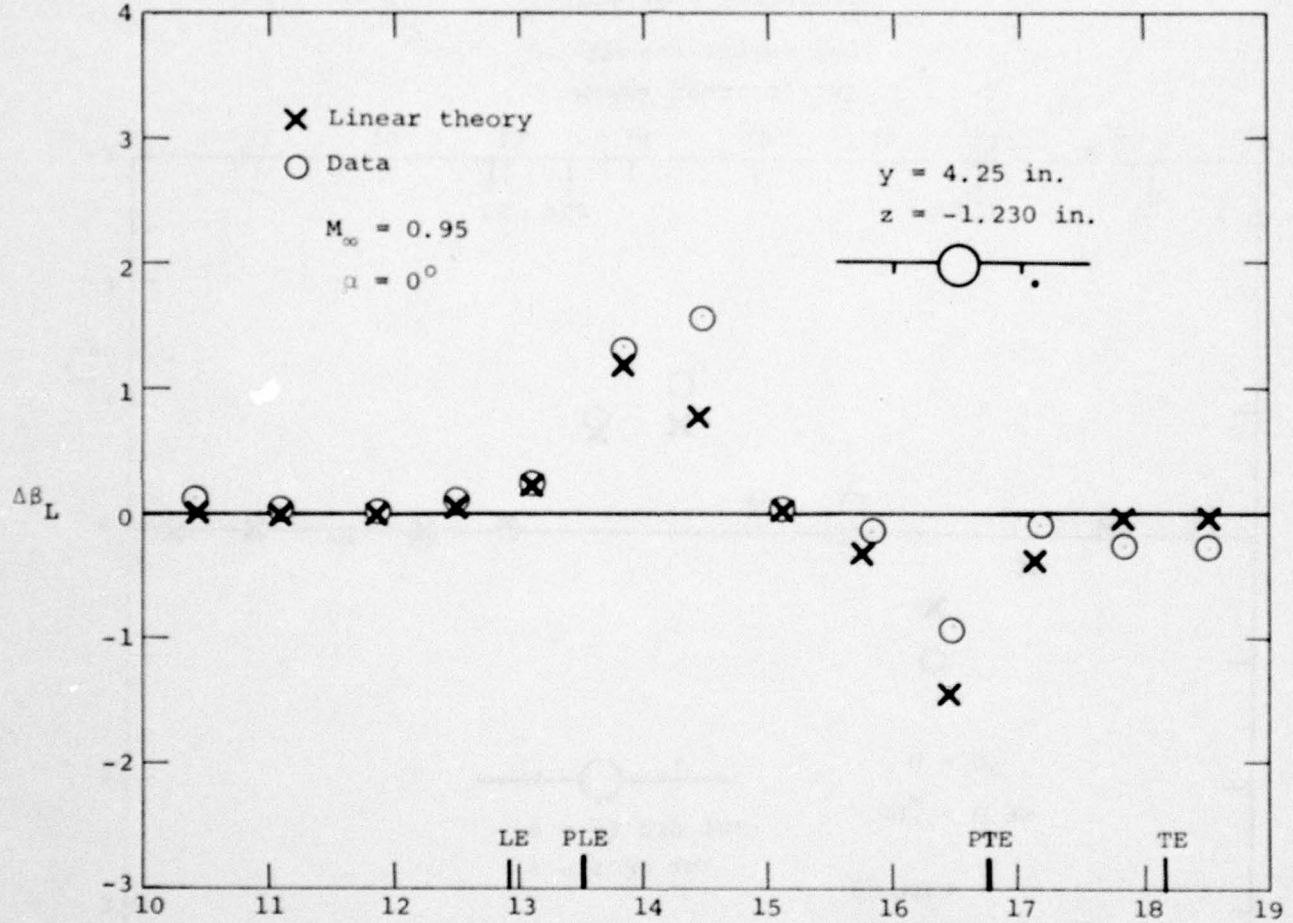

(c) Sidewash angle, deg.

Figure 66.- Concluded.

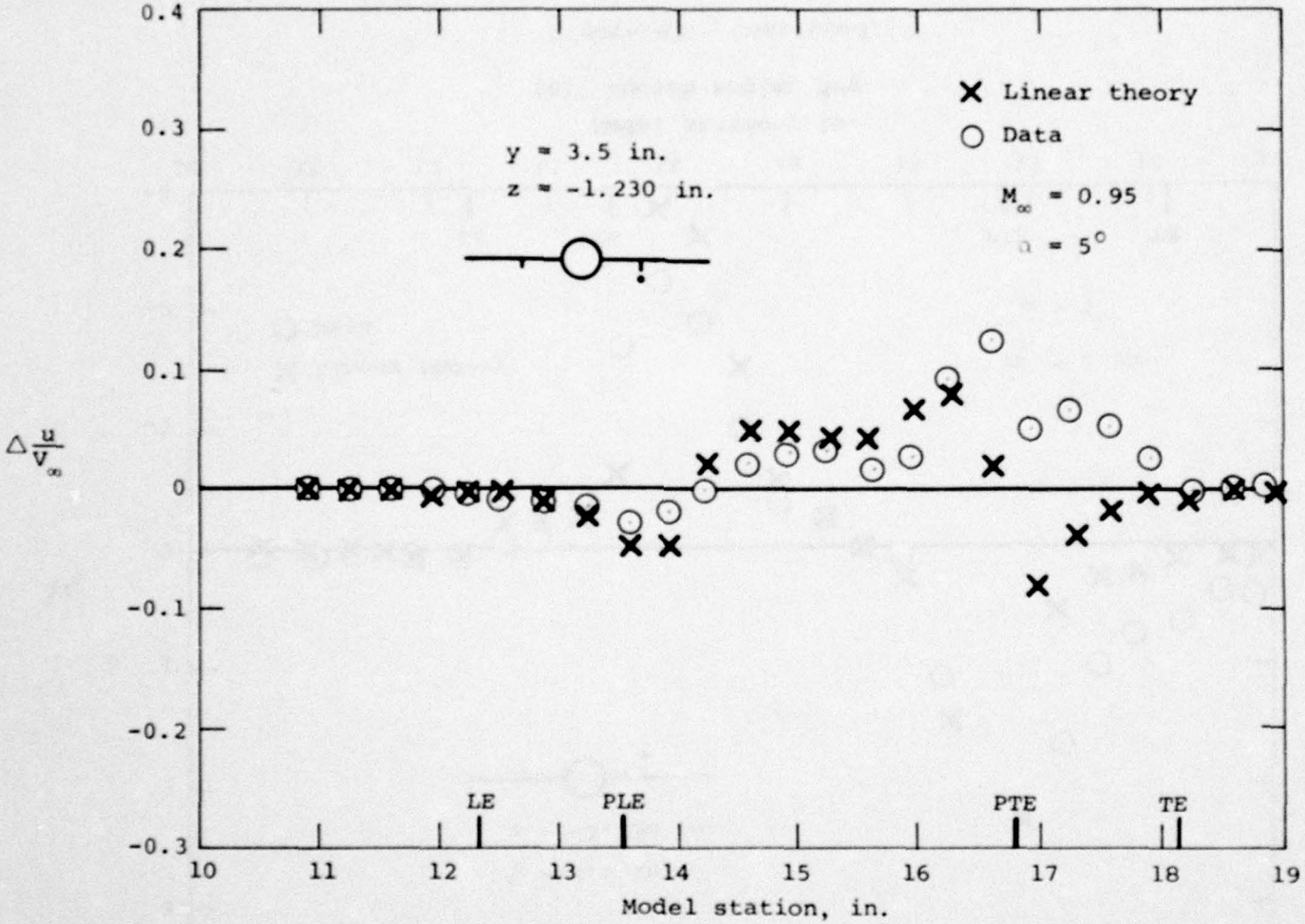

(a) Axial velocity ratio.

Figure 67.- Comparison of measured and theoretical differences between wing-body-pylon and wing-body flow field quantities, $\alpha = 5^\circ$, $M_\infty = 0.95$, y = 3.5 in., z = -1.230 in.

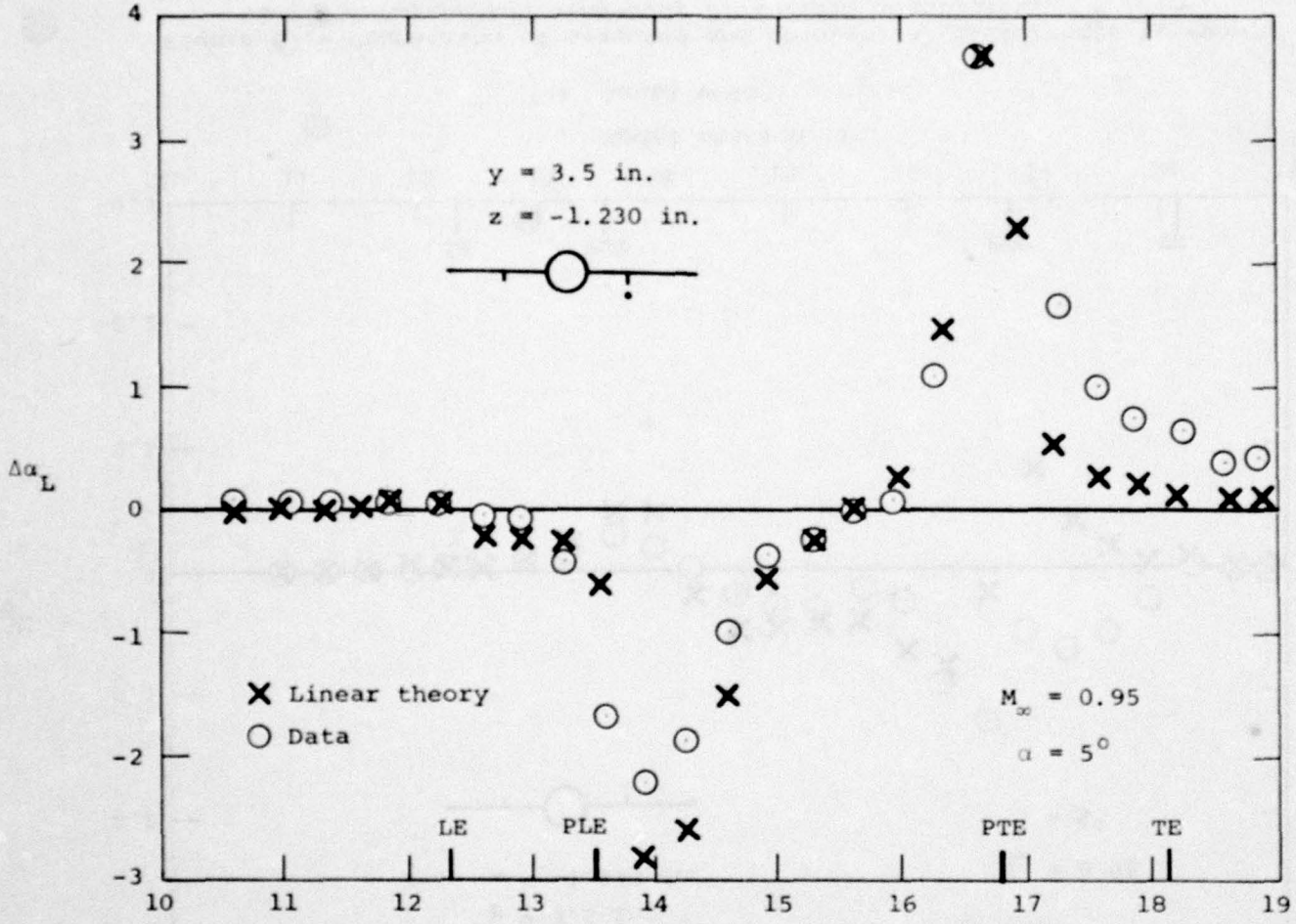

(b) Upwash angle, deg.

Figure 67.- Continued.

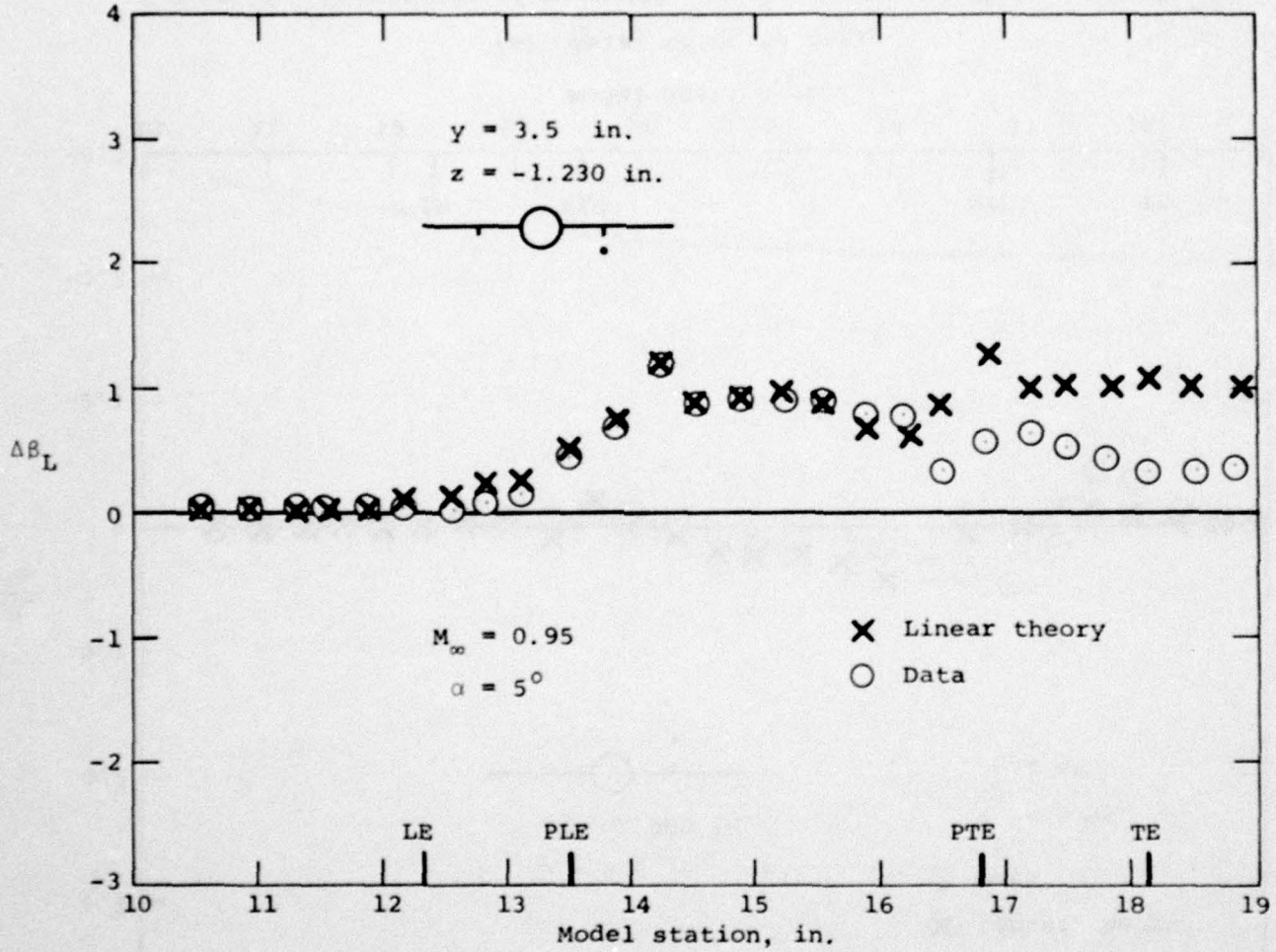

(c) Sidewash angle, deg.

Figure 67.- Concluded.

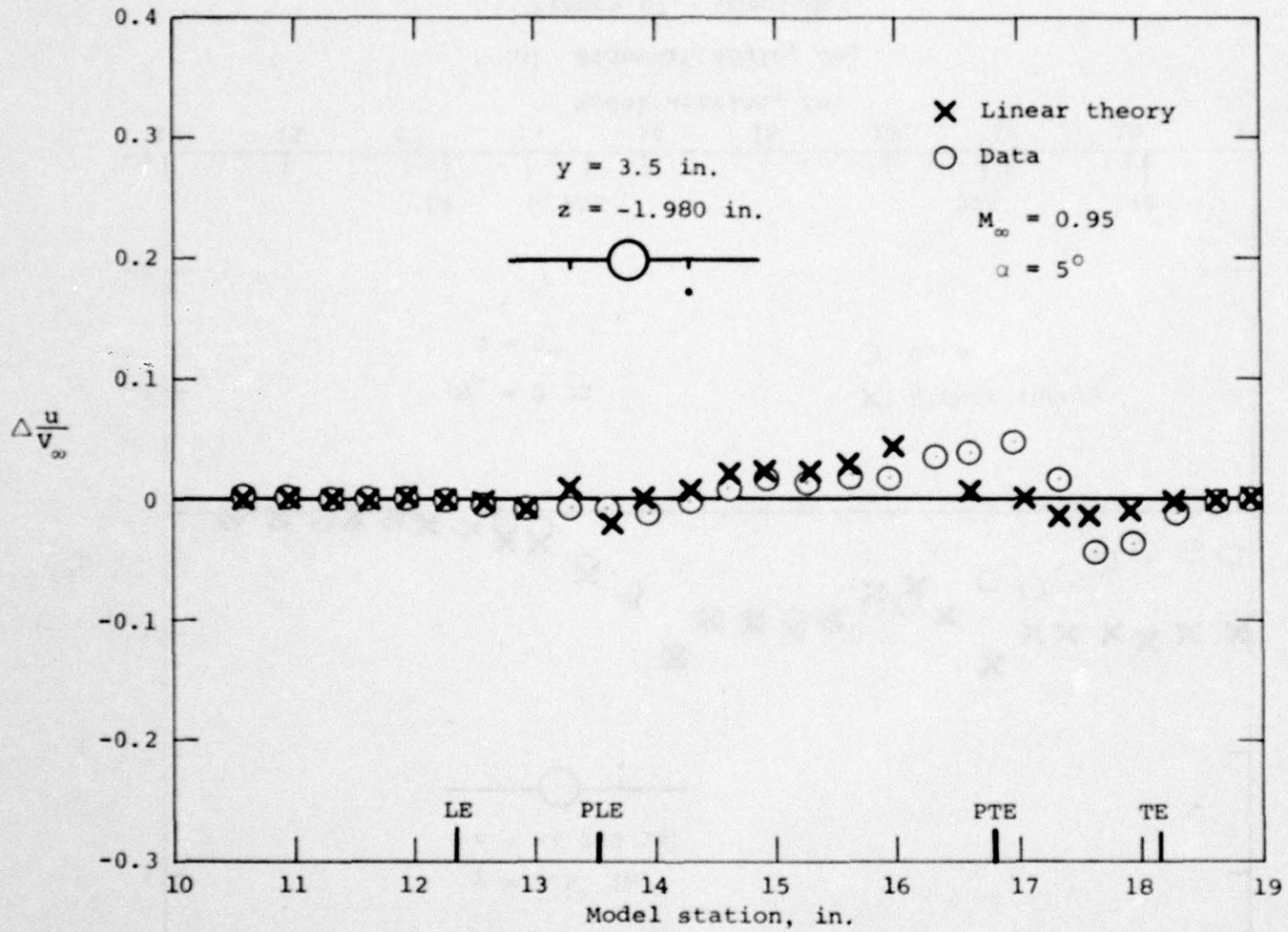

(a) Axial velocity ratio.

Figure 68.- Comparison of measured and theoretical differences between wing-body-pylon and wing-body flow field quantities, $\alpha = 5^\circ$, $M_\infty = 0.95$, y = 3.5 in., z = -1.980 in.

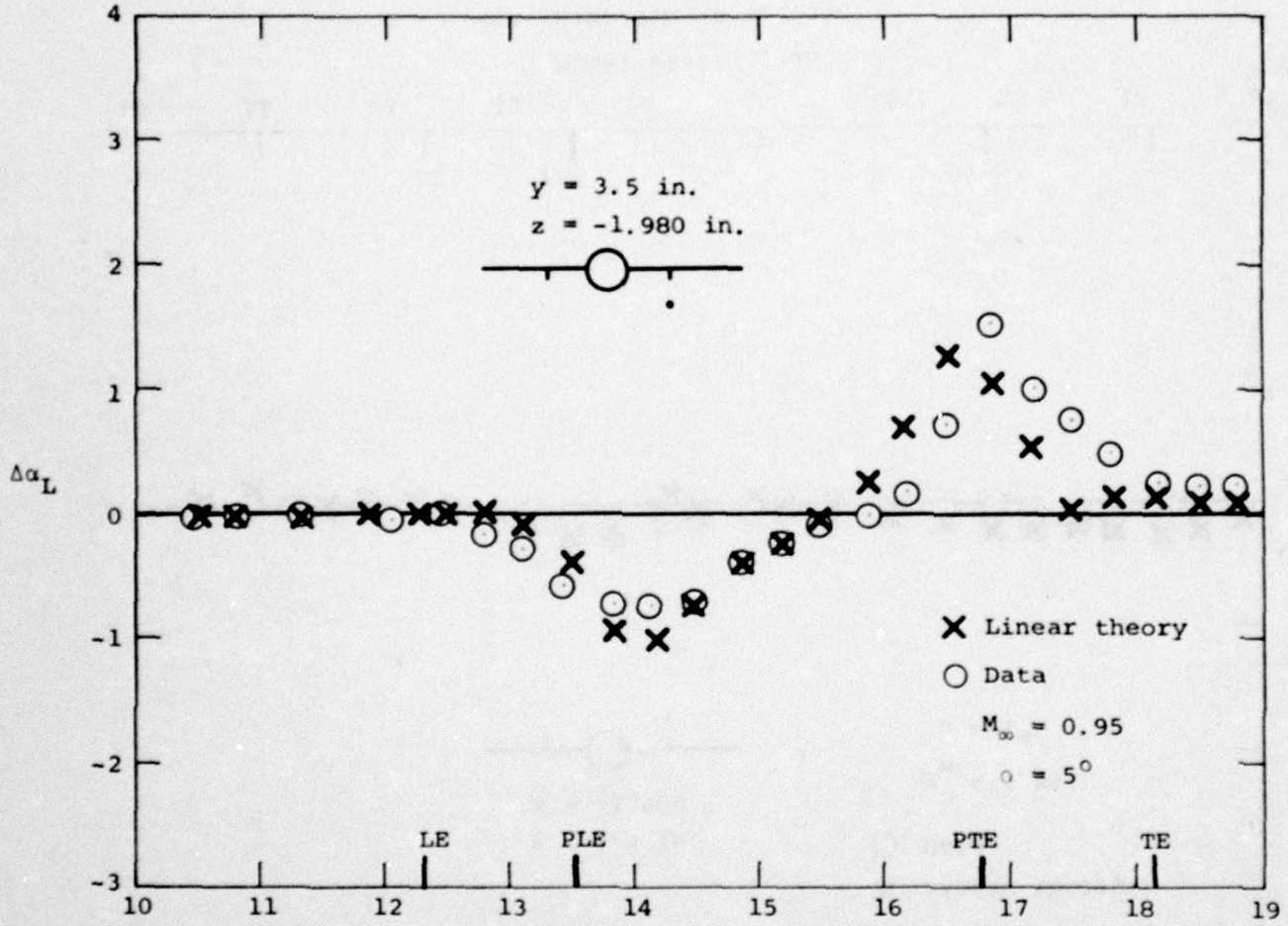

(b) Upwash angle, deg.

Figure 68.- Continued.

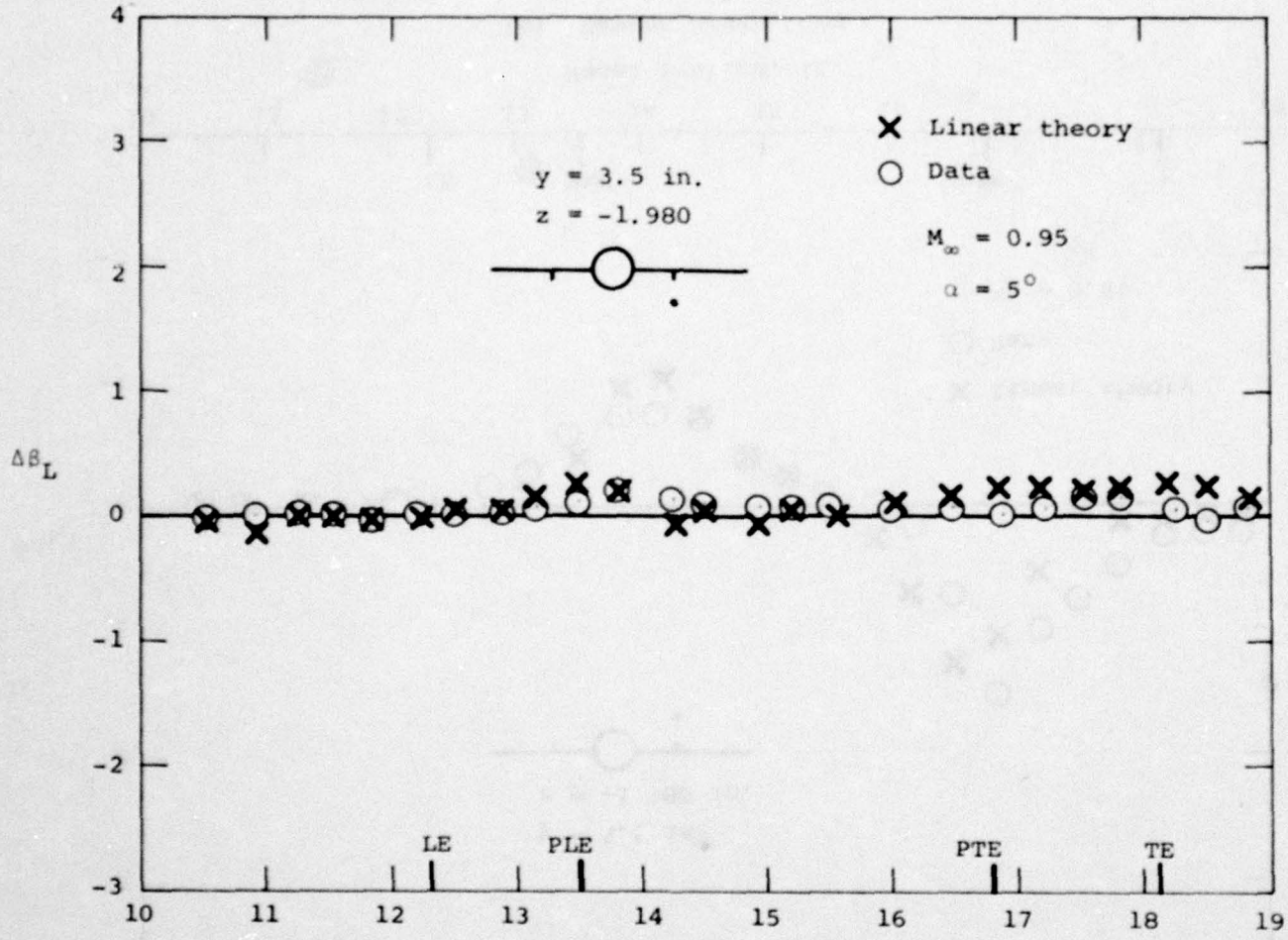

(c) Sidewash angle, deg.

Figure 68.- Concluded.

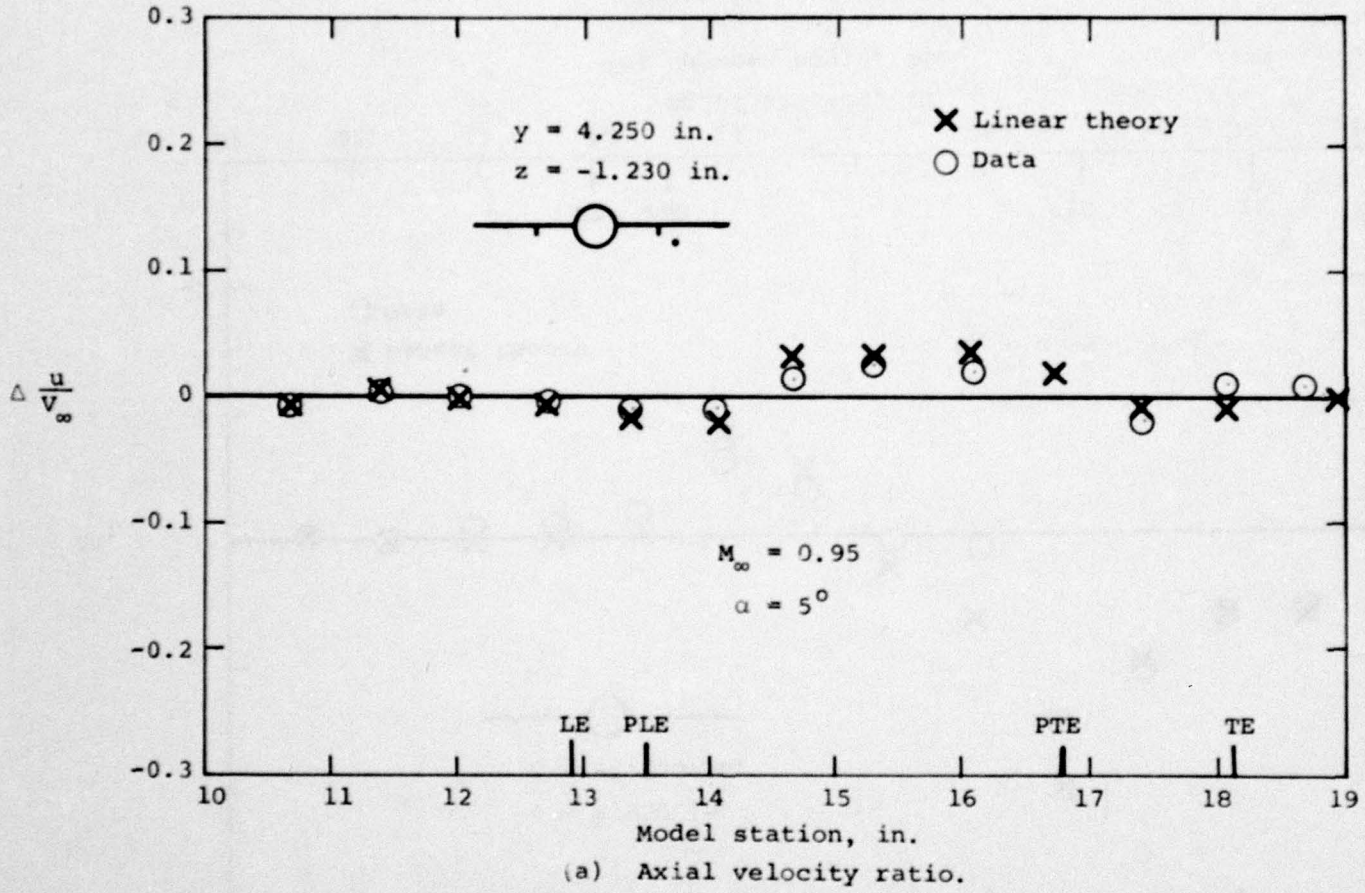

(a) Axial velocity ratio.

Figure 69.- Comparison of measured and theoretical differences between wing-body-pylon and wing-body flow field quantities, $\alpha = 5^\circ$, $M_\infty = 0.95$, y = 4.250 in., z = -1.230 in.

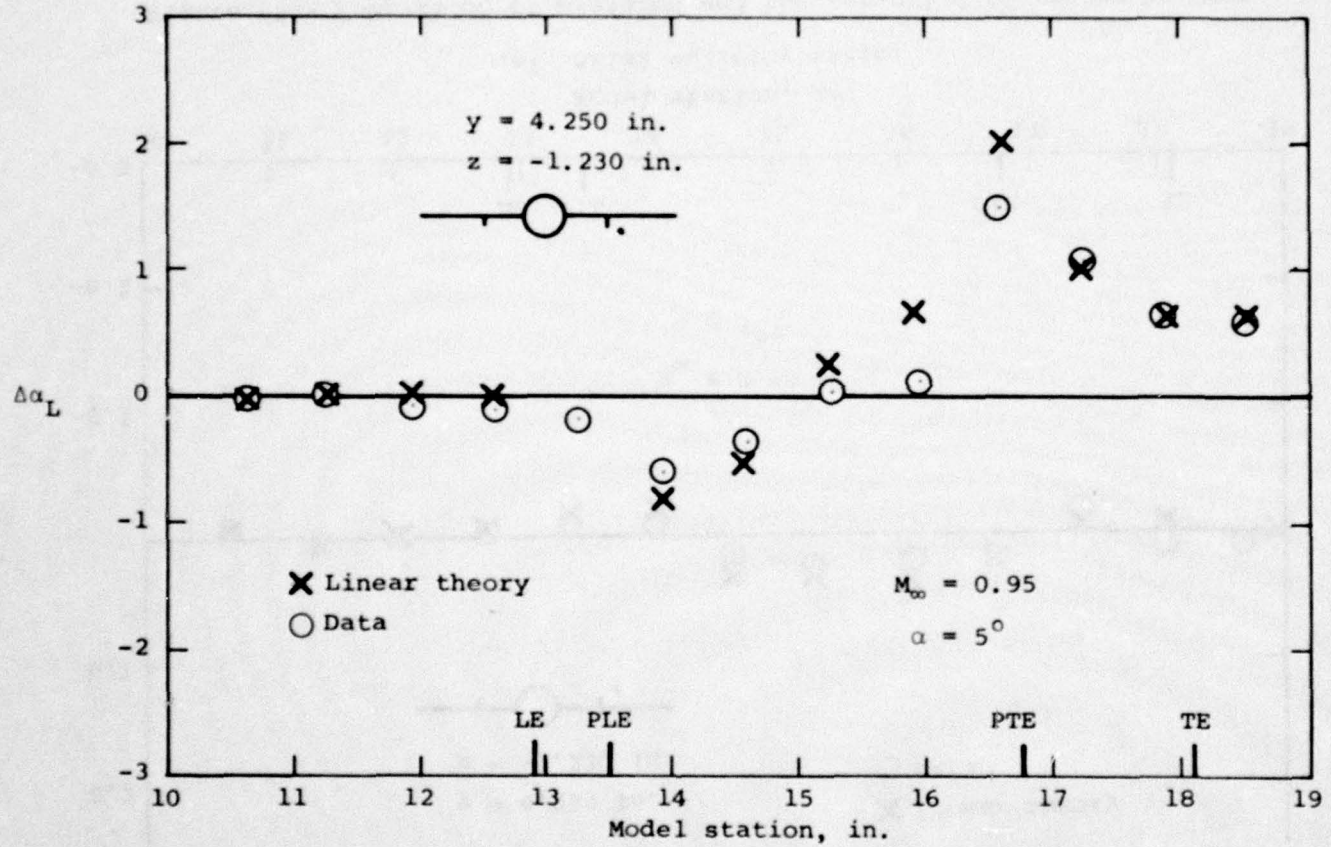

(b) Upwash angle, deg.

Figure 69.- Continued.

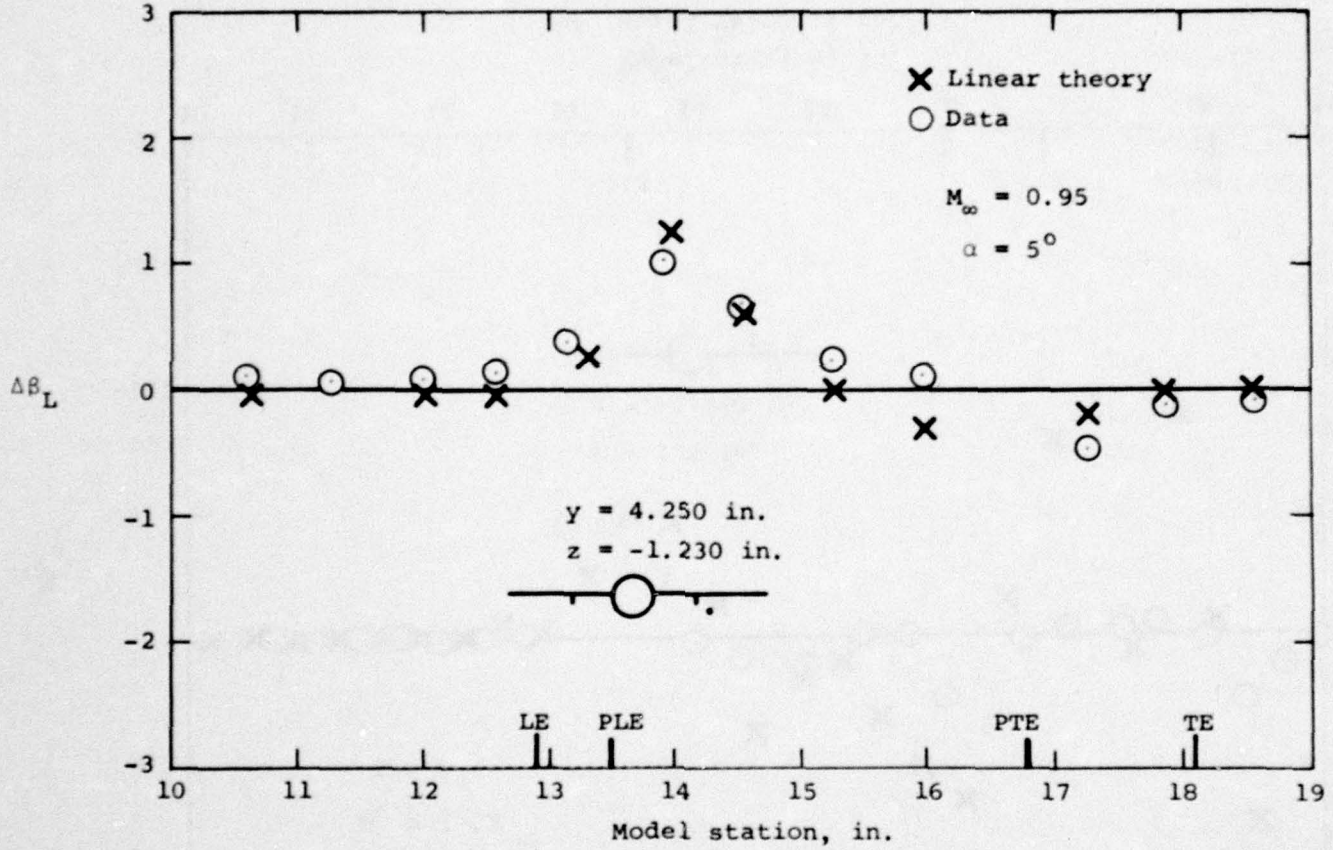

(c) Sidewash angle, deg.

Figure 69.- Concluded.

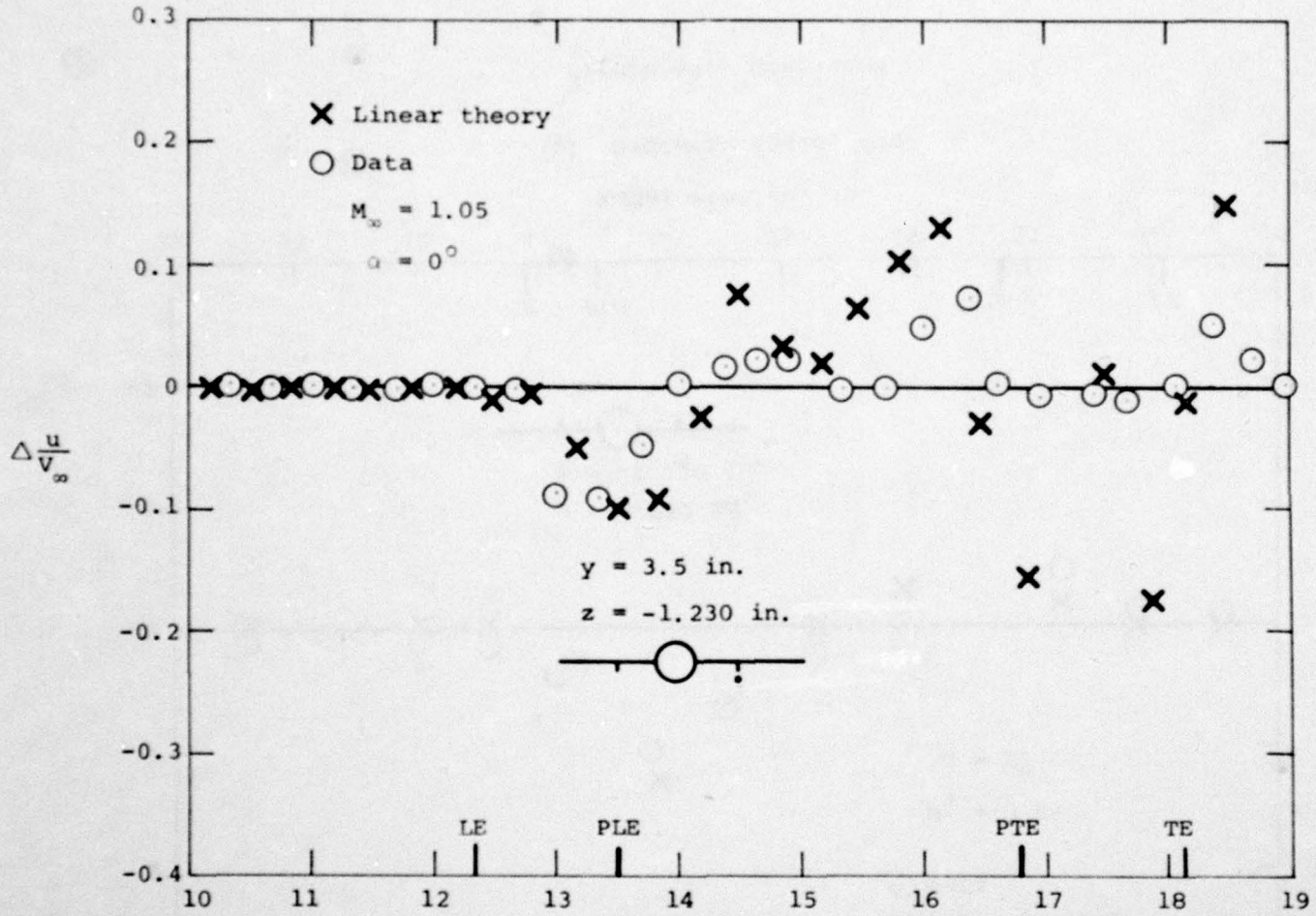

(a) Axial velocity ratio.

Figure 70.- Comparison of measured and theoretical differences between wing-body-pylon and wing-body flow field quantities, $\alpha = 0°$, $M_\infty = 1.05$, y = 3.5 in., z = -1.230 in.

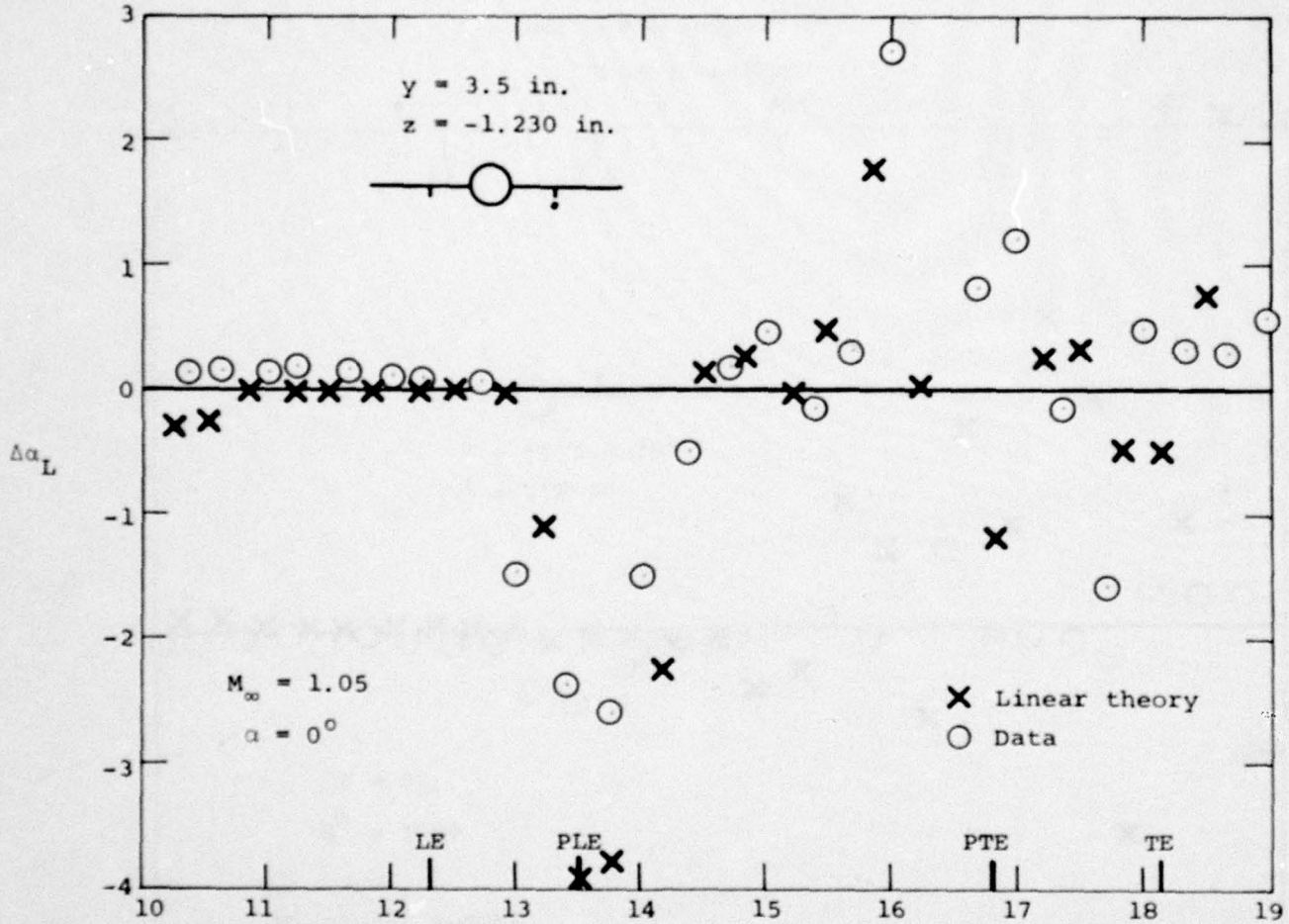

(b) Upwash angle, deg.

Figure 70.- Continued.

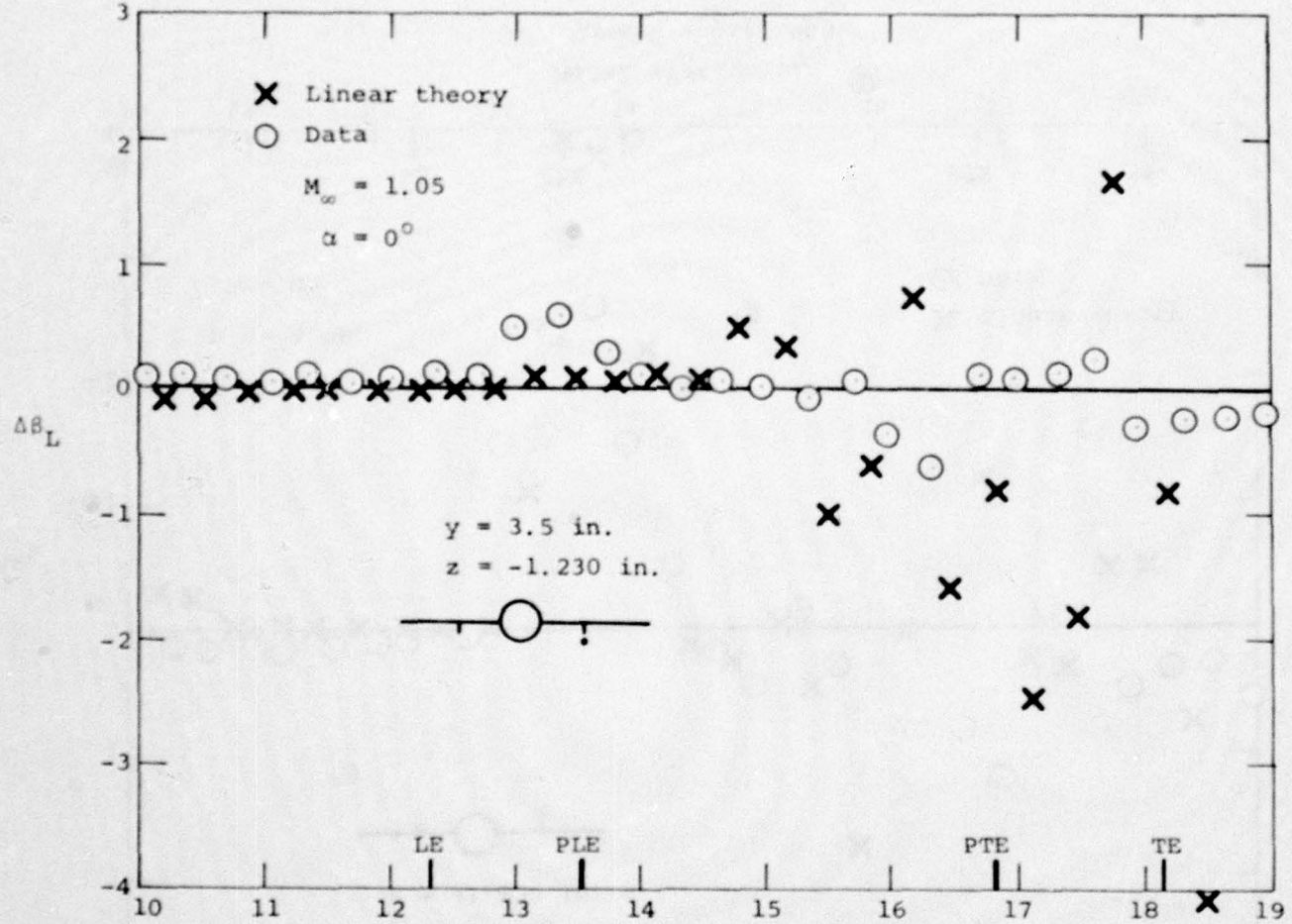

(c) Sidewash angle, deg.

Figure 70.- Concluded.

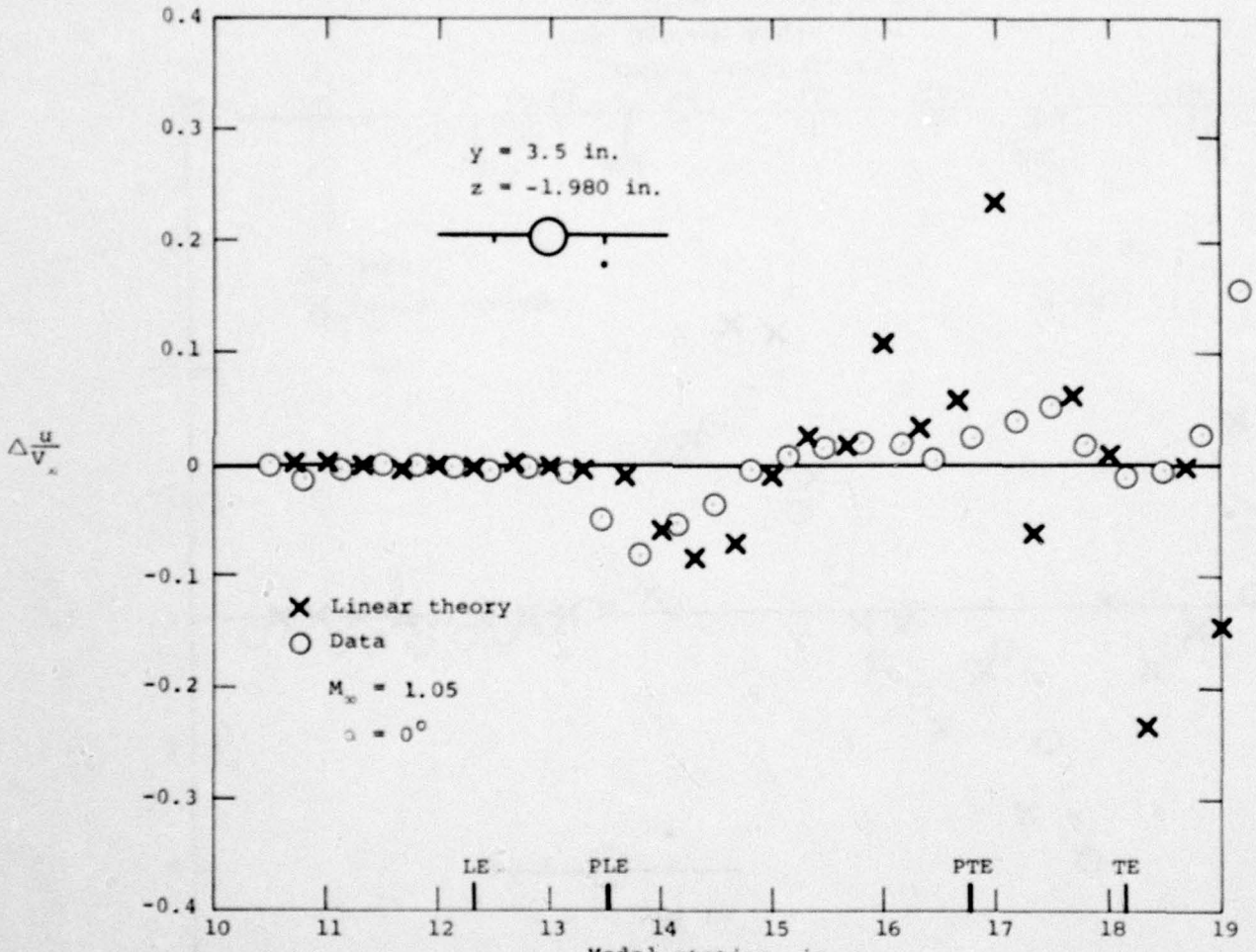

(a) Axial velocity ratio.

Figure 71.- Comparison of measured and theoretical differences between wing-body-pylon and wing-body flow field quantities, α = 0°, M_∞ = 1.05, y = 3.5 in., z = -1.980 in.

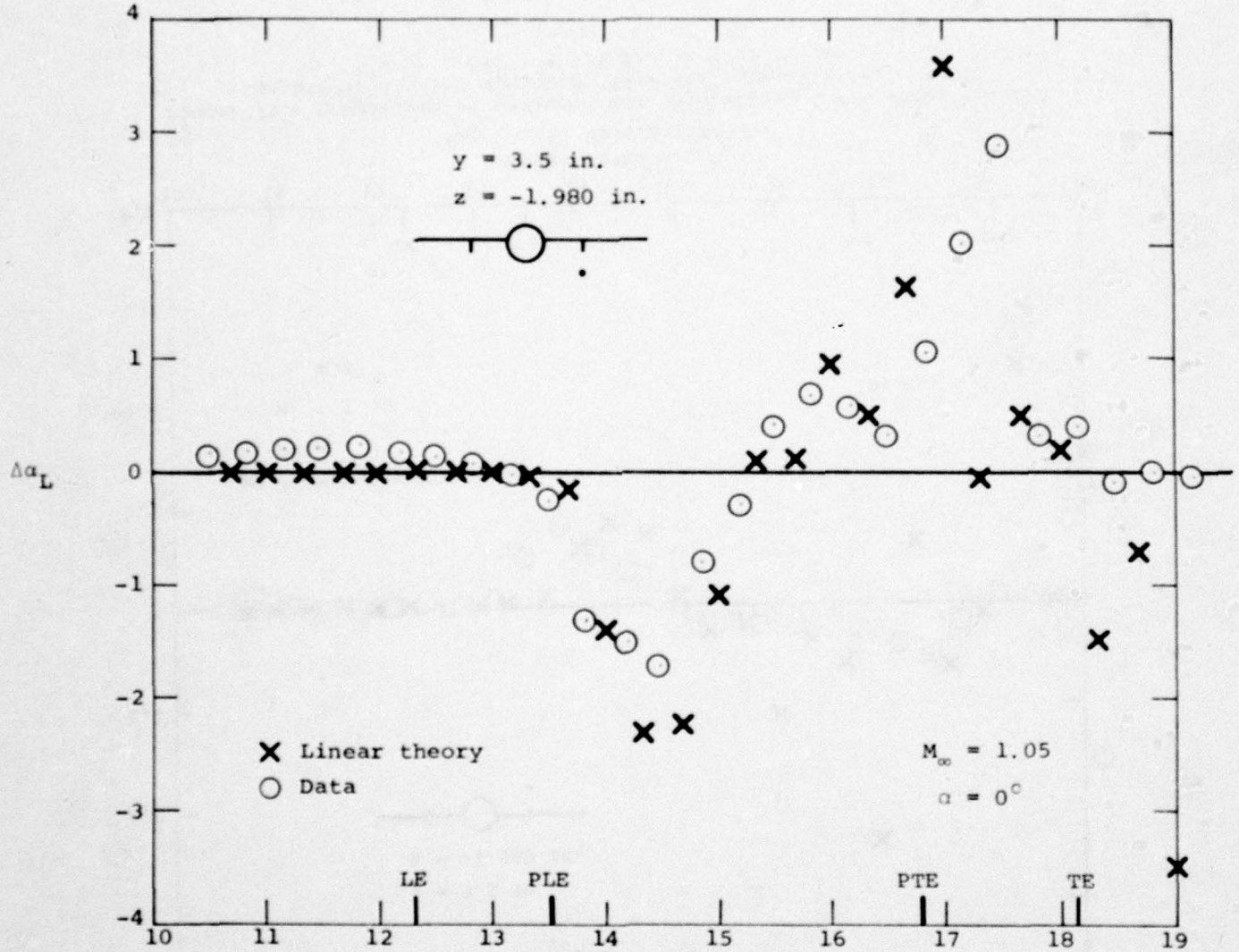

(b) Upwash angle, deg.

Figure 71.- Continued.

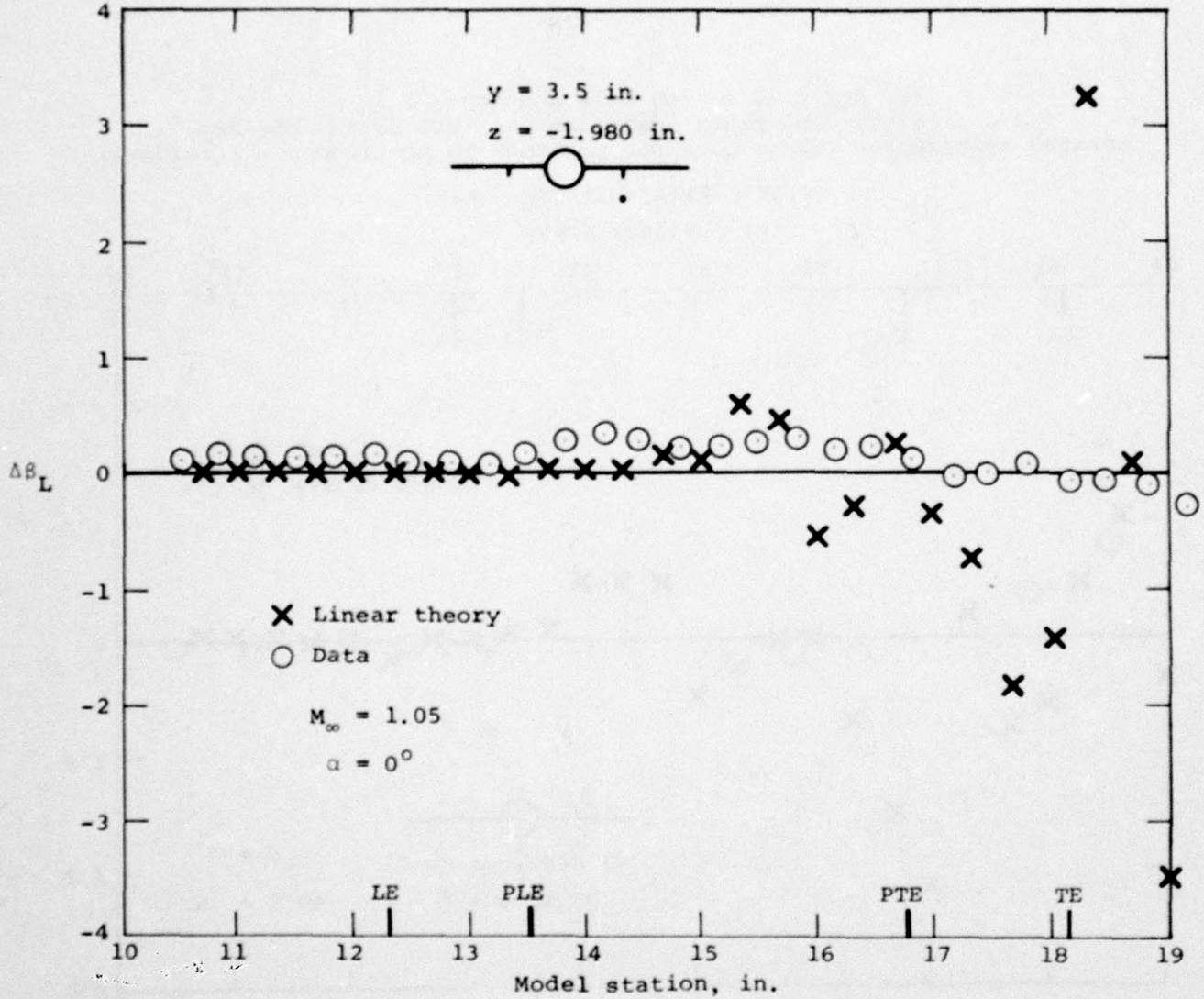

(c) Sidewash angle, deg.

Figure 71.- Concluded.

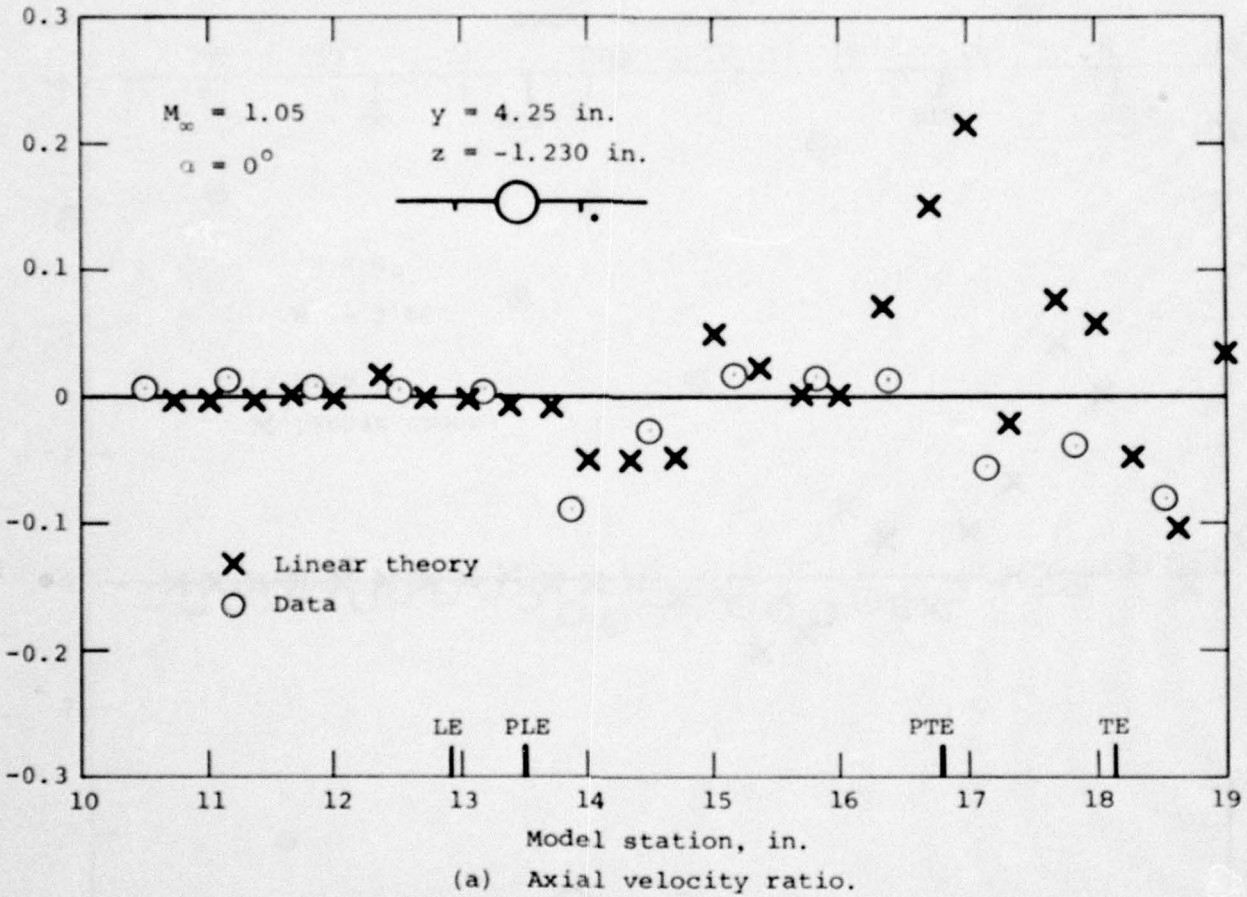

(a) Axial velocity ratio.

Figure 72.- Comparison of measured and theoretical differences between wing-body-pylon and wing-body flow field quantities, $\alpha = 0°$, $M_\infty = 1.05$, y = 4.25 in., z = -1.230 in.

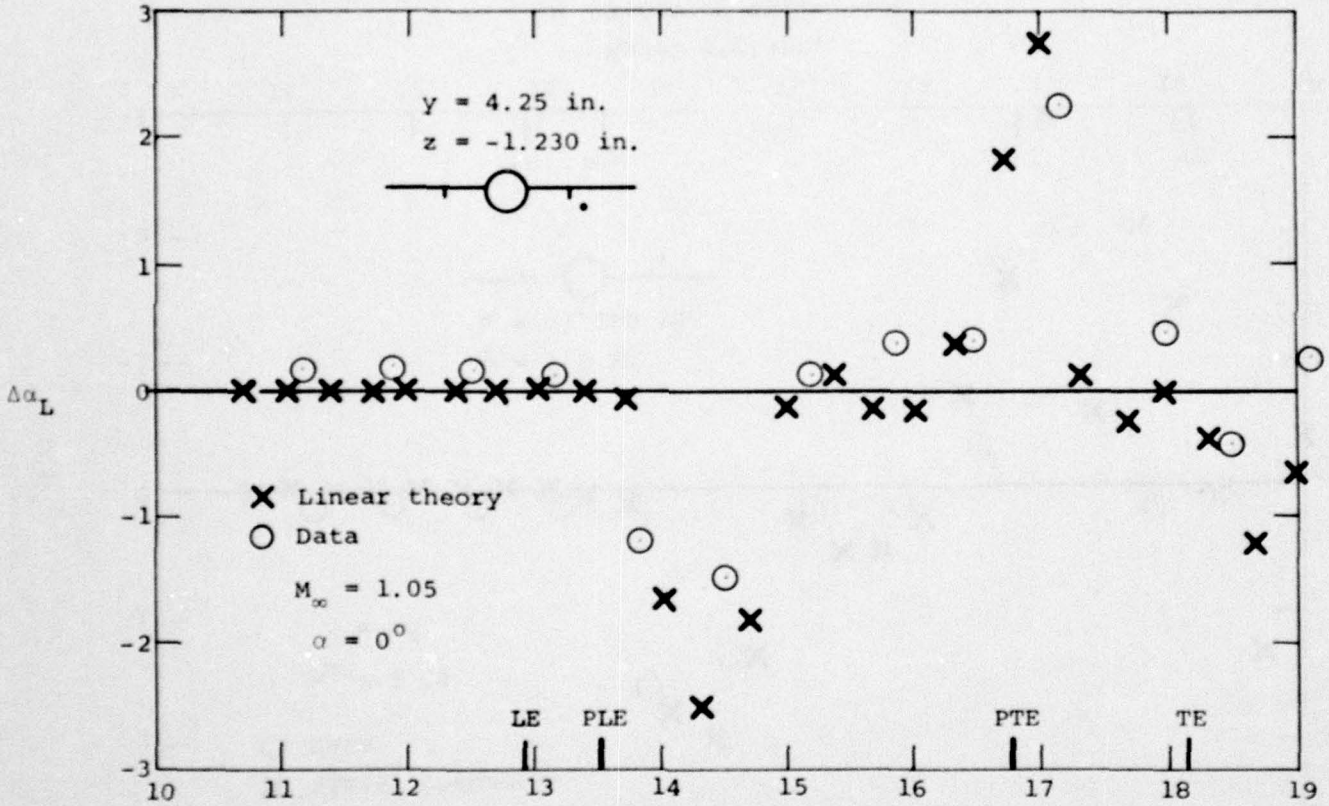

(b) Upwash angle, deg.

Figure 72.- Continued.

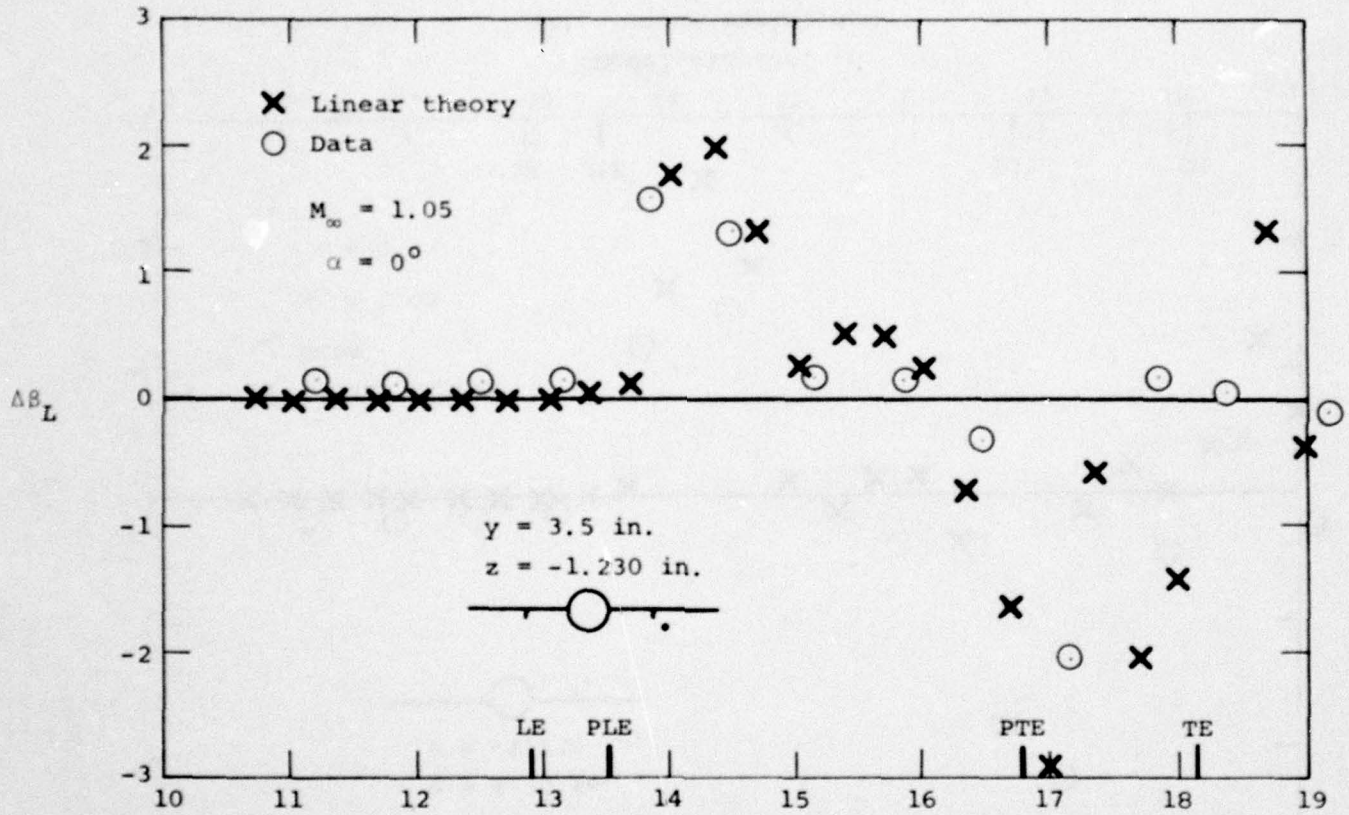

(c) Sidewash angle, deg.

Figure 72.- Concluded.

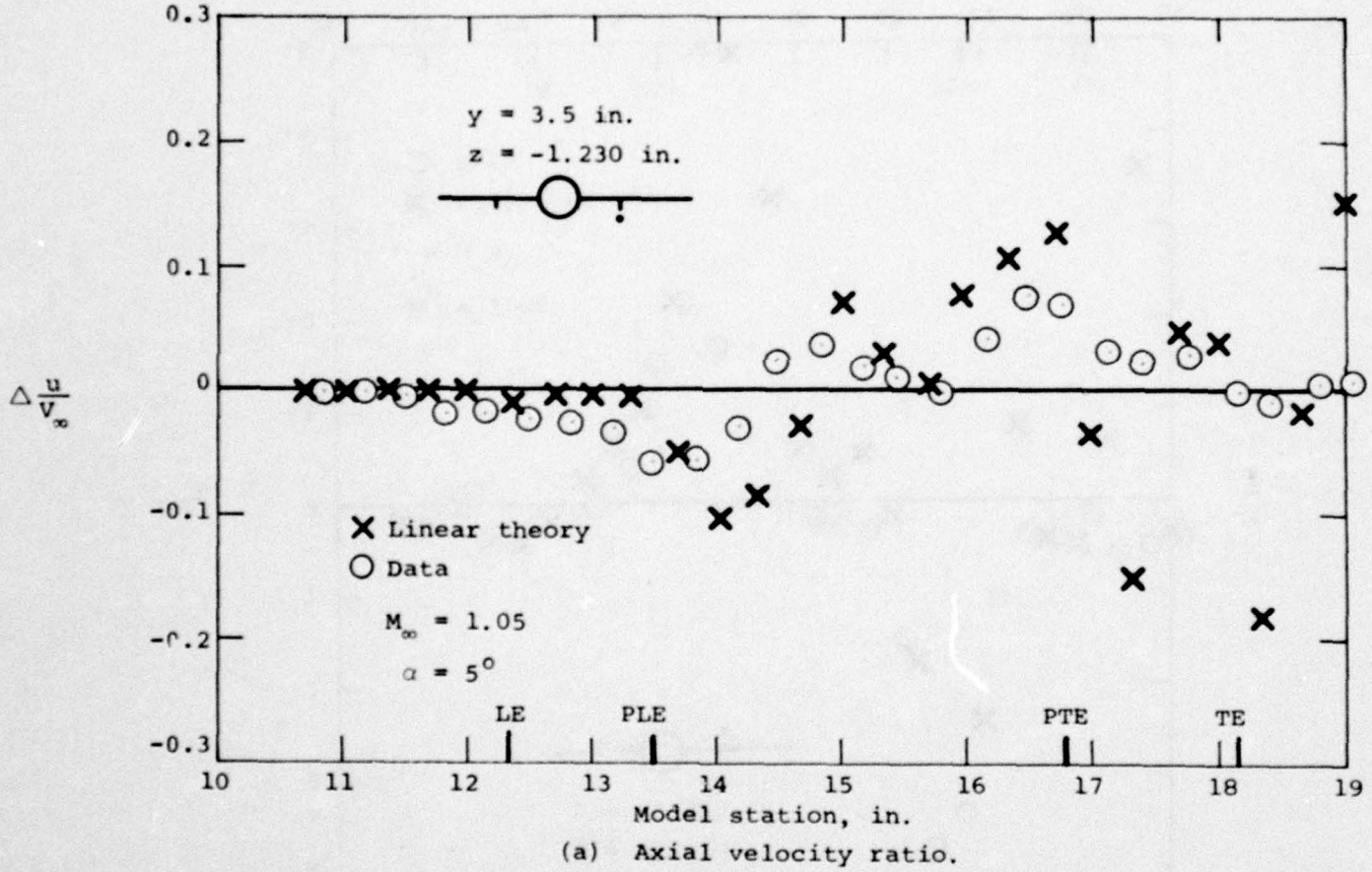

(a) Axial velocity ratio.

Figure 73.- Comparison of measured and theoretical differences between wing-body-pylon and wing-body flow field quantities, $\alpha = 5^\circ$, $M_\infty = 1.05$, y = 3.5 in., z = -1.230 in.

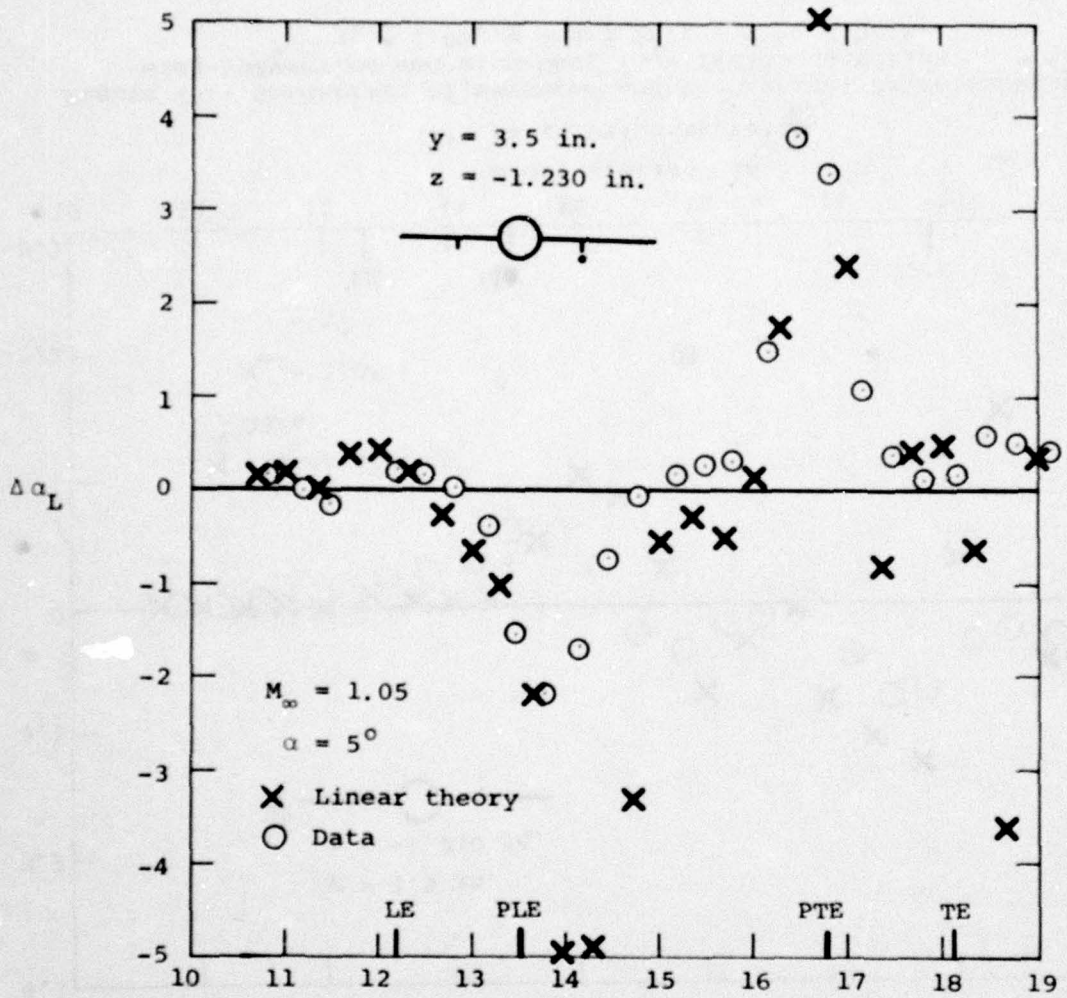

(b) Upwash angle, deg.

Figure 73.- Continued.

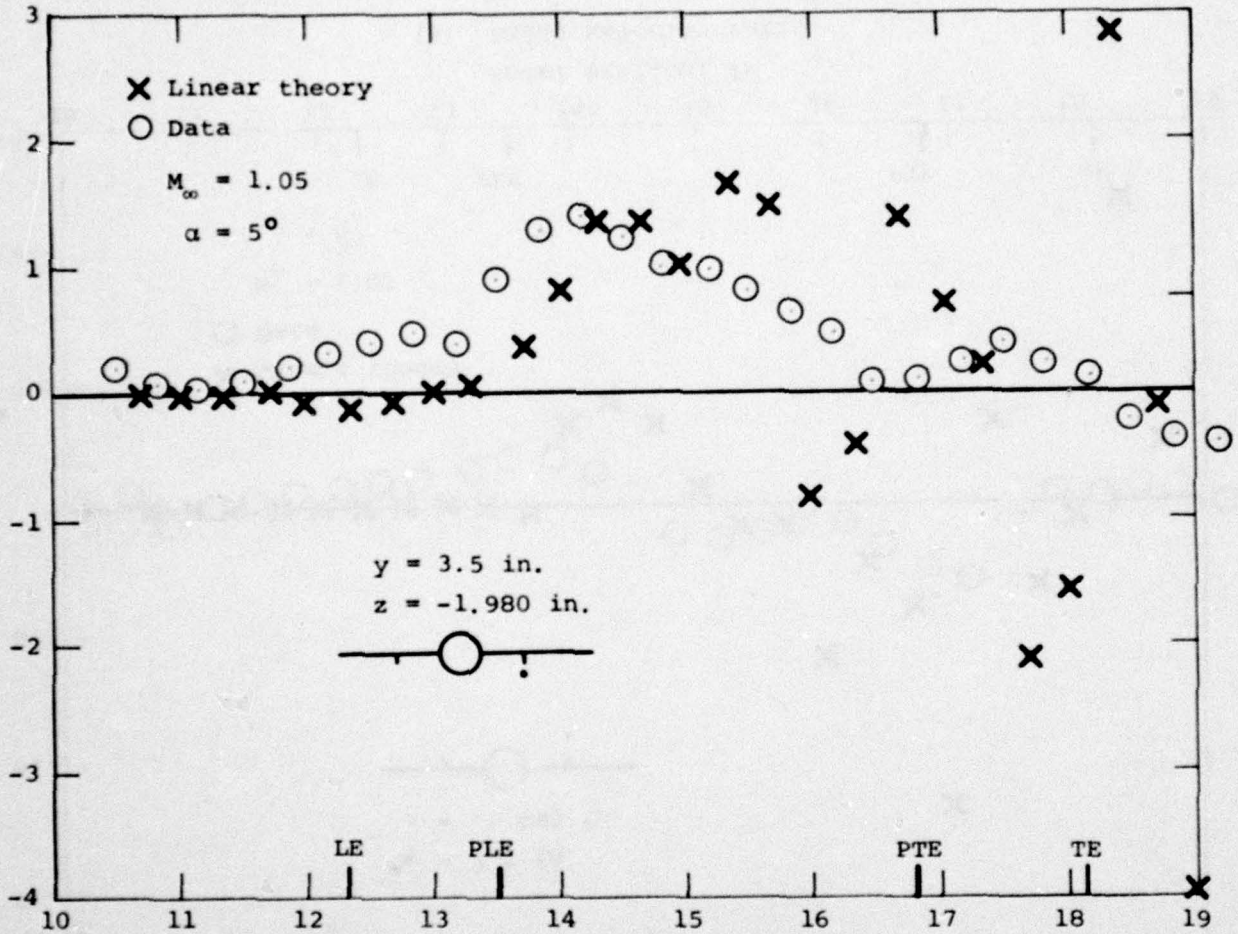

(c) Sidewash angle, deg.

Figure 73.- Concluded.

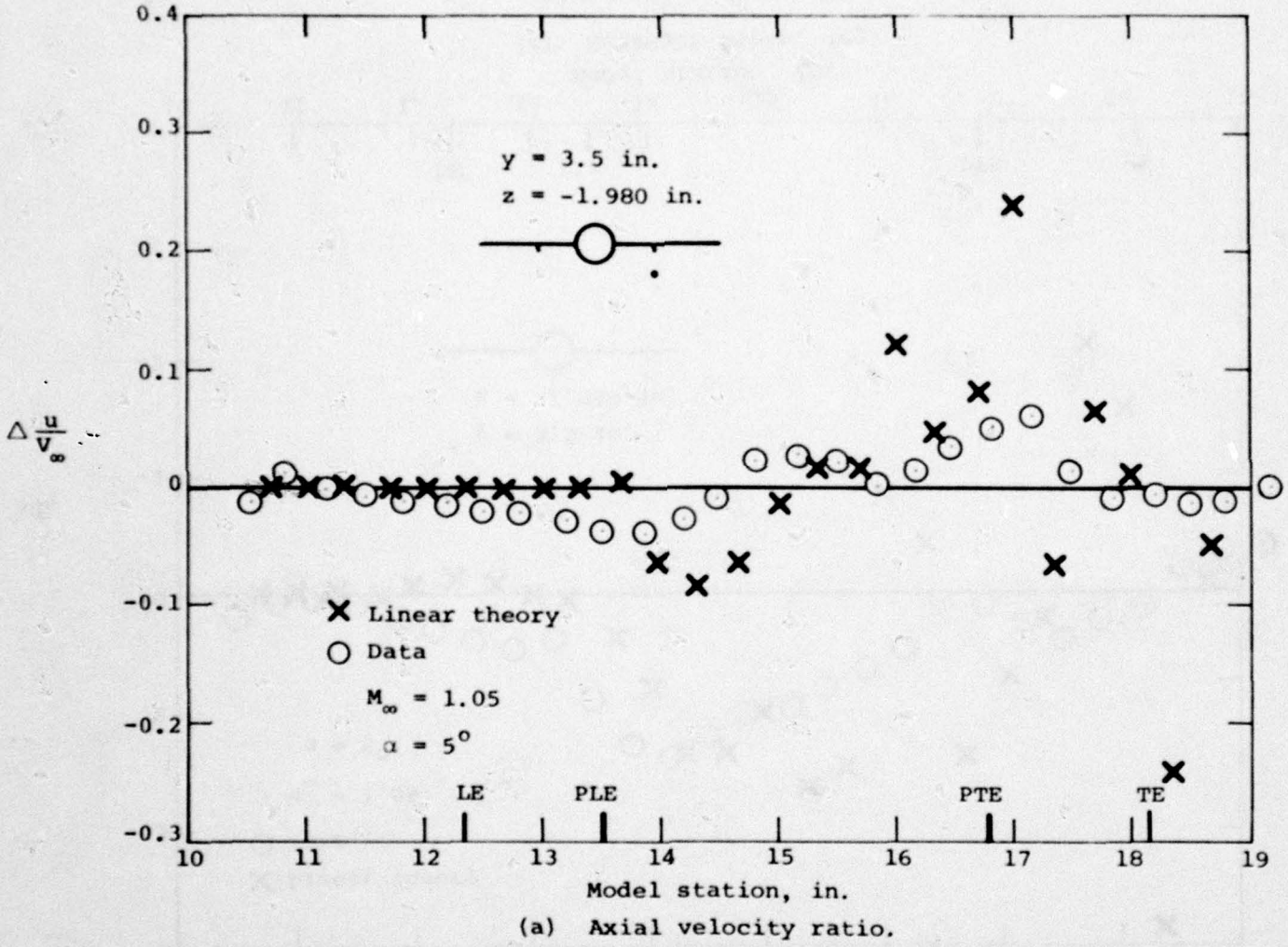

(a) Axial velocity ratio.

Figure 74.- Comparison of measured and theoretical differences between wing-body-pylon and wing-body flow field quantities, $\alpha = 5^\circ$, $M_\infty = 1.05$, y = 3.5 in., z = -1.980 in.

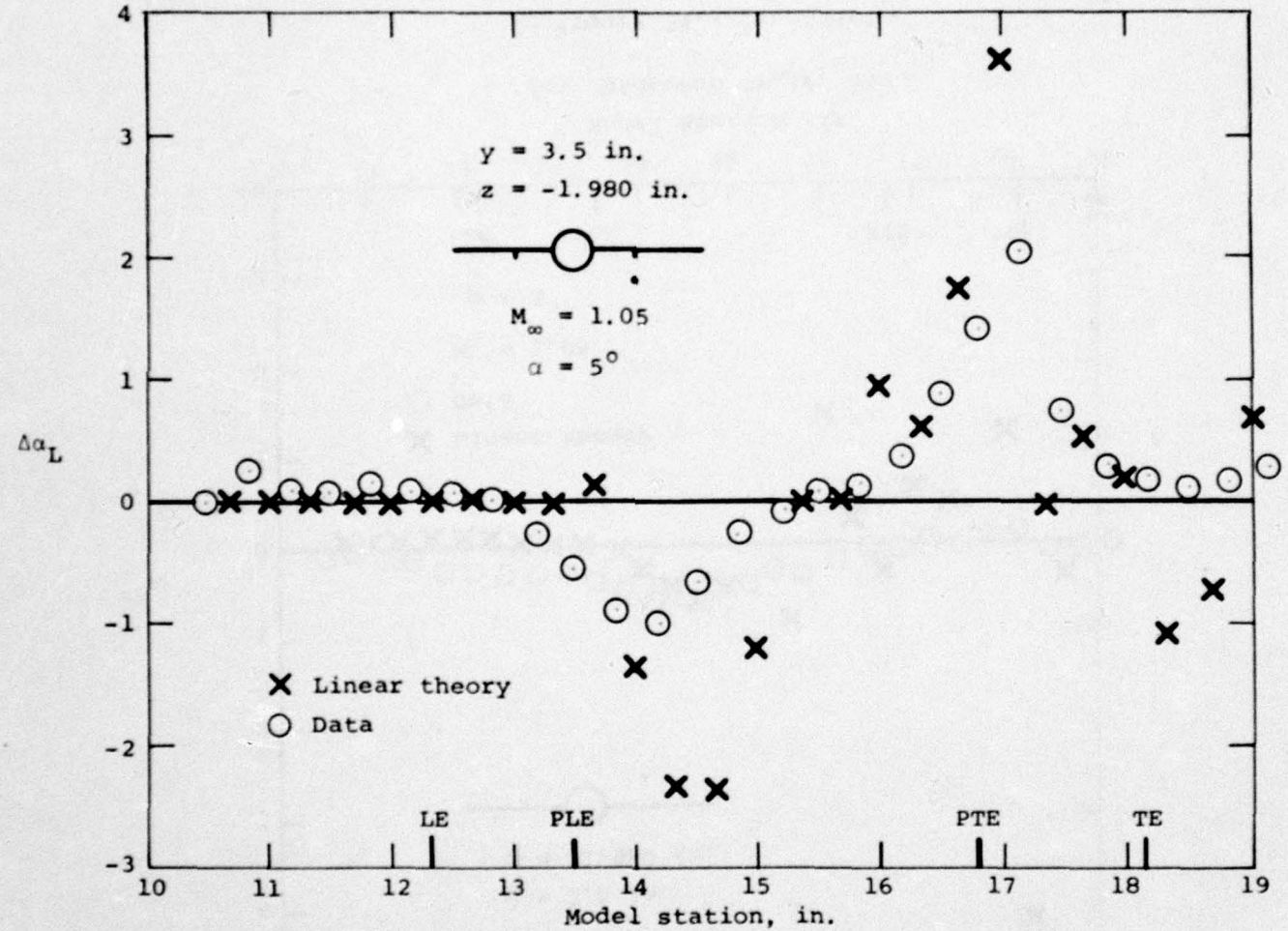

(b) Upwash angle, deg.

Figure 74.- Continued.

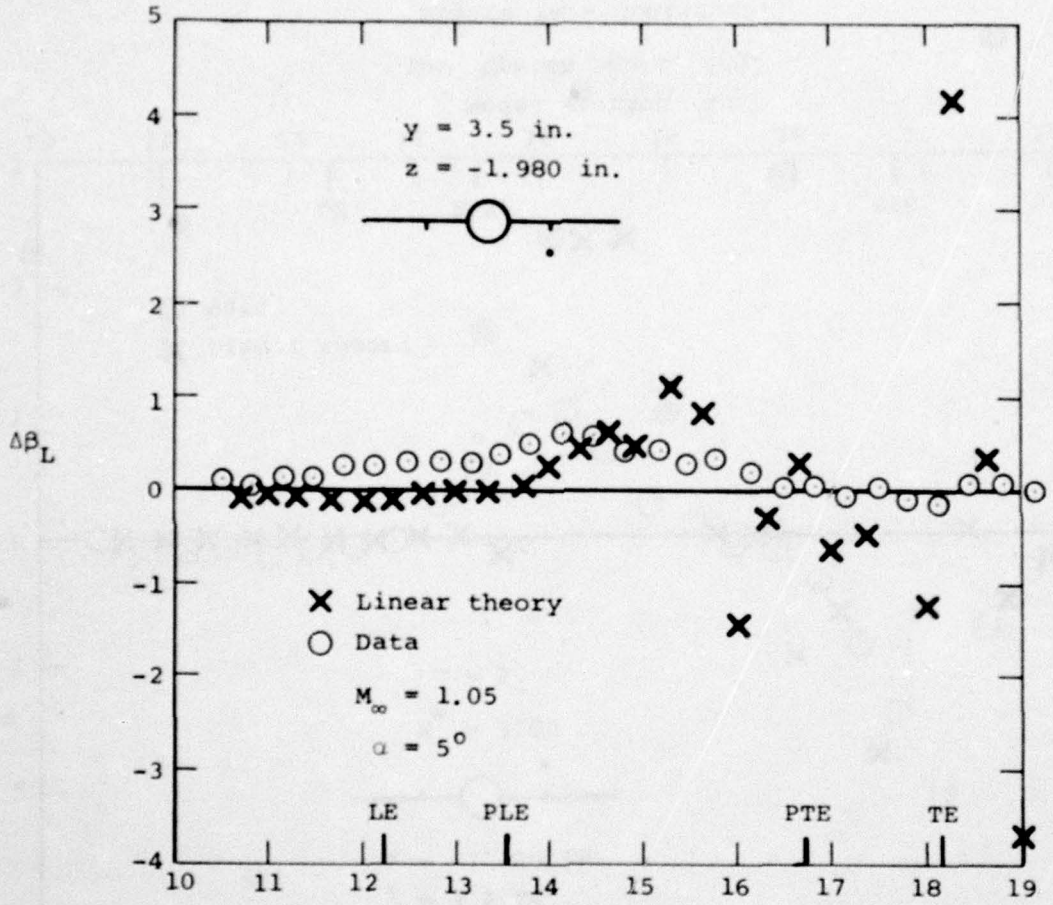

(c) Sidewash angle, deg.

Figure 74.- Concluded.

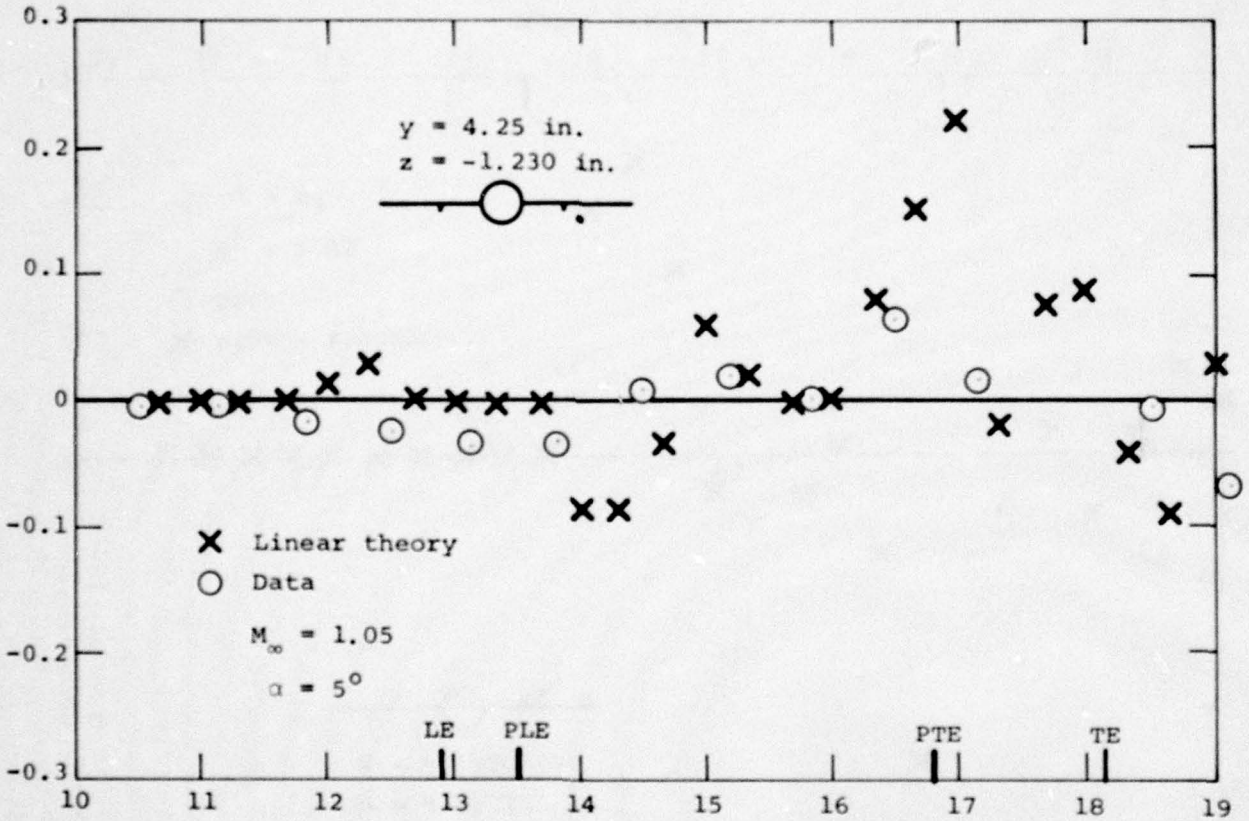

(a) Axial velocity ratio.

Figure 75.- Comparison of measured and theoretical differences between wing-body-pylon and wing-body flow field quantitites, $\alpha = 5^\circ$, $M_\infty = 1.05$, y = 4.25 in., z = -1.230 in.

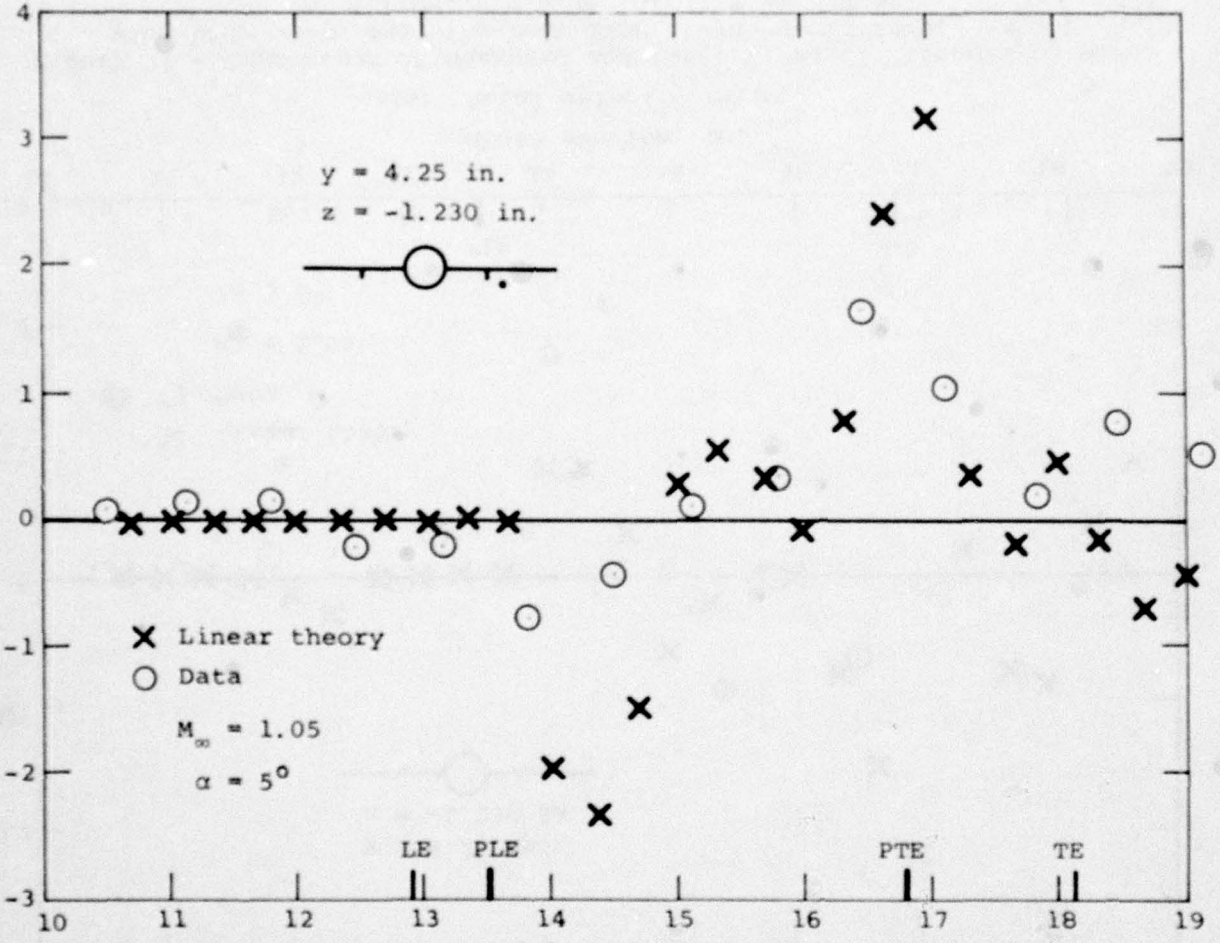

(b) Upwash angle, deg.

Figure 75.- Continued.

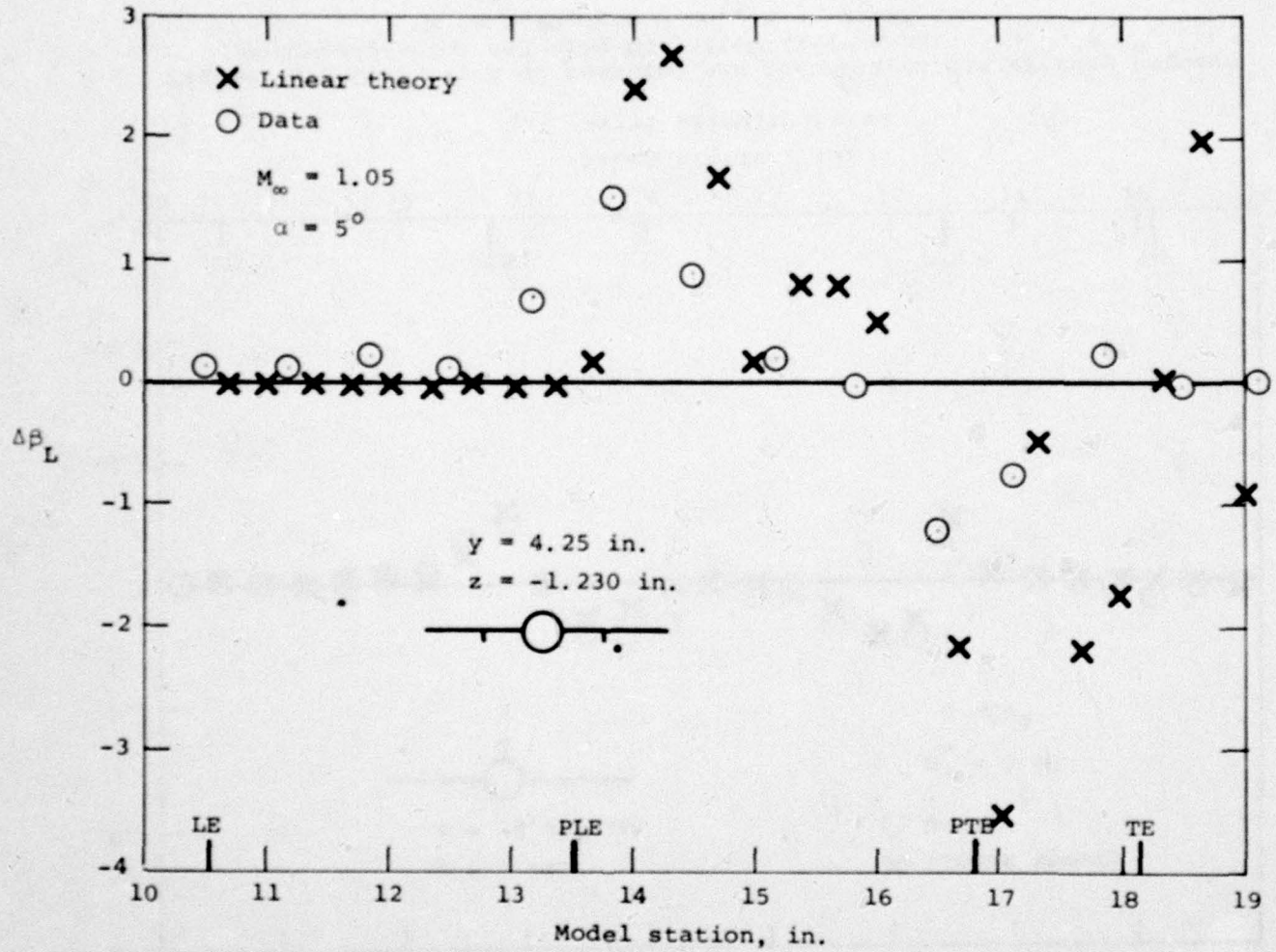

(c) Sidewash angle, deg.

Figure 75.- Concluded.

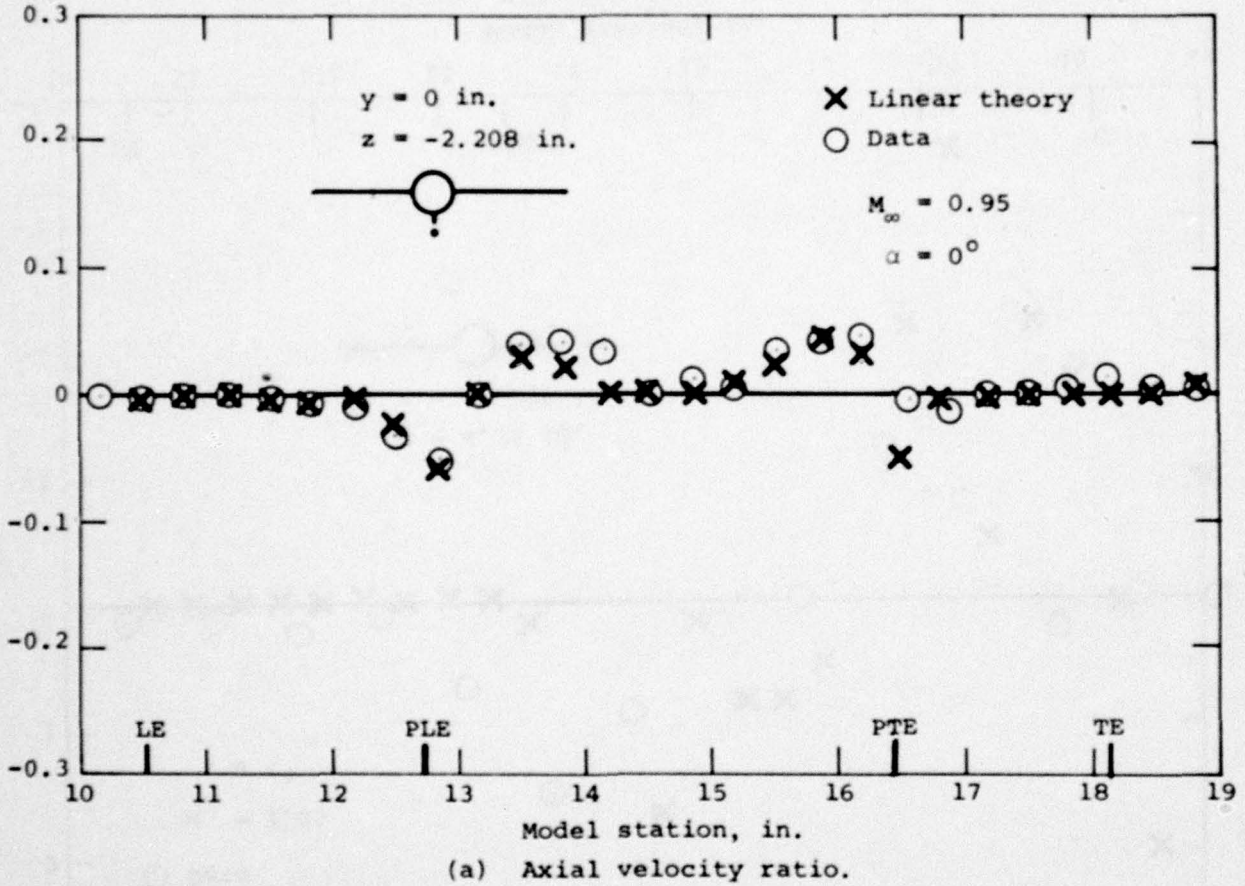

(a) Axial velocity ratio.

Figure 76.- Comparison of measured and theoretical differences between wing-body-pylon and wing-body flow field quantities, $\alpha = 0°$, $M_\infty = 0.95$, y = 0 in., z = -2.208 in.

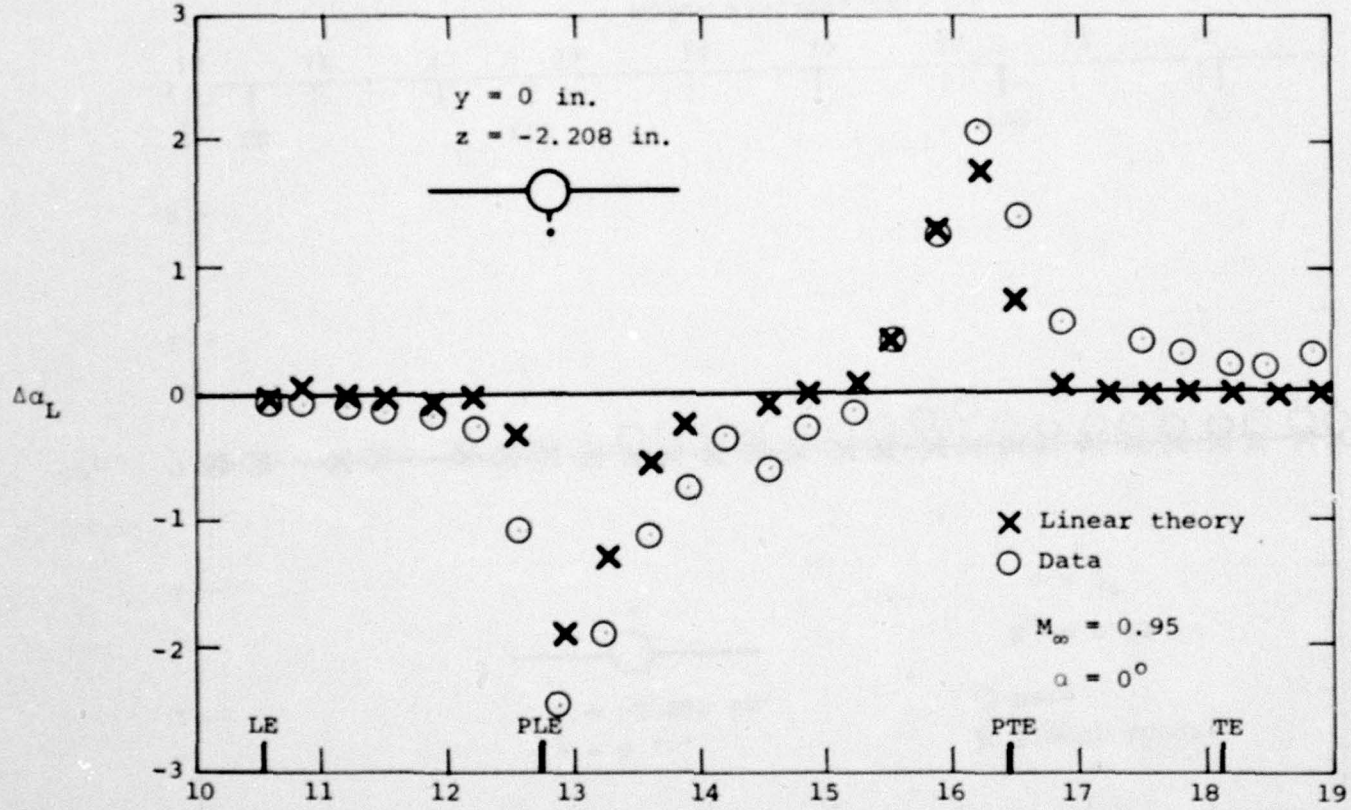

(b) Upwash angle, deg.

Figure 76.- Continued.

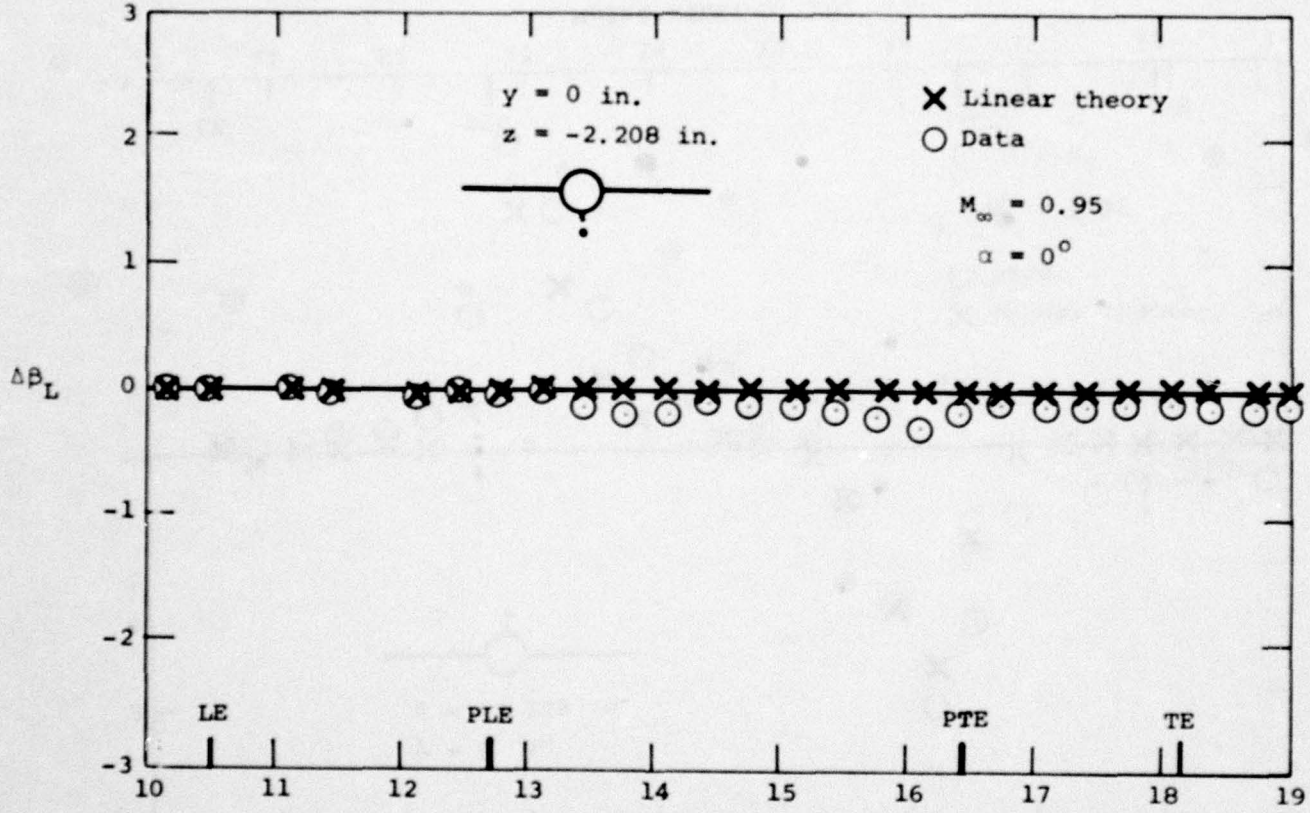

(c) Sidewash angle, deg.

Figure 76.- Concluded.

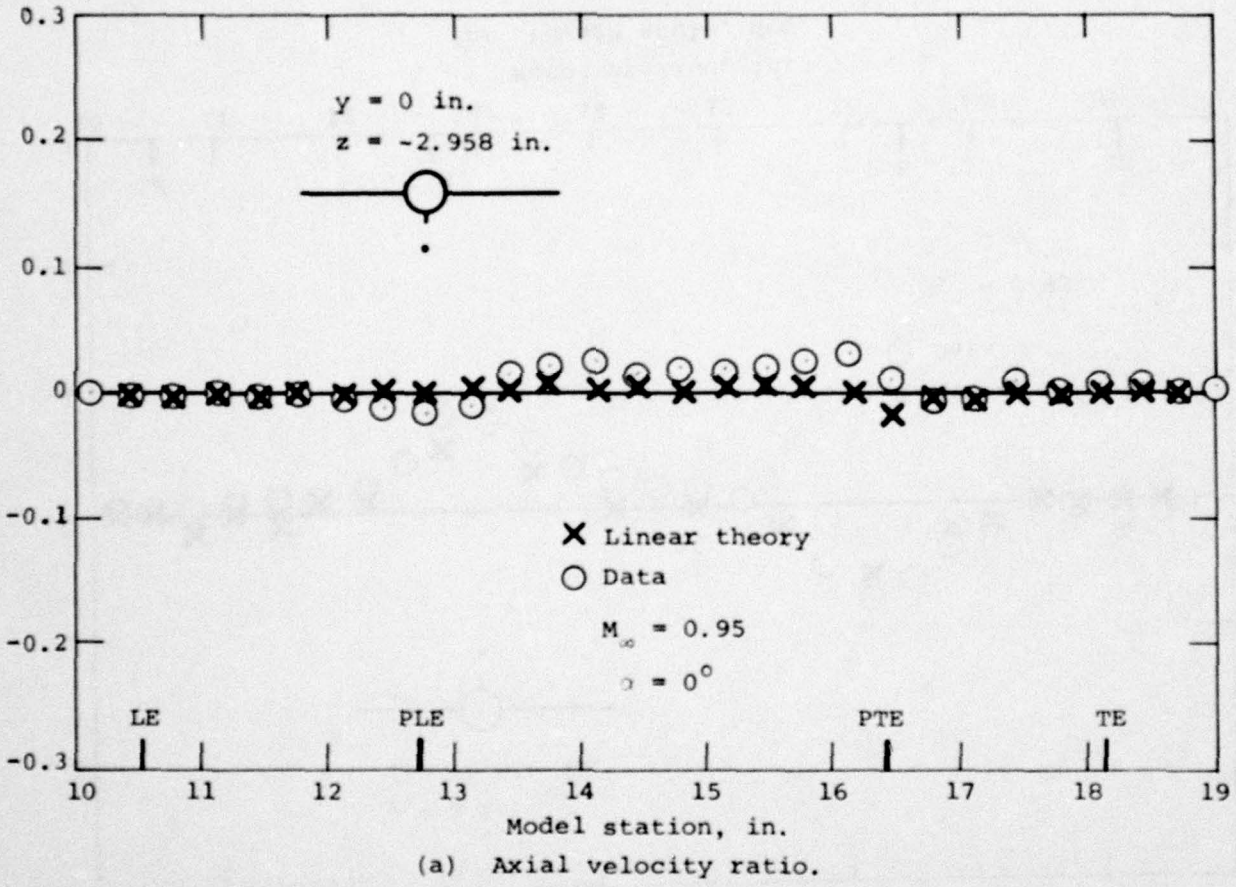

(a) Axial velocity ratio.

Figure 77.- Comparison of measured and theoretical differences between wing-body-pylon and wing-body flow field quantities, $\alpha = 0^\circ$, $M_\infty = 0.95$, y = 0 in., z = -2.958 in.

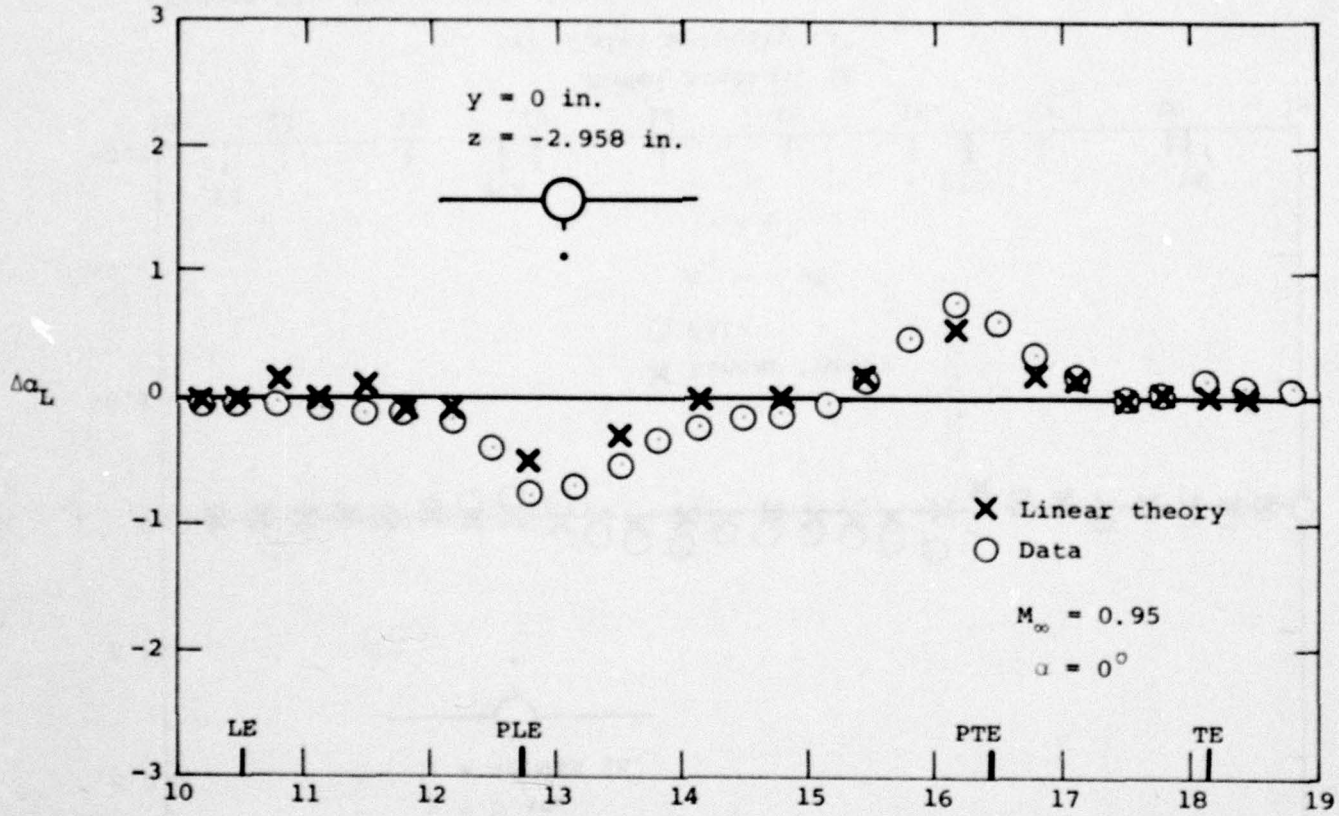

(b) Upwash angle, deg.

Figure 77.- Continued.

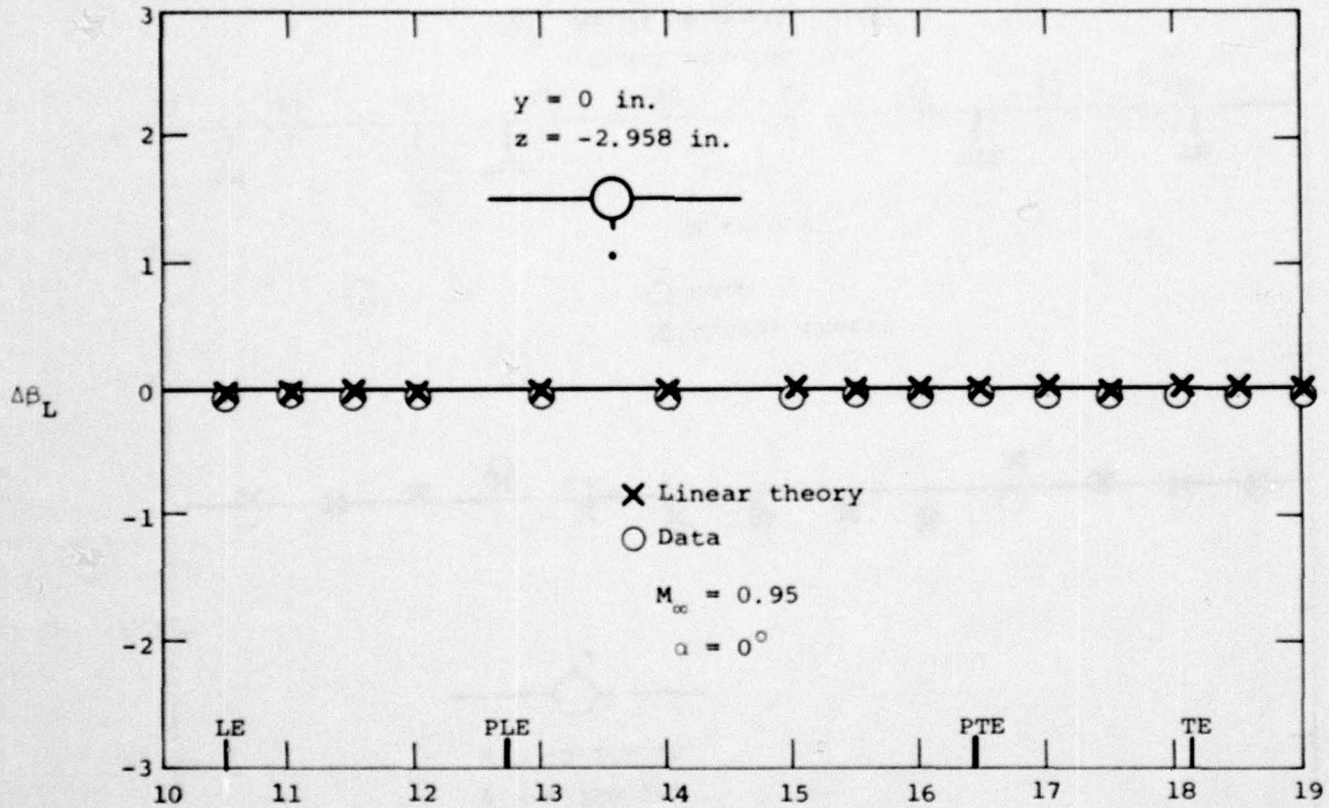

(c) Sidewash angle, deg.

Figure 77.- Concluded.

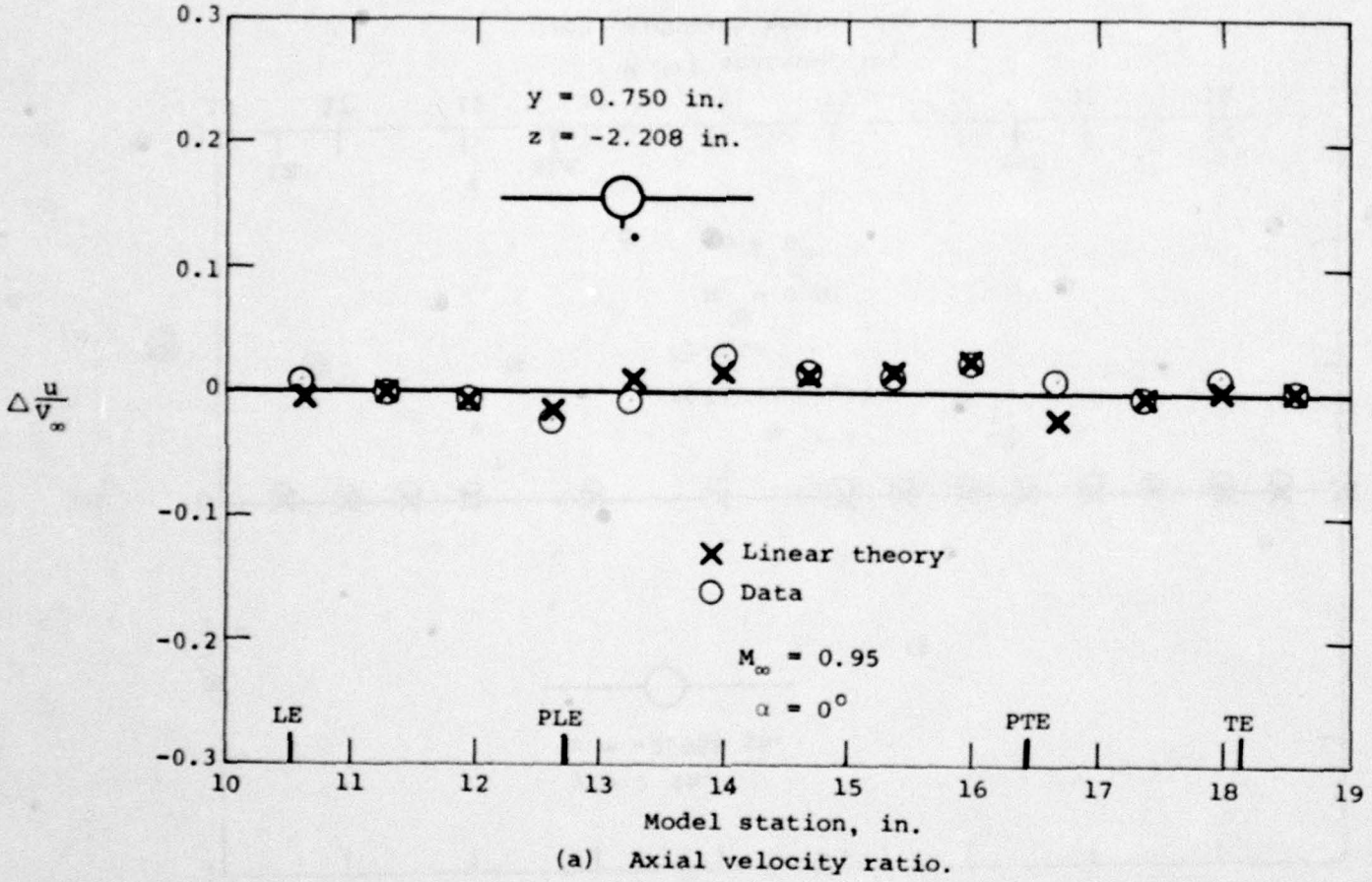

(a) Axial velocity ratio.

Figure 78.- Comparison of measured and theoretical differences between wing-body-pylon and wing-body flow field quantities, $\alpha = 0^\circ$, $M_\infty = 0.95$, y = 0.750 in., z = -2.208 in.

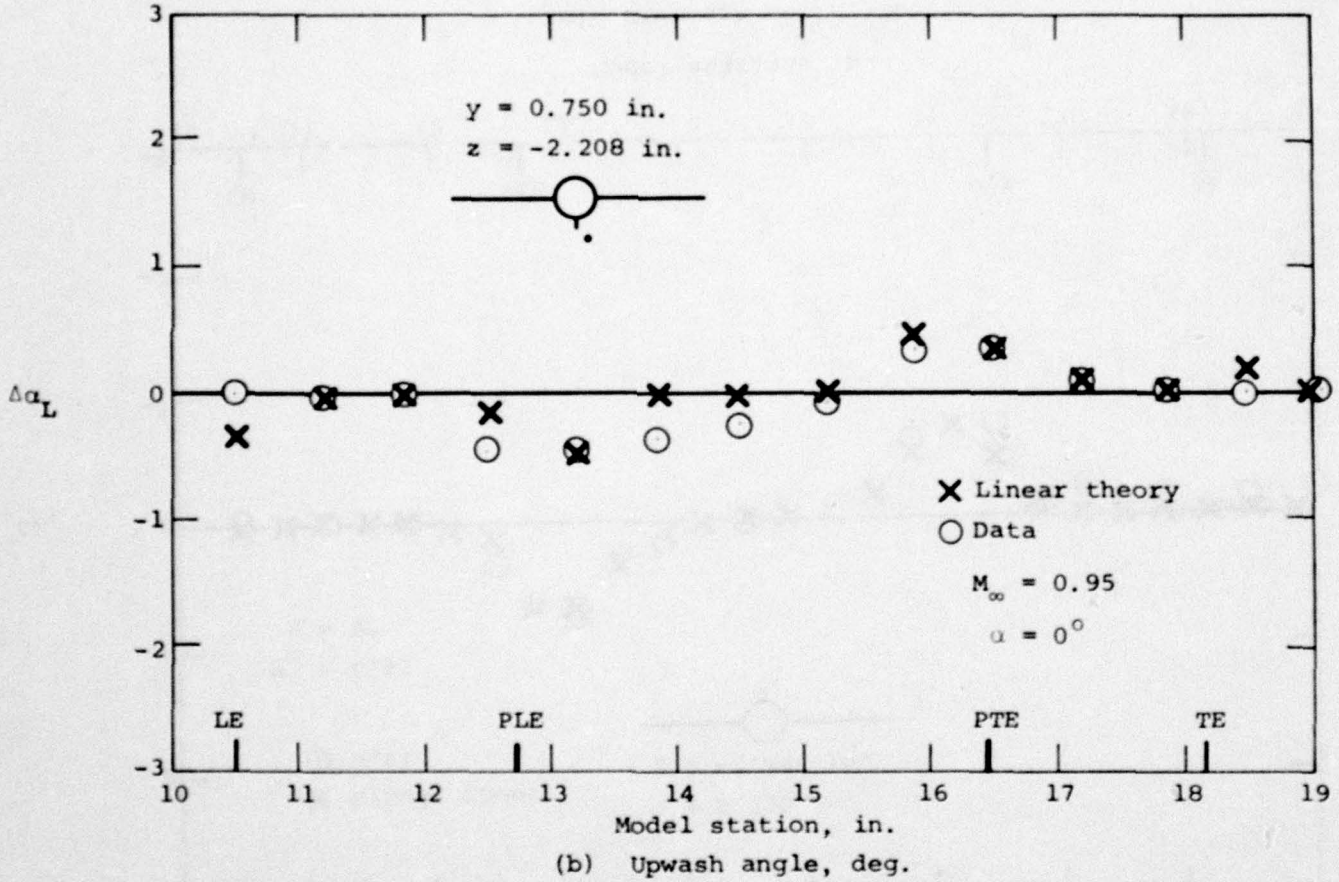

(b) Upwash angle, deg.

Figure 78.- Continued.

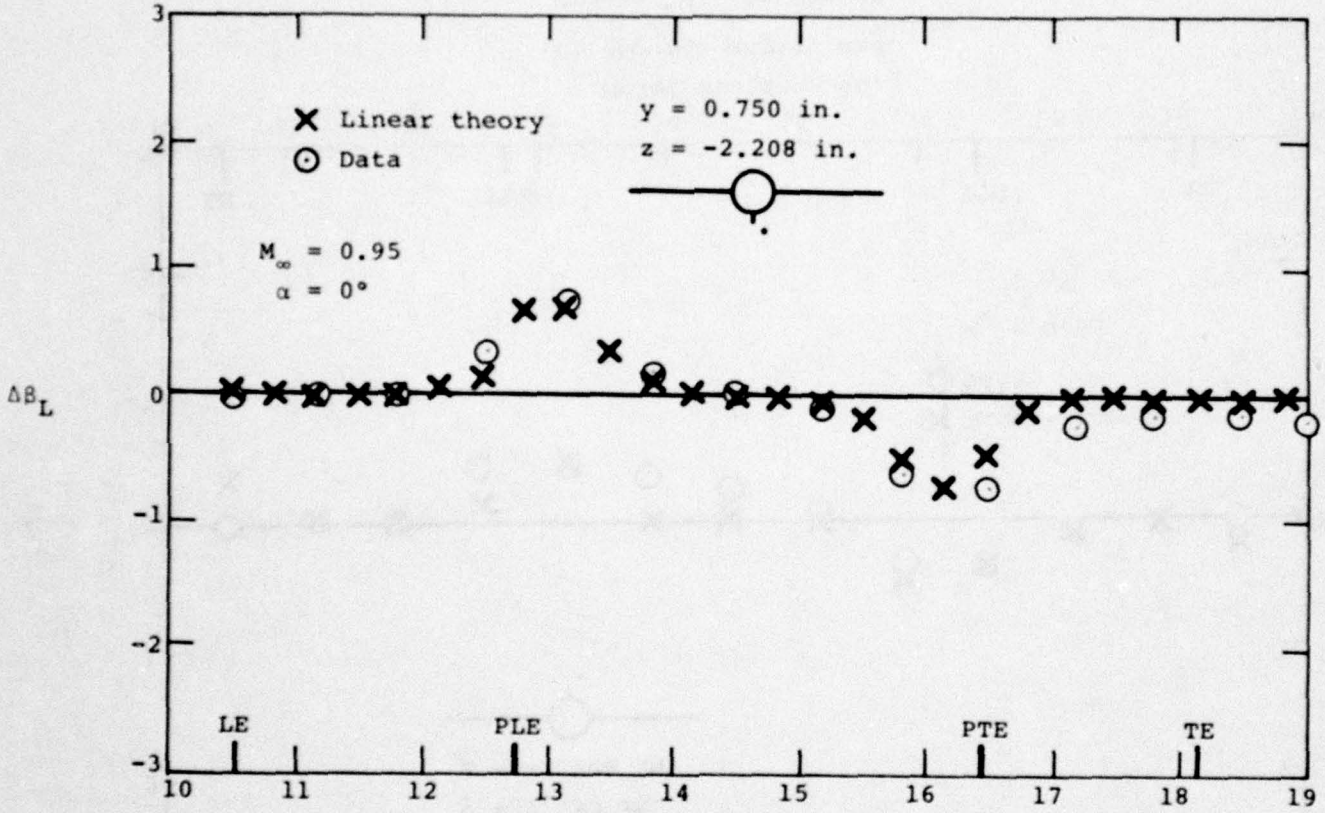

(c) Sidewash angle, deg.

Figure 78.- Concluded.

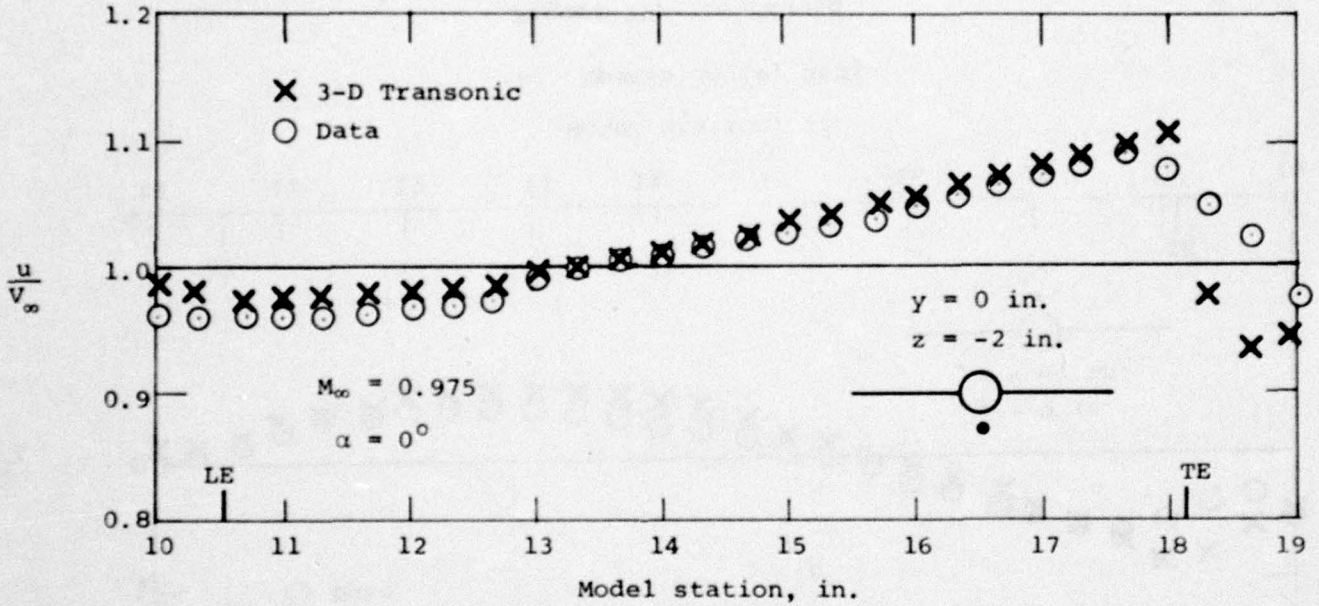

(a) Axial velocity ratio.

Figure 79.- Comparison of measured flow field quantities for wing-body combination with predictions of Bailey-Ballhaus transonic code, $\alpha = 0°$, $M_\infty = 0.975$, y = 0 in., z = -2 in.

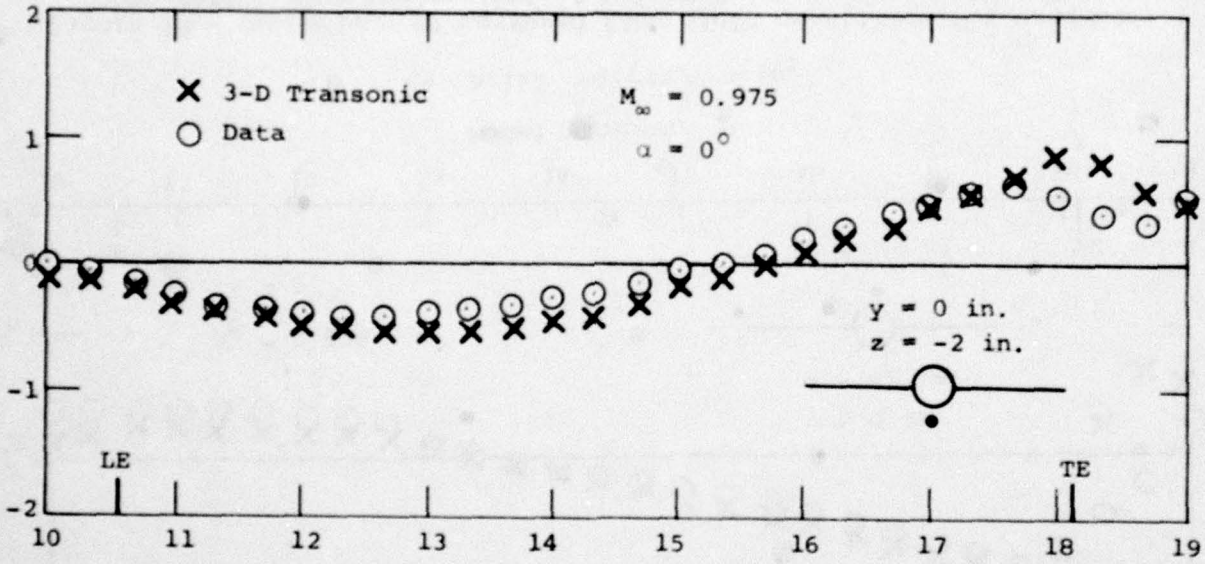

(b) Upwash angle, deg.

Figure 79.- Continued.

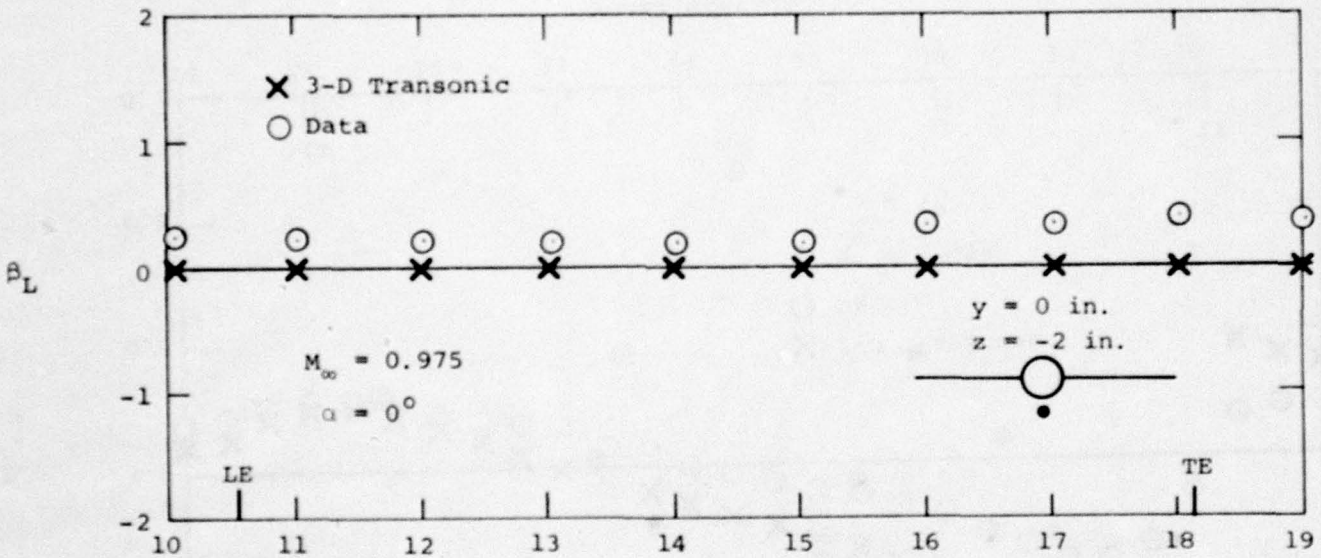

(c) Sidewash angle, deg.

Figure 79.- Concluded.

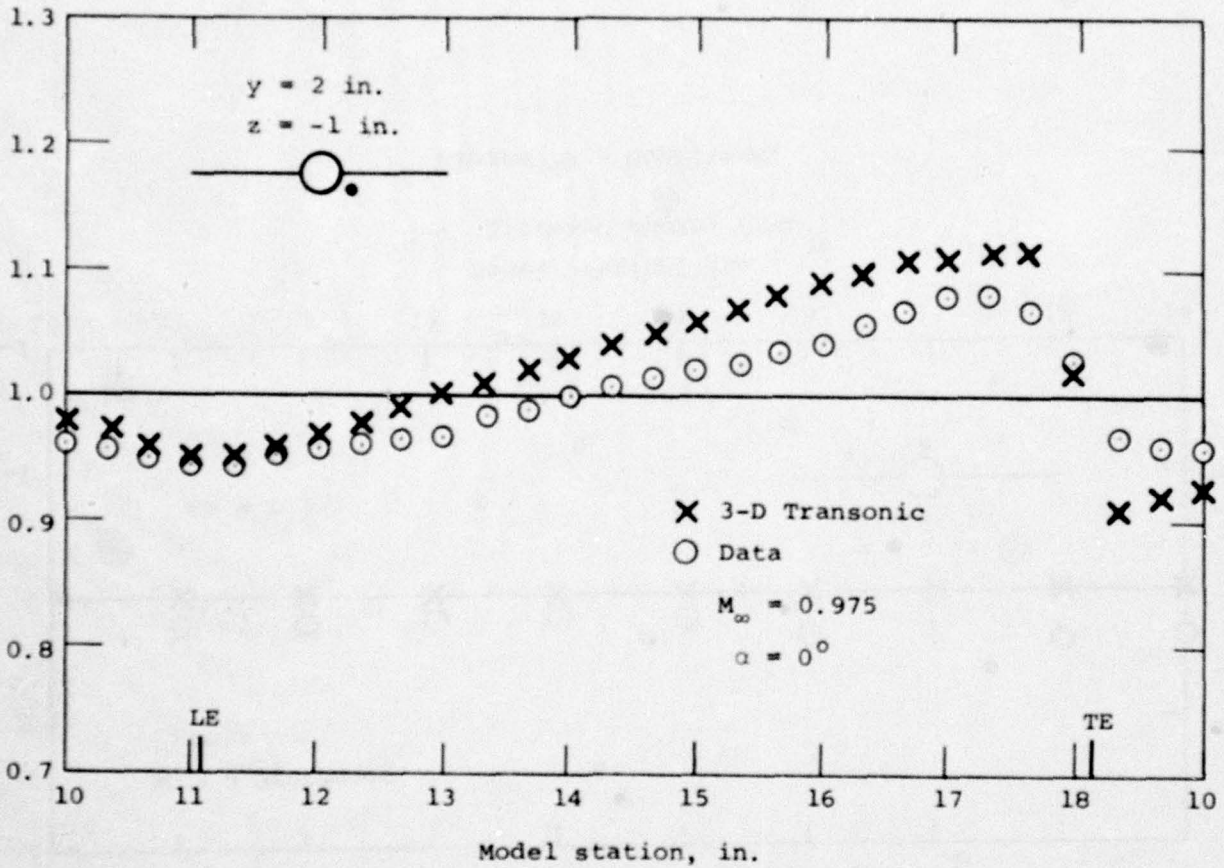

(a) Axial velocity ratio.

Figure 80.- Comparison of measured flow field quantities for wing-body combination with predictions of Bailey-Ballhaus transonic code, $\alpha = 0^\circ$, $M_\infty = 0.975$, y = 2 in., z = -1 in.

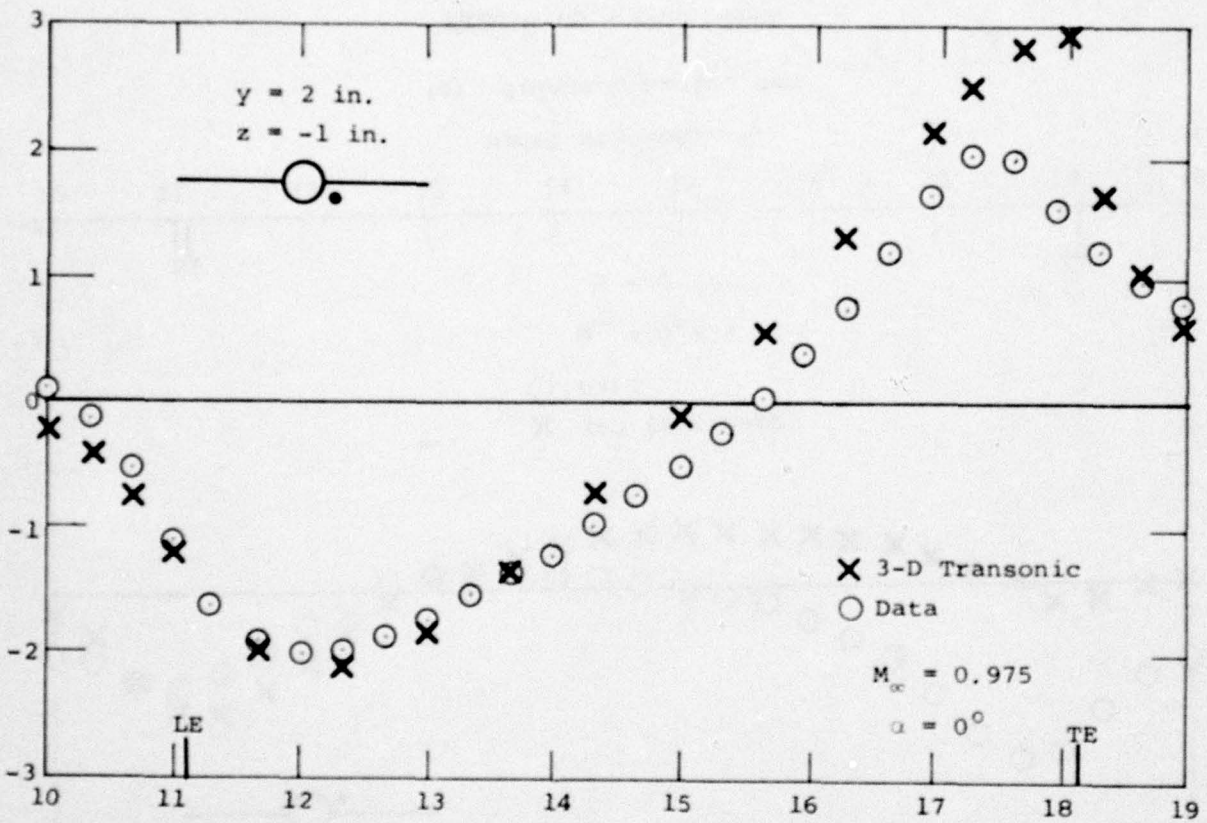

(b) Upwash angle, deg.

Figure 80.- Continued.

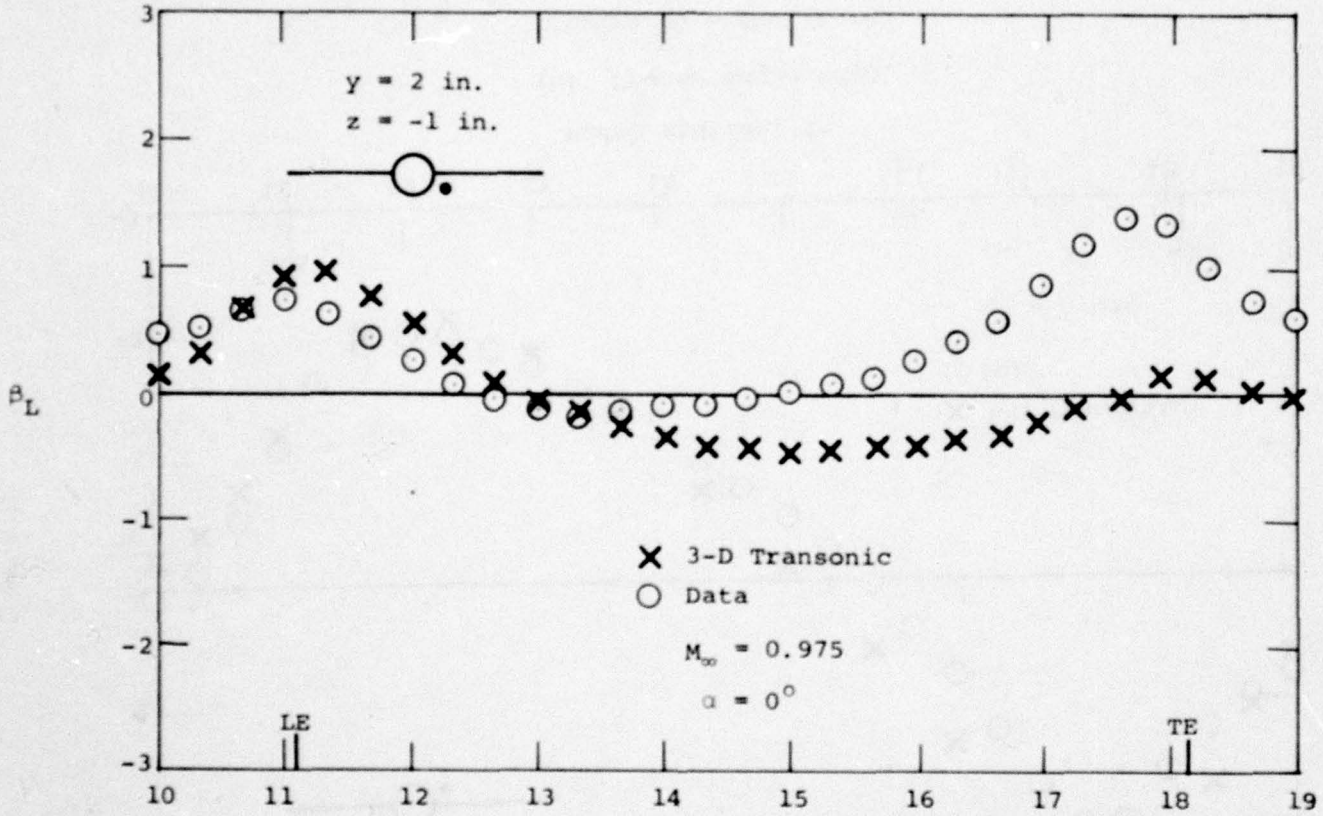

(c) Sidewash angle, deg.

Figure 80.- Concluded.

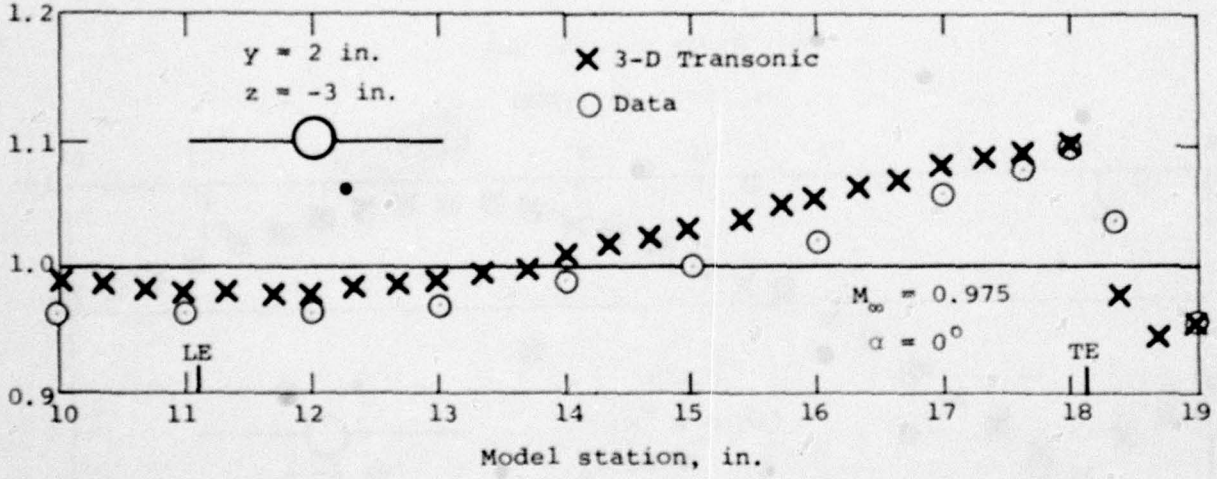

(a) Axial velocity ratio.

Figure 81.- Comparison of measured flow field quantities for wing-body combination with predictions of Bailey-Ballhaus transonic code, $\alpha = 0^\circ$, $M_\infty = 0.975$, y = 2 in., z = -3 in.

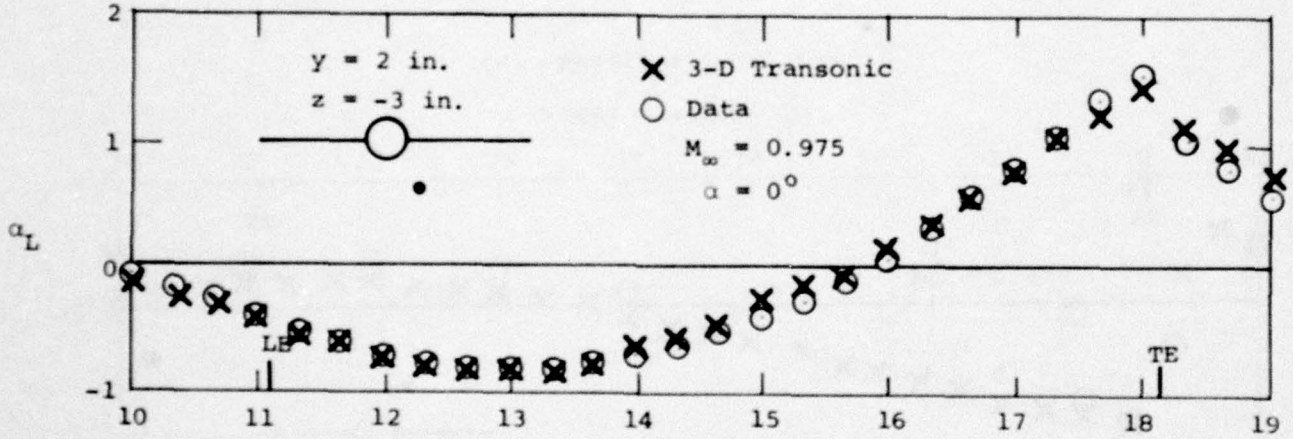

(b) Upwash angle, deg.

Figure 81.- Continued.

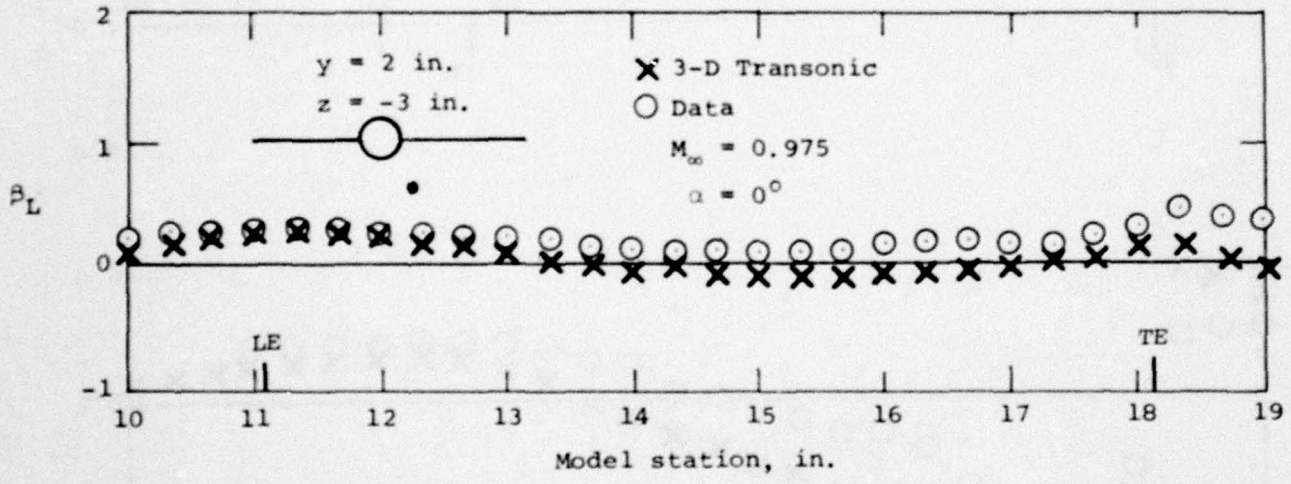

(c) Sidewash angle, deg.

Figure 81.- Concluded.

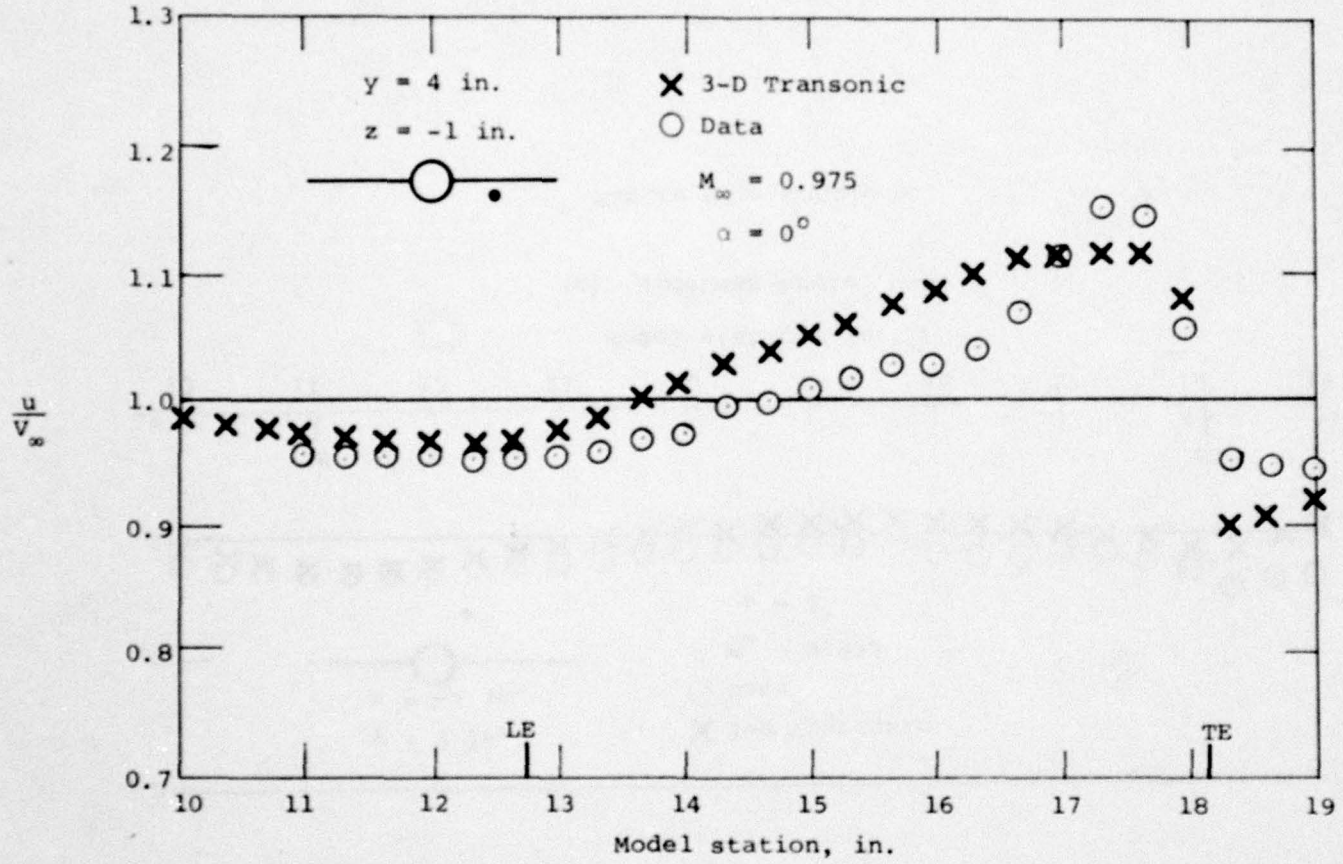

(a) Axial velocity ratio.

Figure 82.- Comparison of measured flow field quantities for wing-body combination with predictions of Bailey-Ballhaus transonic code, $\alpha = 0^\circ$, $M_\infty = 0.975$, y = 4 in., z = -1 in.

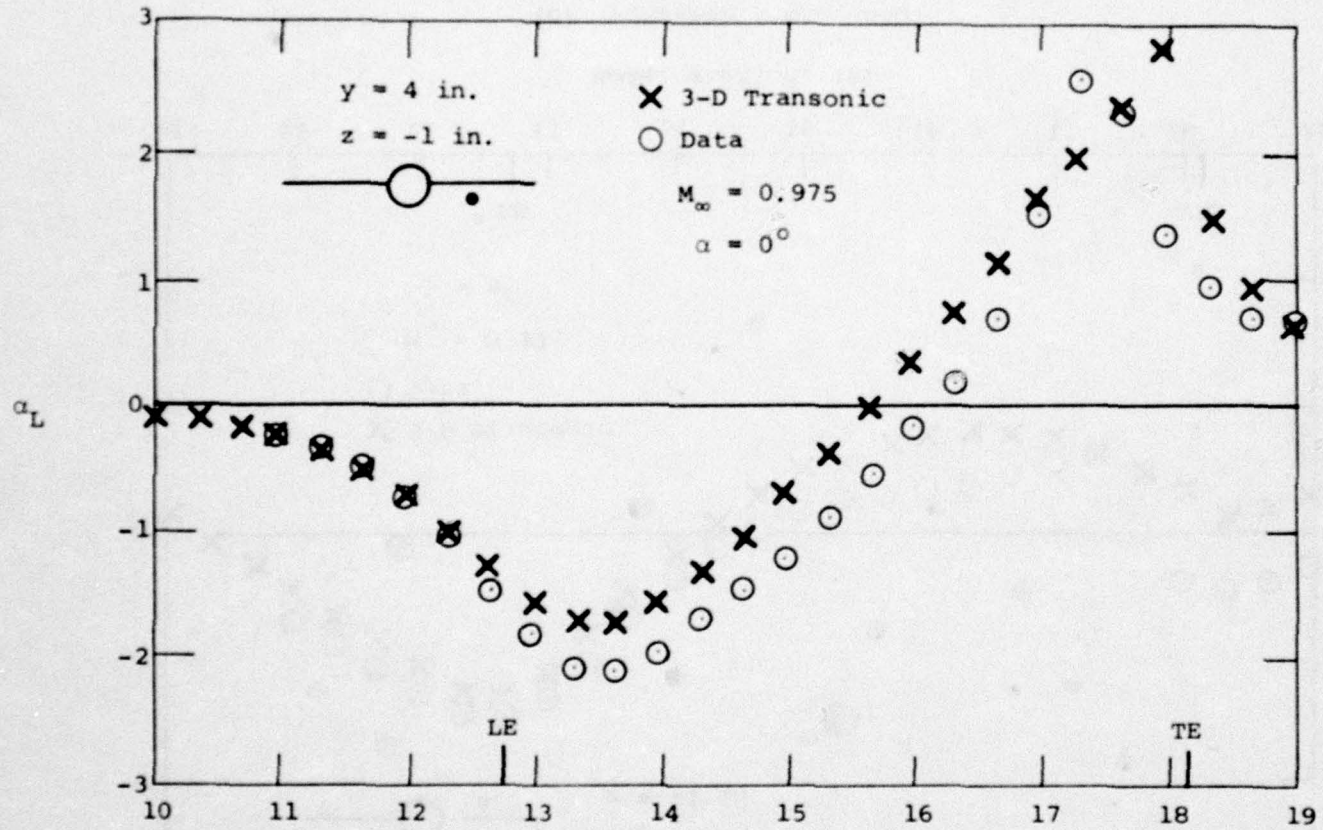

(b) Upwash angle, deg.

Figure 82.- Continued.

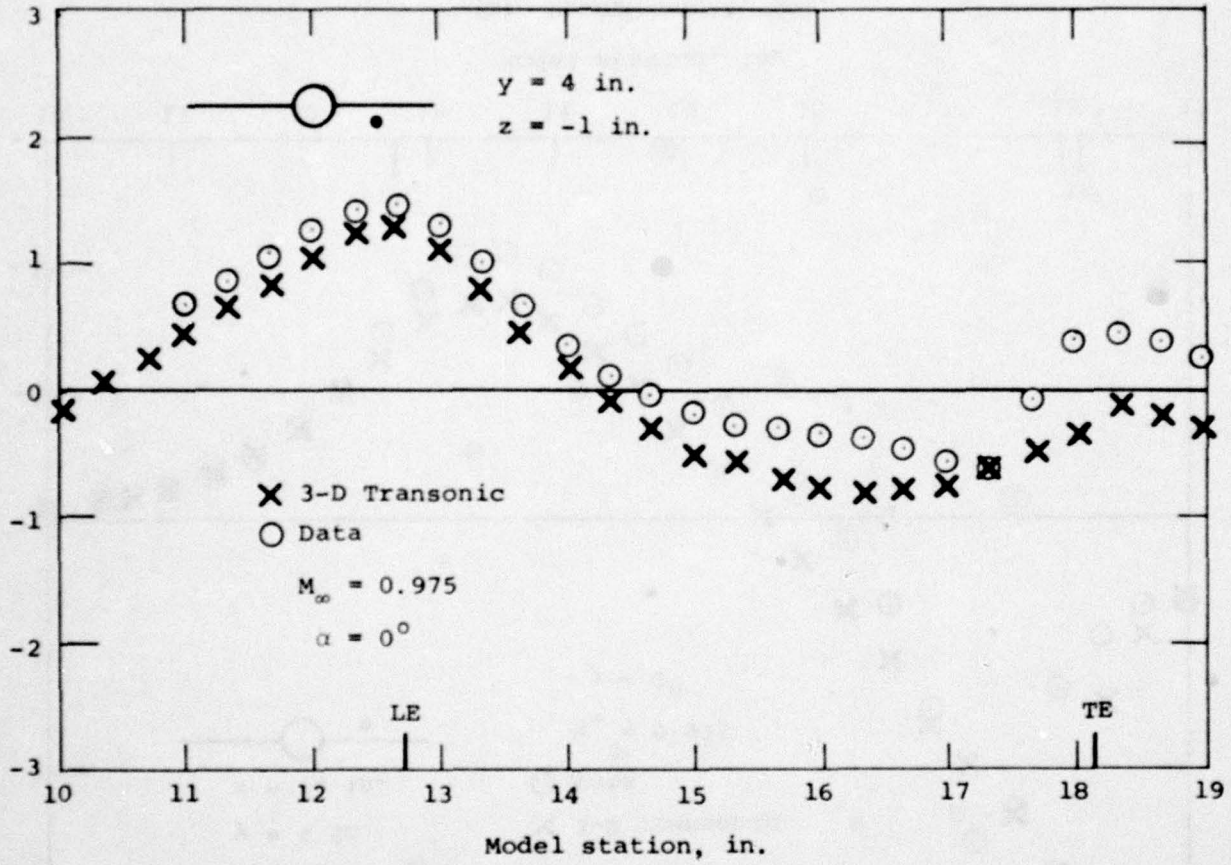

(c) Sidewash angle, deg.

Figure 82.- Concluded.

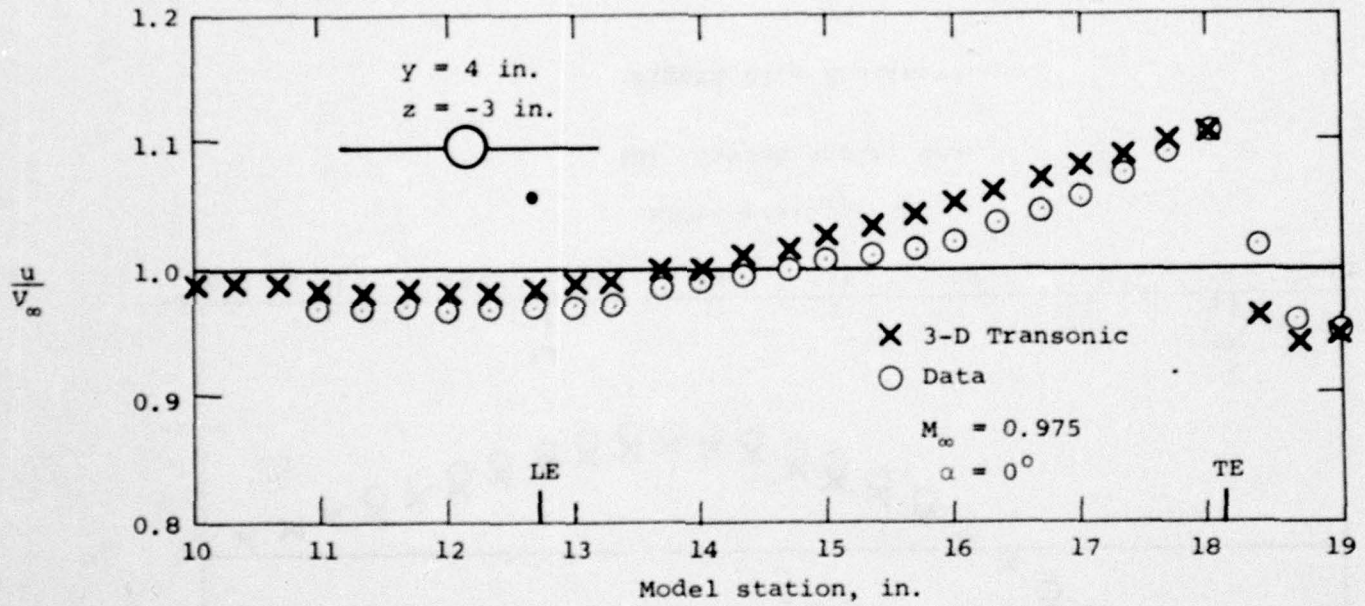

(a) Axial velocity ratio.

Figure 83.- Comparison of measured flow field quantities for wing-body combination with predictions of Bailey-Ballhaus transonic code, $\alpha = 0^\circ$, $M_\infty = 0.975$, y = 4 in., z = -3 in.

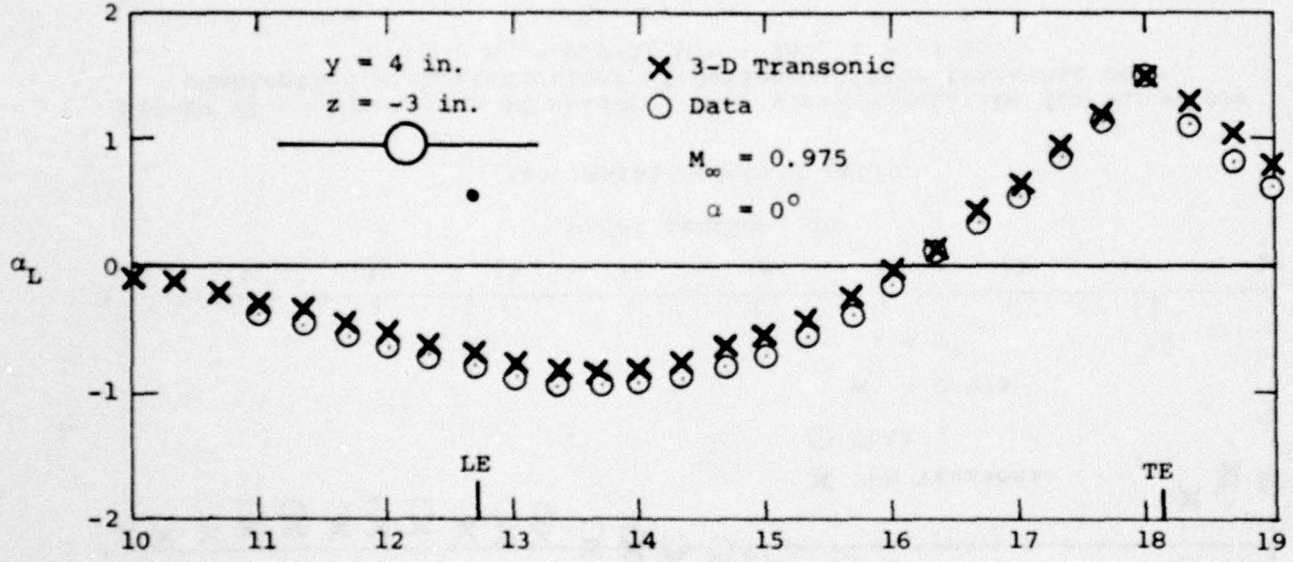

(b) Upwash angle, deg.

Figure 83.- Continued.

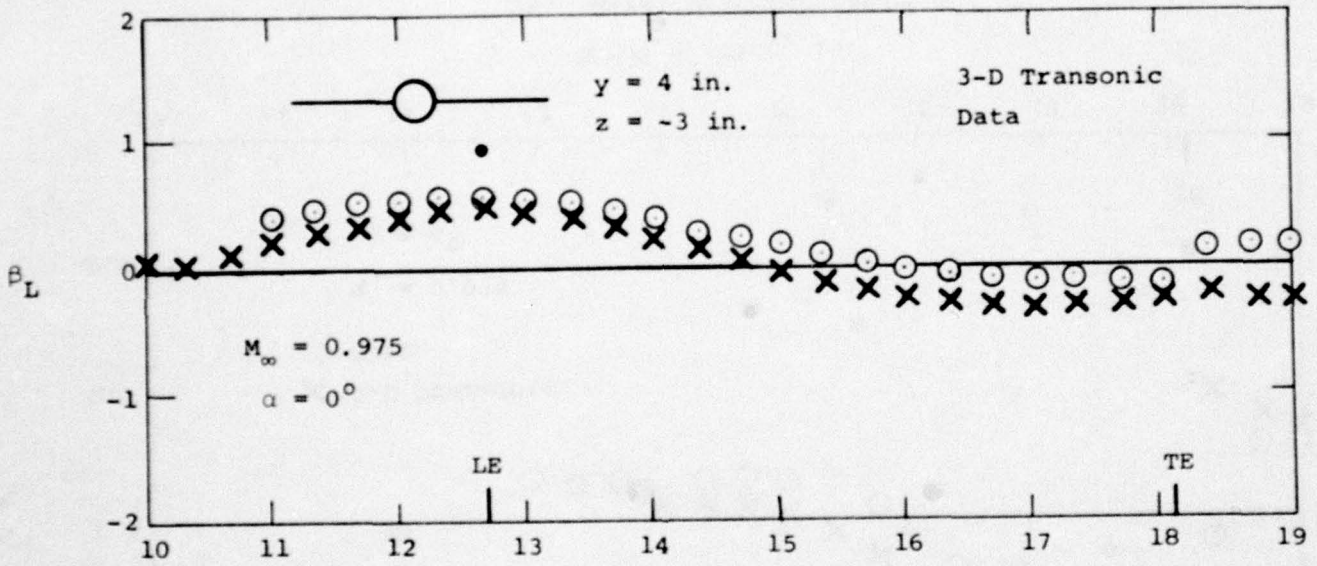

(c) Sidewash angle, deg.

Figure 83.- Concluded.

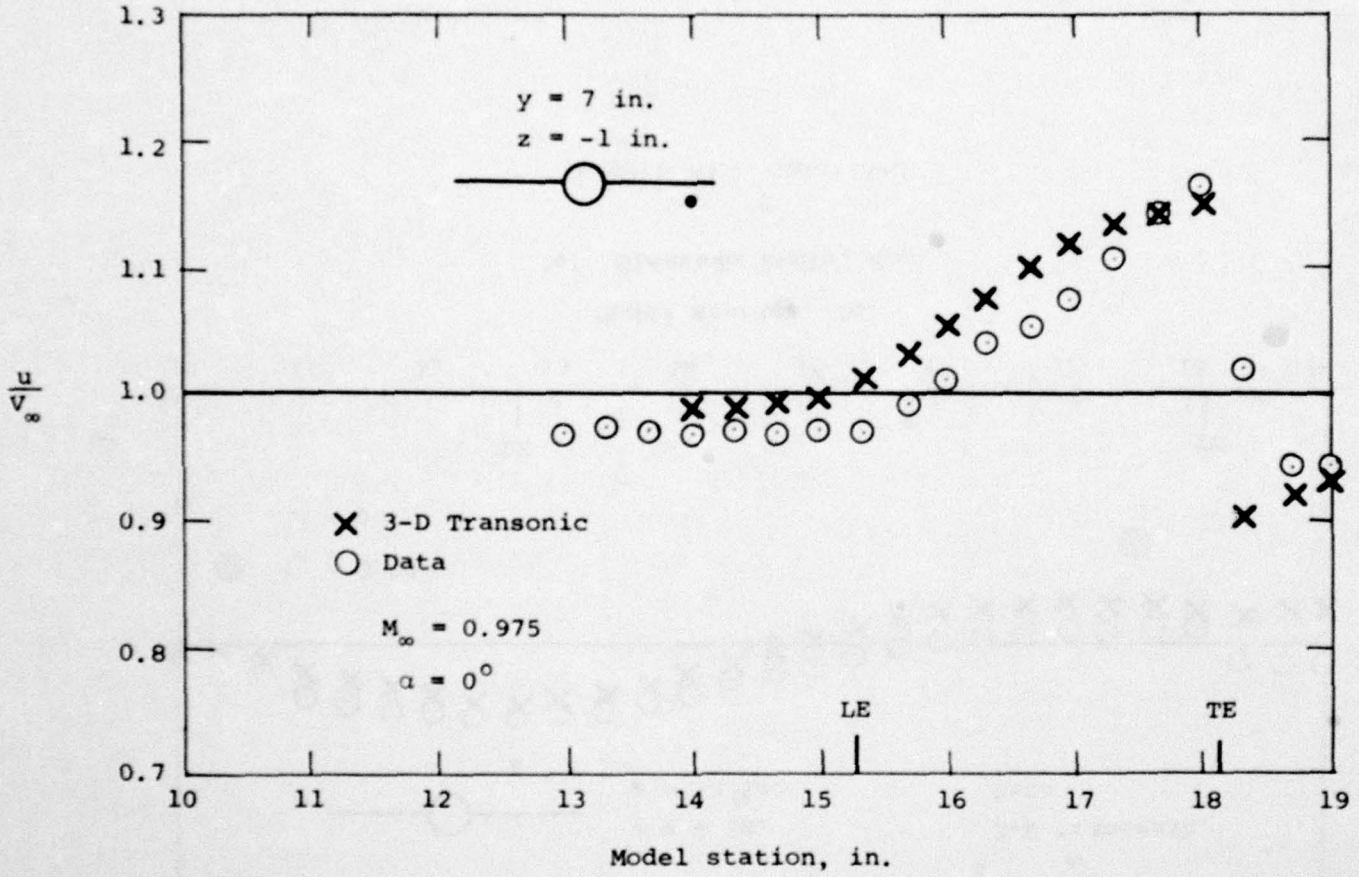

(a) Axial velocity ratio.

Figure 84.- Comparison of measured flow field quantities for wing-body combination with predictions of Bailey-Ballhaus transonic code, $\alpha = 0^\circ$, $M_\infty = 0.975$, y = 7 in., z = -1 in.

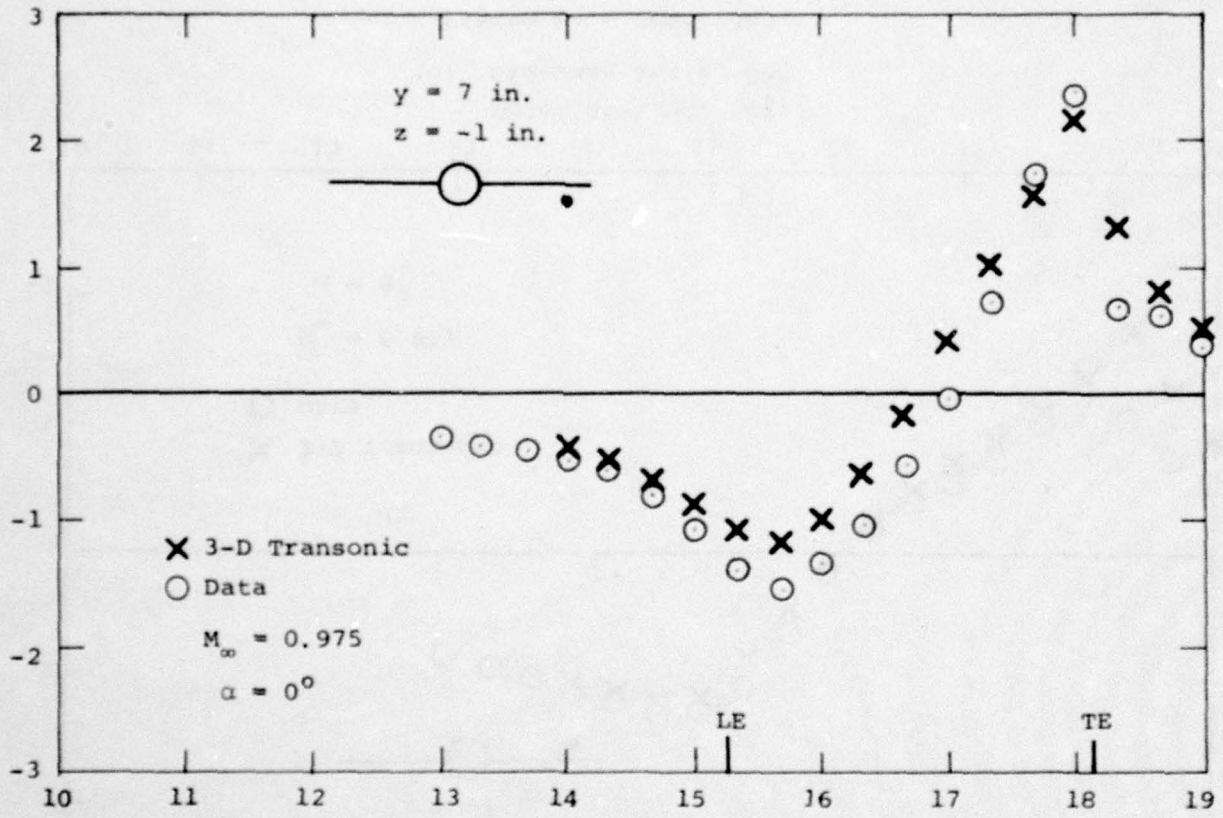

(b) Upwash angle, deg.

Figure 84.- Continued.

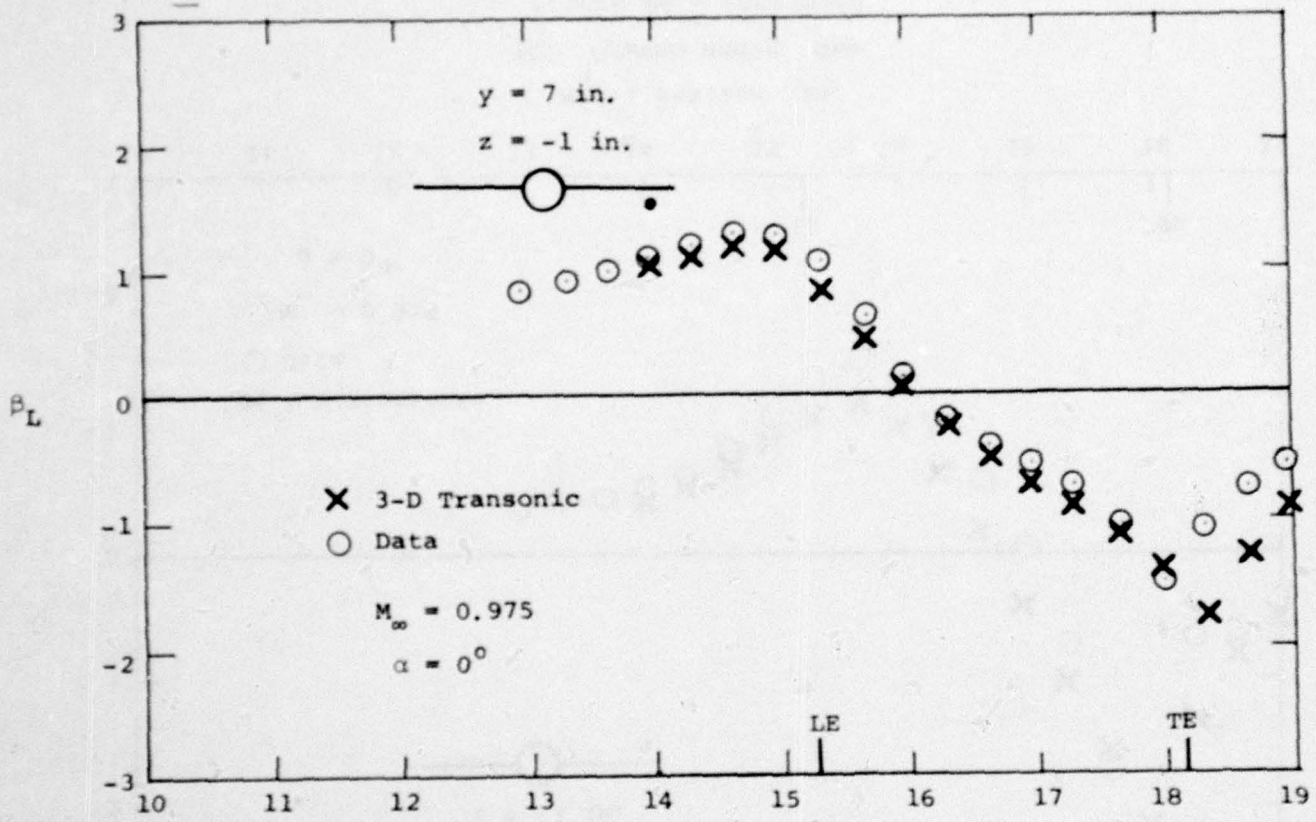

(c) Sidewash angle, deg.

Figure 84.- Concluded.

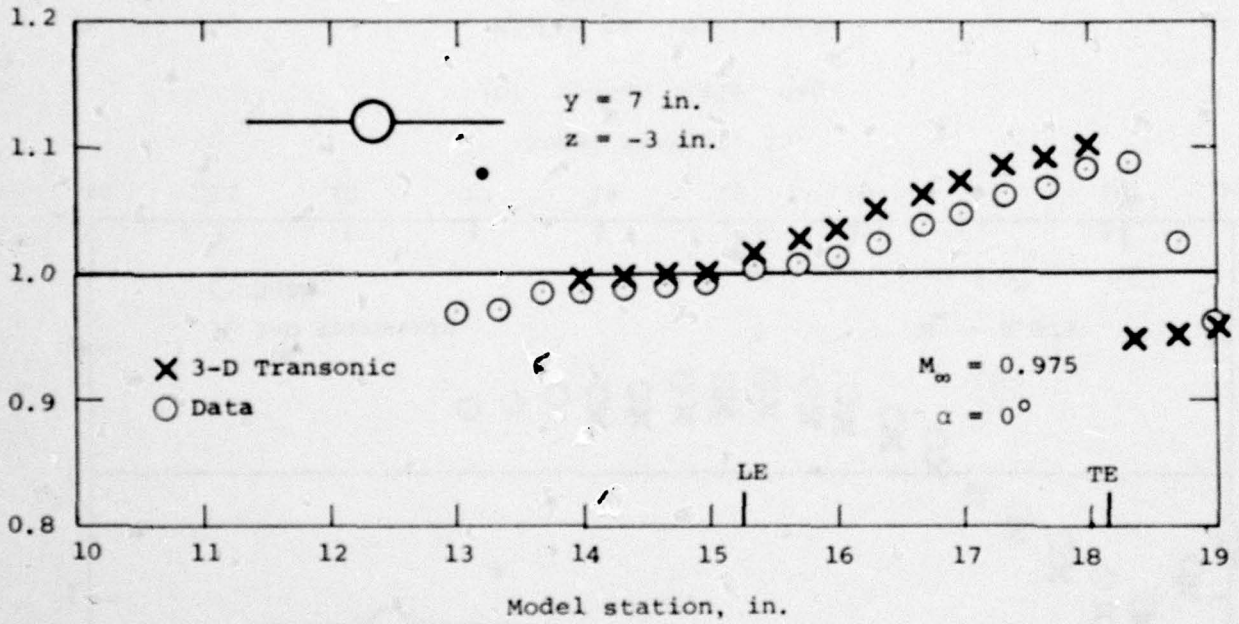

(a) Axial velocity ratio.

Figure 85.- Comparison of measured flow field quantities for wing-body combination with predictions of Bailey-Ballhaus transonic code, $\alpha = 0^\circ$, $M_\infty = 0.975$, y = 7 in., z = -3 in.

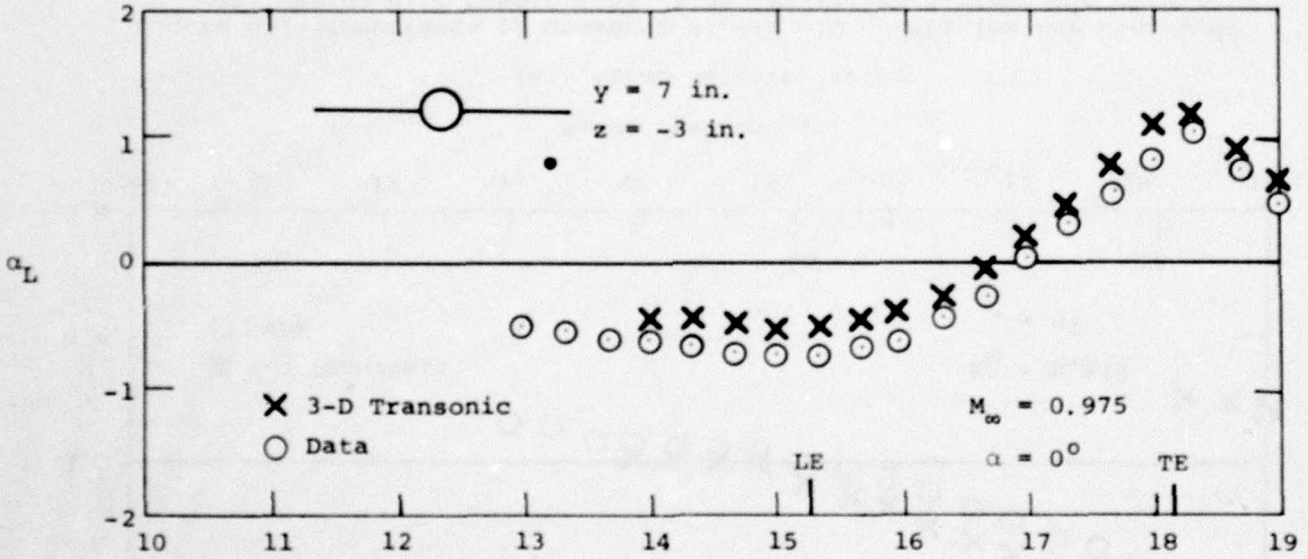

(b) Upwash angle, deg.

Figure 85.- Continued.

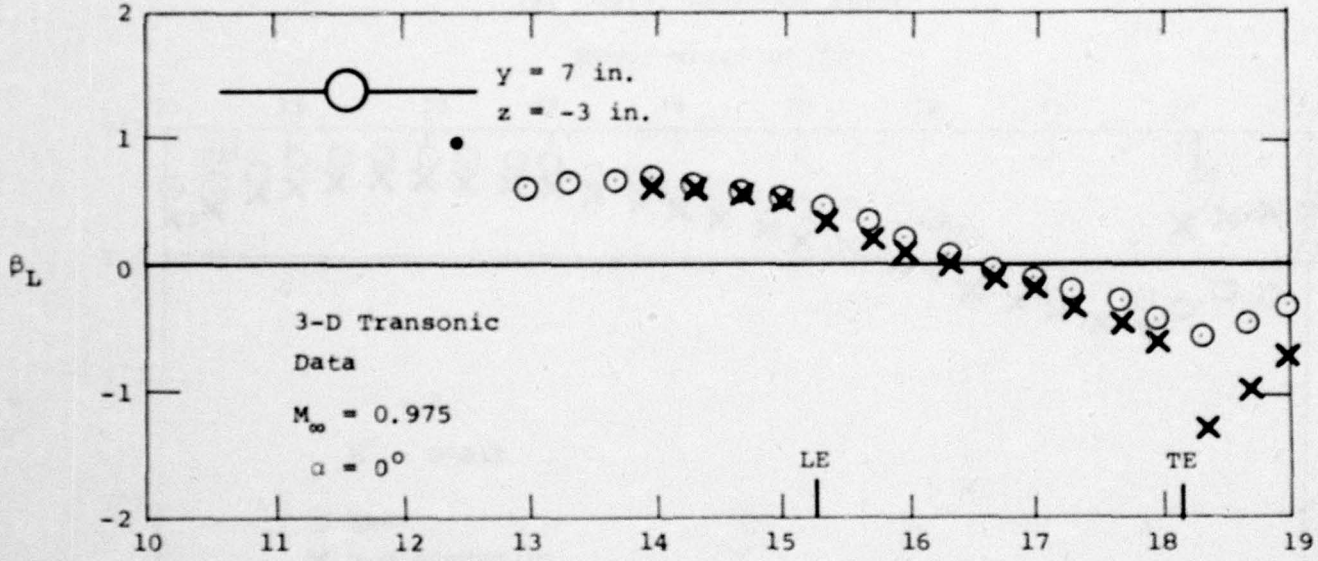

(c) Sidewash angle, deg.

Figure 85.- Concluded.

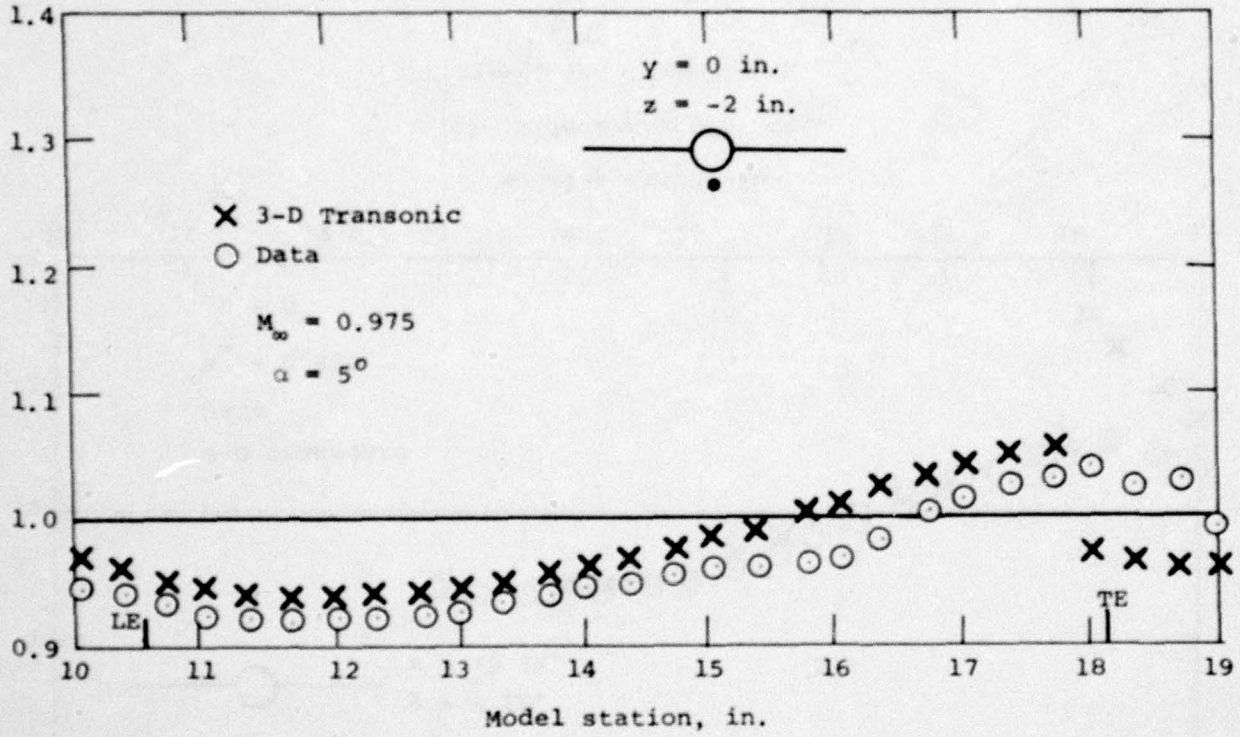

(a) Axial velocity ratio.

Figure 86.- Comparison of measured flow field quantities for wing-body combination with predictions of Bailey-Ballhaus transonic code, $\alpha = 5^o$, $M_\infty = 0.975$, y = 0 in., z = -2 in.

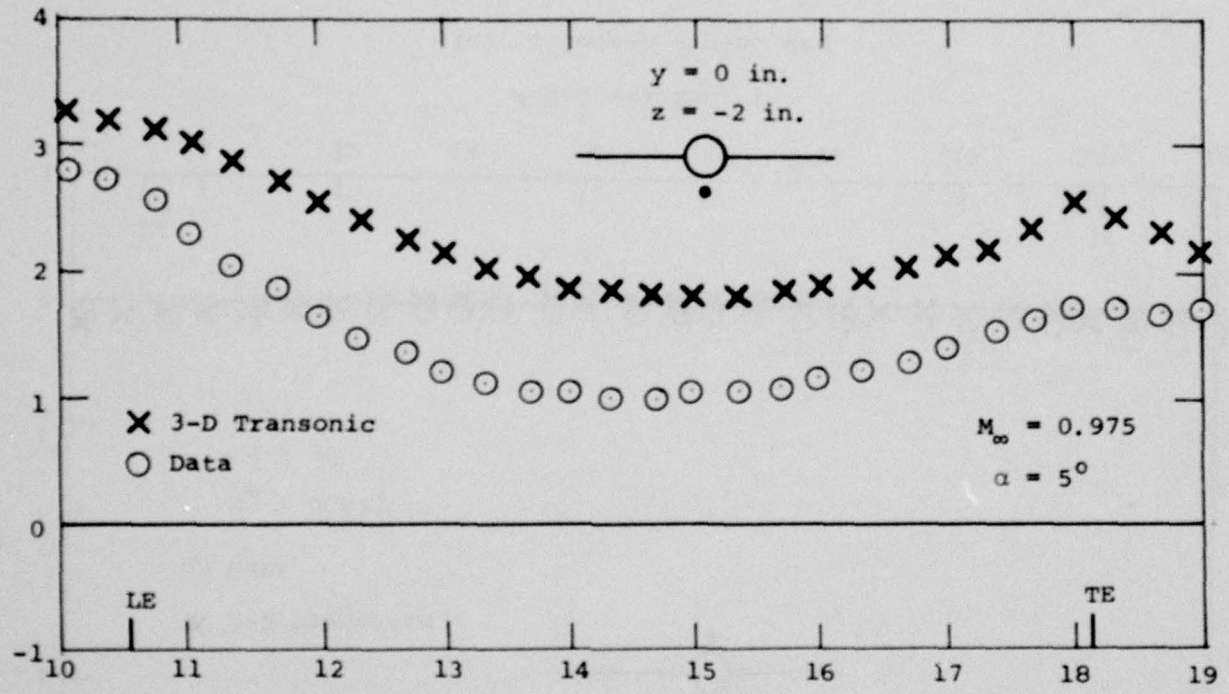

(b) Upwash angle, deg.

Figure 86.- Continued.

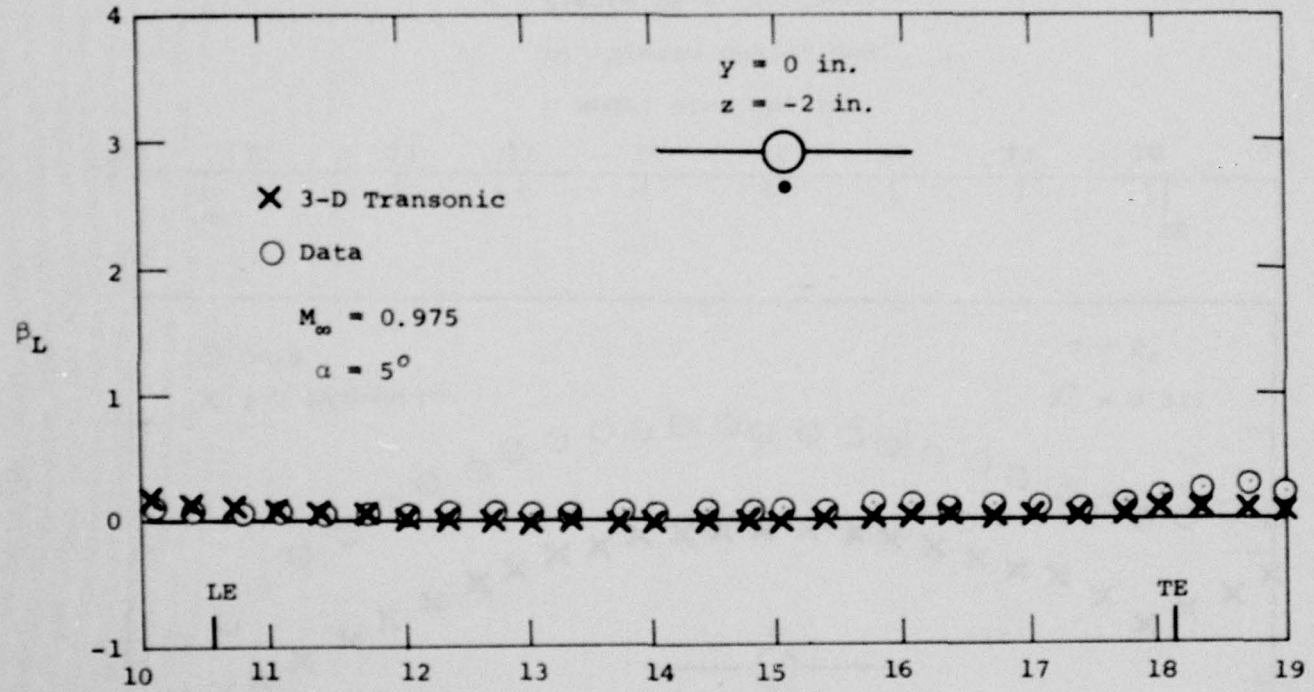

(c) Sidewash angle, deg.

Figure 86.- Concluded.

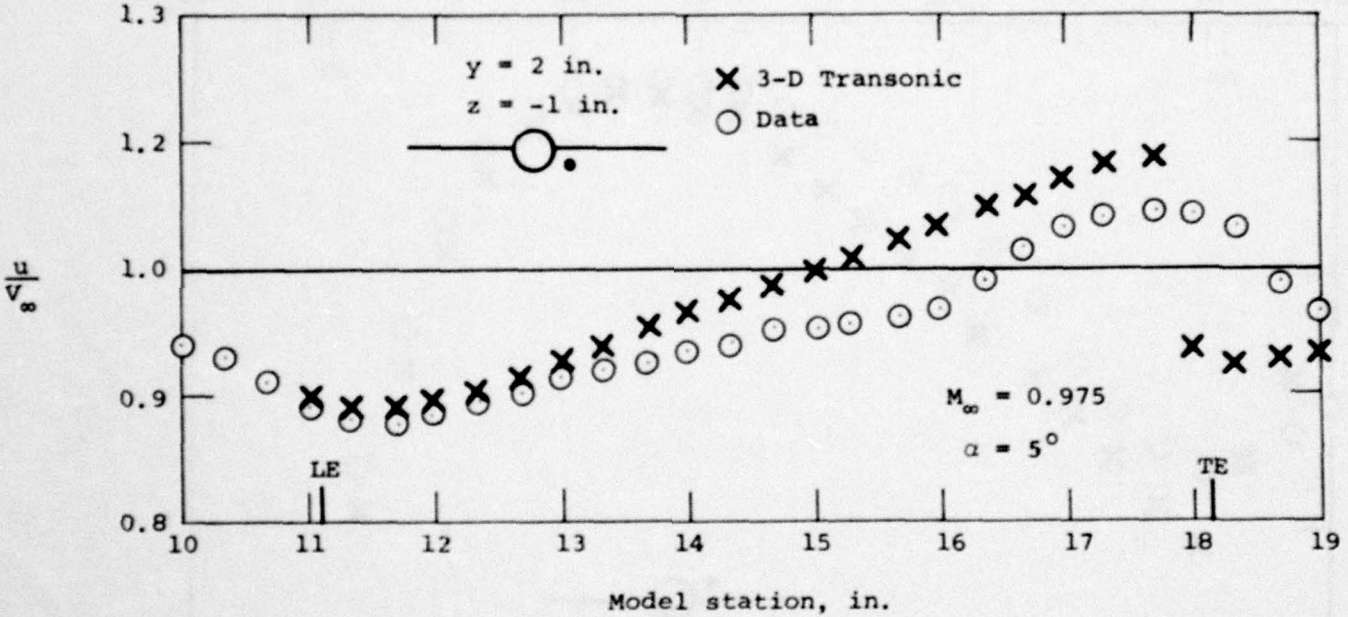

(a) Axial velocity ratio.

Figure 87.- Comparison of measured flow field quantities for wing-body combination with predictions of Bailey-Ballhaus transonic code, $\alpha = 5^\circ$, $M_\infty = 0.975$, y = 2 in., z = -1 in.

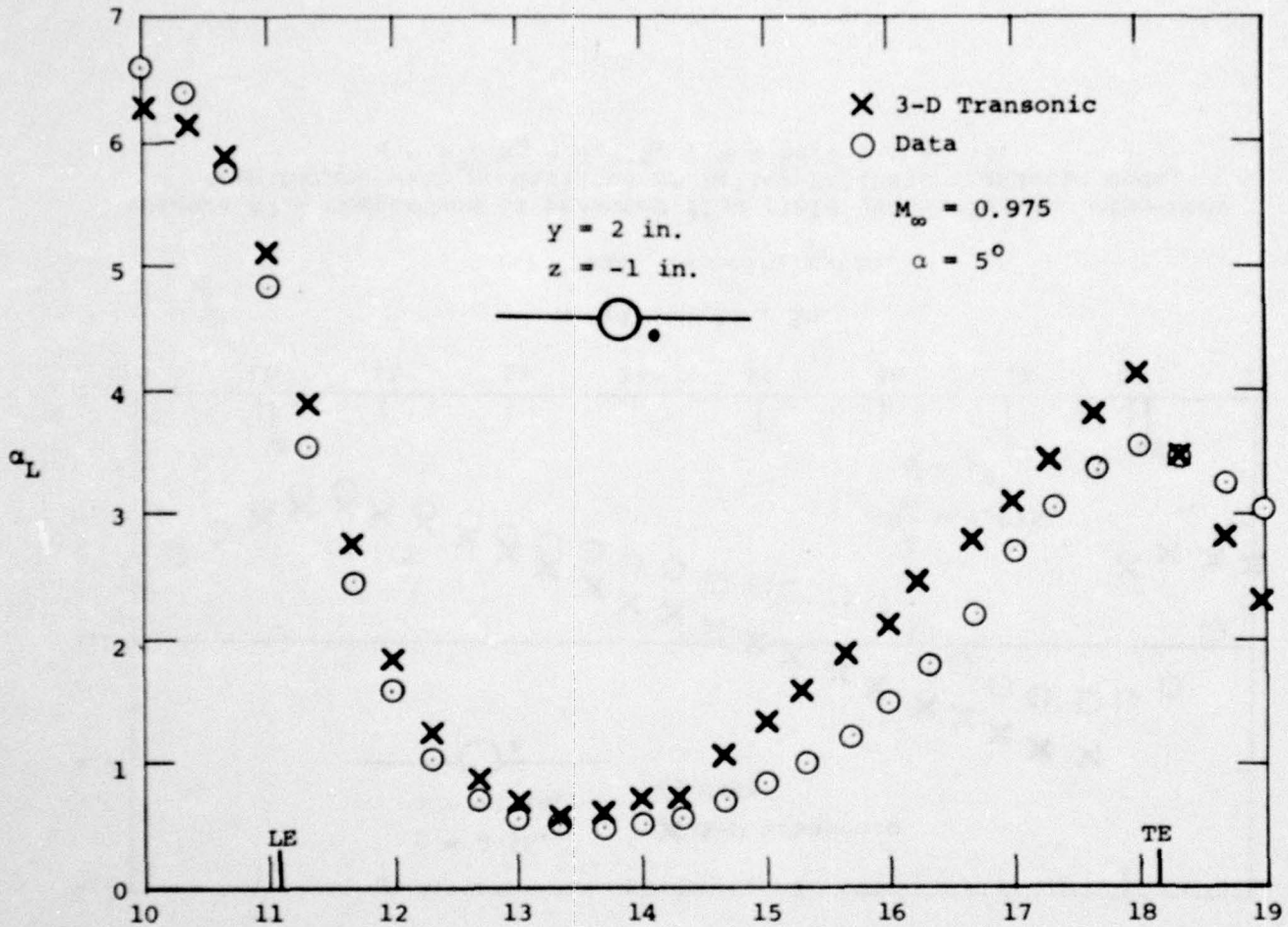

(b) Upwash angle, deg.

Figure 87.- Continued.

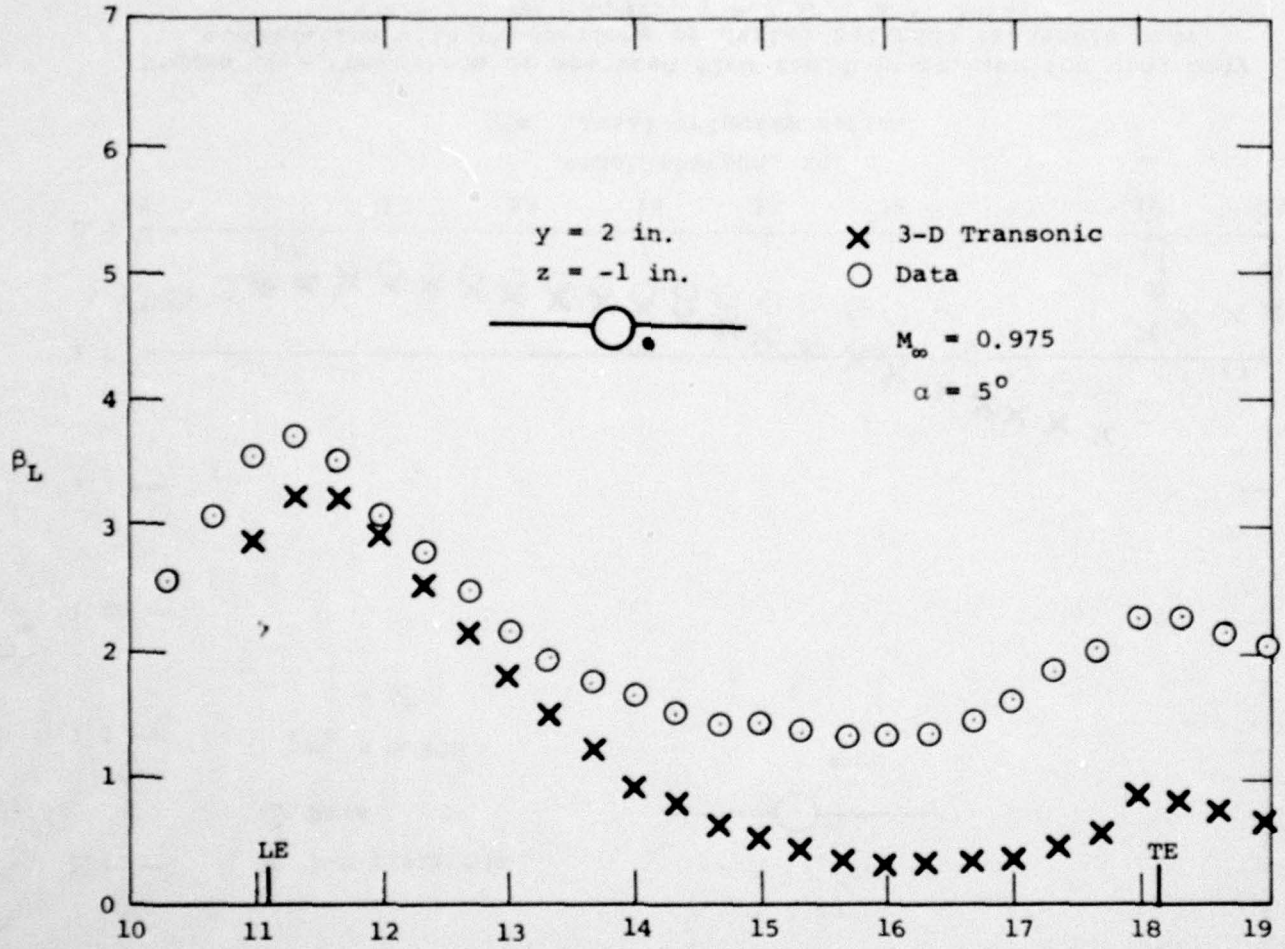

(c) Sidewash angle, deg.

Figure 87.- Concluded.

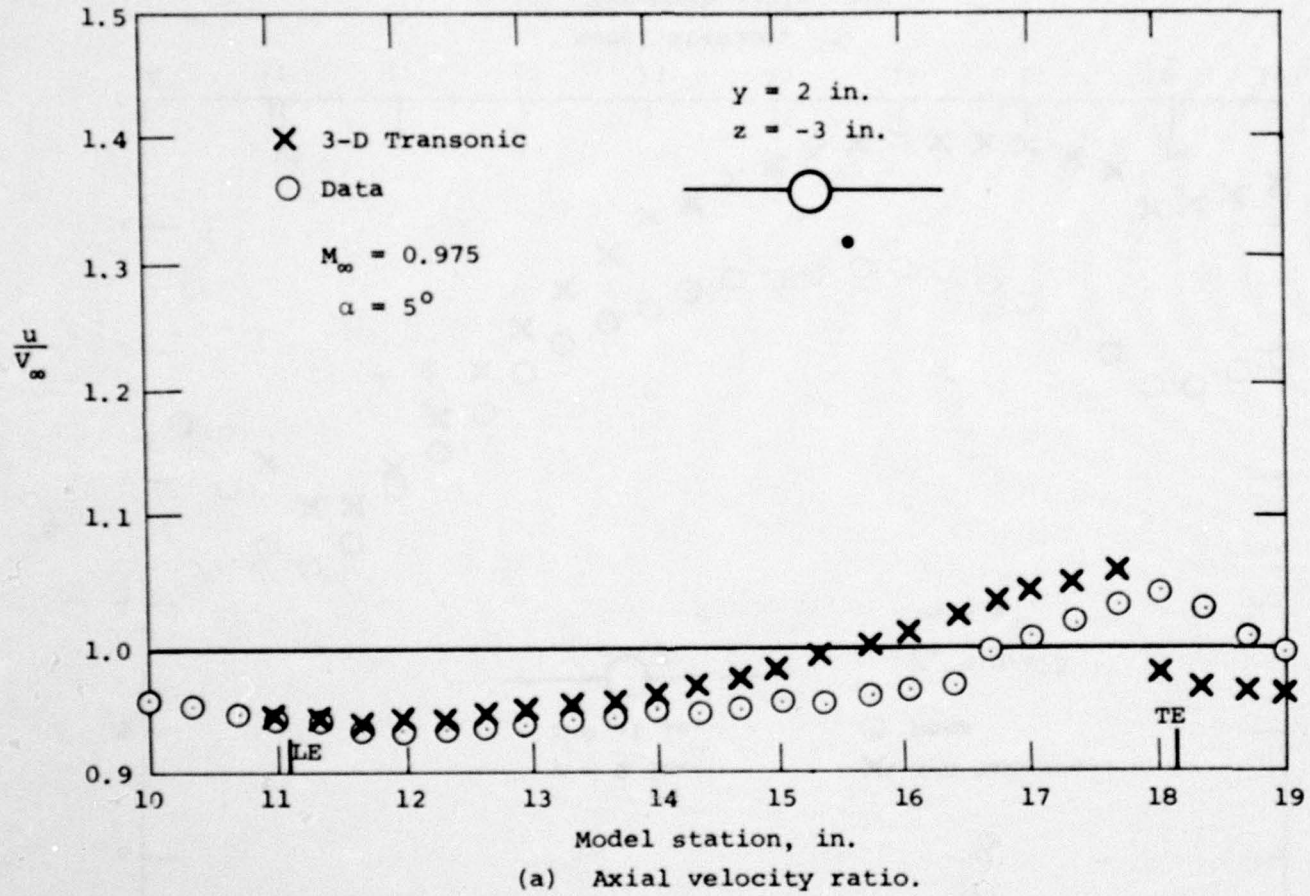

(a) Axial velocity ratio.

Figure 88.- Comparison of measured flow field quantities for wing-body combination with predictions of Bailey-Ballhaus transonic code, $\alpha = 5^\circ$, $M_\infty = 0.975$, y = 2 in., z = -3 in.

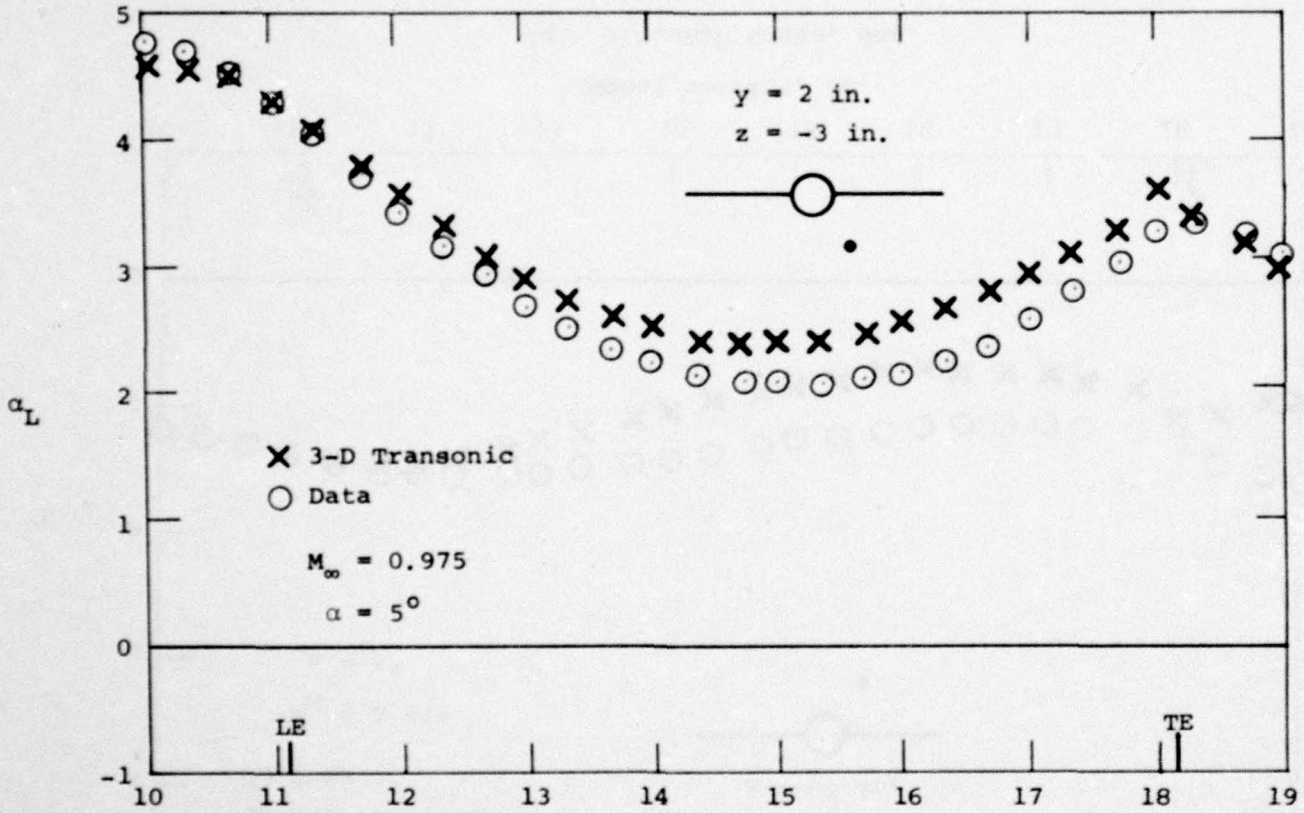

(b) Upwash angle, deg.

Figure 88.- Continued.

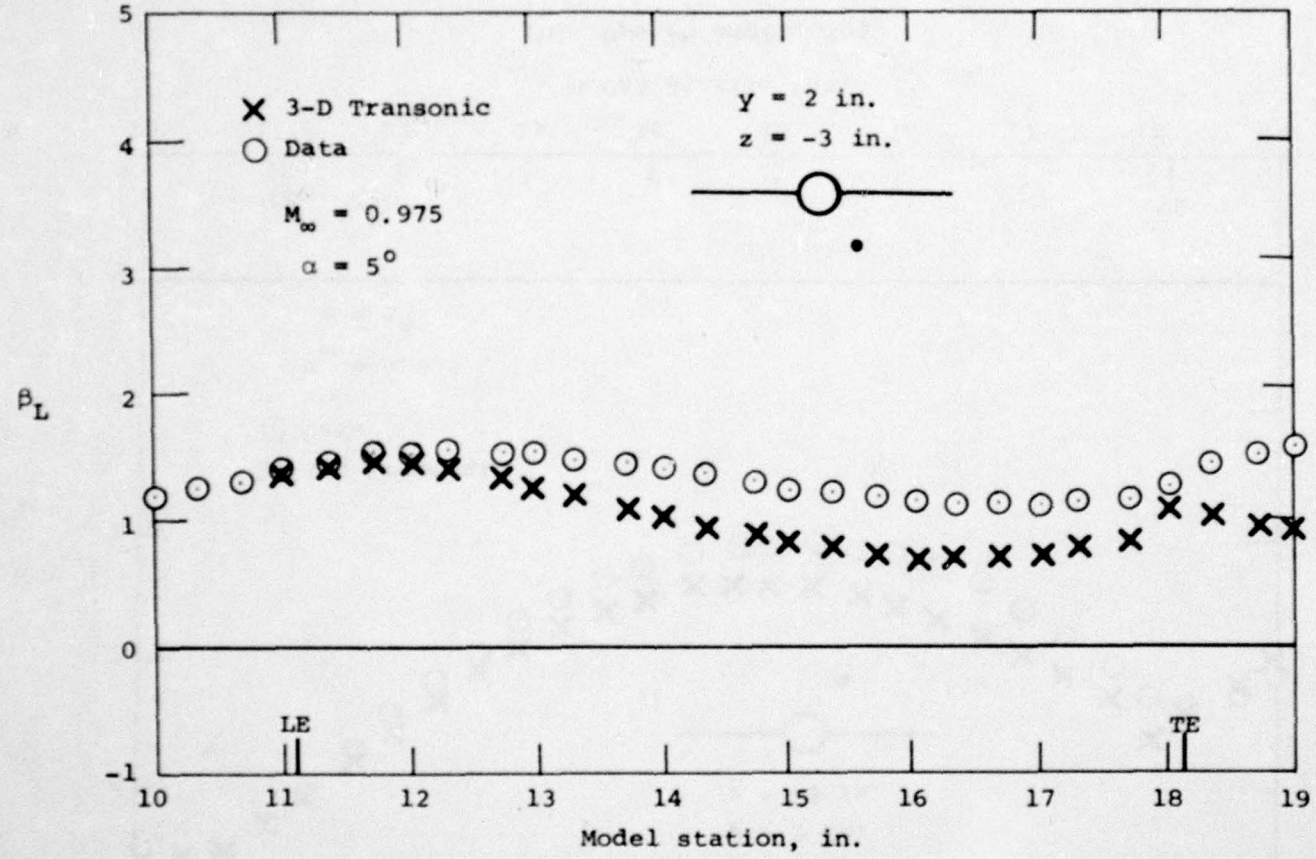

(c) Sidewash angle, deg.

Figure 88.- Concluded.

AD-A078 683 NIELSEN ENGINEERING AND RESEARCH INC MOUNTAIN VIEW CALIF F/G 20/4
THE DEVELOPMENT OF RAPID PREDICTIVE METHODS FOR THREE-DIMENSION--ETC(U)
JUL 79 A J CRISALLI , S S STAHARA F44620-75-C-0047
UNCLASSIFIED NEAR-TR-198 AFOSR-TR-79-1281 NL

4 OF 4
AD-
A078683

END
DATE
FILMED
1-80
DDC

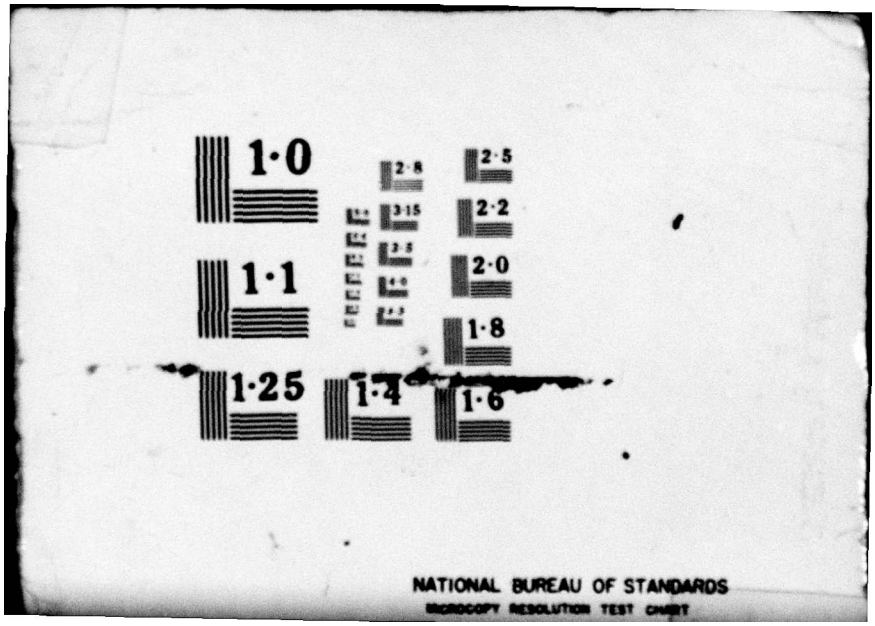
1·0
1·1
1·25
1·4
1·6
1·8
2·0
2·2
2·5
2·8
3·15
NATIONAL BUREAU OF STANDARDS
MICROCOPY RESOLUTION TEST CHART

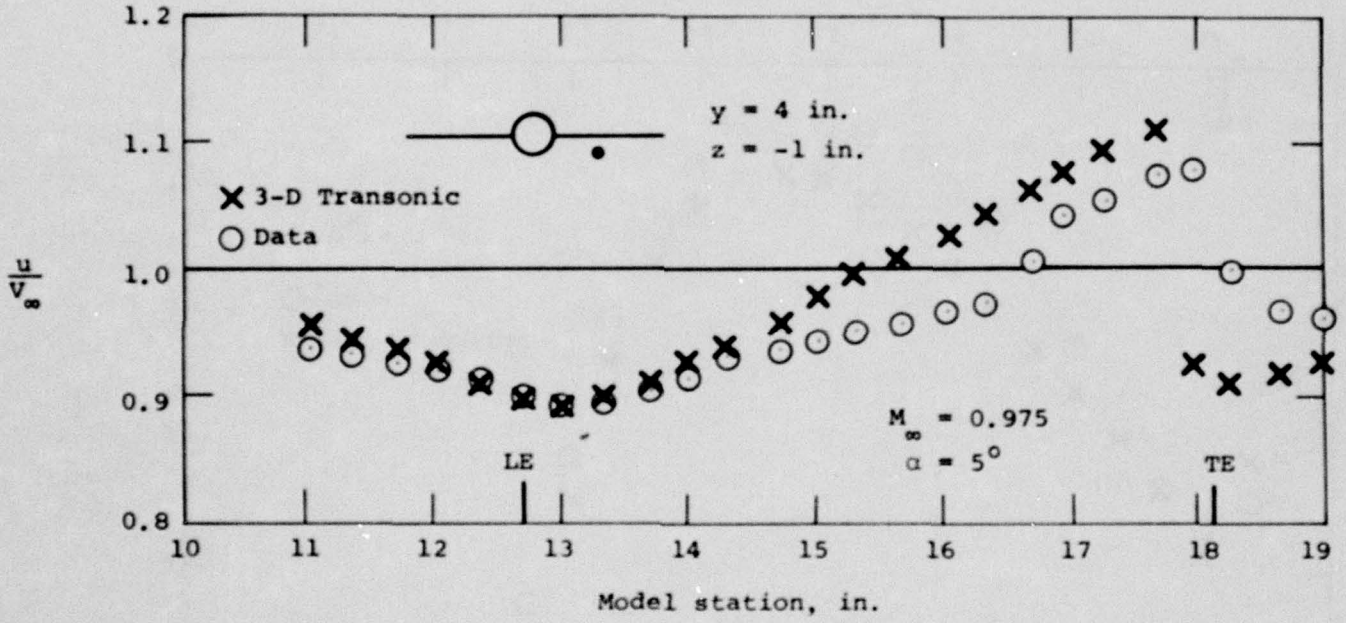

(a) Axial velocity ratio.

Figure 89.- Comparison of measured flow field quantities for wing-body combination with predictions of Bailey-Ballhaus transonic code, $\alpha = 5^\circ$, $M_\infty = 0.975$, y = 4 in., z = -1 in.

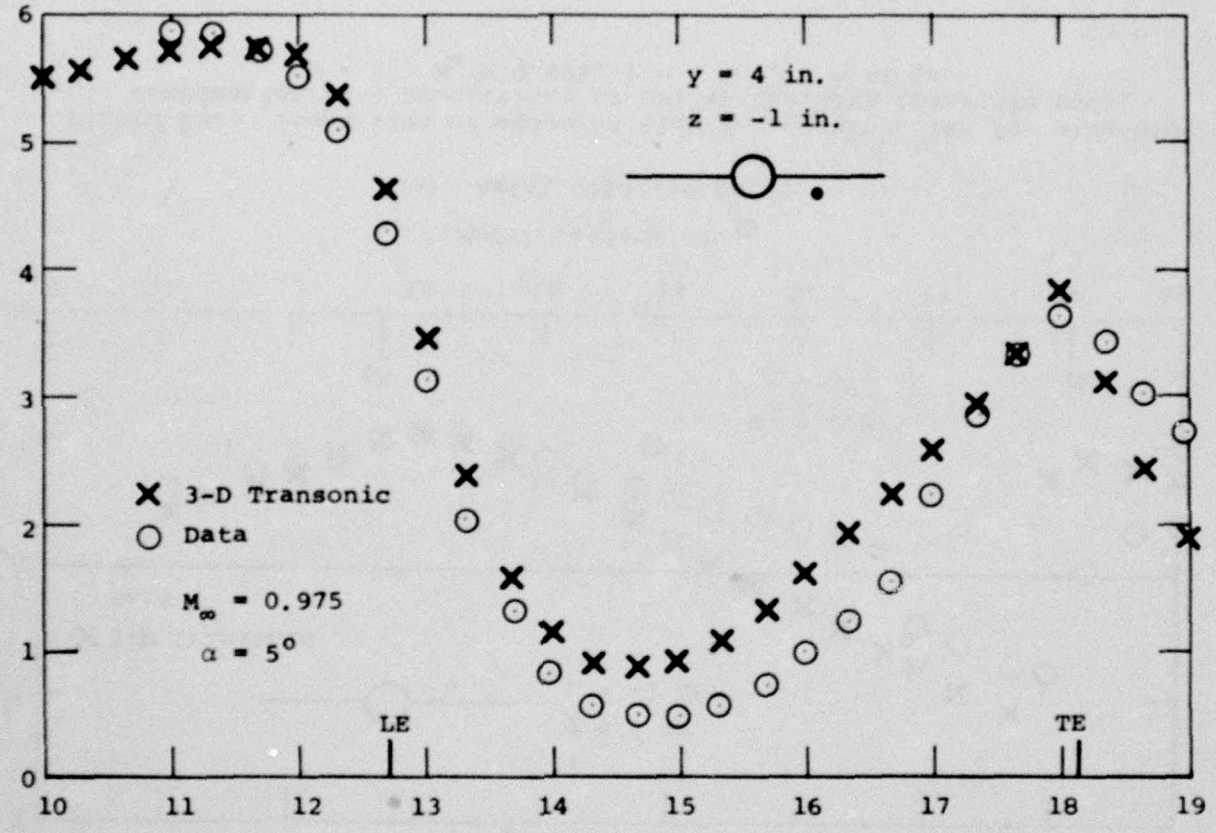

(b) Upwash angle, deg.

Figure 89.- Continued.

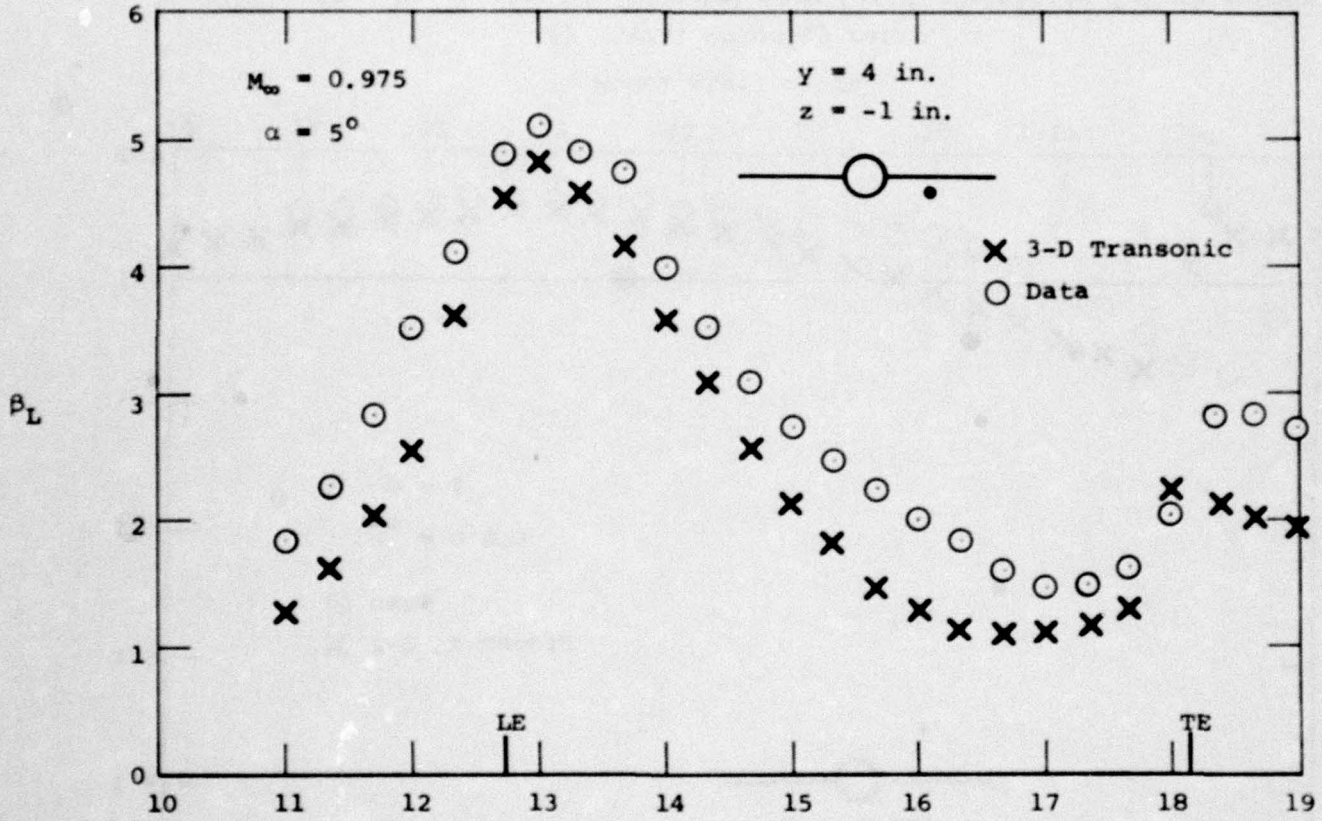

(c) Sidewash angle, deg.

Figure 89.- Concluded.

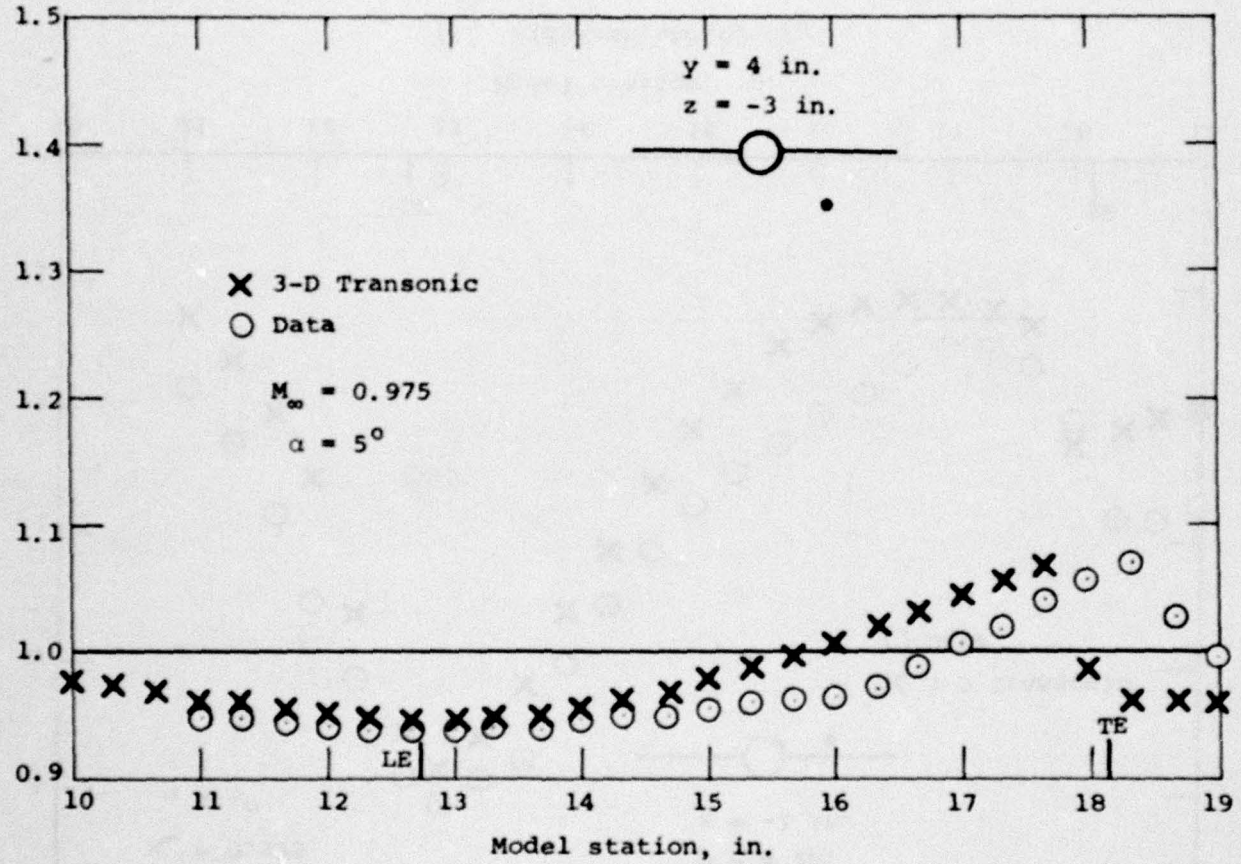

(a) Axial velocity ratio.

Figure 90.- Comparison of measured flow field quantities for wing-body combination with predictions of Bailey-Ballhaus transonic code, $\alpha = 5^\circ$, $M_\infty = 0.975$, y = 4 in., z = -3 in.

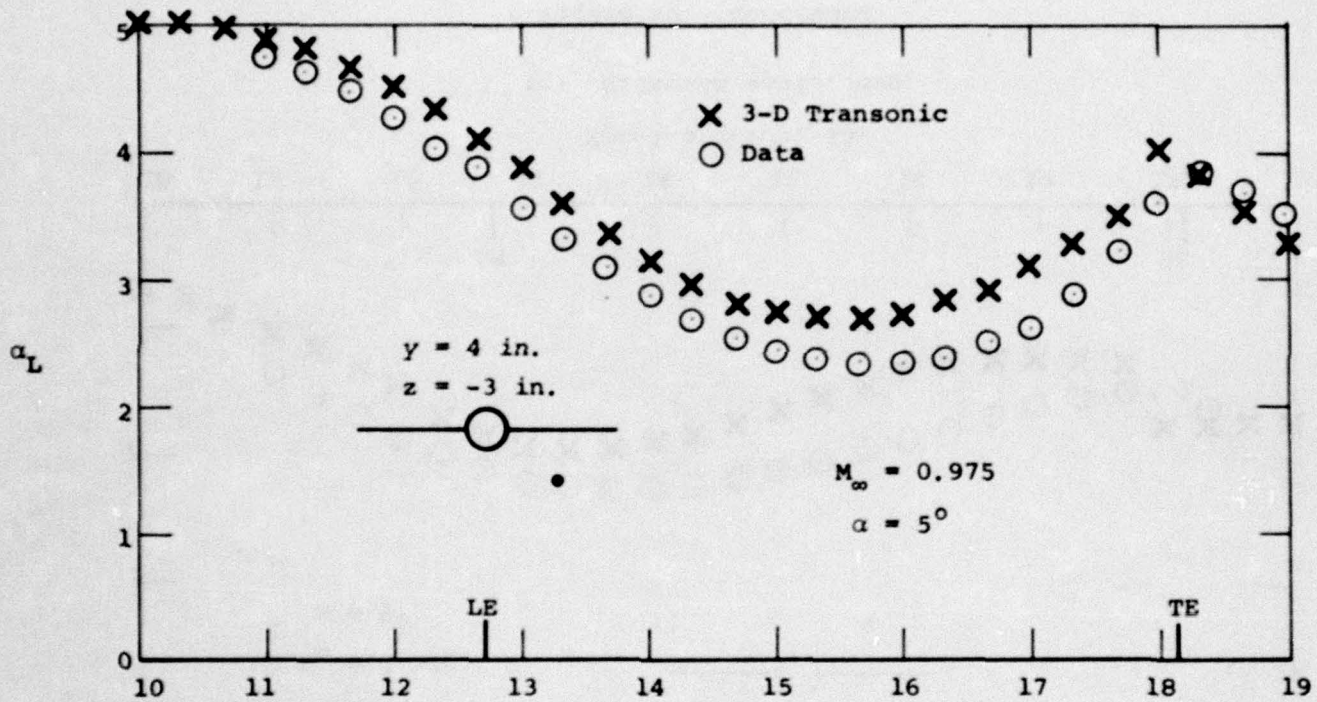

(b) Upwash angle, deg.

Figure 90.- Continued.

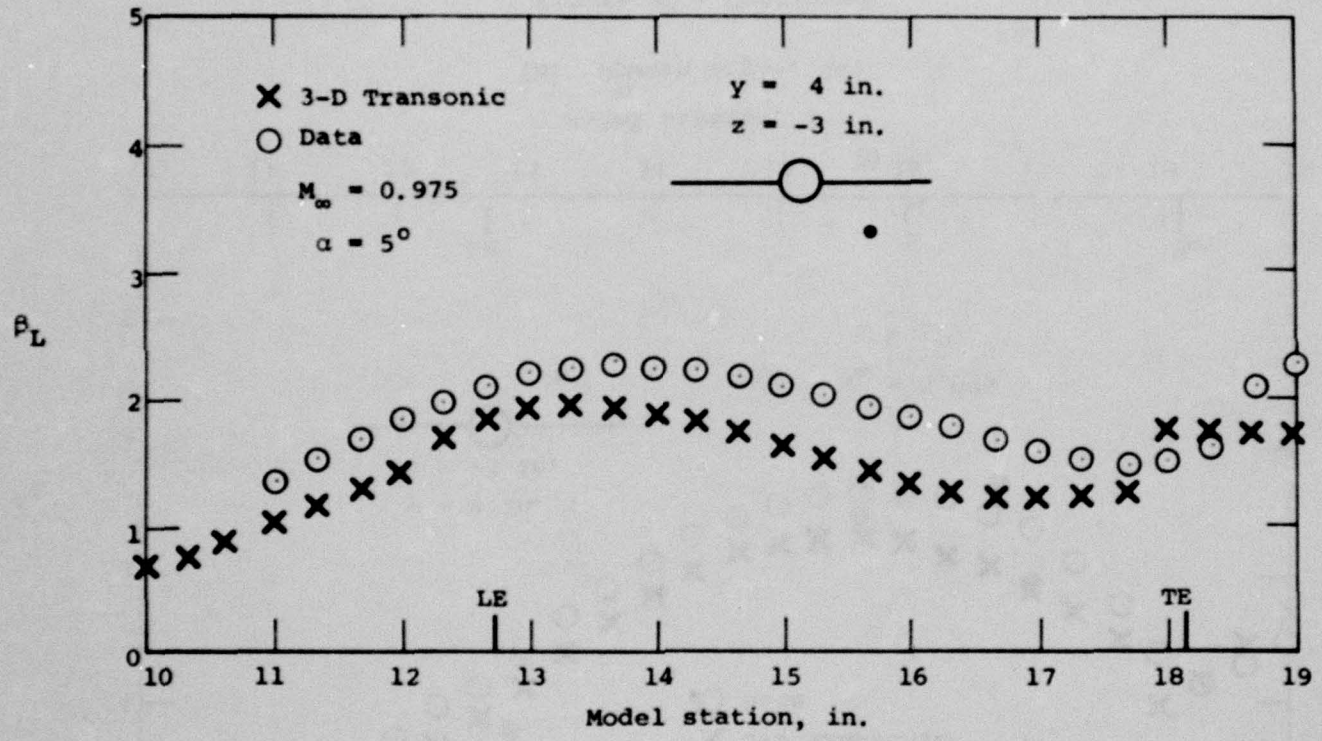

(c) Sidewash angle, deg.

Figure 90.- Concluded.

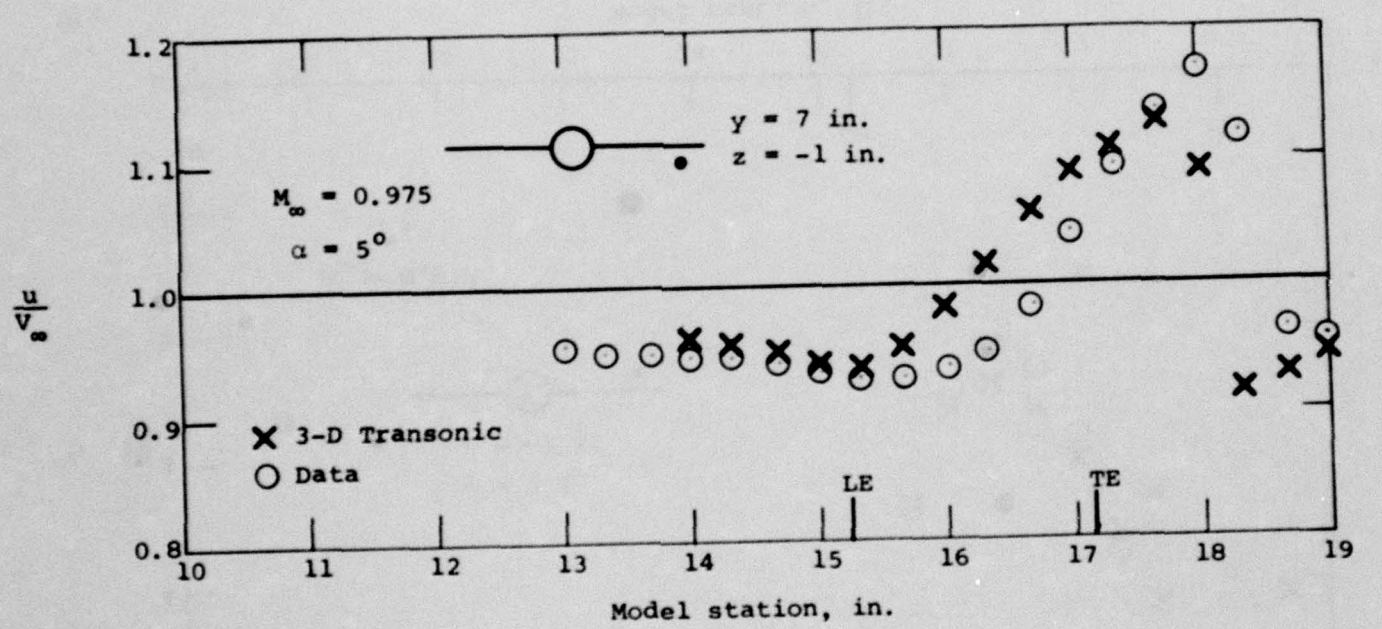

(a) Axial velocity ratio.

Figure 91.- Comparison of measured flow field quantities for wing-body combination with predictions of Bailey-Ballhaus transonic code, $\alpha = 5°$, $M_\infty = 0.975$, y = 7 in., z = -1 in.

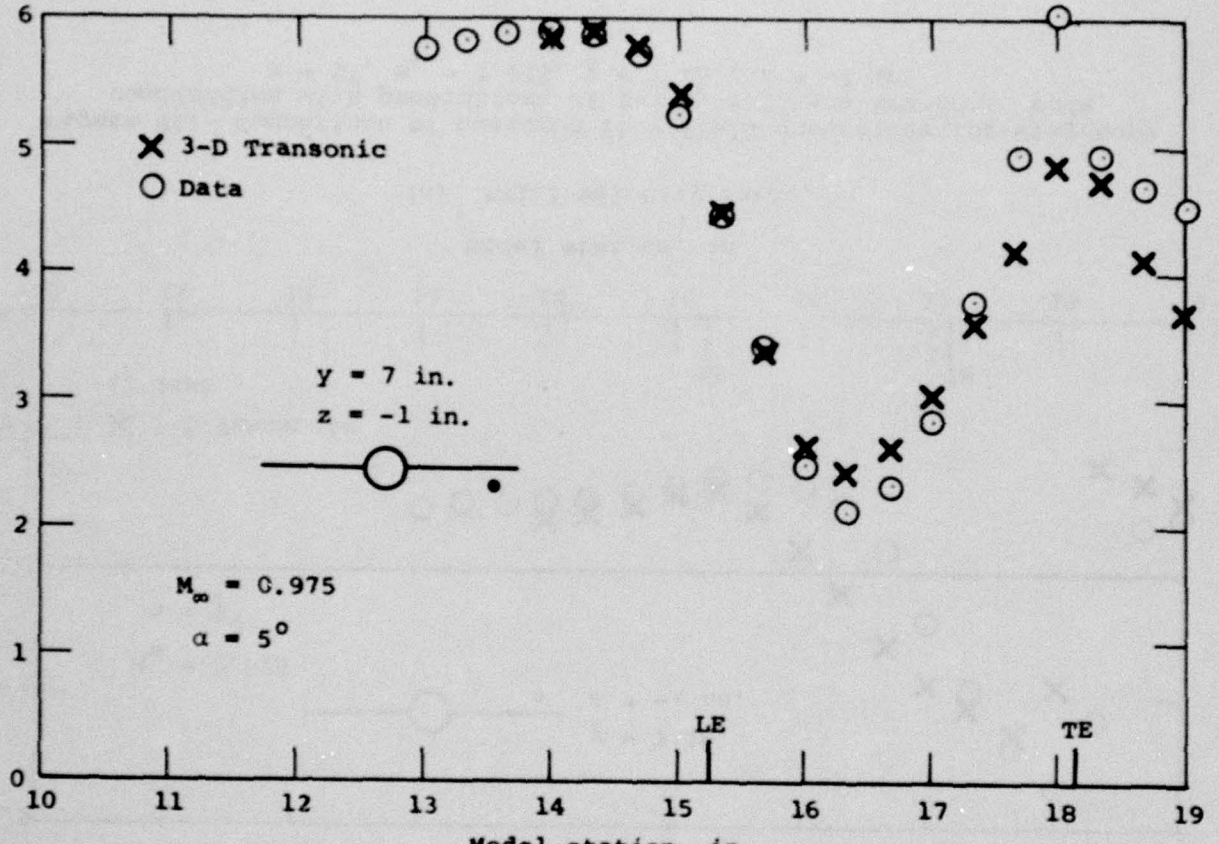

(b) Upwash angle, deg.

Figure 91.- Continued.

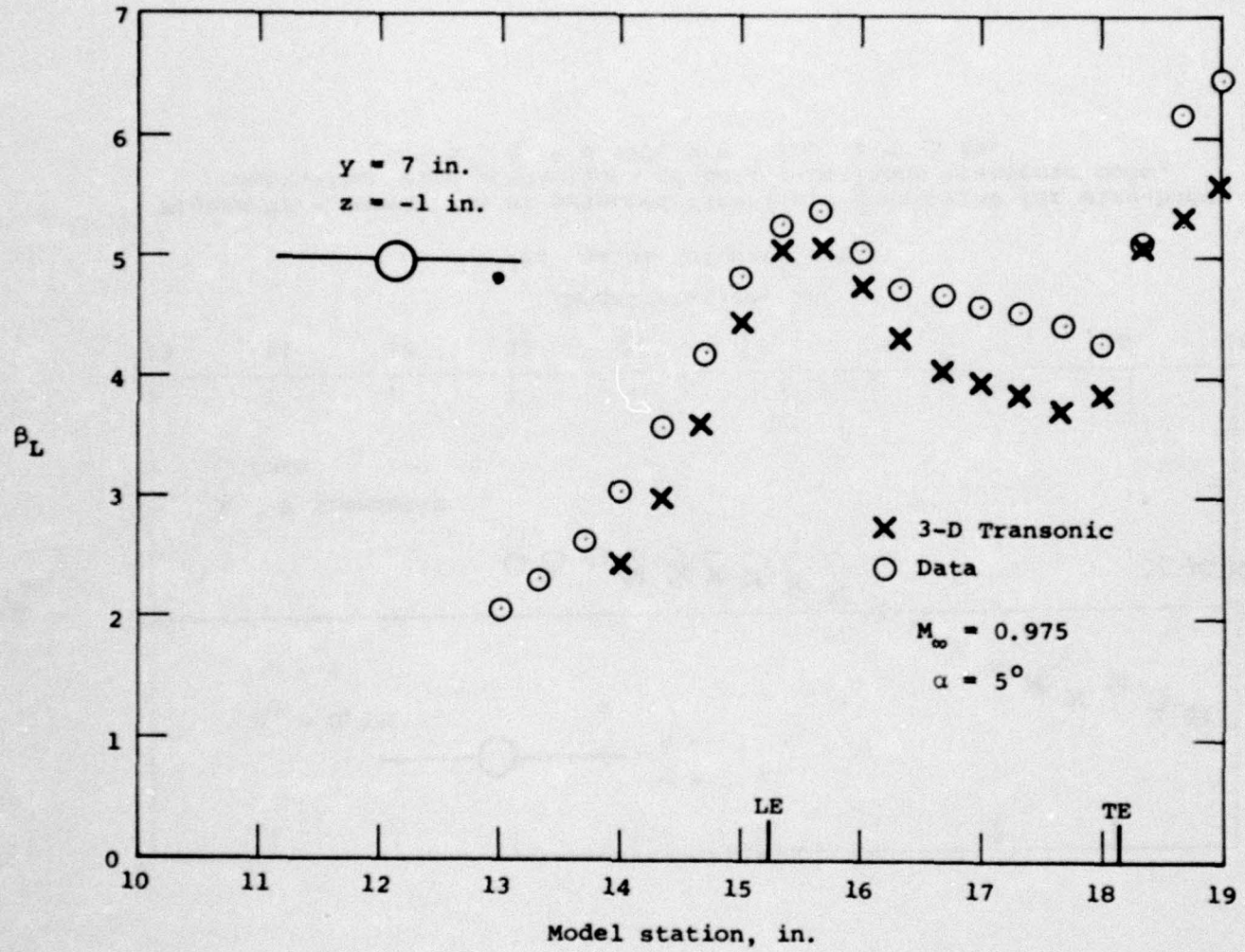

(c) Sidewash angle, deg.

Figure 91.- Concluded.

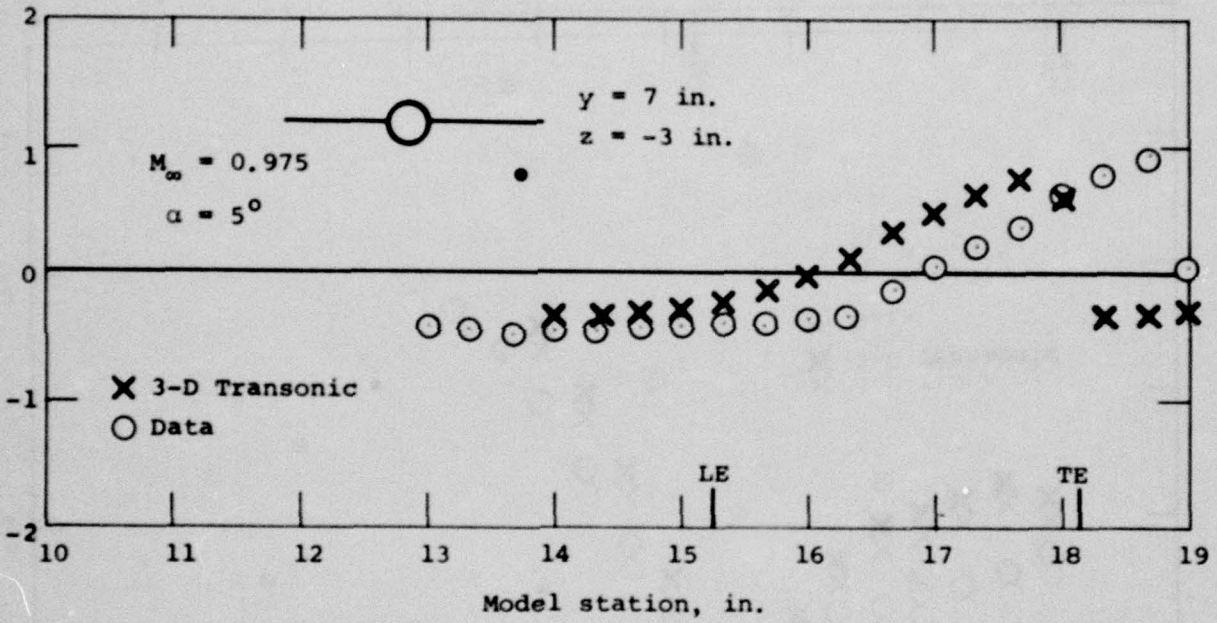

(a) Axial velocity ratio.

Figure 92.- Comparison of measured flow field quantities for wing-body combination with predictions of Bailey-Ballhaus transonic code, $\alpha = 5^\circ$, $M_\infty = 0.975$, y = 7 in., z = -3 in.

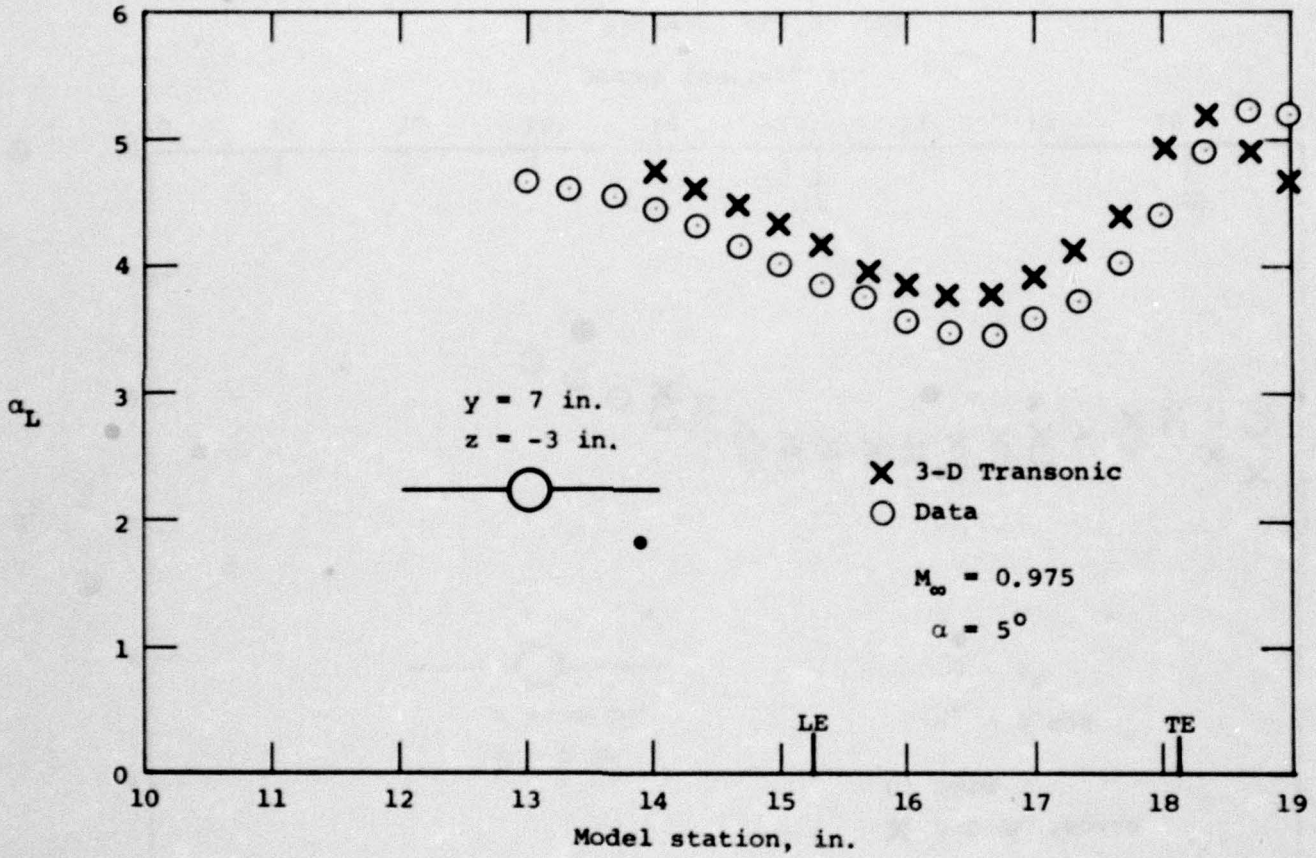

(b) Upwash angle, deg.

Figure 92.- Continued.

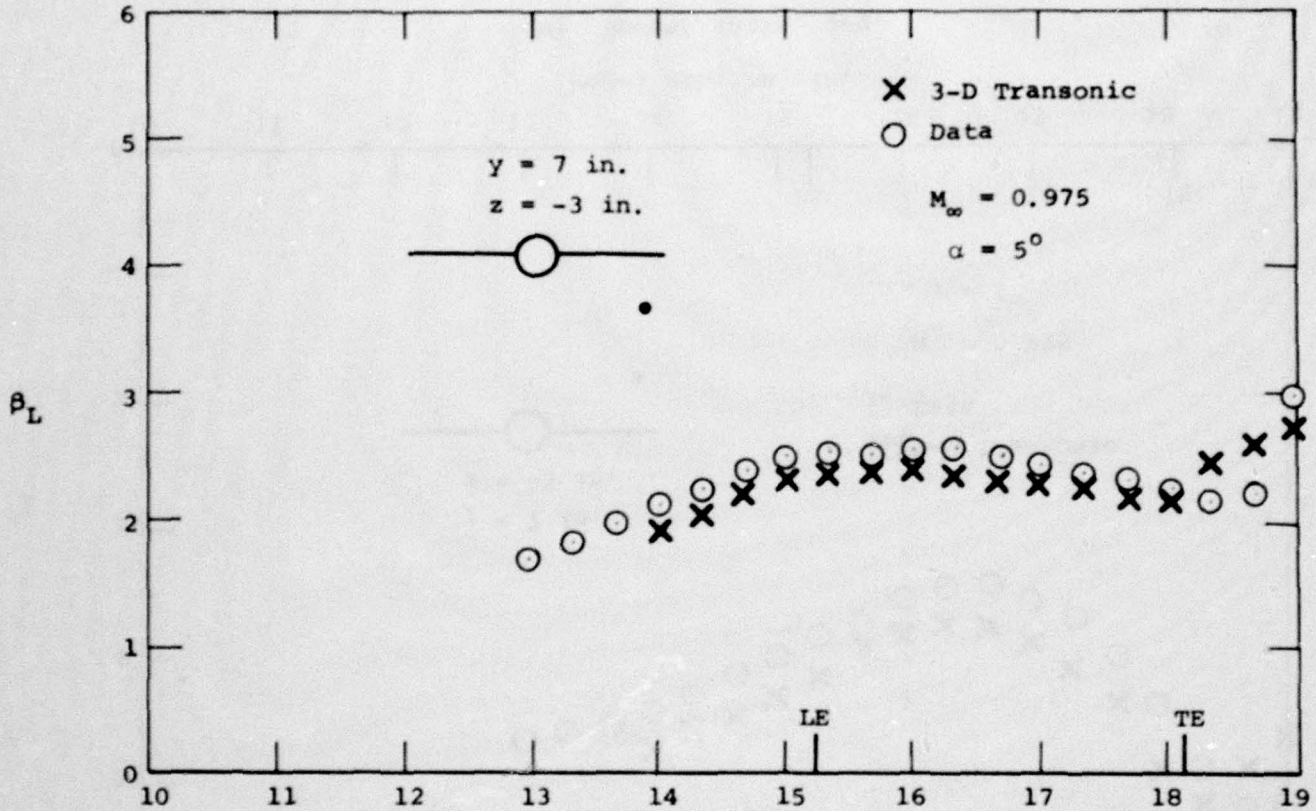

(c) Sidewash angle, deg.

Figure 92.- Concluded.

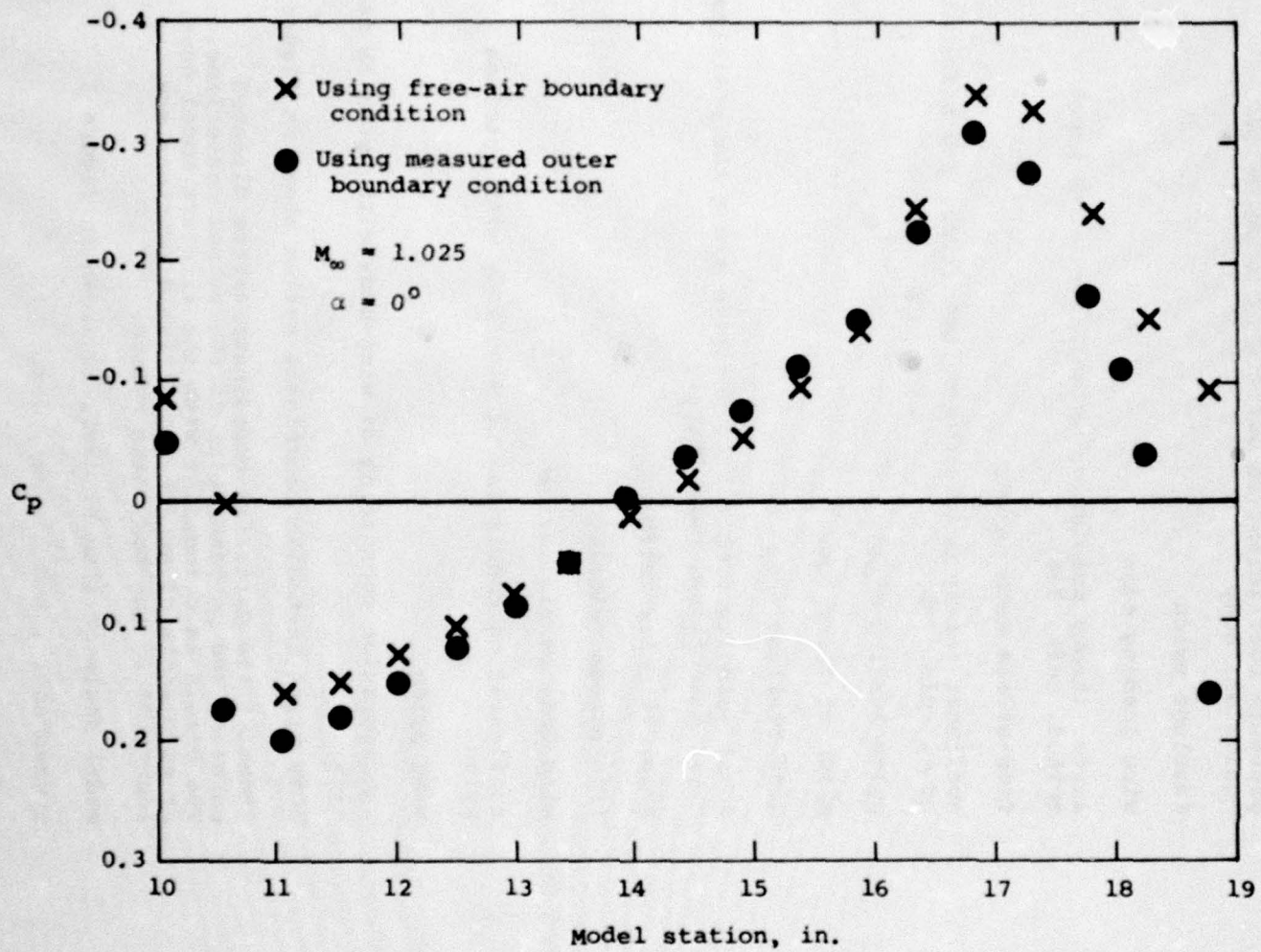

Figure 93.- Comparison of surface pressure coefficients on equivalent body as predicted by nonlinear axisymmetric transonic code, using free-air and measured outer boundary conditions.

SYMBOLS

C_p	pressure coefficient on surface of axisymmetric equivalent body
FP	fuselage pylon
LE	wing leading edge
LT	linear theory predictive method (i.e., 3-D panel method, refs. 5-6)
M_∞	free-stream Mach number
NL	nonlinear theory predictive method (i.e., 3-D transonic code, refs. 7-8)
PLE	pylon leading edge
PTE	pylon trailing edge
TE	wing trailing edge
u,v,w	local velocity components, positive along the positive x,y,z directions, respectively
u/V_∞	axial velocity ratio
V_∞	free-stream velocity
WB	wing-body configuration
WB/FP	configuration consisting of wing-body with fuselage pylon
WP	wing pylon
WB/WP	configuration consisting of wing-body with pylon on each wing
x,y,z	body fixed Cartesian coordinate system shown in figure 1
xt,yt,zt	tunnel-fixed Cartesian coordinate system directed parallel and perpendicular to the tunnel centerline. The origin is coincident with the aircraft model nose at zero angle of attack. Positive directions are identical to the body axis system.
α	model angle of attack, deg., as shown in figure 1
α_L	upwash angle, $\tan^{-1}$ (w/u), deg.
β_L	sidewash angle, $\tan^{-1}$ (v/u), deg.
$\Delta \frac{u}{V_\infty}$	difference between wing-body/pylon and wing-body axial velocities

SYMBOLS (Concluded)

$\Delta\alpha_L$	difference between wing-body/pylon and wing-body upwashes
$\Delta\beta_L$	difference between wing-body/pylon and wing-body sidewashes
ϕ	small perturbation velocity potential for various theories considered in report
$\phi_{2,t}, \phi_{2,B}, \phi_B$	small-perturbation-velocity-potential components of classical transonic equivalence rule described in section 4
$\phi_{3,t+\alpha}, \phi_{3,B}, \phi_B$	small-perturbation-velocity-potential components of extended transonic equivalence rule described in section 5

SECURITY CLASSIFICATION OF THIS PAGE (When Data Entered) Unclassified

REPORT DOCUMENTATION PAGE

READ INSTRUCTIONS BEFORE COMPLETING FORM

1. REPORT NUMBER: AFOSR-TR- 79-1281
2. GOVT ACCESSION NO.
3. RECIPIENT'S CATALOG NUMBER

4. TITLE (and Subtitle): THE DEVELOPMENT OF RAPID PREDICTIVE METHODS FOR THREE-DIMENSIONAL TRANSONIC FLOW FIELDS ABOUT FIGHTER BOMBER AIRCRAFT Part I
5. TYPE OF REPORT & PERIOD COVERED: FINAL 1 Jan 75 - 30 Sep 79
6. PERFORMING ORG. REPORT NUMBER: NEAR TR 198

7. AUTHOR(s): ANTHONY J CRISALLI, JOHN R SPREITER, STEPHEN S STAHARA, JACK N NIELSEN
8. CONTRACT OR GRANT NUMBER(s): F44620-75-C-0047

9. PERFORMING ORGANIZATION NAME AND ADDRESS: NIELSEN ENGINEERING & RESEARCH, INC, 510 CLYDE AVE, MOUNTAIN VIEW, CA 94043
10. PROGRAM ELEMENT, PROJECT, TASK AREA & WORK UNIT NUMBERS: 2307A1, 61102F

11. CONTROLLING OFFICE NAME AND ADDRESS: AIR FORCE OFFICE OF SCIENTIFIC RESEARCH/NA, BLDG 410, BOLLING AIR FORCE BASE, D C 20332
12. REPORT DATE: July 1979
13. NUMBER OF PAGES: 301

14. MONITORING AGENCY NAME & ADDRESS (if different from Controlling Office)
15. SECURITY CLASS. (of this report): UNCLASSIFIED
15a. DECLASSIFICATION/DOWNGRADING SCHEDULE

16. DISTRIBUTION STATEMENT (of this Report)

Approved for public release; distribution unlimited.

17. DISTRIBUTION STATEMENT (of the abstract entered in Block 20, if different from Report)

18. SUPPLEMENTARY NOTES

19. KEY WORDS (Continue on reverse side if necessary and identify by block number)
TRANSONIC FLOW FIELDS
WING-BODY/PYLON COMBINATIONS
TRANSONIC EQUIVALENCE RULE

79 12 18 27

20. ABSTRACT (Continue on reverse side if necessary and identify by block number)

An overall account is presented of the progress made in the development of an engineering predictive method for determining three-dimensional transonic flow fields about parent aircraft, with application to external store separation characteristics. The emphasis of the work reported is on the development of accurate but rapid methods for predicting the transonic flow fields due to wing-body/pylon combinations representative of modern fighter-bomber aircraft. Detailed evaluations of several candidate methods are presented. These were made by extensive comparisons of theoretical results for various flow field properties

DD FORM 1 JAN 73 1473 EDITION OF 1 NOV 65 IS OBSOLETE UNCLASSIFIED

SECURITY CLASSIFICATION OF THIS PAGE (When Data Entered)